SILICON FOR THE CHEMICAL AND SOLAR INDUSTRY XIV

SVOLVÆR, NORWAY

June 11-14, 2018



Editors: Birger Andresen, Lars Nygaard, Harry Rong, Merete Tangstad, Halvard Tveit, Ingrid Gamst Page

The Norwegian University of Science and Technology
N-7491 Trondheim, Norway

ISBN 978-82-692919-2-6

SILICON FOR THE CHEMICAL AND SOLAR INDUSTRY XIV

SVOLVÆR, NORWAY

June 11-14, 2018

Editors: Birger Andresen, Wacker Chemie
Lars Nygaard, Consultant
Harry Rong, Elkem ASA
Merete Tangstad, NTNU
Halvard Tveit, NTNU
Ingrid Gamst Page

The Norwegian University of Science and Technology
N-7491 Trondheim, Norway

Preface

Dear Participants.
Another 2 years has passed since we arranged the last conference in Kristiansand, one of the clusters of silicon production and metallurgical industry in Norway. This year we are reviving one of the features of earlier Silicon conferences; by arranging the conference in one of the more scenic parts of Norway, in Lofoten.
Lofoten is one of the, or maybe the most, visited place in Norway by both domestic and international tourists due to the beautiful contrasts between the mountains and the sea. However, traditionally, Lofoten is known as the area of the Norwegian sea, where fishermen from the whole Norwegian coast came in the winter months to catch the winter-cod. This was the basis of their livelihood for the rest of the year. On a personal note, my own grandfather rowed in a small boat from the shores of Trøndelag 1000 km up north to Svolvær in January every year. It has been said that fishing in Lofoten was the cornerstone of Norway's most important industry in earlier times, and the basis was the brave and unafraid men rowing or sailing hundreds of miles in storms and cold weather.
Today we are in Lofoten to celebrate another cornerstone in Norway; the metallurgical industry. In Norway and worldwide there are opportunities and challenges that needs to be solved by brave men and women within the area of silicon. The base line is always to understand our processes better and be able to use this knowledge to improve our processes and products. In addition, the environmental challenges are emerging as the main driver for steep changes. It can be mentioned that Norway has at a national level agreed to reduce the CO2 emission by 40% in 2030 and be carbon neutral in 2050. 2030 is not many years ahead - it is only 6 conferences away. Other challenges are the scarcity of graphite and the PAH emissions that has reached new levels since the last conference. Things are changing fast and we have to keep up.
The Silicon for Chemical and Solar Industry conference is one of the tools one can use to follow the development within the areas of silicon production and the applications of silicon. By looking at all the references to previous conference proceedings, the conference is proven to be a good tool to keep up with the latest developments within our special field. It is an important arena to be at. The conference could not be arranged without the organizing committee; Birger Andresen (Wacker), Lars Nygaard (Consultant), Harry Rong (Elkem), Halvard Tveit (Elkem) and of course the administrative assistant Ingrid G.Page. The international advisory board consists of Javier Bullon (SilBuCam), Sean Gaal (Dow Corning) and Alan Crawford (Alan Crawford Consulting). They have improved the value of the presentations and their contributions are highly appreciated.

Enjoy the conference,
Prof. Merete Tangstad, Norwegian University of Science and Technology
Head of the Organizing committee

Contents

Preface iii

Nadia Vinck 1
An update of the EU regulatory developments and initiatives in the field of environment and their impact on the European manufacturing of Silicon and its by-products

Jörg Acker, Tim Sieber, Thomas Langner, Steven Herold 11
The impact of lattice strain on the reactivity of silicon

Julia Lyubina, Bodo Frings, Andreas Höfler, Reiner Störger, Stefan Bade 21
Industrial-scale synthesis of high performance Si-based nanopowders for energy storage applications

Eli Ringdalen 29
SiC structures and SiC transformations in industrial Si-production

Karin Fjeldstad Jusnes, Merete Tangstad, Eli Ringdalen 39
Cracks, Disintegration and Phases Transformations in Quartz

Raghed Saadieh, Merete Tangstad, Harald Wegge 51
Cavity formation in silicon furnaces

Evangelos Bertakis, Randi Synnoeve Hegdal Chapana, Ronald Eulenberger 63
CFD modelling for the metallurgical grade silicon production.

Trygve Eidet, Øyvind Mikkelsen 77
The replacement of coal tar pitch – opportunities and constraints

Javier Bullón Camarasa 91
New developments in composite electrodes

Robert Becker, Johann Leye 97
Development and application of PAH free electrode paste

Valdiney Domingos de Oliveira, Rodrigo Silva de Faria, Luciano Biazutti, Gabriel Esteves, Lou Parous 105
Søderberg electrode technology and the potential for higher performance metallurgical silicon for the solar and chemical industry

Matveev A.V., Kvanin A.L., Bleskin G.S., Butakova T.V., Spektoruk A.A. 121
The electrode for submerged arc furnaces production

Sethulaksmy Jayakumari, Merete Tangstad 125
Formation of elemental silicon in β-SiC particles

Andrea Broggi, Merete Tangstad 139
Small scale experiments simulating condensation of SiO and CO in silicon furnaces

Gerhard Traunspurger, Karl Rimböck 153
Carbon Measurements on Silicon Samples

Torbjørn Røe, Kjell Blandhol, Johan Pääaho Svanem, Harry Rong 163
Silicon Content of Silicon Materials

Leili Tafaghodi, Ali Hosseinpour 173
Removal of boron from ferrosilicon alloy using SiO_2-Al_2O_3-CaO slag

Adrian Murgau, Jafar Safarian 183
Solar silicon production through metallurgical route and REC Solar advancements

Denir Paganini Nascimento, Marcelo Aquino Martorano, João Batista Ferreira Neto, Moysés Leite de Lima, Tiago Ramos Ribeiro 193
Effects of forced convection on the micro and macrostructure of metallurgical grade silicon ingots obtained by unidirectional solidification

Thomas J. Preston 205
Stewards of environmentally friendly silicon production for the solar industry

Matthias Colomb, Srinivas Palanki , Nicholas D. Sylvester 217
FTIR Calibration for Detection of High Concentration Chlorosilanes in a Pilot-scale Hydrochlorination Reactor and Comparison with Modeling Results

Sean Gaal, Ryan Schafer, Scott Stachowiak 231
Literature Review - The Effect of Minor Elements on the Production of Trichlorosilane by Direct Chlorination

Alan Crawford, Harry M. Rong, Henning Kjønli, Jan-Otto Hoel, Johan P. Svanem 243
The impact of metallurgical grade silicon phosphorus content on trichlorosilane synthesis and polysilicon purity

Guro M. Wyller, Thomas J. Preston, Marte O. Skare, Hallgeir Klette, Anjitha S. G, Erik S. Marstein 267
Exploring thermal pyrolysis of monosilane trough gas chromatography-mass spectrometry measurements of higher order silanes

Amalie Tysseland, Estelle M. M. Vanhaecke, Ingeborg-Helene Svenum, Edd A. Blekkan, Hilde J. Venvik 277
New approaches to the investigation of carbon formation in the Direct Synthesis of Methylchlorosilanes

John Carberry, Devin Roberts, Robert Tesch, Timothy Wilson 289
Optimizing ZT Power Factor Variables in a Porous Silicon Thermoelectric Material

Alba Ramos, Alejandro Datas, Carlos del Cañizo, Antonio Martí 303
Molten Silicon at the heart of a novel energy storage system

Wojciech Polkowski, Natalia Sobczak, Merete Tangstad, Jafar Safarian, Jian Meng Jiao, Bettina Grorud 315
Silicon and silicon-boron alloys as phase change materials in thermal energy storage units

Sylvain Gouttebroze, Mohammed M'Hamdi 327
Prediction of through-thickness microstructure during metallurgical silicon solidification

Ragnhild Jensen, Jens Christian Fjelldal 335
Fume collection in FeSi/Si plants – Regulations and Technical measures

Erlend Lunnan Bjørnstad, Gabriella Tranell - SFI Metal Production, IMA, NTNU 349
Statistical Model for Locating Micro Slag Droplets in MG-Si production

Halvard Tveit, Mark Breidenthal 357
The EHS Achilles heel of the Silicon Furnace – the potential for energy out of control!

Jørn de Linde 367
Will there be another China?

Author index 373

Participants 1992-2018 375

Silicon for the Chemical and Solar Industry XIV
Svolvær, Norway, June 11 – 14, 2018

An update of the EU regulatory developments and initiatives in the field of health and environment and their impact on the European manufacturing of Silicon and its by-products"

Nadia Vinck [1)]

1) Director EHS & Scientific Issues at Euroalliages, Association of European Silicon and ferro-alloy producers

Abstract

The European best available techniques (BAT) document on Non-Ferrous Metal Industries comprising also the Ferro-alloys and Silicon Industry has been published in July 2017. The related conclusions and BAT-associated emission levels (BAT-AEL) were published as a Commission Implementing Decision in June 2016 according to the legal framework set by the Industrial Emissions Directive or IED. Member States authorities will have to adapt their operating permits accordingly by 30 June 2020. Other EU environmental regulations under revision or recently revised may or will have a direct or indirect influence on the Silicon operating permits, like the chemical Regulation REACH; the Regulation on the control of major-accident hazards; the review of the Priority Substances list within the environmental quality standards (EQS) of EU water framework directive, and last but not least the revision of the Carcinogens at work Directive (CMD) that will incorporate Binding Limit Value for respirable crystalline silica generated by processes. The circular economy package comprising the revision of e.g. the waste framework directive and the landfill directive as well as the revision of REACH might also affect the by-products of the production of Silicon: Silica Fume and the slag. Finally, the fact that Silicon is considered as a critical raw material could have an influence on some EHS regulations. The purpose of this paper is to shed more light on the implementation issues for the Silicon Industry related to these new developments on the EEA territory and to discuss the future trend of the European Environment and Health regulatory framework ahead of the new European elections due to take place in May 2019.

INTRODUCTION

This paper addresses the state of play of the main regulatory developments affecting the production of Silicon. The regulations discussed comprises the Industrial Emissions Directive affecting directly the operating permits with mandatory emission limit levels to be implemented, the impact of the Classification Regulation on other regulations like Seveso or REACH, as well as the Water Framework Directive and the related Environment Quality Standards, Waste Directives and the Carcinogen Directive. Some examples are also outlined. Silica Fume and Silicon slag can also be affected by some other regulations related respectively to nanomaterials or the interface between the waste or the product legal status.

I. Industrial Emissions Directive or IED

Background

The Industrial Emissions Directive [1] or IED (Directive 2010/75/EU on industrial emissions) is the main EU instrument regulating pollutant emissions from industrial installations and hence operating permits.

IED gives a particular role to the BAT-associated emission levels (BAT-AELs) set out in the BAT conclusions. It requires the emissions of the installations concerned not to exceed the BAT-AELs, except in specific cases where the conditions are fulfilled to allow a derogation by the competent authority. Such derogation needs to be justified to the local authority delivering the operating permits on the basis of an assessment demonstrating the disproportionality of the costs of meeting the BAT-AELs against the environmental benefits. Following the publication of a Decision on BAT conclusions in the Official Journal of the EU, Member States have a maximum of 4 years to implement the BAT conclusions through an update of the permits concerned.

The review of the original Non-Ferrous Metal (NFM) best available techniques (BAT) reference document (BREF) - comprising the metallurgical Silicon industry - of 2001 took 10 years. The Commission Implementing Decision 2016/1032 establishing the so-called BAT Conclusions has been published on the 30th June 2016 [2]. The operating permits of the European Silicon plants shall comply with the new values by 30 June 2020, unless derogations would be granted by the local authorities.

Emission limit values

The important issues for the metallurgical Silicon industry are the emissions of dust and fume from the smelting processes [3]. Dust emissions also occur from the storage, handling and pre-treatment of raw materials where diffuse dust emissions play an important role. Depending on the raw material and the process used, other emissions to air are SO_2, NOX, CO, CO_2, polycyclic aromatic hydrocarbons (PAH) and volatile organic compounds (VOCs). The formation of PCDD/F in the combustion zone and in the cooling part of the flue-gas treatment system (de novo synthesis) may be possible.
The BAT-AELs for channelled dust emission to air from Silicon production have been outlined in a previous paper of 2016. As a reminder, the BAT-AEL for channelled dust emission from storage to furnace operation is in a range of 2 to 5 mg/Nm^3. BAT-AEL for Mercury and its compounds, expressed as Hg is in a range of 0.01 – 0.05 mg/Nm^3 and for PCDD/F of 0,05 ng I-TEQ/Nm^3.

The BAT-AELs for emissions to water were also outlined. It must be underlined that there are neither BAT-AELs expressed in kg/y or in kg/t metal nor distinction based on the type of receiving water body (e.g. sea or river). BAT-AELs apply to direct emissions to a receiving water body from the production [3].

Discussion of the impact on Silicon operating permits

The BAT Conclusions for the metallurgical Silicon industry and the related emissions limits values are very strict, in particular for dust emissions, as for other industrials sectors covered by the Non-Ferrous Metals BAT conclusions. The way these emissions

limits values are set by the Commission remains unclear in the absence of a robust and transparent methodology as called by Industry. In principle, the upper end value of a BAT-AEL should be set on the basis of the maximum observed emissions of the plants applying BAT for the pollutant at stake, while the lower end should be set above the lowest maximum observed emissions of the plants applying BAT, after discarding all performances that only occur under specific circumstances. Indeed, the legal obligation for permitting authorities to set the emission limit value for a given pollutant at a level that ensures that, under normal operating conditions, emissions do not exceed the BAT-AEL, has far-reaching consequences.

II. Impact of hazard classification on other regulations

Sometimes clearly disputable (harmonized) classification under the Classification Labelling and Packaging Regulation or CLP can have snowball effects on downstream regulations impacting directly the operating plants on the EU/EEA territory without providing benefit to the health or the environment.

Seveso and transport

The recent EU Court Case related to the harmonized classification of High Temperature Coal Tar Pitch (HTCTP, EC Number: 266-028-2 and CAS Number: 65996-93-2) as acute and chronic for the environment is an illustrative example. HTCTP is a key substance composing the electrode paste used in the electric arc furnaces. The harmonized classification for the environment of HTCTP [4] could trigger the Seveso Directive (Directive on the control of major-accident hazards involving dangerous substances) requirements for Silicon producers (and also their suppliers) which were so far not subject to Seveso [5]. The Silicon producers who would not have been affected are those using only prebaked electrodes in which HTCTP is fully transformed into HTCTP coke. In addition, the contested harmonized classifications triggers under the UN transport regulations a new classification “Class 9 - Miscellaneous dangerous substances” with related requirements under inland water ways (AND), road (ADR) or maritime transport (IMSBC - International Maritime Solid Bulk Cargo Code) regulations, like the use of double-hulled vessels for loads > 0kg AND, or closed/re-enforced doors containers (BK2) under the International Maritime Dangerous Goods (IMDG) Code.

Further to the case lodged by HTCTP European producers and users, the European Court of Justice has decided to annul this environment hazard classification [6]. Due to an appeal lodged by the Commission and three Member States and the related legal uncertainty hence created, the European ferro-alloys and Silicon producers and suppliers of HTCTP have developed via Euroalliages a robust testing strategy together with NIVA (Norwegian Institute for Water research) so as to demonstrate that the mixture of HTCTP electrode paste cannot be classified for the environment. The outcome of the test confirmed that the Søderberg Electrode Paste mixture, composed of HTCTP (CAS n° 65996-93-2) and Carbonaceous material(s) (e.g., Calcined anthracite, filler grains, petroleum coke and others) should not be hazard classified for the environment based on the results from the acute and chronic ecotoxicity tests ([7] Lillicrap A, 2017).

It should be also underlined that SEVESO obligations may be triggered by a relatively insignificant presence of classified impurities in metals alloys, or other materials, although not sufficient to trigger a relevant classification for the overall substance/material. For metal and alloys, in particular in massive form, it is indeed impossible in practice that the presence at 0.1 % of such impurities can cause a release of matter or energy that could create a major accident.

Beginning of December 2017, the European Court of Justice dismissed the Appeal of the Commission. Therefore, the first Judgement was confirmed in stating that HTCTP should not be harmonized classified as Aquatic Acute and Chronic [8].

REACH and CLP Regulations

Other recent decisions on some classification can adversely impact the production and use of Silicon. The TiO_2 case related to biopersistent particles (BP) could seriously affect the classification of all dusts (slags, oxides, metal powders…). Indeed, as a poorly soluble particle (PSP) TiO_2 is proposed to be classified as suspected of causing cancer when inhaled. Therefore, the insolubility of a substance could be associated to a potential biopersistence and hence to a cancer hazard with the related consequences in practice.

Substance considered as very high concern (SVHC) can be subject to further requirements like the authorization or the restriction processes under REACH [9]. With its classification as Carcinogenic, Category 1B, H350 (“May cause cancer”), HTCTP has been identified as SVHC and hence put on the authorization list [10]. This means in practice that users of HTCTP as such or in mixture, like the Silicon sector, are required to apply for an authorization in order to be able to continue to use HTCTP, unless substitutes can be used or exemptions can be applied. Intermediate use can be applied to HTCTP electrode pastes. In the case of the lining, taping hole or repairs pastes, an application for authorisation will have to be lodged, unless substitutes can be implemented. These substitutes should preferably not contain PAHs (Polycyclic Aromatic Hydrocarbon) as sooner or later these substances will also be subject to more stringent regulations. Indeed, Benzo[a]pyrene CAS n° 50-32-8 is already in the pipeline to become subject to authorisation and the following PAHs are under scrutiny by some Members States: Benz(a)anthracene (CAS n° 200-280-6), Pyrene (CAS n° 204-927-3), Benzo[ghi]perylene (CAS n° 205-883-8), Fluoranthene (CAS n° 205-912-4), Benzo(K)Fluoranthene, (CAS n° 205-916-6), Chrysene CAS n° 205-923-4, Phenanthrene (CAS n° 201-581-5).

III. EU Water Framework Directive (WFD)

The objective of the Water Framework Directive or WFD (2000/60/EC – [11]) is to set out strategies against pollution of water by first establishing a list of priority substances (PS) presenting a significant risk to or via the aquatic environment. Environmental quality standards (EQS) for the priority hazardous substances are set for surface waters (river, lake, transitional and coastal). The list of priority substances and their related EQS are published in the Quality Standards Directive 2013/39/EU [12]. Chemical status in a river basin is evaluated by these environmental quality standards (EQS) which must be complied with in all Member States. This also means that ELV (environment limit values) are applied to operating plants where the emissions leave the installation. New

Priority Substances (PS) have been identified since the first list and the EQS of existing PS are going to be revised, like for Nickel.

A number of relevant substances that can be potentially discharged by the Silicon industry is listed in table 1 with their EQS.

Table 1: Some Environment Quality Standard as outlined in Annex I A. of Directive 2008/105/EC

Name of substance	CAS number (1)	AA-EQS (2) Inland surface Waters (3)	AA-EQS (2) Other surface waters	MAC-EQS (4) Inland surface waters (3)	MAC-EQS (4) Other surface waters
Lead and its compounds	7439-92-1	7,2	7,2	not applicable	not applicable
Mercury and its compounds	7439-97-6	0,05 (5)	0,05 (5)	0,07	0,07
Polyaromatic hydrocarbons (PAH) (6)	not applicable	not applicable	not applicable	not applicable	not applicable
Benzo(a)pyrene	50-32-8	0,05	0,05	0,1	0,1
Benzo(b)fluor-anthene	205-99-2	Σ = 0,03	Σ = 0,03	not applicable	not applicable
Benzo(k)fluor-anthene	207-08-9				
Benzo(g,h,i)-perylene	191-24-2	Σ = 0,002	Σ = 0,02	not applicable	not applicable
Indeno(1,2,3-cd)-pyrene	193-39-5				

AA: annual average;
MAC: maximum allowable concentration.
Unit: [µg/l]

(1) CAS: Chemical Abstracts Service.
(2) This parameter is the EQS expressed as an annual average value (AA-EQS). Unless otherwise specified, it applies to the total concentration of all isomers.
(3) Inland surface waters encompass rivers and lakes and related artificial or heavily modified water bodies.
(4) This parameter is the EQS expressed as a maximum allowable concentration (MAC-EQS). Where the MAC-EQS are marked as 'not applicable', the AA-EQS values are considered protective against short-term pollution peaks in continuous discharges since they are significantly lower than the values derived on the basis of acute toxicity.
(5) If Member States do not apply EQS for biota they shall introduce stricter EQS for water in order to achieve the same level of protection as the EQS for biota set out in Article 3(2) of this Directive. They shall notify the Commission and other Member States, through the Committee referred to in Article 21 of Directive 2000/60/EC, of the reasons and basis for using this approach, the alternative EQS for water established, including the data and the methodology by which the alternative EQS were derived, and the categories of surface water to which they would apply.
(6) For the group of priority substances of polyaromatic hydrocarbons (PAH) (No 28), each individual EQS is applicable, i.e. the EQS for Benzo(a)pyrene, the EQS for the sum of Benzo(b)fluoranthene and Benzo(k)fluoranthene and the EQS for the sum of Benzo(g,h,i)perylene and Indeno(1,2,3-cd)pyrene must be met.

EQSs for Pb and Ni and their compounds refer to bioavailable concentrations of the substances. There is a growing confusion between these ELV imposed to operating plants and EQS – indicating the maximum acceptable concentration values in the receiving medium and hence integrating the dilution/dispersion factor - but they are clearly different. A European Court case related to the Water Framework Directive (C-461/13 in 2015 – Weser ruling – [13]) indicated that the Member States are required to refuse authorisation for an individual project where it may cause a deterioration of the status of a body of surface water. The deterioration ban of the WFD is to be examined directly in the authorisation procedure. The only chance of exemption (Art. 4 VII (c)) is the public interest. The disproportionate nature of this provision will be raised by the Industry during the revision of the Water Framework Directive due to take place during the next two years at least.

IV. Carcinogens at work Directive

Current regulatory exposure limits for respirable quartz in Europe are set at Members states levels and range from 0.025 mg/m³ (Ireland, Italy, Portugal) to 0.3 mg/m³ (Poland), with an average of 0.1 mg/m³.

The revision of the Carcinogens Directive (CMD) at work (2004/37/EC – [14] & [15]) introduces in its Annex I "work involving exposure to respirable crystalline silica dust generated by a work process" and sets a Binding Occupational Exposure Limit Value (BOELV) of 0.1 mg/m³ for respirable crystalline silica. The publication in the Official Journal was issued end of December 2017. The transposition in the national laws will have to take place two years after the publication. The CMD obligations apply to any employer and work processes generating exposure to respirable crystalline silica dust. Every workplace situation where such processes are present will have to apply the exposure minimization obligations. If not done yet, a risk assessment has to be carried out and exposure minimization must be applied in accordance with the requirements of the CMD and to respect the 0.1 mg/m³ exposure limit value. Exposure must be monitored. This new European Directive concerns only the control of the exposure of the workers to process-generated RCS. This Directive does interfere with the classification and labelling of products containing crystalline silica. The requirements of the CMD also apply to the exposure to RCS dust generated by the waste management processes. It is also to be noted that surprisingly in 2016 France notified ECHA of its intention to submit a harmonised classification (HCL) for the bulk form crystalline silica (quartz; tridymite; cristobalite) under the category carcinogenicity, and this before having conducted a thorough analysis. This is being in fact conducted *a posteriori* by their expert agency ANSES (Agence nationale de sécurité sanitaire de l'alimentation, de l'environnement et du travail – The French Agency for Food, Environmental and Occupational Health & Safety).

V. Circular economy package

The Circular economy package [16] comprises the current revision of existing regulations like the waste framework directing or the landfill directive, but also an EU Action Plan with measures covering the whole cycle, from production and consumption to waste management and the market for secondary raw materials. A concern for the Silicon sector is the status of slags. Requalification of some wastes as products, based sometimes on years of research is the ideal objective of a circular economy to close the loop. However, the Circular Economy implementation is affected by the non-harmonized status of waste and by-products across Member States. It also complicates the transport of by-products, hence hampering their further use. In addition, in some Member States, to be able to be considered and used as products, some by-products like slags are subject to double regulations as they must comply with both the waste and the products requirements. The conflicting status between product and waste at national or local level jeopardizes valuable use of slags in i.e. constructions road applications which would enable considerable amount of slags to be diverted from landfilling. The issue is mainly at local level where the authorities in charge of waste management are often not (enough) aware of the development related to the chemical regulations and where the various local authorities are still thinking and working in silo.

CONCLUSIONS

The “EHS” Regulations in Europe, which are impacting the metallurgical Silicon production plants are evolving rapidly with an increased complexity. Regulatory requirements are entering more in depth into the production plants. This is accompanied by an increased incoherence and inconsistency across the regulations. This is not necessarily to the benefit of the health and the environment while heavily impacting the companies. There is a conflict between the industrial policy presented as a key driver towards EU 2020, the “European Industrial Renaissance” [17] and the continuous proliferation of regulatory measures adding unilateral costs to industrial operators, complicating operations and negatively impacting the industry’s ability to invest in long term projects. Silicon metal is considered as a critical raw material (CRM) due to its economic importance as essential raw material in a wide range of key uses in Europe and the related absence of substitutes, as well as absence of recycling possibilities. The demand of Silicon is growing while there is no level playing field between the EAA and its main competing regions in terms of policy in the energy, climate and environment fields. This CRM status could help in restoring some balance for the EAA production. Finally, it remains to be seen how the political goal of a “Non-Toxic Environment (NTE, [18]) will be implemented in practice and if or how this NTE will have additional impact on the production plants in the EEA. In this respect, the position of the Metal/Alloys industry is to translate NTE as a “risk-controlled environment” with a fully risk controlled Europe, where hazardous substances are used only when it is certain they will not harm human health or the environment.

References

1. Directive 2010/75/EC on industrial emissions (IED) replacing Directive 96/61/EC on Integrated Pollution Prevention and Control (IPPC) 2010. OJ L 334 of 17.12.2010, p. 17.

2. Commission Implementing Decision (EU) 2016/1032 of 13 June 2016 establishing best available techniques (BAT) conclusions, under Directive 2010/75/EU of the European Parliament and of the Council, for the non-ferrous metals industries 2016. Official Journal of the European Union (OJ) L 174, 30 June 2016, p. 32.

3. Best Available Techniques (BAT) Reference Document for the Non-Ferrous Metals Industries 2017. JRC 107041. Publication Office of the European Union. ISBN 978-92-79-69655-8

4. Commission Regulation (EU) No 944/2013 of 2 October 2013 amending, for the purposes of its adaptation to technical and scientific progress, Regulation (EC) No 1272/2008 on classification, labelling and packaging of substances and mixtures. 2013. OJ L 261, 3.10.2013, p. 5.

5. Directive 2012/18/EU of the European Parliament and of the Council of 4 July 2012 on the control of major-accident hazards involving dangerous substances, amending and subsequently repealing Council Directive 96/82/EC Text with EEA relevance (Seveso III Directive) 2012. OJL 197, 4.7.2012, p. 1–37.

6. Judgement of the Court of 7 October 2015. Case T-689/13. ECLI:EU:T:2015:767

7. Lillicrap A., Gomez T., Macken A. and Allan I. 2017. Ecotoxicological assessment and leaching experiments of Søderberg Electrode Paste. Norwegian Institute for Water Research, project O-162797. Rapport L.NR. 7151-2017 of 19.05.2017. Not published.

8. Judgement of the Court of 22 November 2017. C‑691/15 P. ECLI: EU: T: 2017:882

9. Regulation (EC) No 1907/2006 of the European Parliament and of the Council on the Registration, Evaluation, Authorisation and Restriction of Chemicals (REACH) 2006. OJL 396 of 30.12.2006, p. 1.

10. Commission Regulation (EU) 2017/999 of 13 June 2017 amending Annex XIV to Regulation (EC) No 1907/2006 concerning the Registration, Evaluation, Authorisation and Restriction of Chemicals (REACH) 2017. OJL 150 of 14.06.20117, p. 7.

11. Directive 2000/60/EC establishing a framework for Community action in the field of water policy (Water Framework Directive) 2000. OJ L 327 of 22 December 2000, p. 1.

12. Directive 2008/105/EC of on environmental quality standards in the field of water policy (EQS or Priority Substances Directive) 2008. OJL 348 of 24 December 2008, p. 84.

13. Judgement of the Court of 1st July 2015. Case 461/13. ECLI: EU: C: 2015:433.

14. Directive 2004/37/EC of 29 April 2004 on the protection of workers from the risks related to exposure to carcinogens or mutagens at work 2004. OJ L 229, 29.6.2004, p. 23

15. Directive 2017/2398 amending Directive 2004/37/EC on the protection of workers from the risks related to exposure to carcinogens or mutagens at work 2017. OJ L 345 of 27 December 2017, p. 87.

16. European Commission, Communication from the Commission to the European Parliament, the Council, the European Economic and Social Committee and the Committee of the Regions: Closing the loop - An EU action plan for the Circular Economy 2015. JOC COM (2015) 614 final of 2 December 2015

17. Communication of the Commission « For a European Industrial Renaissance ». 2004. COM/2014/014 final.

18. European Commission. Study for the strategy for a non-toxic environment of the 7th Environment Action Programme. Final Report. August 2017.

The impact of lattice strain on the reactivity of silicon

Jörg Acker, Tim Sieber, Thomas Langner, and Steven Herold
Brandenburg University of Technology Cottbus-Senftenberg, Department of Physical Chemistry, Universitätsplatz 1, D-01968 Senftenberg, Germany

Abstract

The present study is focused on the question of how lattice strain mechanically introduced into silicon alters the chemical reactivity of the silicon atoms that are affected by the strain field on a microscopic length scale. The magnitude and local distribution of lattice strain are extracted from confocal Raman microscopy measurements. The reactivity of Si is expressed by the etch rate of Si after treatment with $HF–HNO_3–H_2SiF_6$ mixtures. Then, the local etch rate is calculated from the local etch depth as determined by confocal microscopy. It has been found that tensile strain leads to the highest enhancement of the etch rate, followed by a compressive strain increase in the etch rate.

Introduction

The terms “mechanochemistry” and “tribochemistry” describe how the introduction of mechanical energy into a chemical system affects its chemical reactivity. Meanwhile, an overwhelming number of applications and examples from inorganic, organic, or polymer solids are known through which chemical reactions can be activated or new reaction pathways far away from the thermodynamic equilibrium can be opened [1,2,3].

In silicon chemistry, there are few known examples of how mechanical energy is used to increase the reactivity of elemental silicon. Bade et al. [4,5] reported about a combination of the vibration milling of Si and hydrochlorination at temperatures up to 450°C. The authors found that this combination leads to a dramatic reduction of the length of the induction period, in particular at low temperatures, to an increased $HSiCl_3$ selectivity, to a higher conversion of HCl and Si with time, and finally to a reduction of the activation energy of thermal activation from 87 $kJ \cdot mol^{-1}$ to a value of mechanical activation of 15 $kJ \cdot mol^{-1}$. The effect of the milling procedure is explained by the enlargement of the specific surface area during milling, the removal of passivating surface layers, and the continuous exposure of fresh surfaces.

Schrader et al. [6,7,8] reported about the activation of the contact mass of the direct reaction of methylchlorosilanes, which shortens the induction period and yields an increase in the utilization rate of Si and an increased selectivity for dimethyldichlorosilane. The authors assume that several effects initiated by the milling process contribute to the higher reaction rate: an increase in the particle surface, a decrease in the primary crystallite size, an increase in the Si lattice constant due to an increased concentration of defects, and finally an increased spin concentration as measured by electron spin resonance.

Recently, Muzafarov [9] reported about the direct synthesis of alkoxysilanes using a “gas phase method with mechanical activation”. Here, CH_3OH or C_2H_5OH is passed over Si that is continuously milled at 250 °C. Compared to the classical reaction, a higher Si conversion at identical temperature, 100% selectivity for $Si(OCH_3)_4$, 30–50% for $HSi(OC_2H_5)_3$, and 70–50% for $Si(OC_2H_5)_4$ were found.

The very general term “mechanical activation” is related to a wide variety of physical effects. In the case of Si, it appears necessary to take further physical phenomena into account that can potentially contribute to observations referred to as “mechanical activation”. Starting from Si in the cubic diamond structure (Table 1) designated as Si-I, mechanical treatment like milling, grinding, polishing, or machining can lead to the formation of various high-pressure modifications (Table 1). High-pressure phases have been identified mainly at the contact interface between Si and the mechanical tool (a mill ball, a polishing grain particle, or an indenter) in the center of an indentation (Figure 1), in wear tracks [10-13], or at the surfaces of the solar wafer after slicing using a diamond-wire sawing technique [14]. The creation of high-pressure phases depends on the magnitude of the applied force, the velocity of loading and unloading, and the temperature at which these processes are performed [12].

Table 1: Modifications of Si.

Modification	Structure/ Space group	Raman signal / cm^{-1}	Ref.
Si-I	cubic diamond/ $Fd\bar{3}m$	300, 521	[11, 14]
a-Si	amorphous	150, 475-485	[11, 14]
Si-III	bc8/ $Ia\bar{3}$	166, 171, 384, 432, 463	[11]
Si-IV	hexagonal diamond/ $P6_3mc$	508	[14]
Si-XII	R8/ $R\bar{3}$	182, 352, 397, 434	[11, 14]
Si-XIII	tetragonal/ $P4_12_12$	200, 330, 475, 497	[22]

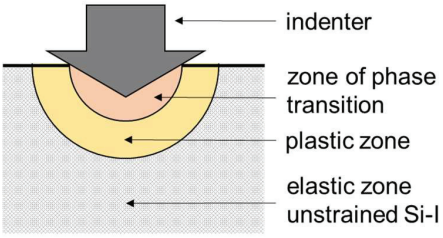


Figure 1. Indentation model with a semi-circle-shaped plastic deformation zone; adapted from [10,12].

Apart from phase transition, a mechanical force applied to Si causes a plastic deformation in a hemispherical volume segment around the indentation center (Figure 1). This volume contains silicon whose lattice is expanded (tensile strain) or compressed (compressive strain) with respect to the dimension of the Si-I unit cell. As shown later in this work, the Si atoms in this zone show a chemical reactivity that is significantly enhanced compared to that of unstrained Si-I.

A versatile method to study the high-pressure phases of Si and lattice strain in Si is Raman microscopy [10,11,15,16]. Single-crystalline Si in the cubic diamond structure (space group Fd3m) leads to one single peak in the Raman spectrum around 521 cm^{-1} with a FWHM ((full width at half maximum)) of about 3 cm^{-1} [15,16]. This single peak represents the three optical phonon modes, one longitudinal (LO) and two transversal (TO), which are degenerated with each other in the center of the Brillouin zone [15,17]. Mechanical stress removes the degeneracy by changing the unit cell dimensions and lowering the symmetry and yields individual shifts in the three phonon modes [15,18,19]. Biaxial compressive stress results in an increase in the Raman shift wavenumber

(> 521 cm^{-1}), and biaxial tensile stress causes a decreasing Raman shift wavenumber (< 521 cm^{-1}) [15]; another signal remains at the position of 521 cm^{-1} (Figure 2). The peak shift of the signal of a strained component, measured at the peak maximum with reference to the peak position of unstrained Si-I, $\Delta\omega$, is a linear measure for the degree of lattice stress [19,20]. The strain components are obtained through peak deconvolution (Figure 2).

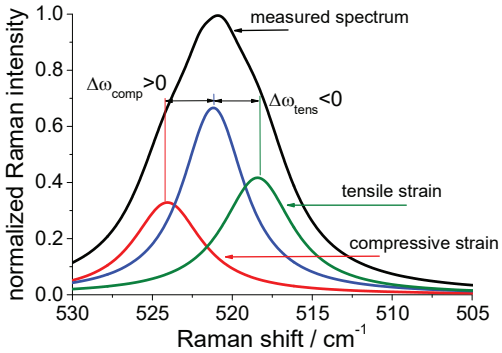


Figure 2. Raman spectrum (black) consisting of unstrained Si as well as Si in tensile and deformation strain. Tensile (green) and compressive (blue) strain component and peak shift, $\Delta\omega$, obtained through peak deconvolution.

Experimental

Silicon surfaces were studied using confocal Raman microscopy (DXR SmartRaman, Thermo Fisher Scientific) in a backscattering configuration equipped with a 532 nm excitation laser and a 900 grooves/mm grating enabling the acquisition of Raman spectra in the 150–1250 cm^{-1} range. A mercury emission source was used as a reference for wavelength correction. The Raman spectra were deconvoluted by using Lorentzian functions representing unstrained Si-I (521 cm^{-1}), Si under compressive strain (> 520 cm^{-1}), and Si under tensile strain (< 520 cm^{-1}) according to the model of biaxial stress [15]. Surface topography and local etch removal were measured using confocal microscopy using the 3D profiler Sensofar PLμ neox equipped with 50x, 100x, and 150x objectives.

For etching experiments, as-cut solar wafer (156 x 156 mm^2) and 15 x 15 mm^2 pieces of as-cut multi-crystalline Si solar wafer were taken from an industrial production process and sliced by diamond-wire sawing and SiC slurry sawing [23]. For scratch experiments, polished semiconductor-grade single-crystalline p-type Si wafers with (100) orientation were used. Scratches were created using a diamond-tip indentation system. Milling experiments were performed in different milling systems using multi-crystalline Si of different quality from various suppliers as starting material. Particles different in size were obtained either by sieving the as-received materials or produced by milling as-received materials followed by sieving.

Etch mixtures were prepared by weighing aliquots from HNO_3 (69% (w/w)) and HF (40% (w/w)), both from Merck (Darmstadt, Germany), as well as H_2SiF_6 (35% (w/w)) from Alfa Aeser (Karlsruhe, Germany). The cleaned samples were immersed in aliquots of always freshly prepared etch solution for a defined time and then rinsed with deionized

water. Before the first etching and after each etch step, the surface was mapped by confocal microscopy and Raman microscopy.

Results and discussion

Lattice strain on the surface of multi-wire-sawn Si wafer

The typical features of a diamond-wire-sawn solar wafer are shown in Figure 3a: there is a pattern of smooth and shiny stripes parallel to rifts with lots of individual fractures and areas of cracks along the rifts. High-pressure modifications were not detected at this surface, but Figure 3b shows that large areas of the wafer surface are covered with amorphous Si. It was previously shown [24] that even diluted etch mixtures entirely remove amorphous Si within a few seconds. The Raman mapping in Figure 3c shows the lateral distribution of the normalized Raman intensities of the tensile strain component. Tensile strain is the most dominant state of Si at the surface, and a considerable fraction of the surface area consists of material with a very high degree of it (red and yellow). Although it is present, the compressive strain component (Figure 3d) covers a smaller fraction of the sample area and only a few regions exhibit a high degree of compressive strain (green).

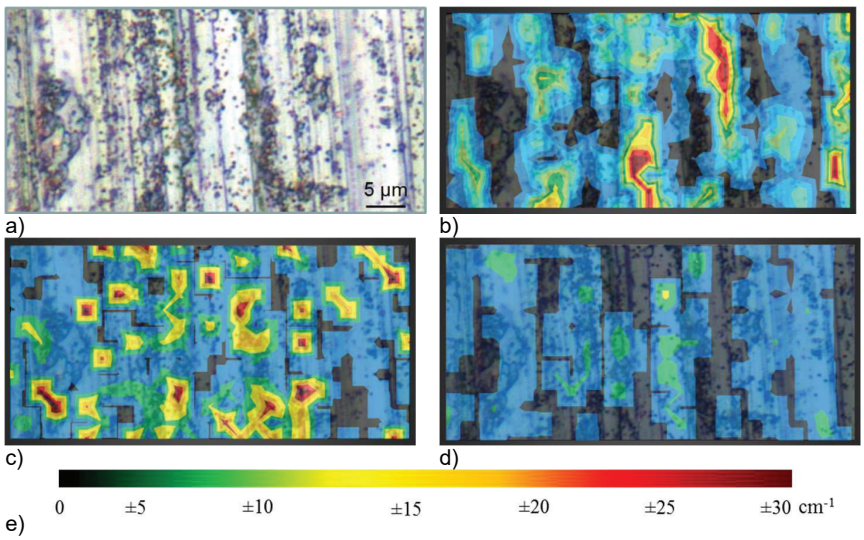


Figure 3. Surface of an as-cut diamond-wire-sawn Si wafer. (a) Optical image of the surface, (b) overlay of the optical image and mapping of the relative Raman intensity at the Raman peak maximum for amorphous Si (red indicates high intensity, blue indicates low intensity, and no color indicates no intensity), (c) overlay of the optical image and mapping of the Raman shift attributed to tensile strain, (d) overlay of the optical image and mapping of the Raman shift attributed to compressive strain, and (e) color scale for (c) and (d) indicating the extent of the Raman shift relative to the Raman peak position of unstrained Si-I.

Etching of the saw damage

The term “saw damage” refers to the topmost layer (up to 3 µm per wafer side) of as-cut solar wafer consisting of pits, fractures, rifts, and cracks. It turned out that etching the saw damage proceeds several times faster than etching the underlying bulk Si (Figure 4). This phenomenon is dependent on the crystallinity of the wafer and independent from the sawing procedure, which underlines the fact that the saw damage has its own reactivity that significantly differs from that of the bulk material. Only after the complete removal of the saw damage do the bulk etch rates show the expected slight difference between multi-crystalline and single-crystalline Si. It should be noted that etching diamond-wire-sawn wafer starts at the most disturbed areas inside the rifts. The shiny areas of the surface are attacked at a later time and lower etch rate. Therefore, the etch rates and etch depths in Figure 4 are averaged values across the entire sample surface.

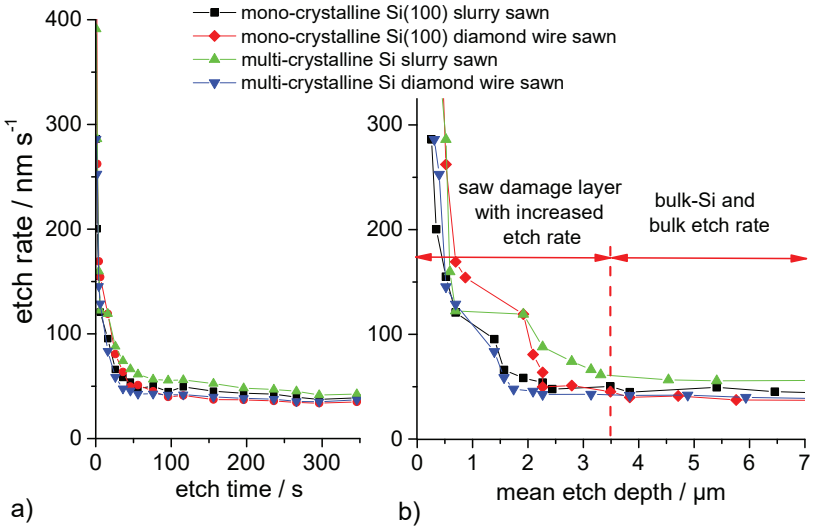


Figure 4. Etch rate (a) as a function of the etch time and (b) as a function of the mean etch depth (calculated for both wafer sides) for different Si ingots and different sawing techniques. The etch temperature is 10 °C, and the composition of the etch mixture is 30% (w/w) HNO_3, 5% (w/w) HF, and 10% (w/w) H_2SiF_6.

Topography analysis of the solar wafer before and after etching

The results of the previous section were obtained for a small surface area on a slurry-sawn as-cut solar wafer. The topography analysis the entire wafer surface (156 x 156 mm^2) before and after etching reveals how the sawing process controls the etch process and the final texture of the solar wafer surface [25]. In order to handle the enormous number of data points, the surface was virtually overlaid with a grid of 21 rows and 21 columns, yielding 441 squares identical in size (7.43 x 7.43 mm^2). Each segment was overlaid by a grid of 3 rows and 3 columns and each of them contains 786.432 individual points. The topography parameters within the 7.43 x 7.43 mm^2 segment were calculated, averaged from all individual points, and attributed to the respective segment as shown in Figure 5.

The silicon carbide (SiC) slurry sawing process uses a smooth steel wire and a slurry of SiC particles with a size in the micrometer range. The slurry is spilled over the wire at the entrance side and transported by the wire into the sawing groove. The term “sawing” is misleading since the SiC particles captured between the wire and the silicon surface are forced to indent into the Si material [26,27]. Due to fractures, Si particles are chipped away and transported to the wire exit. At the wire entrance side where the fresh slurry is added, the large and sharp SiC grains cause fewer but deeper indentations. On their pathway along the sawing groove, the SiC particles ejected at the wire exit side are both smaller in size and rounder, with fewer sharp edges due to abrasion and breakage [28,29]. These smaller and rounder particles generate a higher density of indentation at the wire exit side, resulting in more indentations per area that are shallower compared to the wire entrance side (Figure 5). In consequence, the larger and sharper SiC particles at the wire entrance side create a higher indentation force that results in deeper indentations and a larger strain field. The higher count of smaller and rounder SiC particles at the wire exit side results in a lower indentation force with shallower indentations and a smaller stress field. Comparing the indentation depths before (Figure 5a) and after (Figure 5b) etching reveals that the mean depth was almost homogeneously increased by a factor of roughly 2. However, etching increases the mean depth at the wire entrance side from 1 µm to 2 µm and at the wire exit side from approximately 0.5 µm to 1 µm. At the wire entrance side, 1 µm of depth was removed, whereas at the wire exit side, only 0.5 µm of depth was removed for the same etching time. This corresponds to an etch rate that is two times higher at the wire entrance side compared to the wire exit side because of the higher indentation force and the larger volume of the strain field. This finding confirms the results of the previous section.

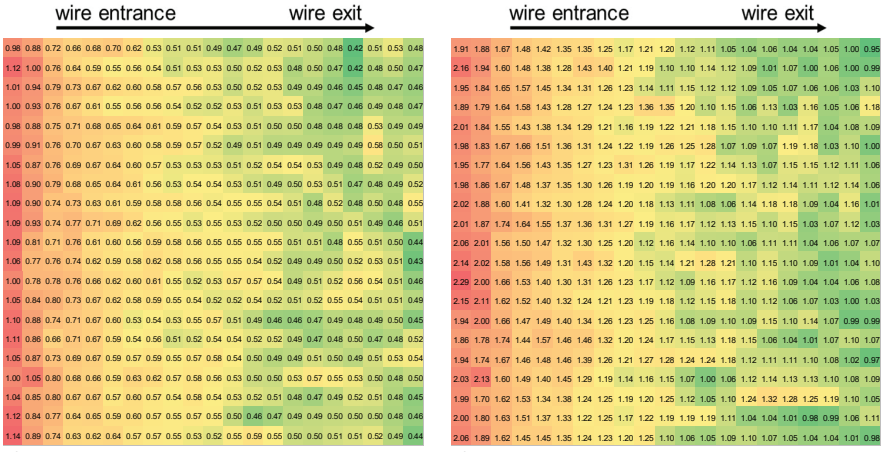


Figure 5. The mean pit depth (in µm) per segment (a) for the as-cut state and (b) after etching across a wafer surface (156 x 156 mm^2).

A quantification of the impact of lattice strain on the reactivity of Si

In order to study the effect of lattice strain on chemical reactivity, polished single-crystalline Si(100) surfaces were scratched with an indentation tool. The Raman

mappings in Figures 6a and b show the positions at which the high relative intensities – indicated by red and dark blue – of tensile-strained Si (Figure 6a) and of compressive-strained Si (Figure 6b) are located. Etching for 40s using an acid mixture consisting of 28% (w/w) HNO_3, 4% (w/w) HF, and 17% (w/w) H_2SiF_6 removes any strain completely (Figures 6c, d). Figure 6f shows the local etch depth as calculated from the confocal images before and after etching. The color scale in Figure 6f shows that the positions with the highest etch depths correlate with the positions of the highest tensile strain.

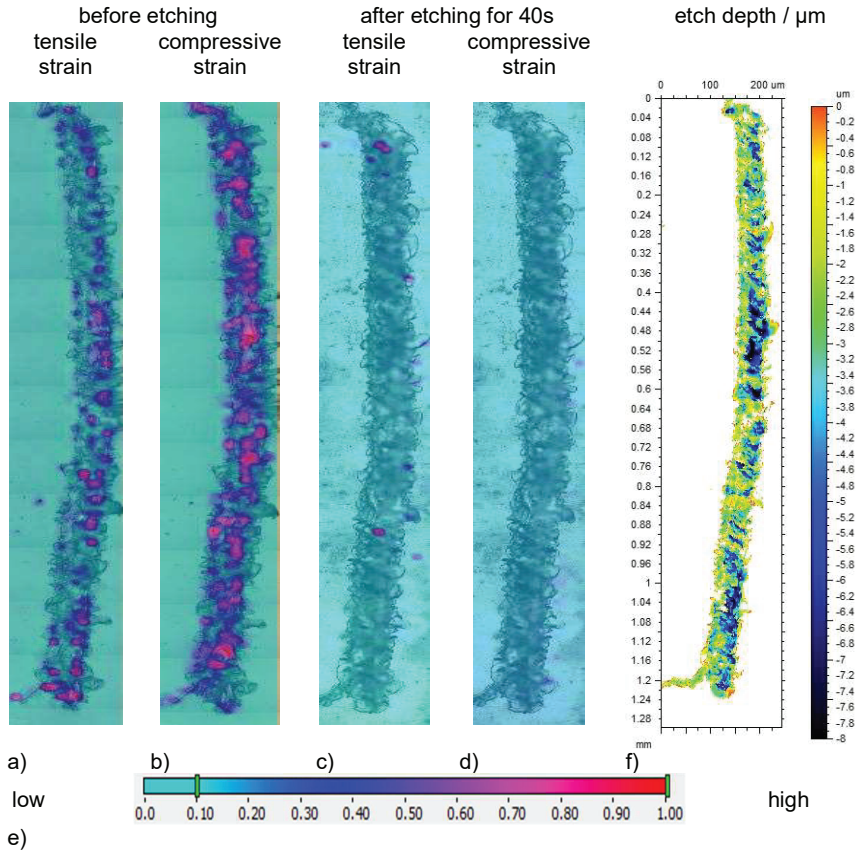


Figure 6. Correlation between lattice strain and etch removal studied on scratch prepared on a polished Si(100) wafer. Confocal microscopic images are overlaid with mappings of the normalized Raman intensities at selected Raman shifts (a) before etching at 517 cm^{-1}, (b) before etching at 525cm^{-1}, (c) after etching at 517 cm^{-1}, and (d) after etching at 525 cm^{-1}. (e) The color scale of the relative Raman intensities is valid for (a) – (d). (f) Etch depth in µm with corresponding color scale. The composition of the etch mixture is 28% (w/w) HNO_3, 4% (w/w) HF, and 17% (w/w) H_2SiF_6.

The spot-by-spot analysis of the scratch yields a quantitative correlation between the local strain state as determined from Raman measurements and the local etch depth as calculated from confocal microscopy images before and after etching (Figure 7). Unstrained Si is etched with an etch rate ranging from 38 to 67 $nm \cdot s^{-1}$. Spots with the

highest observed compressive strain (i.e., the highest peak shift with reference to unstrained Si) are removed with an etch rate ranging from 97 to 348 nm·s^{-1}. Finally, the highest reactivity against the HF–HNO_3–H_2SiF_6 mixture is observed for the spots with the highest degree of tensile strain. Here, the etch rate ranges from 115 to 516 nm·s^{-1}.

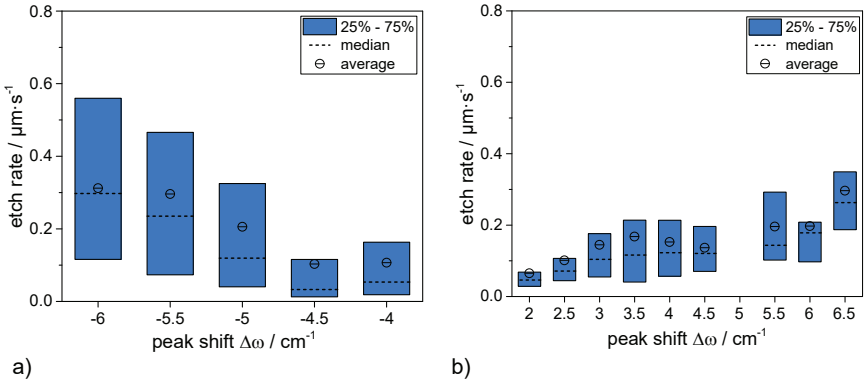


Figure 7. Etch rate as a function of peak shift, Δω, which correlates linearly with the degree of lattice deformation for (a) tensile- and (b) compressive-strained Si. The individual peak shifts are grouped into classes with a width of 0.5 cm^{-1}.The horizontal box dimension covers the range between 25 and 75% of all measured data points. The line within the box indicates the median, and the circle symbol indicates the arithmetic average. The composition of the etch mixture is 28% (w/w) HNO_3, 4% (w/w) HF, and 17% (w/w) H_2SiF_6.

Lattice strain on milled Si particles

Any reaction in industrial Si chemistry uses metallurgical-grade Si that has been previously crushed, ground, or milled. Therefore, Si from very different sources and suppliers was milled by different techniques and the particles were characterized by Raman spectroscopy. Independent from the experimental parameters, particles > 40 µm show the typical shiny surface and the typical half-penny-shaped fracture patterns (Figures 8a, c). Furthermore, the particle surfaces show more or less pronounced defects with micrometer and sub-micrometer size, such as cracks, steps, craters, and pits. Raman analysis showed that the smooth areas consist of unstrained Si-I without exception. Massive plastic deformations are found inside the defects, which mainly consist of tensile-strained Si with typical peak shifts up to 12 cm^{-1}. High-pressure phases and amorphous Si were detected in only a few cases.

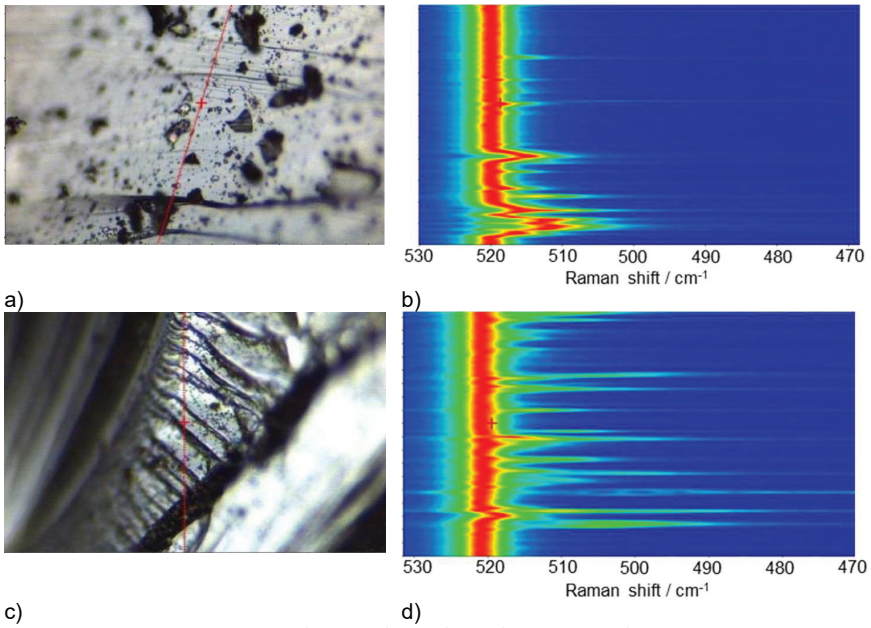


Figure 8. Microscopic images of the surface of two Si particles after milling are shown in panels (a) and (c). Panels (b) and (d) show the normalized Raman intensities of the stacked Raman spectra measured along the red lines marked in (a) and (c) in 1 µm step width. The color scale of the normalized Raman intensities follows the order of red (high intensity), yellow, green, light blue, and dark blue (representing the lowest intensity).

Conclusion

The mechanical treatment of silicon by milling, wafer sawing, or scratching the silicon surfaces can initiate a phase transition and the formation of high-pressure phases, amorphous Si, and plastically deformed Si. Wire sawing, scratching, and milling preferentially leads to tensile-strained Si. Compressive strain seems to be formed to a lesser extent. Amorphous Si and high-pressure modifications are found at higher mechanical load, such as in diamond-wire sawing [14], but very seldom in scratching or milling. The etch experiments show that tensile-strained Si has the highest reactivity against HF–HNO_3–H_2SiF_6 mixtures, followed by compressively strained Si. Assuming that tensile-strained Si also has the highest reactivity against HCl and CH_3Cl, then mechanical activation might be attributed to the formation of this particular strain state. Continuous milling should continuously produce new tensile-strained Si at the particle surface. If these assumptions are valid, then the reaction rate and the Si utilization should increase as stated by Schrader et al. [6-8]. It is yet unknown how a changed selectivity can be explained in the reaction of strained Si with HCl or CH_3Cl. Further efforts are necessary to study the impact of lattice strain in direct reactions of Si and to uncover the nature of "mechanical activation".

References

1. G. Heinicke, Tribochemistry, Akademieverlag, 1984
2. M.K. Beyer, H. Clausen-Schaumann, Chemical Reviews, **105**, 2005, p2921
3. J. Ribas-Arino, D. Marx, Chem. Rev., **112**, 2012, p5412
4. S. Bade, U. Hoffmann, K. Schönert, Int. J. Miner. Process, **44-45**, 1996, p167
5. S. Bade, U. Hoffmann, K. Schönert, Chem. Eng. Comm., **143**, 1996, p169
6. R. Schrader, K. Dreier, K.-H. Werner, Chem. Techn., **20**, 1968, p475
7. R. Schrader, K.-H. Werner, Chem. Techn., **26**, 1974, p302
8. R. Schrader, K.-H. Werner, Chem. Techn., **27**, 1975, p156
9. A. Muzafarov, M. Temnikov, I. Meshkov, A. Zhiltsov, S. Christovalov, V. Kotov, A. Kalinina, M. Gallyamov, M. Pigaleva, I. Elmanovich, *From Silicon to silicones – chlorine free synthesis, prospects and scope*, oral presentation, 9th Silicon Days, Poznan (Poland), 2016
10. A. Kailer, Y.G. Gogotsi, K.G. Nickel, J. Appl. Phys., **81**, 1997, p3057
11. Y. Gogotsi, H. Zhou, S.-S. Ku, S. Cetinkunt, Semicond. Sci. Technol., **16**, 2001, p345
12. V. Domnich, Y. Gogotsi, Rev. Adv. Mater. Sci., **3**, 2002, p1
13. Y. Gerbig, L. Friedmann, M. Vaudin, S. Stranick, G. Stan, W. Osborn, R. Cook, Ultramicroscopy, **163**, 2016, p75
14. A. Bidiville, K. Wasmer, R. Kraft, C. Ballif, Proceedings of the 26th European Solar Energy Conference and Exhibition, 2009, p1400
15. I. De Wolf, Semicond. Sci. Technol., **11**, 1996, p139
16. Y. Gogotsi, Semicond. Sci. Technol., **14**, 1999, p936
17. J.H. Parker, D.W. Feldmann, M. Ashkin, Phys. Rev., **155**, 1967, p712
18. E. Anastassakis, A. Pinczuk, E. Burstein, F.H. Pollack, M. Cardona, Solid State Communications, **8**, 1970, p133
19. I. De Wolf, Journal of Applied Physics, **118**, 2015, 053101
20. R.C. Teixeira, M.B.P. Zakia, J.A. Diniz, J.W. Swart, Materials Science and Engineering, **112**, 2004, p160
21. P.K. Kulshreshtha, K.M. Youssef, G. Rozgonyi, Solar Energy Materials & Solar Cells, **96**, 2012, p166
22. D. Ge, V. Domnich, Y. Gogotsi, J. Appl. Phys., **95**, 2004, p2725
23. H. Wu, Precision Engineering, **43**, 2016, p1
24. S. Herold, Internship Report BTU Cottbus – Senftenberg, 2014
25. J. Acker, T. Langner, B. Meinel, T. Sieber, Mat. Sci. Semicond. Proc., **74**, 2018, p238
26. H.J. Möller, Adv. Eng. Mater., **6**, 2004, p501
27. H.J. Möller, Phys. Status. Solidi A., **203**, 2006, p659
28. A. Bidiville, K. Wasmer, J. Michler, P.M. Nasch, M. van der Meer, C. Ballif, Prog. Photovolt.: Res. Appl., **18**, 2010, p563
29. A. Bidiville, K. Wasmer, M. van der Meer, C. Ballif, Sol. Energy Mater. Sol., **132**, 2015, p392

Industrial-scale synthesis of high performance Si-based nanopowders for energy storage applications

Julia Lyubina, Bodo Frings, Andreas Höfler, Reiner Störger, Stefan Bade
Evonik Resource Efficiency GmbH, Rodenbacher Chaussee 4, 63457 Hanau, Germany

Abstract

Silicon started to find use in lithium-ion battery anodes as it allows a higher specific energy. Widespread application of Si is, however, still limited by the availability of high performance materials that can be produced on an industrial scale. Here, we introduce a novel design and industrial route for the production of Si-based nanopowders optimised for improved electrochemical performance. In particular, it is demonstrated that Si/C composite materials with a specific carbon distribution within the particle maintain their capacity after prolonged cycling compared to pure Si nanoparticles.

Introduction

Nowadays, lithium ion batteries (LIB) represent the majority of batteries used in portable electronic devices and have recently started to be used in automotive applications, leading to a profound growth in the volume of the lithium ion cells produced [1–3]. Technological development in the LIB field is driven by an ever-increasing demand for performance improvement, in particular, by the need to increase the amount of the stored energy. Efforts toward improvement of the major LIB components, i.e. active cathode and anode materials, electrolyte, separator, various additives and coatings, as well as engineering and manufacturing advances result in a steady, albeit incremental, increase of the lithium ion cell specific energy and energy density [2].
The total cell specific energy E_{cell} is given by

$$E_{\mathrm{cell}} = Q_{\mathrm{cell}} U_{\mathrm{cell}}, \tag{1}$$

where U_{cell} is the nominal voltage of the cell and Q_{cell} is the total cell capacity:

$$Q_{\mathrm{cell}} = \frac{1}{\frac{1}{C_{\mathrm{c}}} + \frac{1}{C_{\mathrm{a}}} + \frac{1}{Q_{\mathrm{m}}}}, \tag{2}$$

where C_{c} and C_{a} is the specific capacity of the cathode and anode, respectively, and $1/Q_{\mathrm{m}}$ is the specific mass of inactive battery components in g/Ah [4]. Thus, to maximise the energy stored in a full cell it is necessary to maximise the *reversible* specific capacity and the difference between operating potentials of the cathode and anode. Since the specific capacity of active electrode materials sets an intrinsic limit on the total capacity that can be achieved in a cell, it is imperative to employ materials with a higher specific capacity. The state-of-the-art anode material used in LIB is graphite with a specific capacity of about 370 mAh/g [1]. On the other hand, full electrochemical lithiation of silicon near room temperature leads to the formation of the $Li_{15}Si_4$ phase corresponding to the specific capacity of 3579 mAh/g [5]. Even though currently used cathode materials have a

moderate capacity of 200 mAh/g (e.g. $LiNi_{0.8}Co_{0.15}O_2$), employing an anode with a specific capacity of 1000 mAh/g would bring about up to 30 % gain in the cell capacity (Eq. 2, Refs. [2] and [5]); a combination of a high-capacity anode with a next generation cathode, such as Li-rich $LiNi_xMn_yCo_{1-x-y}O_2$ with a capacity of 300 mAh/g, would double the cell capacity as compared to the current values.

Small amounts of Si are currently added to the graphite-based anodes leading to the commercial availability of 400 to 500 mAh/g anode materials [1]. The ability to integrate higher amounts of silicon into negative electrodes without compromising their cyclability is highly desirable in terms of further cell capacity improvement. However, the use of silicon as an anode material is challenging, mainly due to an extremely large volume expansion of about 300 % [5, 6]. The volume expansion/contraction during cycling leads to electrode decrepitation and disruption of the solid electrolyte interphase (SEI) resulting in a concomitant capacity fade. Control of the silicon particle dimensions at the nanoscale and encasing silicon in a (carbon) matrix are used to mitigate these effects (see Ref. [5] and references therein). It should be noted that sophisticated synthesis methods are frequently required to produce Si-based materials in the form of nanoparticles, nanowires or nanotubes that are not easily scalable for volume production.

Despite better cycling performance of the nanoscale silicon/carbon composite materials compared to that of pure Si or anodes containing coarse Si particles, the capacity retention of Si containing electrodes still needs improvement. Recent studies have shown that the capacity fade in Si-based electrodes is connected to the formation of the crystalline $Li_{15}Si_4$ phase [7]. The formation of $Li_{15}Si_4$ at voltages below 50 mV during the lithiation of silicon leads to significant mechanical stresses and was shown to be responsible for the poor cycling stability of silicon-based electrodes. The use of narrow cycle voltage is one of the methods to prohibit the formation of $Li_{15}Si_4$. This, however, results in a significantly reduced cell energy (the consequence of the reduced U_{cell} in Eq. 1). In addition to having a lower energy, limiting the voltage of the Si-containing electrode may not be practical, because silicon is usually blended with graphite or other forms of carbon. Such electrodes must be cycled to low voltages, so that the graphite or carbon is active. It is, therefore, desirable to prohibit the formation of $Li_{15}Si_4$ without limiting the voltage. The suppression of the $Li_{15}Si_4$ formation can be realised in particles comprising an active Si phase and an inactive matrix phase, such as found in Si-containing alloys and Si/SiOx ($x \leq 2$) composites [5]. However, the inactive phase reduces the specific capacity of the material or can irreversibly trap Li during the first cycle and is, therefore, undesirable.

Here, we report on the synthesis of Si-based nanoparticles with a complex structure where the formation of $Li_{15}Si_4$ is supressed and a high specific capacity is retained. Importantly, such materials can be produced on the industrial scale using a simple gas-phase process.

Experimental

Si-based powders are produced in a hot-wall reactor at 650 °C (unless mentioned otherwise) and ambient pressure. For the synthesis of pure Si powders, monosilane, SiH_4, is injected into the reactor, whereas for the production of Si/C composite powders a mixture of monosilane and ethylene is used. Argon is employed as a carrier gas. The precursor gas concentration in the carrier gas is 20 – 25 vol. % and the residence time is between 3.5 and 4.5 s.

The phase composition and structure parameters were determined by Rietveld refinement of x-ray diffraction data collected in the 2θ range of 15 – 110° with a step of 0.05° using Philips X'Pert Pro diffractometer (Cu Kα radiation). The "average size-strain" method of Langford was used to separate contributions to the overall x-ray line breadth from the

crystallite size <*D*> and lattice strain <*e*> [8]. The x-ray line profile parameters were corrected for instrumental effects. Transmission electron microscopy (TEM) was performed in a JEOL 2010 F microscope. For the TEM study the powders were dispersed in isopropanol and water. The chemical composition was determined using energy dispersive x-ray analysis (EDX) in the TEM.
The electrochemical characterisation was performed on electrodes prepared from a slurry of gas-phase synthesised nanoparticles embedded into a carbon matrix via pyrolysis in argon, an aqueous solution of styrol-butadiene-rubber (SBR in 15 % water, Targray) and multiwall carbon nanotubes (Nanocyl) in a weight ratio of 80:10:10, respectively. The amount of Si in the electrode was > 20 wt. %.The slurry was mixed for 15 min in a ball mill and subsequently coated at a thickness of 130 – 160 µm onto a copper foil (10 µm thickness, SE-Cu58, Schlenk GmbH & Co. KG) and dried. High areal loadings of 4 mg/cm^2 were used. Discs were punched from the coated foil and incorporated into coin cells with Li metal counter electrodes and 1 M $LiPF_6$ in ethylene carbonate/dimethyl carbonate electrolyte. The fist cycle is a forming cycle at C/50, further cycles are run at C/10.

Results and discussion

The use of monosilane as precursor gas in the hot-wall reactor resulted in the synthesis of pure Si nanoparticles according to the reaction:

$$SiH_4 \xrightarrow{650\,°C} Si + 2H_2, \tag{3}$$

whereas the addition of ethylene is used for the preparation of Si/C composites according to the reaction (note, other possible and intermediate reactions are omitted for clarity here):

$$SiH_4 + xC_2H_4 \xrightarrow{650\,°C} Si/C + yH_2. \tag{4}$$

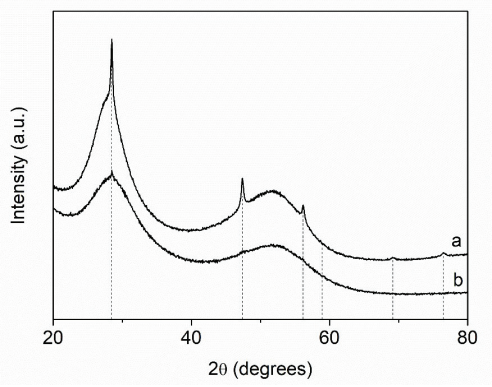


Figure 1: X-ray diffraction patterns of (a) pure Si powders and (b) Si/C powders. Dashed lines represent the Bragg reflection positions of crystalline Si.

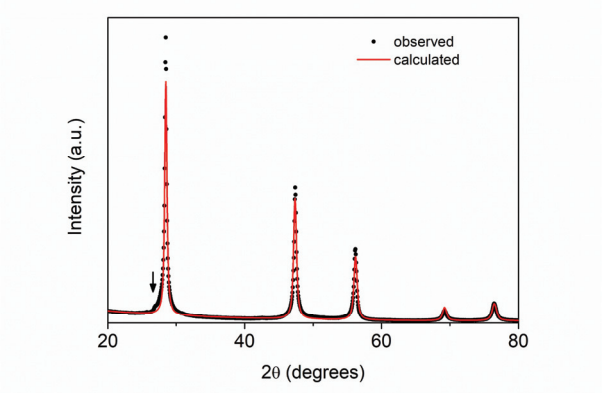


Figure 2: Observed and calculated x-ray diffraction patterns of pure Si powders produced at 750 °C. The calculated pattern shown here is obtained by Rietveld refinement in the assumption that only crystalline Si is present. A small shoulder at the diffraction peak near 28.5° (marked by the arrow) indicates the presence of an amorphous phase, which amounts to about 3 vol. % according to the quantitative phase analysis.

Figure 1 shows x-ray diffraction (XRD) patterns of pure Si and Si/C composite powders obtained in the hot-wall reactor. The pure silicon powder produced by the reaction in Eq. 3 is a mixture of nanocrystalline and amorphous Si: sharper peaks are due to the nanocrystalline Si and two broader peaks (amorphous halo) are due to the amorphous Si (Fig. 1a). According to the quantitative phase analysis, the amount of the crystalline silicon is about 24 vol. %, the rest being the amorphous phase. The amount of the crystalline Si in the Si/C powder produced with the addition of ethylene (Eq. 4) is significantly lower than that in the pure Si powder and is about 4 vol. %.

The choice of 650 °C as an appropriate reaction temperature is guided by envisaged structure and microstructure design aimed at improving material performance in the LIB anode applications. A lower reaction temperature favours the formation of the amorphous Si phase, which has improved cycling performance compared to that of crystalline Si [9–11].

Increasing the temperature above 650 °C results in an increasing crystalline Si fraction. Already at 750 °C, essentially fully crystalline Si with the grain size $\langle D \rangle$ of 45(3) nm is obtained at otherwise identical reaction conditions (Fig. 2). The amount of the crystalline phase is about 97 vol. % and only a minor amount of the amorphous phase (3 vol. %) is present, as is evident from the Rietveld refinement of the XRD pattern (Fig. 2).

Not only the structure, but also the microstructure of the pure Si powders obtained at 650 and 750 °C differ significantly. Fig. 3 shows TEM images of the Si powders. Whereas pure Si nanoparticles obtained at 750 °C are sintered (Fig. 3a), predominantly amorphous nanoparticles produced at 650 °C form agglomerates with no evident sintering between the particles (Fig. 3b). In the crystalline silicon, the reaction with Li is limited by the interface reaction rate and the evolving mechanical stress at the reaction front slows the lithiation and leads to plastic deformation of the lithiated silicon [9]. The crystalline core experiences homogeneous compression, which increases in magnitude as the core size

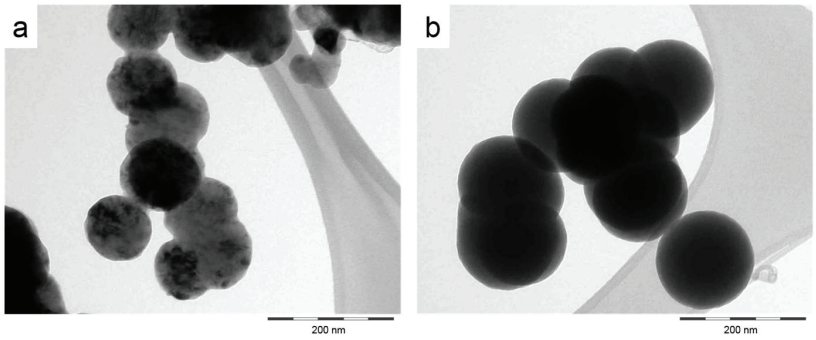


Figure 3: TEM images of pure Si powders produced at (a) 750 °C and (b) 650 °C.

decreases. At the Li_xSi/Si interface, the stress in the lithiated shell is more compressive than in the unlithiated Si core and becomes tensile at the surface of the particle. Inhomogeneous strain during lithiation of Si particles with size of and above 450 nm was shown to be relaxed via crack formation [9].

It is also well known that after the first lithiation, initially crystalline Si remains amorphous during cycling. It is expected that due to the sintered nanoparticle morphology in the Si powder obtained at 750 °C a different stress state at the sintered necks and in the particle that is lithiated from all surfaces will evolve and fracture along the necks can occur. Non-sintered separated Si nanoparticles with the size below 200 nm generally do not fracture [9]. Since the lithiation of amorphous Si is continuous [9, 12], it can be described as a second order-type transformation. During the second order-type transformation, the volume changes smoothly as compared to an abrupt volume change (discontinuity) during the first-order transformation [13] that occurs at lithiation of the crystalline Si [9]. As a result, a lower stress and strain are observed during lithiation of amorphous Si leading to improved cyclability.

As discussed above, the Si/C powders are essentially amorphous with only a small amount of the crystalline Si. It should be noted that a reduction of the amorphous halo intensity and a slight shift of the amorphous halo to higher diffraction angles compared to the pure Si is apparent in the Si/C powders (Fig. 1). These changes in the amorphous halo indicate the formation of the Si and C mixture. A question now arises as to how Si and C are distributed throughout the particle in this silicon/carbon composite powder. The moderate reaction temperature of 650 °C is aimed at prohibiting the formation of SiC, which according to some reports is electrochemically inactive in the cubic form [14] or

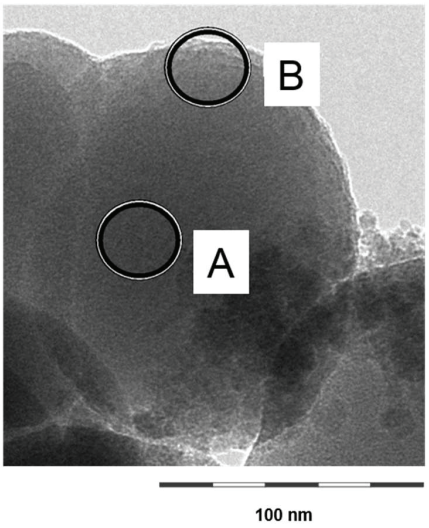


Figure 4: TEM image of Si/C powders. Marked with circles are areas from which EDX spectra were recorded.

is characterised by a lower specific capacity of about 670 mAh/g in the hexagonal structure [15]. Indeed, no reflections that can be attributed to SiC are observed in the diffraction pattern (Fig. 1b).

Figure 4 shows a TEM image of the Si/C composite powder. To study the distribution of Si and C within the Si/C nanoparticle two areas were selected for the EDX analysis: in the centre (A) and close to the surface of the nanoparticle (B). At the particle edge a high C content of about 80 at. % is observed, whereas the Si:C atomic ratio in the area A (particle centre) is about 35:65. The structure of the Si/C composite nanoparticles can thus be described as C-lean in the particle centre and C-rich closer to the particle surface. The underlying mechanism for the formation of this structure can be the initial nucleation of Si nanoparticles in the gas phase which provide a large and highly reactive surface for

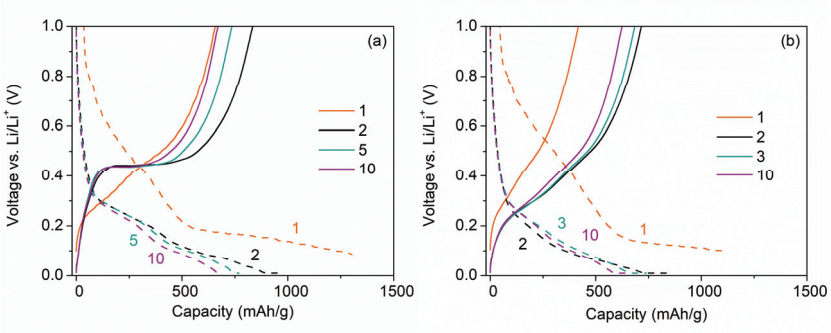


Figure 5: Voltage versus capacity curves for anodes containing (a) pure Si powders and (b) Si/C powders. Solid lines correspond to charge (delithiation) and dash lines correspond to discharge (lithiation). The numbers 1, 2, 3, 5, 10 represent the 1st, 2nd, 3rd, 5th and 10th cycle.

heterogeneous deposition of Si and C species from the reactant gases [16]. The resultant C distribution can be due to a temperature gradient as well as depletion in the Si species along the reactor axis.

This particular Si/C structure is distinctly different from conventional Si@C composites, where Si is coated by/embedded in a carbon layer (see e.g. Ref. [17]) and has direct implication on the electrochemical behaviour. Figure 5 shows voltage versus capacity curves for the pure Si and Si/C composite powders. In the anodes containing pure Si, a characteristic voltage plateau near 0.42 V which is the electrochemical feature of the $Li_{15}Si_4$ formation [7] is observed. In contrast, in electrodes containing Si/C composite powders, the formation of $Li_{15}Si_4$ is effectively suppressed, as confirmed by the absence of the characteristic voltage plateau (Fig. 5b). The sloping voltage curves in the Si/C composites are characteristic of amorphous Si. According to Iaboni and Obrovac [7] the suppression of the $Li_{15}Si_4$ formation occurs under the action of compressive stress. Apparently the specific distribution of C within the Si/C composite nanoparticles leads to a stress state during the expansion/contraction that prohibits the $Li_{15}Si_4$ formation. It should be noted that the electrochemical characterisation was performed on anodes without a composition optimisation and high amounts of Si and Si/C at high areal loadings were used. Nevertheless, it is apparent that the formation of $Li_{15}Si_4$ is detrimental for cycling, i.e. the capacity fade between the cycles 2 and 10 in the Si containing electrode is more pronounced compared to that in the Si/C containing anodes (Fig. 5). Taking into account the amount of Si/C in the electrode the charge capacity of Si/C nanopowders in the first cycle was estimated to be about 3400 mAh/g.

As an additional advantage of Si/C composite powders the beneficial role of carbon should be mentioned. It is well known that bare Si nanoparticles subjected to air are readily oxidised. Elemental analysis of the Si/C composite powder revealed a low oxygen content of 0.6(1) wt. %. The higher C content at the particle surface is advantageous for oxidation protection of the particles, which is desirable in terms of reduction of irreversible Li losses and for improving the workability of the powders during the electrode slurry preparation.

Summary

In this work, a simple and scalable gas-phase synthesis process capable of generating Si-based nanopowders with outstanding electrochemical behaviour is demonstrated. It was shown that the formation of the $Li_{15}Si_4$ phase that is detrimental for cycling can effectively be avoided in the Si/C composite powders. The Si/C powder particles have a particular structure that can be described as C-lean in the particle centre and C-rich closer to the particle surface. The specific C distribution within the particle is apparently responsible for creating a stress state during the expansion/contraction that prohibits the $Li_{15}Si_4$ formation. Furthermore, carbon was shown to be beneficial for oxidation protection and improved workability of the nanopowders.

Acknowledgements

We would like to thank Dr. H. Wiggers and Dr. H. Orthner for experimental support in the preparation of powders and A. Baasner and Dr. S. Dörfler for electrochemical measurements.

References

1. G.E. Blomgren, J. Electrochem. Soc., **164**, 2017, A5019-A5025.

2. T. Placke, R. Kloepsch, S. Dühnen, M. Winter, J. Solid State Electrochem., **21**, 2017, 1939-1964.
3. P. Miller, *Automotive Lithium-Ion Batteries*, Johnson Matthey Technol. Rev., **59**, 2015, 4-13.
4. U. Kasavajjula, C. Wang, A.J. Appleby, J. Power Sources, **163**, 2007, 1003-1039.
5. M.N. Obrovac and V.L. Chevrier, Chem. Rev., **114**, 2014, 11444−11502.
6. M.N. Obrovac and L.J. Krause, J. Electrochem. Soc., **154**, 2007, A103-A108.
7. D.S.M. Iaboni and M.N. Obrovac, J. Electrochem. Soc., **163**, 2016, A255-A261.
8. J.I. Langford, *in* Proceedings of the International Conference on Accuracy in powder diffraction II, edited by E. Prince and J. K. Stalick, U. S. Government Printing Office, Washington, DC, NIST Publication No. 846, 1992, p. 110.
9. M.T. McDowell, I. Ryu, S.W. Lee, C. Wang, W.D. Nix, Y. Cui, Adv. Mater., **24**, 2012, 6034-6041.
10. L. Zhao, D.J. Dvorak, M.N. Obrovac, J. Power Sources, **332**, 2016, 290-298.
11. R. Epur, M. Ramanathan, F.R. Beck, A. Manivannan, P.N. Kumta, Mater. Sci. Engineering B, 177, 2012, 1157-1162.
12. K. Zhao, M. Pharr, S. Cai, J.J. Vlassak, Z. Suow, J. Am. Ceram. Soc., **94**, 2011, S226-S235.
13. J. Lyubina, J. Phys. D: Appl. Phys., **50**, 2017, 053002.
14. I. Kim, G.E. Blomgren, P.N. Kumta, J. Power Sources, **130**, 2004, 275-280.
15. A.L. Lipson et al., J. Phys. Chem. C, **116**, 2012, 20949-20957.
16. N. Rao, B. Micheel, D. Hansen, C. Fandrey, M. Bench, S. Girshick, J. Heberlein, P. McMurry, J. Mater. Res., **10**, 1995, 2073.
17. R.P. Chaukulkar, K.de Peuter, P. Stradins, S. Pylypenko, J.P. Bell, Y. Yang, S. Agarwal, ACS Appl. Mater. Interfaces, **6**, 2014, 19026-19034.

SiC structures and SiC transformations in industrial Si-production

Eli Ringdalen[1],
[1] *Sintef Industry*
Contact: eli.ringdalen@sintef.no

Abstract:

In industrial Si-production, final reduction to silicon is done with silicon carbide SiC as reductant. Carbon added to the furnace will first react with SiO-gas to β-SiC, and at higher temperature transform to other SiC polymorphs grouped as α-SiC. A method has been developed for studying, in laboratory scale, production of β-SiC and its further transformation to α-SiC at temperatures up to 2450 °C. In the laboratory experiments, SiC had to be heated to above 2200 °C to be transformed from β-SiC to α-SiC.

Introduction

Metallurgical silicon (Si) and ferrosilicon (FeSi) are produced in submerged arc furnaces in (SAF) as illustrated in Figure 1.

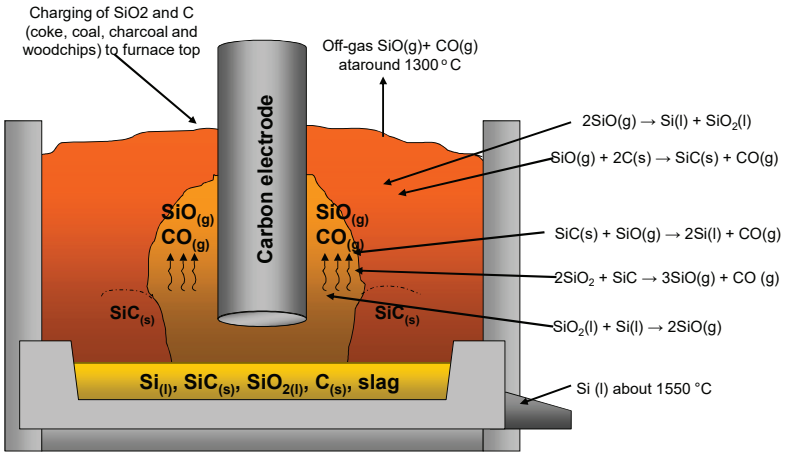


Figure 1: Sketch of Si furnace with critical reactions. Revised after[1].

The two main raw materials are quartz and carbon reductants such as coke, coal, charcoal and woodchips. For FeSi production iron sources are added. Electrical energy, around 11-13 MWh/ton alloy for Si production, is another important input factor. The electrical energy is supplied through electrodes. An electric arc is generated between the electric tip and carbon containing crater walls or liquid silicon bath. This generates a

high temperature zone in the crater where silicon is produced at approximately 2000ºC. Liquid metal, at approximately 1700ºC, is tapped at the bottom of the furnace.

The reduction of silica to Si takes place by the overall reaction (1)

$$SiO_2 + 2C = Si + 2CO \qquad \Delta H^o_{2000^oC} = 687 \text{ kJ/mol} \qquad (1)$$

In industrial furnaces, the reactions take place in several steps as described by Schei et al. [2]. The raw materials are fed to the top of the furnace where the temperature is around 700-1300 °C [3]. In the upper part of the furnace, descending raw materials meet ascending SiO and CO gas. Here carbon react to SiC by reaction (2) and the ascending gases will at decreasing temperature dissociate or react with CO according to reaction (3) and (4). In the lower part of the furnace, where the temperatures reach more than 2000 °C, Si is produced by reaction(7). SiO gas required for this reaction and for SiC production in the upper part of the furnace is produced from SiO_2 by reactions (5) and (6). Dominant reactions and their stability depend strongly on the partial pressures of SiO and CO.

$2C(s) + SiO(g) = SiC(s) + CO(g)$	$\Delta H^o_{1800^oC} = -78$ kJ/mol	(2)
$2SiO(g) = SiO_2(s, l) + Si(l)$	$\Delta H^o_{1800^oC} = -606$ kJ/mol	(3)
$3SiO(g) + CO(g) = 2SiO_2(s, l) + SiC(s)$	$\Delta H^o_{1500^oC} = -1380$ kJ/mol	(4)
$SiO_2(l) + Si(l) = 2SiO\ (g)$	$\Delta H^o_{2000^oC} = 599$ kJ/mol	(5)
$2SiO_2(s, l) + SiC\ (s) = 3SiO\ (g) + CO\ (g)$	$\Delta H^o_{2000^oC} = 1364$ kJ/mol	(6)
$SiC\ (s) + SiO\ (g) = 2\ Si(l) + CO\ (g)$	**$\Delta H^o_{2000^oC} = 167$ kJ/mol**	(7)

Silicon yield is as described by Myrvågnes et al. [4] strongly affected by the rate for reaction(1) and by the SiO-reactivity of carbon materials [5] which is measured by the standard SiO test [6]. SiC is produced at temperatures above around 1500 ºC. The produced SiC will when descend down in the furnace and be further heated up to above 2000 ºC. SiC will as illustrated in Figure 1 form a SiC crust around the cavity at the tip of the electrodes. Electric current will be conducted through the SiC crust and its electric properties are thus also of importance. In the arc, the temperature may reach several thousand degrees. The SiC crust may then be exposed to or form gaseous compounds that require such high temperatures. Reaction (2) between SiO and SiC is described by Schei [2], but not much studied experimentally. It is not known if this reaction is affected by SiC properties. As a basis for future investigations of Si producing reactions, an initial study of changes in structure and properties of SiC in industrial furnaces have been conducted and is presented. Properties of SiC in industrial furnaces is expected to be of importance for reactions in the furnace as well as for energy distribution and material flow. Knowledge about SiC properties and their changes at high temperatures may also be of importance for development of new processes for Si-production.

Properties of SiC and its occurrence in industrial furnaces

The fundamental structural unit of silicon carbide is a covalently bonded primary co-ordinated tetrahedron, either SiC_4 or CSi_4[7,8]. It occurs in a great variety of SiC

polytypes. The cubic polytype is normally referred to as β - SiC. The hexagonal structures (H) and the rhombohedral (R) are all called α - SiC. The number in the polytype name stands for the number of tetrahedron layers in the polytype before it repeats itself. Production of commercial SiC and changes in SiC structures was investigated by Lindstad[9]. It was there found that transformation from β – SiC to α – SiC takes place around 2200°C. In recent experiments by Jayakumari[10] it was observed that the production of SiC is higher with charcoal than coal as a raw material. Once SiC is formed, silicon can easily be produced from charcoal-converted SiC than when compared with coal-converted SiC.

Five industrial Si and FeSi furnaces have been excavated during the last years [11, 12]. Charge with carbon reacted to β SiC was found in all furnaces. The high temperature polymorph α-SiC was found in varying amount in the furnaces, from large amount of crater walls to insignificant amounts.

Experimental

Three principal types of materials have been investigated, commercial coal, commercial SiC and SiC samples taken from excavations of industrial furnaces. The coal has been used to produce SiC that has later been heat treated. Commercial SiC has been heated treated for comparison. SiC found in industrial furnaces have been characterised by the same methods as the raw materials and the products from the experiments. An overview over the materials, experiments and characterisation methods are given in Table 1.

Table 1 Investigated materials and experiments

Exp nr	Raw Material	Produced sample	Experiment	Temperature °C	Gas	Holding time, min	Characterisation methods
1	SiC Thamshavn		Sample from Industrial furnace				XRD, TEM, XPS, Chemical analysis, Microprobe
2	SiC Wacker 12		Sample from Industrial furnace				XRD, TEM, XPS, Chemical analysis, Microprobe
3	SiC Wacker 18		Sample from Industrial furnace				XRD
4	SiC Wacker 104		Sample from Industrial furnace				XRD
5	WM F220		Commercial SiC				XRD, Chemical analysis, Microprobe
6	Coal		Industrial coal, El Cerejon				Microprobe
7	Coal	SiC-4	SiC production ReSiNa furnace	1545	Ar	250	
8	Coal	SiC-5	SiC production ReSiNa furnace	1595	Ar	210	XRD, TEM, XPS, Chemical analysis, Microprobe
9	Coal	SiC-6	SiC production ReSiNa furnace	1645	Ar	240	
10	Coal	SiC-16	SiC production SiO apparatus	1630	Ar		XRD, Chemical analysis, Microprobe
11	SiC WM F220	SiC-1	Heating ReSiNa furnace	2000	Ar	30	
12	SiC WM F220	SiC-2	Heating ReSiNa furnace	2200	Ar	30	
13	SiC WM F220	SiC-3	Heating ReSiNa furnace	2200	Ar	30	XRD
14	Wacker 12	SiC-11	Heating ReSiNa furnace	2000	CO	60	XRD
15	SiC, sample SiC-5	SiC-7	Heating ReSiNa furnace	2000	CO	60	XRD, Chemical analysis, Microprobe
16	SiC, sample SiC-5	SiC-8	Heating ReSiNa furnace	2200	CO		XRD, Chemical analysis
17	SiC, sample SiC-5	SiC-9	Heating ReSiNa furnace	2500	CO		XRD, Chemical analysis
18	SiC, sample SiC-5	SiC-10	Heating ReSiNa furnace	2350	CO	60	XRD, Chemical analysis, Microprobe
19	SiC, sample SiC-5	SiC-12	Heating ReSiNa furnace	2450	CO	4	
20	SiC, sample SiC-5	SiC-13	Heating ReSiNa furnace	2450	CO	5	
21	SiC, sample SiC-5	SiC-14	Heating ReSiNa furnace	2450	CO	7	
22	SiC, sample SiC-5	SiC-15	Heating ReSiNa furnace	2450	CO	45	XRD, Chemical analysis

Materials

The commercial carbon raw materials are a Columbian coal of a type used in industrial Si-production. The commercial SiC used was WM F220 from Washington Mills. This

type of material has often used in laboratory studies of reactions involving SiC. The samples from industrial furnaces are all from Si-furnaces. Two of the samples, Wacker 18 from Wacker fc 4 and Wacker 104 from Wacker fc.1 are from the upper parts of the furnace where the materials have not been exposed to higher temperatures. Two of the samples Thamshavn from Elkem Thamshavn and Wacker 12 from Wacker fc.4 are from the lower, high temperature part of the furnace. Both the high temperature samples are taken from big lumps with large gas channels and with macroscopic crystals of SiC. Macroscopic pictures of the samples are shown in Figure 2 to Figure 5.



Figure 2 *Wacker 104 SiC sample*

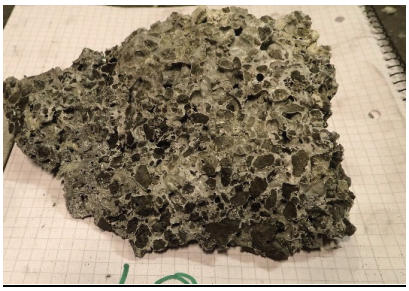


Figure 3 *Wacker 18 SiC sample*

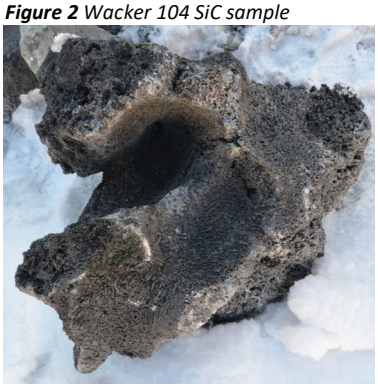


Figure 4 *Thamshavn SiC sample*



Figure 5 Thamshavn, close view

Equipment

Three different types of high temperature experiments were performed. In one experiment SiC was produced from coal in the standard SiO-test apparatus described by Gaal [6]. The two other types of experiments, production of larger amount of SiC from coal and heating of SiC to high temperatures, were both run in the same furnace, a resistance heated graphite tube furnace, able to operate to 2700 °C, the ReSiNa furnace. The furnace has a reaction chamber with possibility for gas purging and a condensation chamber for capturing non-reacted SiO-gas, and is equipped with off-gas measurement system. In the heat-treating experiments, a sample of around 5 grams were placed in the reaction chamber and heated to designated temperature and time. A new set up, shown in Figure 6 was developed for production of larger amount of SiC by reaction (2). The reaction chamber was here divided into a lower part were SiO-gas produced by heating pellets made by a mixture of SiO_2 and SiC. The produced SiO-gas flowed into the upper

part of the chamber filled with coal that reacted with SiO to SiC. The pellets for producing SiO-gas and the temperature was similar to the conditions in the SiO-reactivity test, but the set up allowed use of more material, giving around 30 grams SiC for further heating experiments.

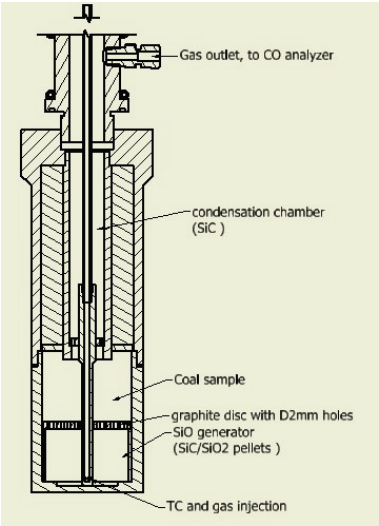


Figure 6 ReSiNa furnace with set up for production of SiC by reaction with produced SiO-gas

Characterization

Raw materials and products were characterised by quantitative XRD, TEM/XPS, chemical analysis and EPMA. Some materials were characterised by all methods and some with fewer as shown in Table 1. The XRD measurements were done by a Bruker D8 Focus X-ray diffractometer using Bruker Topas v5 software and Rietveld-type fitting. The addition of a known quantity of Alumina standard allowed the quantification of the amorphous fraction of the samples. The chemical analyses, done by Sintef Molab, were total carbon (combustion, IR), free carbon (temperature controlled combustion) according to ISO 9286:1997 % SiO_2 was determined by Jis titration and % Si by titration according to Fedorovs method. Based on the chemical analysis, % SiC and % SiO_2 were calculated

$$\% SiC = (C_{total} - C_{free}) \cdot m_{SiC}/m_C = (C_{total} - C_{free}) \cdot 40.1/12.01 = (C_{total} - C_{free}) \cdot 3.339$$

$$\% SiO_2 = 100\% - \%SiC - \%C_{free}$$

Experiments

As shown in Table 1 a total 22 investigations were run. Experiment 1-6 are characterisation of SiC from coal and from other sources, 1-4 are samples from excavations of industrial furnaces, 5 is commercial SiC and 6 is the industrial coal used in further experiments. In experiment 7 to 10 this coal was converted to SiC by SiO - gas at around 1600 °C. In experiment 7 to 9 around 35-gram samples was converted to SiC in the ReSiNa furnace by the new method and in experiment 10 around 5 grams of

coal was converted to SiC in the SiO reactivity test apparatus. The material produced in experiment 10, SiC-5 was in experimented 15-22 heated in CO-atmosphere to different temperatures 2000- 2450 °C. In experiment 11-14 α-SiC was heated to 2000-2200 °C to see if new heat-treatment changed the structure, experiment 11-13 was with commercial SiC and experiment 14 with SiC sample Wacker 12 from excavation if industrial furnace.

Results and discussion

The main results from XRD and chemical analysis are summarised in Table 2. Ratio of the different SiC structures are given relative to total amount of SiC not including % amorphous. This is chosen since % amorphous has not been measured in all samples.

Table 2 XRD and Chemical analysis of investigated samples. % of SiC structures are as % of total SiC not including amorphous

Exp nr	Raw Material	Temperature °C	β SiC 3C	α SiC 2H	α SiC 4H	α SiC 6H	α SiC 8H	α SiC 15 R	Amorphous	Sum α SiC	Free C	SiO2	Free Si	% SiC calc	% SiO_2 calc
1	SiC Thamshavn		0.0	2.6	2.6	67.3	3.1	24.4		100.0	0.1	0.7	1.0	97.6	1.3
2	SiC Wacker 12		6.1	0.0	3.5	66.7	3.7	20.0		93.9	0.1	7.7	0.7	89.6	9.6
3	SiC Wacker 18		100.0	0.0	0.0	0.0	0.0	0.0	30	0.0					
4	SiC Wacker 104		100.0	0.0	0.0	0.0	0.0	0.0	45	0.0					
5	WM F220		0.0	0.0	15.7	81.1	0.0	3.2	21.1	100.0	0.1	1.0	1.0	98.8	0.1
13	SiC WM F220	2200	2.9	1.3	10.1	73.3	4.5	7.9		97.1					
14	Wacker 12	2000	0.0	0.4	1.9	89.1	3.5	5.1		100.0					
6	Coal	0	0.0					0.0	*100*						
10	Coal	1630	100.0	0.0	0.0	0.0	0.0	0.0	16.3	0.0	4.4	2.6	0.5	90.7	4.4
8	Coal	1595	100.0	0.0	0.0	0.0	0.0	0.0		0.0	19.4	0.4	0.6	81.1	-1.2
15	SiC, sample SiC-5	2000	100.0	0.0	0.0	0.0	0.0	0.0	50.7	0.0	20.6	0.2	0.5	81.1	-2.2
16	SiC, sample SiC-5	2200	100.0	0.0	0.0	0.0	0.0	0.0	61.8	0.0	17.9	0.1	0.6	83.1	-1.7
18	SiC, sample SiC-5	2350	33.3	0.0	3.6	50.1	0.0	13.0	36.1	66.7	22.1	0.1	0.5	76.8	0.6
22	SiC, sample SiC-5	2450	45.1	0.0	9.0	45.8	0.0	0.0	71.2	54.9	32.1	0.2	0.8	69.1	-2.0
17	SiC, sample SiC-5	2500	28.1	0.0	3.6	58.0	0.0	10.3	47.3	71.9	24.4	0.1	0.6	76.8	-1.8

Reaction between SiO and coal to β-SiC

The original coal (exp6) is amorphous. Reaction with SiO at around 1600 °C will as expected give β-SiC with some amorphous phase left. No α-SiC was found in samples produced at this temperature. SiO-reactivity test and new method in the ReSiNa furnace gave similar results.

Heating of β-SiC

When heated to 2350 °C, β-SiC was partly converted to α-SiC. Occurrence of the different phases are shown in Figure 7. No phase transformation had taken place at or below 2200 °C. After 60 minutes at 2350 °C, 67 % of the SiC was α-SiC. The main polymorph was 6H with also some 15R. Even after heating to 2500 °C, the samples contained free carbon and amorphous material, most likely a mixture of SiO_2 and C. Only insignificant amounts of free Si were found.

Amount of amorphous phase seemed to vary both with temperature and holding time both below and above 2200 °C with holding time being just as important as temperature. This is also reflected in the total amount of SiC. Due to the low number of experiments, this is only indicative and no clear conclusions can be drawn regarding change in amount of amorphous phase

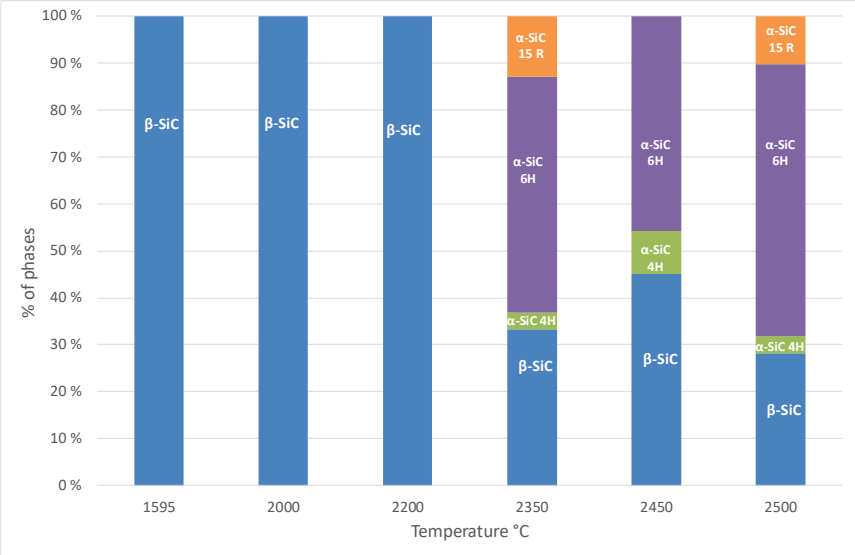


Figure 7 SiC phases in heat treated SiC at different temperatures

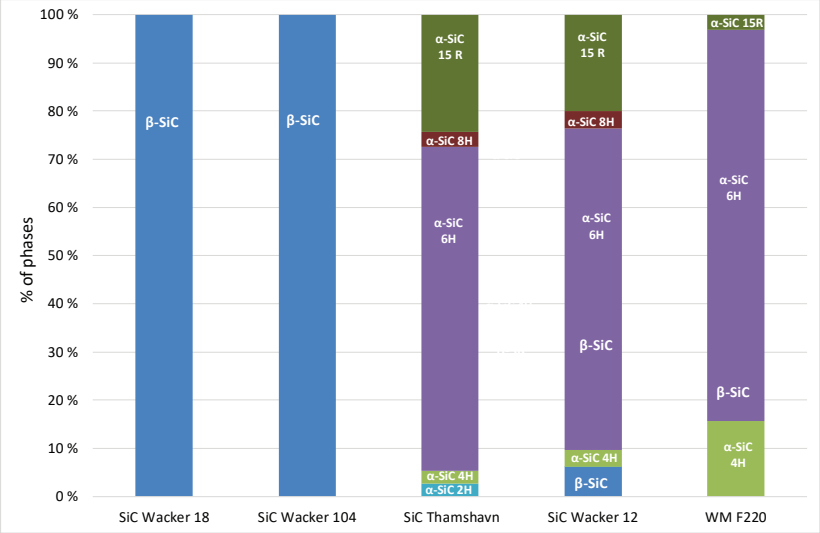


Figure 8 SiC phases in samples from excavations

Comparing SiC from industrial excavations with SiC heated in laboratory.

Samples Wacker 18 and Wacker 104 taken from the upper part, the loose charge in two different furnaces, contained β-SiC as the only SiC phase, similarly to the samples heated up to 2200 °C. Amount of amorphous phase in these were also in the same range, around 50 %. This indicate that the loose charge found in the industrial furnaces have not been exposed to higher temperatures than 2200 °C, but may have been exposed up to these temperatures. The effect of gas phase, SiO in addition to CO in the industrial furnaces and only CO in the laboratory experiments, may affect the results. This has not been investigated.

Samples Thamshavn and Wacker 12 form SiC crust found in the lower part of the furnaces during excavation have as shown in Figure 8 similar content of SiC phases as samples heated to 2350 °C and above. The major difference is that the samples heated in the laboratory still contains considerable amount, up to 45 % β-SiC while this is found only in insignificant amounts in the industrial samples These also had a higher SiC content. The main α-SiC polymorph was in both types 6H.
Comparison of the industrials samples with laboratory heated SiC indicate that the SiC in the SiC crust has been exposed to temperature above 2200 °C, and either considerably longer holding time than the maximum of 60 minutes used in the experiments, or higher temperatures. Also, here the different gas atmospheres may affect the results. The laboratory samples were exposed only to CO, while the industrial samples in addition to CO was also exposed to high concentrations of SiO- gas and may be also gaseous C in the industrial furnace. These effects were not studied and should be further investigated.

Commercial SiC, WM F220 also contained only α-SiC with 6H as the main polymorph, but with less 15 R and more 4H than the industrial samples. Commercial SiC is often used as SiC source when reactions with SiC is studied. The difference in content of the various polymorphs may affect the reaction rates, especially for conditions below 2200 °C were only β-SiC is expected. The effect of SiC polymorphs should in such cases be considered.

Heating and transformation from β-SiC to α-SiC also changed the macroscopic and microscopic structure of the samples as shown in Figure 9. The low temperature material containing β-SiC had a rather smooth macroscopic surface and a microscopic structure revealing the original coal structure. Material heated to 2350 °C that had partly transformed to α-SiC seemed to have small crystals on the surface and a more dense microscopic structure. This resembles the samples from the industrial excavations although these had much larger and prominent t crystals. The changes in structure found by EPMA as well as the TEM and XPS might give useful information regarding mechanisms for phase transformations. This is beyond the scope of this paper and is not further discussed here.

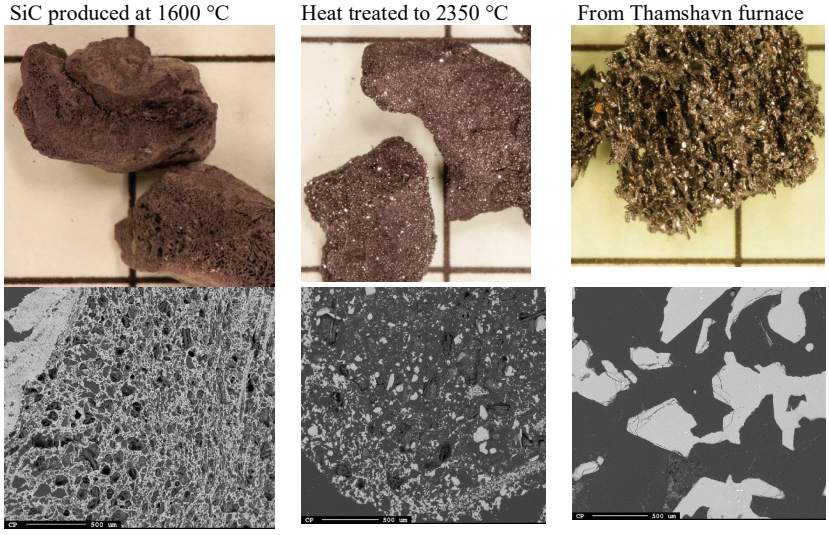


Figure 9 Macroscopic and microscopic appearance of different SiC samples**.**

The observed differences in microscopic structure and in content of the various SiC phases and polymorphs may affect mechanisms and rate for reactions with SiC in industrial furnaces. The work by Jayakumari[10] indicate that properties of SiC are affected by properties of the raw carbon sources while this work indicate that they in addition are affected by temperatures and retention times. To clarify if reactions in the furnace are affected by SiC properties and thus by these parameters are crucial for understanding reactions in the furnace.

Conclusions

SiC produced from coal and SiO- gas at 1600 °C consisted only of β-SiC. This is similar to SiC in loose charge found in upper parts of industrial furnaces. Heat treatment up to 2200 °C did not change the SiC phases while SiC heated to 2350 °C and above contained mainly α-SiC similarly as in the crust in industrial furnaces. This indicates that the loose charge may have been exposed to temperatures up to 2200 °C. Phases present varied with temperature and retention time and has by other been reported to depend on carbon source. It is not known if reactions with SiC are affected by SiC polymorphs. But if this is the case, they will also be affected by the parameters mentioned above.

Acknowledgements

This work has been done by project 235123 Silicon production with use of natural gas SiNG, funded by Elkem as and Research Council of Norway. Cooperation with SFI Metal Production has also contributed to the work. They are all acknowledged.

References

1. Kvande R: Trial Lecture, PHD dissertation, Trondhein, Norway 2008
2. A Schei A., J K Tuset J.K., and H. Tveit, Production of High Silicon Alloys, Tapir forlag, Trondheim, Norway, 1998, ISBN: 82-519-1317-9.
3. Ringdalen, E. and Tangstad, M: Reaction Mechanisms in Carbothermic Production of Silicon, Study of Selected Reactions, Proceedings of International Smelting Technology Symposium (Incorporating the 6th advances in sulphide smelting) held during TMS 2012, Editors: Jerome P Downey, Thomas P Battle, Jesse F White p. 195 – 204. ISBN 978-1-11829-116-0

   Myrvågnes V, Lindstad T: The importance of coal- and coke properties in the production of high silicon alloys; INFACON 12, 2010, Helsinki, Finland
4. Edin H Myrhaug: Non-fossil reduction materials in the silicon process -properties and behaviour, PhD Thesis 2003:67, NTNU, Norway 2003, ISBN 82-471-5619-9
5. S Gaal, T Lindstad, S Hansen, S Prytz: Improved SINTEF SiO reactivity test t, INACON 11, 2007, New Delhi, India
6. Volker Presser, K.G. Nickel: Silica on silicon carbide: Critical Reviews in Solid State Material Sciences, 33;2-99, 2008, ISSN 1040-8436, DOI:10.1080/10408340701718914
7. V. A. Izhevskyi1, L. A. Genova, J. C. Bressiani, A. H. A. Bressiani.: Review article: Silicon Carbide. Structure, Properties and Processing: Cerâmica vol.46 n.297 São Paulo Jan./Feb./Mar. 2000, Print version ISSN 0366-6913On-line version ISSN 1678-4553
8. Lindstad L: Recrystallization of Silicon Carbide, Dr. Ing. Thesis, NTNU, Trondheim, Norway, March 2002
9. Sethulakshmy Jayakumari and Merete Tangstad: Silicon Carbide formation from coal or charcoal in the silicon/ferrosilicon process: Infacon XV: International Ferro-Alloys Congress, Edited by R.T. Jones, P. den Hoed, & M.W. Erwee, Southern African Institute of Mining and Metallurgy, Cape Town, 25–28 February 2018
10. Ksiazek M, Tangstad M, Ringdalen E: Five furnaces, five different stories; Silicon for the chemical and Solar Industri XIII, Norway 2016
11. Tangstad M, Ksiazek M, Faaness B: Zones and Materials in the SI-furnace; Silicon for the Chemical and Solar Industry XII, Norway 2014.

Cracks, Disintegration and Phases Transformations in Quartz

Karin Fjeldstad Jusnes[1)], Merete Tangstad[1)], and Eli Ringdalen[2)]
1) Norwegian University of Science and Technology
2) Sintef Industry

Abstract

Eleven samples from four different quartz types were scanned with X-ray Computed Tomography (CT) to measure the amount of cracks in each sample. All samples were then shock heated at 1500 °C, and sieved at 2, 4, 10 and 20 mm. The different size fractions from one sample from each type were investigated with X-ray diffraction to measure the amount of quartz transformed to either an amorphous state or cristobalite. The amount of transformed quartz varied from type to type, but not from one size fraction to another. The amount of fines below 10 mm, which varied from 6 to 85 %, were compared with the amount of cracks measured. A correlation was found: as the amount of cracks increased, the fines generated by shock heating generally increased. There was no correlation between the amount of fines and the amount of transformed quartz. Type D, which produced the smallest amount of fines, also had the largest amount of transformed quartz.

Introduction

Silicon and ferrosilicon are produced in a submerged arc furnace, where quartz and reduction materials such as coal, charcoal and wood chips, are fed at the top. Electrical energy is supplied to the process through three carbon electrodes. The raw materials descend in the furnace, and several chemical reactions occur. The overall reaction for the process is given in reaction 1. In reality, the process is much more complex. The quartz will first react with either liquid silicon or silicon carbide, as shown in reaction 2 and 3, respectively. The gas produced will ascend in the furnace, and meet the carbon materials added. SiO gas will react with carbon, as seen in reaction 4. The extent of this reaction depends on the SiO reactivity of the raw materials. A higher SiO reactivity is favourable because more SiO will react to produce SiC. The SiO which does not react with carbon will continue to ascend, and in the end be oxidised when it meets oxygen at the charge surface. The two substances, SiO and SiC, are produced in reaction 2, 3 and 4, and liquid Si can then be produced according to reaction 5. The product can be tapped from the bottom of the furnace. Schei et al. [1] gives a thorough explanation of the silicon production process.

$$SiO_2(s) + 2C(s) = Si(l) + 2CO(g) \quad (1)$$
$$SiO_2(s,l) + Si(l) = 2SiO(g) \quad (2)$$
$$2SiO_2(s,l) + SiC(s) = 3SiO(g) + CO(g) \quad (3)$$
$$SiO(g) + 2C(s) = SiC(g) + CO(g) \quad (4)$$
$$SiO(g) + SiC(s) = 2Si(l) + CO(g) \quad (5)$$

The surface of the charge could be up to 1300 °C, but will vary in time depending on the furnace conditions [2]. When the raw materials meet the charge they will be shock heated from room temperature. This sudden increase in temperature could make the raw materials disintegrate in various amounts. For different quartz types, the amount of fines produced will vary. It is favourable to limit the amount of fines in a silicon or ferrosilicon furnace because fines could affect the operations in several ways. When larger particles break up into smaller particles it will make the charge more compact. This would lead to decreased gas permeability in the furnace. An illustration of this can be seen in Figure 1. If the gas flow is hindered, a pressure could build up in the charge and create small outbursts of gas or channelling. Then the SiO gas will have less time to react with the carbon in the upper part of the furnace, and Si atoms are lost from the furnace. This will lower the silicon yield of the process, which has a negative economic effect.

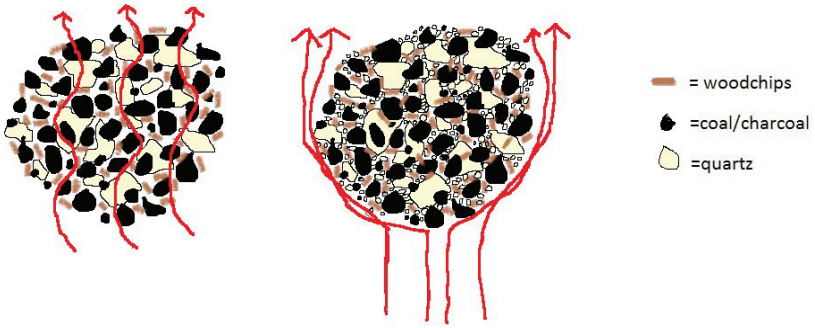


Figure 1: Increased amount of fines will affect the gas permeability in a silicon or ferrosilicon furnace.

When the quartz disintegrate, the surface area available for reactions will increase. It was calculated by Jusnes [3] that for one specific type of quartz the surface area could increase by a factor of 9. This might increase the extent of reaction 2 and 3. It is not favourable for the process that the quartz starts to react high up in the furnace. Then the gas produced will not be in the high temperature zone where it is needed for silicon production. The relative importance of the parameters affected by quartz disintegration, are not fully known.

Several researchers [3]–[6] have investigated the disintegration of different quartz types. Their findings agree that there are large variations in the amount of fines produced from one quartz type to another. In Figure 2, a clear difference in the amount of fines from two quartz types can be seen.



Figure 2: The amount of fines for two different quartz types after shock heating at 1500 °C [3].

This paper investigates if the differences in the amount of fines could be related to cracks in the samples existing before heating. Eleven samples from four different quartz types are scanned with computed tomography (CT) before shock heated at 1500 °C. The amount of cracks are measure for each samples from the CT-scans, and compared to the amount of fines produced after shock heating. The silica phases were also measured for the different size fractions after shock heating, to see if there was a correlation.

Experimental Procedure

Eleven quartz samples were investigated in this study. They were from four different quartz types. The different types are denoted A, D, F and G, and the different experiments within a type are denoted with numbers. The quartz samples were crushed with a hammer to obtain the desirable size of approximately 200 g each. A sample from each type can be seen in Figure 3.

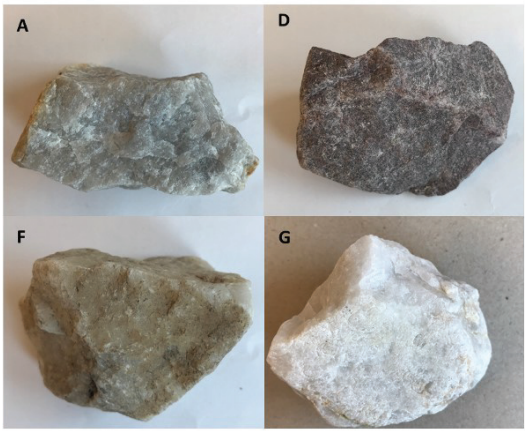


Figure 3: The four quartz types used in this study.

X-ray Computed Tomography (CT)

A X-ray computed tomography was done on all the samples to see images of the cross sections. The scans were performed with a Nikon XT H225 ST instrument. All samples were covered with aluminum foil to make them more stable on the sample holder. The settings for the instrument were 140 kV and 200 µA. The software ImageJ was used to measure the amount of cracks on the pictures.

Shock Heating

A carbon crucible with an inner diameter of 11 cm and height 38 cm were heated to 1500 °C in an induction furnace. A type C thermocouple was used to measure the temperature during the experiments. An alumina tube and a carbon tube protected the thermocouple from the crucible. A piece of Kaowool was placed on top of the crucible during heating to decrease heat loss from the top of the furnace. When the temperature had reached 1500 °C, the quartz samples were placed inside the crucible one at a time, and kept there for 10 minutes. Afterwards, the content in the crucible was poured into a cold graphite crucible to cool. The quartz samples were sieved at 2, 4, 10 and 20 mm and each size fraction weighted. These results were compared with earlier and similar results by Jusnes [3].

XRD-measurements

From each quartz type, a sample was taken from each size fraction of a sample after shock heating. These samples were analyzed with X-ray diffraction to measure the proportion of different silica phases. The samples were milled and then dried overnight at 250 °C to remove any moisture from the samples. To measure amorphous content in the samples, a highly crystalline spike was added to all the samples in a known amount. This, internal standard method, is thoroughly described by Kjelstadli [7]. Back loading equipment was used to prepare samples that could be analyzed in the Davinci 1 Diffractometer. Topas software was used to analyze the result and determine the phases for the different size fractions. Two or three samples were analyzed from each size fraction to confirm the result and determine the sample variance.

Results and Discussion

Crack area

All samples were scanned in the CT instrument. One example image from each sample can be seen in Figure 4, Figure 5, Figure 6 and Figure 7 for quartz type A, D, F and G, respectively. The cracks observed in the samples varied in thickness from 0.05 mm up to 0.2 mm. Some larger cavities were observed in some of the samples. These were up to 2 mm in width. Some of the cracks are easily seen on the images below, while others were not visible except at high magnification in the software ImageJ. Underneath each of the following figures, the observations from studying the whole image sequence are listed. The sequences from each experiment contains more than a thousand images.

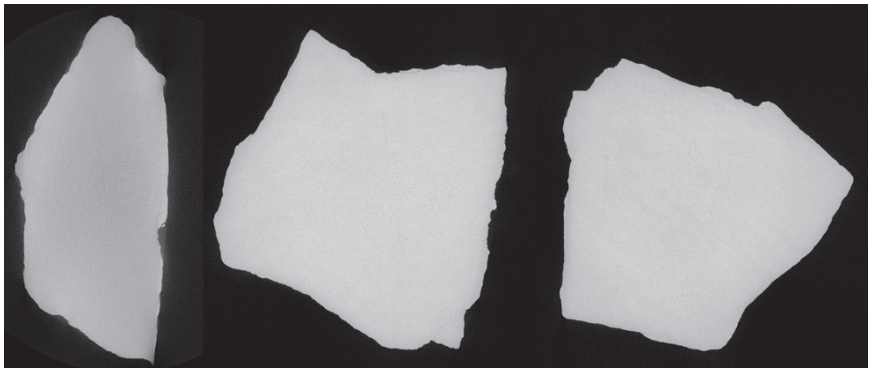


Figure 4: CT images from quartz sample A(4) (left), A(5) (middle) and A(6) (right).

- A(4): few cracks, one small cavity, very homogeneous
- A(5): few cracks, two small cavities, more cracks towards one of the ends
- A(6): few cracks, more cracks towards one of the ends

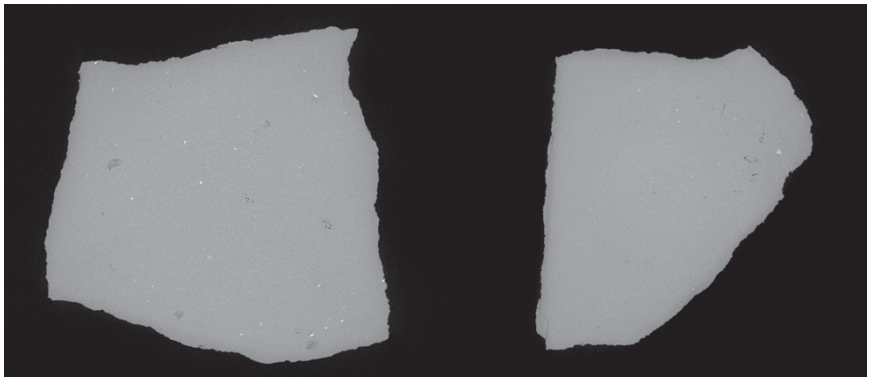


Figure 5: CT images from quartz sample D(4) (left) and D(5) (right).

- D(1): white small dots, porous areas, few cracks
- D(2): white small dots, porous areas, few cracks but clearer than in D(1)

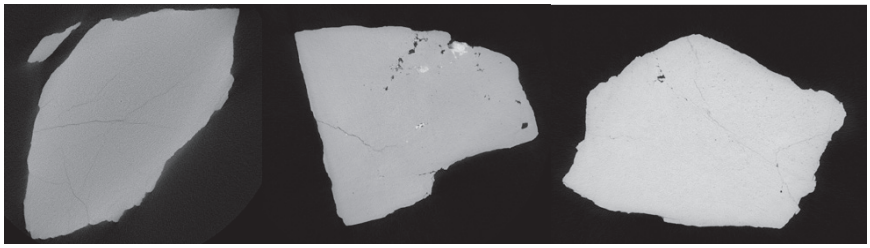


Figure 6: CT images from quartz sample F(4) (left), F(5) (middle) and F(6) (right).

- F(4): more cracks than type A and D, slightly thicker cracks

- F(5): small black holes, cracks with cavities, also independent cavities, white areas
- F(6): cavities through the whole sample, small black dots, cracks

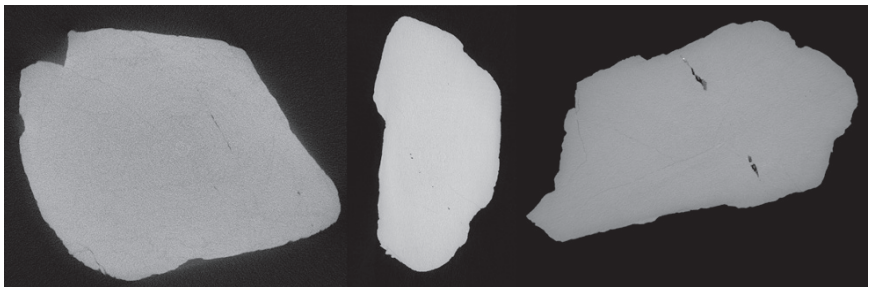


Figure 7: CT images from quartz sample G(1) (left), G(2) (middle) and G(3) (right).

- G(1): many faded cracks, a few cavities along cracks
- G(2): cracks with elongated cavities, fewer but clearer cracks than G(1), minor cavities
- G(3): cracks, cavities, and elongated cavities along cracks, some small black dots, some areas in different grey scale

The amount of cracks were measured and recorded with the ImageJ software. First, the total area was measured, then each crack length were marked and measured. The thickness varied, but an estimated average thickness was used for each image. In Table 1 the average % crack area is listed for each sample. 3-12 images evenly spread out in the sequence were analysed for each sample.

Table 1: The crack area for each quartz sample measured from CT images.

Sample	% crack
A(4)	0.197
A(5)	0.21
A(6)	0.369
D(4)	0.239
D(5)	0.247
F(4)	0.741
F(5)	0.642
F(6)	1.436
G(1)	1.13
G(2)	0.234
G(3)	0.308

Amount of fines

The amount of fines generated by the shock heating varied, as expected based on earlier results [3]. In Figure 8, a sample from each quartz type can be seen. Type D

disintegrated the least, while type F, closely followed by type G, created the largest amount of fines.

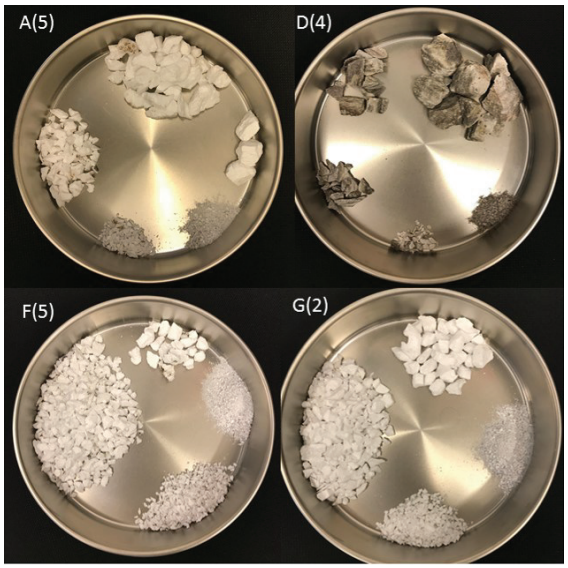


Figure 8: The four quartz types after shock heating to 1500 °C.

From the weighted size fractions from the shock heating, a representation of the cumulative wt% was constructed. It can be seen from the graph in Figure 9 that the amount of fines in different sizes fractions varies a lot. For fines below 10 mm, the number varies from 6 % to 85 %. It can also be seen that there is agreement between the different parallels from the same quartz type, except sample G(1) which is considered to be an outlier. The D type produced the least amount of fines and F type produced the most. This is in agreement with earlier and similar results from Jusnes [3]. A comparison which includes these results can be seen in Figure 10. In both Figure 9 and 10 it can be seen that the variation between quartz types is larger than the variations within a quartz type.

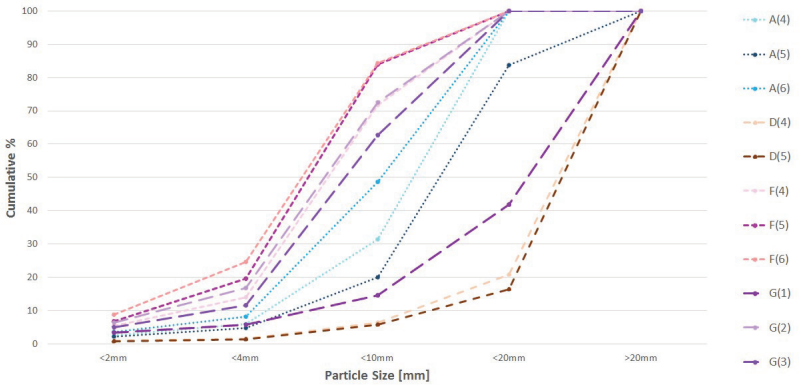


Figure 9: The cumulative representation of the wt% fraction from shock heating different quartz samples to 1500 °C.

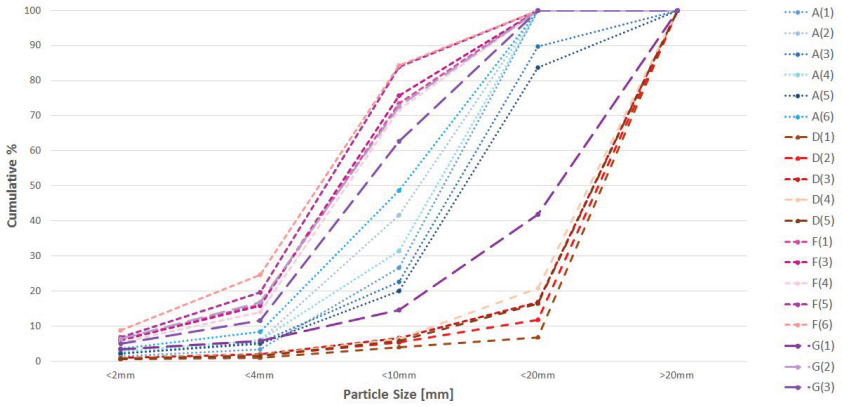


Figure 10: The cumulative representation of the wt% fraction from shock heating different quartz samples to 1500 °C. Results from Jusnes [3] are included in this figure.

Fines and cracks

In Figure 11 the amount of fines below 10 mm and the crack area are plotted together to see if there is any correlation. Sample A, D and G all have between 0.2 and 0.4 % cracks. Sample F has above 0.6 % cracks. Sample G(1) are considered as an outlier. Both the amount of cracks and fines are very different from the other two G samples. If sample G(1) is discarded, an overall trend can be spotted. As the amount of cracks increases, the amount of fines below 10 mm from shock heating also increases.

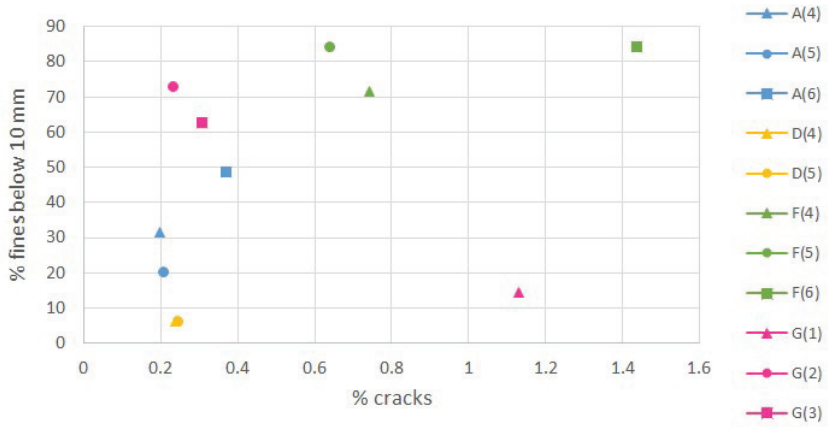


Figure 11: Amount of fines below 10 mm compared with % crack area for the different quartz types A, D, F, and G.

Proportion of phases

The amount of phases from the different size fractions after the shock heating were measured by X-ray diffraction. Both the size fraction and the type of quartz were compared to see any trend in the amount of phases. All quartz types contained between 12 and 36 % amorphous material after shock heating. The amount of cristobalite varied from 1 to 17 %. No clear trend of the different phases could be seen when comparing the different size groups.

When comparing the different types of quartz and amount of phases, a trend is seen. Type D has the largest amount of transformed quartz (amorphous + cristobalite), around 50 % for all samples. This can be seen in Figure 12. Type A has the least amount of transformed quartz, 20-30 %, while type G and F has approximately the same amount of transformed quartz around 30-40 %. This means that the type of quartz has an influence on the proportion of each phase.

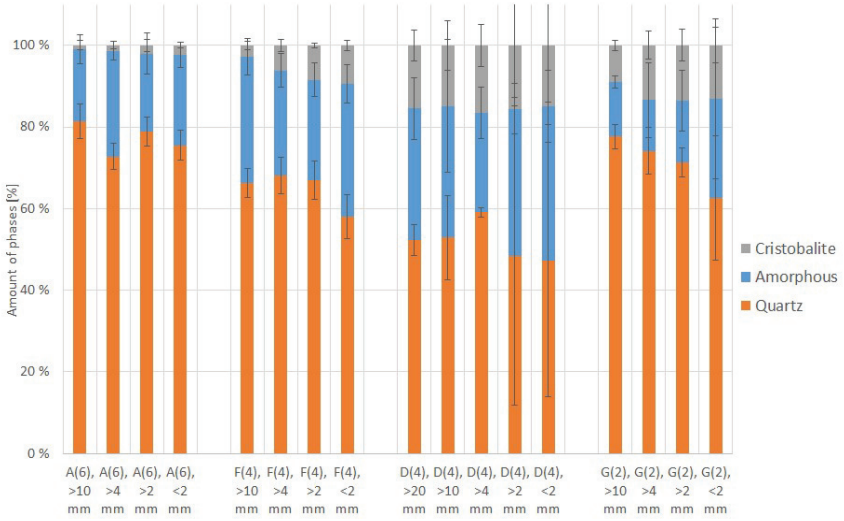


Figure 12: Amount of phases in different quartz types after shock heating to 1500 °C.

Fines and phases

The amount of transformed quartz was compared with the amount of fines generated from the shock heating. No correlation was observed between the two parameters, as can be seen in Figure 13. Every point in this graph is the average from 4-5 measurements of phases in different sized samples. Type D had the largest amount of transformed quartz for all size fractions, but also produced very little fines for both samples tested. Earlier tests with quartz type D also found that it only produced a small amount of fines below 10 mm [3]. This implies that the propensity to transform into other polymorphs is not the determining factor for fines generation, and vice versa.

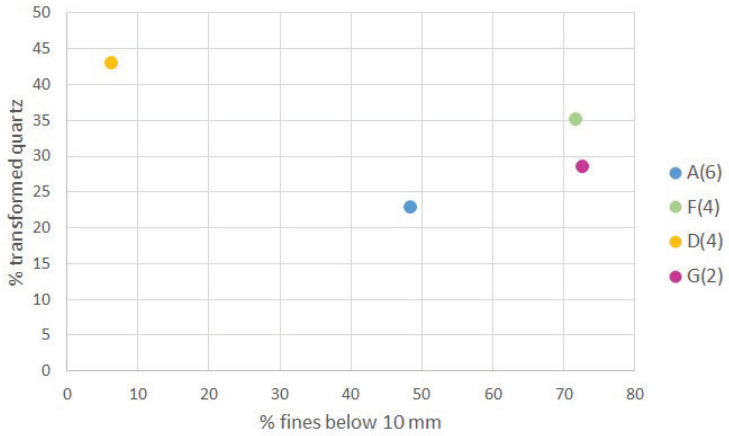


Figure 13: Amount of fines compared with amount of transformed quartz after shock heating to 1500 °C.

Conclusion

Four different quartz types used in silicon and ferrosilicon production have been studied. The aim was to investigate possible correlations between the quantity of fines produced during thermal shock and the amount of cracks in the quartz before testing, or the propensity for quartz to change phase during thermal shock. All 11 samples from 4 different quartz types were scanned with X-ray computed tomography before being shock heated at 1500 °C. After this treatment, the amount of phases were measured in all the size fractions for each quartz. The following were found for the quartz types A, D, F and G.

- The amount of fines below 10 mm varies between 6 and 85 %. D produces the least amount of fines, F the most.
- Shock heating transforms quartz to an amorphous phase and cristobalite, varying between 20 and 50 % transformed quartz.
- In this study X-ray computed tomography was used to measure cracks down to 0.05 mm.
- There is no correlation between the phases measured after shock heating and the different size fractions of the samples.
- There is a correlation between the phases measured and the type of quartz.
- There is a correlation between the amount of cracks measured and the amount of fines generated. The amount of fines increases as the amount of cracks increases. The trend is not very clear.
- There is no correlation between the amount of fines and the proportion of transformed phases. Sample D, which had the largest amount of transformed quartz also had the least amount of fines. This could imply that the propensity to transform into other polymorphs is not the determining factor for fines generation, and vice versa.

Acknowledgment

This paper is published by permission of Elkem AS. Financial support from The Research Council of Norway and Elkem Technology is appreciated, through the project High Temp Quartz – Methods for characterization of quartz properties predicting performance in high-temperature applications with project number 252212.

References

[1] A. Schei, J. K. Tuset, and H. Tveit, *Production of High Silicon Alloys*. Trondheim: Tapir, 1998.

[2] S. T. Johansen, H. Tveit, S. Gradahl, A. Valderhaug, and J. A. Byberg, "Environmental Aspects of Ferro-Silicon Furnace Operations-An Investigation of Waste Gas Dynamics," p. 5.

[3] K. F. Jusnes, M. Tangstad, and E. Ringdalen, "Shock Heating of Quartz used in Silicon and Ferrosilicon Production," presented at the Infacon XV: International Ferro-Alloys Congress, Cape Town, South Africa, 2018, vol. 15.

[4] K. Aasly, "Properties and behavior of quartz for the silicon process," Doctoral Thesis, Norwegian University of Science and Technology, Trondheim, 2008.

[5] F. O. Bakken and C. O. Paulsen, "Thermal stability of quartz for silicon process," Department of Materials Science and Engineering, Norwegian University of Science and Technology, 2013.

[6] E. Ringdalen, "Quartz Properties in the silicon production," presented at the Silicon for the Chemical and Solar Industry XII, 2014.

[7] M. E. Kjelstadli, "Kinetics and Mechanism of Phase Transformations from Quartz to Cristobalite," Master Thesis, Norwegian University of Science and Technology, Trondheim, 2016.

Cavity formation in silicon furnaces

Raghed Saadieh[1,2)], Merete Tangstad[2)], and Harald Wegge[1)]
1)Elkem ASA Technology, Kristiansand, Norway
2) Norwegian University of Science and Technology (NTNU), Trondheim, Norway

Abstract

The production of high silicon alloys plays an important role in the Norwegian economy. In recent years, excavations of various submerged arc furnaces have helped shed light on the internal workings of the production process. It is postulated that one of the key features of Si/FeSi furnaces is the presence of a cavity around the electrodes, resulting from the condensation of SiO(g). Industrial excavations revealed that a cavity is formed in certain furnaces but not all. The focus of this article is to shed more light on the mechanism behind the formation of the cavity using small scale laboratory equipment. Brown and white condensates of SiO has been identified in the experiments and are believed to be the main reason behind cavity formation since they glue the charge together and prevent any further downward movement of the charge. An induction furnace was used to simulate the production of various FeSi alloys under different parameters, including temperature, type of carbon reductants, amount of iron in the system and the effect of a SiO source on cavity formation. It was found that the cavity is formed faster in the case where iron was found in larger amounts and temperature played only a minor effect. The addition of SiO source, as in a $Si+SiO_2$ layer, at the beginning of the experiments had the predict effect of facilitating cavity formation in the case of FeSi75 and 96. On the other hand, for FeSi52, this layer hindered the formation of the cavity and the exact reason behind this behaviour is remains unidentified. Lastly, a mechanism for cavity formation is proposed based on the observations from the experiments.

Introduction

Silicon (Si), second only to oxygen, is the most abundant element in earth's crust [1]. The production of Si and ferrosilicon (FeSi) alloys plays an important role in the Norwegian economy, with Norwegian ferroalloy producers supplying around 10% and 5% of the worldwide production of Si and FeSi respectively [2]. Various FeSi grades are typically denoted as FeSiXY, e.g. FeSi52, where XY is the weight % of Silicon in the alloy. The production processes for Si and FeSi are very similar and are usually carried out in submerged arc furnaces (SAF) of varying capacities. It is a carbothermic production process, where silicon dioxide (SiO2) in the form of quartz is mixed with carbonaceous materials such as coke, coal and charcoal, which act as reductants, transforming the quartz oxide into Si alloy. In the case of FeSi, various iron (Fe) sources, such as scrap iron and ore pellets, are added. Woodchips are the last major component of the raw materials mix and are usually used to ensure good permeability of the charge during Si/FeSi. The large amount of heat required by these processes is supplied by the electric arc through the electrode, and typical energy consumption ranges between 11-13MWh per ton of Si produced [3]. The overall simplified reaction of the process can be written as

$$SiO_2(s)+Fe_xO_y(s)+2C(s)=Si(l)+xFe(l)+(2-y)CO(g)+yCO_2(g) \quad (1)$$

Several articles discussing industrial furnaces excavations have been published recently [4]–[7] and several of these excavations were described in more details in the master thesis of Bø [8] and Andersson [9]. In the work of Ksiazek et. al [4], excavation results from five different furnaces are discussed. According to them, a cavity surrounding the electrodes was not always present and in the case of a furnace producing FeSi52, the production process has been described as running on a coke bed. The discrepancy in the observations of a cavity formation has been attributed to the shutdown routine of the furnace, especially the movement of the electrodes, as well as furnace geometry and operational history. In the doctoral thesis of Myrhaug [10], the internals of a 150kWh pilot scale furnace are presented. He described the presence of two cavities, one near the electrode and another one located in the upper parts of the furnace. The presence of the cavity in the upper parts was attributed to the condensation of silicon monoxide (SiO). Moreover, several small-scale laboratory studies have been carried to investigate the mechanism of cavity formation [11]–[13] where the main focus was on silicon monoxide (SiO) condensation reactions. These investigations were carried out in a 75kW induction furnace using graphite crucibles filled with a combination of silicon carbide (SiC), quartz and carbon reductants. The condensates are believed to act as a binder gluing the charge together and preventing it from sinking further into the hot zone of the crucible. Two types of condensates were evidenced: a white and brown condensate. The white condensate consists of a mixture of SiC and SiO2, and it is assumed to be the product of the following reaction:

$$3SiO(g)+ CO(g) = SiC(s) + 2SiO_2(l,s) \qquad \Delta H_{1500°C} = -1404\ kJ/mol \quad (2)$$

On the other hand, the brown condensate appears to consist of Si droplets dispersed in a SiO2 matrix, and are assumed to be the product of the following reaction:

$$2SiO(g) = Si(l) + SiO_2(s,l) \qquad \Delta H_{1500°C} = -616\ kJ/mol \quad (3)$$

The enthalpies of these reactions were calculated using HSC 7 [14]. In the presence of carbonaceous reductants, SiO(g) will react with C to form SiC according to the following reaction:

$$SiO(g)+ 2C(s) = SiC(s) + CO(g) \qquad \Delta H_{1800°C} = -74\ kJ/mol \quad (4)$$

In the work of Vangskåsen et al. [12], quartz particles extracted from the condensation zone appeared to be surrounded by a thin layer of white condensate followed by a thicker layer of brown condensate. This implies that the white condensate formed at a lower temperature, followed by the brown condensate at slightly higher temperatures. Samples of these condensates were tested for compressive strength, and Vangskåsen [12] reported values as high as 400MPa. He also stated that these condensates were constrained to regions where the temperature (T) was lower than 1700°C. Ksiazek et al came to the same conclusion, stating that the cavity roof was formed around 1720°C, close to the melting temperature of the quartz used in their work. More recently, Sloman et al. [15] developed a mathematical model to describe the Si furnace, which is based on small scale experiments similar to the ones mentioned above. These experiments were carried out in Elkem as are referred to as 'Pilot Furnace Process Simulators'. They found out that the

position of the cavity roof is largely dictated by temperature and is the result of production of SiC and condensation of SiO.
The focus of this paper revolves around the formation of the cavity during the production of Si/FeSi using small-scale laboratory experiments. The effect of temperature, holding time, iron content in the alloy on cavity formation is discussed. In addition, observations relating to the effect of various carbon reductants and Si+SiO_2 layer on cavity formation will be presented. And lastly a mechanism for cavity formation in these small-scale experiments will be suggested.

Experimental

The experiments were carried out in an induction furnace, with a 75kW power limit. The experimental setup is described in detail in the author previous publication [16] and is similar to the setup used in [11]–[13]. Graphite crucibles were filled with industrial raw materials, supplied by Elkem, including quartz, iron ore pellets, coke and woodchips with the end goal of producing various FeSi grades (52, 75 and 96). In addition, in some experiments, a layer of finely crushed Si and quartz was added to the bottom of the crucible to enhance the production of SiO(g). Furthermore, preliminary experiments where coke was substituted with coal or charcoal has been carried out. The chemical composition of the various raw materials used is presented in Table 1. When switching from one FeSi composition to another, only the amount of iron ore pellets was changed. The carbon content in all experiments was chosen to yield a FixC content of 100%. After the start of the experiments, continuous addition of raw materials was carried out to ensure a constant charge level.

Table 1: Chemical composition of the various raw materials used.

	Weight % (Dry basis)				
Raw material	Fix C	Ash	Volatiles	SiO_2	Fe
Coke	90.8	4.7	4.5	-	-
Coal	56.9	4.5	38.6	-	-
Charcoal	74.8	0.5	24.7	-	-
Quartz	-	-	-	99.1	-
Iron ore pellets	-	-	-	-	67.1

The temperature in the crucibles was measured using two Type-C tungsten/rhenium thermocouples, with the reference measurement located at the bottom of the crucible, where the hottest zone is. The other thermocouple, referred to as auxiliary thermocouple, was used to measure the temperature in other areas of interest mainly located at 25cm and 30cm from the bottom of the crucible. At 25cm from the bottom, the temperature near the condensation zone is measured whereas at 30cm from the bottom it served as an indication of the temperature near the top of the charge. The various experimental

conditions used through the experiments are presented in Table 2. Some aspects and results from experiments 1-8 are described in the authors previous work [16]. The holding temperature (T_h) is defined as the set target temperature at which the crucible is held for a defined period, defined as holding time (t_h). The average holding temperature is given calculate over the period of the holding time.

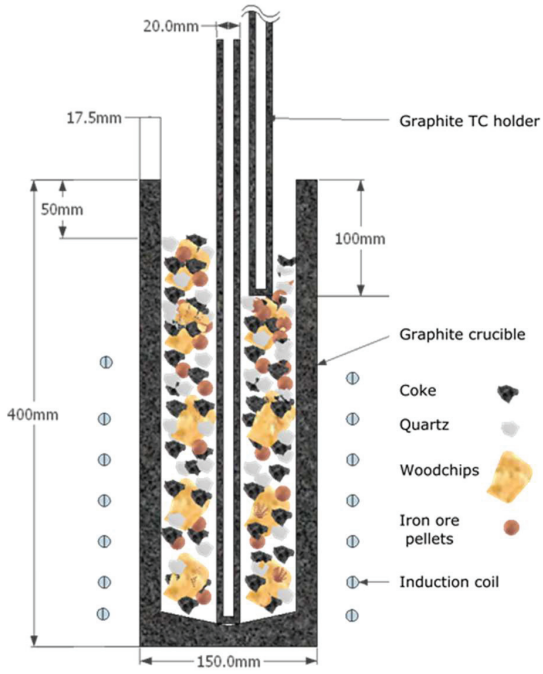


Figure 1: Schematic of the experimental setup, adapted from [16].

At the end of the experiments and after the crucibles have cooled down, a two-component epoxy was added to hold the charge together. The crucibles were then cut longitudinally, and the resulting cross sections were then photographed. Core samples were drilled at various positions in the crucible, and then examined using the scanning electron microscope (SEM). The distinct phases present were identified using the data collected from the energy dispersive spectrometry (EDS).

Table 2: Summary of the experimental conditions.

Experiment	Target Si (wt%)	T_h (°C)	t_h (min)	Type of carbon	$Si+SiO_2$ layer	Aux. TC position (cm)
1 (2)	52	1851 ±1	30	Coke	No	30
2 (3)	52	1885*±14	30	Coke	No	30
3 (4)	75	1854 ±4	30	Coke	No	30
4 (5)	75	1903 ±3	30	Coke	No	30
5 (6)	96	1853 ±4	30	Coke	No	30
6 (7)	96	1900 ±3	30	Coke	No	30
7 (8)	52	1901 ±4	30	Coke	No	30
8 (9)	96	1906 ±3	60	Coke	No	30
9 (10)	52	1907 ±2	30	Coke	Yes	25
10 (11)	75	1907 ±3	30	Coke	Yes	25
11 (12)	96	1906 ±3	30	Coke	Yes	25
12 (13)	52	1905 ±3	30	Coke	Yes	25
13 (14)	52	1905 ±3	30	Coke	No	25
14 (18)	52	1903 ±3	30	Coal	No	25
15 (19)	52	1902 ±2	30	Charcoal	No	25

*The average holding temperature was <1900°C due to a problem with the thermocouple.

Results and discussion

The condensates

After examining various cross sections from the experiments, the brown condensate was very easily distinguishable. On the other hand, the white condensate was harder to observe. Figure 2 shows the brown condensate observed in a sample from experiment 2. A molten quartz particle can be surrounded by a layer of Si droplets in an SiO_2 matrix. The appearance of this layer is very similar to that reported by Vangskåsen et al. [12].

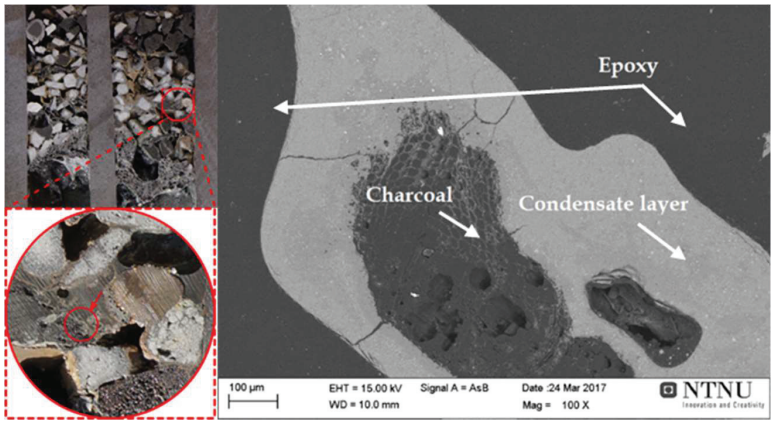


Figure 2: Sample from experiment 2 showing brown condensate layer above the cavity, adapted from [16].

Figure 3 shows the white condensate observed in a sample from experiment 1. A thin condensate layer, less than 200µm thick, can be seen surrounding a coke layer. It was very hard to distinguish the white colour by the naked eye, and the EDS analysis was used to identify the chemical composition of it (Table 3).

Due to the carbon coating of the samples, around 20at% carbon will always be detected. In this case, the average actual carbon content of the white condensate layer is 8.8at%. the molar ratio of [C:O:Si] is approximately 1:4:3 which corresponds to the molar ratio of the products from reaction (2). The appearance of this condensate is very similar to that reported by Vangskåsen et al. [12].

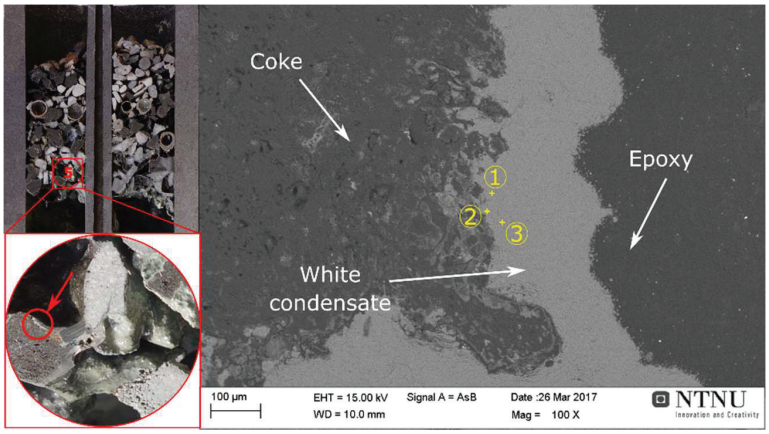


Figure 3: Sample from experiment 1 showing the white condensate layer.

Table 3: EDS point analysis of the white condensate

	Chemical composition (atomic %)			
	C	O	Mg	Si
Point 1	27.1	43.3	0.7	28.9
Point 2	30.1	37.7	0.5	31.6
Point 3	29.2	38.0	0.6	32.2
Average	28.8 ±1.6	39.7 ±3.2	0.6 ±0.1	30.9 ±1.8

Cavity formation

The general trend observed in the experiments is that the cavity formation was strongly correlated to the presence of the condensates mentioned above. And as was already discussed, the condensates are the result of the condensation reaction of SiO(g) as in reactions (2) and (3). Hence, in case a cavity was absent, it can be attributed to lack of SiO(g) generation in the hot zone of the crucible. The interaction between the various experimental parameters on cavity formation is complex and will be discussed in the following sections.

Effect of Fe content and temperature

This section will deal mainly with the results observed in experiments 1-8, which are summarized in Table 4. Cross sections from experiment 2,4,6-8 can be seen in the author previous work [16]. When iron is present in large amounts (experiments 2 and 3) a cavity

was formed. However, at lower iron content, a cavity was not formed (experiments 3-6). Experiment 7 was a duplicate of experiment 2, and similar results was observed. When a cavity was formed, the increase in holding temperature (Th) from 1850°C to 1900°C shifted the cavity roof slightly upwards in the crucible. By increasing the holding time (t_h) to 60min (experiment 8) a crater was formed, and that was for a target composition of FeSi 96. This strongly suggests that the presence of iron lowers the energy requirement for Si reduction. It has been suggested by Chrysanthou et al. [17] that Fe can have a catalytic effect on SiC formation, which will ultimately lead to SiO(g) generation through reaction (5).

$$2SiO_2(s,l) + SiC(s) = 3SiO(g) + CO(g) \qquad \Delta H_{2000°C} = 1353\ kJ/mol \qquad [5]$$

Table 4: Summary of results from experiments 1-8.

Experiment	1	2	3	4	5	6	7	8
Target Si (wt%)	52	52	75	75	96	96	52	96
Cavity formed	Yes	Yes	No	No	No	No	Yes	Yes

Effect of Si+SiO_2 layer

To test the hypothesis that the lack of SiO(g) generation is the previous experiments was the main reason behind the absence of the cavity, another set of experiment was carried out where a Si+SiO_2 layer was added to the bottom of the crucible before the start of the experiments. Theoretically, the SiO(g) generation will occur through the reverse of reaction (3). Results from experiments 9-12 are summarized in Table 5 and cross sections from selected experiments in Figure 4.

Table 5: Summary of results from experiments 9-12.

Experiment	9	10	11	12
Target Si (wt%)	52	75	96	52
Cavity formed	No	Yes	Yes	No

In the experiments 10 and 11, where the target was to produce FeSi75 and FeSi96 respectively, a cavity was formed. This observation validates the hypothesis that SiO(g) will be generated by the Si+SiO_2 layer in the bottom zone of the crucible, which will then condense in cooler zones higher up in the crucible, preventing the charge from sinking. On the other hand, the absence of the crater in the case of FeSi52 was unexpected. The absence of the cavity can be partially attributed to the decrease in Si activity with increasing amount of Fe. As the iron ore pellets are reduced, metallic iron will reach the hot zone and will dissolve the Si in the layer. As a result, the Si activity decreases, and

the equilibrium of reaction (3) shifts to the right, decreasing the production of SiO(g). In other words, the effect of the Si+SiO_2 layer is negated and the system should behave in a similar manner to that in experiments 2 and 7. At this moment, the authors cannot explain the discrepancy observed and further experiments are needed to pinpoint the root cause.

Effect of various carbonaceous reductants

To study the effect of various carbon reductants on cavity formation, coke in experiment 13 has been substituted with coal for experiment 14 and with charcoal in experiment 15. Results from experiments 13-15 are summarized in Table 6 and the cross sections of experiments 14-15 are presented in Figure 5.

Table 6: Summary of results from experiments 13-15.

Experiment	13	14	15
Target Si (wt%)	52	52	52
Type of carbon	Coke	Coal	Charcoal
Cavity formed	Yes	Yes	Yes

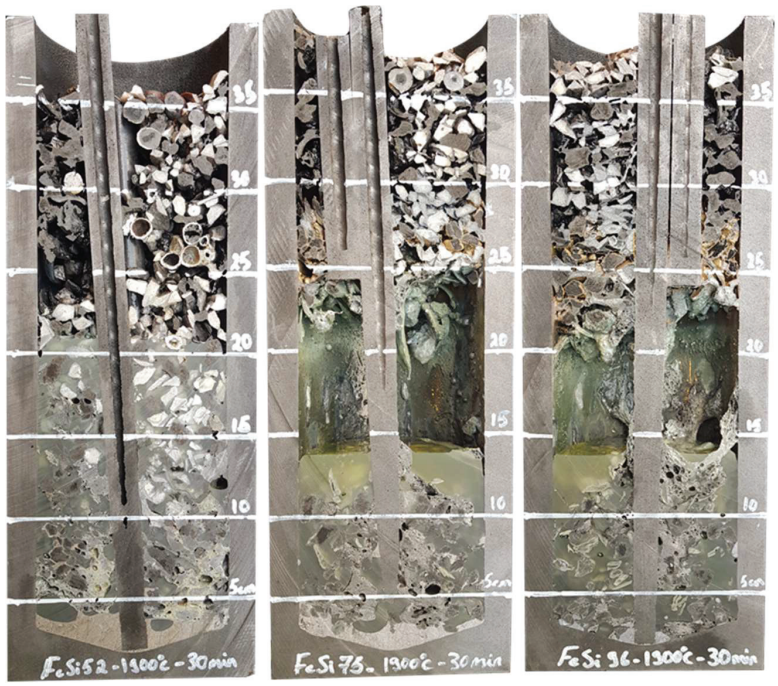


Figure 4: Cross section of experiments carried with Si+SiO_2 layer, from left to right experiment 9,10 and 11.

It is well known that various carbon materials exhibit varying SiO reactivities, defined as the ability of capturing SiO(g) to form SiC according to reaction (4). Charcoals exhibit the highest SiO reactivity followed by coal then coke. The results from experiments 13-15 are consistent and a cavity was formed in all of them. The cavity roof is established at around the same levels in the crucible, around 27.5cm from the bottom. The only difference is by the amount of partially reacted materials in the hot zone, which was the largest in case of coke and smallest for charcoal. This can be explained by the fact that when using coke, the density of the charge is the highest, resulting in more material reaching the hot zone. It can be concluded that the nature of the carbon reductant plays a minor role in cavity formation. Our observation agrees well with those of Sloman et al. [15] who stated that varying the ratio of SiO_2:C in the charge will have a much larger effect on cavity formation than the carbon SiO-reactivity.

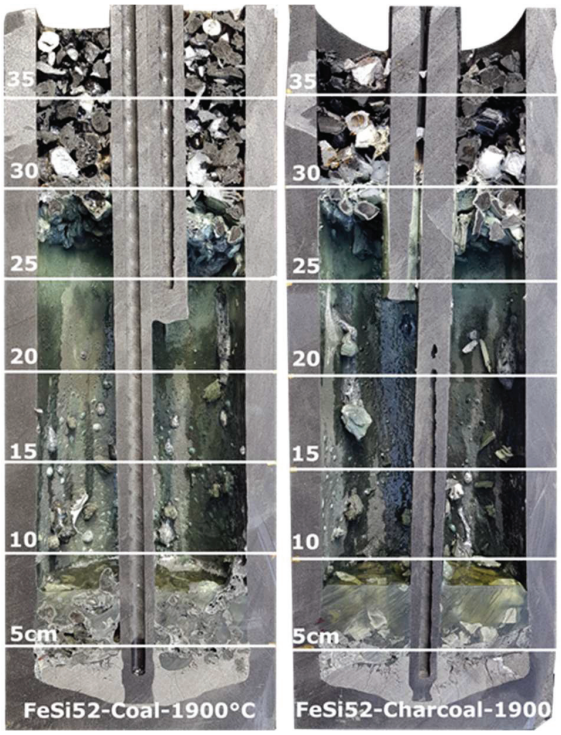


Figure 5: Cross section of experiment 14 (left) and 15 (right).

Cavity formation mechanism

In all the experiments, it was observed that as the temperature inside the crucible increased, the charge top started slowly sinking and fresh batches of raw materials were added. Once the holding temperature was reached, the charge seemed to stop sinking and

hence the charging of raw materials stopped. This is a result of a thermal profile being established in the crucible, preventing further melting of raw materials. This can be seen clearly in experiments where the crater was not formed e.g. experiment 9, where the level of molten materials is constrained to the bottom 10cm from the bottom of the crucible. Once chemical reactions started, raw materials were consumed at the bottom of the crucible, SiO(g) was generated and ascended through the charge. When the temperature was low enough higher up in the crucible, SiO condensed and glued the charge together. A similar mechanism was reported by Vangskåsen et al. [12].

In Figure 6, temperature recorded by the auxiliary thermocouple, located at 25cm from the bottom of the crucible, are plotted versus time. The origin of the x-axis is the point where the holding temperature is reached in the hot zone. When a cavity was not present, i.e. experiment 12, the temperature recorded at that level in the crucible was relatively low and reached a maximum of 1400°C. On the other hand, in experiments 13-15, where FeSi52 composition was targeted, the temperature was the highest and was on average >1700°C. By looking at the cross-sections of these experiments (Figure 4 and Figure 5), the cavity roof is located above the point where the temperature is measured. In experiments 10-11, where FeSi75 and 96 compositions were targeted respectively, the temperature recorded was on average around ~1500°C. By looking at the cross-sections of these experiments (Figure 4 and Figure 5), we can see that the cavity roof is located at the same level as the temperature measured. The higher temperatures observed when cavities are formed are possibly the result of the highly exothermic condensation reactions. In addition, it is also apparent that the melting of quartz plays a key role in determining the size of the zone located above the cavity.

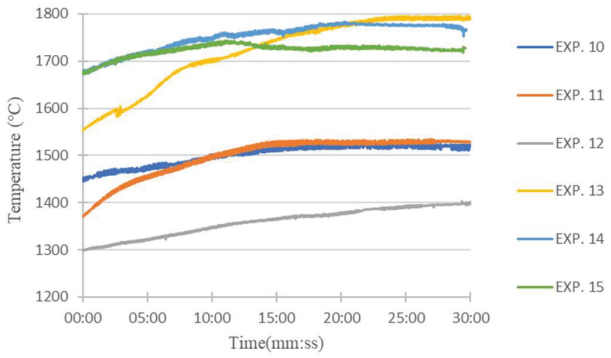


Figure 6: Plot of the auxiliary thermocouple temperature versus time for experiments 10-15.

Conclusions

It was shown that the cavity formed during Si/FeSi production is due to condensation of SiO(g). In accordance with the literature, two types of condensates were identified: a white condensate consisting of SiC+SiO_2 and a brown condensate consisting of Si+SiO_2. The addition of Fe to the system appears to lower the energy required for reactions leasing to SiO(g). Using a layer consisting of Si+SiO_2 as a source of SiO lead to the formation of a cavity in experiments where a cavity was absent. On the other hand, in the presence of large amount of iron, the addition of this layer hindered the formation of the cavity. The substitution of coke by coal or charcoal did not have a significant effect on cavity

formation, and the appearance of the crucibles is very similar. The position of the cavity roof is a function of both temperature high up in the crucible and melting point of quartz, with the former being dependent on the amount of iron present in the system.

Acknowledgments

This paper is partially funded Elkem ASA and published by their permission. The scientific contributions of my colleagues at Elkem are gratefully acknowledged. Special thanks for the Norwegian Research Council for partially funding this industrial PhD program (Project nr. 264146).

References

[1] "silicon | Properties, Uses, Symbol, & Facts | Britannica.com." [Online]. Available: https://www.britannica.com/science/silicon. [Accessed: 24-Apr-2018].

[2] M. Tangstad, *Metal production in Norway*. Oslo: Akademika Publ., 2013.

[3] A. Schei, *Production of high silicon alloys*. Trondheim: Tapir, 1998.

[4] M. Ksiazek, M. Tangstad, and E. Ringdalen, "Five furnaces five different stories," in *Silicon for the Chemical and Solar Industry XIII*, 2016.

[5] M. Tangstad, M. Ksiazek, and J. E. Andersen, "Zones and materials in the Si furnace," in *Silicon for the Chemical and Solar Industry XII*, 2014.

[6] F. A. Weber, L. Parous, and V. D. De Oliveira, "PHASE CHEMISTRY OF DIGOUT SAMPLES FROM A FERROSILICON FURNACE," no. 2, pp. 255–264, 2013.

[7] G. Tranell, M. Andersson, E. Ringdalen, O. Ostrovski, and J. J. Steinmo, "Reaction zones in a FeSi75 furnace - results from an industrial excavation," *Infacon XII Sustain. Futur.*, vol. 1, no. 5, pp. 709–715, 2010.

[8] S. Marie Bø, "Phases and Zones in the Silicon Process," Norwegian University of Science and Technology, 2016.

[9] M. Andersson, "Reaction Mechanisms in the Ferrosilicon Production Process," Luleå University of Technology, 2009.

[10] E. H. Myrhaug, "Non-fossil reduction materials in the silicon process : properties and behaviour," Department of Materials Technology, Norwegian University of Science and Technology, Trondheim, 2003.

[11] M. Ksiazek, M. Tangstad, and E. Ringdalen, "Silicon production in laboratory scale induction furnace," 2015.

[12] J. Vangskåsen and M. Tangstad, "CONDENSATE IN THE METALLURGICAL SILICON PROCESS- REACTION MECHANISMS," no. 2, pp. 255–264, 2013.

[13] M. Tangstad, M. Ksiazek, V. Andersen, and E. Ringdalen, "Small scale laboratory experiments simulating an industrial silicon furnace," *Proc. 12th Int. Ferroalloys Congr. Sustain. Futur.*, pp. 661–670, 2010.

[14] A. Roine, "HSC Chemistry 7." Outotec, 2009.

[15] B. M. Sloman, C. P. Please, R. A. Van Gorder, A. M. Valderhaug, R. G. Birkeland, and H. Wegge, "A Heat and Mass Transfer Model of a Silicon Pilot Furnace," *Metall. Mater. Trans. B*, vol. 48, no. 5, pp. 2664–2676, Oct. 2017.

[16] R. Saadieh, M. Tangstad, and H. Wegge, "Simulation of the Ferrosilicon Process Using Small-Scale Laboratory Furnace," in *Infacon XV*, 2018.

[17] A. Chrysanthou, P. Grieveson, and A. Jha, "Formation of silicon carbide whiskers and their microstructure," *J. Mater. Sci.*, vol. 26, no. 3463, 1991.

Silicon for the Chemical and Solar Industry XIV
Svolvær, Norway, June 11 – 14, 2018

CFD modelling for the metallurgical grade silicon production

Evangelos Bertakis[1)], Randi Synnoeve Hegdal Chapana[1)], and Ronald Eulenberger[1)]
1) Wacker Chemie AG

Abstract

A computational fluid dynamics (CFD) simulation of the freeboard, the smoke stack and the doghouse of an electric arc silicon smelting furnace was configured using a mass and energy balance of the carbothermic process. The model included the combustion of the process gas in the freeboard and the condensation of SiO_2. The microsilica particles were tracked through the computational domain in order to determine the conditions under which the smoke can escape the furnace hood and doghouse. Improvements of the equipment were made based on the findings that lead to a reduction of diffusive dust emissions from the furnace.

Introduction

When the SiO gas from the furnace hearth reacts with oxygen in the air, SiO_2, commonly called dust, is made. If the smoke hood has a sub-optimal design, the dust created above the charge can escape out through the doors of the hood instead of being drawn into the filter by the suction in the smoke hood. This is especially critical when the doors are opened to stoke the furnace and during SiO outbursts. If the doghouse is not designed properly, the dust can escape out into the inner environment instead of being drawn into the filter by the ventilation system. This is especially critical during furnace gassing through the taphole. It is therefore important that the doghouse and smoke hood designs can also handle these cases when dust formation is extensive.

Dust emission both to inner and outer environment is an unwanted part of silicon production. Although dust is a valuable by-product when collected in the filters, it can lead to health problems when emitted to an indoor environment and it is crucial that the doghouse and smoke hood have a design which reduces these emissions as much as possible. With an optimal design, the suction can be improved without simply increasing the suction, which leads to a lower energy consumption. The NOx emissions can also be reduced since the temperature under the smoke hood will be more evenly distributed and hot spots above the charge creating thermal NOx are avoided.

In this work a series of stationary CFD simulations using ANSYS-CFX were performed that led to a better understanding of the flow phenomena in the furnace freeboard and the doghouse. Various design choices for the smoke hood geometry were thus made, while the doghouse was considerably improved, thereby leading to a new patent application [10].

CFD Model

Two different 3D geometries were used with the CFD model, one depicting the furnace freeboard, including the smoke hood and stack, while the doghouse was simulated separately. The geometry was discretized using a tetrahedral grid that was locally refined in order to resolve the narrower passageways of the fluid flow, like e.g. the gaps under the smoke hood doors.

The model is comprised of the physical equations that need to be solved on the grid, the appropriate boundary conditions on every surface and the material properties of all chemical species. The physical equations are:

- The Navier-Stokes equations for continuity and momentum (including buoyancy).
- The Shear Stress Transport (SST) turbulence model equations.
- The thermal energy transport equation.
- The radiation transport equation using the differential approximation (P1) model.
- A transport equation for each of the chemical species in the gas phase except nitrogen that was used as a constraint component.
  - The gaseous chemical species considered in this work are: C_2H_6, C_6H_6, CH_4, CO, CO_2, H_2, H_2O, NH_3, O_2, SiO and SiO_2.
  - The transport equations include the appropriate sink and source terms for each species that are generated by the combustion reactions in the freeboard.

In order to take the condensation of SiO_2 into microsilica particles into account, a mass sink term was implemented in the transport equation for SiO_2 that eliminated that component from the gas phase as soon as it was generated using the reaction rate calculated by the CFD solver. A respective heat source term released the condensation energy in the gas phase. This method has the advantage that the SiO_2 can be defined as a gaseous component using the correct material properties like density and enthalpy while the phase change is modelled separately. The drawback is that an extra transport equation needs to be solved for SiO_2 on the grid, which is superfluous since the SiO_2 mass that gets eliminated by the condensation sink term is then taken into account using a one-way coupled Euler-Lagrange particle tracking model. The one-way coupling here is justified because the microsilica particles are small and their mass and volume fractions in the geometry are negligible. The Euler-Lagrange particle tracking model included the Schiller-Naumann drag force and the turbulent dispersion force.

The Eddy Dissipation Model was used for calculating the reaction rate of the combustion reactions [3]. This model makes the assumption that the chemical reaction is mixing-limited, i.e. that the reaction rate is determined by the mixing between the hot process gas coming from the furnace hearth and the ambient air in the freeboard. This assumption is valid as long as the chemical reactions are fast and the turbulence relatively weak, which is generally true for such combustion reactions and large-scale deflagrations. By making these assumptions the complicated combustion mechanisms that include radicals and several intermediate species as well as the respective Arrhenius kinetic rates can be completely ignored and the reaction rates can be calculated using only the local species concentrations and information provided by the turbulence model.

The Eddy Dissipation Model usually includes two equations, one for taking into account the mixing between the fuel and the oxidizer and the other for taking into account the mixing between the hot combustion products and the fresh reactants that are usually cold and need to be ignited in order to combust. It is postulated that the hot combustion products are those that ignite the cold reactants and the two therefore need to be mixed in order for the reaction to proceed, which could be a rate-limiting step. In the standard formulation of the Eddy Dissipation Model the reaction rate is calculated

using both equations and the smaller of the two is used further in the CFD simulation. This formulation originally aimed at making the model suitable for both diffusion and premixed flames. However, in the case of the silicon furnace, the fuel is preheated in the furnace hearth and is already hot (ca. 1000 ºC) when it meets the air in the freeboard. The hot combustion products are therefore not needed to ignite the fuel and oxidizer. For this reason, the so-called product limiter equation of the Eddy Dissipation Model was turned off and only the one for describing the mixing between the fuel and the oxygen in the air was used. This has the added benefit that the SiO_2 condensation had no adverse effects on the calculation of the reaction rate between SiO and O_2, as it is the case when both equations of the Eddy Dissipation Model are used in multistep reaction mechanisms.

Boundary conditions

The 3D geometry of the CFD simulation starts at the taphole level and ends at the point where the flue gas pipeline meets the trombone air cooler. The outer wall of the crucible was included, as well as the building floors separating the tapping, the charging and the electrode levels. Although the very slow furnace rotation was neglected, the gap between the crucible rim and the charging floor was taken into account in the simulation. Ambient air was thus allowed to flow between the tapping and the charging levels. On the charging floor, the smoke hood with its 10 doors and the area around it was included in the geometry. Under normal operation conditions, all the hood doors were assumed to be fully lowered. Each hood door had two holes and at the fully lowered position remained a 10 cm distance from the crucible rim. Above the charging floor only the smoke stack and the flue gas pipeline were considered. An overview of the geometry is given in Figure 1.

The furnace freeboard was defined by the upper surface of the charge, which means that the CFD simulation did not include the furnace hearth. This is important, since the hearth gas needs to be defined as an inlet gas for the CFD simulation in terms of both amount and chemical composition. The charge surface was empirically separated into three zones around the electrodes for defining an uneven distribution of the process gas. This takes into account that the hearth gas is released into the freeboard mostly through an area around the electrodes and its flow rate diminishes as we move away from the electrodes towards the crucible rim. The composition of the hearth gas was the same in all three zones and its temperature was empirically set at 1000 ºC.

For simulating the freeboard behaviour under stocking conditions, a small round surface was defined between two electrodes. Under normal conditions that surface is included in the inner charge zone. Under stocking conditions the round surface is used to define the inlet of an extra amount of hearth gas that is supposedly released when the upper crust of the charge material is breached. Under normal conditions the mass flow and composition of the hearth gas is estimated using a mass and energy balance for the complete furnace. However, the amount of extra “stocking” gas is calculated based on assumptions for the volume and duration of the gas “burst” that is experienced during stocking. In addition, the composition of the stocking gas is assumed to be 50% v/v CO and 50% v/v SiO and does not include any coal or woodchip volatiles. It is also assumed that a stocking operation must be performed with two doors completely raised in order to provide access to the furnace freeboard. For this purpose the geometry was modified and a new grid was generated.

Within the freeboard, the geometry included the three electrodes, the outer surfaces of the electrode equipment like the pressure ring and the electrode shield as

well as the 10 charging tubes. The freeboard is covered by the water-cooled smoke hood that is connected to the smoke stack, which is mostly indoors. Outside the furnace building the smoke stack is connected to the flue gas pipeline, which defines the outlet of the simulation on which the total amount of flue gas needs to be defined. The entrainment of ambient air in the freeboard was taken into account by defining an "opening" condition on the simulation boundary at the tapping and charging levels. This enables the free flow of 25 °C air at 1 atm into the simulation domain that is then allowed to enter the freeboard under the hood doors, through their holes and through the gaps between doors. However, the "opening" boundary condition does not force a certain amount of air into the domain. Therefore, should the conditions in the freeboard change, as is the case during stocking, the amount of entrained air is allowed to be adjusted dynamically by the simulation software. Under extreme conditions gas will even be allowed to exit the computational domain through the opening surface.

All walls were simulated as smooth with the no-slip boundary condition. For the radiation model all walls were defined as opaque black bodies. All non-cooled surfaces, such as the building floors and the hood doors, were defined as adiabatic. The temperature on the crucible wall was set to 50 °C. The temperature of the electrodes in the freeboard was set to 1000 °C (carbon surface). The temperature on the walls of the water-cooled smoke hood was estimated using data from the water-cooling system and was set to 61.5 °C. Likewise, the water-cooled walls of the chutes and the electrode equipment were given a temperature of 38 °C. In order to simulate the passive cooling of the smoke stack, a heat transfer coefficient of 15 W/(m^{2}K) was set on its surface and the ambient air temperature was set to 25 °C. For the flue gas pipeline that is outside the furnace building a heat transfer coefficient of 25 W/(m^{2}K) and an ambient temperature of 20 °C were used to account for the wind and the cooler environment.

Within the freeboard, several secondary air inlets need to be taken into account. These include the air used for preventing the smoke from escaping through the charging tubes and air blown between the electrodes and the hood for the same purpose. Since composite electrodes are used the furnace considered in this work, the paste tempering air is also allowed to enter the freeboard, although the geometry is strongly simplified at this point. The evacuation of the paste briquette silo also produces an additional air flow that is inserted at the stem of the smoke stack. The radiation boundary condition at all inlets was defined by the simulation software using the local gas temperatures.

The microsilica dust particles were simulated using computational particles, each representing a large amount of real particles. A trajectory is calculated for each computational particle (or "parcel"), thus significantly decreasing the numerical overhead. The trajectories were initialized on the charge surface and the parcel amount was defined relative to the SiO mass flow. This means that the parcel amount was also distributed amongst the charge zones in proportion to the amount of hearth gas at each zone. This also applies for the simulation of a stocking event, which means that a large amount of dust particles is injected through the respective small round surface between the two electrodes which is used as an inlet for the "stocking" gas. Each parcel was attributed a particle diameter using a uniform distribution between 0.1 µm and 0.1 mm.

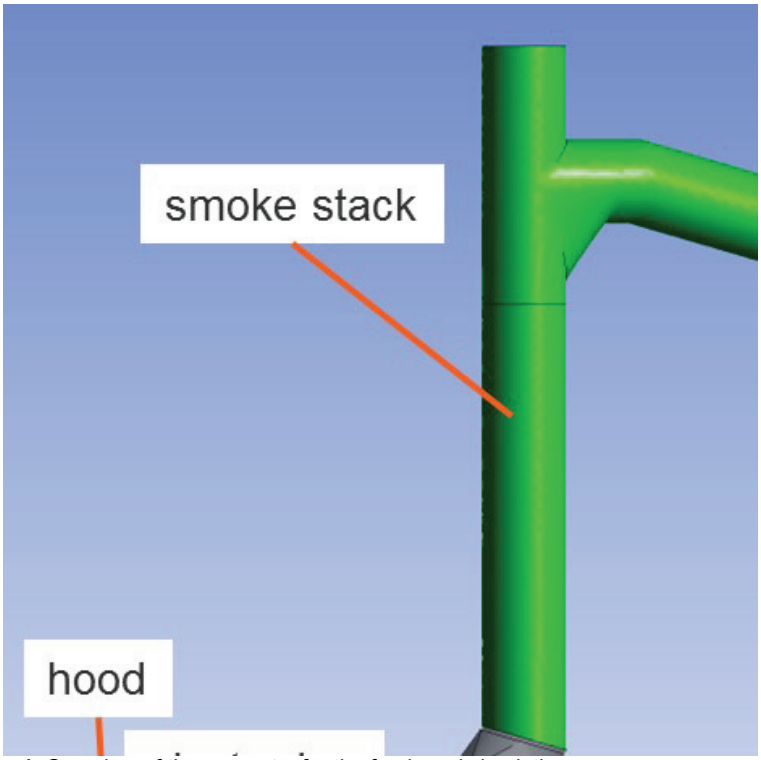


Figure 1: Overview of the geometry for the freeboard simulations.

Mass balance

For the production of silicon the raw materials are quartz, coal, woodchips and limestone, but silicon-rich by-products of the silicon refining process ("sculls") are also recycled in the furnace. In addition, the electrodes are also consumed during the reduction process, so they are also included as a raw material in the mass and energy balance. The composition of each raw material needs to be known in terms of carbon ("fix-C"), volatile matter, humidity, SiO_2 and Si. Using these compositions and the average consumption rate of each raw material, the input mass flow of each component can be calculated.

In a simple mass and energy balance, the volatile mixtures from the coal and the woodchips can be handled as single entities with known mass flows and thermal energy contents. In a more rigorous CFD simulation, however, this approach creates problems when it comes to defining the reactions in the freeboard. In addition, the volatiles of the coal and the woodchips need to be handled separately because of their different energy content. A simplified approach, therefore, does not provide any major advantages in the case of a CFD simulation and it is best to further break down the volatile matter into its constituents.

In order to obtain the composition of coal volatiles in terms of simple chemical species, an ultimate analysis of the coal is needed that will provide its C, H, O, N, S and

V (volatile) content. Using this information, a semi-empirical mass balance is used from the literature with which the evolution of the volatile matter during the thermal decomposition of coal can be predicted [1]. The model output provides the amount of char, CH_4, C_2H_6, CO, CO_2, tar, H_2, H_2O, NH_3, and H_2S in the coal. It is then assumed that the tar can be represented by C_6H_6 for the purpose of simulating the freeboard combustion, which is a reasonable assumption at this point. In this work it was also found that the amount of H_2S was negligible, so this species was not considered further.

For obtaining the composition of the wood volatiles, an ultimate analysis of the wood was used as input for C, H, O, N, S and V but the semi-empirical model had to be modified. It was assumed that all the light hydrocarbons are methane and that no C_2H_6 would be present in the wood volatiles. In addition, the yields for CH_4, CO and CO_2 were expressed as functions of the H and the O in the wood as is done in the original model, but the empirical parameters of these functions were adjusted so that the resulting volatile composition is similar to that published for wood [2]. A result is thus obtained that although empirical in nature is still consistent in terms of mass balance with the measured ultimate analysis of the wood.

The coal and woodchip volatiles were thus represented in the hearth gas of the CFD simulation using the calculated mass flows for CH_4, C_2H_6, CO, CO_2, C_6H_6, H_2, H_2O and NH_3. The water included as humidity in all the raw materials was also added to the water vapour coming from the volatile matter. The hearth gas in the CFD simulation consisted of these species, in addition to the SiO and CO amounts that result from the carbothermic reduction of quartz.

The CO and SiO content of the hearth gas had to be calculated using a mass and energy balance for the whole furnace. For this purpose, the production rate of Si (tapped) was used to determine how much quartz was effectively reduced, which was in turn used to calculate the amount of quartz that was "lost" as microsilica fume. By assuming that all the microsilica comes from the oxidation of SiO in the freeboard, the amount of SiO in the hearth gas is obtained. The amount of CO in the hearth gas was then calculated by adding the CO resulting from both quartz-reduction reactions (producing Si and SiO), plus the CO amounts present in the coal and woodchip volatiles. In total, the reactions considered in the mass and energy balance are:

$$SiO_2 + 2C \rightarrow Si + CO \quad (1)$$
$$SiO_2 + 2C \rightarrow SiO + CO \quad (2)$$
$$C + O_2 \rightarrow CO_2 \quad (3)$$
$$SiO + \tfrac{1}{2}O_2 \rightarrow SiO_2\,(g) \quad (4)$$
$$SiO_2\,(g) \rightarrow SiO_2\,(s) \quad (5)$$
$$CO + \tfrac{1}{2}O_2 \rightarrow CO_2 \quad (6)$$
$$CH_4 + 2O_2 \rightarrow CO_2 + H_2O \quad (7)$$
$$C_2H_6 + 3.5O_2 \rightarrow 2CO_2 + 3H_2O \quad (8)$$
$$C_6H_6 + 7.5O_2 \rightarrow 6CO_2 + 3H_2O \quad (9)$$
$$H_2 + \tfrac{1}{2}O_2 \rightarrow H_2O \quad (10)$$
$$NH_3 + \tfrac{3}{4}O_2 \rightarrow \tfrac{1}{2}N_2 + 1.5H_2O \quad (11)$$

Of these reactions the first three are only used for the mass and energy balance, while all the rest are also present in the CFD simulation. The third reaction accounts for the fate of the excess carbon (if any), that cannot be accounted for in the process products, including the dust and the particle matter captured by the flue gas cyclones. This carbon amount is assumed to combust in the freeboard in the form of small particles or on the

charge surface. Ideally, this combustion could be taken into account in the CFD simulation by using Lagrangian coal particles that are allowed to combust, but this was omitted in favour of keeping the simulation relatively simple. The energy from this reaction is about 5% of the total combustion energy released in the freeboard. Reaction (5), describing the condensation of silica, is not defined in the CFD simulation as a reaction between chemical species, but is instead taken into account using a heat source and mass sink for the gaseous SiO_2 as described earlier.

Energy balance

At the outlet of the simulation the total flue gas mass flow needs to be defined. This can be either measured directly in the flue gas pipeline or it can be calculated using the aforementioned mass balance together with an energy balance and a flue gas temperature measurement. The energy enters the quartz reduction process as electricity and chemical energy in the form of carbon and volatiles. The bulk of the electricity is used for the production of Si and microsilica whereas a small amount is used for bringing the hearth gas up to its temperature. The energy leaves the process stored as chemical energy in the Si-metal and residual heat in both the Si-metal and the flue gas. Another energy amount is removed from the process by the cooling systems of the freeboard hood, the chutes and the electrode equipment.

This cooling energy can be obtained by the mass flow and inlet/outlet temperatures of the cooling water. In the overall energy balance, the energy removed by the cooling system equals the net energy released in the freeboard, i.e. the total amount of freeboard combustion heat, minus the heat necessary to bring the flue gas, including the entrained air, up to its exit temperature. The mass and the energy balance are thus coupled at this point since the calculation of the freeboard combustion heat necessitates knowledge of the hearth gas mass flux and composition. In order to calculate the total amount of air involved in the process the following steps need to be taken:

1. An initial guess for the ambient air amount entrained in the freeboard needs to be made. This air amount needs to be added to the air blown into the freeboard through the chutes etc. as described earlier. A first approximation of the total air amount involved in the process is thus obtained.
2. A temperature for the flue gas must be measured, but a target value can also be assumed if a theoretical scenario needs to be calculated.
3. Assumptions for the ambient air temperature (20 ºC) and the hearth gas temperature (1000 ºC) must be made.
4. The amount of combustion energy released in the freeboard according to reactions (3) – (11) is calculated. In this reaction enthalpy calculation each reactant is at its own inlet temperature while the combustion products are all at the flue gas temperature (defined in step #2).
5. The energy needed to bring the entrained air (all of the N_2 and the excess O_2) from the air inlet temperature to the flue gas temperature is calculated.
6. The algebraic sum of the energies calculated in steps #4 and #5 should equal the energy removed by the cooling system in the freeboard. If not, then the amount of entrained air is adjusted until the energy balance is satisfied.

The flue gas mass flow thus results from the combined mass and energy balance by assuming that all gas-phase reactions are complete. The flue gas at the simulation outlet is thus comprised of the CO_2 and H_2O coming from all combustion reactions and coal/woodchip volatiles, plus the N_2 contained in all the air (reaction (11) is responsible for a negligible amount) together with the residual O_2. It has the advantage that it can

also be used to design a cooling system for the hood that is responsible for most of the energy removed from the freeboard.

Material properties

Each chemical species except SiO_2(s) was defined as an ideal gas. For calculating the heat capacity and enthalpy of each species as functions of temperature, NASA polynomial coefficients were obtained from the literature [4] and given to the simulation software directly. The same polynomials were also used for obtaining the reaction enthalpies in the energy balance. For defining the dynamic viscosity and thermal conductivity, the temperature-dependent data curves were calculated using fitted coefficients from the literature [4] and the parameters of Sutherland's formula were fitted to the data curves for use in the simulation software. The heat capacity, enthalpy, dynamic viscosity and thermal conductivity of the gas mixture were calculated using the ideal mixture assumption. For the radiation properties, however, a different approach was taken in order to save computational time.

The radiation properties that need to be defined are the absorption coefficient, the scattering coefficient and the refractive index. Of these properties, the refractive index was assumed equal to unity and the scattering coefficient equal to zero. These assumptions are acceptable for gasses and low particle number concentrations. Therefore, the absorption coefficient is the only radiation property that can influence the heat transfer and needs to be defined. For this purpose it is assumed that the combustion in the freeboard proceeds very fast so that the absorption coefficient of the gas mixture can be calculated for the final flue gas composition as a function of temperature only. The flue gas composition was obtained using the mass and energy balance and the temperature range covered in this work was 300 K – 2000 K. The partial pressures of CO_2, H_2O, N_2 and O_2 in the flue gas were calculated and used as input for the software RADCAL [5] that provided the effective absorption coefficient of the mixture at temperature increments of 100 K. The data points were used to fit a continuous 5th-order polynomial that was implemented in the simulation software.

For the definition of the condensation heat source term in the energy transport equation, the condensation enthalpy of SiO_2 is needed. This is calculated as the difference between the reference specific enthalpy of the gas phase (obtained using the NASA polynomial) and the reference specific enthalpy of the solid phase published in the literature [7]. The heat capacity of the solid SiO_2 phase in the CFD simulation was defined using a zero pressure polynomial fitted to a curve published in the literature [6].

Doghouse simulations

The CFD simulations of the doghouse covered two modes of operation: one "normal" operation in which the liquid silicon flows out of the taphole together with a nominal amount of hearth gas, and one "gassing" mode in which the hearth gas is increased by an empirical factor of 13. The hearth gas in this case is considered to be 50% v/v CO and 50% v/v SiO. The nominal hearth gas amount was calculated based on the daily silicon production rate using the model published by Næss [8]. The "gassing factor" was set so that the hearth gas at the taphole reached velocities that are usual for severe cases of gassing, as published by Kadkhodabeigi [9]. The temperature of this type of hearth gas was estimated at 1400 °C and was the same for both the normal and the gassing modes. The microsilica dust particles were simulated using the same

methodology as in the case of the freeboard, but the parcel trajectories were initialized at the taphole.

The doghouse simulated in this work features two outlets in an asymmetric orientation, as can be seen in Figure 2. The mass flow of the ventilated gas under normal conditions was set according to the specifications of the ventilation equipment and was distributed equally at each outlet. Under gassing conditions, however, the equipment ventilates a volumetric flow that remains approximately the same, but the mass flow is significantly lower due to the elevated temperature of the flue gas, which is in turn due to the larger amount of hearth gas and the more intense combustion within the doghouse. Under these conditions the total amount of flue gas ventilated was adjusted according to the anticipated temperature, which resulted in approximately half the original amount. In addition, the total mass flow was divided between the two outlets depending on the density (i.e. the temperature) of the flue gas at each outlet.

The fume emitted from the ladle is also estimated using the model by Næss [8] and defined in the simulation as a mixture of SiO and O_2, and N_2. The gas and the respective microsilica particle parcels were initialized on the top surface of the ladle, on which a temperature of 2000 °C was assumed. The walls of the doghouse, the tapping spout, the ventilation ducts and the ladle were all assumed to be adiabatic for the heat convection equation and opaque black bodies for the radiation equation. As in the case of the freeboard simulation, an opening boundary condition allowed the free entrainment of ambient air into the doghouse and through the ventilation ducts. The combustion model was the same as in the freeboard simulation, but only included reactions (4) and (6).

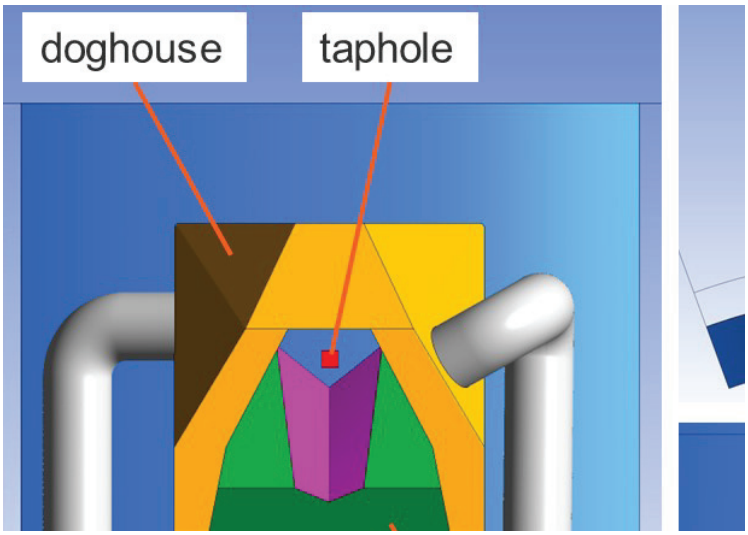


Figure 2: Overview of the geometry for the doghouse simulations.

Results

Freeboard simulations

The results of the freeboard simulation under normal operation conditions can be seen in Figure 3. A 3D temperature isosurface at 1500 K is used in order to visualize the flame. Streamlines are plotted on a 2D surface along the symmetry axis of the smoke hood for depicting the flow of the entrained air and the flue gas. The streamline colours are scaled between 0 m/s (blue) and 15 m/s (red). The most significant feature of the flow is the large eddy shown under the hood on the left. In this simulation the hood doors were at their lowest position, but a 10 cm gap is present between their bottom edge and the crucible rim. The entrained air enters the freeboard through that gap thus forming a wall-bounded jet that flows along the crucible rim and the surface of the charge. After approximately 3 m from entry, the jet meets the rising flame of the hearth gas and thus also rises upwards. Bounded by the hood roof and the doors, the gas thus spins in a counter-clockwise direction (as viewed in Figure 3). The velocity at the circumference of the eddy is about 6 m/s, which is also the entry velocity of the wall-bounded jet. In three dimensions, the eddy is a spiral flow pattern that extends around the hood and serves two purposes:

1. It cools the freeboard flame by providing fresh air from the stocking floor.
2. It pushes the flame towards the centre of the furnace, thus preventing any hot gasses and dust from exiting.

This eddy is of utmost importance for containing the flue gas within the freeboard and the hood design must therefore assist its formation. For this purpose it was decided that it is better to place the doors above the crucible rim instead of next to it. This provides a flat horizontal surface (i.e. the crucible rim) along which the air can flow and enter the freeboard in the form of a wall-bounded jet. In addition, the gap under the doors should be large enough so that a sufficient amount of air can enter, but also small enough so that the air velocity provides enough momentum for the generation of the eddy. For example, the eddy was significantly disrupted when all the doors were raised half-way due to the low velocity. If the gap under the doors is too narrow, the pressure loss at that location will be too large and the entrained air will flow into the freeboard through more favorable openings (e.g. the door holes), that do not produce flow patterns favorable for flame cooling and smoke containment.

Figure 4 shows the flame and flow in the freeboard during stocking. It can be seen that the burst of “stocking” gas that is injected upwards leads to a much larger flame in the centre of the furnace. The amount of hot combustion gasses and the gas expansion in the freeboard are so large that the flame hits the ceiling of the smoke hood and flows along the inner wall which leads to a respective hot-spot on the smoke hood. This behaviour also disrupts the air entrainment eddy, which is actually reversed in this case. In Figure 4 the eddy on the left rotates clockwise, which means that the gas flow is reversed. The trajectories of the microsilica particles that can be seen on Figure 5, indicate that the smoke leaves the freeboard through the holes on the doors, the gaps under the doors, and, most importantly, through the doors that need to be opened during stocking, although the flame itself remains contained by the smoke hood.

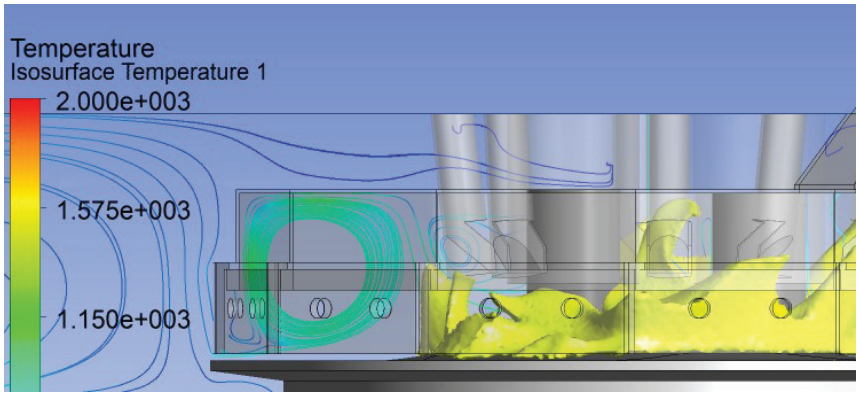


Figure 3: Representation of the flow in the freeboard under normal conditions. The eddy on the left rotates counter-clockwise.

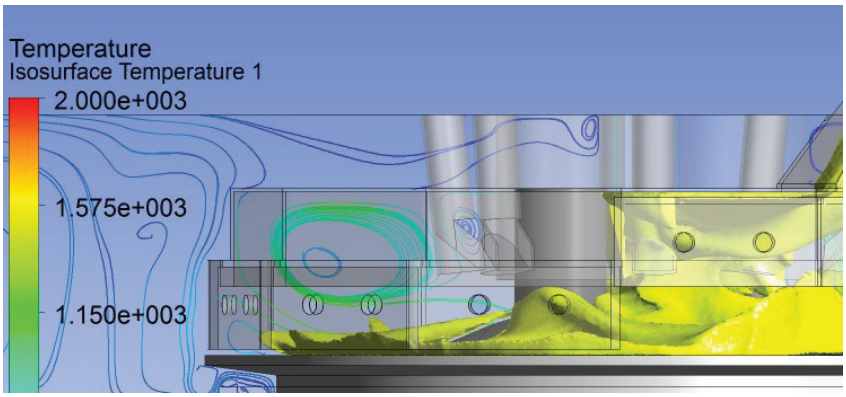


Figure 4: Representation of the flow in the freeboard during stocking. The eddy on the left rotates clockwise.

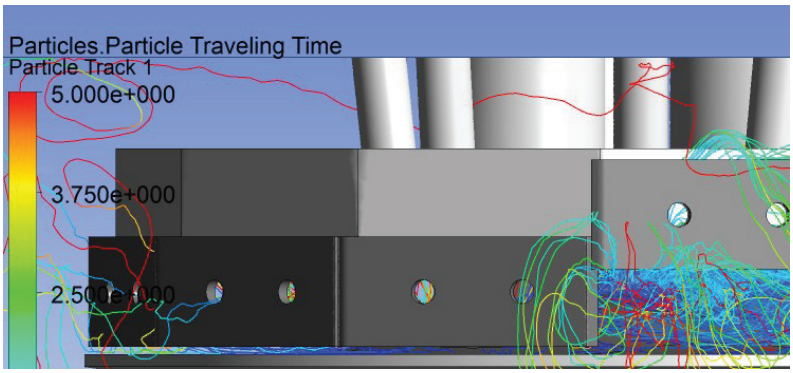


Figure 5: Trajectories of silica particles during stocking, showing smoke exiting the freeboard.

Doghouse simulations

In the present doghouse design, the two suction ducts are placed asymmetrically which under normal conditions has two major advantages:

1. The duct at the back, i.e. closer to the taphole, is responsible for capturing the fume coming from the taphole, but it also captures a certain amount of fume from the ladle. The duct at the front, i.e. over the ladle, is responsible for capturing the fume emitted by the ladle.
2. The asymmetrical placement also avoids the appearance of a stagnation point between the two suction ducts, which is typical of fluid flows with two symmetrical inlets or outlets. In the case of the doghouse this would be a strong disadvantage because the fume-emitting taphole is located midway between the two outlets.

The simulated velocities in the doghouse can be seen in Figure 6. On the left are the velocities under normal operation whereas on the right are the velocities under gassing conditions. The velocities are visualized on a 2D surface that goes through the middle of the doghouse. The color scale is adjusted in each picture so that the red color always represents the highest velocity in that representation. Under normal conditions the highest velocities in the doghouse are caused by the ventilation that accelerates the gas inwards. This acceleration is performed by both ducts and not only captures the ladle fume, but also the incoming gas prevents the fume emitted by the taphole from escaping by forming a counter-flow barrier. This can also be seen in Figure 7 in which the microsilica particle trajectories are visualized. On the left (for the normal operation) the particles coming from the taphole all have short residence times (below 0.2 s, blue lines) and are all vented by the duct at the back. The particles coming from the ladle have residence times of about 0.5 s (green lines) and are mostly vented by the duct at the front, but some also reach the back of the doghouse and are vented by the duct at the back.

The simulated temperatures in the doghouse can be seen in Figure 8. On the left are the temperatures under normal operation whereas on the right are the temperatures under gassing conditions. The temperatures are visualized on a 2D surface that goes through the middle of the doghouse using the same color scale. It can be seen that the flow in the doghouse gets much hotter under gassing conditions and that a very strong gas jet exits the taphole that can also be seen in Figure 6 (right). In this case the pressure gradient provided by the two ducts is too weak to manage and divert this jet, and a different mechanism is therefore necessary in order to prevent it from escaping. For this reason, the top walls of the doghouse, and especially the frontal plate, are sloped. The frontal plate provides a surface for the jet to hit and thus lose momentum. Since hot combustion gasses have the tendency to rise, this creates a backwards flow as shown in Figure 6 (right) and Figure 8 (right), where a counter-clockwise rotating eddy can be discerned in the top half of the doghouse. This means that the hot plume, after having lost most of its momentum, is forced to recirculate in the doghouse. The sloped walls eliminate any “blind” corners where the smoke can accumulate out of reach and instead streamline it towards the openings of the suction ducts where it can be vented away. In Figure 7 (right) the circulating dust cloud can be seen on the top of the doghouse, from which it is also evident that no dust can escape.

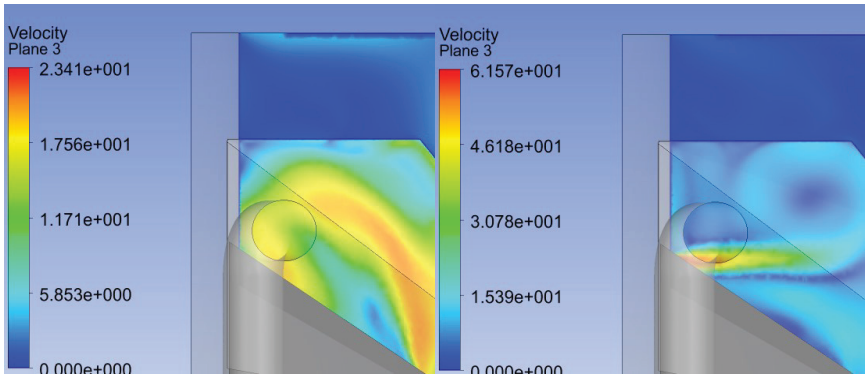


Figure 6: Gas velocities in the doghouse under normal operation (left) and gassing conditions (right).

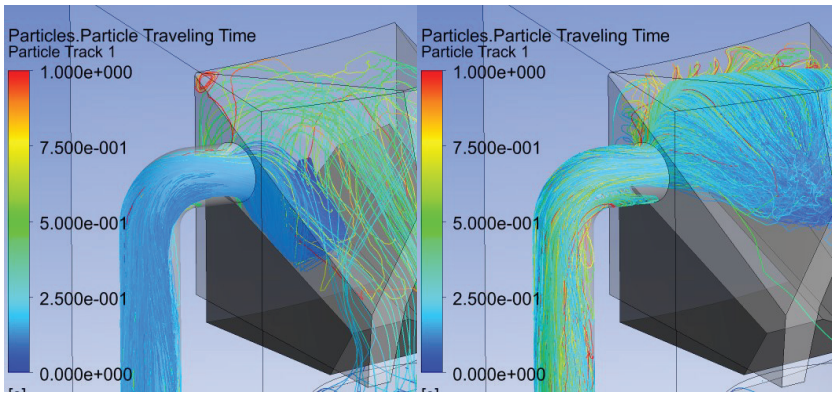


Figure 7: Trajectories of microsilica particles emitted by the ladle and the taphole under normal operation (left) and gassing conditions (right).

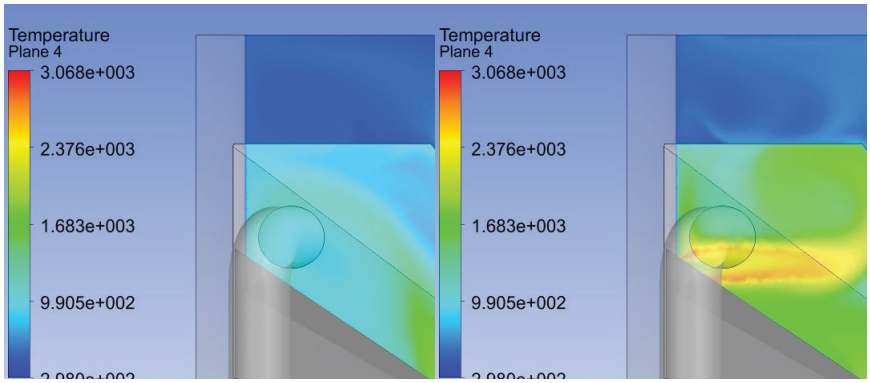


Figure 8: Temperatures in the doghouse under normal operation (left) and gassing conditions (right).

Conclusion

The gas flow phenomena in the freeboard and the doghouse of a silicon furnace could be visualized and interpreted using CFD simulations. For the case of the freeboard smoke hood, the CFD simulations led to design decisions that under normal conditions improved the suction and cooled the freeboard flame. It was also shown, however, that additional equipment advancements are necessary in order to prevent dust emissions during stocking. For the case of the doghouse, a new design was developed that can capture the smoke even if the furnace is gassing. This improvement led to a patent application for the asymmetrical design of the suction duct pair, that divides the suction load and eliminates any stagnation points, as well as the sloped wall design of the doghouse, which streamlines the smoke and prevents it from accumulating [10].

Acknowledgements

The authors would like to acknowledge the contributions by Mr. Eirik Andersen Rotevatn and Mr. Einar Olav Schei that provided many valuable insights and data.

References

1. D. Merrick, *Mathematical models of the thermal decomposition of coal (1. The evolution of volatile matter)*, Fuel, **62**, 1983, p534
2. K. W. Ragland, D. J. Aerts, A. J. Baker, *Properties of wood for combustion analysis*, Bioresource Technology, **37**, 1991, p161
3. B. F. Magnussen and B. H. Hjertager, *On mathematical modeling of turbulent combustion with special emphasis on soot formation and combustion*, Symposium (International) on Combustion, **16**, 1977, p719
4. B. J. McBride, S. Gordon, M. S. Reno, *Coefficients for calculating thermodynamic and transport properties of individual species*, NASA Technical Memorandum **4513**, 1993
5. W. L. Grosshandler, *RADCAL: A narrow-band model for radiation calculations in a combustion environment*, NIST Technical Note **1402**, 1993
6. P. Richet, Y Bottinga, L Denielou, J. P. Petitet, C Tequi, *Thermodynamic properties of quartz, cristobalite and amorphous SiO2: drop calorimetry measurements between 1000 and 1800 K and a review from 0 top 2000 K*, Geochimica et Cosmochimica Acta, **46**, 1982, p2639
7. L. Peng, W. Qisui, L. Xi, Z. Chaocan, *The molar formation enthalpy of nano-SiO2 with different surface area*, Journal of Thermal Analysis and Calorimetry, **95**, 2009, p667
8. M. K. Næss, *Mechanisms and kinetics of liquid silicon oxidation*, Norwegian University of Science and Technology, Thesis for the degree of Philosophiae Doctor, Trondheim, 2013
9. M. Kadkhodabeigi, *Modeling of Tapping Processes in Submerged Arc Furnaces*, Norwegian University of Science and Technology, Thesis for the degree of Philosophiae Doctor, Trondheim, 2011
10. E. Bertakis, R. Eulenberger, E. O. Schei, Hood for Si-metal tapping, patent application number PCT/EP2018/054384.

Silicon for the Chemical and Solar Industry XIV
Svolvær, Norway, June 11 – 14, 2018

The replacement of coal tar pitch – opportunities and constraints

Trygve Eidet[1)] and Øyvind Mikkelsen[1)]
1) Elkem Carbon AS

Abstract

High temperature coal tar pitch (CTPht) is completely dominant as the binder in use for electrode paste and other carbon materials that carbonize in-situ in metallurgical use. The dominance is based on excellent material properties for the applications, availability, cost and more than 100 years of technical optimization around this material.

On the other hand, due to the content of polycyclic aromatic hydrocarbons (PAH), CTPht has been defined as a "substance of very high concern" under the European Chemicals Legislation REACH. In 2017 CTPht was published on the list of substances included in REACH Annex XIV ("Authorization List"). In principle, this requires all users of CTPht in Europe to apply for authorization of the use, but exception has been achieved for Søderberg electrode paste with reference to intermediate status based on harmonized European industry position.

Elkem Carbon has an ongoing program on binders for metallurgical carbon materials. The scope of the program is to find substitutes for the high temperature coal tar pitch (CTPht).

This paper discusses the regulatory status and use of coal tar pitch, and testing of materials with CTPht replaced.

Regulatory status of products containing coal tar pitch

ECHA (European chemicals agency) is the public body in the EU responsible of implementing the union's chemicals legislation [1]. ECHA has made, and is managing, a regulation of the EU named REACH [2]. REACH is the regulation for Registration, Evaluation, Authorization and Restriction of Chemicals.

Due to its content of polycyclic aromatic hydrocarbons (PAH), CTPht (EC / List no. 266-028-2) has been defined as a "substance of very high concern" under REACH. In 2017 CTPht was published on the list of substances included in REACH Annex XIV ("Authorization List») [3]. In principle, this requires all users of CTPht in Europe to apply for authorization of the use, but exception has been achieved for Søderberg electrode paste with reference to intermediate status based on harmonized European industry position [4]. Figure 1 shows the regulatory status of products containing CTPht on a timeline.

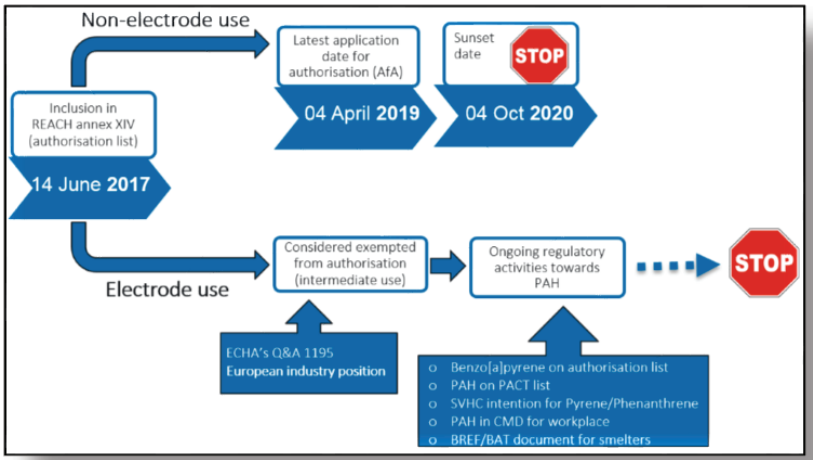


Figure 1: Timeline for the use of high temperature coal tar pitch (CTPht) in the EU.

According to ECHA, the use of high temperature coal tar pitch in Søderberg electrode paste is considered as *intermediate*, and is thus exempted from authorization requirements under REACH (Regulation, ECHA Q&A 1195). This means that the use of CTPht in Søderberg electrode paste has been exempted from authorization requirement by REACH, and can still be marketed in Europe without authorization. Other carbon products containing CTPht must be authorized for use in commercial products.

Note that it will be illegal under REACH, to utilize electrode paste for *other* functions than electrode use after October 4th, 2020.

Authorization is a tedious process, as REACH places the burden of proof on companies. To comply with the regulation, companies must identify and manage the risks linked to the substances they manufacture and market in the EU. They must demonstrate to ECHA how the substance can be safely used, and they must communicate the risk management measures to the users. If the risks cannot be managed, authorities can restrict the use of substances in different ways. In the long run, the most hazardous substances should be substituted with less dangerous ones.

Elkem Carbon has a program in order to develop products where CTPht is replaced with more environmentally friendly solutions when technically possible. Driving the development of carbon products without CTPht are the aim to reduce worker exposure to polycyclic aromatic hydrocarbons (PAH) both in the carbon industry and at customer sites, to reduce emissions of PAH to the environment, and to improve the sustainability of metal production.

The program of product development activities focuses on the whole product portfolio range, and solutions have been commercially implemented to some products, while other areas are still under development, see “Products with alternative binders”, below.

The new binder solutions are sought after in a wide range of material sources from purely bio-based materials to more classical fossil materials. There is even one coal tar pitch binder on the market that is not restricted by the REACH regime, as it is defined by a different EC number than the standard pitches (Pitch, coal tar, high-temp., heat-treated, EC / List no. 310-162-7), but this will be challenged by the new, more chemically defined, materials on the on the list of substances included in REACH Annex XIV ("Authorization List»), see figure 1.

Coal tar pitch

Fundamental aspects of coal tar pitch

Coal tar pitch is a unique material that has properties very well suited as a binder in metallurgical metal production. This binder consists almost exclusively of polycyclic aromatic hydrocarbons (PAH), which from a material *function* perspective is ideal, but from an environmental perspective is a challenge, see above.

Due to the good technical performance of the binder, the utilization and optimization of CTPht-based carbon materials has lasted over the last century [5]. Even though other binders also have been in use [6,7,8,9,10], technology and analytical methods in the metallurgical carbon material science have been adapted to pitch as the main binder in use.

CTPht is the binder of choice for carbon electrodes and other carbon materials utilized in metallurgical applications [11,12]. As shown in figure 2, it has the ability to form a well-ordered, graphitizable carbon structure upon heat treatment. The micrograph in figure 2 is taken from a pitch sample in the early phase of heat treatment, before solid carbon is formed, and the spheres shown are *mesophase* spheres. The mesophase is a state where the pitch still has liquid-like properties, and at the same time crystal-like structure.

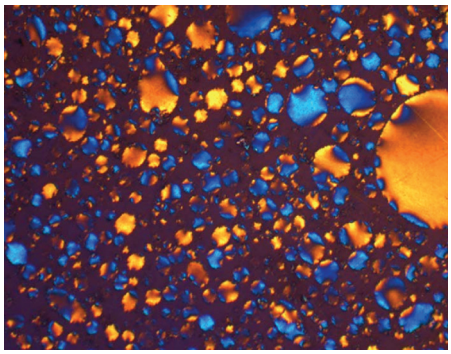


Figure 2: Polarized light micrograph of coal tar pitch *mesophase spheres*, a state where the pitch still has liquid-like properties and at the same time crystal-like structure. Structure visualized by using cross-polarizing filters and λ-plate on a reflecting light metallurgical microscope.

Upon further heat treatment, after mesophase formation, coke structure is formed. As the CTPht is an aromatic substance, the whole volume of the material has the ability to form mesophase, and condense into anisotropic structures. Figure 3 shows the results from FT-ICR-MS analysis of CTPht and an aliphatic petroleum derivative. The plot is showing double bounding equivalents (y-axis) versus number of C-atoms in the molecules. It is evident that the two substances are very different. The petroleum derivative displays a much larger range of molecular weights and little aromaticity, whereas the pitch is purely aromatic.

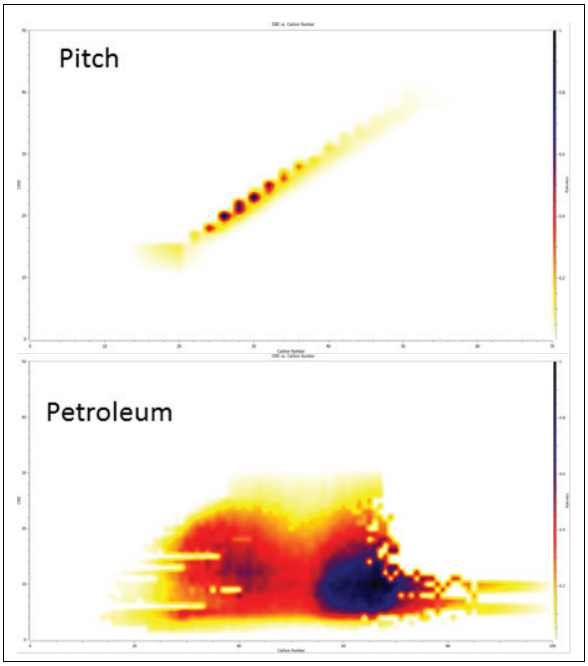


Figure 3: Results from FT-ICR-MS showing double bounding equivalents(y-axis) versus number of C-atoms in the molecules for pitch and a petroleum derivative. Dark colours indicate high concentration.

Another unique feature stemming from the almost purely aromatic nature of CTPht, is the gas released during heat treatment of pitch. Aromatic components with low boiling points may vaporize from the pitch, and thus pose a risk of PAH emissions to the surroundings, but the gaseous reaction product from the condensation to coke, is almost purely hydrogen, as illustrated in figure 4 [13]

The property of releasing low amounts of gas during carbonization is important in the formation of solid, dense, strong, carbon materials with good conductivities.

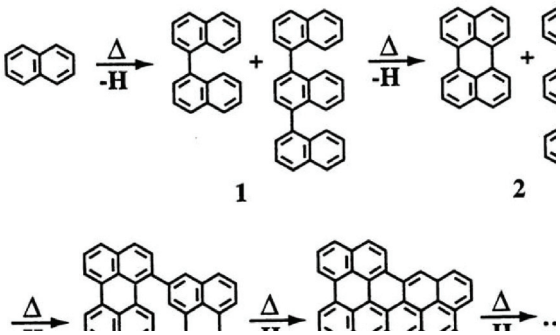
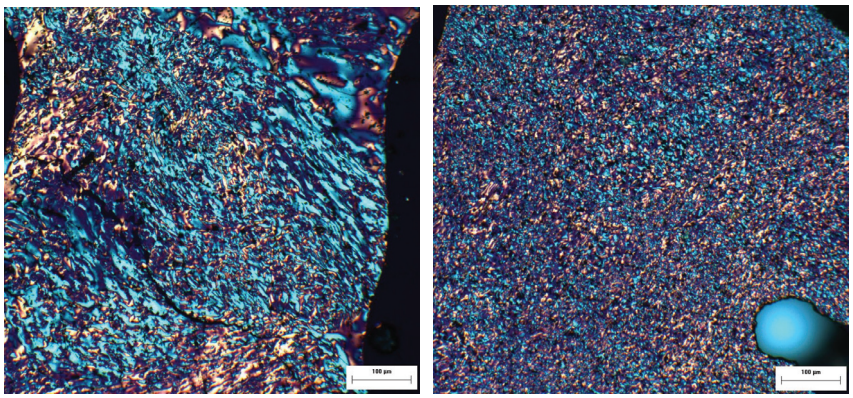


Figure 4: Mechanism of aromatic growth during heat treatment of CTPht [13].

The aromatic growth via mesophase in the coal tar pitch, allows the formation of well-ordered graphitic structure elements, as illustrated in figure 5. This enables the formation of large, well ordered structure elements in the coke formed during carbonization.



(a) Coal tar pitch after carbonization. (b) Alternative binder after carbonization

Figure 5 Polarized light micrographs of a typical coal tar pitch (a) and an alternative binder (b) by using cross-polarizing filters and λ-plate on a reflecting light metallurgical microscope.

With the well-ordered structure as illustrated in figure 5, comes a low concentration of graphite lattice edges and imperfections in the structure. This is equivalent to a low number of active sites for reactions to occur, and is a determining factor in the chemical integrity of the carbon material, and an inherent advantage of carbon materials formed from highly aromatic precursors.

From above, it is clear that no known materials possess the same set of properties as coal tar pitch, and it is not realistic to find a unique solution applicable to all the different materials and processes where CTPht is used in the metallurgical industry. In

this case, environmental improvements of the chemical composition will generally come at the cost of less ideal technical function and more expensive materials.

Søderberg electrode binder requirements

Figure 6 shows a sketch of a metallurgical furnace with the Søderberg electrodes included.

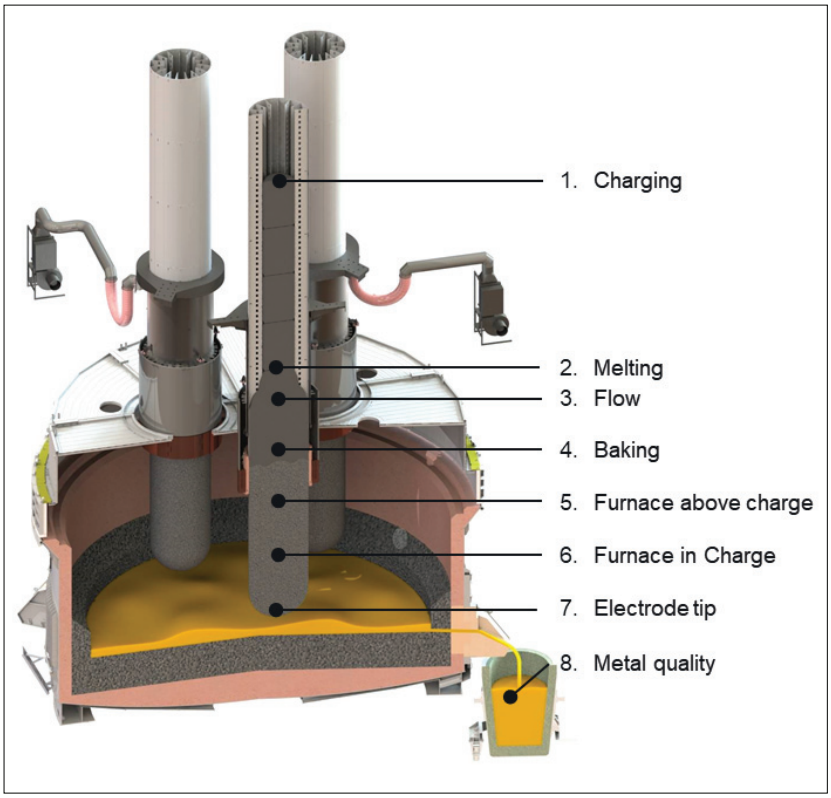


Figure 6: Furnace with cross section of electrode visible. Indications show critical parts of the electrode function.

As the indications in figure 6 show, the Søderberg electrode paste passes through the critical parts of the electrode function during its consumption, all posing demanding requirements to the paste, and inherently, its binder.

1. The charging of electrode paste is where the paste is transferred into the electrode column. The requirements from the paste in this area are structural integrity during handling, minimum dust emissions, and maintained geometric shape. This means that the binder must be in a solid state with a certain strength in order for the electrode paste to be handled in the traditional formats: cylinders or briquettes.

2. Melting happens when the electrode paste is heated above the melting point of the binder. It is critical for a well-functioning Søderberg electrode that this happens in the right height in the electrode, see 4. Baking. The molten paste, and the unmolten electrode paste above it, provides the pressure required in order to achieve good conditions for the steps below. The melting process requires certain rheology versus temperature properties from the binder. This is a complex interaction between the binder and the dry aggregate of the paste. The transfer from solid to liquid paste must also happen without too high vapor pressures of light components, and without toxic emissions.

3. The molten electrode paste must demonstrate the right flow inside the electrode column. In the macroscale, it must flow out to fill the whole electrode column cross section. In the microscale, the paste must flow and give coalescence into a monolithic carbon structure with adequate density and homogeneity. It is important that the binder facilitate densification before carbonization.

4. The baking process is extremely critical for good electrode function. In this process conductivities, strength, chemical integrity etc. in the solid electrode material are established. If the paste bakes too late, disastrous consequences in the form of a soft electrode breakage may occur.

The baking must yield a strong, solid electrode, able to carry the mechanical and electrical load where the temperature is too high for the electrode casing to carry the loads. The baked electrode must give sufficient anchoring to the casing. Ideally, this means that the baking isotherm is in/above the contact clamps. The mechanical stress distribution after baking must be low enough to prepare the electrode for thermal and mechanical stress and -shock.

Obviously, electrical resistivity of the electrode material must allow for low energy consumption and the right ohmic heating distribution. Also, thermal conductivity and thermal expansion must enable thermal shock resistance required.

During baking, the binder must be able to form a solid phase with the has the properties described here, and in addition the properties mentioned in 5.-8. below.

5. The electrode exposed in the furnace above the furnace charge needs the ability to withstand stresses, as described above. In addition, chemical integrity versus furnace atmosphere is required.

6. The electrode exposed in the furnace charge needs the ability to withstand stresses, as described above. In addition, chemical integrity versus process gasses, and mechanical wear resistance are required.

7. The most extreme conditions to which the electrode material may be exposed is at the electrode tip. Here high temperature properties must be adequate.

8. Impurities in the electrode material will end up in the metal, and the electrode cannot be composed from raw materials with unacceptable impurity concentrations with respect to metal quality.

Product development with alternative binders

Metallurgical technology is generally adapted and optimized with respect to the use of coal tar pitch binders in the carbon materials. Thus, large investments in new technologies could be required in order to accommodate materials based on other binders. This is not economically viable. Development of materials with new binders must then focus on finding alternatives that can be implemented with current technology.

Elkem Carbon's developments are focused on fulfilling all requirements posed to the materials in metallurgical use, as exemplified in "Søderberg electrode binder requirements", above. On the other hand, only CTPht has the exact properties of CTPht, and other solutions inside current technology will tend to be less ideal with respect to technical performance. The targets of the change being reduced exposure for workers and reduced harmful emissions to the environment.

Examples of testing alternative product vs requirements.

Electrode exposed in the furnace charge

To test if function requirements as described in "Søderberg electrode binder requirements" were met, baked electrode materials were exposed to furnace charge conditions in a "furnace simulator". This is a test where furnace charge is heated in a crucible to reaction temperatures, and reaction products and material conversions are observed after the test. This procedure is normally used for testing of raw materials for the furnace process, but Elkem Carbon has utilized it to expose carbon electrode materials to furnace charge conditions, as shown in figure 7.

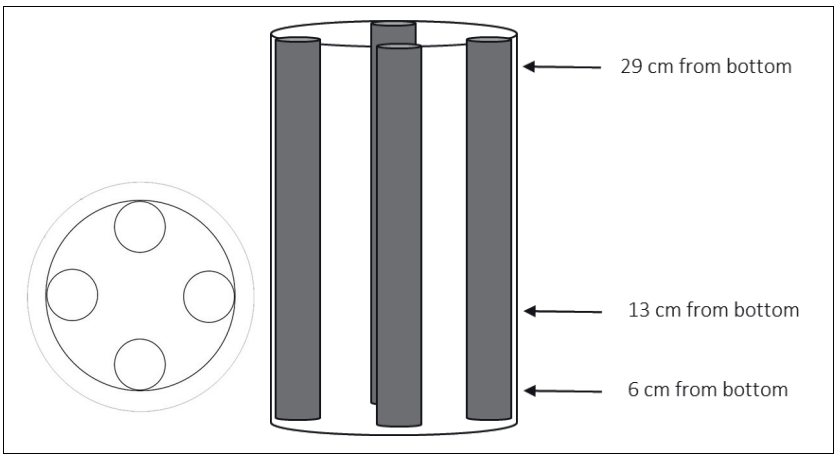


Figure 7: Test crucible set up. Four test samples placed in graphite crucible seen from above and from the side. Analysis levels indicated. Furnace charged filled around the samples.

The test is performed by heating the samples covered in furnace charge in an induction furnace. In this case, typical Si-furnace feed was used to generate conditions similar to the silicon process. The baked electrode samples were analysed after exposure to look for conversion of the electrode carbon to SiC/Si.

Analysis of samples 6 cm from bottom level

Due to the furnace design, the highest temperature is reached at the bottom of the crucible. Figure 8 shows SEM-images of the for samples 6 cm from the bottom of the crucible. The materials in the test were CTPht based material and PAH-free material with two types of dry aggregate composition.

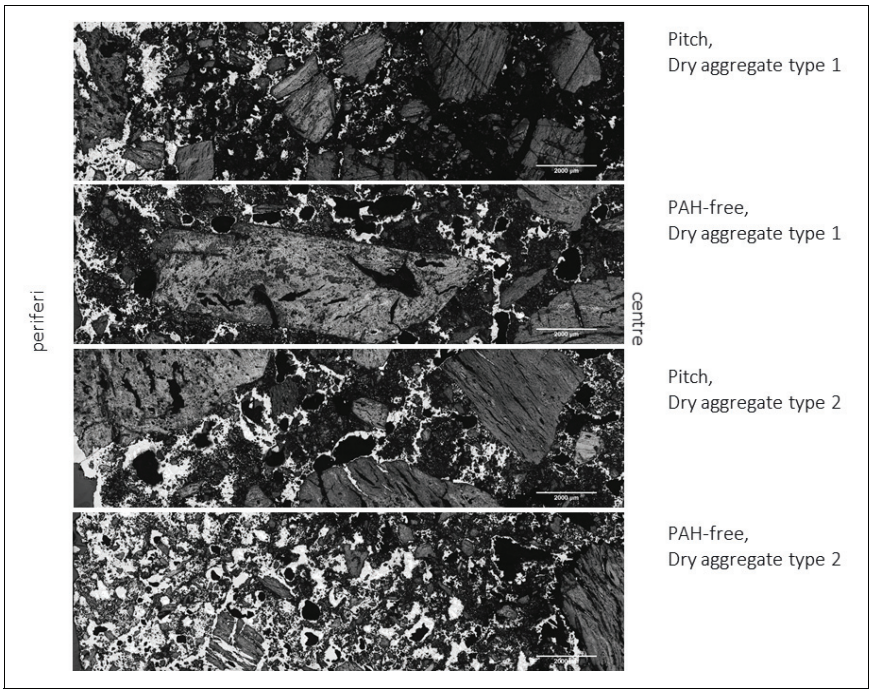


Figure 8: SEM-images of the for samples 6 cm from the bottom of the crucible. The materials in the test were CTPht based material and PAH-free material with two types of dry aggregate composition.

White regions in the SEM images from the electrode samples are converted to SiC and Si. The images show that the 6cm samples have been severely exposed to furnace gases and high temperatures since a large portion of the material has been converted. Especially the binder/fines are to a large extent converted to SiC/Si. It can be seen that dry aggregate type 2 is more converted than type 1, and PAH-free samples are more converted than pitch samples. Still for dry aggregate type 1, the differences between pitch and PAH-free are small.

Analysis of samples 13 cm from bottom level

Figure 9 shows SEM-images of the for samples 13 cm from the bottom of the crucible.

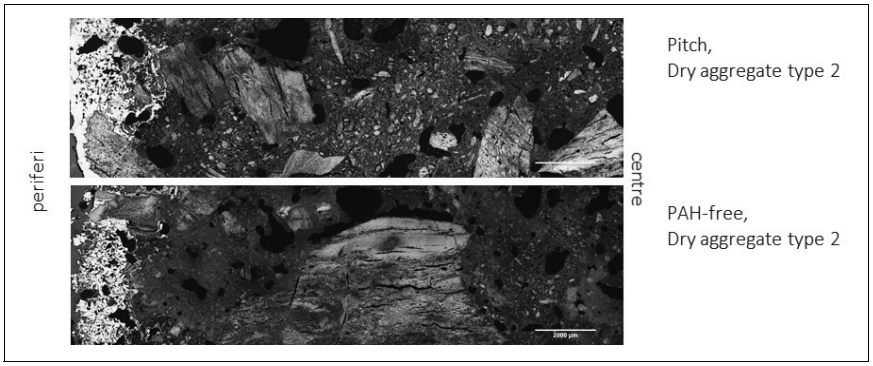


Figure 9: SEM-images of the for samples 13 cm from the bottom of the crucible.

White regions in the SEM images from the electrode samples are converted to SiC and Si. The 13cm samples have been less exposed to furnace gases and high temperatures than the samples in figure 8. Conversion to SiC/Si was only taking place at the periphery. Only small differences between the samples can be observed.

Analysis of samples 29 cm from bottom level

Figure 10 shows SEM-images of the for samples 29 cm from the bottom of the crucible.

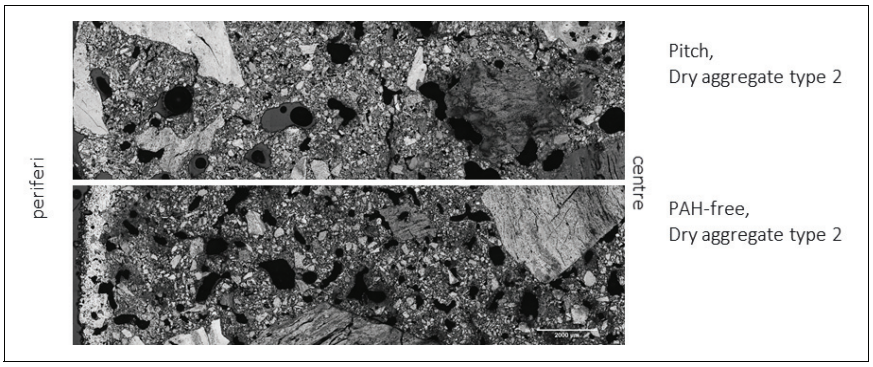


Figure 10: SEM-images of the for samples 29 cm from the bottom of the crucible. The materials in the test were CTPht based material and PAH-free material with two types of dry aggregate composition.

White regions in the SEM images from the electrode samples are converted to SiC and Si. The 29cm samples have been least exposed to furnace gases and high temperatures. Conversion to SiC/Si was only taking place at the periphery surface. Only very small differences between the samples can be observed.

Weight loss during heat treatment

Limited gas release over a wide temperature range, allowing limited porosity formation, is a requirement well fulfilled by CTPht.

Figure 11 shows weight loss curves of samples under nitrogen atmosphere for a tamping paste with bio-based binder, regular tamping paste and electrode paste (self-flowing).

Note that the volume represented by the evolved gas normally is higher from bio-material due to smaller molecules lost in the evaporation processes.

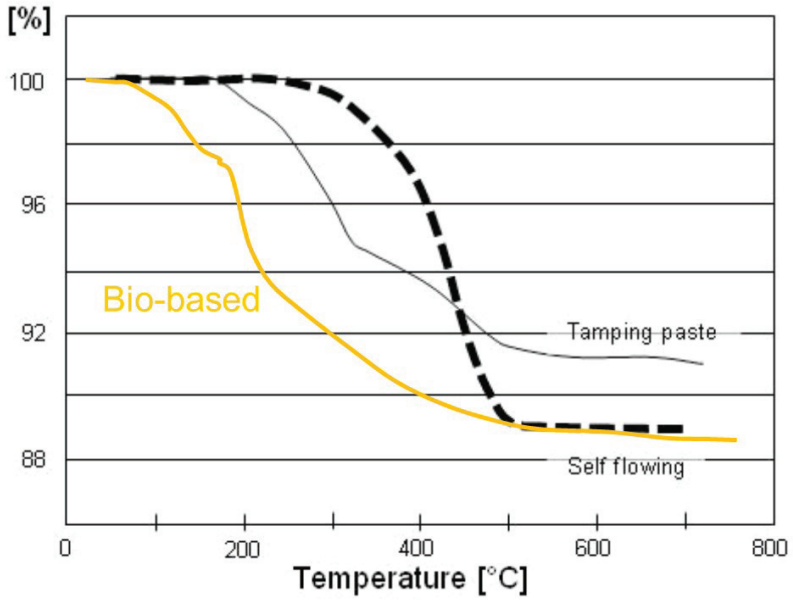


Figure 11: Weight loss curves of samples under nitrogen atmosphere for a tamping paste with bio-based binder, regular tamping paste and electrode paste (self-flowing).

This example shows that the requirement of gas release over a wide temperature range was achieved also with the bio-based binder, but the release happened at a lower temperature range.

Products with alternative binders

The Elkem Carbon program of product development activities focuses on the whole product portfolio range, and solutions have been commercially implemented to some products, while other areas are still under development.

The new binder solutions are sought after in a wide range of material sources from purely bio-based materials to more classical fossil materials. Note that it will be illegal under REACH, to utilize electrode paste for other functions than electrode use after October 4th, 2020, see figure 1.

Cathode ramming paste

ELSEAL® Type G is Elkem Carbon's PAH free solution for cathode ramming paste in aluminium cells. The product was developed with a new binder in a system with more than 25 years proven performance of Elkem Carbon's concept. The new binder system has a slightly lower coke yield compared to coal tar pitch based binders. Despite this, properties such as density, open porosity and mechanical strength are at the same level as comparable coal tar pitch based products. This product is manually handled and installed, and thus requires minimum exposure risk. The binder developed for this solution is purely bio-based, and has no PAH issues.

Ramming paste for use in tapping spouts, runners, carbon lined ladles etc.

Also, a paste for lining of tapping spouts, runners, carbon lined ladles and for tap hole repairs was developed, ELTAP® SMB. This product is in most cases manually handled and installed, and thus require minimum exposure risk. In addition, baking of the installed material occurs near to worker environment, and may represent a PAH-issue for ferro-alloy producers. The binder applied for this product is bio-based, and has no PAH issues.

Tap hole plugging- and repair pastes

Elkem has decided not to utilize CTPht in the tap hole plugging- and repair pastes product range, and alternative materials are under development. For tap hole plugging application, it is already clear that the properties without CTPht are acceptable

For paste used in demanding repair conditions, coal tar pitch is still the preferred solution in some cases. Until alternative solutions are developed and commercialized, Elkem will base these materials on the still accepted CTP (Pitch, coal tar, high-temp., heat-treated, EC / List no. 310-162-7), but promising results have already been seen with alternative binders, and new products are currently being tested.

Søderberg electrode paste

"Søderberg electrode binder requirements", above, indicates that the most challenging Elkem Carbon product to develop with new binder systems is the Søderberg electrode paste. In this application, there are numerous, partly contradicting, strict requirements. The technical and economic potential impacts to the metal production are large, and low willingness to compromise on performance from the users is expected.

Challenges on meeting requirements related to inherent binder properties, *e.g.* conductivities, reactivities, and volatiles, pose significant technical risk. In taking short-cuts here, one may even increase the potential for safety issues.

From a technical perspective, fortunately, the use of high temperature coal tar pitch (CTPht, EC / List no. 266-028-2) in Søderberg electrode paste is considered as intermediate and is thus exempted from authorization requirements under REACH (Regulation, ECHA Q&A 1195). This means that the use of CTPht in Søderberg electrode paste has been exempted from authorization requirement by REACH, and can still be marketed in Europe without authorization.

Elkem Carbon is working on the development of a PAH-free electrode paste (ELSEP® E), and promising results have been obtained, see table 1. It is clear that CTPht based paste performs better than the new alternative paste on important parameters like electrical resistivity, reactivity and strength. However, for most of the properties the results for the alternative paste is in an acceptable range, at least for some of the ferroalloy processes. Ultimately, this may result in a more diversified product range adapted to the conditions in different metallurgical applications. Optimization of the paste is still ongoing.

Table 1: Properties of PAH-free Søderberg electrode paste (ELSEP® E) and reference with standard CTPht.

Property	Unit	ELSEP® E	Reference CTPht
PAH		<100ppm	~20%
Plasticity	%	10-90	30-40
El.res.	μΩm	70-85	60-70
CTE 950-20 °C	10^{-6}K	~4	~4
Porosity	%	23-25	21-23
BAD	kg/m^3	1350-1400	1375-1425
Thermal conductivity	W/mK	~4	~4
CO_2 reaction residue - CRR	%	35-45	70-80
Air reaction residue - ARR	%	15-25	65-75
Compr. Strength	Mpa	10-15	19-23
Diametr. Strength	Mpa	1.5-2.5	1.5-2.5

CONCLUSIONS

Current EU legislation on the use of coal tar pitch, CTPht, require authorization of the use in products, but exemption has been made for electrode paste.

When developing metallurgical carbon materials based on new binder systems, detailed understanding of technical requirements is vital, and it is important to realize that some test regimes and measurement techniques are developed for coal tar pitch, and may not be directly applicable to other binders.

It has been demonstrated that CTPht can be replaced by more environmentally friendly solutions in many metallurgical applications.

The substitution of coal tar pitch in metallurgical carbon products is a challenging task, and may not be possible in all current technical applications within economically viable frames.

ACKNOWLEDGEMENTS

This paper is published by permission of Elkem Carbon AS. The contributions of colleagues are gratefully acknowledged, especially the help from the Elkem Carbon R&D laboratory team, our environmental legislation specialists and the product responsible colleagues.

References

1. European Chemicals Agency, https://echa.europa.eu/
2. Regulation 1907/2006, (Registration, Evaluation, Authorisation and Restriction of Chemicals), https://echa.europa.eu/regulations/reach/understanding-reach
3. REACH Annex XIV ("Authorization List»), https://echa.europa.eu/authorisation-list
4. ECHA Q&A, https://echa.europa.eu/support/qas-support/qas, 1195, 22.06.16
5. Søderberg, C.W., Norske Elektrokemisk Ind AS. 1919. *Electrode for electric furnaces and process for manufacturing the same*, U.S. Pat. 1,440,724 A
6. Tandberg, R., 1943. *Method of manufacturing continuous electrodes*. U.S. Pat 2,495,148 A
7. Blackmore, K.A.E., Georgia Pacific LLC. 1983. *Lignosulfonate/urea binder for particulate composites*. U.S. Pat. 4,704,230 A.
8. Franke A. J., F. L., Sturm A., Kaiser H. (1986). *Soederberg pot operation with tar-free paste*. Light metals (New York). p 689.
9. De Carvalho, J. R. D., et al., Albras Aluminio Brasileiro SA. 2001. *Anode, a process for the manufacture thereof and a process for the production of aluminum*. U.S. Pat 6,235,184.
10. Eidet, T., Guldhav, A.Y., Olsvik, A., Sørlie, M. (2004) *PAH Emissions from Søderberg Anodes with standard and PAH-Reduced Binder Pitches*, Light Metals (New York), p. 527
11. Marsh, H., Ed. *Introduction to carbon science*. Butterworths, Cornwall, England, 1989.
12. Marsh, H., Heintz, E.A., Rodríguez-Reinoso, F., Ed. *Introduction to carbon technologies.* Alicante: Universidad, 1997.
13. Zander M. *Chemistry and Properties of Coal-tar and Petroleum Pitch*, In Sciences of Carbon Materials. Marsh H. and Rodríguez-Reinoso F. (2000), 205-258. University of Alicante, Alicante.

NEW DEVELOPMENTS IN COMPOSITE ELECTRODES

Javier Bullón Camarasa
SilBuCam S.L. La Coruña, Spain

Abstract

The extremely big price increase in graphite electrodes in the last year has changed the profitability of composite electrodes for silicon metal submerged arc furnaces compared with other possibilities. Graphite makers explain that the prices will not return to previous levels, and that this price change will strongly affect the electrical steel industry, their main market. However, reasons for using graphite are completely different in the steel industry than in the silicon sector, which means other solutions, can be applied to silicon metal and other ferroalloys. In this paper, we explain the advantages of using a metallic core instead of graphite, made primarily with silicon, in particular for the silicon furnaces.

The core in the composite electrode

The graphite core is important in the composite electrode because it is the mechanical support of the carbonaceous material as well as the plunger of the extrusion effort. When the slippage of the electrode is done, a hydraulic effort is made in the slippage rings of the graphite, while the casing rings remain closed. With this effort, the casing-carbon addition is broken and only the carbonaceous material slips without silicon contamination. For that, the mechanical characteristic is the more important in the electrode core.

Graphite electrodes are used in steel industry as electrical conductor to produce the arc with the raw materials in the electrode bottom. The weak area is the connection between electrodes that is made by the nipples designed to conduct the electrical current and in favours of accumulate the breakage in this area instead of the electrode core. The electrical conduction is less important in the composite electrode because the bigger amount of the electricity goes by the outside paste as in the electrode prebaked or in the normal Soderberg electrodes.

It is also true, in the composite electrode the graphite core is a baked carbon and a good conductor of furnace heat, which is why Soderberg paste is baked at a higher level around the graphite. That is why the composite electrode can slip faster than the normal Soderberg electrodes, as is necessary in the silicon production. A presentation on

mathematical model temperatures in the contact clamps area of the electrodes was made years ago at the Silicon for Chemical and Solar Industry Conference in Tromsø.

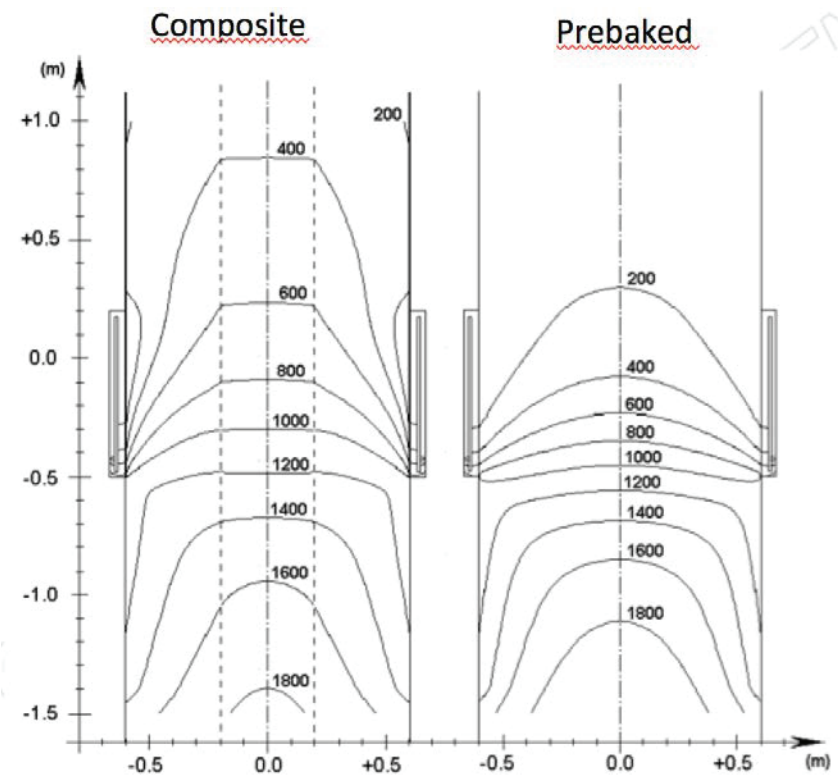


Figure 1: Temperature distribution in the electrode contact clamps area in composite and prebaked electrodes, Bullón & Bermúdez et al. (2000).

It is important to remember that carbon does not contaminate silicon. There are not many elements that do not contaminate, which makes substituting the graphite for other elements difficult, except if you return to the prebaked electrodes. Nevertheless, there is a cheap and better solution, as we will explain later.

The main problem with graphite is the very low mechanical characteristic. Its values in tensile and flexural strength are a little better than the prebaked, but much lower than the metallic elements, and the producer cannot guarantee the value. In other words, you must use a big electrode diameter to avoid as much as possible the mechanical break in the long electrode column, which can be four times longer than in steel furnaces.

The new core for the composite electrode

The question is: Is there a material with mechanical characteristics equal to or better than graphite, and which does not contaminate the silicon? We had not posed this question before, as graphite was a very common material and not very expensive. Twenty years ago the composite electrode was around one third of the prebaked electrode price but now the difference is much smaller. Now, considering the current graphite electrode situation, the answer is: Yes, there is, and this material is the silicon itself, which is also very good news for the silicon makers, as they can consume their own product.

Of course, the silicon made by the solar industry is not the good way forward, but there is an existing material, well-known for other applications and close to our sector which can be used: the Al-Si alloys and more specifically, the hypereutectic Al-Si alloy. To understand its application well, we can take a look of the Al-Si diagram:

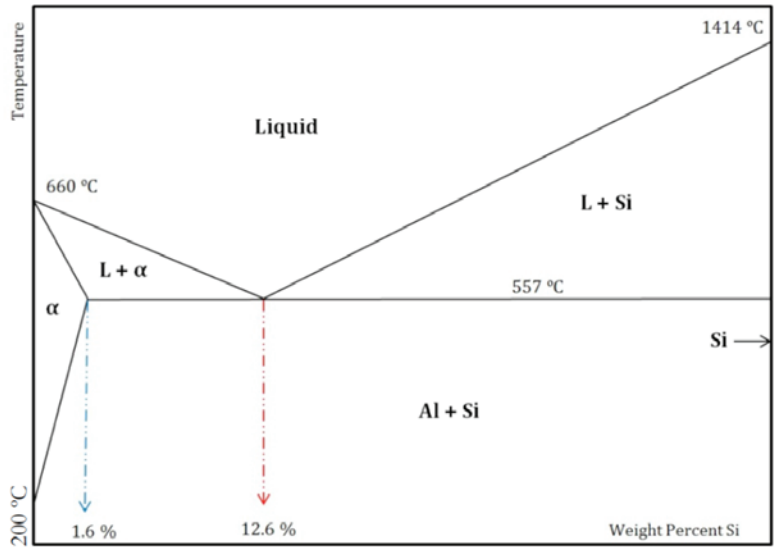


Figure 2: The schematic phase diagram of Al-Si

The diagram is very clear: the higher the silicon level, the higher the melting temperature, which is important because we want to bake the paste before losing the mechanical support of the core, similar to the fins in the normal Soderberg electrode. As the paste becomes rigid at 300 ºC, we are thinking of first approach in an alloy of minimum 50% Silicon, and the rest Aluminium and some other elements in small amount.

The hypereutectic Al-Si

The hypereutectic Al-Si is an existing material with current applications in aerospace and machinery, with much lower density than the steel, and good mechanical and

thermal characteristics. There are companies specialized in this field and we need to explain to them what a silicon furnace is, what an electrode is, and what the core in the composite electrode is. Moreover, we do not want to pay a much higher price than the raw materials: the silicon or the aluminium. Today, the main characteristics are: lower corrosion, low density, lower expansion coefficient, good machinability etc., which are not very interesting in our sector, but it has high strength, as well as good thermal and electrical conductivity, which are important for the core in the electrode.

A table of the mechanical properties of the Al-Si hypereutectic alloys can be obtained on the internet:

Table 3. Mechanical properties of Al-Si hypereutectic alloys

MECHANICAL PROPERTIES, TYPICAL VALUES OSPREY CE ALLOYS

	CE17F	CE17MF	CE13F	CE11F	CE9F	CE7F	CE6F
Chemical composition	Al-27%Si	Al-27%Si	Al-42%Si	Al-50%Si	Si-40%Al	Si-30%Al	Si-20%Al
Tensile strength, ultimate	>160	175–312[3]	205	193	181	>100	N/A
Yield strength, MPa	100	282	147	189	-		N/A
Bend strength (three point), MPa	-	-	300	300	300	270	319[1]
Young's modulus, GPa	91.8	91.8[2]	101.9	121.4	118	129.2	130
Rigidity modulus, GPa	35.8	35.8[2]	42.2[2]	48.6	46	51.6	N/A
Poisson's ratio	0.28	0.28[2]	0.27[2]	0.29	0.29	0.26	N/A
Density, g/cc	2.6	2.6	2.55	2.51	2.47	2.43	2.35[2]
Hardness, Hv	60	75–132[3]	90	-	230	-	N/A

1) Test pieces 4 mm x 3 mm x 40 mm
2) Calculated values
3) Depending on heat treatment condition

The producer of this material, https://www.materials.sandvik/en/products/ce-alloys/product-properties/#tab-mechanical-properties, is looking at the main characteristic for controlled expansion alloys, called "CE alloys". For the electrode core, in our silicon sector, the controlled expansion is not the most important factor but, is a good example of how the Al-Si product can be ready in a very short time.

Comparison between graphite and AlSi50

In terms of tensile or flexural strength, the graphite values are very small compared with the values of the hypereutectic Al-Si alloys. The nipple used for connexion between electrodes is better, but still very low. In the composite electrode, the diameter decision of the graphite electrode is taken by the weight of the column, with the more critical area being the nipple section and the top of the column.

Another problem to consider is that the values indicated in the graphite specifications are always with the sentence: "The values given in this catalogue are for purpose of information only and do not constitute any contractual obligation", because it is a brittle material. For that reason, if you want to avoid expensive electrode breakage, a bigger diameter than what is necessary theoretically for the electrode weight must take into account.

Moreover, metallic core has tensile or flexural strength values that are much bigger than the graphite. In particular the Al-Si 50 has values in the order of 193 MPa and the

graphite has only around 10 MPa, meaning a section of 500 mm graphite core diameter, which is the normal in 1250 mm electrode, can be substituted for less than 120 mm AlSi50 metallic core diameter, for the same effort.

The big graphite advantage is its increased mechanical and electrical characteristic with higher temperatures. Metals are just the opposite, with their values diminishing very fast and disappearing in the melting. In the new core, we must take into account that a cylinder of 120 mm diameter is not convenient, as when the metal disappears in the area of the contact clamps, a hole in the electrode will remain, making the electrode weaker. For that, it is better to make a tube instead of a cylinder with the same surface and mechanical resistance, introducing a precursor of silicon carbide inside the tube. Therefore, when the metal has melted and disappeared, it will be replaced with silicon carbide, which will remain unchanged until the bottom of the electrode and the furnace. Others important details must be also taken into account in this new technology of metallic core, the ELMET composite electrode, which can be also apply to others ferroalloys by substituting the Al-Si alloys with normal steel and can directly compete with the current casing with fins

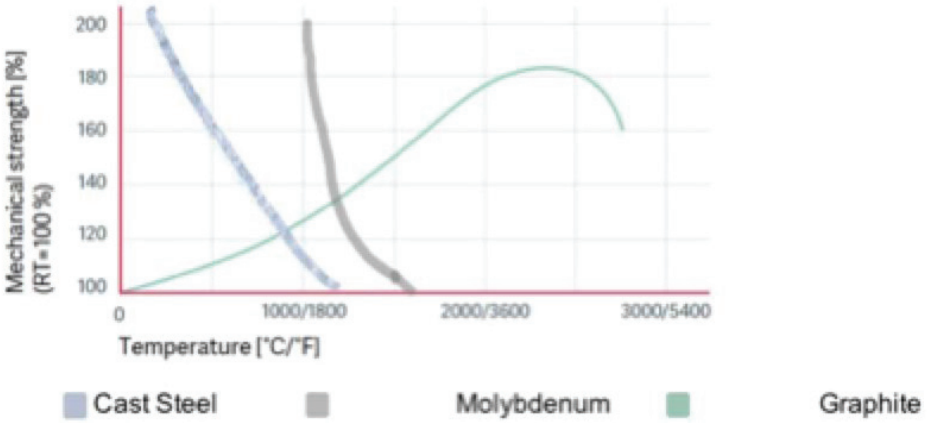


Figure 3: Hot bending strength in various high temperature materials

As far as silicon contamination is concerned, the 100 cm^2 new metallic core represents a weight of 32 kg/m, where 16 kg are aluminium. Making some numbers, the normal daily electrode consumption of one 24 MW silicon furnace is 2 meters, which means 32 kg of aluminium will go to the silicon. The normal daily production of this kind of furnace is 45 tonnes. Aluminium contamination by the metallic core represents 0,07 %, which is not important in front of the normal aluminium contamination coming basically from the quartz. In many furnaces, depending of the quartz origin the aluminium in the tap hole can be in between 0,3 % and 0,8 %, the metallic core aluminium contamination is lower than 10% of the total. Moreover, it is very well known aluminium is one of the easiest contaminants to eliminate by blowing air/oxygen in the ladle. It is very possible than in the future we can use Al-Si alloys with more than 80% in silicon, with some others small addition in very low level.

Conclusions

A new metallic core is proposed for the composite electrode, replacing the graphite used today with many advantages from a mechanical point of view, and using silicon as the main element, which does not contaminate silicon production. Also, the cost would be much lower and using the silicon product as raw material, the sector will be free of the extremely big price increase of the graphite or other carbon electrodes. The system is patent pending and supposes a new step in the electrode technology for the submerged arc furnaces. The principle can be the same for the ferroalloys and we can propose the name "ELMET" for this new electrode technology. The next step is to test this new development in an existing furnace.

References

1. V. Gallego, J. Bullón – The use of a compound electrode for the production of silicon metal. Silicon for the Chemical Industry II. Loen 1994.
2. J. Bullón, V. Gallego, R. Boisvert, J. Dubois – Experiences in 1995 with the new compound electrode for silicon metal. Iron and Steel Institute. Orlando 1995.
3. J. Bullón, V. Gallego, D. Ksinsik and R. Boisvert – New developments in the Compound Electrode for the Silicon Metal Production. Silicon for the Chemical Industry. Sandefjord June 1996.
4. J. Bullón, M. Lage, A. Bermudez, F. Pena – Development in 1996 of the new electrode for silicon metal. Iron and Steel Institute. Dallas 1996.
5. A. Bermúdez, J. Bullón, F. Pena – Thermoelectrical simulation of electrodes for reduction furnaces. Computational Science for the 21ST Century. London 1997.
6. J. Bullón, A. Bermudez, F. Pena – The new compound electrode current situation and thermoelectric studies. Infacon 8. Beijing 1998.
7. J. Bullón, J. García, A. Bermúdez, F. Pena – Mechanical resistance in the compound electrode. Iron and Steel Institute. New Orleans 1998
8. A. Bermudez, F. Pena, J. Bullón – A finite element method for the thermoelectrical modelling of electrodes. Commun. Numer. Meth. Engn. 14 (1998)
9. J. Bullón, A. Bermudez, A. Lorenzo, P. Salgado – Development of the Elsa-Compound electrode for silicon metal and its mathematical model. Silicon for the Chemical Industry. Tromso 2000.

Development and application of PAH free Electrode Paste

Robert Becker[1)], Johann Leye[1)],
1) Rheinfelden Carbon GmbH & Co KG

Abstract

Electrode Paste for silicon metal production is used in various electrode technologies today. Traditional Electrode Paste is based on coal tar pitch as a binder. Coal tar pitch is rated carcinogen and genotoxic. In Europe and the western world there is a big pressure to ban the use of coal tar pitch for Söderberg application within the next 2 years.
This work is presenting our investigations of alternative binders, the results in production furnaces and setting a question mark on existing specifications for Söderbergpaste. The results we learned from production use may open new possibilities in composite technology.

Coal tar pitch (CTP) as a binder

Legal Situation

Coal tar pitch, high temperature, CAS number 65996-93-2, is identified as
CMR (carcinogenic, mutagenic and reprotoxic) according to Article 57 (a)
PBT (persistent, bioaccumulative and toxic), according to Article 57 (d) and
vPvB (very persistent and very bioaccumulative) according to Article 57 (e)
of Regulation (EC) 1272/2008[1] and (EU) 944/2013 (REACH)[2].
Due to that classification it was put on the candidate list for substances of very high concern (SVHC) on January 13th, 2010. On June 13th, 2017 the European Commission decided to put pitch on Annex XIV, authorisation list, of the REACH regulation with sunset date October 10th, 2020[3].

Consequences

This classification automatically leads to extensive impacts for the application. When handling and emitting hazardous substances, it is essential to consider the use of alternatives. Substitution is a general legal provision mentioned in Framework Directive 89/391/ECC[4] and Chemical Agents Directive 98/24/EC[5]. Using and handling carcinogenic and mutagenic substances requires substitution analysis (Carcinogens and Mutagens Directive 2004/37/EC[6]).
Regarding authorisation there are two solutions. First option is to declare the application as an intermediate use. Intermediate use is exempted by authorisation. This classification might not be granted by the European Chemical Agency (ECHA). There is a risk that the authorities might not accept that approach.

The second option is to apply for authorisation. If there are alternatives available on the market, authorisation will not be possible.
In addition to the substitution dictate, the Industrial Emission Directive 2010/75/EU need to be considered.
The most challenging substance with regard to "Best available Techniques" (BAT) is the Emission level for Benzo[a]pyrene which is a key indicator for all polyaromatic hydrocarbons (PAH), 0,001 – 0,01 mg/Nm^3.

Binder for Electrode Paste

Coal tar pitch is a mix of various aromatic hydrocarbons. The melting point is a function of the average molecule weight. For Electrode Paste application a melting point of 60 up to 100°C is used[3].

In the self-baking electrode the temperature of the paste slightly increases from room temperature (RT) to approx. 3000°C at the tip of the electrode. The binder is connecting the granular carbon, adding mechanical strength and electrical conductivity, which is essential for electrode use[7].

There are several reasons why the aromatic hydrocarbons in coal tar pitch are the best to fulfil both needs properly:

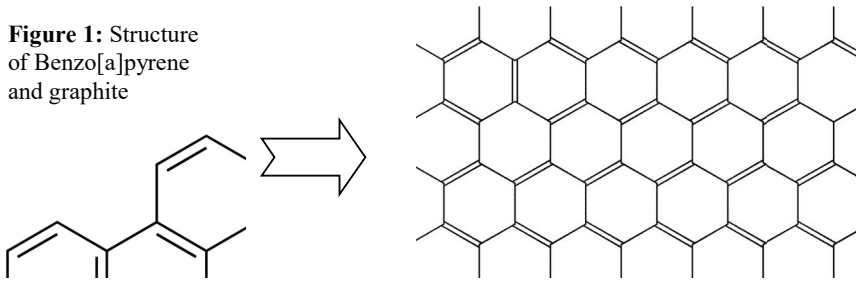


Figure 1: Structure of Benzo[a]pyrene and graphite

As shown in Figure 1 the medium sized PAH (like BAP) are perfect structured to be converted into graphite – unfortunately they are the most toxic substances in CTP.

Coal tar pitch high temperature (CTPht) can easily be transformed to graphite particles by temperature only, forming a mechanical strong and electrical conductive binder coke.

Due to the large range of molecule weight, the hardening process starts at 500°C and is finished at around 700°C. This large temperature window is important for the process to avoid mechanical or thermal tensions.

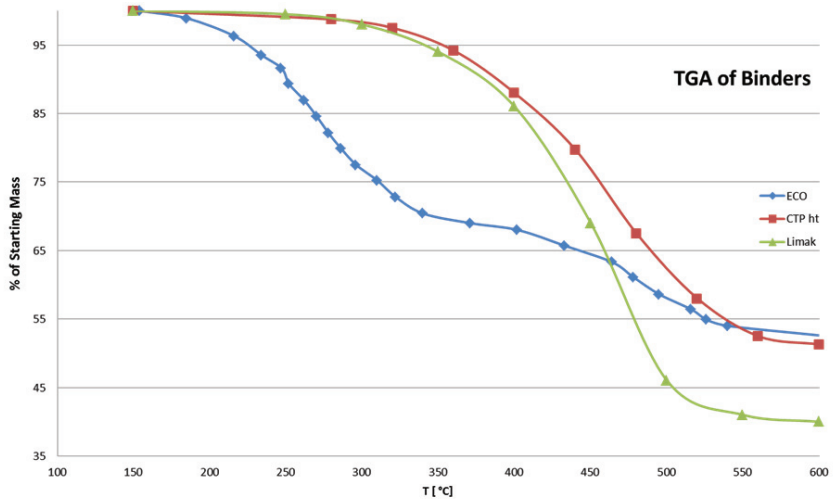
Other binding systems based on mono-structural molecules are hardening much faster, in the worst case with exothermic reactions. The result is a brittle and by micro cracks damaged binder matrix.

For the application of Electrode Paste the large temperature window (while hardening) is essential.

Based on these principles we worked on lots of industrial products with large molecule weight distribution and more aliphatic origin. The final product after baking must be graphite. The chain structure has to be converted to ring structures. This could be slightly supported by additives.

The best results ended up in a very poor binder system we named LIMAK.

Figure 2:



Coking value is the most important figure to characterize binder properties (amount of binder coke in the paste).
Positive indications for LIMAK at this stage were the shape of the curve and the mechanical stability of the coke residue.

The lab results using LIMAK binder were not promising accordingly.

	LIMAK paste	CTP paste	
baked app. density	1,4	1,5	g/cm3
electrical resistivity	95 -120	70	µΩm
flexural strength	3	7	MPa
crushing strength	10	25	MPa

Anyway we had to take the risk for an industrial test – from the lab tests this was the best paste without PAH's. We found a partner and started charging one small electrode in Ferrosilicon production. We scheduled the test before a long maintenance stop to minimize the risk.
Making the first electrode autopsy was a big surprise. The LIMAK electrode looked perfect – no cracks neither on the surface nor inside the electrode.
Cutting the removed electrode vertical and taking cores for investigation was even more surprising.

Figure 3: Sampling the LIMAK electrode

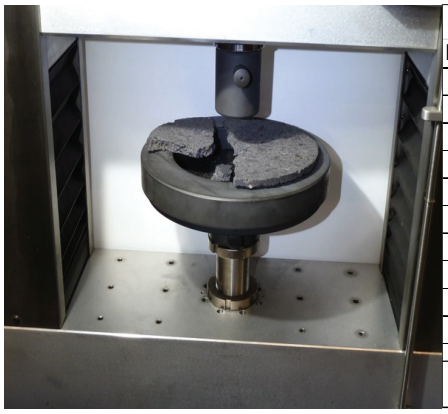


LIMAK 30	density	spez.el. resistivity (µOhmm)	bending strength (MPa)	thermal conduct. (W/mk)	crushing strength (MPa)
top	1,395	34,2	2,04	32,18	7,34
↓	1,429	34,0	3,20	31,87	9,20
	1,419	47,6	3,24	25,49	10,08
↓	1,441	37,0	4,20	32,57	13,06
bottom	1,418	32,7	3,48	33,54	10,75
Ø	**1,420**	**37,1**	**3,23**	**31,13**	**10,09**
2σ	**0,034**	**12,2**	**1,56**	**6,43**	**4,20**

Figure 4: Physical data of the electrode (top = direct below the contact clamps, bottom = close to the tip of the electrode)

To have some more indications on the flexibility or the brittleness of baked electrodes we developed a measurement system we named bulge test.

Figure 5: Bulge test arrangement and data



LIMAK 30 Bulgetest		stress N/cm²	strain %
1	center	2,51	28,4
2	↓	2,62	27,1
3		2,58	30,2
4		2,42	22,9
5		2,81	26,2
6		3,06	23,0
7		2,81	25,4
8		2,80	23,9
9	↓	2,97	25,5
10	casing	2,99	26,6
	Ø	2,76	25,92

26% strain is given by bending the plate (10mm thickness) 2.6 mm before it breaks.

That is extraordinary for Electrode Paste - we never measured such values before.Summary LIMAK binder and electrode performance:

Limak binder does not match the specifications for CTPht binders at all.
Coking value is low.
Volatiles are high
Softening point is high
Quinoline insolubles vs. toluene insolubles are not applicable.

Lab tests for paste:
poor mechanical properties
very high el. resistivity
low shrinkage during baking

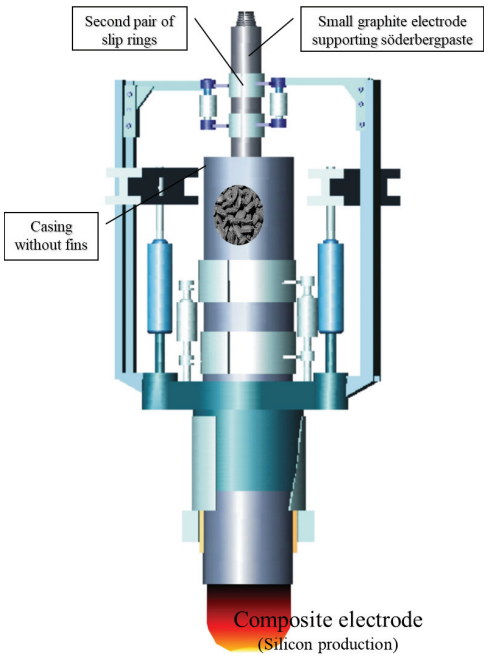
Furnace results:
low density,
low mechanical strength
perfect electrical resistivity,
high thermal conductivity
outstanding elasticity

In Söderberg furnaces LIMAK pastes are covering all needs, running on electrode diameters between 0.9 and 1.9 m.
The baking zone is high compared to CTPht pitch based pastes. This is a big advantage in Söderberg furnaces. Specific paste consumption is slightly higher.
Thermal shock resistivity is good.

LIMAK paste in Silicon Metal Production

LIMAK based pastes are running in composite technology furnaces[8] for silicon metal production as well.

Figure 6: Typical electrode arrangement for composite electrodes



The thermal profile in a composite furnace is very different from Söderberg furnaces. The graphite core is dominating heat transfer to the top and is bending the isotherms up in the centre. Each nipple area is influencing the isotherms and baking conditions on top. When the 500°C isotherm is above the contact clamps problems with lowering the electrode may get severe.

Measuring the baking zone in composite can be done by the Cavigli voltage[9]. Our customers reported an increase of the baking zone by 20-30 cm in average, when using LIMAK paste. Of course this is not a fixed number – it differs from furnace design and paste quality.

When we started to use LIMAK in composite, small problems came up with sticking. In well managed furnaces the paste performed normal. When the power reached a certain level (Furnaces run on more than100%) the baking level exceeded above the contact clamps and lowering of the electrodes was disturbed.
Today several furnaces are running with LIMAK paste without any problems. Specific paste consumption is normal.

For some furnaces running with extreme high power we have to modify the paste and from the furnace design there are a lot of possibilities to bring the baking zone down.

Conclusions:

- PAH free pastes are working in Industry, proven by various furnaces and industries.

- Without taking some risk from production sites this work on coal tar free products would have had no chance to proceed. Thanks to our friends for their help and patience.

- Specifications have to be adapted to new systems - sometimes they are blocking the right conclusions and decisions.

In times when coal tar pitch is doubling the price within a year and graphite electrode prices increase with a factor of 10, it is helpful to have alternatives from other industries.

The problematic high baking zone with LIMAK binder in composite (caused by the high thermal conductivity of the core) is pushing new ideas.

Today we are working on a project to get rid of the graphite core in composite. A high baking zone of the paste is one key for success. This will solve electrode problems and save a lot of costs for the silicon smelters.

References

1. Regulation (EC) No 1272/2008 of the European Parliament and the Council of 16 December 2008 on classification, labelling and packaging of substances and mixtures, amending and repealing, Directives 67/548/EEC and 1999/45/EC, and amending Regulation (EC) No 1907/2006. Available at: http://eur-lex.europa.eu/LexUriServ/LexUriServ.do?uri=OJ:L:2008:353:0001:1355:en:PDF
2. Commission Regulation (EU) No 944/2013 of 2 October 2013 amending, for the purposes of its adaptation to technical and scientific progress, Regulation (EC) No 1272/2008 of the European Parliament and of the Council on classification, labelling and packaging of substances and mixtures. Available at: https://eur-lex.europa.eu/legal-content/EN/TXT/?uri=celex%3A32013R0944
3. ECHA publication. Available at: https://echa.europa.eu/de/substance-information/-/substanceinfo/100.060.007
4. Council Directive 89/391/EEC of 12 June 1989 on the introduction of measures to encourage improvements in the safety and health of workers at work, Official Journal of the European Communities L 183 of 29June 1989. Available at: http://eur-lex.europa.eu/LexUriServ/LexUriServ.do?uri=OJ:L:1989:183:0001:0008:EN:PDF
5. Council Directive 98/24/EC of 7 April 1998 on the protection of the health and safety of workers from the risks related to chemical agents at work, Official Journal of the European Communities L 131 of 5 May1998. Available at: http://eur-lex.europa.eu/LexUriServ/LexUriServ.do?uri=OJ:L:1998:131:0011:0023:EN:PDF
6. Directive 2004/37/EC of the European Parliament and of the Council of 29 April 2004 on the protection of workers from the risks related to exposure to carcinogens or mutagens at work (codified version), Official Journal of the European Union L 158 of 30 April 2004. Available at: http://eur-lex.europa.eu/LexUriServ/LexUriServ.do?uri=OJ:L:2004:229:0023:0034:EN:PDF
7. L. F. King, W. D. Robertson, *Coal tar and petroleum pitches as binders for Soderberg electrodes,* ACS Fuels,18, No.4, 1973, p.145–154
8. J. Bullon, V. Gallego, *The use of a compound electrode for the production of silicon metal. Electric Furnace Conference Proceedings*, Vol. 52, Iron & Steel Society, Warrendale, PA, 1994, 371–374
9. M. Cavigli, *Self-baking electrode structure and method of operating same,* US3624261A, 1970

Søderberg electrode technology and the potential for higher performance metallurgical silicon for the solar and chemical industry

MSc. Dipl. Eng. Valdiney Domingos de Oliveira[1], Dipl. Eng. Rodrigo Silva de Faria[1], Dipl. Eng. Luciano Biazutti[1] , Dipl. Eng. Gabriel Esteves[1] , Dipl. Eng. Lou Parous[1]
1) Viridis.iQ GmbH, von-Emmich-str 4, 78467 Konstanz, Germany

Abstract

Metallurgical Silicon is becoming increasingly a critical raw material and industry wide efforts are being made to develop high performance, customized Silicon materials for the production of lower cost derivatives for the solar and chemical sectors. These industries continue to grow at a rapid pace and increasingly demand higher quality feedstock with a focus on lower costs over the entire value chain. Over the past decades, one initiative that many TCS and MCS producers have used is the addition of selected catalyst to the metallurgical Silicon feedstock as a way to increase downstream performance. In parallel, development in silicon smelting electrode technology has undergone changes in the past years with a trend away from prebaked solid electrodes towards graphite core electrodes with Søderberg paste. More recently, volatility in the supply and price of graphite core composite electrodes has shocked the industry and has furthered the trend of developing 100% Soderberg paste electrodes for metallurgical silicon production. The conflation of the two trends of 100% Søderberg paste electrodes and the demand for higher performance metallurgical silicon with catalyst has resulted in the development of the alternative electrode technology with 100% Søderberg paste which can be used to add specialized and tailored catalyst to increase the reactivity and selectivity of the produced silicon in the TCS and MCS downstream sectors while reducing costs and supply risks. The aim of this article is to explore the possible benefits of capitalizing on the electrode trends with improving performance of metallurgical Silicon in TCS and MCS production processes.

Overview of Søderberg electrodes for Silicon production

Introduction

The Søderberg electrode is considered to be a self-baking electrode because the electrode paste and calcination occurs inside the actual furnace in the vertical tubular casing. The components of the Søderberg electrode for Silicon production are similar with that used for Ferrosilicon production with a principle difference being the material used in the casing. Various casing options are available depending on producer needs and materials characteristics. It´s very import that that the specific engineering aspects are considered during the system design and built into the design by experienced and qualified experts. Lastly, process operational experience is key to successful implementation and capitalization of the economic benefits of the technology. The following figure shows the principle components of the Søderberg electrode column.

The electrode itself is made of a metallic casing with internal radial fins for structural support that are also used for conductivity of the electrical energy to provide the calcination of the electrode. The fins also have the function to increase the mechanical and flexural strength of the electrode column (in the crude paste area and under contact pads region during the self-baking process at high temperatures). As the electrode is consumed in the furnace, additional segments of casting, ribs and electrode paste are added in the upper part of the column much like additional segments are added in other electrode types. This conjunct that is prepared prior to the welding/addition process on top of the electrode column.

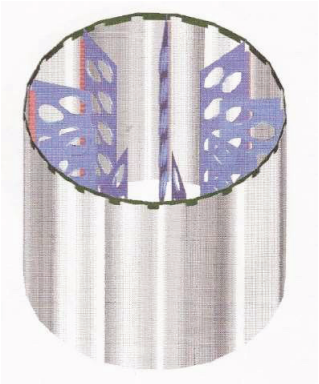


Figure 1: Example of the internal stainless steel ribs

History of using Søderberg electrodes in Silicon

The use of Søderberg electrodes has been well established for the ferroalloy production industries and was developed initially by the precursor company to Elkem, Elektrokjemisk, in the early 1900s. The use of Søderberg electrodes for ferrosilicon and other ferroalloys, as well as for slag cleaning processes has been a revolutionary achievement for those processes and the dissemination of the technology is widespread. Historically, Søderberg electrodes have not been adapted in a similar widespread manner for Silicon production due in part to the operational challenges in using non-Iron based casing materials, unwanted contamination of the Silicon with the casing material, and lastly the equally unwanted contamination of Iron in the Silicon caused from the structural fins of the casing that are normally made from stainless steel.

The cost savings of using Søderberg electrodes in Ferrosilicon production was eventually seen as providing a value contribution to Silicon production and its use in Silicon production was driven by market forces. In Brasil, Silicon producers were highly dependent on imported prebaked electrodes from Europe and were forced to seek cheaper alternatives. Similarly, European Silicon producers were seeking competitive advantages again lower cost competitors in Norway and the United States and eventually developed what is now known as the composite electrodes.

Presently, a few companies have succeeded in fully adapting the use of Søderberg electrodes to the production of Silicon in submerged arc furnaces of various sizes. These companies are mainly in South America and over the past 20 years have perfected the practical use of this technology in both the engineering of the electrode column as well as the operational nuances required for this electrode variant. To this day, it is believed that at least three Silicon production facilities in Brasil still use the technology in the production of Silicon. The following table shows the History of the development and consolidation of Søderberg electrode technology for Silicon production in Brazil.

Company	Country	Year	Active Power (MW)	Electrode Diameter(mm)
CBCC	Brazil	1997	12.8	1060
CBCC	Brazil	1998-2001	15.0	1060
CBCC	Brazil	2001-present	20-24	1300
Italmagnesio	Brazil	2001	17.5	1143
Italmagnesio	Brazil	2002	17.5	1143
Italmagnesio	Brazil	2003	17.5	1143
Rima	Brazil	2002-2003	20,21	1143
Rima	Brazil	2004-2011	20,21	1205
Rima	Brazil	2012	26 - 27	1320

Figure 2: History of Søderberg electrode technology in Brazil.

Self-baking process description

The Søderberg electrode is a system of three components: electrode paste, metal casing and stainless fins, along with rivets for the connection of the fins to the casting and

possibly additional components such as measurement probes of various materials. As the purpose of the electrode is to conduct a high electrical current, the electrical conductivity is an important component in the electrode. As the temperature increases, conductivity in the metal casting is reduced, but is increased in the carbon paste. With a proper of metal to carbon ratio, the metallic casing and the calcinated electrode paste acquire the same conductivity at a specific temperature. With increasing temperature, the conductivity of the paste increases as the metallic casing and ribs melt resulting in a baked carbon electrode suitable for conducting current on its own. The following figure is shows an overview of the self-baking process in the tubular casing.

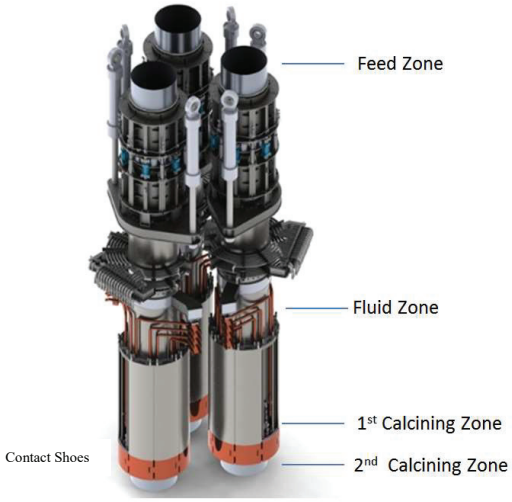


Figure 3: Viridis.iQ Alternative Søderberg electrode column (source Virdis.iQ)

- Feed Zone: column top, where new segments of liners are welded and where the solid Electrode paste is fed.
- Fluid Zone: Where the temperature increases and the paste receives certain amount of heat causing the paste to flow and fill the entire interior of the shirt.
- 1st Calcinating Zone: where the electrode paste transitions from a liquid to conductor with high mechanical strength. Pyrolysis removes the volatiles thru the pores of the electrode depositing crystals and increasing strength
- 2nd Calcinating Zone: the electrode graphitizes and forms the electrode itself performing its basic function, which is to allow the formation of the arc and the consequent generation of heat to the reduction process.

Søderberg Column Equipment

The main equipment used in the Södeberg electrode column can be divided into two main areas: the upper column and the lower column as well as the power system, as explained below.

1) Upper column – The slipping device, mainly the upper and lower slipping rings, the pressure control system, the regulating cylinder for the column, etc.
2) Lower column – The pressure rings, water cooled jackets, electrode tube, contact clamps/pads, etc),
3) Power system – includes the cooling pipes, insulation system and air heating and insuflating system

There are various considerations that should be noted in the electrode equipment design, of which a few are outlined below.

- It is important and essential that the coking of the electrode paste take place entirely and must occurs before the temperature level of shirt reaches 630 °C.
- Sufficient heating systems and fans are well designed to provide proper temperature profiles for the contact shoes.
- The interface between the electrode column equipment and the electrode itself (casing) must to be kept under pressure to avoid dust accumulation.
- The contact pads should be designed in the high conductivity material and provide a design to cover the expansion of the paste and melting of the electrode casing material in between the electrode and internal contact pad facings.
- Pressure rings should be designed considering one segment per contact pad and the system should be able to operate at lower pressure ranges with high accuracy..
- The cooling circuit on the contact pads should allow the operator to regulate the flow and temperature of the water in order to help the control of self-baking curve during start and ramp ups.
- The paste feeding system should allow the feeding process to be handled in a smooth way in order to avoid damage during this process
- Thermal control of the electrode column should be installed properly in the right positions on electrode.
- Pressure control of the regulating cylinder, as well as load cells to control the electrode column weight will help the electrode management during the production process
- The electrical insulation chain of the electrode column should be technically designed to mitigate operational risks
- The electrode casing and fins conjunct should be designed to ensure the heat and electricity transference from the contact plates to the electrode, as well as the formation of the electrode to support the paste in the solid and liquid transition state.
- The internal ribs of the electrode must be designed for the optimal heat and electrical transference and the conjunct of the ribs and the casting material must be carefully designed for the mechanical demands of the entire electrode.

Cost Benefits of Alternative Søderberg Electrodes

The implementation of the Søderberg electrode various substantial cost benefits to Silicon production.

Table 1: Qualitative benefits of Alternative Søderberg Electrodes

Benefit	***Description***
Operational Costs	The Søderberg electrode operational cost is lower than prebaked and composite electrodes[13].
Improved Process Control and Product Quality	Higher operational process controls are needed which benefit the overall production process and require additional operator training and in depth process knowledge, resulting in higher product quality.
Catalyst Addition	Addition of specialized catalyst for downstream applications is possible with the substitution of the internal ribs with catalyst containing materials.

The authors have published previously a simulation of the cost advantages of Alternative Søderberg Electrodes considering the following basecase scenario. The results of the simulation are shown following.

- 24 MW SAF
- 1271 mm electrode dia (types)
- 50in PB 4TPO m-f, 52Al10SS Alt, 50450 C
- Low ash coal + charcoal
- 84 kg/t, 2.55[1] kg SiO_2/t
- 10.75 MWh/t
- Viridis.iQ process design assumptions

Capital Equipment Cost Benefits

In terms of capital equipment costs, due to the fact that the composite electrode requires a higher level of control and an additional slipping system, the capital expenditures expected for the Alternative Søderberg electrodes column is slightly higher than the other standard technologies. The Søderberg electrodes could be operated with similar equipment (with a simple observation that the design of the electrode column either for prebaked or Søderberg electrodes must permit operating the slipping clamps and lower electrode column parts at lower pressures with good accuracy). One important point of this initial equipment comparison is the flexibility that the operator will have if the electrode installation is planned to operate with Søderberg electrodes or Prebaked electrode. In both cases, the flexibility will allow the plant to convert between the two technologies without significant problems so long as there is a well-developed transition plan involving the operational staff. The slight difference between the Søderberg electrodes and Prebaked electrodes from the capital costs standpoint is

[1] Calculated value by Viridis.iQ GmbH metallurgists - Based on global reaction (SiO_2(s) + 2C(s) = Si(l) + 2CO(g)) the stoichiometric consumption of a 98% pure quartz (98% of SiO_2), silicon recovery of 88% and final product with 99% of Si (Silicon) and up to 2.8% of losses in Quartz handling process, the calculated Silicon consumption is 2,55 tons of Quartz per ton of Silicon.

related to the level of automation and the need for machinery to prepare the casing and fins.

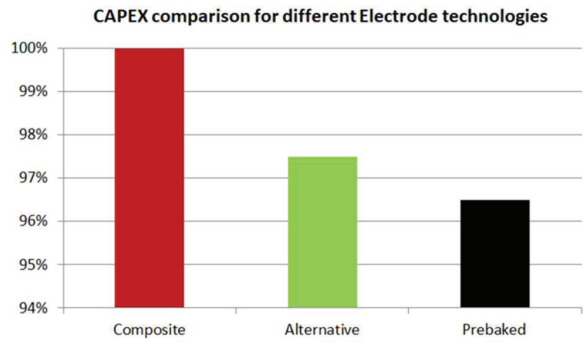


Figure 5: Electrode technologies comparison (normalized) (source Viridis.iQ)

Operational Cost Benefits

Considering the mentioned basecase scenario, under the same operational circumstances in terms of Silicon yield and Overall Equipment Effectiveness (OEE), the authors estimate the expected Operational Costs for the Søderberg electrodes versus prebaked and composite electrodes. The scenario was used as a reference and inputs from the Viridis.iQ data base, such as budgetary offers from the main prebaked, graphite and Søderberg paste suppliers, as well as quotations for Aluminum, Steel (both used in the casings for Extruded and Søderberg electrodes. The labor cost for the casing preparation, based on Viridis.iQ estimates was calculated. The results are shown in the following graph in a normalized basis.

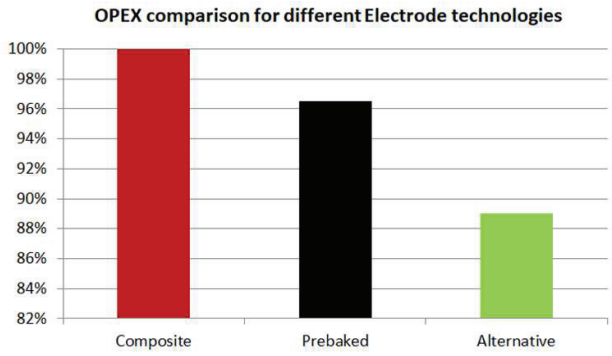


Figure 6 Electrode technologies comparison (normalized) (source Viridis.iQ)

Catalyst usage in MCS and TCS processes

Overview of catalysts usage

The effects principally copper based catalyst in the industrial TCS and MCS process is well documented, although specific industrial usage feed rates and copper concentrations in the reaction mass are relatively unpublished for proprietary reasons. In all cases, catalyst is externally added to the mgSi feed as are promoters - not to be confused with the promoter impact of various impurities that are already in mgSi such as Al, Fe, etc. The following is only meant to be a primer on the subject and not a comprehensive review.

In MCS, the use of copper[1] catalyst (CuCl, CuO, Cu_2O, Cu,) along with zinc and tin promoters is well established. Phosphorus can also be used as a promoter. The addition of Phosphorus to the mgSi is a working example of adding a catalyst / promoter to MCS[2]. Without use of copper + Zn + Sn, the MCS process reaction does not work at all and thus the common use of various nuances forms of Cu, Zn and Sn, along with absolute amounts and ratios of Cu/Zn, Zn/Sn, Sn/Cu are kept as closely guarded secrets among main MCS producers. Lastly, each producer has developed optimal process parameters and methods to operate their facility that best fits their overall plant design and knowledge base, not to mention their established mgSi quality and composition. This includes the actual form of copper used (CuCl, CuO, Cu_2O or Cu).

In TCS, there are two main process routes that are industrially used.

Hydrochlorination	$Si + 2H_2 + 3SiCl_4 \rightarrow 4HSiCl_3$ and	(1)
Direct Chlorination	$Si + 3HCl \rightarrow HSiCl_3 + H_2$	(2)

While both routes can proceed on its own without a catalyst, there are benefits from using catalysts. There are no known industrial applications of TCS Direct Chlorination (TCS-DC) production using catalyst but TCS Hydrochlorination (TCS-HC) is known to use catalyst in industrial applications. Unlike the MCS process, the TCS-HC reaction can be run successfully without use of external catalyst but results in lower TCS yield, which is the main reason the catalyst is used in practice as the catalyst can increase yields in practice. Impurities present in the mgSi feed, such as Al and Fe, always provide in-situ catalysis for the TCS-HC reaction; however the use of an external catalyst, principally copper based, helps drive the TCS-HC reaction closer to equilibrium and higher TCS yield[3].

Copper is the preferred externally added catalyst can be added in the form of copper oxide, metallic copper or copper chloride. Cu_3Si (Eta phase) is believed to be the catalytically active form of copper in the TCS-HC reaction, as is the case for the MCS process. In MCS studies meant to identify the form of copper in MCS beds, the Eta phase is generally seen as the catalytically active form of copper[4]. The eta phase is generally assumed to be formed based on the following reaction:

For TCS	$3Cu\ (g) + Si\ (s) \rightarrow Cu_3Si\ (s)$	(1)
For MCS	$12CuCl\ (g) + 7Si\ (s) \rightarrow 4Cu_3Si\ (s) + 3SiCl_4\ (g)$	(2)

If CuCl is not the external catalyst used, then other forms of Cu (i.e. CuO / Cu_2O or Cu) must be converted to CuCl first.

Catalyst concentration and activity

Industrial catalyst concentration feed rates into the reaction mass are not published due to proprietary reasons. However, lab concentration rates are disclosed from patents and other studies on the subject[5,6]. For MCS, the lab rate catalyst concentration rates are approx. 3% - 5% by weight of the reaction mass while for TCS-HC the rates are 1%-5% by weight of the reaction mass. As most lab scale reactors run with higher copper catalyst than industrial plants, the authors will assume a mid-range for the copper catalyst concentration in subsequent discussion of 3%.

The external copper catalyst used in the MCS process (along with Zn and Sn promoters) and TCS-HC are mainly surface reactions. In MCS, Copper diffuses into the surface of the silicon particle and creates an alloy which releases Silicon and creates a diffusion front that moves deeper into the particle until the kinetics are exhausted[7]. In theory, the number of surface reaction sites would lead to a higher reaction rate in both processes. It can be surmises that the mgSi had a dopant concentration of the catalyst embedded in the particles, on the surface and throughout, the reaction rate also would accelerate.

Addition of copper to mgSi

Some mgSi smelters have experimented with doping of mgSi with Copper in an effort to increase the reaction rates for TCS-HC and MCS customers. The high segregation rates of Copper in Silicon along with the traditional slow cooling of mgSi ingots upon casting results in ample opportunity for the added dopant to segregate to the heterogeneous grain boundaries of the mgSi cast ingot resulting in, once crushed and ground to a powder, a wide variability in concentration level of the catalyst from particle to particle. This heterogeneity can cause uneven results in the TCS and MCS reactors and has been the rationale for adding catalyst externally to the ground mgSi powder at the TCS-HC and MCS reactor site. Lastly, externally added CuCl must be converted to Cu_3Si (Eta phase) before the intended catalysis effect takes place. It is likely that if mgSi is doped with copper in the liquid state, on cooling, the copper would form Cu_3Si and therefore be readily available in the active form without the need for an external catalyst addition[2]. The Cu_3Si (eta phase) has been reported to be an important copper source in the MCS direct process in the catalysis of the reaction.

Bulk casting of mgSi generally takes place in large ingot moulds at the smelter site which undergo forced convection cooling before being crushed and ground into a powder for TCS-HC and MCS customers. A few TCS-HC and almost all MCS producers have their own grinding plant which allows them to size the mgSi to correct specifications before adding to their process. Heterogeneous impurity concentrations in cast ingots have been reported by «Møll, et al»[8] due to the slow cooling of standard Silicon casting processes. Slow ingot cooling is well known to impart wide ranging

[2] The authors plan further work on this subject

grain sizes in the ingot which is where most of the mgSi impurities are concentrated in the center of the ingot[8]. Upon crushing and grinding, the Silicon is more friable at the grain boundaries and therefore smaller grains tend to break more easily, resulting in most of the impurities being concentrated in the lower size fractions.

W. Kurz, et al showed the temperature vs time data in different positions for a Silicon ingot with 10 cm thickness. Fast temperature degradation is seen initially at the surface and then slower for deeper sections of the ingot as the heat transfers through thicker cooler sections.

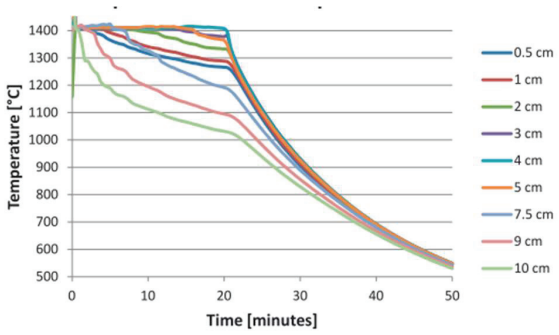


Figure 7: Temperature vs time in different position – 10 cm cast. Source: [12]

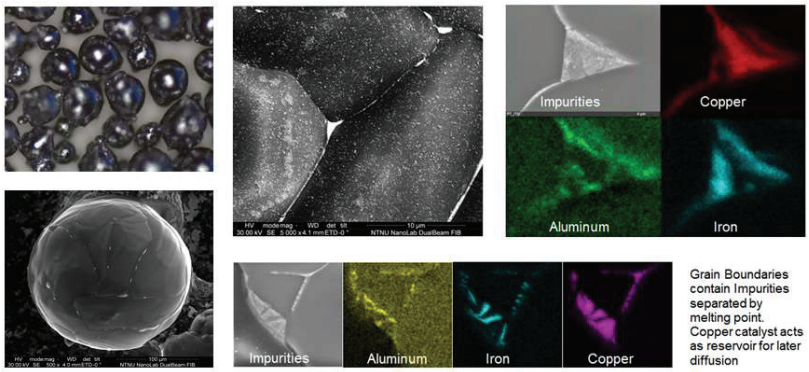
Adding Copper to Silicon via ladle addition would lead to high segregation in cast ingots due to the slow cooling characteristics of ingot casting. Based on operational experience, ingot cooling rates are on the order of 17 °C/min and literature reference of Copper diffusivity[12] in Silicon is known. Based on slow cooling rates and high diffusivity, it can be concluded that the normal casting methods in the Silicon industry would lead to Copper being agglomerated at the lattice defect sites with lower activation energy and later will move towards grain boundaries. The final result is a copper distribution with high segregation in the silicon solid. Thus slow cooling and Copper addition in the ladle would lead to highly segregated material and this correlates to known results of adding Copper to Silicon for us in Polysilicon and MCS production.

The authors propose that adding Copper in the Søderberg electrode column via fin substitution would result in the Copper being present as intermetallic bonds in the Silicon versus the grain boundaries and would not lead to this segregation upon cooling. Additional work is needed to validate this theory.

Previous work by the authors tested extremely rapid cooling techniques, namely gas atomization of Silicon with dopant levels of Copper as a possible improvement in performance of metallurgical Silicon. Gas atomization has a cooling rate of approximately 10^4 °C/sec versus a much slower 17 °C/min as in traditional casting. As expected, the Copper dopant, as well as other metallic impurities in the Silicon collected in the grain boundaries of the atomized Silicon and protruded through the surface of the particles. Future work on this subject will include evaluating the phases of Copper present in the grain boundaries as well as a determination of the grain size of atomized Silicon, both subjects could affect the performance of catalyst doped Silicon in the

TCS-HC and MCS process. Atomized Silicon with catalyst dopant is uniquely different that cast Silicon in two main aspects:

- The physical dispersion of the liquid Silicon creates natural barriers that prevent the catalyst from segregating beyond the liquid surface of the particle. As the particles sizes can be manipulated with gas pressure, temperature and speed, the already small sizes of the particles upon cooling means the catalyst is homogeneous throughout all particles.
- The fast cooling rate of the gas atomization process is such that even within the particle the segregation rate of the catalyst is much slower that the solidification of the particle. Precise studies of the cooling rate of gas atomized Silicon versus the



segregation rate of Copper in Silicon have not been validated.

Figure 9: Previous work by author on copper in grain boundaries of gas atomized Silicon

Many works on the subject emphasize that the effect of the Cu_3Si catalysis for TCS-HC or MCS is limited to the surface leading to the inference that Copper buried inside the particle as in atomized Silicon would not be as effective. However, this inference has not been fully evaluated and remains unclear if a distributed network of catalyst evenly distributed in a fine grain Silicon particle with surface negatively impacts the reaction in HC-TCS or MCS. The authors believe the segregation front, as described in literature, would be enhanced as it moves from the surface of the particle and encounters additional reservoirs of catalyst, thereby actually improving the performance of the reaction.

Adaptation of Søderberg electrodes

Catalyst addition in the smelting process

It is known that at least one Silicon producer has experimented with adding Copper to at the refining stage in order to achieve high Copper content in the final product for use at

a specific Polysilicon customer. The same experiments were performed at difference Silicon producer with the goal us adding Copper for eventual MCS consumers. The results from these experiments were mixed as the volatility of the distribution of the Copper in the mgSi ground mgSi was less than ideal. Given the high segregation rates and the cooling methods for Silicon ingots, this result would be expected. Silicon smelters are generally reluctant to add Copper to silicon due to possible contamination into other product grades for customers that are sensitive to Copper content. Therefore, any serious strategy to add Copper to Silicon would likely be limited to smelters who have exclusive production contracts with TCS or MCS customers that would allow for the management of this risk. Another option is for fully integrated MCS and TCS producers who own and operate mgSi smelters, to have production protocols that allow for Copper addition.

The main method for adding Copper to mgSi is simply the addition of copper source to the ladle before tapping ensuring the dissolution of the Copper during the refining step. Once Copper has been added, the subsequent casting of the Copper doped Silicon occurs normally. The authors propose that a different route for Copper addition is possible in combination with the use of 100% Søderberg electrodes for Silicon production.

Introduction of Copper in the Alternative Søderberg electrode column

As discussed in the previous section, the Alternative Søderberg electrode consists of the casing, the fins and the paste itself. It is feasible that the internal fins of the column are made with different materials. This component of the electrode column could be designed based on a Copper based material, i.e. Copper metal or a Copper alloy, that could be used as catalyst in the downstream application for Chemical processes. The mechanic strength and electrical conductivity of that specific fin design as well as the complete assembly characteristics (thermal, mechanic and electrical) must be carefully evaluated with careful consideration of the safety limits of the flexural strength, conductivity and tension support. Various fin designs are possible based on evaluation of the stresses on the electrode during production.

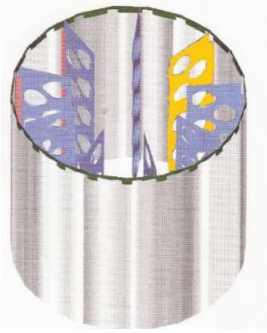


Figure 11: Example of substitution of one fin with Copper based material

The substitution of one or more of the fins with Copper material will affect various aspects of the electrode column, namely:

Thermal Conductivity	Higher thermal conductivity is expected which supports and improves baking process of the column.
Electrical Conductivity	Higher electrical conductivity of the electrode from the Copper fins will reduce the heating of the electrode
Thermal Expansion	Due to disparate expansion coefficients of the two fin materials, adjustments in the fin thickness and dimensions of the Copper fin will be required.
Melting Point	The lower melting point of Copper is a detriment to the structural aspect of the column, but should not impact to a large degree as the temperature of the fins at the contact plate region will be below the melting point and the engineering of the column should be made with these limits in mind to avod failures

The addition of Copper in the Alternative Søderberg electrode column must be considered in regards to the eventual transference of the Copper to the final Silicon project. The internal furnace composition which consists of various forms of SiC, Si and other phases represent a complex environment that is not easily estimated without extensive testing. Kamfjord 2012 and Myrhaug in 2003 affirm that 79% to 80% of the Copper added to the furnace will be carried to final product (Silicon), which considers no segregation due to the high temperatures of the middle and lower reaction zones and indicate that high levels of Copper would reach the tapped Silicon. Additionally no Copper will be lost via oxidation in the refining process based on the Elligham Diagram. Synthetic slagging of Silicon with high Copper content is not recommended to avoid equilibrium dislocation during the refining process.

The authors estimate that the substitution of three thicker fins of the Alternative Södeberg electrode with Copper would add approx. 0.0920% ppm to the Silicon final product. Additionally, Copper contamination of the Silica Fume is expected to be minimal based on literature references that approximately 20% of the Copper added to the furnace would reach the Micro Silica. This is clearly not sufficient in terms of the targeted 3% Copper addition as stated previously, however, such an addition of Copper in the fins of the Søderberg electrode would provide a base level of Copper that would reduce the future addition of Copper catalyst at the Polysilicon and MCS site and would reduce minor amounts of Iron contamination from the Stainless Steel fins. Additional work on the subject is required to examine the full range of benefits of adding Copper catalyst via Søderberg electrode in combination with gas atomization to provide a high performance Silicon material for end use applications.

Acknowledgements

This paper is published by permission of Viridis.iQ GmbH. The contributions of our colleagues are gratefully acknowledged.

Conclusions

Søderberg electrodes have been used extensively in the production of Ferrosilicon due to the lower operational costs compared to Prebaked carbon electrodes. Adaptation of Søderberg electrodes for Silicon has been successful in Brasil as an alternative to Prebaked and Composite electrodes and has seen a resurgence of interest. Søderberg electrodes can provide an easy method for adding catalyst to Silicon via the substitution of one of the fins of the electrode with a catalyst bearing materials, namely Copper. The use of Copper as a catalyst for the Polysilicon and MCS production processes is well established and Copper based catalyst are routinely added to Silicon material at the site to increase performance. The authors propose the addition of Copper catalyst to the Søderberg electrode column as a manner to provide a baseline level of Copper to the Silicon that can bring benefits to the vertically integrated Polysilicon or MCS producers by reducing the need to add excess Copper catalyst, reduce the addition of Iron the Silicon via the removal of some of the Stainless Steel fins in the electrode, and providing a highly homogenous Silicon material via the use of extreme rapid cooling of Silicon such as gas atomization that can be a marked improvement over standard casting methods due to segregation effects. Further work on the subject is needed to validate the effects of the Copper addition in the electrode column and the phases present in the final Silicon.

References

[1] Ward, W. J.; Ritzer, A.; Carroll, K. M.; Flock, J. W., Catalysis of the Rochow Direct Process, J. Catal. 1986, 100, 246.

[2] Dow Corning Patent US 4,898,960.

[3]A. Crawford, Cost saving of using a metallurgical grade silicon with higher trichlorosilane yield in the hydrochlorination based polysilicon process, Silicon for the Chemical and Solar Industry XIII, L. Nygård, B. Pachaly, H. Rong, M. Tangstad, H. Tveit, I. Page Eds., (Kristiansand, Norway), 2016, p. 201-218.

[4] John M. Bablin, Larry N. Lewis, Aqueous Leaching Technique for the Determination of Eta Phase (Cu3Si) in MCS Beds, Silicon for the Chemical and Solar Industry V, H.A. Øye, H.M. Rong, L. Nygaard, G. Schtissler, J.Kr. Tuset (Trondheim, Norway), 2000, p. 347-364.

[5] A. Crawford, et al (cross reference 3)

[6] Ward, et al (cross reference 1)

[7] W. Banholzer and Micheal C. Burrell, Characterization of Reactive Areas in the Direct Process for the Production of Methylchlorosilanes, GE Research and Development Center, p. 269

[8] Maria Førde Møll, KH Berget, E Myrhaug, M Onsoien, and H Tveit, The Main Reasons to develop an improved casting process for silicon, Proceedings of INFACON XIII, Almaty, Kazakhstan, p. 763.

[9] Jose Joaquim Cardoso, Eletrotermia - Fornos Eletricos a Arco., Volume I and II. 1987.

[10] Engineering ToolBox, (2005). Thermal Conductivity of Metals. [online] Available at: https://www.engineeringtoolbox.com/thermal-conductivity-metals-d_858.html [Accessed 02 05 2018].

[11] Aleksandar Mitrašinovic, Characterization of the Cu-Si System and Utilization of Metallurgical Techniques in Silicon Refining for Solar Cell Applications, Department of Materials Science and Engineering, University of Toronto, 2010

[12] W. Kurz, D.J. Fisher., Fundamentals of solidification, Uetikon-Zuerich, Switzerland ; Enfield, N.H. : Trans Tech Publications, 1998

[13] V.D. Oliveira, et all, Electrode Technology comparison for Silicon production – a brief overview, Infacon XV: International Ferro-Alloys Congress, Cape Town – South Africa, 2018

THE ELECTRODE FOR SUBMERGED ARC FURNACES PRODUCTION

Matveev A.V.[1)], Kvanin A.L.[1)], Bleskin G.S.[2)], Butakova T.V.[2)], Spektoruk A.A.[2)]
1) ENERGOPROM R&D center, Moscow, Russia
2) NOVOSIBIRSK ELECTRODE PLANT, Novosibirsk, Russia

Abstract

The principle of a conventional Submerged Arc Furnaces (SAF) is the heat produced by the electrical arc between the electrode and the materials mix in the bottom of the furnace .. The energy is transmitted to the furnace bottom by carbon electrodes. The power of the furnace is the product of the area resistance and the square of the electrode current. Therefore, a limited increasing electrode current may result in a relatively large increasing load. Characteristic of the process in SAF is that the electrode penetrates through the raw material downward until the furnace bottom thought the different raw materials changes . In this way, the furnace efficiency and productivity are very sensitive to electrode properties like specific electrical resistance (SER), heat resistance etc. ENERGOPROM GROUP is producing several types of carbon electrodes for SAF and one of the best options is fully graphitized carbon electrodes that will help to achieve high furnace efficiency as well as low energy/electrode consumption.

Reduction of carbon electrode waste in SAF

Carbon electrodes as energy transmitter to the furnace are undergo several important transformations which can effect on it efficiency. The temperature of electrode column is increasing as it goes deeper in the furnace. As you can see on the fig.1 the temperature distribution in electrode column leads to oxidation, the phase transition of carbon electrode material in graphite, and puffing effect [1], as well as some portion of the electrode can take part in silicon reduction. Therefore, the main issues that can be emphasized are: losses at furnace top zone to burning/oxidation at temperatures above 500°C, the electrode will participate in silicon reduction reaction, an electrode can drop stubs because of cracks development during the rapid graphitization [1] in silicon furnace. It is not easy to estimate total losses due to the above but in worst cases, it can reach up to 7% of electrode material. Such losses of electrode is high enough and can be reduced by using graphitized electrodes.

EPM group produces several types of carbon electrodes (please see fig.2). First three grades (MCM-A, MCM-C, MCGM) are anthracite based and contain graphite in different ratio. The production process of these grades includes several steps like paste preparation, forming, baking of carbon electrode in special furnace at temperature up to 1100°C and machining. It means that the electrode material does not undergo any phase or material transformation before reaching again 1100°C but at higher temperatures, we cannot ignore it. For the last grade (MGM - graphitized electrode), the final step of heat

treatment is graphitization in Acheson furnace at the temperature up to 2900°C. It provides the unique properties for this electrode. The main average values of different electrode grades properties you can find in table 1. It easily can be seen that the SER is lower (only 9.5 vs 20-30 for other grades) and thermal conductivity is much higher (95 vs 10-28 for other grades) for a graphitized electrode. In addition, it should be noted much lower ash content in MGM electrodes, which is due to the absence of anthracite among the raw materials.

Let's talk about advantage of graphitized electrode for furnace operation. Graphitized material allows us to increase current up 9 A/cm^2 (7 A/cm^2 for other grades recommended as max current), and also can increase the load of the furnace . The better in comparison to other electrode types thermal conductivity allows achieving the lower shutdown-normal operation recovery time and higher starting current in case of a graphitized electrode. Also graphite material provides reduction of electrode losses due to lack of oxidation, non-participation in silicon reduction and no electrode stubs dropping in furnace, no tip losses due to absence of puffing effect.

In general, the lower up to 20% electrode consumption can be achieved.

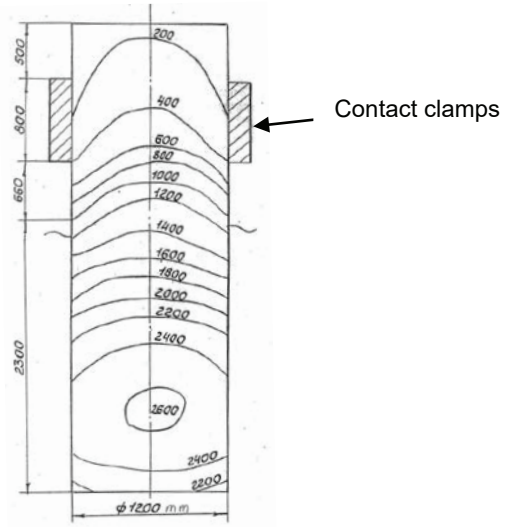


Figure 1: Temperature distribution in electrode column in °C from length in mm (Y axis).

CARBON ELECTRODES

GRADES		GRAPHITE	ANTHRACITE
Carbon electrode, Grade A (MCM-A)	50%		50%
Carbon electrode, Grade C (MCM-C)	55%		45%
Carbo-graphitic electrode (MCGM)	80%		20%
Graphitized electrode (MGM)	100%	Graphitized (petroleum coke + pitch)	

Figure 2: Carbon electrode grades produced by ENERGOPROM GROUP company.

Conclusion

Usage of MGM (graphitized) electrodes in SAF allows decreasing specific electrode consumption due to low rate of electrode body oxidation, reduction of electrode losses in silicon reduction reaction, also absence of graphitization effect prevent tip losses in the furnace. From operational point of view, it is possible to decrease shutdown-normal operation recovery time, which has positive effect on silicon production rate. In addition, this grade successfully used for running up new furnaces worldwide and can be recommended as the best option due to very high heat resistance in comparison with usual carbon electrodes.

Table 1: The average values of ENERGOPROM GROUP carbon electrodes main properties.

Properties	MCM-A	MCM-C	MCGM	MGM
SER, μΩm	29	27	20	10.5
Tensile strength, MPa	4.2	4.2	4.5	5.0
Bending strength, MPa	10.0	10.0	13.0	12.0
Thermal conductivity, W/(m K) at 20 °C	11.5	13	28	110
CTE, (20-520)°C in 10-6 × K-1	3,4	3,4	3,5	2.9
Apparent density, g/cm3	1,60	1,60	1,63	1,62
Ash, %	1,9	1,8	1,0	0,6

References

1. I. Letizia, “Puffing test: a high-temperature laboratory method for evaluating the graphitizability of carbons”, High Temperatures – High Pressures, 9（1977）291-296.

Formation of elemental silicon in β-SiC particles

Sethulakshmy Jayakumari[1] and Merete Tangstad[1]
1) NTNU, Department of material science and engineering.

Abstract

Silicon Carbide (β-SiC) is the main intermediate compound in the production of silicon (Si) and it plays a major role in controlling the energy distribution in the silicon production furnace. Knowledge about the features of β-SiC particles formed from different carbon materials and thereby the production of silicon may leads to advancement in the silicon industry. A laboratory induction furnace was used to investigate the features of Si formation from β-SiC particles by using different carbon materials such as charcoal, coal or pet-coke. A mixture of SiO_2 + Si was utilized as the raw material for the generation of $SiO_{(g)}$. The formation of elemental Si in β-SiC particles is observed at 1750°C. The transformation of carbon (C) to β-SiC particles is more efficient with charcoal followed by coal and pet-coke respectively.

1. Introduction

The industrial production of silicon happens theoretically at 1811ºC by carbothermal reduction from quartz in submerged arc furnaces [1]. Thermodynamic factors such as temperature, partial pressures of the gases inside the furnace as well as the purity and quality of the raw materials that are added during the process are the different factors to be considered. For a significant silicon yield, quartz (SiO_2) having large Si content and the type of carbon source (C), which should be more reactive towards the SiO gas must be selected. During the scenario of silicon production process, several reactions are occurring at the different zones of the furnace. The reactions that are happening at the inner zone of the furnace where the temperature is 1800°C and above are;

$2SiO_2$ (s,l) + SiC (s) → 3SiO (g) + CO(g) (1)
SiO_2 (s,l) + Si (l) → 2SiO (g) (2)
SiC (s) + SiO (g) → 2Si (l) + CO (g) (3)

Reaction (3) confirms that the compound SiC is the main intermediate product necessary for the production of silicon as well as the formation of SiO gas according to reaction (1). SiC is producing at the upper zone of the furnace where the temperature is 1700°C and below along with some other reactions are:

SiO (g) + 2C (s) → SiC (s) + CO (g) (4)
3SiO (g) + CO (g) → $2SiO_2$ (s,l) + SiC (s) (5)
2SiO (g) → SiO_2 (s,l) + Si (l) (6)

Reaction (1) and (2) are the $SiO_{(g)}$ producing reactions, when $SiO_{(g)}$ rises, this can be captured by reacting with C according to reaction (4). If the $SiO_{(g)}$ is not completely captured by the C materials, it condenses according to reaction (6) where the temperature is below 1700°C. For the maximum silicon yield, it is very important to capture the $SiO_{(g)}$ either by reacting with SiC or by forming condensates rather than

leaving through the off gas. The kinetics of the reaction (4) depends on the reactivity of $SiO_{(g)}$ towards the carbon material and the partial pressure value of $SiO_{(g)}$ coming from the furnace inner zone.
Figure (1) shows the equilibrium partial pressure of SiO as a function of temperature for reaction (2) and (4) together with the silicon producing reaction (3) was calculated by using HSE software [13]. Before the temperature reaches 1600ºC, P_{SiO} produced according to reaction (2) is high enough for the production of SiC according to (4). If the SiO gas is not completely captured by the C materials, the rest will rise upwards and condenses at the low temperature region (<1700ºC) according to reaction (6).

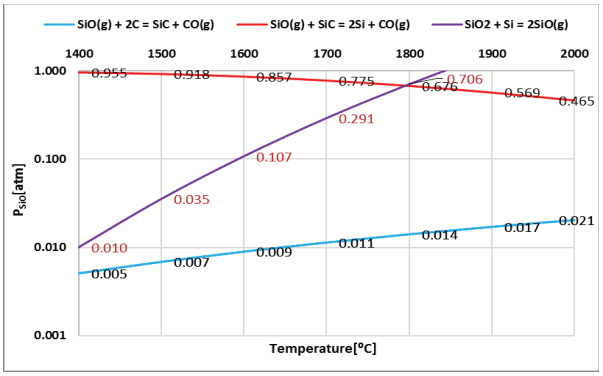


Figure 1: Equilibrium conditions for reactions (2), (3) and (4) [13].

Previous works quantified the reactivity of SiO with different carbonaceous materials. Different carbon materials shows different reactivity towards SiO gas. Charcoals typically have a high reactivity followed by chars and coals, whereas metallurgical cokes and most petroleum cokes shows a low SiO reactivity and are summarized in figure (2) [4].

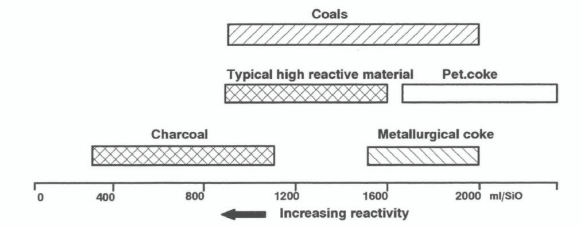


Figure 2: Reactivity towards with $SiO_{(g)}$ for different carbon materials [4]

The main goal of this work is investigating the formation of silicon from β-SiC particles by generating SiO gas from a mixture of (SiO_2 + Si). Charcoal, coal and pet/coke were used for the production of β-SiC particles. Experiments and results with charcoal and coal were recently published [2]. In the current article we are discussing the β-SiC formation experiments with charcoal and coal along with pet-coke. Previous literature regarding silicon production in SiC and carbon particles, as well as SiO generation are described below. **Tangstad et al. (2010)** observed Si formation from SiC particles at temperatures 1500ºC and 1760ºC, which are lower than figure 2 indicates, around

1800°C [8]. This is also in accordance with the observations of charcoal with metallic Si in the low temperature zone (zone 7 purple color in figure 3a) during the investigation of the effect of bio carbon and study of the reaction mechanisms in the silicon process by **Myrhaug et al. (2003)**, shown in figure 3(a) [3]. **Vangskåsen et al. (2012)** also studied the metal producing mechanism in the silicon process. During their study, the material consumption (SiO_2+SiC) was very low for temperatures below 1820°C as no SiO gas was produced. A temperature above 1900°C was needed for a noticeable change in the charge consumption. An excavation from pilot scale experiment for the production of silicon were carried out. Formation of silicon in SiC particles were observed in the low temperature zone during the pilot scale experiment as shown in position 5 in figure 3(b) [7].

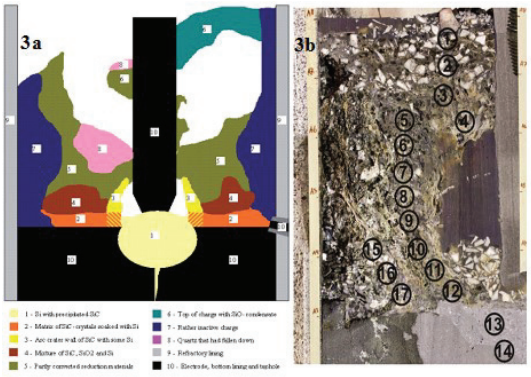


Figure 3(a): Illustration of different zones found after a pilot scale experiment [3] and **Figure 3(b):** Cross-sectional figure showing different zones after a pilot scale experiment for Si production.

Andersen et al. (2010) studied the kinetics of the high temperature reactions (1) and (2) and concluded that both reactions are temperature dependent. An exponential increase of reaction rate were observed for both the reactions at 1450-1723°C. For reaction (1) a constant or a slight decrease in the reaction rate from 1723-1770°C and a significant increase of reaction rate from 1770-2000°C were observed. For reaction (2), a reduced rate of reaction due to viscosity of liquid silica at 1723-1860°C was seen, but from 1860-2000°C the reaction rate increases again as the equilibrium pressure exceeds one bar [10]. **Bao et al. (2013)** studied the kinetics of the same reactions (1) and (2) in a thermal gravimetric apparatus under Ar atmosphere in the temperature range of 1550-1820°C. At temperatures lower than 1550°C, both reactions were very slow and then increases exponentially to 1730 and 1820°C until the charge materials were almost consumed. At temperatures 1550-1730°C, the ($Si+SiO_2$) mixture reacts maximum 1.5 faster when compared the reaction with a mixture of ($SiC+SiO_2$). However, the reaction with a mixture of ($SiC+SiO_2$) dominates at around 1800°C [9]. **Tangstad et al. (personal communication)** studied the reaction rate of (1) with various polymorphs of SiO_2. It was seen that when increasing the SiC amount higher than the stoichiometric amount, the reaction rate per gram of SiO_2 increased and there was not any noticeable difference reported between different polymorphs of quartz [11].

2. Raw materials, method and apparatus

A laboratory induction furnace (IF75) was used to study the features of Si formation in β-SiC particles. A mixture of (SiO_2+Si) were used as the raw materials for the production of SiO gas according to reaction (2). Carbon materials (C) such as either charcoal, coal or pet-coke were used for the conversion of SiC by $SiO_{(g)}$. The compositional analysis of charcoal, coal, pet-coke and quartz obtained from the producer are shown in table (1). The silicon used in this study was 99.99% pure silicon.

Table 1: The compositional analysis of coal, charcoal, pet-coke and quartz.

Contents (DB-Dry Basis)	*Coal (%)*	*Charcoal (%)*	*Pet-coke (%)*
Fix C (DB)	58.36	**90.32**	**89.8**
Ash (DB)	1.06	1.62	0.2
Volatiles (DB)	40.58	8.06	10
Fix C (after heating)	**91.9**		

Contents	*SiO_2*	*Fe_2O_3*	*Al_2O_3*	*CaO*	*TiO_2*	*MgO*	*Na_2O*	*K_2O*	*P_2O_5*
Wt:%	**99.82**	0.0352	0.1157	0.0058	0.0031	0.0028	0.004	0.0205	0.0014

From table (1), the fix C (DB- Dry basis) amount in coal is 58.36%, was less compared to charcoal and pet-coke. Heat treat (calcination) of coal was done at 1200°C for 20 minutes, in order to remove the volatiles thereby increasing the fix C amount from 58.36% to 91.9%. However, industrially, coal is used directly and throughout the process coal transformed to char and then transformed to SiC. The reasons why heat-treated coal used for the experiments are; **(i)** Removing the volatiles and make the fix C amount near to the fix C in charcoal and pet-coke. **(ii)** In order to make the consistency in particle size (5-10 mm) for experiments, as using coal leads to expansion, thereby leads to big particle size [2].

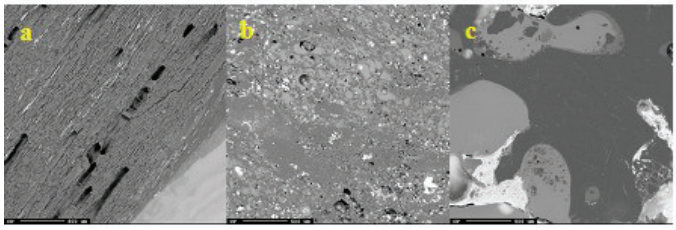


Figure 4(a), (b), (c): EPMA images of charcoal/coal/pet-coke showing porosity and cell wall thickness.

Table 2: Porosity measurement in wt. % of charcoal/coal/pet-coke

Carbon materials	*Charcoal*	*Coal (calcined)*	*Pet-coke*
Porosity (%)	73.4	53.9	17.5

Figure (4a), (4b) and (4c) representing the EPMA images of charcoal/coal/pet-coke respectively showing the structural variation such as pore size, shape and cell wall thickness in three different carbon materials. A 10% in weight iodoform added epoxy resin was used for carbon material sample preparation for EPMA or SEM material characterization, since this gives a good contrast between the carbon particle and the matrix during imaging [14]. The light grey region is the iodoform contained epoxy resin medium and the dark region is the carbon particle. From figure (4a,) the EPMA image of charcoal, it can be seen that the pores are homogeneous, evenly distributed and large in number. The cell walls between the porous layers in charcoal is very thin, whereas in coal figure (4b) a combination of thick and thin cell walls was observed. From Figure (4c) image form pet-coke, the pores were very big and the cell walls between the pores were very thick when compared with the other two. Table (2) represents the porosity (%) of the three carbon materials and the corresponding values were well coordinated with the images figure (4a,b,c). **Videm et al (2000)**, during their studies based on reactivity and petrography of cokes showed that high porosity with thin cell walls were favorable for good SiO reactivity in the silicon and ferrosilicon process [12].

Experiments with charcoal/coal/pet-coke were performed at four different temperatures for the production of β-SiC particles, thereby observing the formation of Si in β-SiC particles. A graphite crucible of length 40 cm, inner diameter 11.5 cm, was used, where one can use particles close to industrial size up to 20 mm in diameter. A mixture of (SiO_2+ Si) of 5-10 mm in size were added initially, as the raw materials for the production of SiO gas according to reaction (3). Then carbon particles of about 5-10 mm in size was placed on the top of (SiO_2 + Si) mixture. Two thermocouples were used, TC_1 (Thermocouple 1) was placed on the top of the (SiO_2 + Si) mixture in order to measure the temperature distribution in the charge mix. TC_2 (Thermocouple 2) was placed in the middle region of the carbon layer to assess the temperature distribution in the carbon layer. The schematic representation of the complete experimental set up for the study is shown in figure (5).

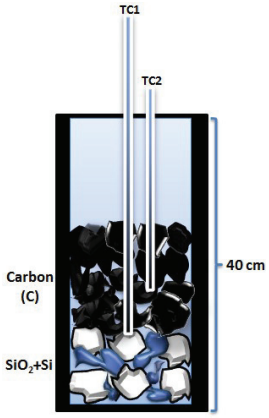


Figure 5: Experimental set up for the production of Si in β-SiC particles.

The graphite crucible filled with charge materials is placed in the induction furnace, heated up and when the target temperature reached held it for one hour. Experimental conditions and charge mixtures used for experiments with coal/charcoal/pet-coke are listed in tables below. The experiments at 1900^0C with charcoal were stopped after 15min holding time owing to problems with thermocouples.

Table 3: Experimental conditions by using charcoal as raw material at four different temperatures [2].

Exp: with charcoal	*Charge mixture (5-10 mm) molar ratio*	*Crucible weight (empty)*	*Crucible weight with complete set up*	*Heating rate*	*Target temperature °C*	*Holding time*
1	SiO_2:Si:C = 1:1:4	5584 g	6725 g	25^0C\min	1750^0C	60 min
2	SiO_2:Si:C = 1:1:4	5773 g	6866 g	25^0C\min	1800^0C	60 min
3	SiO_2:Si:C = 1:1:4	5721 g	6862 g	25^0C\min	1850^0C	60 min
4	SiO_2:Si:C = 1:1:4	5783 g	6923 g	25^0C\min	1900^0C	15 min

Table 4: Experimental conditions by using charcoal as raw material at four different temperatures [2].

Exp: with coal	*Charge mixture (5-10 mm) molar ratio*	*Crucible weight (empty)*	*Crucible weight with complete set up*	*Heating rate*	*Target temperature °C*	*Holding time*
1	SiO_2:Si:C = 1:1:4	5669 g	7242 g	25^0C\min	1750^0C	60 min
2	SiO_2:Si:C = 1:1:4	5501 g	7079 g	25^0C\min	1800^0C	60 min
3	SiO_2:Si:C = 1:1:4	5747 g	7313 g	25^0C\min	1850^0C	60 min
4	SiO_2:Si:C = 1:1:4	5665 g	7241 g	25^0C\min	1900^0C	60 min

Table 5: Experimental conditions by using pet-coke as raw material at four different temperatures.

Exp: with petcoke	*Charge mixture (5-10 mm) molar ratio*	*Crucible weight (empty)*	*Crucible weight with complete set up*	*Heating rate*	*Target temperature °C*	*Holding time*
1	SiO_2:Si:C = 1:1:4	5722 g	8159 g	25^0C\min	1750^0C	60 min
2	SiO_2:Si:C = 1:1:4	5517 g	7958 g	25^0C\min	1800^0C	60 min
3	SiO_2:Si:C = 1:1:4	5639 g	8084 g	25^0C\min	1850^0C	60 min
4	SiO_2:Si:C = 1:1:4	5663 g	8119 g	25^0C\min	1900^0C	60 min

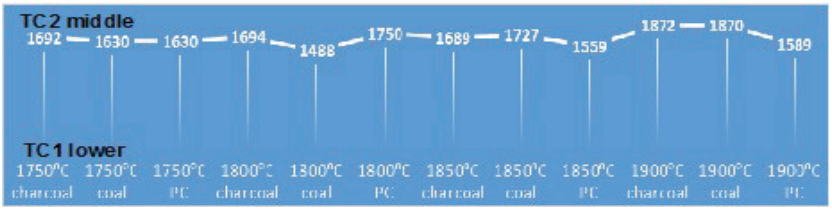


Figure 6: Temperature measurements on the top of the (SiO_2 + Si) mixture (TC1 lower) and the corresponding temperature between the carbon layer (TC2 middle) for experiments with coal/charcoal/pet-coke (PC).

Figure (6) shows the temperature distribution on the top of the (SiO_2 + Si) mixture (TC1 lower) and the corresponding temperature between the carbon layer (TC2 middle) for experiments with coal/charcoal/pet-coke (PC). First of all, there will be a temperature gradient from bottom to the top of the crucible while working with the induction furnace. During the experiment at 1800^0C with coal, the thermocouple inserted in the graphite rod, which was placed at the middle layer (TC2), got displaced up accidently, that is the reason why the measured temperature was a bit low (1488^0C). During the experiments with 1900^0C charcoal and coal, when the target temperature was reached, the TC2 slumps down from its original position close towards the (SiO_2 + Si) mixture. This might be the reason why the measured temperatures at the middle layer was comparatively high with these two experiments. Yet another speculation why the temperature near the middle layer varies from 30-311^0C at different target temperatures with charcoal/coal/pet-coke is that the amount of raw materials that were added for the three set of experiments were different. The density between different carbon materials are different, so in order to fill 10 cm layer of carbon materials, the amount of (SiO_2+Si) mixture were added for three different C materials varies according to the stoichiometry. Therefore, the raw material heights in the crucible for experiments with different C materials are different. Therefore, the positions of the thermocouples at the middle and lower layers, where the temperatures were measured in experiments with three different C materials, are different. In a similar experimental setup, Jusnes et al (2016) measured the vertical temperature gradient of the crucible and their temperature gradient data shows similar results as the data obtained in the present study, figure (6), with some exceptions [6].

3. Results and discussion

The schematic representation of crucible cross-section after the experiment is illustrated in figure (4). The assumption is that, during the experiment SiO gas produces first according to reaction (2) followed by SiC producing reaction (4) and the Si producing reaction (3) respectively. In figure (4) the order of these reactions are represented as I, II and III. Samples were collected from the middle (C transformed to SiC) and lower regions (C transformed to SiC and Si, figure 4) of the crucible are considered for XRD (X-ray diffraction), chemical analyses and EPMA (Electron Probe Micro Analysis). Since the samples from the top part have only unreacted carbon materials covered by a thin layer of condensates\volatiles, it was not analysed further.

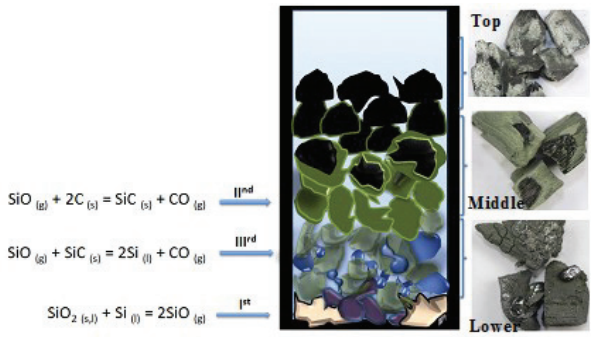


Figure 5: Schematic representation of the crucible cross-section after the experiment with induction furnace [2]

Figure (8), (9) and (10) represents the amount of β-SiC particles and (β-SiC+Si) that are collected from the graphite crucible at different temperatures by using different carbon materials (refer to figure 4) measured in centimetres. From the figures, the amount of unreacted coal/charcoal/pet-coke was high at low temperatures. When the temperature increases the carbon materials is more reactive with SiO (g) and produces more β-SiC particles and (β-SiC+Si). The production of SiC from charcoal/coal/pet-coke is higher from 1800ºC-1850ºC. Production of pure silicon starts from 1750ºC and by increasing the temperature, a gradual increase in this layer was observed. It was observed that the amount of β-SiC particles was less and (β-SiC+Si) particles is higher from pet-coke. We assume that the reason for this observation may be that when the temperature increases the voids between the pet-cokes get clogged with condensates which may block the passage for the SiO gas to rise upwards and reacts with the pet-coke. So once the β-SiC formed with pet-coke, the SiO gas coming from the charge materials may not rise upwards but stays in the crucible lower region, and reacts with the already produced β-SiC particles thereby increasing the formation of Si. When the temperature increases the amount of unreacted pet-coke was comparatively high compared to charcoal/coal as raw material.

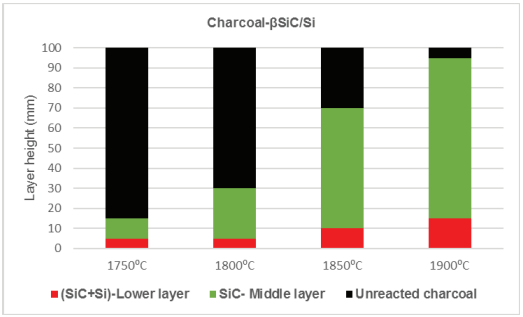


Figure 6: Amount of unreacted C, β-SiC particles and (β-SiC+Si) formed after experiments with charcoal at different temperatures [2].

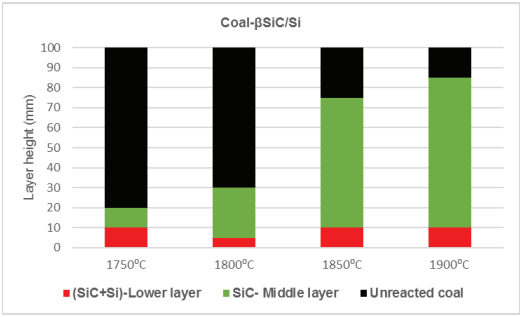


Figure 7: Amount of unreacted C, β-SiC particles and (β-SiC+Si) formed after experiments with coal at different temperatures [2].

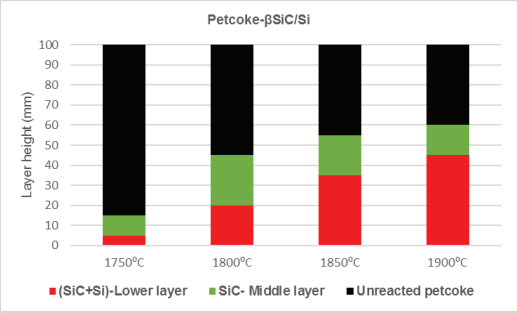


Figure 8: Amount of unreacted C, β-SiC particles and (β-SiC+Si) formed after experiments with pet-coke at different temperatures [2].

Figure (11), (12) and (13) shows the XRD analysis of particles after experiment with charcoal/coal/pet-coke collected from the middle and lower regions of the crucible at four different temperatures. From the XRD analysis, the SiC particles that are obtained from charcoal/coal/pet-coke are identified as the cubic form, which is 3C-SiC polytype (β-SiC). It can also be seen that elemental silicon was present at all temperatures. Very interestingly, there is hardly any carbon peak observed from charcoal converted SiC particles, whereas the carbon peak is very strong in pet-coke converted SiC particles followed by coal converted SiC particles. This also confirms that the complete conversion of SiC is possible by using charcoal as a raw material followed by coal and pet-coke.

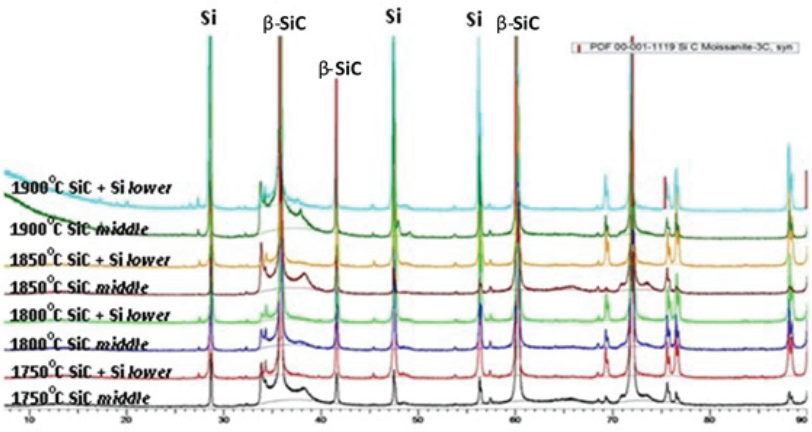


Figure 9: XRD analysis of SiC particles from charcoal [2].

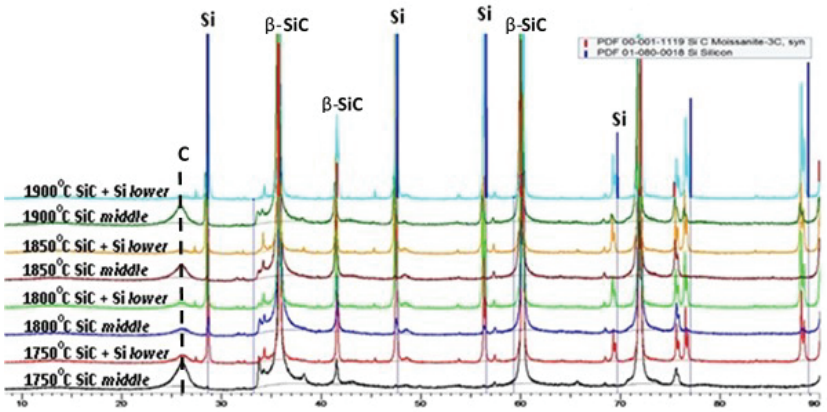


Figure 10: XRD analysis of SiC particles from coal [2].

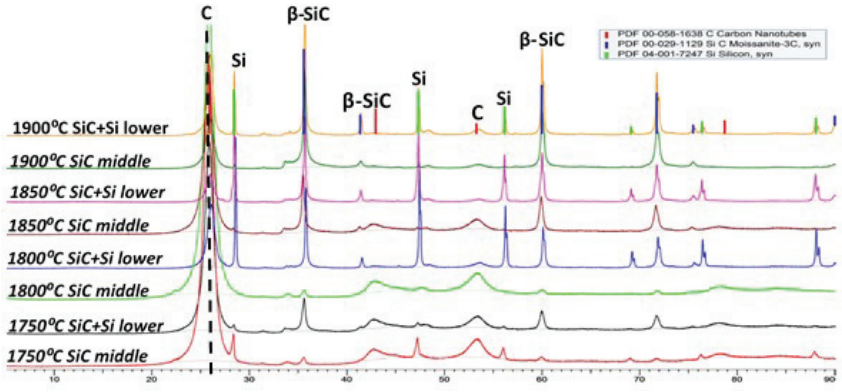


Figure 11: XRD analysis of SiC particles from pet-coke.

Chemical analysis of SiC particles that are collected from the middle and lower regions of the crucible were carried out to know the amount of SiC, free carbon and elemental silicon content. From the chemical analysis data the amount of SiC as well as the elemental silicon produced from charcoal/coal/pet-coke at different temperatures were calculated. From figure (14), the chemical analyses of samples from the middle layer it was seen that the amount of SiC obtained is comparetively higher with charcoal followed by coal and petcoke.This also indicates that charcoal has the highest SiO(g) reactivity compared with data form coal/pet-coke according to reaction (4). This is in good agreement with the studies based on the reactivity of different carbon materials [4].

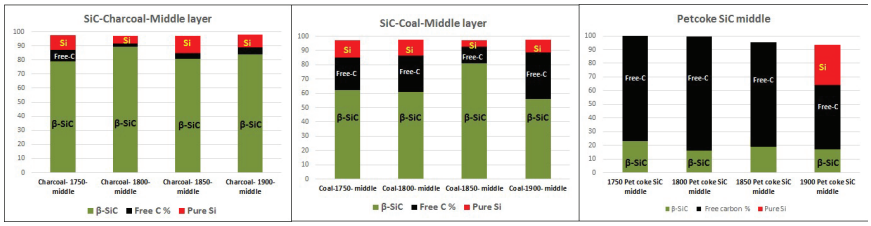


Figure 12: Chemical analysis of samples that are collected from the middle layer after experiments with charcoal/coal/pet-coke.

Figure (15) shows the amount of SiC, free carbon and elemental silicon content present in SiC particles that were collected from lower part of the crucible from charcoal/coal/pet-coke at four different temperatures. Here the amount of SiC is higher for coal compared to charcoal and pet-coke, while the amount of elemental silicon was higher for charcoal than with coal and pet-coke. This means that once SiC was formed, silicon can easily be produced from charcoal-converted SiC than when compared with coal-converted SiC and pet-coke converted SiC. However, a higher temperature was needed for the maximum conversion of SiC from coal/petcoke as a raw material.

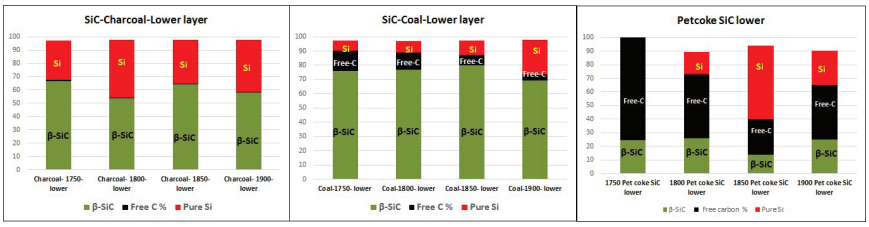


Figure 15: Chemical analysis of samples that are collected from the lower layer after experiments with charcoal/coal/pet-coke.

Figure (16), (17) and (18) are the EPMA images of SiC particles from charcoal/coal/pet-coke that are collected from the middle and lower region of the crucible after induction furnace experiments at 1750ºC and 1900ºC. The dark grey region in the images is SiC, which was formed according to reaction (4) and the light grey region mostly seen in the samples that are collected from the lower region of the crucible is the formation of elemental silicon along with SiC according to reaction (3). A detailed structural difference of charcoal/coal/pet-coke after exposed with SiO gas can easily be seen in the EPMA images. From the images, the topo-chemical reaction that the amount of SiC is high at the outer layer and decreases when it goes towards the center of the particle can also be seen. The rate of reaction will slow down as the thickness of the SiC layer increases, since the SiO has to diffuse through the already formed SiC layer to reach the unreacted carbon for complete conversion, which agrees with previous studies [3], [5]. The production of silicon was observed even at 1750°C, which is interesting since the silicon production happens theoretically at 1811ºC [2]. This is due to a higher SiO pressure in these experiments compared to the industrial furnace. From the pet coke chemical analysis, hardly any silicon was present at 1750°C, but the corresponding EPMA image (figure (18) 1750°C SiC pet-coke lower) shows the formation of elemental silicon at low temperature. Silicon production in this condition

may be owing to the presence of SiO (P_{SiO}) alone, where as in industrial conditions the total pressure is the sum of P_{SiO} and P_{CO}. This is in accordance with the elemental silicon production at lower temperatures based on previous studies [3], [7], [8].

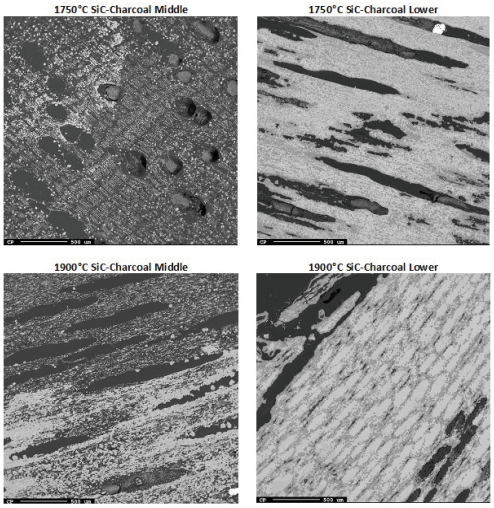


Figure 16: EPMA images of SiC particles from charcoal that are collected form the middle and lower layer after experiments at 1750ºC and 1900ºC [2]. (Light grey phase is elemental silicon and grey phase is SiC)

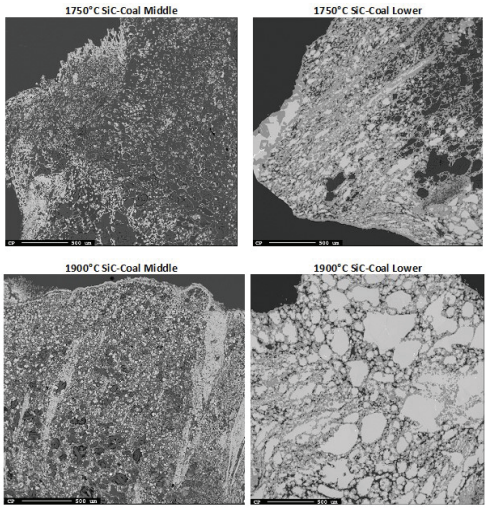


Figure 17: EPMA images of SiC particles from coal that are collected form the middle and lower layer after experiments at 1750ºC and 1900ºC [2]. (Light grey phase is elemental silicon and grey phase is SiC)

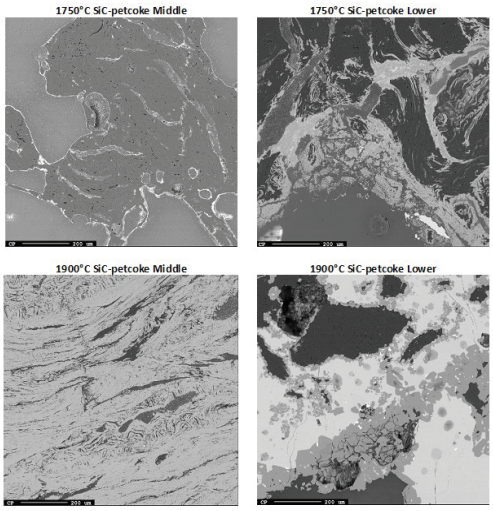


Figure 18: EPMA images of SiC particles from pet-coke that are collected form the middle and lower layer after experiments at 1750ºC and 1900ºC. (Light grey phase is elemental silicon and grey phase is SiC)

Conclusion

As a preliminary study, in order to investigate the features of SiC formation with charcoal, coal and pet-coke an induction furnace was used. The induction furnace experiments shows that it is possible to produce silicon at low temperature (1750ºC) on a laboratory scale. From this study, it can be confirmed that around 10-15% of silicon may be produced quite high in the industrial furnace within the SiC particles, the region where the temperature is low. We observed that the production of SiC is higher with charcoal followed by coal and pet-coke as a raw material. Once SiC is formed, silicon can easily be produced from charcoal-converted SiC than when compared with coal-converted SiC and pet-coke converted SiC. In the industrial furnace during the production of silicon and ferrosilicon, at high temperatures the Si produced in SiC particles higher up in the furnace will easily mix with the rest of the silicon produced at the region where the SiC consumption takes place.

Acknowledgement

SFI Metal Production has funded this work, an 8 year Research Centre under the SFI-scheme (Centres for Research-based Innovation, 237738). The authors gratefully acknowledge the financial support from the Research Council of Norway and the partners of SFI Metal Production.

References

1. A. Schei, J.K. Tuset and H. Tveit, *Production of high silicon alloys*, Tapir Forlag, ISBN 82-519-1317-9, Norway, 1998

2. S. Jayakumari and M. Tangstad, *Silicon Carbide formation from coal or charcoal in the silicon/ferrosilicon process,* Infacon XV International ferroalloy conference, 2018.
3. E. Myrhaug, *Non-fossil reduction materials in the the silicon process – behavior and properties*, PhD thesis, Norwegian university of science and technology, 2003.
4. O. Raaness and R. Grey, *Coal in the production of silicon rich alloys*, Infacon 7, Trondheim, Norway, 1995.
5. A. Schei and S. A. Halvorsen, *A stoichiometric model of the silicon process*, Proceedings from the Ketil Motzfeldt Symposium, 1991.
6. K. Jusnes, *Parameters affecting softening and melting of quartz*, Master thesis, Department of material science and engineering, NTNU, 2016.
7. J. Vangskåsen, *Metal producing mechanisms in the carbothermic silicon process*, Master thesis, Department of material science and engineering, NTNU, 2012.
8. M. Tangstad, M. Ksiazek, V. Andersen and E. Ringdalen, *Small scale laboratory experiments simulating an industrial silicon furnace*, The twelfth international ferroalloys congress Sustainable future, June 6-9, Helsinki, Finland, 2010.
9. S. BaO, M. Tangstad, K. Tang and E. Ringdalen, *Production of SiO gas in the silicon process*, Thirteenth international ferroalloy congress, Almaty, Kazakhstan, 2013.
10. V. Andersen, *Reaction mechanism and high temperature reactions in the silicon process,* Master thesis, Department of material science and engineering, NTNU, 2010.
11. M. Tangstad, *Reaction rates of $2SiO_2+SiC=3SiO+CO$ in pellets at elevated temperatures,* Personal communication.
12. T. Videm, R.J. Grey, R.M. Patalsky, *Reactivity and petrography of cokes for ferrosilicon and silicon production,* Int. J. of Coal Geology 43, 2000, p243-256.
13. HSC Chemistry version 7.1, Outotech research center, Finland.
14. C. O. Gomez, D. W. Strickler and L. G. Austin, *An iodized mounting medium for coal particles,* Journal of electron microscopy technique, 1984.

Small scale experiments simulating condensation of SiO and CO in silicon furnaces

Andrea Broggi, Merete Tangstad

1) *Ph.D. candidate at the Norwegian University of Science and Technology (NTNU), Department of Materials Science and Engineering, Alfred Getz vei 2, 7034 Trondheim, Norway.*
2) *Professor at the Norwegian University of Science and Technology (NTNU), Department of Materials Science and Engineering, Alfred Getz vei 2, 7034 Trondheim, Norway*

Abstract

Condensates generated from SiO(g) and CO(g) can influence the silicon yield in silicon production, thanks to their high silicon content and mechanical properties. Despite condensation products subtract silicon from the high temperature zone, they hinder losses of SiO(g) from the process. In this study, SiO_2 and SiC pellets have been used to create SiO(g) and CO(g) in an electric tube furnace, at different Ar flows. These gases will condensate on SiC substrates between 1150 and 1800ºC. Condensates composition, morphology and topography have been characterized by using BSE- and SE-SEM, EDS, XPS and EPMA. Two compounds have been found: a SiO_2-SiC and Si-SiO_2 mixture. The first is a nanometric whiskers web, generated in a wide temperature range and in high amounts. Changes in microstructure occur through the condensation temperature range, but the composition fluctuates in a small interval. The Si-SiO_2 condensate consists of elemental silicon microspheres immersed in a molten SiO_2 matrix at high temperatures. SiO_2 goes mainly to the SiO2-SiC mixture. Experiments at higher Ar flows reduce the condensates mass and shift the condensation temperature ranges to colder areas. Longer holding times will enhance clogging.

Introduction

Metallurgical silicon is produced by the reduction of silica by carbonaceous materials in electric arc furnaces. The thermodynamics of silicon production are well known nowadays. However, the kinetics are difficult to predict. SiO(g) develops as an intermediate product, whereas CO(g) is the main by-product in silicon production. SiO(g) contributes to the formation of Si in the high temperature zone (1800-2000ºC) by reaction with the solid intermediate SiC [1]. A flow of SiO(g) towards the off-gas system reduces the Si yield. The condensation reactions of SiO(g) and CO(g) is triggered between 1400 and 1800ºC in many industrial furnaces [2-10]. SiO_2, SiC and Si precipitate according to: [11-14]:

$$3\ SiO(g) + CO(g) \rightarrow 2\ SiO_2\ (s,l) + SiC(s) \quad (1)$$

$$2\ SiO(g) \rightarrow Si\ (s,l) + SiO_2\ (s,l) \quad (2)$$

The condensation products and the unreacted molten quartz create a cavity above the liquid silicon pool. The cavity roof will entrap SiO(g) and CO(g) thereby avoiding Si

losses to the off-gas system. Some of the SiO(g) is condensed on the surface of the raw materials added to the furnace. The materials accumulated in the cavity roof and the upper part of the charge are put back in the cycle by stoking [1,13]. This solution is nowadays a common practice in industrial processes. Another solution is an increase in the heat supplied to the electrode. This procedure weakens the condensate, until it melts and flows to the silicon production zone. The additional heating implemented on electrodes leads also to fast consumption, as well as an increased difficulty in the process control [4]. Silica and SiC will also move downwards with the other raw material to the reaction zone.

Previous laboratory scale experiments led to the characterization of brown, white and blue condensates [12-13, 15-19]. The first is a mixture of Si and SiO_2, whereas the second and third are made of SiO_2 and SiC. The white and blue condensates produced on some of these works [12,15-16] show structural and compositional similarity with the SiO_2-SiC nanowires produced from reaction between quartz and carbon [20-26]. The mechanism of formation suggested for the nanowires needs further confirmation. Many of the reactions proposed are not happening in silicon production, since their ΔG° would be positive in the temperature range corresponding to the condensation zone. Some works hypothesize that SiO(g) can generate a metastable solid phase SiO(s), which disproportionates at atomic scale [27-29]. The structure of SiO(s) has been widely modelled and discussed [30-33]. The interface cluster model proposed by Hohl and Achim [32] got closest to the TEM analyses performed so far, but it needs further experimental confirmation. Topographic and surface analysis of condensates can be crucial to understand their mechanical properties and the mechanism of formation.

In this work, SiO(g) and CO(g) are produced from SiO_2 and SiC by Reaction -1. Compositional and microstructural analysis through different characterization techniques will identify the main condensates and their relations with Reaction 1 and 2. Temperature measurements will assess temperature intervals for condensation products and the points where the condensates will start clogging the system. Once the produced condensates are weighted, a mass balance will clarify how Si, SiC and SiO_2 distribute themselves between the different condensation products.

Experimental

The main raw materials are quartz named Quartz20 (SiO_2 >99% wt.) and SiC (95%wt. SiC) from Washington Mills. The powder size range between 0.5 and 50 µm. The powders were mixed for two hours starting from a molar ratio SiO_2:SiC 2:1, and then pelletized at room temperature, with water as binder. The pellets final diameter ranged between 1 and 2 mm. The pellets underwent drying for 6 hours at 110°C and calcination for 30 minutes at 1200°C. 20 g of pellets served as SiO(g) + CO(g) generating material.

A cylindrical graphite crucible containing pellets were inserted in an electric graphite tube furnace. The graphite sheath dimensions were 265 mm height and 150 mm diameter. It consisted of two parts: a gas production chamber at the bottom, and a condensation crucible mounted above. The condensation crucible had an inner diameter of 25 mm and a height of 150 mm. SiC particles with diameter ranging between 10-20 mm filled this part up to 13 cm from the bottom of the condensation chamber. Their purpose was to capture the gas for condensation on their surface. Interactions between SiO(g) and SiC(s) was considered negligible in the condensation chamber.

After reducing the pressure in the system down to 150 mbar at room temperature, Ar(g) or He(g) were injected. The total pressure in the furnace was set to 1 atm. An alumina tube carried the inert gas down to the bottom of a cylindrical graphite sheath. The

terminal part of the alumina tube was glued to a graphite gas lance, and placed at temperatures where alumina would not evaporate or sag in such extreme conditions [34]. The inert gas flowed upwards through the pellets, carrying the SiO(g) and CO(g) produced by the pellets. An overview of the apparatus is given in Figure 1.

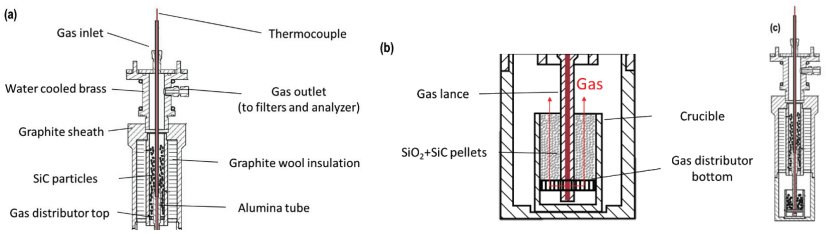


Figure 1: Schematic overview of the ReSiNa furnace setup. (a) Condensation chamber; (b): Gas production chamber; (c) Overview.

The holding temperature was set to 2000°C for all the experiments in the gas production chamber. Heating and cooling rates were fixed at 50°C/min and 35°C/min respectively. The variables are inert gas flow and holding time. A temperature gradient would generate inside the condensation chamber. A C-type thermocouple was inserted for each experiment at a fixed position, to monitor the thermal history at a fixed point. This means that temperature measurements were carried out while condensation went on. Each experiment is marked with a number from 1 to 5, corresponding to the conditions in Table 1, and by a letter from *a* to *e*, defining each experiment repetition. The temperature profile was computed for condition 4. He(g) was used in Experiment 1, whereas Ar(g) was supplied in the remaining conditions. The computed gradients for experiment 3-5 are shown in Figure 2. The curves are extrapolated by using a second grade polynomial regression. The values in bold were measured experimentally. They correspond to the temperature during the plateau. This means that the Experiment 3, 4 and 5 are assumed to share the same temperature profile, as the temperature gets constant few minutes after the holding temperature at 2000°C was started. The temperature profile as a function of time computed for Experiment 4 proves this assertion. Each point on the graph is separated from each other by a distance of 1 cm. The coordinate y=0 corresponds to the bottom of the condensation chamber. A thermal history was not collected for the measurement at y=0.

Table 1: Holding time at maximum temperature and Ar gas flow

Experiment	Time (h)	Ar flow (l/min)
1	1	0.4
2	1	0.05
3	0.5	0.02
4	1	0.02
5	4	0.02

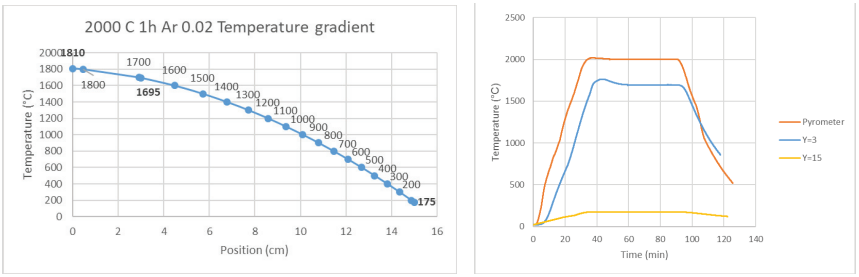


Figure 2: Left: Temperature gradient generated in condition 4; Right: Thermal history at different positions in condition 4

Once the experiment was finished, the SiC inert particles covered in condensates were weighted and sorted as a function of position, and therefore temperature. A condensation profile is created. Such drawings would track the physical appearance and composition of the condensate, and eventual coexistence of different condensates in the same temperature range.

After each experiment, all the condensates accumulated on the graphite parts were removed by using SiC sand paper. Some SiC substrates were isolated for metallographic analysis. The samples were mounted in an iodoform-containing epoxy that grants higher contrast for carbon-containing materials [35]. A 10% in wt. iodoform was added into the resin and stirred thoroughly until it mixed completely. Then, the solution was cooled down to 10°C, and the hardener was added in the proportions specified by the resin producer. Back-scattered (BSE) and secondary-electron (SE) images were taken with a Hitachi SU-6000 FE-SEM. EPMA (Electron Probe Micro-Analysis) was carried out on the samples used for the metallographic analysis by using a JEOL JXA-8500F. Points showing different contrasts were selected to detect the relative mass percentage of Si, O and C. All the signals collected from the EPMA analysis of this compound came from a defocused area of 10µm diameter. Perturbation in the measurements might come from carbon coming from sample preparation.

XPS chemical analysis was performed on a Kratos Axis Ultra. The source used was an aluminium monochromatic source with K_α wavelength at 417 nm. The analysis covered an area of 500x700 µm, whereas the penetration depth ranges around 10 nm. The chemical shift of the obtained signals was calibrated by taking the C-C bond signal as reference at 285 µm.

Results

Condensate characterization

Five kinds of mixtures have been sorted according to their colour. They are called blue, white, orange, grey and brown condensate. Figure 3 shows the SE images of the first three kinds of condensates. The condensation compounds do not interact nor diffuse into the SiC particles placed in the condensation chamber.

The blue condensate appears as a thin layer on the SiC particles. It is formed between 1150-1250°C and always found together with the white condensate. It can also appear at the bottom of the condensation chamber, between 1750 and 1800°C. It appears as a thick web of disordered whiskers, with thickness of 20-80 nm in diameter and several

hundred µm in length. The white condensate (1250-1800°C) appears as a foamy, light and weak layer. When scratched, layers of blue condensate appear. The white condensate consists of an intricate forest of treads and nodules. The average diameter of the treads ranges between 50 and 100 nm, whereas the nodules range between 0.25-1 µm. These results match with findings from Mølnås and Vangskåsen [12,15]. The nodules density increases with the condensation temperature in the condensation crucible. The orange condensate appears only at high He flows in experiment 1. Its microstructure consists of nanowires and nodules in higher concentration. The blue, white and orange condensates are very similar in compositions. The blue condensate was analysed by XPS only, because of its low thickness. The compositions are very close to a mixture of SiO_2 and SiC in a molar ratio 2:1. These condensates will be referred from now as SiO_2-SiC mixtures. Table 2 summarizes the results of the characterization analysis.

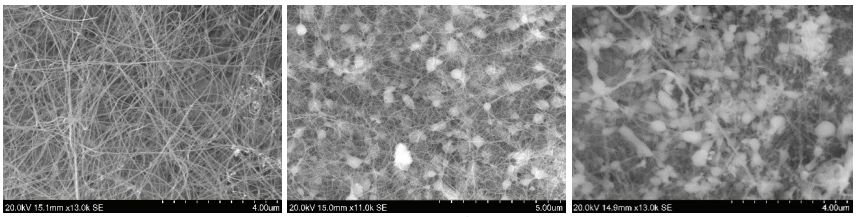


Figure 3: Blue, white and orange condensates, SE images experiments 2a, 2a and 1a

Table 2: Characterization of SiO_2+SiC mixture (%at.)

Element	Theoretical (SiO_2:SiC 2:1 molar)	EPMA (White, 28 points)	EPMA (Orange, 6 points)	XPS (Blue, 3 points)
Si	37.5%	34.3 ± 1.3%	35.3 ± 2.7%	38.3%
O	50,0%	47.7 ± 1.7%	44.7 ± 2.3%	42.5%
C	12.5%	18.0 ± 2.5%	20.1 ± 4.4%	19.2%

A grey, strong and foamy layer is formed close to the highest temperature ranges of the white condensate (1550-1700°C). This layer consists of oriented wires of length ~1 mm and diameters between 1-4 µm. These wires are made of spherical building blocks piled up together (Figure 4). Table 3 shows the results from the characterization. The composition is close to the SiO_2-SiC mixtures. Some white or blue SiO_2-SiC mixture can be present between the wires. This condensate was found in low amounts compared to the others, therefore it will not be the main focus of this work.

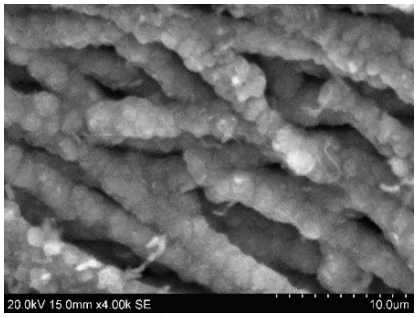


Figure 4: Grey condensate, SE-image from Experiment 4a

Table 3: Characterization of grey Si-SiO_2 mixture (%at.)

Element	Theoretical (SiO_2:SiC= 1:2 molar)	EPMA (11 points)
Si	37.5%	36.1 ± 0.6%
O	50,0%	52.7 ± 0.4%
C	12.5 %	14.8 ± 0.9%

A brown, glassy material appears in the temperature range 1700-1780°C. The white SiO_2-SiC and SiC particles act as substrates. The SiC substrate stick together as if the brown compound was molten during condensation. The morphology matches with previous works [2, 8, 12-13, 15-16, 28]. BSE images show spheres embedded in a darker matrix. EPMA mapping from Figure 5 shows areas with 90%wt. Si where the spheres appears, also the green stream in the Si-mapping corresponds to the silica matrix. The Si-particle size ranges between 0.25 and 2.5 µm. Figure 6 shows that the brown condensate can embed the grey SiO_2-SiC mixture. This might create perturbations in the received signal during characterization. It was concluded that the brown condensate is a mixture of Si and SiO_2 in a molar ratio 1:1 (Table 4).

Table 4: Characterization of brown Si-SiO_2 mixture (%mol.)

Element	Theoretical (Si:SiO_2 1:1 molar)	EPMA (14 Points)	XPS (1 point)
Si	50.0%	43.1 ± 2.6%	44.5%
O	50.0%	49.4 ± 0.4%	49.4%
C	0 %	7.5 ± 2.6%	6.1%

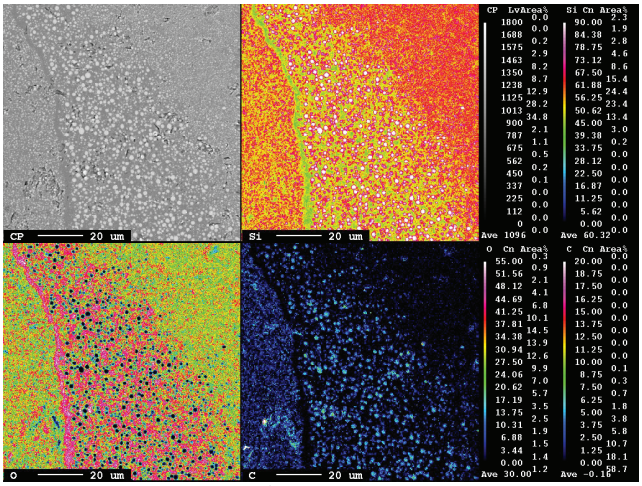


Figure 5: EPMA mapping of brown condensate, Experiment 4a

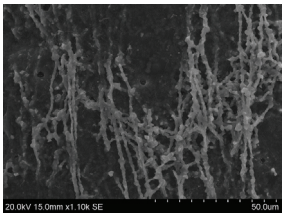


Figure 6: SE-image of brown condensate embedding the grey wires, Experiment 4a

Condensation profiles

Figure 7 shows the condensation profiles of the experiment producing the highest amount of condensate for each experimental condition. Shades of different colours cover the same temperature interval if two condensates are present in the same positions. The thicker the transversal lines, the higher the relative amount of condensate in that temperature interval. Where no colour is shown, the SiC substrate did not capture any condensate. Since the temperature gradient was not computed for the first two conditions, the positions are shown in the scale to the left of the picture. For conditions 3-5, the same temperature profile was assumed to be present, and a scale with the computed temperature gradient is associated on the left side of each condensation profile. After separating the condensate manually from the substrate, it was noticed that at least half of the condensate weight is located between 1600-1800°C for conditions 3-5. Table 5 shows the measured weight of condensate, according to its composition. The data written in bold refer to the condensation profile shown in Figure 7.

The circle diagrams in Figure 8 summarize the distributions of SiO_2, SiC and Si between the different condensates compositions. It is assumed that all Si and SiC respectively go to the Si-SiO_2 and SiO_2-SiC condensates. These results have been computed by assuming the theoretical equilibrium compositions for Si-SiO_2 1:1 molar and SiO_2-SiC 2:1 molar mixtures. The amount of Si generated during condensation can

reach up 12%wt. of the total condensates mass. SiO_2 mostly goes to the SiO_2-SiC condensate. Strong Ar flow reduces Si content in the condensates.
Experiment 3 is the only one where some of the pellets are unreacted. The amount of pellets leftovers ranges around 1 gram for this experiment. Time does not affect the temperatures at which each condensate starts forming. SiO(g) is lost in different ways during the experiment. It can diffuse into the graphite sheath, forming a layer of SiC up to 400 µm thick. Si is also formed within this layer. This phenomenon occurs only on the graphite wall of the gas production chamber. Other causes for gas losses can be found in the condensates generated in the off-gas system [13] and outside the sheath. The condensate mass balance disregards the compounds generated by diffusion of SiO(g) into graphite. Finally, when the inert gas flow flow increases, the condensation yield decreases and the temperature range for the formation of white and blue condensate becomes wider.

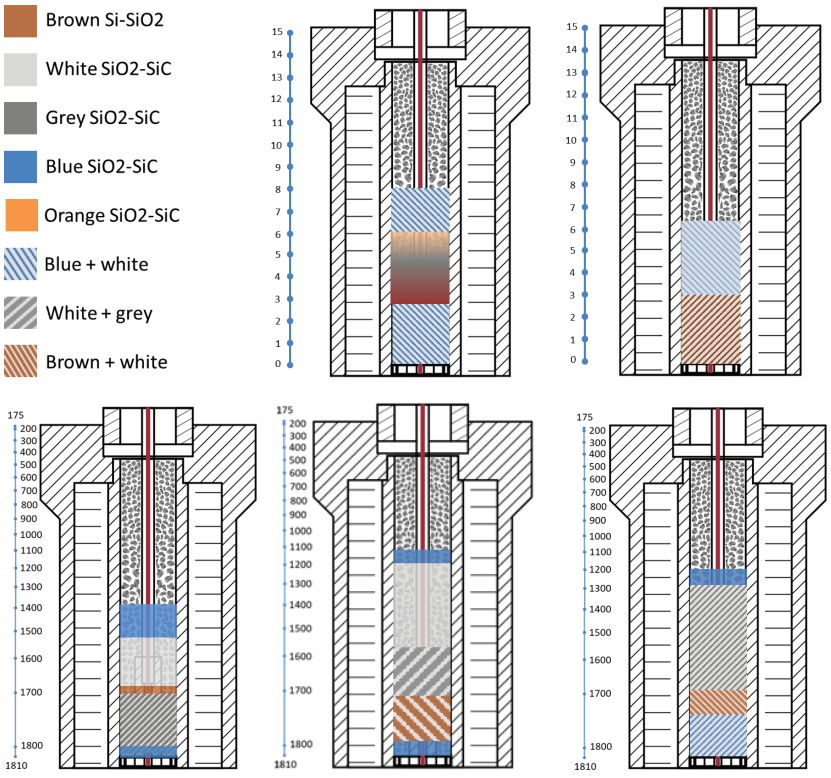


Figure 7: From left to right: condensation profiles of experiments 1b, 2a, 3a, 4a, 5a. Scales in cm for conditions 1-2 and in °C for conditions 3-5

Table 5: Weight of condensates collected in each experiments

Exp.	Si-SiO_2 (g)	SiO2-SiC (g)	Si (g)	SiO2 in Si-SiO2 (g)	SiO2 in SiO2-SiC (g)	SiC (g)
1a	0	1.43	0	0	1.07 (75%)	0.36 (25%)
1b	**0.38**	**1.71**	**0.12 (6%)**	**0.26 (12%)**	**1.28 (61%)**	**0.43 (21%)**
2a	**1.40**	**2.61**	**0.45 (11%)**	**0.95 (24%)**	**1.96 (49%)**	**0.65 (16%)**
3a	**0.10**	**0.88**	**0.03 (3%)**	**0.07 (7%)**	**0.66 (67%)**	**0.22 (23%)**
4a	**1.65**	**3.70**	**0.53 (10%)**	**1.12 (21%)**	**2.78 (52%)**	**0.93 (17%)**
4b	0.10	1.38	0.03 (2%)	0.07 (5%)	1.03 (70%)	0.34 (23%)
4c	0.70	1.98	0.22 (8%)	0.48 (19%)	1.49 (55%)	0.50 (18%)
4d	1.28	1.90	0.41 (13%)	0.87 (27%)	1.42 (45%)	0.47 (15%)
4e	0.12	1.78	0.04 (2%)	0.08 (5%)	1.34 (70%)	0.45 (23%)
5a	**0.20**	**1.14**	**0.06 (5%)**	**0.14 (10%)**	**0.85 (64%)**	**0.28 (21%)**

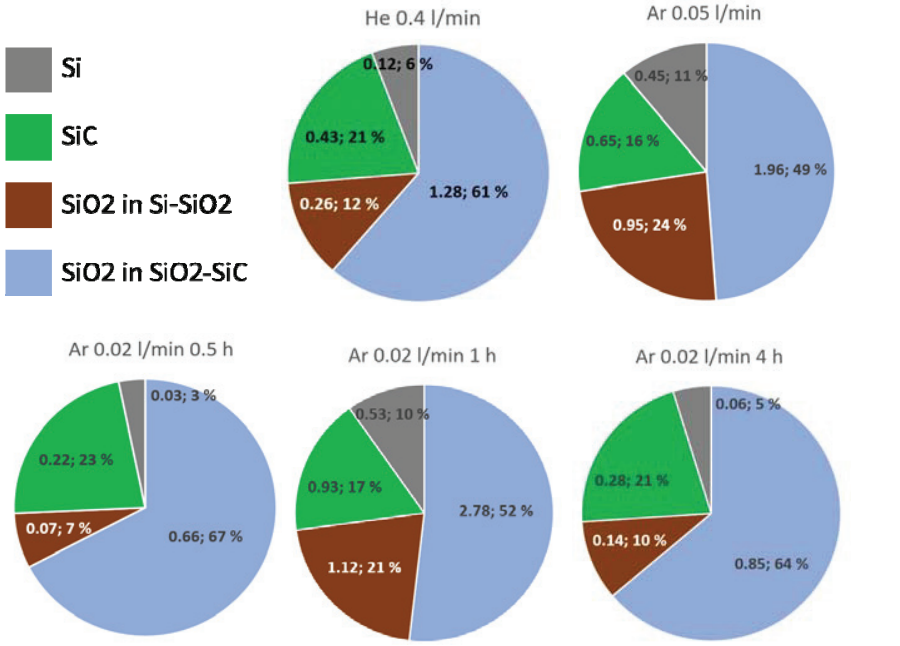


Figure 8: Distribution of Si, SiC and SiO_2 in the different phases

Discussion

SiO_2–SiC mixture

Samples covered in white condensate often turn blue after casting in epoxy and polishing, which means that the blue condensate can form before the white. In fact, blue

condensate is found at lower temperatures, and consequently at lower SiO(g) partial pressures. Another hint proving the validity of this theory is the increasing presence of nodules at higher temperatures in all the experiments. This is in good agreement with research done by Hu [21] and Mølnås [12]. From a TEM analysis, Hu [21] confirmed that the nodules are a mixture of Si and SiO_2 at nanometric scale. This is in good agreement with the intermediate cluster model computed by Hohl and Achim [32]. An higher increase in the nodule dimension and presence corresponds to a higher partial pressure of SiO(g) in the system. The shell layer should react to temperature changes as a mixture of SiO_2 and Si. It would be rather a SiO_x mixture, with x close to 2. For the sake of simplicity, a stoichiometric composition for silica was assumed. Materials undergoing softening, like silica itself, tend to assume a spherical shape, to reduce their surface energy. Therefore, an increase in condensation temperature makes the nodules larger, spherical and more abundant.

Even though the starting materials for the SiO(g)+CO(g) mixture are different, the final condensation product is the same in microstructure and composition. Therefore the wires are forming a core-shell structure, with a 3C-SiC core and an amorphous SiO_2-shell layer [36]. In the mechanism proposed by Hu [20-21], the gas condensates forming a SiC nucleus (Stage I). Then, SiC whiskers will grow (Stage II) and at the same time they will be covered into SiO_2 (Stage III). In the oxide-assisted growth, the shell phase limits the lateral growth of the core-phase, thus developing nanowires in a preferential crystalline direction. The chemical reactions proposed by Hu must be revised after this experiment. No elemental carbon is present in the raw materials. As a consequence, the Boudouard reaction becomes negligible, and the formation of SiO(g) and CO(g) occurs faster, since the energy is not used for the production of the SiC intermediate. One of the reactions proposed during stage I, according to Hu [21] is

$$SiO_2 + C = SiO(g) + CO(g) \quad (3)$$

In silicon production, this reaction is going through an intermediate step producing SiC and CO(g). The already formed SiC reacts with SiO_2 to produce SiO(g) and CO(g) according to Reaction 1. In fact, the Si-SiO_2 condensates, which are the main product of this reaction, generates only at high temperatures, above 1700°C.

Since the white condensate covered a very wide temperature range in the crucible, the composition is compared between different positions. Figure 9 clearly shows that neither temperature nor Ar flow influence the composition of the condensate produced at different positions of Experiment 3a. The only thing varying is the amount of condensate generated, and the local density of nodules.

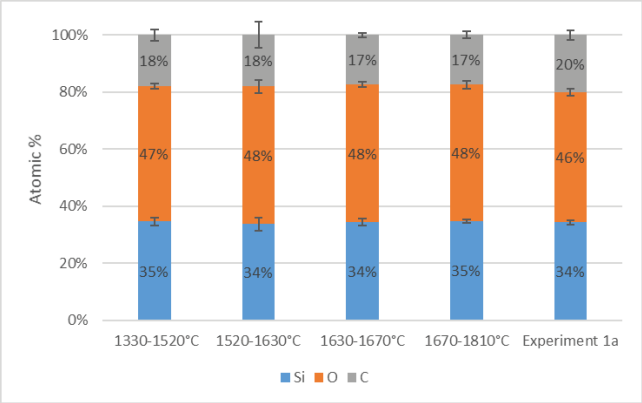


Figure 9: Characterization of SiO_2-SiC mixtures from different temperatures. Samples from experiment 4a and 1a. Theoretical composition for the white condensate was assessed to be 37.5% Si, 50% O and 12.5% C. The bars shows uncertainties at one standard deviation

The white SiO_2-SiC mixture is the first condensate responsible of the clogging effect in the crucible. It is useful to define a *stoking temperature* as the lowest temperature in the crucible where the SiC particles do not flow when the condensation chamber is put upside down. From this point down, it is necessary to stoke the SiC inert particles from the top of the condensation chamber. Stronger clogging is present down in the highest temperature ranges where the brown Si-SiO_2 mixture appears. The stoking temperature is strongly depending on the holding time and inert gas flow. At higher flows the profile is shifted to lower temperatures, and the stoking point follows this trend. The nanowires create a solid with large porosity, whereas the SiO_2 nodules decrease the space between the pores. A higher the partial pressure of SiO(g) corresponds to a higher temperature and density of nodules. Stronger Ar flow create gas channels and make clogging less likely to happen. It is important to state that the stoking point may vary consistently with the charge size. The system would clog easily if the charge was packed more efficiently.

Table 6: Stoking points. Scale in cm for conditions 1-2 and °C for conditions 3-5

Exp.	1	2	3	4	5
Stoking point (cm; °C)	6.4	3.0	1520-1580	1620	1390

Si–SiO_2 mixture

The brown condensate is the product of Reaction 2 [14-16]. Si has a lower melting point than silica. When cooling, silicon is still liquid, whereas the matrix is solid. Si assumes a spherical shape and subsequently enlarges to reach its lowest internal energy value. The mechanism of growth is Ostwald-ripening. Lower particle size implies lower growth times. Areas with smaller particles are exposed to lower temperatures. Vangskåsen [15] and Ksiazek and Kero [13] also observed Si spheres surrounded by a glassy SiO_2 matrix. However, they did not observe wires embedded in the matrix, as it

happened for the grey condensate. Dimensions and interfaces between Si spheres in the two compounds coincide in composition.
Nucleation and growth of Si-SiO_2 mixture occurs simultaneously with the SiO_2-SiC formation. This hypothesis confirms the results of Vangskåsen [15-16], where the brown condensate is sandwiched between two layers of white SiO_2-SiC mixture. There is no clear correlation between the diameter of the Si spheres and the temperature in the condensation crucible. An hypothesis for the mechanism is the disproportionation of SiO(g) into Si and SiO_2. Intermediate steps involving SiC are also a possibility, since C was still detected during EPMA analysis of the brown condensate. Reaction 2 would be the overall producing reaction for the Si-SiO_2 mixture, but SiC contained in the condensates or in the SiC substrate can also react with SiO(g) above 1700°C according to:

$$SiC(s) + SiO(g) = 2\ Si(l) + CO(g) \quad (3)$$

Other hypothesis would involve the generation of a SiO(s) single phase, which then disproportionates into Si and SiO_2 [27-28].

Conclusion and further challenges

SiO_2 and SiC have been used to produce a stoichiometric mixture of SiO(g) and CO(g). The gas deposits with different microstructures and composition on an inert SiC substrate. The condensates can be divided into two categories. The SiO_2-SiC mixtures are composed of nanowires with a SiC crystalline core and a SiO_2 amorphous outer layer. SiO_2 is generated in excess at higher temperatures, and accumulates between the wires as nodules. This compound contains most of the generated SiO_2. The Si-SiO_2 mixtures consist of micrometric scale oriented treads. Si spheres are packed together by a glassy SiO_2 matrix. SiO(g) disproportionation happens at a higher extent because of the higher temperature. Condensation clogs the setup from 1390°C up. The first clogged particles change their positions according to the gas flow and time. At least half of the condensate is generated between 1600 and 1800°C.
A TEM analysis can confirm the core-shell structure of the SiO_2-SiC nanowires, the composition of the SiO_2 nodules and the interface between the Si spheres and the SiO_2 matrix in the Si-SiO_2 condensate. Further experiments with different condensation substrates can be performed. Condensation mainly occurs on the SiC crust generated in the furnace. However, it would be useful to assess how condensation occurs on quartz or carbon substrates, or on the condensates themselves.

Acknowledgments

The authors would like to thank Morten Peder Raanes for the EPMA and Ingeborg-Helen Svenum (SINTEF) for the XPS analysis. The present study was supported by Elkem AS and the EnergiX program of the Research Council of Norway through project 269431 SiNoCO2.

References

1. Tangstad, M. *Metal Production in Norway*. 1st ed., Akademika Forlag, 2013.
2. Ksiazek, M., Tangstad, M. and Ringdalen, E. (2016) *Five furnaces five different stories*, in. “Silicon for the Chemical and the Solar Industry XIII”, Kristiansand, Norway, pp. 33–42.

3. Otani, Y., Saito, M., Usui, K., Chino, N. *The inner structure in submerged arc furnaces*, in. ”6th Internationl congress of electro heat. N.12, discussion N117D”, Brighton, England, 1968
4. Schei, A., Tuset, J,, Tveit, H. *Production of High Silicon Alloys*. 1st ed., Tapir, 1998.
5. Schei, A. *The Chemistry of Ferro-Silicon Production.* Tidsskr Kjemi Bergvesen Met, vol. 27, **8** , 1967, pp. 252–158.
6. Schei, A., Rong, H., Øye, H.A. *Impurity Distribution in Silicon,* in “Silicon for the Chemical Industry”, 1992, pp. 11–23.
7. Schei, A., and O. Sandberg. *Selected Topics in High Temperature Chemistry*. 1966.
8. Tangstad, M., Ksiazek, M. and Faaness, B., *Zones and Materials in the Si furnace*, in. “Silicon for the Chemical and the Solar Industry XII”, Trondheim, Norway, 2014.
9. Poch, W., and A. Dietzel. *The Formation of Silicon Carbide from Silicon Dioxide and Carbon*. Ber. Dtsch. Keram. Ges., vol. 39, 1962 , pp. 413–26.
10. Kurosawa, T., Yagihashi, T., Ochiai, S., Naramura, T. *Several Aspects on the Products in a Silicon-Making Electric Furnace*., Trans. Nat. Res. Inst. Metals, vol. 14, 1972, p. 22.
11. Fei, L., and M. Tangstad. *Use of Agglomerated Raw Materials in Si Production*. In “Silicon for the Chemical and the Solar Industry XIII”, Kristiansand, Norway, 2016, pp. 259–68.
12. Mølnås, H. *Investigation of SiO-Condensate Formation in the Silicon Process*. Internal report, 2010.
13. Ksiazek, M. and Kero, I. *Challenging in transporting the off-gases from the Silicon process*, in. “Takano International Symposium on Metals and Alloys” Vol. 3, 2015.
14. Ringdalen, E. *Phase transformations in quartz and its effect on furnace operation*, in. “Silicon for the Chemical and the Solar Industry XIII”, Kristiansand, Norway, 2016, pp. 269–278.
15. Vangskåsen, Jørund. *Investigation of the Cavity Formation in the Silicon Process*. Internal report, NTNU, 2011.
16. Vangskåsen, Jørund, and Øystein Høgsand. *Investigation of Cavity and Condensate Formation in the Silicon Process*. Internal report, NTNU, 2011.
17. Kuhn, W. E. *The Formation of Silicon Carbide in the Electric Arc*, Journal of the Electrochemical Society, vol. 110, **4**, 1963, pp. 298–306.
18. Tangstad, M., Ksiazek, M., Andersen, V., Ringdalen, E. *Small scale laboratory experiments simulating an industrial silicon furnace*, in. “The twelfth International Ferroalloys Congress, Sustainable Future”, Helsinki, 2010, pp. 661–670.
19. Tangstad, M. and Ksiazek, M. *Investigation of white and brown condensate*. Internal report, Sintef: Trondheim. 2010
20. Hu, P., Dong, S., Gui, K, Deng, X, Zhang, X. *Ultra-Long SiC Nanowires Synthesized by a Simple Method.*, RSC Advances, vol. 5, **81**, 2015, pp. 66403–08.
21. Hu, P., Pan, R., Dong, S., Jin, K, Zhang, X. *Several Millimeters Long SiC-SiO2 Nanowires Synthesized by Carbon Black and Silica Sol*. Ceramics International, vol. 42, 2016, pp. 3625–30.

22. Wei, J., Li, K., Li, H., Fu, Q., Zhang, L. *Growth and Morphology of One-Dimensional SiC Nanostructures without Catalyst Assistant.* Materials Chemistry and Physics, vol. 95, **1**, 2006, pp. 140–44.
23. Wang, J., Liu, S., Ding, T., Huang, S., Qian, C. *Synthesis, Characterization and Photoluminescence Properties of Bulk-Quantity β-SiC/SiO2 Coaxial Nanowires*. Journal of Material Chemistry and Physics, vol. 135, 2012, pp. 1005–1011.
24. Wang, X. J., Tian, J.F., Bao, L.H., Hui, C., Yang, T.Z., Shen, C.M., Gao, H.-J., Liu, F., Xu, N.S. *Large Scale SiC/SiO2 Nanocables: Synthesis, Photoluminescence, and Field Emission Properties.* Journal of Applied Physics, vol. 102, **1**, 2007, p. 014309.
25. Saito, M., Nagashima, S., Kato, A. *Crystal Growth of SiC Whisker from the SiO(g)-CO System*. Journal of Materials Science Letters, vol. 11, **7**, 1992, pp. 373–76.
26. Liu, H., Huang, Z., Huang, J., Fang, M., Liu, Y.-G., Wu, X. *Thermal Evaporation Synthesis of SiC/SiO2 Heterojunctions and Their.* Jounal of Materials Chemistry C, vol. 2, **37**, 2014, pp. 7761–67.
27. Hass, G. *Preparation, Structure, and Application of Thin Films of Silicon Monoxide and Titanium Dioxide*. Journal of the American Ceramic Society, vol. 33, **12**, 1950, pp. 353–60.
28. Brewer, Leo, and Russell Edwards. *The Stability of SiO Solid and Gas*. Journal of Physical Chemistry, vol. 58, **4**, 1954, pp. 351–58.
29. Kolobova, K. *Some Properties of Silicon Monoxide*. All-Union Institute of Refractories, vol. 12, 1967, pp. 42–43.
30. Philipp, H. R. *Optical Properties of Non-Crystalline Si, SiO, SiO2 and SiO2*. Journal of Physics and Chemistry of Solids, vol. 32, **8**, 1971, pp. 1935–45.
31. Tempkin, R. J. *An Analysis of the Radial Distribution Function of SiO2.* Journal of Non-Crystalline Solids, vol. 17, 1975, pp. 215–30.
32. Hohl, and Achim. *An Interface Clusters Mixture Model for the Structure of Amorphous Silicon Monoxide (SiO).* Journal of Non-Crystalline Solids, vol. 320, **1**, 1950, pp. 255–80
33. Schulmeister, K., and W. Mader. *TEM Investigation on the Structure of Amorphous Silicon Monoxide.* Journal of Non-Crystalline Solids, vol. 320, **1**, 2003, pp. 143–50
34. Jonas Einan Gjøvik, private communication, NTNU, Trondheim, Norway, 2017.
35. Gomez, C. O., Strickler, D.W., Austin, L.G. *An Iodized Mounting Medium for Coal Particles*. Journal of Electron Microscopry Technique, vol. 1, 1984, pp. 285–87
36. Broggi, A. *TEM analysis of condensates from silicon production*, to be published in 2019.

Silicon for the Chemical and Solar Industry XIV
Svolvær, Norway, June 11 – 14, 2018

Carbon Measurements on Silicon Samples

Karl Rimböck [1] and Gerhard Traunspurger [1]

1) WACKER *Chemie AG, Burghausen, Germany*

Abstract

In the present study, we applied a multiphase carbon analysis method, which is a tool for monitoring the quality of *WACKER*'s polycrystalline silicon products, also to metallurgical grade silicon – the feedstock for chlorosilane synthesis. We found the combination of static and dynamic measurements of surface carbon contaminations to be suitable to not only evaluate the quality of the raw material, but also predict its performance in chlorosilane production with respect to the formation of carbon-containing side products. Key to the success of the methodology at hand is the correlation between specific thermogram areas and extent of the formation of a certain side product. Our results are summarized in this communication.

Introduction

Industries that use polycrystalline silicon (polysilicon) as feedstock (photovoltaic and electronics) are calling for high quality of the raw material, with continuously raised standards over the last decades, thereby forcing the polysilicon producers to ensure efficient control over up- and downstream processes. The producers, meanwhile, have to have an eye on their manufacturing costs whilst quality requirements gain in importance and competition stiffens [4]. These constraints form a challenging overall package for producing operations and associated units from research and development as well as quality management – even more so, when the prospective relevance of renewable energy sources is considered; with solar powered systems being the most attractive and promising among the mainstream technologies [1,2,3].

In order to provide the market with high quality polysilicon suitable for usage in semiconductor devices, the levels of contaminants have to be strictly controlled – especially those of metals (*e.g.* chromium, cobalt, iron, nickel and copper), boron, carbon, oxygen and phosphorus. Although the polysilicon production processes were constantly refined and optimized, there are still questions to be answered and problems to be solved: formation of side products and other impurities as well as purification problems, which have not changed much since the "early days". Generally, boron and carbon are the elements, which are most difficult to remove by classical distillation technologies [5].

As far as carbon is concerned, concentrations in the lower ppba-regions are typical for polysilicon products. Even in comparatively low-lying ranges, carbon levels of as low as 20 to 120 ppba in the polysilicon bulk were shown to cause defects in the silicon

crystal structure, which in turn significantly influence the electrical properties of the respective semiconductor device [6,9]. The polysilicon producers‘ general options to ensure pure products are apparent: either it is the elimination of the source of contamination or the removal of the respective impurities during downstream-processing before deposition. Especially the latter can be highly energy-intensive, which is why an early identification of potential contaminations is key to maintain a cost efficient process.

It is well established that metallurgical grade silicon is not only a major carbon source itself, but also a carbon-vehicle for contaminations from mechanical comminution and separation processes. Most of the carbon does not react under the reaction conditions of chlorosilane syntheses and will be concentrated in the contact mass or discharged from the reactors. Smaller fractions of the carbon introduced *via* metallurgical grade silicon, however, do react under these reaction conditions and form undesired side products. Some of these compounds have boiling points similar to trichlorosilane and, therefore, are difficult to separate by distillation [5,6,7,11]. Up to now, this was particularly problematic since the latter fraction of carbon contaminations could not be detected before the metallurgical grade silicon was used in production [7].

In this publication, the development and the implementation of a new methodology is presented that allows for the evaluation of metallurgical grade silicon with regard to the formation of carbon-containing side products and, ultimately, its applicability for the synthesis of chlorosilanes.

Theory

Despite the efforts to access semiconductor grade polysilicon by means of direct purification of metallurgical grade silicon, the rod deposition of trichlorosilane (“*Siemens* Deposition”) is still – even after over 60 years – the most important production route towards hyperpure silicon. Trichlorosilane is mainly prepared by reacting metallurgical grade silicon with a reactive gas mixture containing hydrogen chloride in fluidized bed reactors (chlorosilane reaction [CSR] & hydrochlorination). An alternative route towards polysilicon resorts to the deposition of monosilane. This process includes trichlorosilane production coupled with redistribution reactions. Figure 1 provides a highly simplified block process flow diagram of *WACKER*’s closed-loop polysilicon production process.

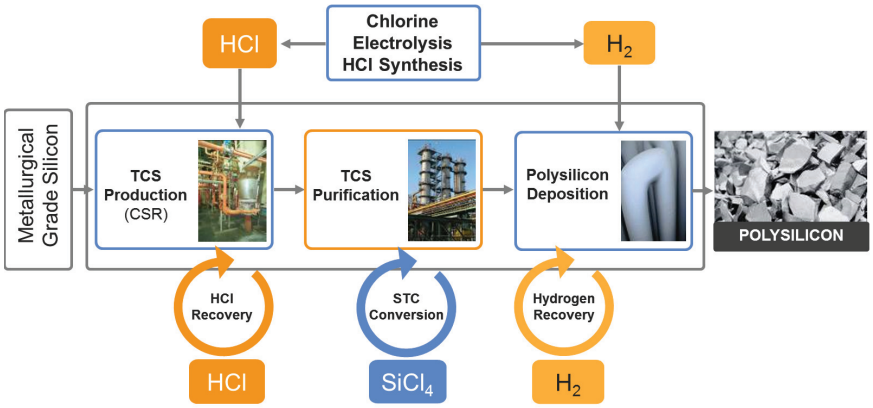


Figure 1: Simplified depiction of *WACKER*'s closed-loop polysilicon production process starting from metallurgical grade silicon (CSR ≙ chlorosilane reaction).

The formation of byproducts is immanent in chemical reactions or processes. Alongside the main products of the chlorosilane reaction, several byproducts are formed. To which extent these compounds are being formed is dependent on a vast variety of factors and, in addition, the respective contributions of these factors to their formation are weighted differently. For instance, fluctuating chemical compositions of metallurgical grade silicon result in varying interdependencies as well as, ultimately, inconstant product mixtures.

Regarding polysilicon purity, side products that are of most interest during chlorosilane synthesis include the trichlorides of boron and phosphorus, (chloro-)phosphine(s), lower hydrocarbon homologues and chloromethylsilanes. Basically, most of the reactive carbon, boron and phosphorus species are introduced to the chlorosilane reaction *via* metallurgical grade silicon – the lower the boron and carbon levels in metallurgical grade silicon, the higher the potential for cost savings since those would allow for simplified purification processes [5,6,7,11].

Literature only offers a blurry picture when it comes to anatomizing the chemical processes of carbon species in chlorosilane syntheses starting from metallurgical grade silicon, *viz*. the chlorosilane reaction and the hydrochlorination. Most commonly, you will merely find the distinction between "obviously unreactive" (*e.g.* silicon carbide) and "obviously reactive" (*e.g.* oil) carbon species [8,5;11,7,12].

Initial work towards an analytical foundation for the matter at hand has been performed by *Rong et al* and was presented as an "analytical method to measure different forms of carbon in silicon" in their conference paper back in 2012 [8], where the authors also gave an introductory overview of carbon in metallurgical grade silicon production. During their investigations, the authors found that the measurement of the total carbon content is unsuitable for correlations with byproduct formation in chlorosilane syntheses, which is why the focus was laid on surface carbon contaminations. They worked with *LECO*'s multiphase carbon analyzer *RC612*, which suits the purpose of targeting only the contaminations on the silicon surface, since it operates at temperatures below 1100 °C. Their study also showed that the amount of surface carbon is dependent on factors such as measurement temperature and particle size.

In view of the apparent correlation between surface carbon contaminations and the formation of carbon-containing side products, figure 2 gives a schematic overview on corresponding ideas about general reaction pathways for the chlorosilane reaction.

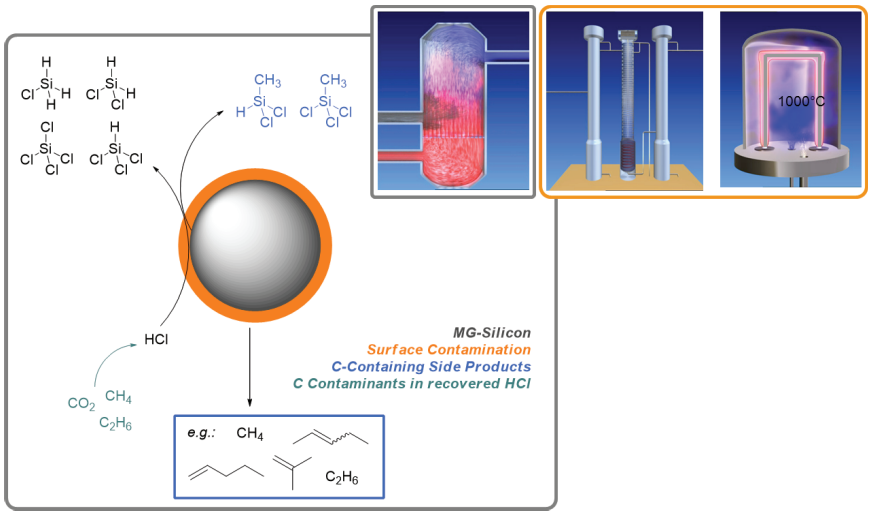


Figure 2: Formation of main and side products during the chlorosilane reaction in a schematic overview.

The group of the carbon-containing side products is dominated by two subgroups: lower hydrocarbon homologues and chloromethylsilanes. Both subgroups represent highly undesired side products since they not only partly reduce the yield but also require further efforts during downstream processing [6,7]. As already mentioned above, having access to appropriate analytical methods is key in order to help understanding and, eventually, optimizing chemical processes. We hypothesized that the first step towards the latter would be to reveal a correlation between presence and nature of different carbon species and specific byproducts. In doing so, it should then be possible to predict the reaction outcome – preferably, solely based on a simple and fast analytical method without having to resort to additional performance, interpretation and evaluation of single-case experiments on lab- and/or plant-scale.

Given the implications of carbon contaminations on the production of polysilicon, it seemed therefore desirable to revisit multiphase carbon analysis, which *WACKER* already had successfully implemented to monitor purity of its polysilicon products [13]. Hence, an optimized analytical setup with a detection limit (LOD) of 12 ppbw C was available for our investigations (setup of *Rong et al.* 25 ppmw C [8]).

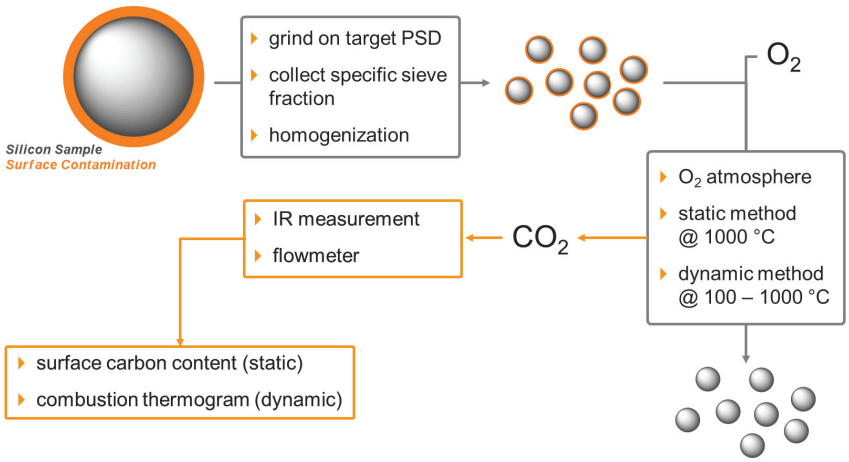


Figure 3: Basics of multiphase surface carbon analyses on silicon samples.

With multiphase carbon analysis it is possible to differentiate various forms of carbon by the temperature at which they combust and is thereby enabling the user to determine the elemental, inorganic and organic carbon contents of respective samples by applying a temperature ramping method (DIN19539). The analyzer is equipped with a resistance-heated, tubular combustion furnace, which can be operated at either a specifically programmed temperature set point (static method) or temperature ramp (dynamic method). While the former method simply yields the surface carbon content, the latter additionally furnishes a "combustion thermogram", which enables to draw conclusions on presence and nature of different carbon species. A downstream infrared spectrometer measures the intensity of the resulting carbon dioxide signal, which is then converted into a carbon concentration.

Experimental

At this point, it is worth dwelling on basic concepts and definitions, which are not completely self-explanatory:

- *free carbon*: this term groups carbon species that react with oxygen up to a temperature of 700 °C in a combustion device, preferably in a combustion furnace of a multiphase carbon analyzer. This group generally consists of organic carbon compounds, i.e. various synthetic materials, oils, fats and greases. (Please note that we chose to redefine the term "*free carbon*" which was introduced by *Rong et al.*[8])

- *surface carbon*: here, all carbon species are included, which are present on the surface of the metallurgical grade silicon particles – comprising free carbon as well as carbon species that show a reaction with oxygen above temperatures of 700 °C. The latter group is mainly made up of inorganic carbon species, *e.g.* carbides, carbonates and carbon allotropes.

- *total carbon*: alongside the surface carbon, this group also includes carbon species, which are part of the bulk of the metallurgical grade silicon particles.

We started with gathering a variety of metallurgical grade silicon materials from different sources and preparing the respective particulate silicon lab samples. In order to ensure comparability among the samples with respect to both carbon measurements and lab test performance we were aiming for a highly reproducible sample preparation (*i.e.* grinding, sieving and homogenization).

We used a batch-operated lab-reactor, which was run under standard reaction conditions [7] for the chlorosilane reaction with pure hydrogen chloride. The product gas stream was condensed and the respective condensate samples analyzed for product composition via off-line gas chromatography. Depending on the concentration and type of the byproducts, each sample was classified with a performance grade, which are predicated on risk potentials for *WACKER*'s real production processes. Each carbon-containing byproduct was evaluated separately according to cost estimates for its removal from the production process. These evaluations were then weighted by the respectively observed byproduct ratios and, eventually, combined to yield the performance grade. The performance grades range from 1.0 (best) to 6.0 (worst).

In parallel, particulate silicon samples (sieved fraction between 100 and 200 µm), which have been taken prior to use in the chlorosilane reaction, were analyzed by multiphase carbon measurements. Here, two basic methods have proved to be essential: the static and the dynamic measurement method. Each sample was measured thrice in both operation modes, thereafter, the results were averaged. The specific operation modes used in our investigations are shown in table 1.

Table 1: Parameter settings for operation modes used in this study.

Parameter	Static Method	Dynamic Method
O_2-flow [$Lmin^{-1}$] (purge)	4.0	4.0
O_2-flow [$Lmin^{-1}$] (carrier gas)	0.75	0.40
measurement time [s]	55	120
sample amount [g]	2.5	2.5
measurement temperature [°C]	1000 ($C_{surface}$) and 700 (C_{free})	100-1000 ($C_{surface}$) and 100-700 (C_{free})
temperature gradient [$Kmin^{-1}$]	0	120
analytical detection limit for C	20 ppbw	80 ppbw

Results and Discussion

In their study [8], *Rong et al.* were able to analytically differentiate between total carbon content and free carbon content of metallurgical grade silicon. We wanted to add another level of differentiation: reactive *vs*. unreactive carbon species and their relative level of impact on the chlorosilane reaction, *viz*. we wanted to correlate the content of

reactive carbon species with the extent of formation of specific carbon-containing side products of the chlorosilane reaction.

To meet this end, we started with generating and collecting data with carbon analyses (*i.e.* with static and dynamic measurement methods and temperatures up to 1000 °C) and lab-reactor tests for all silicon samples, which we selected in the run-up of this study. As far as the investigation is concerned, we were pleased to find that there were not only remarkable differences in terms of surface carbon content across all silicon samples but also regarding the presence of carbon species. Further analysis of the gathered data provided us with evidence that there is a possibility to draw a line between reactive and unreactive carbon species. In figure 4 we plotted examples for combustion thermograms of silicon samples and highlighted the areas, which group signals of reactive and unreactive carbon compounds, respectively.

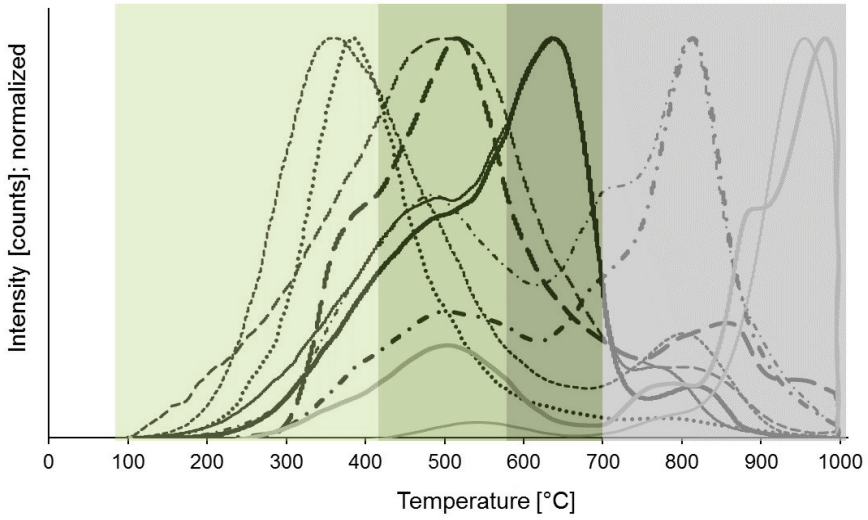


Figure 4: Exemplary, normalized thermograms of silicon samples and distinction between reactive (highlighted in green) and unreactive carbon species (grey area).

We assumed that the application of lower measurement temperatures would allow us to only – or at least mainly – target the reactive carbon species and thereby enable an attempt of directly correlating the free carbon content with the extent of carbon-containing byproduct formation. We subsequently analyzed all samples once again at lower temperatures of up to 700 °C. Indeed, this turned out to be an expedient way of correlating free carbon levels (*via* static method) and total byproduct concentration. In addition, we were also able to retrace the formation of specific carbon-containing byproducts (*i.e*. hydrocarbons, dichloromethylsilane and trichloromethylsilane) with the aid of the thermograms (*via* dynamic method). We identified the following correlations:

- peaks between 300 and 400 °C correlate with the formation of hydrocarbons
- peaks between 450 and 550 °C correlate with the formation of trichloromethylsilane

- peaks between 600 and 650 °C correlate with the formation of dichloromethylsilane

It should be noted that the dynamic method – for now – has to be considered as a semi-quantitative screening technique, which is capable of indicating the relative byproduct distribution. Nevertheless, these findings seemed sufficient to expect a certain level of predictive capability. This expectation was gratifyingly confirmed, as we successfully predicted the performance grade for a new silicon sample (red curve, figure 5), solely based on the results from the static and dynamic measurements.

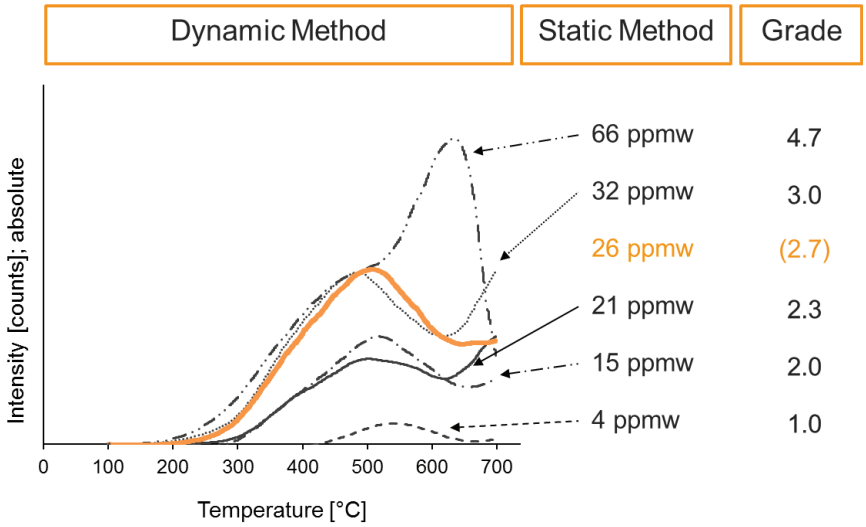


Figure 5: The combination of static and dynamic measurements can be used to predict the performance grade of silicon samples.

In all further cases, in which we tested the prediction of the performance of new silicon samples we observed the same result: predicted and conventionally determined grades matched reliably. Clearly, the combination of static and dynamic measurements is a powerful analytical tool for chlorosilane manufacturers with high quality standards, which is why *WACKER* has implemented this system in its routine monitoring of metallurgical grade silicon [14].

Conclusion

From previous work, we knew that multiphase surface carbon analysis is a formidable tool for gaining new insights into our processes. In view of the results provided by *Rong et al.*, its application to particulate metallurgical grade silicon was revisited and we were pleased to find that this study led us to an expedient analytical tool, which allows for predicting the performance of silicon materials in the chlorosilane reaction regarding the formation of carbon-containing byproducts. Our experiments have shown that the static and dynamic measurements are best performed at temperatures up to 700 °C, since we found that carbon species, which combust at higher temperatures had no impact on product distribution.

Together with other currently running studies, the presented method offers another promising avenue for exploring reactivity patterns and mapping out reaction pathways in metallurgical-grade-silicon-based chlorosilane syntheses.

References

1. H. Graßl, J. Kokott, M. Kulessa, J. Luther, F. Nuscheler, R. Sauerborn, H.-J. Schellnhuber, R. Schubert, E.-D. Schulze, *World in Transition - Towards Sustainable Energy Systems*, German Advisory Council on Global Change, London, **2003**, ISBN 1 84407 882 9.
2. World Energy Council, *World Energy Issues Monitor 2017 – Exposing the New Energy Realities*, **2017**, ISBN 978 0 946121 65 6.
3. World Energy Council, Accenture Strategy, Paul Scherrer Institute, *World Energy Scenarios 2016 – The Grand Transition*, **2016**, ISBN 978 0 946121 57 1.
4. J. Bernreuter, *Silicon for the Chemical and Solar Industry* **2016**, *XIII*, 361–364.
5. H. Kohno, T. Kuroko, H. Itoh, *Silicon for the Chemical Industry* **1994**, *II*, 165–170.
6. T. Lobreyer, K. Hesse, *Silicon for the Chemical Industry* **1998**, *IV*, 93–100.
7. K. Hesse, U. Pätzold, *Silicon for the Chemical Industry* **2006**, *VIII*, 157–166.
8. J. P. Svanem, T. Røe, A. P. Ruff, H. Kjønli, B. Eik-Nes, H. M. Rong, *Silicon for the Chemical and Solar Industry* **2012**, *XI*, 145–156.
9. R. C. Newman, *Rep. Prog. Phys.* **1982**, *45*, 1163–1210.
10. D. C Lynch, M. A. Lynch, *Silicon for the Chemical Industry* **2004**, *VII*, 307–318.
11. W. C. Breneman, H. J. Dawson, *Silicon for the Chemical Industry* **1998**, *IV*, 101–112.
12. A. Crawford, *Silicon for the Chemical and Solar Industry* **2016**, *XIII*, 201–217.
13. G. Traunspurger, L. Fabry, R. Pech, DE102012202640 A1.
14. K. Rimböck, G. Traunspurger, U. Pätzold, PCT/EP2018/053210.

Silicon for the Chemical and Solar Industry XIV
Svolvær, Norway, June 11 – 14, 2018

Silicon Content of Silicon Materials

Røe, Torbjørn[1)], Blandhol, Kjell[2)], Svanem, Johan Pääaho[1)], Rong, Harry[1)]
1) Elkem Silicon Materials, Fossegrenda 13, N-7038 Trondheim, Norway
2) Elkem Technology, Fiskaaveien 100, N-4621 Kristiansand, Norway

Abstract

Even though mentioned in almost all specifications, analysis reports, material summaries and naturally being of importance to all producers and consumers of silicon, a common understanding of how the silicon content of silicon should be understood, determined and presented is not in existence. Silicon cannot be measured directly to high accuracy and therefore the silicon content must be calculated based on the content of other elements. It is widely accepted that it is practically impossible to measure all elements in the periodic table in order to calculate the silicon content. Therefore, we suggest two ways for producers to report the silicon content based on analysis of main and some selected trace elements in silicon either by XRF (X-ray fluorescence) or by ICP (Inductively Coupled Plasma Optical Emission Spectroscopy) methods:

XRF Method: Si wt% = 100wt% - Fe wt% - Al wt% - Ca wt% - Ti wt% - 0.1 wt%

ICP Method: Si wt% = 100wt% - Fe wt% - Al wt% - Ca wt% - Ti wt% - B wt% - P wt% - Mn wt% - Cu wt% - Ni wt% - Cr wt% - Mg wt% - V wt%

Other intentionally introduced metallic elements must be separately subtracted.

Elements measured below detection limit of the analytical instrument used are subtracted using the full detection limit.

The ICP method is perceived as the most accurate method for calculating silicon content. However, for practical reasons, silicon content will often be calculated using the XRF method as this is both faster and less costly than using the ICP method.

In documents where silicon content is specified, the applicable method must be referred. In cases where the method is not referred, the ICP method shall prevail.

Both these methods are valid for silicon with silicon content > 96 wt% (by XRF-method). For silicon where the XRF method determines a silicon content above 99.7 wt%, the silicon content should be calculated using the ICP method.

This paper is also a call for all who refer to silicon content to include how this content is determined.

Silicon content of Silicon

What is silicon content for you?

Even though silicon has been produced and used, bought and sold, imported and exported, named and branded using the silicon content of this silicon as a main parameter for both internal and external use, there is no specification defined in standards, industry, academia or governmental organizations on how this content should be defined and determined.

The issue we try to solve with this paper can be addressed by trying to define the silicon content of materials within the scope for this paper. A normal definition of metallurgical silicon is that the Si content is > 96wt% [1]. Initially, this seems reasonable and is not possible to misunderstand.

But: Main issue-when determining Si-content is that silicon in itself is not possible to measure with good accuracy. The best analytical method has a relative uncertainty of +/- 0,5% (assumed based on data for ferrosilicon [2]). Methods to do direct determination of silicon content are not in normal use in the silicon industry.

As this direct determination is not used or deemed useful, the other route to find content of silicon, can be a residual calculation, which subtracts elements in the material that is NOT silicon from 100%.

Following this, a possibility to determine the actual content of silicon in a sample is to measure all other elements besides silicon in the periodic system and subtract these from 100% to determine actual content. Even though possible in theory, in practical terms measuring more than 100 other elements in order to determine the Si-content is impossible, highly costly, and generally irrelevant because the trace content will have no meaningful impact on the actual silicon content.

Therefore, a uniform residual calculation for calculating silicon content needs to be used by producers and consumers of silicon. Although the precise residual calculation formula will vary depending on purity, the residual calculation standard is otherwise accepted by industry.

Silicon content

An interesting point when looking at silicon content is that most producers and consumers of metallurgical silicon do not use the silicon content value for any material sorting or judgement of usefulness of the silicon.

For most practical considerations and evaluation, it is the content of other elements contained in silicon that is considered when looking at the usefulness of the material. Content of iron, aluminium, calcium, titanium, phosphorus, etc. are usually the values considered rather than the silicon content of the material.

That said, it is normal to report a silicon content both in specifications, product data sheets, certificates, and other documentation. As it is silicon that is bought and sold, it seems logical that the amount must be ensured to a minimum value. These are often given as a percentage number, normally without any given context to how the number is calculated or measured.

It is also a problem in import/export of silicon, where the limitation (e.g.) between high purity silicon and metallurgical silicon is given as a percentage number (99.99%) without any defined calculation method [3]. As high purity and lower purity silicon are treated differently, a common understanding of how these numbers should be understood would be beneficial.

Surface effects

A complicating fact in determining silicon content is that silicon will form a native oxygen layer on the surface when exposed to air [4]. If oxygen bound to the surface is to be included in calculation, it would mean that purity would depend heavily on average particle size – contrary to current consensus in industry, where surface bound species are omitted when considering purity.

As example, including surface oxygen – or other surface adsorbed species would in effect mean that high purity silicon powder (>99.99%) does not exist if the powder has been exposed to air.

Surface oxidation by air will also have a time effect, making actual determination of purity something that must be determined at any time when it is questioned. For instance, both when the silicon material leaves the silicon producer's country and when the silicon material arrives the silicon consumer's country – this is not practical.

Similarly, carbon content, can also be significantly influenced by adsorption from air, and may show a varied content based on timing when sample is taken and analysed.

This does not mean that surface bound or adsorbed elements are unimportant for users of silicon, and does not mean that analysis of carbon and oxygen should not be done, only that including these in calculation of silicon content is both difficult, ever-changing, and not correct.

How is Si content given by laboratory scale suppliers?

A normal way to specify silicon content for R&D qualities are on metals basis, for instance as done by Sigma Aldrich where purity is given to 99.999% on a "trace metal basis" (product 267414) [5] or by American Elements, where purity is given to 5N (99.999%), with a reference to "Total metal impurities: 0.001% max." [6]

The reference to total metal impurities is in line with omitting surface elements (oxygen/carbon/nitrogen). As there are no limits to what metals are included, it would mean that any serious dispute over purity require a lot of analysis to determine ALL existing metals (> 80) in order to conclude about silicon content.

Similar materials, aluminium and titanium

The standard for determination of aluminium content in unalloyed Al is to withdraw from 100% the sum of all metallic elements present in amounts higher than 0.0010% for refined Al, or 0.010% for unrefined Al [7].

The indirect determination of content is similar to the proposed methods for silicon, even though no list of elements to be subtracted is given for aluminium.

A similar indirect calculation is also used for determination of titanium content in titanium [8].

Analytical equipment

The typical method used to analyze metallurgical silicon is the X-ray fluorescence [9]. For higher purity materials and/or to analyze specific elements of interest the normal method is Inductively Coupled Plasma Optical Emission Spectroscopy (ICP-OES) [10]. Calculation of silicon content will be based on either of these two measurement methods.

Measurement of elements in and on silicon

Measurement by WD-XRF

For metallurgical silicon, the content of Fe, Al, Ca and Ti are as a minimum measured by all producers, and normally also by consumers. The XRF is the standard workhorse for measuring most elements of interest, mainly because the method gives the result very fast. However, the XRF will have limitations for light elements (Boron, Carbon… [12]), and is not suited for measuring very low levels and with very high accuracy (typically, detection limit is about 0.0010 wt%). WD-XRF (Wavelength dispersive X-ray Fluorescence) is chosen as measurement tool, as it is the most widely used technique today.

Measurement by ICP-OES

For measurement of low levels of elements and also light elements, the method of choice will normally be ICP. To our knowledge, ICP-OES is the most widely used method for these measurements and is the method of choice.

Other measurements

Naturally, other measurement methods are available and used based on need for other chemical data. For normal metallurgical silicon these include combustion analysis for O, C, S, N, Atomic absorption, and others. For determination of silicon content, these methods are not included. ICP-MS is another technique possible to use, but is mainly applied for high purity Solar and Electronic grade silicon, and normally not used for metallurgical grade silicon.

Suggested standard methods for calculation of silicon content

XRF-method

The XRF method (1) measures iron, aluminium, calcium and titanium by XRF and subtract these elements and a lump sum of 0.1% from 100% to calculate the silicon content:

Si wt% = 100wt% - Fe wt% - Al wt% - Ca wt% - Ti wt% - 0.1 wt% (1)

The 0.1 wt% is subtracted as a lump sum of metallic elements in silicon not separately subtracted. (The 0.1 wt% does not include surface effects.)

Elements measured below detection limit are subtracted using the full detection limit of the analytical instrument used. For other metallic elements intentionally added to the material, the silicon content is calculated by additional subtraction of these elements.

The maximum theoretical silicon content possible to calculate by this method is 99.9 wt%.

ICP-method

The ICP-method subtract elements measured by ICP-OES. In this case we have selected the main and trace elements that are normally found in silicon. Si content can here be calculated by (2):

Si wt% = 100wt% - Fe wt% - Al wt% - Ca wt% - Ti wt% - B wt% - P wt% - Mn wt% - Cu wt% - Ni wt% - Cr wt% - Mg wt% - V wt% (2)

Elements measured below detection limit are subtracted using the full detection limit of the analytical instrument used. For other metallic elements intentionally introduced to the material, the silicon content is calculated by additional subtraction of these elements.

The maximum theoretical Si-content possible to calculate by the ICP-method is 100%.

Choice of method

The two methods will normally not give the same Si content for the same sample. Since the ICP method includes more elements and no subtraction of a lump sum, it will normally give a better residual calculation of actual silicon content. The ICP-method is therefore the method of choice for determination of accurate silicon content of a material and will prevail if the method is not referred.

The ICP-method is preferred towards applications that require a high silicon content and generally low levels of metallic elements, as the XRF method is less accurate for higher silicon content and unable to measure silicon content above 99.9%. For high purity materials, the ICP method should be the method of choice.

As guideline for choice of method of calculation, authors will recommend that content calculated by the XRF method is reviewed to determine if ICP method should be applied. Recommended method for final calculation of Si-content is:

Si content by XRF (1)	Method applicable
< 96 wt%	(outside scope)
96 – 99,7 wt%	ICP or XRF
> 99,7 wt%	ICP

For high purity qualities (> 99.7 wt% Si), the 0.1 wt% lump subtraction of metallic elements will be a large part of the total subtracted value. With a measured silicon content of 99.8 wt% by the XRF method the lump sum will be 50% of the total subtracted value. This is too high compared to real content of trace elements for a sample with these low amounts of Fe, Al, Ca and Ti. With a measured silicon content of 99.7 wt% by the XRF method the lump sum will be 33% of the total subtracted value. The 0.1 wt% subtracted is still too high compared to real content.

Due to the high expected relative error, we recommend that purity above 99.7 wt% should be measured by the ICP-method.

Validity of methods

In this paper the focus is on metallurgical silicon, and qualities with slightly higher purity. We have set the lower limit of our given calculations to 96 wt% (as calculated by the XRF method), as this fits the normal understanding of what is a metallurgical silicon. On the upwards purity, there will be limitations on how low levels of trace elements the given methods can measure, and hence how high purity of silicon can be calculated by these methods.

Examples of residual calculation

Normal metallurgical silicon

For a given silicon quality, specification values measured by XRF analysis are reported to:
Fe < 0.40 wt%, Al < 0.20 wt%, Ca < 0.10 wt%, Ti < 0.05 wt%

In this case the minimum Si content, can be calculated to:
100 wt% - 0.4 - 0.2 - 0.1 - 0.05 - 0.1

Si > 99.15 wt% (XRF)

A specific sample within the above specification, analysis by XRF show

Fe = 0.335 wt%, Al = 0.131 wt%, Ca = 0.052 wt%, Ti = 0.025 wt%

Using the XRF method will give: **Si = 99,357 wt%** (XRF) for this sample (Si wt% = 100 wt% - 0.335 - 0.131 - 0.052 – 0.025 - 0.1)

Higher purity silicon

For a specific sample, the following values were measured by both XRF and ICP:

Element		ICP-OES	WD-XRF
Fe	wt%	0.0025	0.0020
Al	wt%	0.0010	<0.0010
Ca	wt%	0.0002	<0.0010
Ti	wt%	0.0002	<0.0010
B	wt%	0.0003	<0.0010
P	wt%	0.0004	<0.0010
Mn	wt%	0.0002	<0.0010
Cu	wt%	0.0002	<0.0010
Ni	wt%	<0.0002	<0.0010
Cr	wt%	0.0002	<0.0010
Mg	wt%	<0.0002	<0.0010
V	wt%	0.0002	<0.0010

For this case, the two different methods will give the following results:

XRF: Si minimum content: 100 –0.002 –0.001 –0.001 –0.001 –0.1 = **99.895 wt%**

ICP: Si minimum content: 100 – (total max included elements) = **99.9942 wt%**

(In this case, the XRF method shows a content of silicon > 99.7 wt%. Therefore, the ICP-method should be used to report the silicon content.

Higher purity silicon with alloy

For a specific sample, the same elements were measured by both XRF and ICP. But here the sample is intentionally alloyed 1% brass (80 wt% Cu, 20 wt% Zn). As intentionally introduced elements have to be subtracted separately, both Cu and Zn must be additionally subtracted from the XRF method, while Zn must be additionally subtracted from the ICP method.

Element		ICP-OES	WD-XRF
Fe	wt%	0.0025	0.0020
Al	wt%	0.0010	<0.0010
Ca	wt%	0.0002	<0.0010
Ti	wt%	0.0002	<0.0010
B	wt%	0.0003	<0.0010
P	wt%	0.0004	<0.0010
Mn	wt%	0.0002	<0.0010
Cu	wt%	0.8000	0.8000
Ni	wt%	<0.0002	<0.0010
Cr	wt%	0.0002	<0.0010
Mg	wt%	<0.0002	<0.0010
V	wt%	0.0002	<0.0010
Zn	wt%	0.2000	0.2000

As a consequence, calculated minimum silicon content in both methods are reduced by 1 wt%.

XRF: **98,895 wt%**
ICP: **98,9942 wt%**

Standardizing measurements of silicon

ISO - work

There is need for a common understanding of how silicon content should be understood, and there is also a need for further standardization of how analysis and control of analysis equipment is done.

Elkem is in the process of initiating work on ISO standardization of how determination of the main and trace elements in metallurgical silicon via both WD-XRF and ICP-OES. As work on standardization of silicon and silicon analysis is long overdue, we hope many other companies and organizations will join in on this work.

References

1. USGS Minerals Yearbook 2014, Silicon, by Emily K. Schnebele, retrieved from https://minerals.usgs.gov/minerals/pubs/commodity/silicon/myb1-2014-simet.pdf
2. S. Velken, *Analysemetoder for silisium i stål, rujern og ferrolegeringer Litteraturoversikt*, Meddelelse nr. 6 fra Metallurgisk komité, mars 1955, Norges Teknisk-Naturvitenskaplige Forskningsråd, Trondheim (in Norwegian), retrieved from The National Library of Norway: https://www.nb.no/nbsok/nb/77a29bd13da7fe5d122d6db43dbe8f25?lang=no#0
3. Listing of the Harmonized Tariff Schedule (2018 HTSA Revision 4), retrieved from https://hts.usitc.gov/current, (chapter 28)
4. Patent. Inventor: Francis Dubrous, Assignee: Ferropem SAS, Priority date 1991-01-11, retrieved from https://patents.google.com/patent/US5429866
5. Product data, 267414 Aldrich. Silicon powder -60 mesh. Retrieved from: https://www.sigmaaldrich.com/catalog/product/aldrich/267414?lang=en&region=NO
6. Product data SI-E-05-P, American Elements (5N) 99.999% High Purity Silicon Powder, retrieved from https://www.americanelements.com/5n-99999-high-purity-silicon-powder-7440-21-3
7. British standard BS EN 573-3:2003 (pt. 4.2)
8. Product data TI-M-05-P, American Elements (5N) 99.999% Titanium Powder, retrieved from https://www.americanelements.com/titanium-powder-7440-32-6
9. ThermoFisher Scientific, XRF technology, retrieved from https://www.thermofisher.com/us/en/home/industrial/spectroscopy-elemental-isotope-analysis/spectroscopy-elemental-isotope-analysis-learning-center/elemental-analysis-information/xrf-technology.html
10. Wikipedia, *Inductively coupled plasma atomic emission spectroscopy*, retrieved from https://en.wikipedia.org/wiki/Inductively_coupled_plasma_atomic_emission_spectroscopy
11. Portable XRF Services, *Why light elements are difficult to measure with portable XRF*, retrieved from https://www.pxrfs.com.au/light-elements-difficult-measure-portable-xrf/

Silicon for the Chemical and Solar Industry XIV
Svolvær, Norway, June 11 – 14, 2018

Removal of boron from ferrosilicon alloy using SiO_2-Al_2O_3-CaO slag

Leili Tafaghodi Khajavi[1)], Ali Hosseinpour[1)]
1) University of British Columbia, Vancouver, Canada

Abstract

In this study slag treatment has been used in order to remove boron from a ferrosilicon alloy. In this process, silicon is initially alloyed with iron (as a solvent metal) to produce an alloy of 80% Si-20% Fe. Various mixtures of Al_2O_3-SiO_2-CaO were used to find the optimum composition for boron removal. The partition ratio of boron between the slag and Si-Fe alloy at 1873 K (1600 °C) was determined using the B concentrations obtained by ICP-OES. The effect of basicity and oxygen potential on boron removal is also investigated.

Background

Siemens process is currently the most common industrial method for producing high purity silicon. This process involves conversion of silicon to gaseous compounds, which makes it an energy intensive route. Thus, developing a cost-effective and energy-efficient silicon purification process has been the driving force behind many recent studies [1-3]. Metallurgical techniques such as solvent refining and slag refining can be utilized to overcome the energy problems in production of solar grade silicon (SoG-Si) [4]. The energy consumption of these processes is considerably lower than Siemens and Siemens-like processes (~130 kW h/kg vs. ~20 kW h/kg) [5]. In addition, the energy payback time of a photovoltaic system using metallurgical route is about 1.1 years while this figure is about 1.3 years for a photovoltaic system using Siemens process [6].

Solvent refining is a process in which silicon is alloyed with another metal. When the silicon-metal melt is cooled to below the liquidus line, impurities are rejected from the solid silicon phase and they are trapped in molten alloy phase. B is considered as one of the most detrimental impurities in Si because of its high segregation coefficient (the ratio between the concentrations of an impurity in liquid phase to that in solid phase). A suitable metal for alloying with Si to remove B is one that has low solid solubility in Si and also high affinity for B [4]. Al [7,8], Cu [9-11], Mg [12], Sn [13], Ni [14] and Fe [15-18] are some of the alloying agents that have been used for solvent refining of silicon in previous studies.

Slagging is another refining technique which involves the removal of impurities from silicon through oxidation followed by dissolution in slag phase. Slag components are chosen in a way that the melting point of slag does not exceed the melting point of silicon. Also, slag should not be miscible with Si and should chemically tend to combine with impurities rather than silicon [19]. Removing impurities such as B is challenging because of its smaller affinity for oxygen compared with silicon. Thus, slag composition should be carefully adjusted in order to achieve effective B removal via

slag treatment. Eq. 1 shows the overall reaction (oxidation and dissolution) of B removal through slag treatment.

$$[B] + 3/2\ O^{2-} + 3/4\ O_2 \rightarrow BO_3^{3-} \quad (1)$$

As it is clear in Eq. 1, concentration of oxygen ions and partial pressure of oxygen (PO2) are crucial factors in B removal process. Eq. 2 and 3 show the reactions in which oxygen ions and oxygen gas, required for B removal, are produced. Slag basicity and oxygen potential are two counterbalancing factors which means simultaneous increase of these factors is impossible. This is due to the fact that basic oxides have a great affinity for SiO2 in slag. Thus, increasing the CaO content of slag leads to lower activity of SiO2 [22].

$$CaO \rightarrow Ca2^{+} + O^{2-} \quad (2)$$
$$SiO_2 \rightarrow Si + O_2 \quad (3)$$

B partition ratio (which is defined as the ratio of B concentration in slag to that in silicon) is a decisive factor which is used to examine the efficiency of the removal process. Many researches have been conducted on increasing the partition ratio of B through changing the slag composition. Contradictory effects of oxygen potential and slag basicity result in low partition ratio of B. Among all the binary, ternary and quaternary slags used, the highest partition ratio of B (5.5) was reported for binary of SiO_2-48.3 mol% CaO at 1823 K (1550 ºC) [20]. Therefore, a combination of solvent refining and slag refining has been proposed as a route for improving the partition ratio of B [21, 22].
In the current work, partition ratio of B were measured between different compositions of CaO-SiO_2-Al_2O_3 slag and Si-Fe alloy at 1873 K (1600 ºC). A critical value of oxygen potential for B removal which corresponds to maximum B removal, was calculated. Finally, the effect of basicity on partition ratio values was isolated through normalized distribution parameter.

Materials and Methods

Si and Fe powders were used as the main components for preparing the ferrosilicon alloy at 1600 ºC. This alloy may be referred to as master alloy hereafter. B was also added to the master alloy as the initial impurity. CaO, Al_2O_3 and SiO_2 powders were used as the slag components (Table 1). Five grams of pre-melted Fe-Si alloy was charged in an alumina crucible together with five grams of the desired composition of CaO-SiO_2-Al_2O_3 slag. Then, the crucible was placed in a vertical tube furnace at 1600 ºC for 8 hours. The equilibrium time was determined via preliminary experiments. During all of the experiments, argon was purged with the flow rate of ~8 lit/h into the furnace to avoid the oxidation of the samples. After equilibrium, the sample was quenched in a water bath by opening the bottom cap of the furnace. The schematic of the experimental set up is shown in Figure 1.
The slag phase was separated from the alloy phase and each phase was ground for chemical analysis. The alloy phase was digested using a mixture of sulfuric, nitric and hydrofluoric acid. The slag phase was fused with sodium hydroxide at 450 ºC. Subsequently, the fused slag was digested in diluted nitric acid. The B contents of alloys and slags were measured by inductively coupled plasma optical emission spectrometry (ICP-OES).

Table 1: Composition of the slags equilibrated with Fe-Si alloy and the associated partition ratios.

Samples	CaO (wt%)	Al_2O_3 (wt%)	SiO_2 (wt%)	L_B
1	40	5	55	0.91
2	40	7	53	0.98
3	40	10	50	3.20
4	40	15	45	5.31
5	40	20	40	4.61
6	40	30	30	1.74
7	40	35	25	1.48
8	20	15	65	1.09
9	25	15	60	0.82
10	30	15	55	1.35
11	35	15	50	1.52
12	45	15	40	11.42

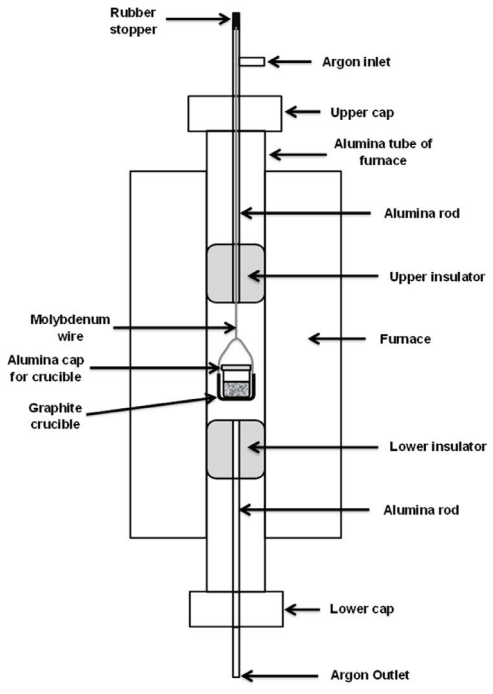


Figure 1: Schematic of the experimental set up

Results and Discussion

The effect of oxygen potential and basicity on B partition ratios is explained in this section.

Effect of oxygen potential

In order to investigate the effect of oxygen potential on B removal from Fe-Si alloy, SiO_2/Al_2O_3 ratio of slag was changed while the CaO content was kept constant at 40 wt%. The first seven compositions of Al_2O_3-SiO_2-CaO ternary presented in table 1 were chosen for this purpose. The effect of SiO_2/Al_2O_3 ratio on B partition ratios is presented in table 1 and figure 2.

B removal reaction (Eq. 1) shows that P_{O2} is one of the factors that can enhance the B removal process. Thus, it is expected to observe an increase in L_B values by increasing the SiO_2 content of slag. Figure 2 shows that the expected trend is achieved before the SiO_2/Al_2O_3 ratio of 3. On the other hand, increasing the SiO_2 content of slag results in a more acidic slag (lower concentration of oxygen ions) because optical basicity values for SiO_2 (0.48) and Al_2O_3 (0.6) show that SiO_2 is more acidic [23]. Thus, further increase of SiO_2/Al_2O_3 ratio decreases the L_B values. In other words, when P_{O2} surpasses a critical value, L_B decreases due to the stronger effect of basicity drop. The highest L_B recorded in present work, by changing the oxygen potential of slag, is 5.31 at SiO_2/Al_2O_3 of 3.

The critical oxygen potential ($P_{O2,\ critical}$) is defined as an oxygen potential associated with the highest removal. In other words, balance of partial pressure of oxygen and concentration of oxygen ions results in the highest partition ratio at this point. Therefore, P_{O2} at SiO_2/Al_2O_3 ratio of 3 is considered as the $P_{O2,\ critical}$ for B removal. P_{O2} for all slag compositions in this study are presented in table 3. These values are calculated from the equilibrium constant $\left\{\frac{a_{Si}.P_{O2}}{a_{SiO2}}\right\}$ for Si/SiO_2 equilibrium (Eq. 3). By obtaining the equilibrium constant of Eq. 3 (from HSC 5.1 thermodynamic database), activity coefficient of silicon in molten Fe-Si (0.977) [24] and activity of silica in CaO-SiO_2-Al_2O_3 ternary [25], the P_{O2} value for each slag composition was calculated. Thus, $P_{O2,\ critical}$ for B removal process is calculated as approximately 9×10^{-18} atm in this study.

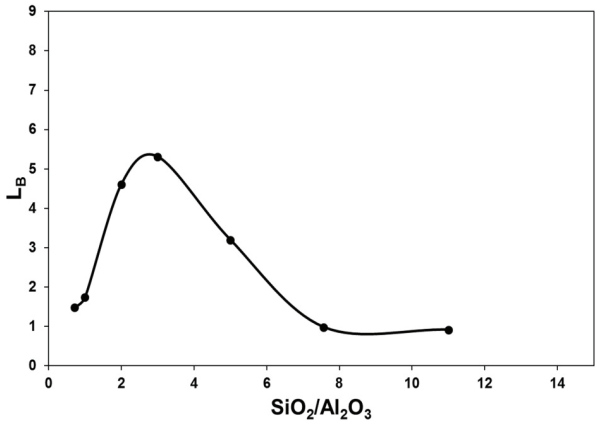


Figure 2: Effect of oxygen potential on boron partition ratio.

Effect of basicity

Basicity of slag is another crucial factor that is used for improving impurity removal from silicon. The effect of basicity on partition ratio of B was investigated through changing the CaO/SiO_2 ratio in Al_2O_3-SiO_2-CaO ternary, with Al_2O_3 content fixed at 15 wt%. Slags 8 to 12 and slag 4 in table 1 were chosen for this purpose. Partition ratio results are shown in table 1 and figure 3.

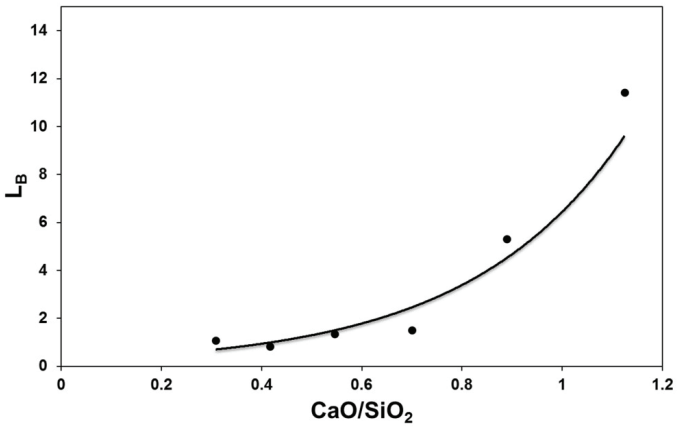


Figure 3: Effect of basicity on boron partition ratio.

The highest value of L_B is achieved when the CaO/SiO_2 ratio is equal to 1.125. This means the slag with the highest basicity is the most successful in removal of B. Because of the aforementioned conflictive relationship between basicity and oxygen potential of slag, it is expected to observe a negative parabola when L_B values are plotted against CaO/SiO_2 ratio. However, as shown in figure 3, B partition ratio increases exponentially when the CaO/SiO_2 ratio of slag changes in the range of 0.31 to 1.125. P_{O_2} calculations for different slag compositions show that even the $P_{O_2}$of slag with highest CaO/SiO_2 ratio is still higher than $P_{O_2,\ critical}$ for B ($1.40 \times 10^{-17} > 9.01 \times 10^{-18}$ atm). This means the expected maximum value of L_B cannot be observed in the range of CaO/SiO_2 ratio in this study.

Borate capacity

As it was stated before, B enters the slag phase according to reaction ([B] + 3/2 O^{2-} + 3/4 $O_2 \rightarrow BO_3^{3-}$) Eq. 4 expresses the equilibrium constant of B removal reaction:

$$K_1 = \frac{a_{BO_3^{3-}}}{a_B\, a_{O2}^{3/4}\, a_{O2-}^{3/2}} = \frac{C_1(B) f_{BO_3^{3-}}}{[B]\, f_B\, P_{O2}^{3/4}\, a_{O2-}^{3/2}} = \frac{C_1(B) f_{BO_3^{3-}}}{C_2\, [B]\, \gamma_B\, P_{O2}^{3/4}\, a_{O2-}^{3/2}} \qquad (4)$$

Where f_B is activity coefficient of B in liquid alloy and $f_{BO_3^{3-}}$ is activity coefficient of BO_3^{3-} in slag phase with respect to 1 mass% standard state. C_1 is the conversion factor of mass percent of BO_3^{3-} to mass percent of B in the slag phase. C_2 is the constant required for converting the standard state of dissolved B from 1 mass percent B to pure liquid B. Eq. 4 can be rearranged to isolate the partition ratio of B as Eq. 5. In these

equations, C_3 is equal to C_1/C_2. Also, K is the equilibrium constant $\left(\frac{a_{Si}.P_{O2}}{a_{SiO2}}\right)$ for Si/SiO_2 equilibrium.

$$L_B = \frac{(B)}{[B]} = K_1\, C_3\, \frac{\gamma_B\, P_{O2}^{3/4}\, a_{O2-}^{3/2}}{f_{BO_3^{3-}}} = K_1\, C_3\, \frac{\gamma_B\, a_{O2-}^{3/2}}{f_{BO_3^{3-}}} \left(\frac{K\quad a_{SiO_2}}{a_{Si}}\right)^{3/4} \qquad (5)$$

In order to isolate the effect of basicity when the slag composition is changing, borate capacity is defined based on the oxidation reaction of B (Eq. 1). Borate capacity is only dependent on slag composition and temperature.

$$C_{BO_3^{3-}} = \frac{Mass\%BO_3^{3-}}{a_B P_{O2}^{3/4}} = \frac{K_1 a_{O^{2-}}^{3/2}}{f_{BO_3^{3}}} \qquad (6)$$

To calculate the borate capacity, mass percent of borate was calculated from the impurity content of slag phase measured by ICP analysis. By obtaining the equilibrium constant of Eq. 2.18, activity coefficient of silicon in molten Fe-Si (0.977) [24] and activity of silica in $CaO\text{-}SiO_2\text{-}Al_2O_3$ ternary [25], the P_{O2} value for each slag composition was calculated.

Activity of B in liquid Fe-Si was calculated using Henrian activity coefficients and mole fraction of B in the alloy phase (measured by ICP analysis). The activity coefficient values were calculated from literature by Gibbs-Duhem integration method

$$RT \ln \gamma_{i\ in\ Fe-Si\ melt}^{\circ} = X_{Si\ in\ Fe-Si\ melt}\, RT \ln \gamma_{i\ in\ molten\ Si}^{\circ} + X_{Fe\ in\ Fe-Si\ melt}\, RT \ln \gamma_{i\ in\ molten\ Fe}^{\circ} - G_{Si-Fe\ melt}^{excess} \qquad (7)$$

The excess Gibbs energy of mixing for Fe-Si melt was calculated from Miettinen's work [26], knowing that the mole fraction of Si and Fe in the alloy is constant in all samples and is equal to 0.89 and 0.11, respectively.

The borate capacity values obtained in this study are presented in figure 4. There's a linear relationship between the borate capacity and optical basicity of the slags. For the sake of comparison the borate capacity values were also calculated using the results of Jakobsson and Tangstad [27]. Similar values for borate capacity was expected considering the use of the same ternary system and the same temperature in these studies. Figure 4 shows that there's excellent agreement between the results of the current work and that of Jakobsson and Tangstad [27].

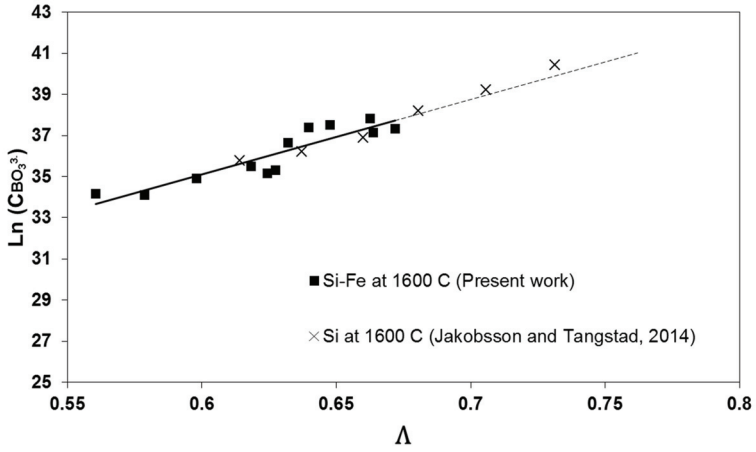


Figure 4: Borate capacity of slag vs. optical basicity

Comparison with solvent refining and slag refining

In order to compare the current process with solvent refining and slag refining, the expected final B content of silicon (or alloy) is calculated for all three processes (Figure 5). For the sake of consistency, the calculations were based on 100 ppm of B in the starting material. Using solvent refining and slag refining boron content can be reduced to as low as ~25ppm [15] and ~35ppm [27] respectively. However, combining the two, B concentrations as low as 8ppm can be achieved.

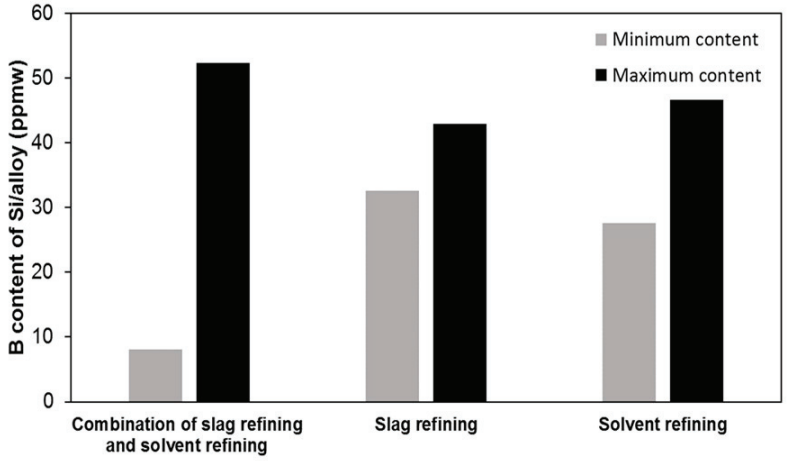


Figure 5: Comparison boron removal efficiency for slag refining, solvent refining and combination of slag and solvent refining.

Conclusions

A metallurgical refining route is proposed for removing B from silicon. Partition ratio of B between slag of $CaO-SiO_2-Al_2O_3$ and alloy of Si-Fe was measured at 1600 ºC (1873 K). Oxygen potential and basicity of slag are two competing factors that influence the B removal process. Therefore, a critical oxygen potential value, at which a balance between these two factors is achieved, was calculated. The highest L_B value of 11.42 was achieved for the slag with highest CaO/SiO_2 ratio. Thus, it is proposed that the slag with the highest basicity and oxygen potential equal to $P_{O2,\,critical}$ can result in the highest B removal yield. Effect of basicity was isolated through normalizing the L_B values with P_{O2} and the relation between borate capacity and optical basicity of slag. Boron removal efficiency for individual slag refining and solvent refining.

References

1. P. Wang, H. Lu, and Y. Lai, Journal of Crystal Growth, **390**, 2014, p 96.
2. B. Gao, S. Nakano, H. Harada, Y. Miyamura, T. Sekiguchi, and K. Kakimoto, **352**, 2012, p 47.
3. X. Gu, X. Yu, K. Guo, L. Chen, D. Wang, and D. Yang, Solar Energy Materials and Solar Cells, **101**, 2012, p 95.
4. M. D. Johnston, L. T. Khajavi, M. Li, S. Sokhanvaran, and M. Barati, JOM, **64**, 2012, p 935.
5. G. Bye and B. Ceccaroli, Solar Energy Materials and Solar Cells, **130**, 2014, p 634.
6. R. Glöckner and M. de Wild-Scholten, 27th EUPVSEC, Frankfurt, Germany, 2012, p 24.
7. T. Yoshikawa and K. Morita, Journal of Crystal Growth, **311**, 2009, p 776.
8. I. Obinata and N. Komatsu, Sci Rep RITU, **29**, 1957, p 118.
9. A. M. Mitrašinović and T. A. Utigard, Silicon, **1**, 2009, p 239.
10. A. M. Mitrašinović and T. A. Utigard, Metallurgical and Materials Transactions B, **43**, 2012, p 379-387.
11. J. Juneja and T. Mukherjee, Hydrometallurgy, **16**, 1986, p 69.
12. K. Masumoto and H. Kaneko, Trans. Nat. Res. Inst. Met, **1**, 1959, p 36.
13. X. Ma, T. Yoshikawa, and K. Morita, Journal of Crystal Growth, **377**, 2013, p 192.
14. Z. Yin, A. Oliazadeh, S. Esfahani, M. Johnston, and M. Barati, Canadian Metallurgical Quarterly, **50**, 2011, p 166.
15. L. Tafaghodi Khajavi, K. Morita, T. Yoshikawa, and M. Barati, Metallurgical and Materials Transactions B, **46**, 2015, p 615.
16. L. Tafaghodi Khajavi, and M. Barati, Metallurgical and Materials Transactions B, **48**, 2017, p 268.
17. S. Esfahani and M. Barati, Metals and Materials International, **17**, 2011, p 823.

18. S. Esfahani and M. Barati, Metals and Materials International, **17**, 2011, p 1009.

19. H. Liaw and F. S. d'Aragona, Solar Cells, **10**, 1983, p 109.

20. L. A. V. Teixeira, Y. Tokuda, T. Yoko, and K. Morita, ISIJ international, **49**, 2009 p 777.

21. X. Ma, T. Yoshikawa, and K. Morita, Metallurgical and Materials Transactions B, **44**, 2013, p 528.

22. M. Li, T. Utigard, and M. Barati, Metallurgical and Materials Transactions B, **45**, 2014, p 221.

23. K. Mills and S. Sridhar, Ironmaking & Steelmaking, **26**, 1999, p 262.

24. J. Chipman, J. Fulton, N. Gokcen, and G. Caskey, Acta metallurgica, **2**, 1954, p. 439.

25. K. Kume, K. Morita, T. Miki, and N. Sano, ISIJ international, **40**, 2000, p 561.

26. J. Miettinen, Calphad, **22**, 1998, p 231.

27. L. K. Jakobsson and M. Tangstad, Metallurgical and Materials Transactions B, **45**, 2014, p 1644.

Silicon for the Chemical and Solar Industry XIV
Svolvær, Norway, June 11 – 14, 2018

Solar silicon production through metallurgical route and REC Solar advancements

Adrian Murgau[1)], Jafar Safarian[2)]
1) REC Solar Norway AS, Fiskaaveien 100, Kristiansand, Norway
2) Norwegian University of Science and Technology (NTNU), Alfred Getz Vei 2, 7491, Trondheim, Norway

Abstract

The production of solar grade silicon (SoG-Si) has been very important in the last two decades with regard to the rapid PV growth and installation of solar modules around the world as silicon is the main material used for the fabrication of solar cells. Production of SoG-Si through metallurgical route is a young and emerging technology in which this important material is being produced through a more sustainable approach that the traditional and more recent developed chemical processes. The Elkem Solar process operated by REC Solar Norway is the only commercial metallurgical process and it is compared with the other invented metallurgical processes. Moreover, the main steps of the Elkem Solar process, slag refining and acid leaching are described. In addition, the key issues about the production, energy consumption and carbon foot print are presented and compared with literature. It is shown that the Elkem Solar process has an advantageous situation compared to the main chemical processes and is well positioned for the future.

Metallurgical processes for solar-grade silicon production

The metallurgical route for the production of silicon for photovoltaic applications has a more recent development than the chemical route in the recent years. In the chemical route, Siemens reactor and Fluid Bed Reactor (FBR) are the main existing technologies for solar silicon production, where the amorphous silicon produced from Si-containing gases is called polysilicon. The chemical route and its comparison with metallurgical processes was discussed before [1], and the main advantage of the metallurgical processes is claimed to be the lower energy consumption per unit mass of silicon product. The energy use for the production of silicon through chemical route by Siemens technology and Si deposition from trichlorosilane (TCS) is around 170 kWh/kg Si, considering metallurgical silicon (MG-Si) production and different recycling scenarios [2]. The energy consumption in FBR technology is claimed by RECSiLICON to be 80-90% less than the Siemens reactor [3], which may provide roughly around 75-95 kWh/kg Si, including MG-Si production. The energy consumption of the developed and under development integrated solar-grade silicon (SoG-Si) production processes is lower than chemical technologies and in the ranges of 30-60 kWh/kg Si, including MG-Si production. Figure 1 shows the main developed metallurgical processes for making SoG-Si, and as we see for many processes MG-Si production in submerged arc furnace (SAF) is the initial stage, except the Evonik Solar process, formerly known as SolSilc process. The MG-Si production in SAF is a well-known process [4] in which silicon

metal is produced is through a high temperature carbothermic process in which the process has usually 80-90% Si yield, where quartz in the main charge material. In general, more than 50% of the required energy is supplied as the chemical energy in the form of carbon and volatiles, the rest is electric energy. The amount of CO_2 emission is depending on the furnace Si yield, off gas characteristics of the furnace, gas combustion, and so on. In general, the total amount of CO_2 emission is higher than the above reported 7.5 kg CO_2 [5]. Among these processes, only Elkem Solar process is applied in large commercial scale production.

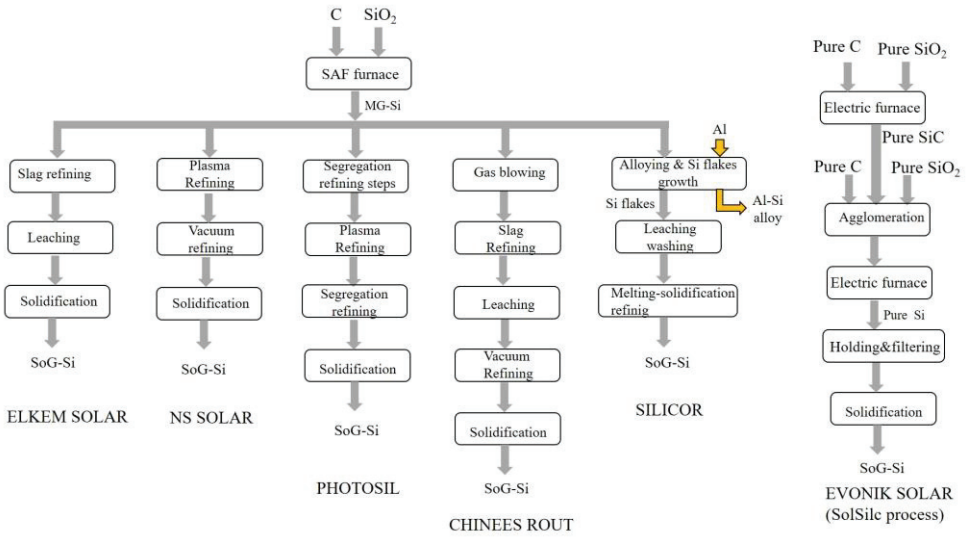


Figure 1: The main developed and under development processes for production of SoG-Si through metallurgical processes.

Elkem Solar process

As observed in Figure 1, the Elkem Solar process is consisted of MG-Si production in SAF followed by slag refining, acid leaching and solidification refining processes. These processes and the main developments in Elkem Solar are described as follows.

Slag refining

The produced silicon in SAF is refined through a slag refining technique in which the more active elements than silicon are removed through their absorption into a liquid slag phase. The slag refining is in particular helpful to remove the dissolved boron impurity, where the boron removal reaction may be through the following reaction:

$$3/2\ (SiO_2) + 2\ \underline{B} = 3/2\ Si + (B_2O_3) \qquad (1)$$

The mechanism of B removal in slag refining is depending on the slag type and chemical composition and a couple of chemical reactions may be involved for B

oxidation into B_2O_3. For instance, if Na_2O-SiO_2 or CaO- Na_2O-SiO_2 slags are interacted with silicon melt, the B removal can be through oxidation by Na_2O at the slag/metal interfacial area as described previously [6,7]. As SiO_2 is the main component of any slag that is used for slag refining, chemical reaction (1) can be always employed to study the equilibrium conditions. An important thermodynamic parameter which shows the potential and effectiveness of slag refining process is the distribution coefficient of B between the slag and the silicon metal phase, which is expressed as:

$$L_{\mathrm{B}} = \frac{\%B}{\%B}$$

Where *(%B)* and *[%B]* are the equilibrium mass percentages of B in slag and silicon, respectively. The magnitude of L_B for many slag systems have been studied and a wide range of L_B-values has been reported in literature. Figure 2 illustrate the reported L_B-values for typical calcium-silicate metallurgical slags.

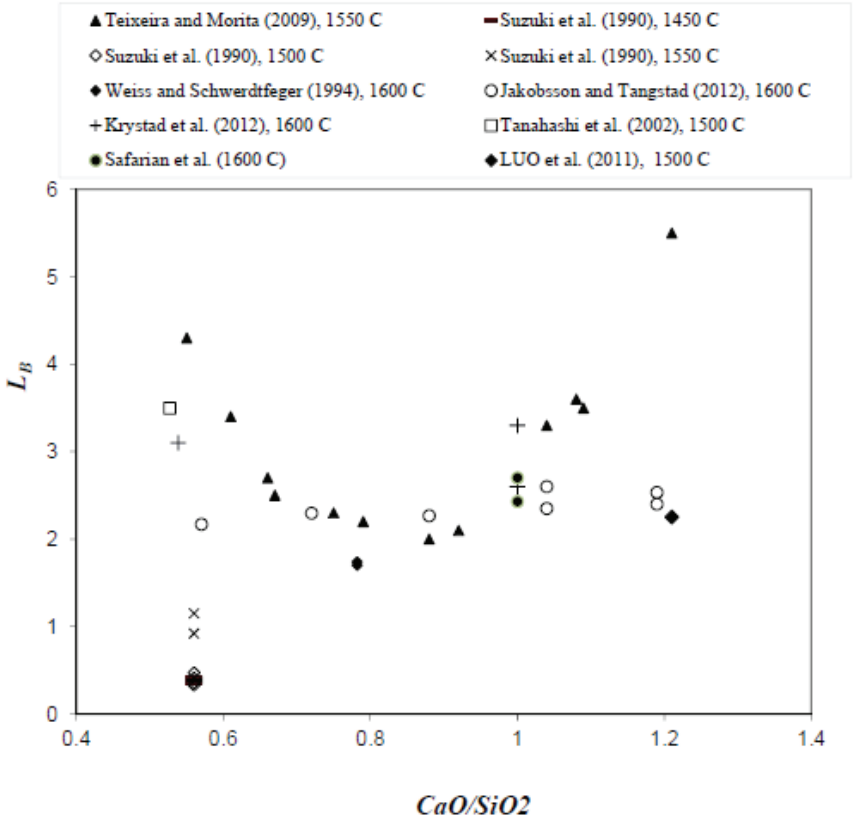


Figure 2: The distribution of B between different slags and silicon (L_B) versus the slag basicity from Literature [8,9,10,11,12,13,14,15].

As seen, L_B is dependent on slag type, slag composition and temperature. Obviously, larger L_B-value is important and it provides more effective slag refining process.

Acid leaching refining

The growth of primary silicon grains from silicon melt is accompanied with the significant segregation of the impurities at the grain boundaries. This is due to the very small distribution coefficient of the impurity elements between liquid and solid silicon phases. Except B and P with 0.8 and 0.35 distribution coefficients, many impurities are mainly precipitated between the primary silicon grains (along grain boundaries) and they can be removed through milling and acid leaching of silicon. In particular, Fe, Ca, Ti and Al have low distribution coefficients as 6.4×10^{-6}, 8×10^{-3}, 2.0×10^{-6} and 2.8×10^{-3}, respectively. These elements are precipitated along the grain boundaries in the form of silicides as the formation of silicides is more favourable from thermodynamics point of view than precipitation of metals or other compounds. It has been shown that the leachability of silcides is different, for instance $CaSi_2$ is more leachable than $Ca_xAl_ySi_z$, $Al_xFe_ySi_z$ and $FeSi_2$, respectively [16]. The research activities for many years about the refining by acid leaching was on purification of MG-Si under different conditions and different acids such as Sulphuric acid, hydrochloric, hydrofluoric and aqua regia were used [17, 18 ,19]. In general, higher purities can be obtained for smaller particles size of silicon [19,20,21], higher leaching temperature [22] and it is dependent on the type of acid [23, 24], and acid concentration [22, 24].

The addition of a refiner metal into silicon has shown that it is more practical and efficient for the acid leaching refining process. In this case the refiner metal must provide a leachable silicide as the main secondary phase, which is precipitated between the primary silicon grains and can be easily washed away in leaching. This silicide may contain some metallic impurities, or silicides of the metallic impurities and when it is leached, the impurities may be removed by chemical or physical mechanisms as described previously for using Mg as the refinier metal [21]. Different metals such as Ca [25 ,26], Mg [21,22,24,27], Cu, Fe, Ti, Zr, etc. have been used as the refiner metal. However, only Ca and Mg can be successfully used as they do not provide problems for introduction of other metallic impurities and not significant loss of silicon. Figure 3 shows an schematic of the Ca- and Mg-doped silicon samples and the mechanism of how the impurities are removed. When Ca is used as the refiner metal siloxane ($Si_6H_6O_3$) [25], which is a greenish jelly phase is separated from the silicon grains, while when Mg is used the other leaching reaction products are gaseous and leaving the system.

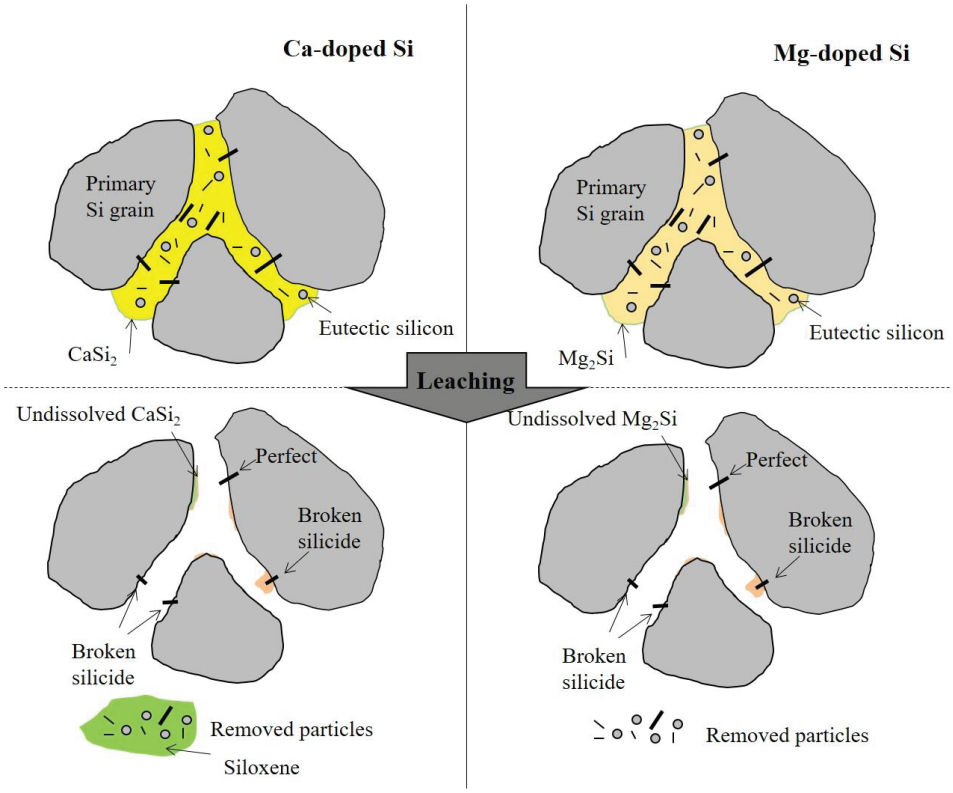


Figure 3: The mechanism of acid leaching refining of Ca and Mg-doped silicon and the removal of the impurities.

Elkem Solar and REC Solar production developments

The development of the current process started in 1975. By the end of the 1990's the 5 process steps that we know today were mature enough to start upscaling from lab size to industrial size. Elkem Solar was incorporated as an own organizational entity in 2001. Investment decision for building the new 5000 MTY solar plant at Fiskaa, Norway, was taken in 2006, production started in 2009. The Fiskaa plant is currently operating at 8000 TPY speed.

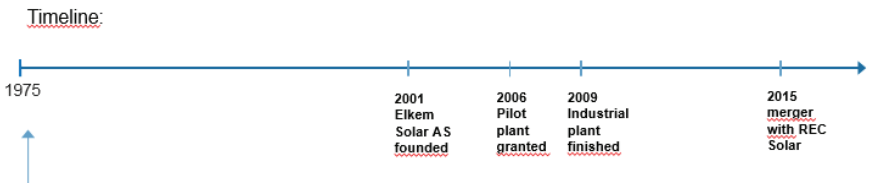


Figure 4: The timeline for the production developments in Elkem Solar/REC Solar.

REC Solar, the biggest European manufacturer of solar panels started qualification of Elkem Solar Silicon (ESS) feedstock in late 2013. Within months, ESS was qualified for mass production of high quality solar panels at the plant in Singapore. In 2016 the two companies were merged together in to a group that now has the unique opportunity to utilize the synergies in a value chain that spans from quartz to finished module. Same year, the ingot plant in Herøya, Norway was acquired, modernized and customized to become the first plant that takes full benefit of ESS. The Herøya plant produces currently 4000 MTY of multi crystalline blocks and is competitive in the harsh business environment because it leverages on several advantages: high knowledge of metallurgical processes, automation (the plant is operated by 7 workers per shift) and flat Scandinavian organizational model that keeps down the indirect headcount. The form factor of the ESS brick has been optimized (Fig. 5) to the crucible which allows for production of the tallest ingots in the industry further lowering the costs. Its rectangular shape makes it ideal for robot handling. Automation of crucible filling eliminates one of the most tedious jobs in the solar business, reduces cost and improves furnace safety and operation.



Figure 5: Crucible filled with ESS at the left and with chunks from the chemical route to the right. The ESS charge is 50% heavier.

The integration with REC Solar gave opportunity to optimize electrical properties to the PERC cell architecture where, due to co-doping, a very stable, linear resistivity profile can be obtained as seen in Figure 6.

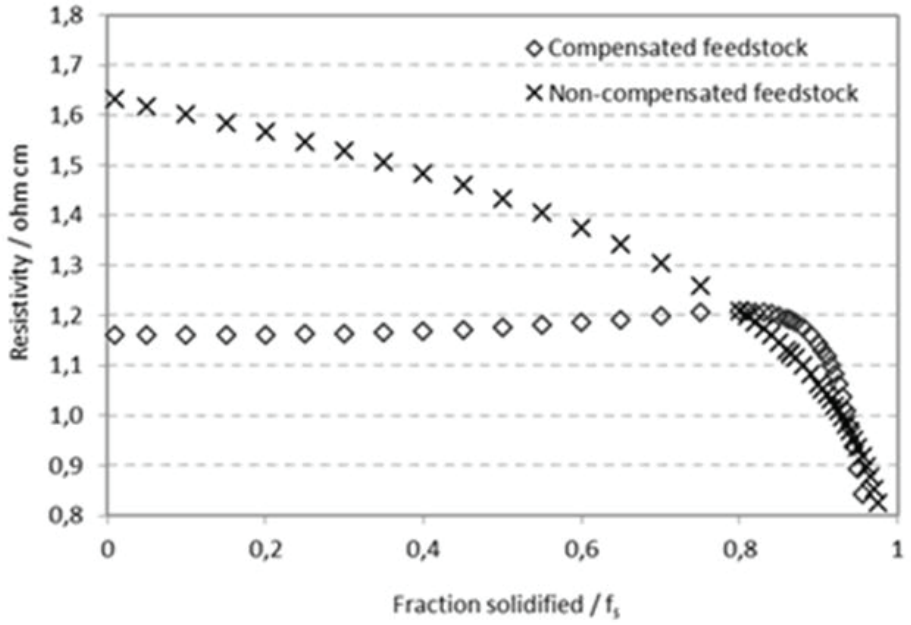


Figure 6: Example of resistivity profile with a non-compensated silicon feedstock (boron doped) and a compensated silicon feedstock with co-doping with gallium.

Today's multi-crystalline production modules manufactured based on ESS perform up to 300 Wp which is at par with main stream mono but at lower cost and with a lower environmental footprint.

Energy consumption

Lower energy consumption in the metallurgical route (30-60 kWh/kg Si) than chemical route (~ 170kWh/kg Si) is one of the biggest advantages of silicon purification by metallurgical processes. It is worth noting that the reported electric energy consumption for the chemical processes is usually excluding the energy consumption for the production of MG-Si in SAF. Among the illustrated processes in Figure 1, the Elkem Solar process has currently the lowest electric energy consumption of approx 32 kWh/kg Si of which 12 kWh is dedicated to the MG-Si production in SAF and the rest is for silicon purification to solar grade.

The base-line level for ESS production is approximately 40 kWh/kg. Current level is a result of volume expansions and value chain integration which allows for taking back to feed-stock production silicon units from ingot operations.

Carbon footprint

The carbon footprint for the production of PV modules has been studied through many life cycle assessments (LCAs) in recent years. According to NREL study, the carbon

footprint is in average around 40 g CO_2/kWh for a PV power plant, where PV modules are fabricated from crystalline silicon with 13.2-14% efficiency and 30 years lifetime [28]. Form this emission, 60-70 % is related to the whole value chain from raw materials to fabricated module, 21-26% is related to power generation and operational processes, and 5-20% related to downstream processes. This may roughly show that the carbon footprint for the making crystalline silicon PV modules is 24-28 g CO_2/kWh. The conversion of this number to solar silicon production process is, however, difficult due to many unknowns, in particular the source of energy use for the production of silicon in SAF and also its further purification.

A large portion of CO_2 in solar silicon production is related to the source of electric energy used for SAF process. The CO_2 emission for using fossile fuels such as coal and natural gas is 0.8-1.0 and 0.42-0.62 kg/kWh, respectively [29]. While, for using renewable energies such as solar, geothermal, wind and hydro the CO_2 emissions are around 0.07, 0.04, 0.015-0.035, 0.012 kg CO_2/kWh, respectively [29]. As we see the lowest carbon footprint in silicon production in the whole value chain, including the electric energy production is for the case of using hydropower for SAF process and further refining steps. Regarding the production of electricity in Norway by hydropower and not significant CO_2 emission in the slag refining, acid leaching and solidification steps, the CO_2 emission for Elkem Solar process is around 10.8 kgCO_2/kg SoG-Si. Table 1 shows the comparison of CO_2 emissions in Elkem Solar process in Norway and polysilicon production in different geographical locations. As this table shows the CO_2 emission in the metallurgical process is much lower than the chemical process.

Table1: Global warming potential expressed as kg CO_2 equivalents /kg silicon for the production of solar grade silicon as expressed in the background material for the French PV tender provided by ADEME.

Origin of solar grade silicon	Kg CO2 eqv/kg silicon
Norway, Elkem Solar plant as approved by ADEME	**10,87**
Germany, Polysilicon	87,724
China, Polysilicon	141,023
Japan	75,104
South Korea	85,535
USA	93,149
Rest of the world	107,093

The application of biocarbon in silicon is a sustainable approach and it has been the subject of research and development in Elkem and it has been pronounced using 20% charcoal in its silicon furnaces in 2021. This means less CO_2 emission compared to the SAF process with using only coal.

Perspectives

The success of solar and its ability to become the preferred source of energy is set by achieved cost reduction as well as future potential for further improvements. Compared to the mature Siemens process, ESS is still an emerging technology with a very steep development curve. The cost of ESS has been halved twice since the start of the Fiskaa plant to current level of below 10$/kg and a target to half it again. It is necessary to

maintain this trend, for REC Solar Norway as well as for the solar business. Further cost reduction is enabled by technology development on following lines of work:

1. Decarbonization. The Elkem Solar process has the unique feature to introduce silicon units at several points in the value chain. As such, it is unique in its ability to be operated entirely on low value, secondary silicon units with 0 carbon emissions. This trip has started with downstream integration and continues with the incorporation of fines from dusts and sludges from the entire PV value chain.
2. Development of smart processes focused on high throughput, low cost automation and digitalization.
3. Yield improvements, most notably from shaping operations and wet chemical processing.
4. Operational improvements to increase volume, life time of critical components and uptime of the plants
5. Circular economy to reduce utilization of virgin materials and waste of feedstocks, fuels, process gases, etc.

Summary

The production of solar silicon through metallurgical route at REC Solar is an emerging technology in which slag refining, acid leaching and solidification processes are employed. This young metallurgical process has been significantly developed since it started production in 2009. The process is able to produce larger silicon ingots than the other processes, and it has significantly lower energy consumption than the other commercial processes. Moreover, the carbon footprint for ESS production is much lower than the chemical processes for polysilicon production. The production cost of unit mass of ESS has been significantly decreased in the last 9 years and the process competes well with the other commercial processes.

Acknowledgement

This work was performed within the Research Centre for Sustainable Solar Cell Technology (FME SuSolTech, project number 257639), co-sponsored by the Norwegian Research Council and research and industry partners.

References

1. J. Safarian, G. Tranell, M. Tangstad: Energy Procedia, 2012, vol. 20, pp. 88-97.
2. J.O. Odden, G. Halvorsen, H. Rong, R. Gløckner, Silicon for the Chemical and Solar Industry IX, Oslo, Norway, June 23-26, 2008, pp. 1-16.
3. www.recsilicon.com
4. A. Schei, J. Kr. Tuset, H. Tveit, Production of high silicon alloys, Tapir, Trondheim, 1998.
5. BAT Reference Document for the Non-Ferrous Metals Industries, Integrated Pollution Prevention and Control, European Commission, 2014.

6. J. Safarian, G. Tranell, M. Tangstad: Met. Mat. Trans. B, 2013, vol. 44, pp. 571-583.
7. J. Safarian, G. Tranell, M. Tangstad: Met. Mat. Trans. 2E, 2015, pp. 109-118.
8. K. Suzuki, T. Sugiyama, K. Takano, N. Sano: J. Jpn. Inst. Met. vol. 54**, 1990, pp.** 168 – 172.
9. T. Weiss, K. Schwerdtfeger: Met. Mat. Trans. B, vol. 25b, 1994, pp. 497-504
10. L.A:V. Teixeira, Y. Tokuda, T. Yoko, K. Morita: ISIJ Int. vol. 49, 2009, pp. 777-782.
11. D.W. Luo, N. Liu, Y.P. Lu, G.L. Zhang, T.J. Li: Trans. Nonferrous Met. Soc. China, vol. 21, 2011, pp. 1178-1184.
12. D.W. Luo, N. Liu, Y.P. Lu, G.L. Zhang, T.J. Li: Trans. Nonferrous Met. Soc. China, vol. 21, 2011, pp. 1178-1184.

13. L.K. Jakobsson, M. Tangstad: International Smelting Technology Symposium, Ed. J. P. Downey, T.P. Battle, J.F. White, TMS 2012, Orlando, FL, USA, pp. 179-184.
14. E. Krystad, K. Tang, G. Tranell, JOM, 64, 2012, pp 968-972.
15. M. Tanahashi, Y. Shinpo, T. Fujisawa, C. Yamauchi: J. Min. Mat. Proc. Inst. Japan, vol. 118, 2002, pp. 497-505.
16. F. Margarido, J. P. Martins, M. O. Figueiredo, and M. H. Bastos, Hydrometallurgy, vol. 34, no. 1, pp. 1–11, 1993.
17. W. Voos, "Production of pure silicon,"US Patent 2972521, 1961.
18. L. P. Hunt, V. D. Dosaj, J. R. McCormick, and L. D. Crossman, 12th IEEE Photovoltaic Specialists Conference, 1976, pp. 125–129
19. J. Dietl, Sol. Cells, vol. 10, no. 2, 1983, pp. 145–154.
20. L. Huang et al., Hydrometallurgy, vol. 161, 2016, pp. 14–21.
21. S. Espelien, J. Safarian, AIMS Energy, 5 (4) (2017), pp. 636-651.

22. S. Espelien, G. Tranell, J. Safarian, Energy Technology 2017, San Diego, CA, February 26th (2017), pp. 355-365.
23. I. C. Santos, A. P. Goncalves, C. S. Santos, M. Almeida, M. H. Afonso, and M. J. Cruz, Hydrometallurgy, vol. 23, 1990, pp. 237–246.
24. J. Safarian, S. Espelien, 33rd European Photovoltaic Solar Energy Conference and Exhibition, Amsterdam, Netherland, 2017, pp.480-482.
25. A. Schei, International seminar on refining and alloying of liquid aluminium and Ferro-alloys, 1985.
26. T. Shimpo, T. Yoshikawa, and K. Morita, "Thermodynamic study of the effect of calcium on removal of phosphorus from silicon by acid leaching treatment," Metall. Mater. Trans. B, vol. 35, no. April, pp. 277–284, 2004.
27. J. Safarian, G. Tranell, 32nd European Photovoltaic Solar Energy Conference and Exhibition, 20-24 June 2016, Munic, Germany, pp.1011-1014.
28. www.nrel.gov
29. Postnote update: Carbon footprint of electricity generation, Parliment Office of Science and Technology, UK, No 383, June 2011.

Effects of forced convection on the micro and macrostructure of metallurgical grade silicon ingots obtained by unidirectional solidification

Denir Paganini Nascimento[1,2)], Marcelo Aquino Martorano[1)], João Batista Ferreira Neto[2)], Moysés Leite de Lima[2)] and Tiago Ramos Ribeiro[2)]

1) *University of São Paulo, Department of Metallurgy and Materials, São Paulo, Brazil. dpnascimento@usp.br*
2) *Laboratory of Metallurgical Processes, Center for Metallurgical and Materials Technology, Institute for Technological Research – IPT, São Paulo, Brazil.*

Abstract

The effects of forced convection on the micro-macrostructure and the macro segregation of metallurgical grade silicon ingots obtained by unidirectional solidification were investigated. Solidification was carried out by extracting heat from the melt through the bottom of a crucible in contact with a water-cooled base. In one experiment, a graphite disk rotating at a controlled velocity was immersed into the silicon melt to force convection during the directional solidification process. After solidification, the resulting ingots of 100 mm height showed a purified region with: clearly aligned columnar grains, without intermetallic precipitates, and which probably solidified with a planar solid-liquid interface. With forced convection the length of the purified region increases from 8 to 80 mm, indicating an increase in the macrosegregation of impurities and in purification. Chemical analyses along the longitudinal axis of the ingots confirmed the larger macrosegregation of impurities promoted by convection. Convection movement transports impurities within the liquid and are well-known to increase macrosegregation, but a heat and mass transfer mathematical model indicates that it might also increase the stability of a planar solid-liquid interface, preventing formation of cells/dendrites and, therefore, facilitating solute transport from the solid-liquid interface into the bulk liquid, which increases macrosegregation.

Introduction

The growing demand for silicon in photovoltaic applications triggered the development of alternative more economic routes for production of solar grade silicon [1]–[4]. In the metallurgical route, the metallurgical grade silicon (~ 98.5%Si) is refined to achieve the purity of the solar grade silicon (>99.999%??). One of the main steps of the metallurgical route is the unidirectional solidification, in which most of the metallic impurities are removed [5] by their macrosegregation to one of the ingot ends, leaving purer silicon behind. The intensity of macrosegregation is related to the solute partition coefficient, given by:

$$k_0 = \frac{C_S^*}{C_L^*} \quad (1)$$

where C_S^* and C_L^* are the solute concentrations of a specific impurity in the solid and liquid, respectively, in thermodynamic equilibrium at a given temperature. Lower k_0 values are

associated with greater macrosegregation of the specific impurity. Except for B, P, and O, most metallic impurities in silicon have $k_0 \ll 1$, giving rise to intense macrosegregation during controlled directional solidification and, therefore, higher purity ingots [6]. Melt convection increases the transport of impurities during solidification [7] and can suppress the formation of cells and dendrites, keeping a planar solid-liquid interface [8]. As a result, melt convection should increase the intensity of impurity macrosegregation. These effects have not been examined in the directional solidification of metallurgical grade silicon, despite its importance for the metallurgical route of solar grade silicon production. The objective of this work is to study the effects of forced melt convection on the micro-macrostructures and macrosegregation of impurities in metallurgical silicon ingots obtained by directional solidified. Experiments of directional solidification with and without forced convection were carried out and a mathematical model of heat and mass transport was built to help in the investigation.

Experimental procedures

Directional solidification experiments

Two directional solidification experiments of metallurgical grade silicon were carried out: one without and another with forced convection. A charge of 7.5 kg of metallurgical grade silicon was melted in an open-air induction furnace. After melting, liquid silicon was transferred to a graphite-clay crucible positioned inside a resistance furnace pre-heated to $1600℃\ (1873K)$ and consisting of two parts (Figure 1). In the upper part, there are heating elements of $MoSi_2$, a funnel to transfer the melt into the crucible, protection alumina sheaths for thermocouples, and a duct for argon injection on the melt surface for protection against oxidation. The lower part contained the graphite-clay crucible placed on a water-cooled copper base. The water-cooled base extracts heat, whereas the crucible lateral wall is thermally insulated by refractory blocks to promote directional solidification. Two thermocouples were positioned within the melt to record the temperatures along the experiments in two positions, one near the crucible base and another near the melt surface. After melt transfer into the crucible and thermal stabilization of the temperature (20 mins), the water-cooled base was brought in contact with the crucible bottom to begin solidification. The heating elements were kept on all the time during the experiments, supplying heat to the top of the melt to increase the temperature gradient and decrease solidification velocity. The heating elements were turned off only when the melt temperature reached about $1000℃$, indicating that solidification had ended. In the experiment with forced convection, a graphite disc rotating at 360 rpm was immersed into the liquid near its free surface, approximately 85 mm from the bottom of the crucible. A shaft connected this disc to an electric motor. The disc was kept in the liquid until the solidification interface reached the melt top, when it was pulled out of the remaining liquid [9]. The resulting ingots were cut longitudinally to reveal their micro and macrostructures and samples were extracted from its axis for chemical analyses by ICP-OES.

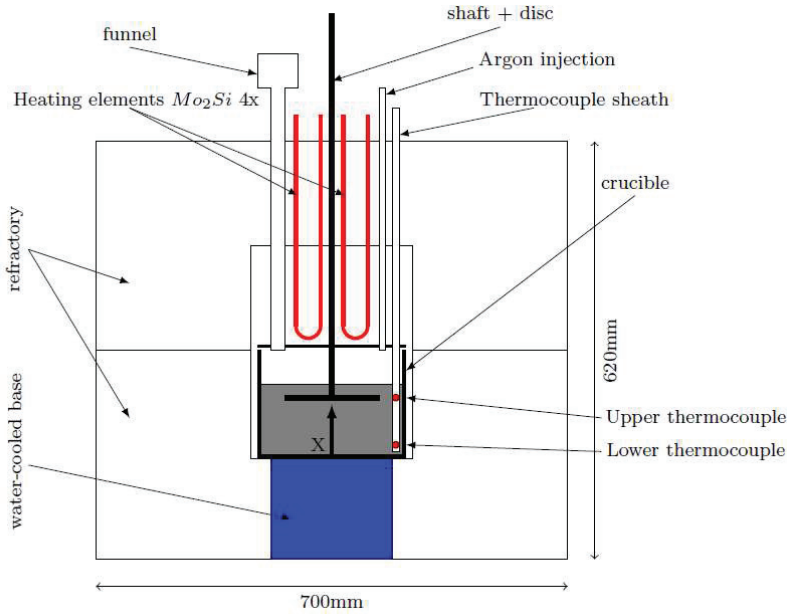


Figure 1 – Schematic drawing of the furnace used in the experiments. The disk-shaft setup was used only in the experiment with forced convection.

Mathematical model of directional solidification

The heat transfer in the silicon during the unidirectional solidification of the ingot was modelled according the enthalpy method for a pure metal using the unidimensional equation [10]:

$$\frac{\partial H}{\partial t} = \frac{\partial}{\partial x}\left(K\frac{\partial T}{\partial x}\right) \tag{2}$$

where H is the enthalpy per unit volume, K is the effective thermal conductivity, T is temperature, t is time and x is the distance from the crucible base along its longitudinal axis. The effective thermal conductivity (K) was calculated with the conductivities of the solid (K_S) and liquid (K_L), given in Table 1, weighed by their local volume fractions. To approximately consider the effect of forced convection, the value of K_L was increased five times. This procedure is sometimes adopted in solidification models [11]. Although the metallurgical grade silicon contains several impurity elements, a binary Si-Fe diluted alloy was assumed as a first step to the development of a more comprehensive model. Material properties used in the simulations are listed in Table 1. The curves of temperature as a function of time measured with the two thermocouples were used as boundary conditions of the first type and, therefore, the calculation domain was set equal to the distance between them. Equation (2) was solved by the finite volume method, with an explicit formulation [12].

Table 1 - Silicon-Iron alloy properties [13], [14] adopted in the simulations: slope of *liquidus* line ($\boldsymbol{m}$), iron diffusion in liquid silicon ($\boldsymbol{D_{Fe}}$), thermal conductivity in solid and liquid ($\boldsymbol{K_S}$ and $\boldsymbol{K_L}$), heat capacity of solid and liquid ($\boldsymbol{C_{pS}}$ and $\boldsymbol{C_{pL}}$), heat of fusion ($\Delta\boldsymbol{H_S}$) and $\boldsymbol{T_f}$ fusion temperature.

Property	Value	Property	Value	Property	Value
$m\ (K \cdot \%^{-1})$	-5.1	k_0	$8.0{\cdot}10^{-6}$	$C_{pS}\ (J \cdot kg^{-1} \cdot K^{-1})$	1050
$D\ (m^2 \cdot s^{-1})$	$1.8{\cdot}10^{-8}$	$K_S(W \cdot m^{-1} \cdot K^{-1})$	28	$C_{pL}\ (J \cdot kg^{-1} \cdot K^{-1})$	968
$C_0(\%)$	0.14	$K_L(W \cdot m^{-1} \cdot K^{-1})$	58.5	$\Delta H_S(J \cdot kg^{-1})$	$1.80{\cdot}10^{6}$
$T_f\ (K)$	1685				

Results and Discussion

Micro and macrostructures of the ingots

The macrostructure of the ingot from the experiment without forced convection consists mainly of columnar grains with serrated boundaries without any apparent common orientation (Figure 2(a)). However, there is a layer thickness of approximately 8 mm adjacent to the ingot base with columnar grains of straight boundaries and common orientations, approximately parallel to the heat extraction direction. Within this layer, no intermetallic particles are seen, which seems to indicate that solidification occurred with a planar solid liquid interface, i.e., without cells/dendrites. The microstructure within this layer (Figure 2(c)) shows silicon carbide particles formed by the interactions between melt and crucible wall, but no intermetallic particles. Outside this layer (Figure 2(b)), intermetallic particles are seen.

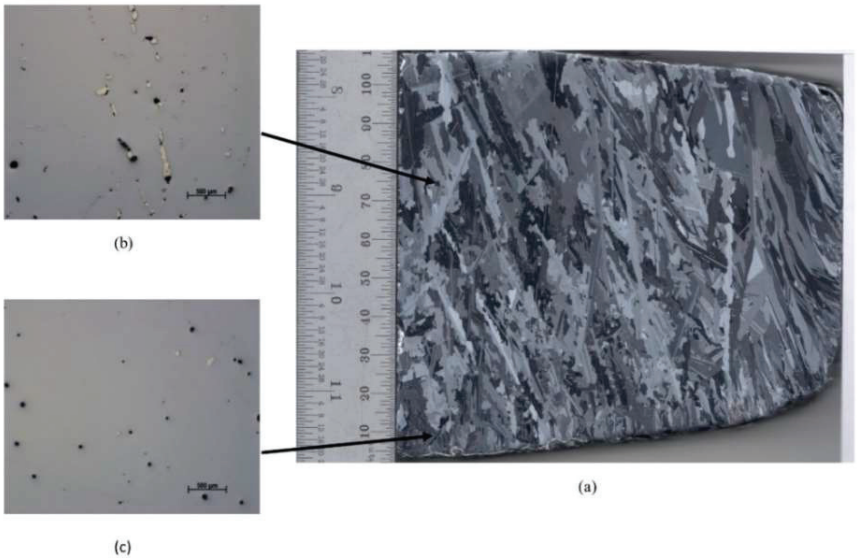


Figure 2 – Experiment without forced convection: (a) macrostructure of the ingot; microstructures at (b) 75 mm and at (c) 8mm from the ingot base.

The macrostructure of the ingot obtained with forced convection is given in Figure 3(a), showing mainly columnar grains with straight and well-defined boundaries, approximately aligned with the heat extraction direction. This grain structure, which without convection was present only in an 8 mm layer near the ingot base, has been extended up to 80 mm with forced convection. At the top of this ingot, however, there is a layer of approximately 20 mm containing again grains with serrated boundaries and without common orientations. Intermetallic precipitates were seen only in this top layer, as illustrated in Figure 3(b) and (c). Therefore, a planar solid-liquid interface was probably maintained during most of the ingot solidification, up to the ingot top layer.

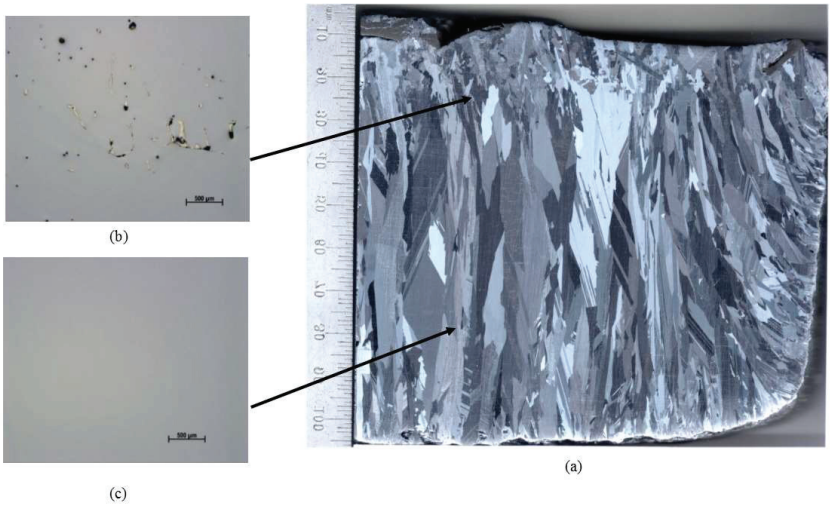


Figure 3 - Experiment with forced convection: (a) macrostructure of the ingot; microstructures at (b) 80 mm and at (c) 25 mm from the ingot base.

The profiles of Fe and Al concentrations along the ingot axis as a function of the distance to the ingot base are given in Figure 4(a) and (b), respectively. All profiles show macrosegregation of these elements to the ingot top, as expected, because it was the last part to solidify. For both elements, concentrations decreased below the detection limit of the analytical technique when forced convection was introduced, showing a significant increase in macrosegregation and, thus purification. In the ingot obtained with forced convection, the region where concentration increased above the quantification limit coincided with the existence of the intermetallic precipitates observed in the top layer. Consequently, the absence of precipitates indicates very low impurity concentrations, confirmed by chemical analysis. The presence of intermetallic precipitates, on the other hand, might also indicate that solidification occurred in the presence of cells/dendrites.

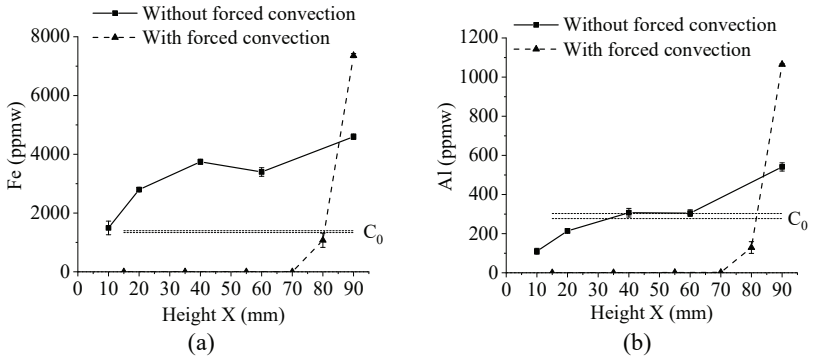
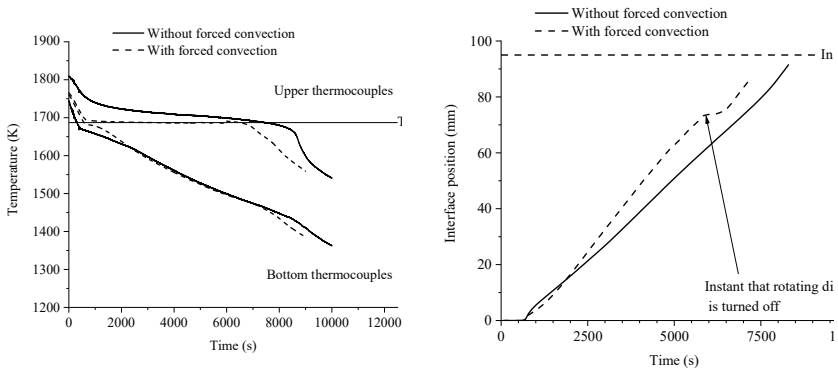
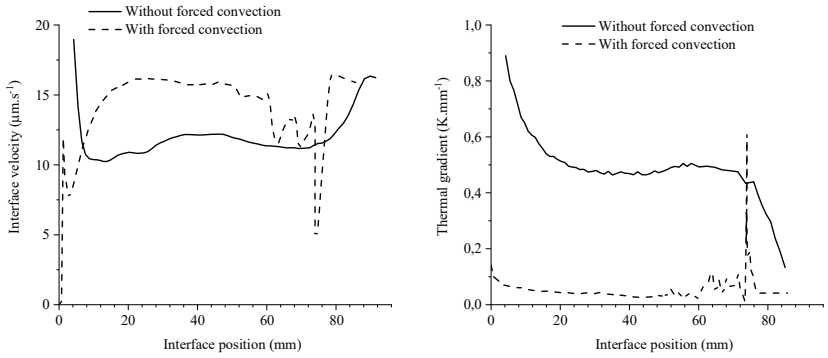


Figure 4 – Profiles of impurity concentration as a function of distance to the ingot base for the experiments without and with forced convection: (a) Fe with $\boldsymbol{C_0 = 1368 \pm 32 ppmw}$ and (b) Al with $\boldsymbol{C_0 = 290 \pm 13 ppmw}$. The quantification limit (QL) in either cases is 0.5ppmw.

Heat and mass transfer analysis of directional solidification

Using the mathematical model described previously and the measured cooling curves given in Figure 5(a) as boundary conditions, the solid-liquid interface position (Figure 5(b)), the interface velocity (Figure 5(c)), and the temperature gradient (Figure 5(d)) in the liquid adjacent to the interface were computed for the two experiments. The interface position for the case with convection was usually ahead of that without convection (Figure 5(b)), corresponding to a larger interface velocity, as illustrated in Figure 5(c). This is consistent with the higher cooling rate observed in the cooling curves of the experiment with forced convection (Figure 5(a)). In this experiment, the thermal gradient at the interface is significantly lower than that without convection, which can be easily explained by the vigorous convective liquid mixing.





(c) (d)

Figure 5 – For the conditions without and with forced convection: (a) measured cooling curves and (b) calculated interface position as a function time are given. Also shown are the calculated (c) interface velocity and (d) temperature gradient as a function of the interface position.

To verify the conditions for the presence of a planar solid-liquid interface, the interface velocity, V (Figure 5(c)), and the temperature gradient, G_L (Figure 5(d)) obtained with the heat transfer model were used to calculate the constitutional supercooling at the liquid adjacent to the solid-liquid interface. The constitutional supercooling can be defined as the difference between the *liquidus* temperature gradient and the actual temperature gradient at this liquid. The *liquidus* temperature gradient was obtained from the impurity concentration gradient calculated as suggested by Hurle [8], who defined a stagnant liquid layer of thickness δ adjacent to the interface. Within this stagnant layer, there is only impurity diffusion, whereas outside the impurity concentration is assumed uniform because of strong convective mixing. The final expression for the constitutional supercooling (S_{conv}) at the liquid adjacent to the solid-liquid interface is [8]

$$S_{conv} = -\frac{mVC_{L\infty}(1-k)}{D[k+(1-k)e^{-\Delta}]} - G_L \tag{3}$$

where, m is the slope of *liquidus* line, $C_{L\infty}$ is the solute concentration in the liquid outside of the stagnant layer, D is the solute diffusion coefficient of Fe in the liquid, Δ is the convective-diffusive parameter, given by

$$\Delta = \frac{V\delta}{D} \tag{4}$$

which indicates the importance of the impurity transport by liquid convection relative to that by diffusion. The solute concentration $C_{L\infty}$ was calculated by Scheil equation, as proposed by Pfann [15], given by:

$$C_{L\infty} = C_0 f_l^{(k-1)} \tag{5}$$

where C_0 is the initial concentration of impurity and f_l is the global fraction of liquid in the crucible, estimated by the ratio of the interface position to the ingot height (95 mm). According to the constitutional supercooling criterion [16], when constitutional supercooling is absent ($S_{conv} \leq 0$), solidification occurs by the migration of a planar solid-liquid interface. On the other hand, when this supercooling exists ($S_{conv} > 0$), cells/dendrites might form and grow at the planar interface. The stagnant liquid layer adopted by Hurle [8] is part of a simple technique to consider the effects of convection in the diffusion field of the liquid adjacent to the interface. The stagnant layer thickness decreases when the severity of convection increases. Consequently, increasing convection results in a decrease of Δ and, thus, also in S_{conv}, increasing the stability of a possible planar interface. The impurity transport away from the interface is facilitated in the absence of cells/dendrites (planar interface). Therefore, by setting $\delta \rightarrow 0$, i.e., $\Delta \rightarrow 0$, the minimum constitutional undercooling obtained by vigorous convection can be obtained as

$$S_{min} = -\frac{mVC_{L\infty}(1-k)}{D} - G_L \tag{6}$$

Note that when $S_{min} > 0$, convection alone cannot stabilize a planar interface for a given solidification condition. On the other hand, by setting $\delta \rightarrow \infty$, i.e., $\Delta \rightarrow \infty$, the effects of convection are neglected and the maximum constitutional undercooling, which is actually the original constitutional undercooling [16], is obtained by

$$S_{diff} = -\frac{mV\ _0(1-k)}{Dk} - G_L \tag{7}$$

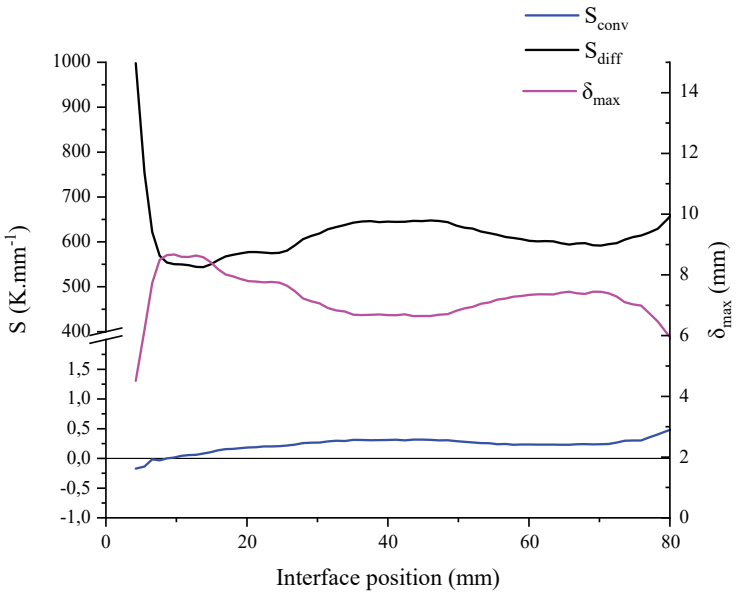
In this case, $C_{L\infty} \rightarrow C_0$, because the bulk melt outside the stagnant layer will have the initial solute composition C_0, since the liquid is semi-infinite ($\delta \rightarrow \infty$). Note that, when the solid-liquid interface is planar and $S_{diff} > 0$, i.e., there exists constitutional supercooling, the stability of this planar interface is probably a result of liquid convection. The minimum convection intensity, which corresponds to the maximum stagnant layer thickness (δ_{max}), to keep a planar interface stable can be calculated by setting $S_{conv} = 0$ in Eq. (3), giving

$$\delta_{max} = -\frac{D}{V}\ln\left(-\frac{mVC_{L\infty}}{G_L D} - \frac{k}{1-k}\right) \tag{8}$$

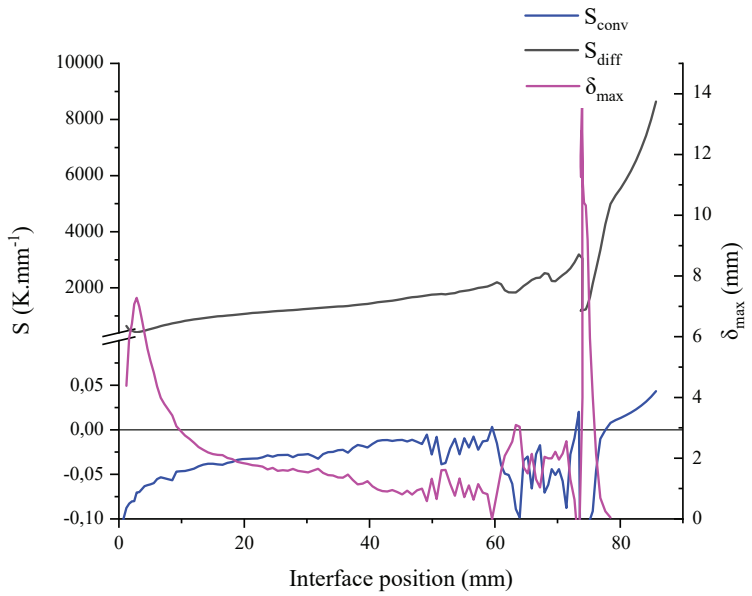
Note that lower δ_{max} values indicate greater convection intensities required to keep the stability of a planar interface. The parameters S_{conv}, S_{diff}, and δ_{max} were calculated for the solidification conditions in the two experiments, considering a Si-Fe binary alloy (table 1) with $C_0 = 1368\ ppm$. To obtain S_{conv}, the value of δ was chosen in agreement with experimental results. For example, in the experiment without convection, an ingot bottom layer of $8\ mm$ was observed with columnar grains and without intermetallic particles, which might indicate the existence of a planar solid-liquid interface. Therefore, $\delta = 8.7\ mm$ ($\Delta = 5.0$) was chosen to make $S_{conv} = 0$ at $x = 8\ mm$. For the experiment with forced convection, the same strategy gives $\delta = 0.23\ mm$ ($\Delta = 0.19$) to make $S_{conv} = 0$ at $x = 80\ mm$.

Since $S_{diff} > 0$ in the two experiments, liquid convection might have stabilized the planar solid-liquid interface during solidification of the ingot region without intermetallic particles. The S_{conv} curves, Figure 6 (a) and (b), show that, for the adopted δ thickness

value, $S_{conv} = 0$, changing from negative to positive at the end of the region without intermetallic particles. Note that δ is larger for the experiment without forced convection ($\delta = 8.7\ mm$) than that for the experiment with convection ($\delta = 0.23\ mm$), which is consistent with the greater intensity of liquid convection in the latter case. When forced convection is absent, natural convection caused by radial temperature gradients in the crucible might be important for solute transport and, therefore, for the constitutional undercooling, as observed during solidification in Bridgman furnaces [17]. In this case, a few authors obtained δ values in the range between 4 and $8\ mm$ [14], [18], [19], in reasonable agreement with the value calculated here ($\delta = 8.7\ mm$). The curves of δ_{max} as a function of position indicates the severity of convection required to keep a planar interface at that specific position. It can be seen that more vigorous convection (lower δ_{max} values) is needed to keep a planar interface in the forced convection experiment. As shown in Figure 5(c) and (d), the interface velocity is larger and the temperature gradient at the interface is lower for this experiment, which are conditions that destabilize the planar interface and, thus, require more intense convection to keep it stable. In this experiment, convection increases the impurity transport adjacent to the interface and decreases the gradient of impurity concentration, which decreases the gradient of *liquidus* temperature and, consequently, decreases the constitutional undercooling.



(a)



(b)

Figure 6 – Calculated parameters S_{conv}, S_{diff}, and δ_{max} as function of interface position in the experiments (a) without and (b) with forced convection

Conclusions

Experiments of directional solidification of metallurgical grade silicon were carried out to investigate the effects of forced convection on microstructure, macrostructure, and macrosegregation of impurities in the resulting ingots. Without forced convection, the ingot macrostructure consists mainly of columnar grains with serrated boundaries and without any apparent common orientation. Nevertheless, a layer of 8 mm thickness exists adjacent to the ingot base with columnar grains of straight boundaries and a common orientation approximately parallel to that of the heat flux. Intermetallic precipitates are seen outside of this layer, but are absent within it. When forced convection is introduced by a rotating disc (360 rpm) near the melt free surface, the layer of columnar grains with straight boundaries (observed in the previous ingot) is extended to about 80 mm, including most of the ingot. In this region, intermetallic precipitates are absent and the concentration of impurities, e.g. Fe and Al, are below the quantification limit of the analytical technique, showing an increase in macrosegregation and higher purification. A numerical mathematical model of heat and impurity transfer shows that, despite the obvious convection effects of increasing solute transport, forced convection might also have increased the stability of a probable planar solid-liquid interface, preventing cell/dendrite formation and, therefore, facilitating the transport of impurities from the interface into the bulk liquid.

Acknowledgements

The authors want to acknowledge the CAPES and FIPT grants provided to D.P. Nascimento, CNPQ (311206/2014-0), FAPESP (2017/22361-6) and Cia Ferroligas Minas Gerais-MINASLIGAS for the metallurgical grade silicon supplied.

References

[1] E. Øvrelid, M. Juel, M. P. Bellmann, and B. A. Tuffour, "Refining of solar grade silicon by directional solidification," in *Silicon for the Chemical and Solar Industry IX*, 2008, p. 91.

[2] G. Bye and B. Ceccaroli, "Solar grade silicon: Technology status and industrial trends," *Sol. Energy Mater. Sol. Cells*, vol. 130, pp. 634–646, 2014.

[3] T. R. Ribeiro, M. L. Lima, J. B. Ferreira Neto, J. B. V. Neira, and A. A. Lotto, "Metallurgical route to produce solar grade silicon," in *Silicon for the Chemical and Solar Industry XIII*, 2016, pp. 343–354.

[4] D. Lynch, "Winning the global race for solar silicon," *JOM*, vol. 61, 11, pp. 41–48, Nov. 2009.

[5] P. Woditsch and W. Koch, "Solar grade silicon feedstock supply for PV industry," *Sol. Energy Mater. Sol. Cells*, vol. 72, 1–4, pp. 11–26, Apr. 2002.

[6] J. P. Garandet, "New Determinations of Diffusion Coefficients for Various Dopants in Liquid Silicon," *Int. J. Thermophys.*, vol. 28, 4, pp. 1285–1303, Oct. 2007.

[7] J. A. Burton, R. C. Prim, and W. P. Slichter, "The Distribution of Solute in Crystals Grown from the Melt. Part I. Theoretical," *J. Chem. Phys.*, vol. 21, 11, pp. 1987–1991, Nov. 1953.

[8] D. T. J. Hurle, "Constitutional supercooling during crystal growth from stirred melts—I," *Solid. State. Electron.*, vol. 3, 1, pp. 37–44, Jul. 1961.

[9] J. B. Ferreira Neto, "Processo e equipamento para purificação de silício grau metalúrgico por solidificação direcional sob convecção forçada," Patent BR 13 2017 006280 4, 2017.

[10] V. Voller and M. Cross, "Accurate solutions of moving boundary problems using the enthalpy method," *Int. J. Heat Mass Transf.*, vol. 24, 3, pp. 545–556, Mar. 1981.

[11] M. Rappaz, "Modelling of microstructure formation in solidification processes," *Int. Mater. Rev.*, vol. 34, 3, pp. 93–123, 1989.

[12] S. V Patankar, *Numerical Heat Transfer and Fluid Flow*, 1st ed. USA: Hemisphere Publishing Corporation, 1980.

[13] K. C. Mills and L. Courtney, "Thermophysical properties of silicon," *ISIJ Int.*, vol. 40, pp. S130–S138, 2000.

[14] M. A. Martorano, J. B. Ferreira Neto, T. S. Oliveira, and T. O. Tsubaki, "Macrosegregation of Impurities in Directionally Solidified Silicon," *Metall. Mater. Trans. A*, vol. 42, 7, pp. 1870–1886, Jul. 2011.

[15] W. G. Pfann, "Principles of Zone Melting," *J. Met.*, vol. 4, pp. 747–753, 1952.

[16] W. A. Tiller, K. A. Jackson, J. W. Rutter, and B. Chalmers, "The redistribution of solute atoms during the solidification of metals," *Acta Metall.*, vol. 1, 4, pp. 428–437, Jul. 1953.

[17] P. W. Bridgman, "Certain Physical Properties of Single Crystals of Tungsten,

Antimony, Bismuth, Tellurium, Cadmium, Zinc, and Tin ," *Proc. Am. Acad. Arts Sci.*, vol. 60, 6, pp. 305–383, 1925.
[18] A. Rouzaud, D. Camel, and J. J. Favier, "A comparative study of thermal and thermosolutal convective effects in vertical Bridgman crystal growth," *J. Cryst. Growth*, vol. 73, 1, pp. 149–166, Oct. 1985.
[19] S. Ren *et al.*, "Removal of Cu, Mn and Na in multicrystalline silicon by directional solidification under low vacuum condition," *Vacuum*, vol. 115, 2, pp. 108–112, May 2015.

Stewards of environmentally friendly silicon production for the solar industry

Thomas J. Preston[1)]
1) Institutt for energiteknikk, Box 40, 2027, Kjeller, Norway

Abstract

Making electricity available is a great motivating factor for our industry: we help bring brighter futures to the globe. There are many paths we can take as a community. Solar energy enjoys high public approval across the globe. There are economic advantages to operating in an environmentally friendly manner. It is in our best interest to act in the planet's best interest. Here I present some opportunities we face and some success stories of how we are reaching them.

Introduction

Access to energy has long been a key indicator for humanity's well-being. Be it the food energy to feed a population, the mechanical energy to build and maintain our living spaces, or the electrical energy to enable steps forward in technology, ready access to energy is critical. For too long, we as humans have focussed on the roll-out of energy availability while turning a blind eye to other consequences. We are undergoing an energy revolution. You and I, as members and interested parties of the silicon production industry, hold enough sway to sculpt that future and to avoid the mistakes of the previous energy revolutions.

Electrification of primary and secondary schools improves their ability to serve their pupils, and solar energy is contributing [1]. Delivery of healthcare requires consistent electricity sources, and already their cost to use solar energy is less than previous fossil-fuel based solutions [2]. Food security may also be linked to energy access [3]. Water cleanliness and abundance are inextricably linked to the form of energy production, because use of water at power plants competes with use at home for drinking and irrigating [4]. Global strife and multinational cooperation will affect total CO_2 emissions in the coming decades [5].

The way we drive today's and tomorrow's silicon production affects far more than our own industry. It is my intention with this contribution to share a vision of why we should work towards that future, to take a quick foray into why there are inherent problems in silicon refining, and -to highlight both bright and troubling spots. I close with a personal take on how we can work together to be stewards of the global solar energy team. The references I supply herein are woefully incomplete. They are meant to be entry points for interested readers into other avenues of research rather than to be a comprehensive assembly of information.

Teamwork among renewable industries

Silicon-based photovoltaic systems are one piece of a multi-faceted energy solution. There are, furthermore, many ways to implement this technology. We can expect a mixture of electricity sources as we move to a renewable mix, and we can expect that the right mixture can be mutually beneficial to all actors. Wind, solar, electrical energy

storage in batteries, chemical energy storage in hydrogen and liquid fuels, and potential energy storage in hydro dams can all contribute to a carbon-neutral energy system. I suspect that cooperation among nations and technologies, rather than competition among these sectors, will bring about the fastest change [6].

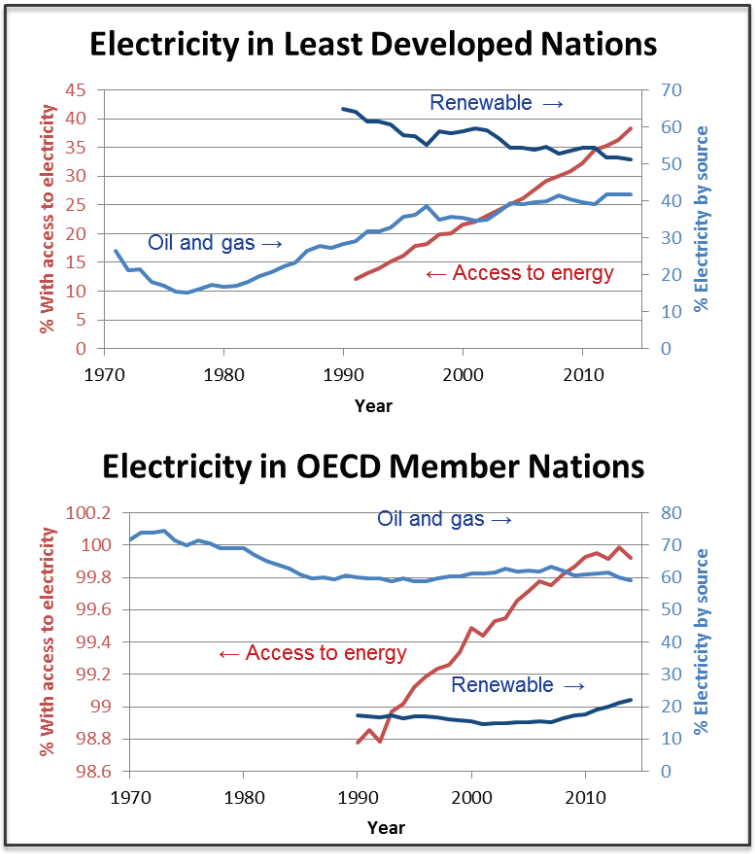


Figure 1: Access to electricity and its source. Electricity access is increasing, year on year, for the people in the Least Developed Countries (top panel), although the production by renewable sources is decreasing. Electricity access is near 100% for OECD Member nations (bottom panel, used as a proxy for developed nations) and the fraction produced by renewables is increasing. Data from The World Bank [7-12].

There is a heavy focus on large-scale solar development. "World's largest solar plant" or "World's cheapest production tendered" make great headlines. Such stories serve as advertising for our cause of developing the solar silicon industry. We must be cognizant, however, of regions lacking distributed electrical grids. According to the World Bank, and as shown in the top panel of Figure 1, less than 40% of the nearly 1 billion people in the Least Developed Countries have access to electricity [7]. Even though the trend of those with access is moving in the right direction, the fraction of renewable energy production in those counties is declining [8, 9]. This trend is contrary

to that shown in the bottom panel of Figure 1 for OECD countries [10-12], which I use as a proxy for developed nations.

There is a strong correlation between wealth and energy use [13]. To bring ready access to cheap electricity is to bring wealth. It is difficult to reduce energy demand if we wish to roll out our electrical generation to more markets: the more people with access, the more the demand. At-home energy storage with batteries makes installation of solar panels more useable. Other energy storage solutions for power-plant scale solar installations can do the same. Big or small, nearby or far away, supporting the entire renewable sector supports our silicon industry.

Public support behind renewables

Public support of the silicon industry is vital for us to thrive. Developments that people like are easier to sell. When it comes to large-scale renewable energy developments, exactly what affects a population's attitude (their thoughts) and behavior (their actions) is under study. Batel and Wright propose, in the first instance, promoting renewable energy as social change [14].

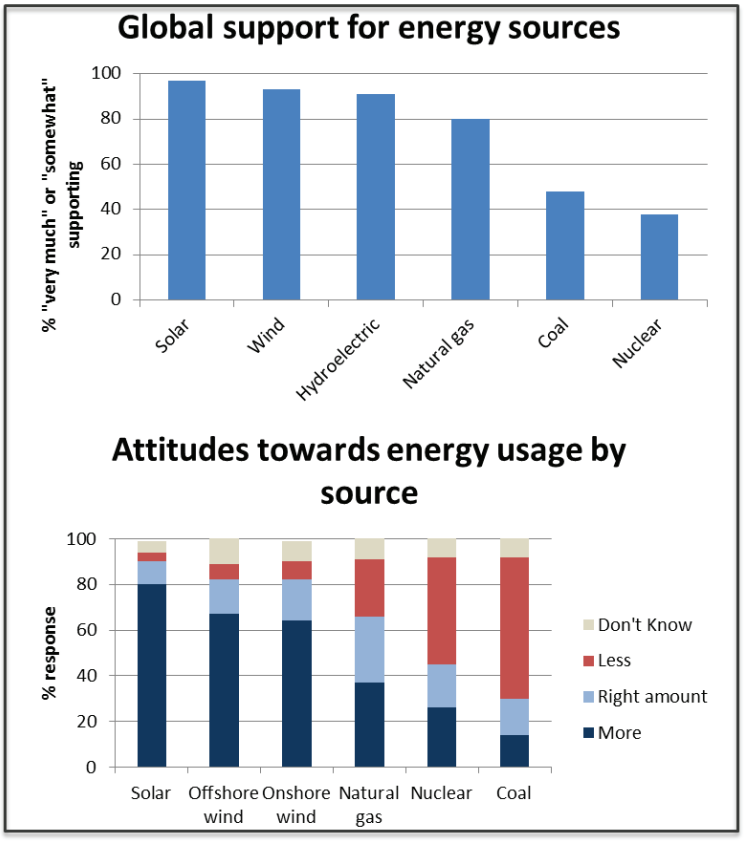


Figure 2: Desire for use of renewables is high around the world. There is strong support for solar (top panel). Furthermore, people want more solar to be used (bottom panel). Data from Ipsos [16] (top) and Ørsted [17] (bottom).

If we in the industry will sell our technology as a social change, so too must we be smart in our production. I will take up this theme further in the next section on silicon production, but, to say it in broad strokes, we must avoid backlashes in the future by making smart choices now.

There are two clear economic reasons to keep on the public's good side. First, people are willing to pay extra for electricity produced from renewable sources [15]. Second, global support for renewable energy sources is incredibly high. A global survey [16] from Ipsos in 2011, shown in the top panel of Figure 2, provides credence to that which many of us already know: there is global support for renewable energy solutions. A survey [17] from Ørsted of residents in 13 countries in 2017 shows that solar is still the favored renewable technology, shown in the bottom panel of Figure 2. Let us, therefore, find ways to ensure this momentum in our silicon-based solar energy industry.

Environmental friendliness is an asset

From dust to dust

The silicon-based solar energy industry needs to have a broad environmental vision. From the silica we harvest, to the methods we use to convert it to silicon, to the byproduct we generate, to the final product we sell, to the waste product the consumer must deal with in end of life - it should all be in our sphere of understanding. Cutting energy use, developing new methods, and making the best product we can are good business.

What makes it difficult in silicon production?

Silica, the ore of silicon, is an abundant resource. Because Si is the second most abundant element in the Earth's crust and because SiO_2 is its most common form, we have a good supply. The problem, if you will, is a chemical one.

The Earth is an oxidizing environment. Silica, SiO_2, is the fully oxidized state of silicon. It is our job, therefore, to rid silica of its oxygen and to produce clean silicon. Reduction of SiO_2 to metallic silicon, Si, changes the oxidation state of silicon from +4 to 0. The standard enthalpy of formation of SiO_2 is -859.4 kJ/mol. This large, negative number means that it takes a lot of energy to remove the O atoms from the Si. Table I shows the enthalpy of formation of several binary oxides. The table is sorted by the right-most column, which gives the enthalpy of formation per gram non-oxygen element: running the chemistry backwards to make metallic silicon from silica requires lots of energy. For this reason, it is imperative that we take stock of these energy costs and their attendant effects on the environment.

The industrial conversion of SiO_2 to Si, however, proceeds through several more steps than via the direct removal of O. The first conversion to make metallurgical-grade silicon

$$SiO_2 + C \rightarrow Si + 2CO, \quad (1)$$

shows that carbon is consumed and CO is produced. Despite the over-simplified chemistry shown in Equation 1, here are three quick interpretations: 1) the process consumes C, which is supplied by mined or harvested C sources; 2) the process

produces CO, which must be dealt with; and 3) the process consumes energy in the form of electricity. Typical purities after this first refining step are about 98-99% Si.

Table 1: Binary oxides, ordered by stability per gram of non-oxygen element.

Formula	ΔH_f / kJ·mol^{-1}	ΔH_{fX} / kJ·g$_X^{-1}$
CO_2 (g)	- 393.5	-32.8[1]
Al_2O_3	-1669.8	-30.9
SiO_2	**- 859.4**	**-30.6**
MgO	- 601.8	-24.8
CaO	- 635.5	-15.9
ZrO_2	-1100.6	-12.1
Cr_2O_3	-1128.4	-10.9
MnO_2	- 519.7	- 9.5
SnO_2	- 580.7	- 8.9
Fe_2O_3	- 822.2	- 7.4

[1]This column lists ΔH_{fx}, a contrived value to highlight the energy demand per gram non-oxygen element, X.

Solar applications require much higher purities. Figure 3 shows the limits for impurities for various grades of solar-grade silicon [18]. The left axis shows atomic concentration in ppb, the right axis in %Si. Metallurgical grade silicon, which would be

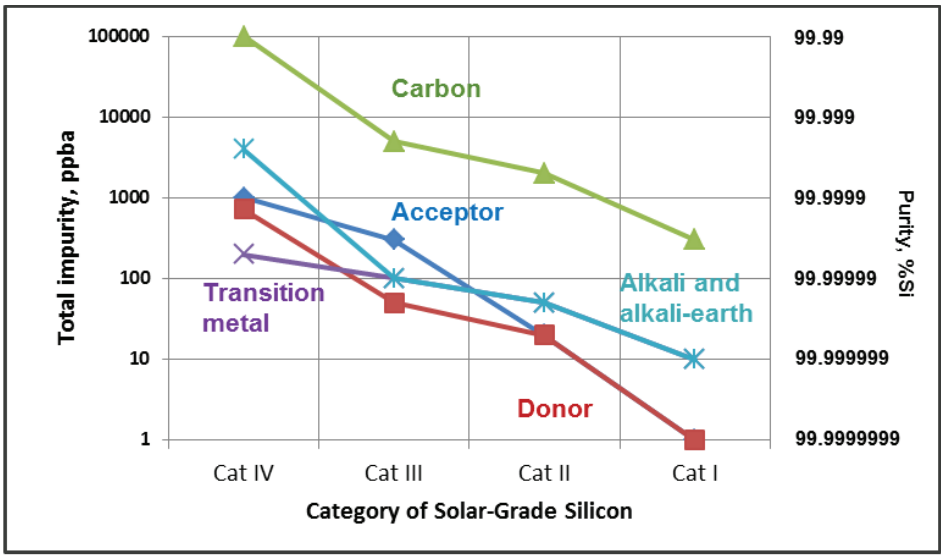


Figure 3: Purity requirements for solar-grade silicon. In general, the more pure the material, the more energy required to make it. Data from Ref [18].

two decades above the range of Figure 3, requires energy to bring impurities to the acceptable levels given in the figure. From a historical perspective, production of solar-grade Si came from the electronics and semiconductor industry, which have minimum

tolerances near or smaller than the lower range of this graph. Tailoring production to purity demands, and thus minimizing energy costs, is a focus for the industry. See the section on Challenges and Opportunities for further discussion.

Making the new energy mix

The silicon-production industry is in the curious position of being able to craft, literally, its own future. We make the new energy we need to make our product. Let us take a base case of converting 50% of current global fossil fuel consumption (about 12.3 TW/year) with solar energy. Let us also require reaching 50% solar by the year 2038, a reasonable target for reaching the goals set forth by the Paris agreement. To do so, we will need approximately 300 000 tons of solar-grade silicon per year. We must be aware of the environmental costs to reach such a target using current practices. A satisfactory option is to use our own solar panels for production. We must use the change we wish to see.

An emerging theme for the solar industry is to use silicon for lithium intercalation in the anodes of lithium-ion batteries. As mentioned above, co-location of solar harvesting plus electrical storage can help provide a stable source of renewable electricity. Such products have rather separate demands on purity and production, so I leave the details of future production needs elsewhere.

The industry can contribute on multiple fronts to sculpting a viable, electrified future: we build the solution we need. The earlier we can build up, the faster our production comes from clean sources of energy. We must act now and act correctly. We cannot expect that misdeeds now will be forgiven in the future. There isn't the patience to ask users and society to wait for the payback to kick in as we slowly shift to a green energy mix.

Current success stories

There are several ways in which the industry is already making a more environmentally friendly product: making established techniques more energy efficient, siting old and emerging technologies near renewable energy producers, and developing new technology to address the needs of the solar industry. More opportunities abound. There are myriad novel contributions and reviews available on this topic. A recent text is a good place to start [19].

Energy gains in established technology

Just as the solar-cell processing industry continually improves the efficiency of cells, the silicon-production industry decreases the energy demands of producing the silicon itself. A recent study posits that savings of 15-17 kWh/kg-Si amounts to an energy savings that is analogous to about a 1% increase in baseline efficiency of the modules [20]. The so-called Siemens process, the workhorse of the silicon production industry, is geared towards production of electronics-grade silicon. Thus, it produces silicon of higher purity than is typically required for solar applications.

The maturity of the technology, however, contributes to its continued use in the solar industry. We cannot expect its dominance to disappear overnight. As a recent example, seemingly simple improvements such as how to deliver the electricity to heat the Si rods in a Siemens reactor may lead to improved processing [21]. Other improvements are certainly possible.

Emerging tech with new energy sources

Two emerging technologies may threaten established production. REC Solar Norway (formerly Elkem Solar) produces solar-grade silicon using the so-called upgraded metallurgical silicon route. The process avoids both the gasification and deposition processes inherent in the Siemens process. Doing so reduces the energy demand by a factor of 5-10 [22]. Furthermore, by siting the production in Norway, with its nearly 100% renewable electrical production, the CO_2 produced per kg Si is 3-5 times less than conventional processes [22].

The second comer, pyrolysis of silane in a fluidized bed reactor, is operated by REC Silicon. In this process, tricholorosilane ($SiHCl_3$) is converted to silane (SiH_4), which is then flowed into a reactor containing solid silicon seed particles. Silicon from the SiH_4 accretes at the particles, thereby making the particles heavier and causing them fall out of the reactor. Despite the extra processing step to produce silane, the pyrolysis is efficient and leads to an overall energy demand less than half of the Siemens process [23]. Their two production facilities are located in regions dominated by renewable energy mixes, thus beating the typical "US mix" assessments of 20% renewable [24]. The facility in Moses Lake, Washington, USA, is served by 66% hydro from the Grand Coulee Dam [25], and the Butte, Montana, USA, facility is served by 78% renewable electricity [26].

New technology, new energy sources

The industry should be prepared for even newer technologies to enter production. REC Solar Norway continues to improve its process and to increase its silicon production in hydro-powered Norway. Dynatec, a newcomer to silicon production, has shown remarkably low energy consumption in its silane-based centrifugal reactor. They state 5 kWh/kg-Si as their current record [27] for the silane-to-silicon conversion step.

Challenges and opportunities

We should recognize that to name current challenges is also to highlight opportunities. Table 2 lists the top 10 Si producing nations [28], including ferrosilicon production. The countries are ranked, however, by dividing annual Si production by each nation's gross domestic product (GDP). Although the unit is meaningless, and thus omitted from the table, the ranking is informative. Bhutan and Iceland produce only ferrosilicon, but could be considered markets with refining potential. Norway, next on the list, devotes a large fraction of its economy to Si production. Russia and China are nearly equal, but China is by far and away the global leader in tons of production.

China

It's not all rosy in silicon production in China. There, environmental costs are typically downplayed compared to economic gains [29]. We again see that the high electricity consumption works against the environmental gains of rolling out silicon-based PV [30]. These authors do highlight, however, that these costs are only about 4.5% of those from the present-day coal-based electricity in China. Their major suggestions are to decrease material and energy use, and to improve waste water treatment during production. In the EU and in the USA, these are demands placed on producers already by law. Established and new producers in the Chinese market would be wise to heed such warnings.

Table 2: Silicon production, ordered by tons of Si divided by GDP.

Country	Annual Si production / tons·yr^{-1}	GDP / Trillion USD	(Si production / GDP)
Bhutan*	78	2 321	3 x 10^{-2}
Iceland*	75	24 848	3 x 10^{-3}
Norway	380	392 052	1 x 10^{-3}
Russia	747	1 469 341	5 x 10^{-4}
China	4 600	11 937 562	4 x 10^{-4}
South Africa	84	344 064	2 x 10^{-4}
Spain	81	1 307 170	2 x 10^{-5}
Brazil	100	2 080 916	5 x 10^{-5}
France	121	2 574 807	5 x 10^{-5}
United States	396	19 362 129	2 x 10^{-5}

Future regions and other regions

There are other parts of the globe to consider. Russia, South Africa, and Brazil rank high on Table 2, yet receive minimal mention. Iceland and Bhutan produce large amounts of ferrosilicon, but do not refine it further. Oceania, Southeast Asia, and Africa are missing from the table completely. If we imagine silicon as a global solution, we should be ready to imagine production that is spread around the globe.

New technologies

Certain aspects of the silicon production industry are reticent to change. It is difficult to adopt new technologies when it's going "well". Global installation of solar panels [31] reached a new high in 2017, and that growth will likely increase in 2018. Listed herein are three challengers to the Siemens process: upgraded metallurgical silicon, fluidized-bed pyrolysis from silane, and centrifugal pyrolysis from silane. Despite their advantages, they still produce only a fraction of the global solar-grade silicon. A mixture of adopting new technologies and adapting existing technologies will be a good way forward.

What of the next wave of technology? I opened this monograph with a call to provide electricity to the developing world. I also mentioned that silica is an abundant resource and can be found the world round. Perhaps there is new technology out there than can lead to production on smaller scales. Perhaps tomorrow's silane factory can be located in Lagos, Nigeria or on a farm in Peru. There's plenty of room at the bottom [32].

Summary

This contribution represents a call to action for the industry. Here I provide a list of how I feel the industry can continue to lead the way.

- Take a personal stake
- Promote other renewable sectors
- Ensure continued momentum in silicon-based energy harvesting
- Advertise recent improvements in energy use and pollution control
- Be willing to explore new technologies and new markets

References

1. United Nations Department of Economic and Social Affairs, *Electricity and education: The benefits, barriers, and recommendations for achieving the electrification of primary and secondary schools*, https://sustainabledevelopment.un.org/content/documents/1608Electricity%20and%20Education.pdf, Published: 2014, Accessed: 8 April 2018.

2. A. Franco, M. Shaker, D. Kalubi, S. Hostettler, *A review of sustainable energy access and technologies for healthcare facilities in the Global South*, Sustainable Energy Technologies and Assessments, **22**, 2017, 92-105.

3. P. Sola, C. Ochieng, J. Yila, M. Iiyama, *Links between energy access and food security in sub Saharan Africa: an exploratory review*, Food Security, **8**, 2016, 635-642.

4. United Nations, *Securing Access to Water and Energy*, Published: 2014, Accessed: 8 April 2018.

5. P. Andrews-Speed, C. van der Linde, K. Keramidas, *Conflict and cooperation over access to energy: Implications for a low-carbon future*, Futures, **58**, 2014, 103-114.

6. F. Creutzig, J.C. Goldschmidt, P. Lehmann, E. Schmid, F. von Blucher, C. Breyer, B. Fernandez, M. Jakob, B. Knopf, S. Lohrey, T. Susca, K. Wiegandt, *Catching two European birds with one renewable stone: Mitigating climate change and Eurozone crisis by an energy transition*, Renewable & Sustainable Energy Reviews, **38**, 2014, 1015-1028.

7. The World Bank, *Access to electricity (% of population) Least Developed Countries: UN Classification*, https://data.worldbank.org/indicator/EG.ELC.ACCS.ZS?locations=XL, Published: 2014, Accessed: 9 April 2018.

8. The World Bank, *Renewable electricity output (% of total electricity output) Least Developed Countries: UN Classification*, https://data.worldbank.org/indicator/EG.ELC.RNEW.ZS?locations=XL, Published: 2014, Accessed: 9 April 2018.

9. The World Bank, *Electricity production from oil, gas and coal sources (% of total) Least Developed Countries: UN Classification*, https://data.worldbank.org/indicator/EG.ELC.FOSL.ZS?locations=XL, Published: 2014, Accessed: 9 April 2018.

10. The World Bank, *Access to electricity (% of population) OECD Members*, https://data.worldbank.org/indicator/EG.ELC.ACCS.ZS?locations=OE, Published: 2014, Accessed: 9 April 2018.

11. The World Bank, *Renewable electricity output (% of total electricity output) OECD Members*, https://data.worldbank.org/indicator/EG.ELC.RNEW.ZS?locations=OE, Published: 2014, Accessed: 9 April 2018.

12. The World Bank, *Electricity production from oil, gas and coal sources (% of total) OECD Members*, https://data.worldbank.org/indicator/EG.ELC.FOSL.ZS?locations=OE, Published: 2014, Accessed: 9 April 2018.

13. S. Sorrell, *Reducing energy demand: A review of issues, challenges and approaches*, Renewable & Sustainable Energy Reviews, **47**, 2015, 74-82.

14. S. Batel, P. Devine-Wright, *Towards a better understanding of people's responses to renewable energy technologies: Insights from Social Representations Theory*, Public Understanding of Science, **24**, 2015, 311-325.

15. J.J. Soon, S.A. Ahmad, *Willingly or grudgingly? A meta-analysis on the willingness-to-pay for renewable energy use*, Renewable & Sustainable Energy Reviews, **44**, 2015, 877-887.

16. Ipsos MORI, *Strong global opposition towards nuclear power*, https://www.ipsos.com/ipsos-mori/en-uk/strong-global-opposition-towards-nuclear-power, Published: 2011, Accessed: 9 April 2018.

17. Ørsted, *Green Energy Barometer*, https://orsted.com/en/Barometer, Published: 2017, Accessed: 8 April 2018.

18. C. del Cañizo Nadal, S. Binetti, T. Buonassisi, Purity Requirements for Silicon in Photovoltaic Applications, in: B. Ceccaroli, E. Øvrelid, S. Pizzini (Eds.) Solar Silicon Processes, CRC Press, 2017.

19. Solar Silicon Processes, B. Ceccaroli, E. Øvrelid, S. Pizzini (Eds.), CRC Press, 2017.

20. D. Ravikumar, B. Wender, T.P. Seager, M.P. Fraser, M. Tao, *A climate rationale for research and development on photovoltaics manufacture*, Applied Energy, **189**, 2017, 245-256.

21. Z.F. Nie, P.A. Ramachandran, Y.Q. Hou, *Optimization of effective parameters on Siemens reactor to achieve potential maximum deposition radius: An energy consumption analysis and numerical simulation*, International Journal of Heat and Mass Transfer, **117**, 2018, 1083-1098.

22. E. Øvrelid, S. Pizzini, The MG Silicon Route, in: B. Ceccaroli, E. Øvrelid, S. Pizzini (Eds.) Solar Silicon Processes, CRC Press, 2017.

23. T. Torvund, *Silane-Based Fluidized Bed Reactor (FBR) Technology Development*, in: International Silicon Industry, Xi'an, China, 2016.

24. US Energy Information Administration, *What is U.S. electricity generation by source?*, https://www.eia.gov/tools/faqs/faq.php?id=427&t=3, Published: 2018, Accessed: 9 April 2018.

25. Grant Public Utility District, *Fuel Mix*, http://www.grantpud.org/your-pud/what-we-do/power-generation/renewable-energy/fuel-mix, Published: 2016, Accessed: 9 April 2018.

26. Northwestern Energy, *Environmental stewardship: our commitment in action*, http://www.northwesternenergy.com/docs/default-source/documents/environment/nwe_enviroreport_2017_web.pdf, Published: 2017, Accessed: 9 April 2018.

27. Private communication, W.O. Filtvedt, 2018.

28. United States Geological Survey, *Silicon Statistics and Information*, https://minerals.usgs.gov/minerals/pubs/commodity/silicon/, Published: 2017, Accessed: 9 April 2018.

29. Z.X. Wang, W. Wei, *External cost of photovoltaic oriented silicon production: A case in China*, Energy Policy, **107**, 2017, 437-447.

30. M. Xie, J. Ruan, W. Bai, Q. Qiao, L. Bai, J. Zhang, H. Li, F. Lv, H. Fu, *Pollutant payback time and environmental impact of Chinese multi-crystalline photovoltaic production based on life cycle assessment*, Journal of Cleaner Production, **184**, 2018, 648-659.

31. United Nations Environment Programme and Bloomberg New Energy Finance, *Global trends in energy investment 2018*, https://drive.google.com/file/d/1SmhaI-WAcmEMqR8R9oL5Fxn0cZ0kfY8Z/view, Published: 2018, Accessed: 9 April 2018.

32. A.J.G. Hey, R.P. Feynman, Feynman and computation : exploring the limits of computers, Westview Press/Perseus Books, Cambridge, Mass., 2002.

Silicon for the Chemical and Solar Industry XIV
Svolvær, Norway, June 11 – 14, 2018

FTIR Calibration for Detection of High Concentration Chlorosilanes in a Pilot-scale Hydrochlorination Reactor and Comparison with Modeling Results

Matthias Colomb[1)], Srinivas Palanki B[2)], and Nicholas D. Sylvester C[3)]
1) *Mitsubishi Polysilicon America Corp., Theodore, AL 36582*
2) *Department of Chemical Engineering, Lamar University, Beaumont, TX 77710*
3) *Department of Chemical and Biomolecular Engineering, University of South Alabama, Mobile, AL 36688*

Abstract

Researchers analysing chlorosilanes in the silicon industry typically use gas chromatography (GC) technology with a chomosorb W packed column to determine chemical concentrations. Industrial experience with the GC technology for measurement of chlorosilane gas concentrations has resulted in less than satisfactory results with line plugging, six-way valve leaks, and damage to sensitive electronics. Due to shortcomings of the GC technology, an industrial Fourier transform infrared (FTIR) spectrometer was calibrated with a custom-built dilution system to study a newly built pilot-scale hydrochlorination fluidized bed reactor. The FTIR provided conversion data on the reactor without the problems typical of the GC analyser. The FTIR data was compared with yield predictions from a hydrodynamic model of the fluidized bed reactor and were found to be in good agreement with less than 4% difference.

Introduction

The silicon industry typically uses gas chromatography (GC) technology with a chromosorb W packed column to determine chlorosilane gas concentrations [1, 2]. A GC machine was used industrially to study silicon chemical vapor deposition (CVD) reactors. CVD reactors pass trichlorosilane (TCS) and hydrogen gas across polysilicon seed rods thereby resulting in the deposition of additional polysilicon. The process produces by-product gases of silicon tetrachloride (STC), dichlorosilane (DCS), and hydrogen chloride (HCl). Chlorosilane gases such as STC, TCS, and DCS are difficult to study as they immediately react with moisture, even moisture naturally occurring in the air as humidity. The use of GC technology in this application led to frequent maintenance problems. Problems resulted from chorosilane polymers such as hexachlorodisilane (HCDS) forming a sticky fouling on piping when condensed. Some sample tubing internal to the machine had an inner diameter of a sixteenth of an inch. The slightest introduction of moisture would result in plugging by the formation of silicon suboxides and silicon dioxide. Furthermore, leaks occurred at a frequency of about every two weeks in the six-way sampling valve. Chlorosilane leaks from the valve form HCl gas. This gas was drawn into the delicate GC electronics through a fan thereby causing failure of the circuit boards and other electronics. The HCl gas reacted with moisture in the air and deposited on the valve as a highly acidic green aqueous solution thereby etching the valve and requiring a rebuild or replacement. The leaking

gas also caused a build-up of silicon suboxides and silicon dioxide on the valve which resulted in damage to the valve parts by abrasion.

The development of a pilot-scale hydrochlorination fluidized bed reactor at an industrial silicon plant required a gas analyser to determine its performance. The process flow diagram of the fluidized bed reactor is shown in Figure 1.

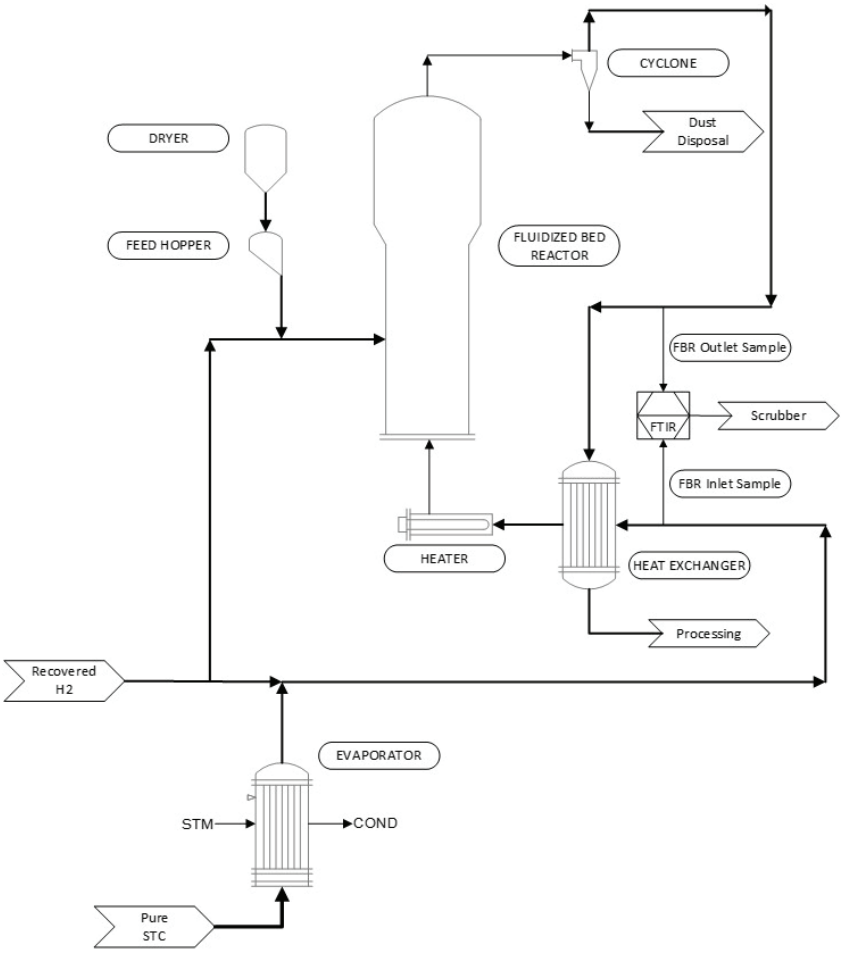


Figure 1: Process flow diagram of the hydrochlorination system.

The reactor produces TCS from STC and metallurgical silicon (MeSi) by the hydrochlorination reaction [3] of Eq. 1.

$$Si_{mg} + 3SiCl_4 + 2H_2 \rightleftharpoons 4SiHCl_3 \quad (1)$$

Mui and Seyferth [4] proposed that the hydrochlorination process takes place by a two-step reaction:

$$SiCl_4 + H_2 \rightleftharpoons SiHCl_3 + HCl \quad (2)$$

$$Si_{mg} + 3HCl \rightleftharpoons SiHCl_3 + H_2 \quad (3)$$

$$(Overall)Si_{mg} + 3SiCl_4 + 2H_2 \rightleftharpoons 4SiHCl_3 \quad (4)$$

Process and Plant Safety [5] states that analytical equipment in severe service conditions may require regular maintenance. Therefore, an analytical machine with few maintenance requirements was desirable. Two machines that had potential to meet the requirement of less maintenance were studied for this reaction: an industrial FTIR and an industrial GC. The industrial GC improved the standard design by protecting the sensitive electronics with a nitrogen purge, contained less moving parts, did not use a six-way valve, and had an airless oven. Most importantly, the industrial GC required calibration on at least a weekly basis. Considering the FTIR, there are no moving parts in the analysed gas stream as the gas simply passes through a flow cell. The FTIR manufacturer specialized in fabrication of systems tolerant to dry HCl gas. The wetted parts: O-rings, flow cell, and windows were designed to tolerate dry HCl gas. The design was given to greater portability and could easily be contained in a cart. The FTIR does not require daily or weekly calibrations. The advantages of the FTIR made it superior to the GC technology and it was chosen to monitor the conversion of the pilot-plant reactor.

The conversion of the hydrochlorination pilot-scale fluidized bed reactor was predicted with a hydrodynamic model and the mathematical predictions were compared with results from an inline FTIR. Kunii and Levenspiel [6] developed a model for fluidized bed reactors based on first principles. The Kunii and Levenspiel [6] model was slightly modified by Colomb *et al.* [7] and was used to predict the conversion in the laboratory-scale hydrochlorination fluidized bed experiments of Cygon [8] and Sill [9] with less than 9% difference between yield predicted and experimentally observed. Given the small difference between experimentation and prediction from the model, the model was considered validated. Since the Kunii and Levenspiel [6] model is based on first principles, the model could be scaled, and was used to predict conversion in the pilot-scale fluidized bed reactor. The model predictions were compared to the measurements made by the FTIR analyser.

FTIR Calibration

Fourier infrared transform spectroscopy (FTIR) with a deuterated triglycine sulfate (DTGS) detector and two 15cm flow cells in series for a total path length of 30 cm was chosen to gather chemical concentration data from the pilot-scale reactor. Two materials were considered for the cell windows, potassium bromide (KBr) and zinc selenide (ZnSe). Both window materials are compatible with dry HCl gas. KBr windows have superior optical qualities; however, they haze when exposed to moisture. Cell windows may be exposed to moisture in the event of failure in the nitrogen purge system, if moisture contaminates the process gas, during transportation of the FTIR system, and when the windows are cleaned. For this reason, ZnSe windows were chosen for the cells. The FTIR was calibrated for the expected concentration ranges of the inlet and exhaust streams of the FBR reactor given the design conditions. The cell temperature

was set to 70 °C at a pressure of 5 psig. A dilution system, as shown in Figure 2, was constructed to calibrate the FTIR for various concentrations of trichlorosilane (TCS) and silicon tetrachloride (STC). Calibrations were also performed with cylinders of calibration gas for the chemicals dichlorosilane (DCS), water, and hydrogen chloride (HCl). The matrix gas for all calibrations was nitrogen because it was readily available and non-flammable. Although the matrix gas for the FBR reactor was hydrogen, the difference in matrix gas is thought to have a minimal impact on the calibration of the FTIR.

A cylinder of either pure liquid TCS or liquid STC was filled in-house. The liquid cylinder was connected to the dilution system and the head space was pressurized by a gas cylinder of research grade nitrogen. The liquid stream from the bottom of the cylinder was connected to a Horiba LVF20PO series liquid mass flow controller (MFC). The MFC is calibrated for either TCS or STC. The maximum flow rate is 0.05 g/min with an accuracy of ±1% of full scale. The appropriate MFC was left in-line while the tubing to the off-line MFC was physically removed. The metered liquid stream was sent to heat traced lines connected to an evaporator cylinder packed with quartz wool.

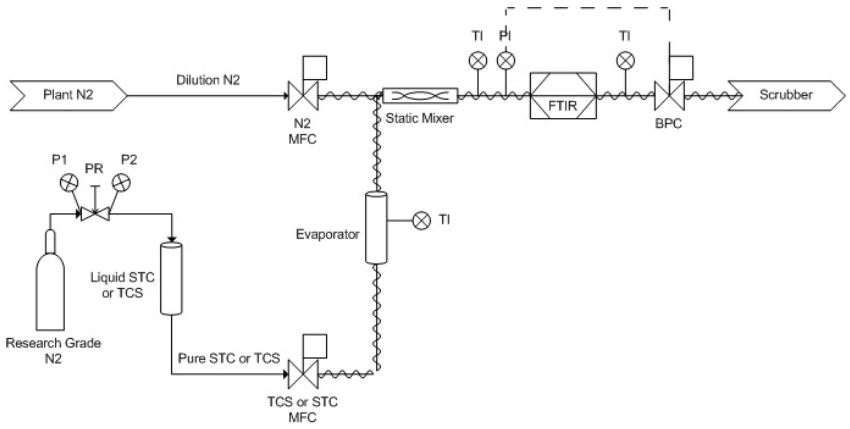


Figure 2: Process flow diagram of dilution system.

Plant nitrogen was metered to a tee where it was mixed with the vaporized chlorosilane gas. Nitrogen was metered by one of two MKS MFCs model 1179A. One unit was constructed for 50 sccm maximum and the other was constructed for 10,000 sccm maximum. The accuracy of the units is ±1% of full scale.

To ensure complete mixing, the combined streams were passed through a Koflo® static mixer model Stratos ¼-21. The blended stream was sent through the analyser and the pressure in the analyser was controlled by an MKS model 148J control valve, model 121A pressure transducer, and model 1249A controller. The pressure transducer has a maximum reading of 2000 Torr and is accurate to 0.5% of the reading. The exhaust gas was then sent to a scrubber for treatment.

The system was thoroughly purged with plant nitrogen before start-up. The general heat tracing for the tubing was set to 120 °C and the heat tracing for the evaporator was set to 150 °C with a single reference point controller. The FTIR cell temperature and

pressure were allowed to stabilize at 70 °C and 5 psig. At this point a scan was taken with the FTIR of the nitrogen sweep. The scan results were checked for moisture contamination. If the moisture was below 20 ppm, a background scan was taken. At this point flow of either TCS or STC was started. The experiment was executed for at least three hours. A data point at a higher concentration could be obtained after the completion of the previous experiment; however, a lower concentration could not be calibrated for unless the system was thoroughly purged with nitrogen again. Calibration points for STC were obtained at 1%, 10%, 15%, 25%, 30%, and 35%. Calibration points for TCS were obtained at 5% and 15%.

Certified calibration gas cylinders accurate to ±5% of stated concentration were also used to generate calibration scans. DCS was calibrated with two cylinders one of 120 ppm and one of 1,000 ppm concentration. HCl was calibrated with four cylinders at 104.7 ppm, 728 ppm, 1,020 ppm, and 9,988 ppm concentration. Water was calibrated with three cylinders at concentrations of 10.2 ppm, 113 ppm, and 460 ppm so that the quality of drying purges could be determined. STC was calibrated by bottle for concentrations of 1,010 ppm and 10,122 ppm. Finally, TCS was calibrated at concentrations of 10 ppm and 1,007 ppm.

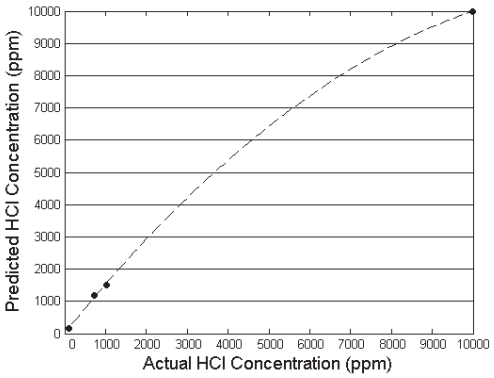


Figure 3: FTIR calibration curve for HCl.

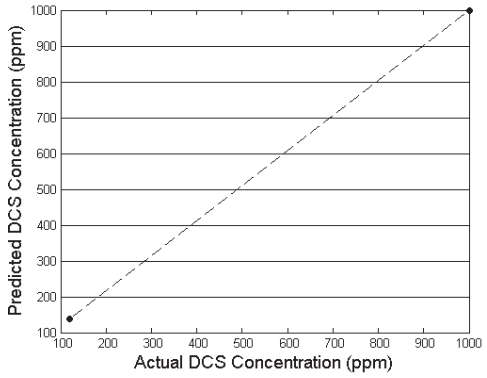


Figure 4: FTIR calibration curve for DCS.

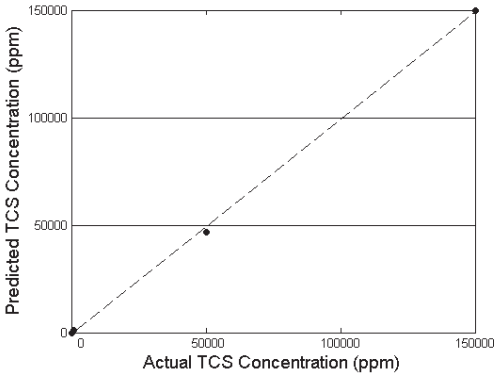


Figure 5: FTIR calibration curve for TCS.

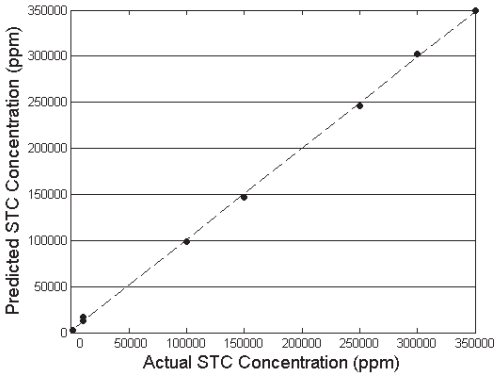


Figure 6: FTIR calibration curve for STC.

The calibration scans were sent to the analyser company to be processed into a method file. The method file was used for these experiments and exhibited a linear trend for TCS and STC, which is a typical result for the DTGS detector of the FTIR. The resulting calibration curves are shown in Figures 3, 4, 5, and 6. The HCl curve in Figure 3 is not linear. This non-linear behaviour was observed on similar FTIR units on-site that were produced and calibrated by another manufacturer.

For concentrations of TCS up to 1000 ppm, the analysis window was set to wavenumbers 2215-2306 cm^{-1} and 747-892 cm^{-1} that include a sharp peak at 2262 cm^{-1} and 810 cm^{-1}. The absorption calibration spectrum of TCS at 1000ppm is shown in Figure 7.

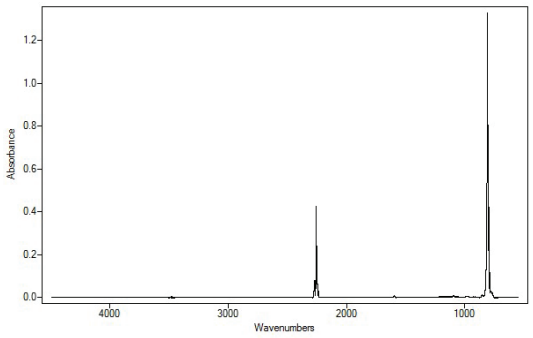


Figure 7: Absorption calibration spectrum of TCS at 1000 ppm.

To prevent peak saturation and to keep a linear calibration, the analysis window for TCS concentrations higher than 1000 ppm was shifted to wavenumbers 1400-1900 cm^{-1} and 900-1140 cm^{-1} , with a sharp peak at 1607 cm-1 and relatively broad peaks at 986, 1063, 1097 cm^{-1}. The resulting absorption calibration spectrum for TCS at 15% concentration is shown in Figure 8.

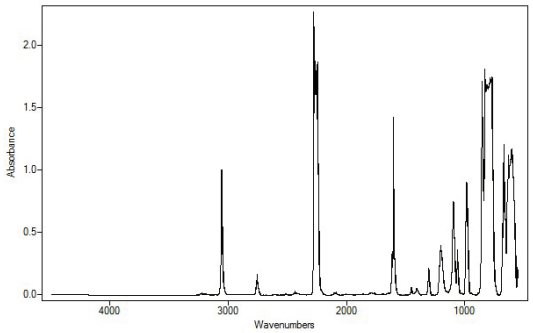


Figure 8: Absorption calibration spectrum of TCS at 15%.

For concentrations of STC up to 1%, the analysis window was set to wavenumbers 930-1120 cm^{-1} with a relatively broad peak at 1045 cm^{-1}. The absorption calibration spectrum of STC at 1% follows in Figure 9.

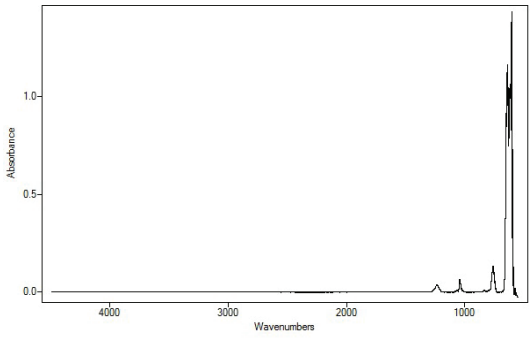


Figure 9: Absorption calibration spectrum of STC at 1%.

As was necessary for TCS, the STC analysis window was shifted to prevent peak saturation and to maintain linearity. For concentrations greater than 1%, the analysis window was set to wavenumbers 1048-1142 cm^{-1} with a peak at 1065 cm^{-1}. The resulting absorption calibration spectrum for STC at 35% concentration is shown in Figure 10.

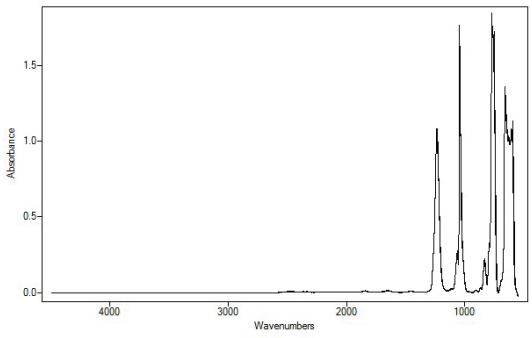


Figure 10: Absorption calibration spectrum of STC at 35%.

The analysis window for DCS was chosen as wavenumbers 930-1140 cm^{-1}, which contained a split peak at 947 cm^{-1} and 962 cm^{-1}. HCl had an analysis window set to wavenumbers 2551-3100 cm^{-1} for concentrations up to 1020 ppm. The analysis window contained the peaks typical for HCl; 22 large peaks separated by about 18 cm^{-1}. At a concentration of 1% HCl, four large peaks were selected near the end of the signal at wavenumbers 2510-2682 cm^{-1} to prevent signal saturation and to maintain a predictable fit of the data. The calibration spectrums of DCS and HCl are found in Figures 11 through 13.

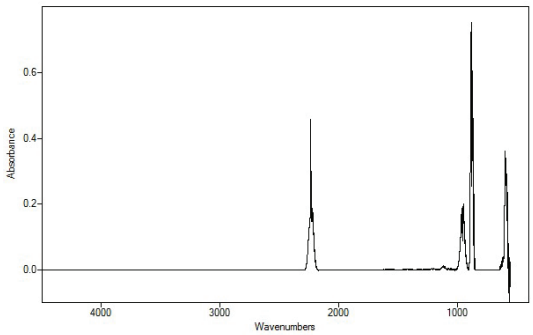


Figure 11: Absorption calibration spectrum of DCS at 1%.

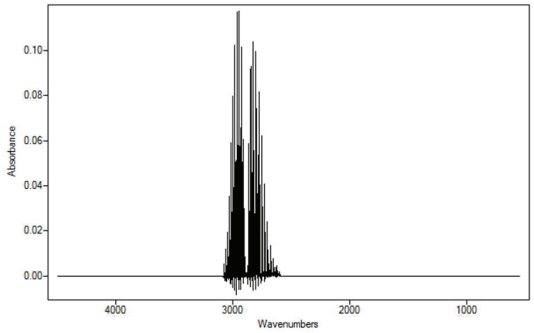


Figure 12: Absorption calibration spectrum of HCl at 1000 ppm.

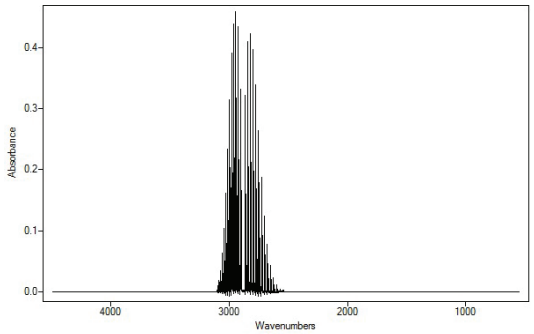


Figure 13: Absorption calibration spectrum of HCl at 1%.

With the newly calibrated method file, the FTIR was ready for service and was placed in-line with the pilot-scale FBR reactor.

Reactor Analysis

An experimental test plan was developed for the pilot-scale FBR reactor to test conversion while varying important process conditions like, inlet gas temperature, inlet gas flow rate, and the ratio of hydrogen to STC. The test plan is detailed in Table 1.

Table 1: Experimental Test Plan.

Experiment	Temp Heater ($^{\circ}C$)	Bottom Press (PSIG)	Molar Ratio (H_2/STC)	W_{Cu} (wt%)	u_0 (m/s)
1	572	111	1.53	1	0.155
2	562	120	1.20	1	0.125
3	574	111	1.51	1	0.154
4	558	86	1.51	1	0.188
5	558	111	1.39	1	0.145
6	423	117	0.819	1	0.091
7	477	116	0.813	1	0.098

The theoretical yield of TCS for each experiment was predicted by the mathematical hydrodynamic model of Colomb *et al.* [10] which is based on a modified version of the Kunii and Levenspiel [6] fluidized bed reactor model. As the model information is available from Colomb *et al.* [10], it is only briefly discussed. The mathematical model considers the fluidized bed as a bubble phase surrounded by a cloud phase traveling through the bed emulsion as shown in Figure 14.

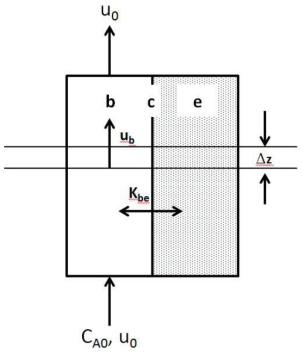


Figure 14: Phases and mass transfer in the bubbling fluidized bed for the hydrochlorination reaction.

The reactant gas (STC) enters the reactor through the distributor as small bubbles that grow in size as they travel up the reactor. There is little reaction in the bubble phase as the fraction of solid reactant there is sparse. The gas must then pass through the bubble to a cloud under a mass transfer resistance (∂K_{be}). The bulk of the reaction occurs in the emulsion phase where the reactant gas is in contact with a higher fraction of solids. The change in concentration of STC, hydrogen, and TCS (C_{ib}) is described by Eq. 5

$$-u_0 \frac{dC_{ib}}{dz} = f_b \varrho_{si} v_i (\gamma_{Fe} r_{Fe_x Si_y} + \gamma_{Cu} r_{Cu_x Si_y})_b + \delta K_{be} (C_{ib} - C_{ie}) \qquad (5)$$

with the subscript *i* denoting the chemical species STC, hydrogen, or TCS. The mass transfer of chemicals from the bubble phase to the emulsion phase is set equal to the reaction that occurs in the emulsion as shown in Eq. 6.

$$\delta K_{be}(C_{ib} - C_{ie}) \cong f_e \varrho_{si} v_i (\gamma_{Fe} r_{Fe_x Si_y} + \gamma_{Cu} r_{Cu_x Si_y})_e \quad (6)$$

The mass transfer rate is a strong function of bubble size. The size of the bubble along the reactor height is solved by a subroutine based on Werther's [11] model as described by Eq. 7.

$$\frac{d}{dz} d_b = \left(\frac{2\epsilon_b}{9\pi}\right)^{1/3} - \frac{d_b}{3\lambda u_b} \quad (7)$$

The reaction kinetic data were developed by Becker [12] who also presented an equation for the calculation of yield for the reaction as shown in Eq. 8.

$$Y_{SiHCl_3} = \frac{3\dot{n}_{SiHCl_3,OUT} * 100}{4\dot{n}_{SiCl_4,IN} + \dot{n}_{HCl,IN}} \quad (8)$$

The yield available from the mathematical model prediction was compared with the yield calculated by FTIR analysis and is presented in the following section. The calculation methodology with the FTIR results is available from Colomb et al. [10].

Results

The predicted yield of the pilot-scale fluidized bed reactor, by the hydrodynamic model was compared with the yield provided analytically by the FTIR. The results of the study are shown in Table 2 and Figure 15.

Table 2: Pilot-Scale Reactor Results.

Exp	Temp Heater ($^{\circ}C$)	Bottom Press (PSIG)	Molar Ratio (H_2/STC)	x_{HCl} (mol%)	W_{Cu} (wt%)	u_0 (m/s)	F_{TCS} (Norm)	Y_{TCS} (mol%)	Y_{TCS} Pred (mol%)	Difference %
1	572	111	1.53	1.7	1	0.155	1.00	20.3	19.2	5.44
2	562	120	1.20	2.8	1	0.125	0.866	17.7	18.0	-1.77
3	574	111	1.51	1.8	1	0.154	0.948	19.4	19.2	0.922
4	558	86	1.51	1.8	1	0.188	0.975	19.9	18.5	6.88
5	558	111	1.39	2.0	1	0.145	0.899	18.4	18.3	0.064
6	423	117	0.819	4.6	1	0.091	0.512	10.3	11.0	-6.59
7	477	116	0.813	4.6	1	0.098	0.676	13.7	13.6	1.11

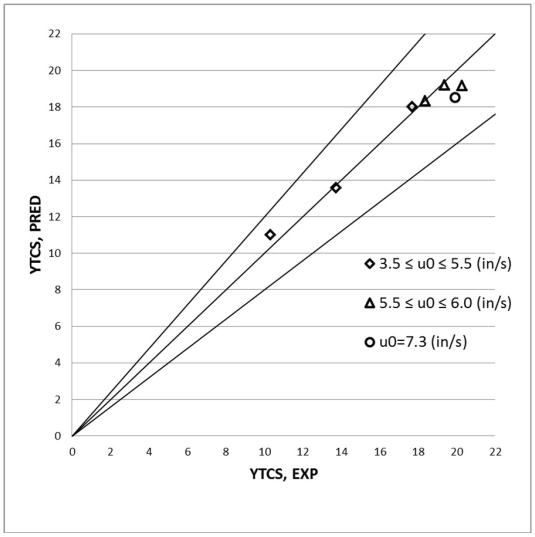


Figure 15: Parity plot of pilot-scale hydrochlorination experimental yield vs predicted results. Solid black lines show boundary of ±20% percent difference

The results are in excellent agreement with an average difference between yield predicted by the mathematical model and the yield as determined by FTIR of less than 4%. The calibration of the FTIR remained reliable over three years' time. It should be noted that the laser was not changed in the period of analysis. The problems of plugging and maintenance typical of the GC machine were not present with the FTIR. FTIR technology has been adopted as a standard for chlorosilane concentration measurement for industrial applications at the polysilicon plant.

Conclusions

An FTIR gas analyser was calibrated for the detection of chlorosilane gases. The technology was investigated as an alternative to the industry standard of using GC technology. The FTIR provided reliable results as checked against mathematical predictions from a fluidized bed model of Colomb et al. [10] developed for a pilot-scale hydrochlorination reactor. The experimental tests on the pilot-scale reactor spanned over three years' time. In this time, the FTIR required no recalibration. There were no issues with leaks or plugging of the unit. The FTIR technology was considered superior to the GC technology alternative and has been adapted as the standard concentration measurement system for chlorosilane gases in the production areas of the polysilicon plant.

Notation

C	component concentration, mol^1m^{-3}
d	diameter, m
d_b	bubble diameter, m
f	volume of solids per volume of bed
K	gas interchange coefficient, s^{-1}
$\dot{n}$	molar flow rate, mol^1s^{-1}
r	reaction rate, $mol^1s^{-1}kg_{cat}^{-1}$
u_0	superficial velocity, m^1s^{-1}
u_b	average bubble velocity, m^1s^{-1}
v	stoichiometric coefficient
Y_{SiHCl_3}	yield of TCS, *see Eq.8*, %
z	reactor height, m

Greek letters

δ	bed fraction in bubbles
ε	fraction of voids in the bed
ε_b	local bubble gas holdup of Werther [11] correlation
γ	fractional weight of catalyst
λ	average duration of life of a bubble, s
ϱ	density, kg^1m^{-3}

Subscripts

b	bubble phase
Cu_xSi_y	copper catalysed reaction
e	emulsion phase
Fe_xSi_y	iron catalysed reaction
i	component (*STC*, H_2, *TCS*)
IN	actual feed stream
mg	metallurgical grade silicon
OUT	product stream
Si	silicon

References

1. Mui, J., *Investigation of the Hydrochlorination of $SiCl_4$*, Final report., JPL Contract 956061, (1983).
2. Li, K.Y., Peng, S.H., and Ho, T.C., *Hydrochlorination of Silicon in a Fluidized-Bed Reactor*, AIChE Symposium Series, pp.114-125, Vol. 84, No. 262, (1988).
3. Mara, W.C., Herring, R.B., and Hunt, L. P., *Handbook of Semiconductor Silicon Technology*, Noyes Publication / William Andrew Publishing, Norwich, NY (1990).
4. Mui, J., and Seyferth, D., *The Hydrogenation of $SiCl_4$*, Final report., JPL Contract 955382, (1981).
5. Hauptmanns, Ulrich, *Process and Plant Safety*, Springer, New York, NY (2015).
6. Kunii, D., and Levenspiel, O., *Fluidization Engineering*, 2nd ed., Butterworth-Heinemann, Newton, MA (1991).
7. Colomb, M. A., Palanki, S., and Sylvester, N. D., *Modeling the Hydrochlorination Reaction in a Laboratory-Scale Fluidized Bed Reactor*, Powder Technology, pp. 242-250, Vol. 292, (2016).
8. Cygon, P., *Reaction Studies for the Hydrochlorination of Silicon in a Laboratory Fluidized Bed System*, Diss., U of Cologne, (1999).
9. Sill, T., Buchholz, S., Weber, R., and Mleczko, L., *Thermodynamic, Mechanistic and Reaction Engineering Aspects of Hydrochlorination of Silicon*, Silicon for the Chemical Industry V, Trondheim, Norway (2000).
10. Colomb, M. A., Palanki, S., and Sylvester, N. D., *Experimental verification of scalable model for the hydrochlorination reaction in a pilot-scale fluidized bed reactor*, Powder Technology, pp. 989-998, Vol. 301, (2016).
11. Werther, J., *Scale-up Modeling for Fluidized Bed Reactors*, Chem. Eng. Sci., pp.2457-2462, Vol. 47, No. 9-11, (1992).
12. Becker, F., *Modeling and Simulations of Hydrochlorination of Silicon to Trichlorosilane for the Development of a Technical Fluidized Bed Reactor*, Diss., RWTH Aachen U, (2005).

Literature Review
The Effect of Minor Elements on the Production of Trichlorosilane by Direct Chlorination

Sean Gaal, Ryan Schafer and Scott Stachowiak
Dow Silicones Corporation, 2651 Salzburg Rd, Midland MI 48640, USA

Abstract

Trichlorosilane (TCS) is an important raw material used in the production of polysilicon, a range of silicones and fumed silica. It can be produced in a reactor at suitable conditions from metallurgical silicon and hydrogen chloride gas, with various by products including silicon tetrachloride and disilanes. The yield of TCS from these processes is critical, but is reported to be heavily influenced by just about all of the available operating parameters, such as temperature, reactor type, reactor scale, silicon composition, catalyst and to a lesser extent, operating pressure. This paper reviews the operating parameters with a focus on the silicon impurities described in literature, highlighting common themes and contradictions.

Introduction

The production of trichlorosilane (TCS) is inherently simple, it is the exothermic reaction of hydrogen chloride and silicon. However, there are many interacting factors which influence the process, such as the chemical composition and particle size of the silicon, catalysts, reactor type, geometry and scale, as well as the temperature and pressure of the reaction. The combination of these factors determines the productivity and yield of TCS relative to other chlorosilanes, principally silicon tetrachloride (STC).

The literature investigating the production of TCS is limited. Data is often provided from small laboratory tests that sometimes have brief references to industrial scale operations, although occasionally some industrial information is provided.

When investigating a process, such as the production of TCS from silicon and hydrogen chloride, it is important to assess how well the laboratory model replicates the larger industrial process. How well do the laboratory tests, which are small scale models, reflect the actual industrial production of TCS? Do the results correlate?

This paper discusses the reaction hydrogen chloride with various silicon compositions for the production of trichlorosilane.

Reactor Type

Literature describes several types of reactors for the production of TCS, including fixed bed reactors, vibrating fixed bed reactors, stirred bed reactors and fluidised bed reactors (FBR) (1-3), however, it is stated (4) that industrially this reaction is always performed in a fluidised bed reactor. In contrast, published data is often from laboratory scale tests, where a ranged of fixed beds and occasionally small fluidised beds are used.

A large industrial fluidised bed reactor is not chemically, thermally or physically uniform, while a fixed bed reactor such as those often used in laboratory tests are significantly more uniform. They can be considered a small cell within a larger industrial process, but care must always be taken when extrapolating.

Occasionally small scale tests with equipment described as fluidised beds are also employed, such as described by Hoel et al. (2, 3), who published a range of results using two different reactors:

1. A quartz tube embedded in an aluminium block heated to 350 °C or 500 °C, with a 15 °C increase for the actual reaction due to the exotherm, using 1 gram of silicon with a particle size of 180 to 250 µm which was reacted with a mixture of 10 ml/min HCl(g) and 10 ml/min Ar. Results were measured with a GC, with selectivity defined as TCS/(TCS+other silanes).
2. A steel tube embedded in an aluminium block heated to 325 °C, producing a temperature of 340 °C in the reactor, using 5 grams of silicon, 180 to 250 µm. The gas mixture was 280 ml/min HCl and 20 ml/min Ar. Dimensions or details of the test equipment are limited, except that there was a continuous addition of silicon powder to maintain a total of 5 grams silicon in the reactor. Selectivity is measured with a GC. Reaction pressure was 1.15 barg.

These laboratory tests are not unusual, but it should be noted that Hoel et al. (3) claims a temperature range of 250 – 1100 °C and a pressure of 0.5 to 30 atmospheres, but all tests were performed between 340 °C and 515 °C, at atmospheric pressure or slightly above, in a fixed bed, without vibrations as employed by some researchers (5) or in a small laboratory fluidised bed. The results are reported as a function of time, while others sometimes (6) report only a single value for the selectivity. In addition, Hoel et al. (2, 3) is diluting the reactive HCl gas with argon, although the second test has a lower proportion than the other two, the purpose of this is not explained. Thermodynamically, this will have a small effect (1), but it changes the gas dynamics. It would have been helpful if they had compared the fixed bed, laboratory continuous fluidised bed and industrial process, but it is interesting that the later work (2) only references tests in the laboratory continuous fluidised bed.

Many authors have investigated the role of iron in the reactor (5-9), so the use of iron as the reactor vessel in the second method above should be considered with caution. Coleman (10) states that industrial reactors for TCS production are made from steel, but the larger size of these reactors make the wall less likely to interact significantly with the silicon, as could easily be the case for such small scale tests.

The reader should also consider that if fluidised bed reactors are used exclusively on an industrial scale (4), but the majority of reported information is from a scale of grams, how comparable are these relationships? This is obviously problematic, as an industrial fluidised bed is expected to have very different circulation than a reactor with 5 grams, such as described above (2, 3). It would be interesting to have more details of the laboratory fluidised bed, to understand the fluidisation regime, if the particles are circulating or if they are maintaining their relative location, but especially how it correlates to large scale performance.

Wakamatsu et al. (8) gives some guidance, stating that “It is often observed that the TCS selectivity in the industrial reaction is usually lower than in the experimental one, and that the TCS selectivity in the industrial reaction decreases if the reacted residue particles are not withdrawn successively from the reactor.” Andersen et al. (7) also noted that in the laboratory tests “TCS selectivity was as high as 99.2% … in the reactor studies. This is very high selectivity compared to what is obtained in industrial processes, where the usual selectivity is around 80-90%”. Results that differ from the process they are modelling by such a large degree need to be carefully studied before reaching conclusions.

The outcome of these comparisons is that small scale tests are often extrapolated to determine operating conditions for optimal production of TCS, but caution must be used when drawing conclusions from such small batch tests, sometimes with inert gases and often at higher temperatures. It is assumed that by adjusting different parameters, it is feasible to produce examples and data for nearly any purpose. Presumably, the value of these tests are when they are used at industrially relevant conditions, validated against real processes, generally for screening purposes.

This is not a criticism of the various published works, but instead an indication of the care that must be exercised when translating and extrapolating results from extremely small scale physical models. The often quoted aphorism “All models are wrong but some are useful” (11) should be considered, as the published data provides no comparison or validation of the laboratory data with the industrial process.

Particle Size

The particle size range reported in literature for laboratory scale synthesis of TCS is from 20 µm - 5000 µm (4, 6). Laboratory tests are often in the range of 150 µm – 200 µm. Noort et al. (12) states that the chemical industry requires the silicon to be ground from 500 µm to 1000 µm, with all material below 75 µm removed. Parous et al. (13) and Portal (14) note that material less than 45 µm is removed after grinding, either for safety or fluidisation benefits. Coleman (10) states that an average particle size of 160-180 µm is desired, with a maximum size of 400 µm and minimal material below 50 µm, removing the lower size range as it has poor selectivity. Kohno et al. (15) indicates a preferred particle size for an industrial process of 74 µm to 300 µm, indicating that the commercial operation at that time was operating in the range most often investigated in small scale tests.

Laboratory tests by Lobreyer et al. (6) showed that the reaction between silicon and hydrogen chloride starts at lower temperatures for 50-100 µm particles compared to 315-400 µm particles, but that once the reaction started it was vigorous and consumed most of the HCl, as can be expected for an exothermic system. They also reported the selectivity of different silicon compositions and particles sizes, with no clear indication of a preferred particle size between 50 µm and 500 µm.

As shown from these references, there is little agreement of the optimal size, except that it is noted that fluidisation is difficult when using either very fine or very coarse particles. The only clear conclusion that can be drawn is that the optimal particle size for a TCS reactor is dependent on the specific reactor, the chemical composition of the

silicon and catalysts present, the operating temperature, reactor design and size, as well as many other factors.

Reactor Operating Conditions

Temperature

The reactor temperature distribution will have a very strong influence on the synthesis of TCS, while laboratory tests, even laboratory scale fluidised bed reactors, will be relatively isothermal. Goebel et al. (16) discussed that it was beneficial to control the temperature distribution of the reactor, such that the reaction was 300 – 400 °C, but that the temperature should drop to less than 250 °C at the top of the reactor.

Reactor conditions are regularly reported (or claimed in patents) over a wide range, often from 250 – 1100 °C and 0.5-30 atm (2, 3, 17, 18) with some early work involving copper from 200 – 300 °C (19), but most reported data concentrates on the range of 250 – 400 °C, with laboratory tests generally above 340 °C.

Kohno et al. (15) broadly discusses industrial conditions, reporting that the selectivity of TCS increases at lower temperatures, plotting a selectivity of 89 – 91% over the range of 285 – 305 °C. Details of the industrial reactor are not disclosed, but corresponds to other sources claiming an operating temperature of 280 – 320 °C (20) or simply above 300 °C (16), with a focus on a lower temperature above the reaction zone. This is also interesting, if a lower temperature in the reactor is important, then presumably there must be a role. As time has progressed, the range of temperatures claimed in patents has increased dramatically, with most recent patents claiming from 250 °C to 1100 °C (2, 3, 17, 18).

The temperature required for the reaction with high purity polysilicon varies dramatically. Lobreyer (6) reported that polysilicon started to react at 320 °C, while Samori et al. (9) found that polysilicon did not react with hydrogen chloride, even at 650 °C. Ehrich et al. (5) found that in laboratory tests the reaction initiated at around 300 °C, but that with the addition of copper 240 °C was possible, which is similar to the results from Wagner (19) for copper additions.

Samori et al. (9) published results as low as 240 °C with a sample of metallurgical silicon. Since there are examples of laboratory tests in the industrially relevant range of 285-305 °C (15) or 300 °C (1, 10, 16), it is not clear why so many laboratory tests are performed at 340 °C and as high as 515 °C, which is recognised in the literature to be significantly higher than industrially relevant for this reaction (1).

When considering temperature, the theme industrially is to operate at the lowest possible temperature with sufficient reactivity to sustain the reaction, which will provide the highest selectivity of TCS. The laboratory tests also confirm this trend, even if they are generally performed at significantly higher temperatures than industrially relevant.

Pressure

The pressure mainly influences productivity (2, 10) by increasing the mass of hydrogen chloride that can be added to the reactor while maintaining the required fluidisation, although Andersen (1) discusses that higher selectivity is expected when considering Reaction (1) through Le Chatelier's principle.

$$Si_{(s)} + HCl_{(g)} = SiHCl_{3(g)} + SiCl_{4(g)} + H_{2(g)} \quad (1)$$

Silicon Composition

The production of metallurgical silicon (MG-Si) is extensively described in literature, Schei, Tuset and Tveit (21) is the most regularly cited. The most important aspects of this process for the production of TCS is the chemical composition, which is controlled by the selection of raw materials and to some extent the refining process. The most common impurities in metallurgical silicon are Fe, Al, Ca, Ti, Mn, V, Ni, Cr, P and B, of which only the aluminium and calcium can be removed by oxygen refining. Twenty years ago, Ehrich et al. (5) stated that there were very few reports that described the "role of individual silicon impurities on the reactivity and selectivity" and although there are publications since then, they are primarily a few conference papers and patents describing results from small scale tests.

There is a lot of focus in the literature on not just the elements present, but the phases and way they are added. For example, individually iron and aluminium added to the reactor increases reactivity, but have no or minimal effect on selectivity, while together as a Al-Fe-Si ternary phase it increases the reactivity and reduces the selectivity (1), at least at higher temperatures. There are catalytic effects in the synthesis of TCS, both positive and negative, these will be discussed below, individually and in combination where possible.

Polysilicon

When comparing the role of different elements in the process, it is common to include polysilicon in the testing as a basis for comparison. However, the results are not always consistent, which considering the simplicity of the system should raise concern with the test methods. In this case, the polysilicon can easily be commercially procured, so the purity should be extremely high. The process to prepare the polysilicon, sometimes melting, then grinding and classify the silicon, combined with the reactor materials of construction and cleanliness must account for the different results. This strongly suggests that the smallest change in experimental procedure could result in large variations in the results.

Lobreyer et al. (6) showed that polysilicon had a lower reactivity, in general agreement with others, requiring a higher temperature to start reacting than metallurgical Si under the same conditions, but it always had the highest selectivity of TCS at all temperatures and silicon particle sizes. When using a very fine particle size of 50 – 100 µm the reactivity improved, with the reaction starting as low as 310 °C, while larger particles required higher temperatures to initiate.

Ehrich et al. (5), following the work of Lobreyer et al. (6), published that 360 °C was required to initiate the reaction with polysilicon, using a coarser silicon particle size. Andersen et al. (7) found similar results, with 370 – 385 °C required to initiate the reaction, again with a more realistic particle size, as suggested by literature (1, 10, 12-15).

Samori (9) found that polysilicon did not react with hydrogen chloride at all, even at temperatures up to 650 °C, possibly there were more impurities present for other investigations or the polysilicon was more heavily oxidised, but this again highlights the variations and sensitivity of the test methods.

Catalysts

Suitable catalysts can also be added directly to the reactor, as has been well recognised since the initial commercial production of chlorosilanes, with examples of suitable catalysts such as "nickel, tin, silver, copper, antimony, manganese and titanium" (19) listed as early as 1950, with clearer examples published in the following years. There are several patents discussing the use of catalysts in TCS production, but that should be balanced by conclusions that additional catalysts are not required (10), instead the required elements are already available in metallurgical silicon, it is only necessary to control them at the required concentrations and combinations. Harder et al. (20) found that the impurities that accumulate in a reactor are beneficial to the reactor selectivity. By recycling a proportion of the contact mass at the end of a campaign, it is possible to restart the reactor with higher selectivity. This indicates that small scale laboratory experiments may have significantly lower concentrations of impurities than an operating reactor, depending on how long the reactor is operated, calling in to question the validity of short laboratory tests compared to industrially relevant conditions.

Silicides

Acker et al. (22) discussed the role of silicides in the synthesis of TCS, using a Calvert DSC they were able to show that the TCS yield decreased in the following order:

$$Si > NiSi_2 > FeSi_2 > NiSi > FeSi > Fe_2Si > Ni_2Si$$

Of course, the reaction of disilicides, $NiSi_2$ and $FeSi_2$, yields monosilicides, NiSi and FeSi, respectively. Buseth et al. (23) studied the reactivity of different phases with hydrogen chloride, concluding that $FeSi_2$ was one of the least reactive phases, while Al_3FeSi_2 was the most reactive studied, which agrees well with Andersen (1) who found that the combination of iron and aluminium was important, while individually they had little effect.

Most elements present in the TCS reactor will be present as either silicides or chlorides, besides the occasional slag particles present as oxides (24).

Iron

Iron is the largest impurity in metallurgical silicon, essentially all of the iron that enters the furnace is found in the metallurgical silicon. For any industrially relevant production of TCS, metallurgical silicon is the only commercially available source of silicon and it is not practical to reduce the concentration of iron below around 0.3% (21), due to the

cost associated with high purity raw materials and production limitations. Typical concentrations of iron in metallurgical silicon used for TCS production is reported to be 0.4% to 0.5% (10), but studies have explored metallurgical silicon up to 2.6% iron (9).

Andersen (1) found that iron had a small negative effect on the reactivity and slowly reduced the selectivity of TCS as temperature increased, but that in combination with aluminium there was a much larger negative effect which increased with temperature. Interestingly, when Andersen extrapolated the combined effect of iron and aluminium down to 300 °C, a midpoint in the reported industrial temperature (1, 10, 12-15), the effect on selectivity was negligible. Ehrich (5) also reported that iron and aluminium had little effect on the reactivity.

Samori (9) and Wakamatsu (8) both found that iron chloride reduced the selectivity of TCS, while also noting that it is formed when iron in the metallurgical silicon reacts with hydrogen chloride, so it will always be present in the reactor. If $FeSi_2$ has a very low reactivity, as reported by Buseth et al. (23), the discrepancy between the effect of iron and iron chloride may be explained by the time required for the iron to be chlorinated.

A limitation on high iron silicon was also discussed by Kohno et al. (15), where they discussed the accumulation of a residue inside the reactor predominately Ca, Fe, Si and Cl. During the reaction silicon is chlorinated and leaves as a gas, but many of the other elements form solid chlorides that may have trouble leaving the reactor. Even elements that may have minimal effect on the reaction, need to be removed to maintain reactor volume.

Aluminium

Unlike iron, it is possible to oxidise the aluminium in silicon during the refining process (21), removing it to the slag phase. In this way, it is economically viable to produce a range of aluminium concentrations. There is a wide interpretation of the optimal aluminium concentration and role within the process.

Samori (9) found that aluminium increased selectivity; an aluminium concentration of 0.561%, the highest they tested, produced the highest TCS selectivity of all Si samples tested. Wakamatsu (8) also found that aluminium improved selectivity, especially when iron chloride and phosphorus were high, mitigating the negative impact of other impurities. When tests are published showing the impact of various elements, it is important to consider all of the additional elements and phases in the silicon, as this can easily mask the actual result.

Andersen (1) found that aluminium by itself had minimal effect on the selectivity, but that with iron there was a large effect at higher temperatures. Interestingly, Andersen also suggested that by extrapolating the effect of iron and aluminium back to the industrial operating temperature of 300 °C, that the effect on selectivity is minimal.

Calcium

Calcium is relatively easily removed through refining metallurgical silicon. Andersen (1) found that calcium forms calcium chloride and reduces the selectivity by blocking

the surface of the silicon, although it was also found that $Al_6CaFe_4Si_8$ increased selectivity. This again shows that it is not the element that is critical, but the phases in the process that influence the selectivity.

Titanium

Buseth et al. (23) found that all titanium phases studied had a very low reactivity, while Andersen (1) reported that it had no effect on either the reactivity or selectivity, alone or in combination with iron, up to 0.8% titanium, but that $TiSi_2$ itself had a very high reactivity.

Sobota and Alber (17) claim that phosphorus above 30 ppm reduces the TCS selectivity, but that by adding titanium this effect is reduced at a temperature of 360 °C. There is mixed data for the effect of small increases in phosphorus, such as the data presented by Hoel et al. (3), even if that was not the focus of the patent, so it is difficult to understand if titanium is able to suppress a problem, especially when there is little data supporting the existence of the problem at these concentrations (9).

Phosphorus

Sobota and Alber (17) claim that phosphorus above 30 ppm reduces the TCS selectivity, as discussed above for titanium. Hoel et al. (3), in a patent focused on chromium additions, tested silicon with phosphorus from 17 to 150 ppm, with all of the other impurities equal (Samples B and F). The low phosphorus (17 ppm) sample was tested at 340 °C with 89% TCS, while the high phosphorus sample (150 ppm) was tested at 365 °C with 89% TCS. This indicates that at moderate phosphorus levels, even at a slightly higher temperature, phosphorus may actually enhance TCS selectivity, as it should be remembered that all researchers have found that selectivity decreases as temperature increases.

Wakamatsu et al. (8) found that adding 0.2% red phosphorus in the presence of iron reduced TCS selectivity by 22%, but that adding just 500 ppm phosphorus the effect was minimal. They also noted that the effect of phosphorus at high concentrations could be mitigated to a large extent by the addition of modest amounts of aluminium.

Copper

The use of copper as a catalyst promotes the reactivity of silicon (19), with the reaction initiating as low as 200 °C. Ehrich et al. (5) investigated the effect of adding 0.5% copper to either pure silicon or metallurgical silicon increases TCS selectivity. However, when comparing the TCS selectivity with normal metallurgical grade silicon, as reported by other researchers, there is little difference at 300 °C. Hoel et al. (2) claims a copper concentration of 40 ppm – 10,000 ppm in the metallurgical silicon enhances selectivity, but the data presented does not support this claim, except with the addition of barium. Copper is shown to enhance the reactivity, but TCS selectivity is the most critical.

Chromium

Hoel et al. (3) claim that by adding 50 to 1000 ppm of chromium at 515 °C it is possible to increase the selectivity of TCS by 15-20%, but it is not clear why the tests are

performed at such a high temperature relative to the practical industrial operating reactor temperatures. At a more moderate temperature of 340 °C, the increase was only 2.5-3.0% when 2 wt% chromium was added to the reactor half way through the test. Assuming that these are optimal examples and adapting a suggestion from Andersen (1) to extrapolate the effect of chromium back to 300 °C, based on the above data, it is possible to produce Figure 1. It can be seen that when the available data, linearly extrapolated to 300 °C, results in a slight negative enhancement of the selectivity (reduction in selectivity). This illustrates the importance of data at the actual temperature of interest and how experimental data at high temperatures can be used to indicate an improvement that may not have a significant impact at the industrially relevant temperature.

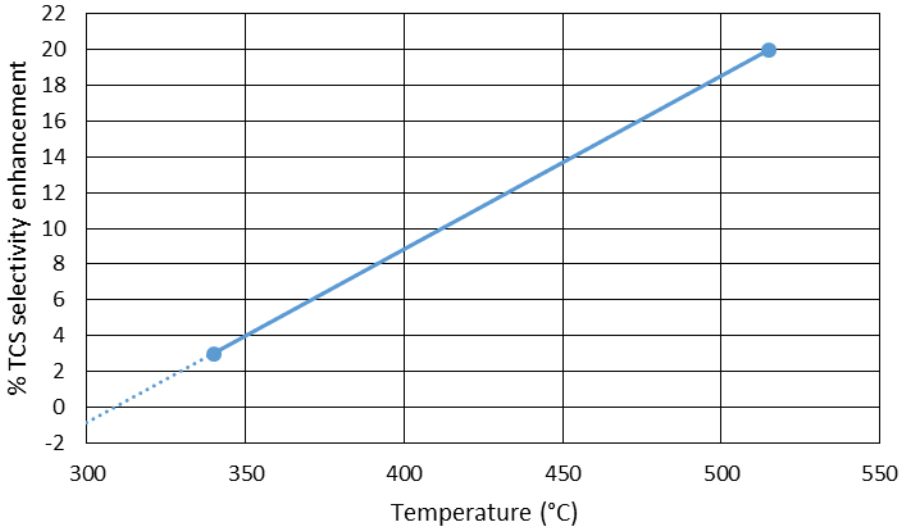


Figure 1 – The effect of chromium additions as a function of temperature, extrapolated back to 300 °C (3).

Manganese

Andersen et al. (18) claim that manganese in metallurgical silicon above 100 ppm reduces TCS selectivity, although again all tests were performed at elevated temperatures. Interestingly, the results presented show the hydrogen chloride conversion rather than the TCS selectivity for most of the samples, with essentially no difference except that the % Si converted was less when a high concentration of manganese was present. The reported tests were performed with up to 14,000 ppm manganese, but the claim is that manganese should be below 100 ppm for high selectivity. Interestingly, the presented data indicates essentially no difference between 930 ppm and 10,000 ppm manganese. Possibly more data exists, but most of the data presented focuses on a loss of reactivity, rather than the selectivity.

The last figure in the patent (18) shows the effect of adding manganese at discrete times. Each addition is equivalent to about 3,000 ppm of manganese, significantly higher than the proposed limit of 100 ppm. The selectivity drops after each addition, but it is not

until significantly after the second addition that the results deviate significantly from the control, where no manganese was added. Even then, the final result with a total of 1.8% manganese was a loss of only 3% selectivity. These results were also generated at 350 °C, significantly above industrially interesting temperatures and known to significantly increase any possible influence on selectivity. It does not seem that there is sufficient data presented to support the claim that manganese should be below 100 ppm for optimal TCS selectivity at 300 °C, which is reflected in the current status of the patent.

Nickel

Nickel was the first catalyst listed by Wagner (19) in 1947, however, it seems that this was not supported by data. Subsequent work has found that although nickel silicides may be reactive (22, 25), it actually reduces the TCS reactivity and selectivity (1).

Barium

Hoel et al. (2) claim that barium is able to improve TCS selectivity with additions as low as 40 – 50,000 ppm to the silicon, with a target of at least 250 ppm barium accumulated in the reactor. The examples are very limited, all at 340 °C, which as discussed is higher than literature states is the industrial operating temperature (1, 10, 12-15). The patent examples indicate that small additions of copper provide no benefit, but still claims 40-10,000 ppm copper as a benefit, both with barium and by itself.

Conclusion

The effect of minor elements on the production of trichlorosilane has been investigated in small scale laboratory equipment by a handful of groups, but there is very limited data published that compares these results with industrial production.

The small scale tests show that the source and combination of impurities have a large influence on the results. The phases of each minor element is critical, with iron and aluminium individually having very limited influence on the process, but together, especially at higher temperatures, significantly reduced the trichlorosilane selectivity. However, as the temperature was reduced towards the industrially reported temperature of 300 °C the effect was minimised. Similar effects were noticed with phosphorus and iron chloride, which both reduced the selectivity, but when aluminium was added to the process the effects were mitigated.

It is also clear from the available literature that the laboratory test method has a large influence on the results. The simplest test would be when using polysilicon, which essentially contains no impurities, however various researchers investigating polysilicon reactivity and selectivity were not in agreement.

Laboratory tests have shown large differences in the results as a function of temperature, however, they are almost exclusively performed at significantly higher temperatures than the industrial process, without any published comparisons.

To fully appreciate the effects of different minor elements it is necessary to couple these small scale tests with larger scale industrial operations.

References

1. Andersen GK. *Reactor Studies of the Trichlorosilane Process*: Norges Teknisk Naturvitenskapelige Universitet - NTNU; 2003.
2. Hoel JO, Kjoenli H, Rong HM, Roe T, Bjordal J, *Method for Production of Trichlorosilane and Silicon for Use in the Production of Trichlorosilane* Patent Application WO2012021064. Feb. 16, 2012.
3. Hoel JO, Rong HM, Roe T, Oye HA, *Method for Production of Trichlorosilane and Silicon for Use in the Production of Trichlorosilane* Patent Application US2007/0086936. Apr. 19, 2007.
4. J M Bill J, Merkh CW, *Silicon and Catalyst Material Preparation in a Process for Producing Trichlorosilane* Patent Application US2009/0060818. Mar. 5, 2009.
5. Ehrich H, Lobreyer T, Hesse K, Lieske H. *Action of Copper in Trichlorosilane Synthesis*. Silicon for the Chemical Industry IV; June 3-5, 1998; Geiranger, Norway. p. 113-122.
6. Lobreyer T, Hesse K, Ehrich H, Lieske H. *Study of Selectivity in Trichlorosilane Producing Reactions*. Silicon for the Chemical Industry III; June 18-20, 1996; Trondheim, Norway. p. 147-155.
7. Andersen GJ, Hoel JO, Rong H, Oye HA. *Selectivity and Reactivity of the Trichlorosilane Process*. Infacon IX - The Ninth International Ferroalloys Congress; 3-6 June 2001; Quebec City, Canada. p. 352-357.
8. Wakamatsu S, Hirota K, Sakata K. *Study of Selectivity in Trichlorosilane Producing Reactions*. Silicon for the Chemical Industry IV; June 3-5, 1998; Geiranger, Norway. p. 123-132.
9. Samori H, Enokuchi M, Aimoto T, Nagase N, Oda H, Momose H. *Effect of Trace Elements in Metallurgical Silicon on Trichlorosilane Synthesis Reaction*. Silicon for the Chemical Industry III; June 18-20, 1996; Trondheim, Norway. p. 157-167.
10. Coleman L. *Best Practices for Fluidized Bed Reactors in the Hydrochlorination Process*. Silicon for the Chemical and Solar Industry XII; June 23 – 26, 2014; Trondehim, Norway. p. 113-122.
11. Box GEP. *Robustness in the Strategy of Scientific Model Building*. Robustness in Statistics: Academic Press; 1979. p. 201–236.
12. van-Noort WCJ, Stap Pvd, Waal Jvd. *Silicon Milling & Explosion Prevention*. Silicon for the Chemical and Solar Industry XII; June 23 – 26, 2014; Kristiansand, Norway. p. 29-36.
13. Parous L, Weber F, Oliveira VDd, Herbst W. *Effect of Trace Elements in Metallurgical Silicon on Trichlorosilane Synthesis Reaction*. Silicon for the Chemical and Solar Industry XIII; June 12-16, 2016; Kristiansand, Norway. p. 43-52.
14. Portal J. *The Use of Rhodax® Interparticle Crusher in Silicon Industry*. Silicon for the Chemical and Solar Industry XI; June 25-29, 2012; Bergen-Ulvik, Norway. p. 43-52.
15. Kohno H, Kuroko T, Itoh H. *Quality Requirements for Silicon Metal in Polysilicon Production*. Silicon for the Chemical Industry II; Jun 8-10, 1994; Leon, Norway. p. 165-170.
16. Goebel T, Haeckl W, Muenzer W, Paetzold U, Sofina N, *Composition Analysis of a Gas or Gas Stream in a Chemical Reactor and Method for Preparing Chlorosilanes in a Fluidized Bed Reactor* Patent Application US2016/0131584A1. May 12, 2016.
17. Sobota M, Alber A, *Preparation of Trichlorosilane* Patent Application US2016/0176717. Jun. 23, 2016.

18. Andersen G, Hoel JO, Rong HM, Roe T, Oye HA, *Method for Production of Trichlorosilane, Method for Production of Silicon and Silicon for Use in the Production of Trichlorosilane* Patent Application WO2006/031120. Mar. 23, 2006.
19. Wagner GH, *Chlorosilanes* US Patent No. 2499009. Issued Feb. 28, 1950.
20. Harder P, Swenson T, Williams D, *Process for Preparing Monohydrogentrihalosilanes* Patent Application US2016/099833. Jun. 23, 2016.
21. Schei A, Tuset J, Tveit H. *Production of High Silicon Alloys*. Trondheim, Norway: Tapir; 1998.
22. Acker J, Rover I, Roewer G, Bohmhammel K. *Formation of Silicides in the System Metal-Silicon-Chlorine-Hydrogen: Consequences for the Synthesis of Trichlorosilane from Silicon and Hydrogen Chloride*. Silicon for the Chemical Industry V; May 29 - June 2, 2000; Tromso, Norway. p. 121-134.
23. Buseth T, Forwald AG, Rong HM, Skofteland B, Sorheim H, Hoel JO. *Surface Studies of Silicon in the Tcs Process*. Silicon for the Chemical Industry V; May 29 - June 2, 2000; Tromso, Norway. p. 135-150.
24. Forwald AG, Rong HM, Vogelaar GC. *Oxygen in Silicon; Occurence and Influence on the Direct Process to Methylchlorosilanes*. Silicon for the Chemical Industry II; Jun 8-10, 1994; Leon, Norway. p. 107-119.
25. Acker J, Bohmhammel K. *Reactivity of Intermetallic Compounds: A Solid State Approach to Direct Reactions of Silicon*. J Phys Chem B. 2002;106:5105-5117.

Silicon for the Chemical and Solar Industry XIV
Svolvær, Norway, June 11 – 14, 2018

The impact of metallurgical grade silicon phosphorus content on trichlorosilane synthesis and polysilicon purity

Alan Crawford[1)], Harry M. Rong[2)], Henning Kjønli[2)], Jan-Otto Hoel[2)] and Johan P. Svanem[2)]

1) Alan Crawford Consulting LLC, 259 Greenmore Court, Bozeman, Montana, USA 59715
2) Elkem ASA, Fossegrenda 13, 7038 Trondheim, Norway

Abstract

Phosphorus is an important impurity to consider in the industrial synthesis of trichlorosilane (TCS) for use in production of polysilicon. Metallurgical grade silicon (MGS) is the primary source of phosphorus entering any industrial polysilicon plant. Some phosphorus present in MGS is converted to volatile compounds. Some of these compounds have boiling points close to TCS. Removal of volatile phosphorus compounds from TCS prior to conversion of TCS to polysilicon is important especially for production the highest purity grades of polysilicon. There are no disclosed volatile phosphorus compound removal unit operations (analogous to use of silica gel to remove boron trichloride). TCS-based polysilicon plants that are integrated with fumed silica and / or organofunctional silane production units have an easier time to reliably produce highly pure TCS capable for production of the lowest phosphorus content polysilicon. Volatile phosphorus compounds are rejected by distillation during the TCS purification process to TCS and silicon tetrachloride (STC) feed streams used in production of organofunctional silanes and / or fumed silica. Without an economically viable method to divert sufficient amounts of TCS and / or STC away from polysilicon production, stand-alone TCS-based polysilicon plants are challenged to reliably produce the lowest phosphorus content polysilicon. All TCS-based polysilicon plants, and specifically stand-alone plants, can benefit from use of low phosphorus content MGS. Low phosphorus content MGS consumption minimizes production of volatile phosphorus compounds. Phosphorus has been shown in laboratory work to reduce the yield of TCS in the direct chlorination synthesis reaction. Laboratory quantification of the phosphorus distribution from the MGS shows that significantly more phosphorus is converted to volatile phosphorus compounds in the hydrochlorination reaction compared to direct chlorination. Most phosphorus entering the direct chlorination process remains in the solid phase and does not contaminate the reaction product.

Trichlorosilane Synthesis

There are three primary industrial routes for synthesis of trichlorosilane (TCS): 1) Hydrochlorination; 2) Direct chlorination and 3) Hydrogenation.

Hydrochlorination

The process to produce TCS ($HSiCl_3$) by reaction of ground metallurgical grade silicon (MGS), hydrogen and silicon tetrachloride (STC; $SiCl_4$) has been given several names. The

original name used by Union Carbide was STC hydrogenation, which was later shortened to hydrogenation. In recent years the terms “cold hydrogenation” and “cold conversion” have been used in China. Hydrochlorination (HC) has become the most widely used name and is used in this paper. The overall equilibrium reaction is written:

$$Si\ (s) + 2H_2\ (g) + 3SiCl_4\ (g) = 4HSiCl_3\ (g) \quad (1)$$

Union Carbide researchers [1] discovered the HC reaction (Reaction 1) in 1948 as part of research for an alternate route to produce TCS. Work on HC was abandoned around 1950 and not restarted until 1976 when the Jet Propulsion Laboratory (JPL) Low Cost Solar Array project started. Through the JPL project, Union Carbide developed a viable commercial route to produce silane (SiH_4). TCS synthesis by HC was the first step in the overall Union Carbide silane process. The first industrial plant to synthesize TCS by HC was built in Moses Lake, Washington, USA. Union Carbide produced polysilicon rods from silane in Moses Lake using modified Siemens technology developed by Komatsu (Japan).

The HC reaction is an equilibrium reaction that has a maximum TCS yield determined by the thermodynamics given by the operating conditions. The available thermodynamic data for the reaction products are not accurate, resulting in a wide range of calculated equilibrium values for TCS selectivity. Therefore, each producer develops their own thermodynamic data for calculating maximum TCS selectivity.

The reaction is typically run in a fluid bed reactor (FBR) and is slightly endothermic (ΔH_{rxn} = 10.4 kcal/gmole-Si) [2] assuming there is no anhydrous HCl co-feed. Reaction temperature is controlled by superheating feed streams of hydrogen and STC. An acceptable reactor operating temperature is 520 – 550^o C and typical operating pressures are 10 – 34.5 barg (150 – 500 psig). Higher temperature, higher pressure, longer gas residence time in the reaction mass, MGS composition, MGS particle size distribution (PSD) and the use of externally supplied catalyst facilitate pushing the reaction closer to equilibrium TCS yield. Detailed discussions of HC reaction chemistry can be found in several references [2, 3, 4, 5, 6, 7, 8].

Dichlorosilane (DCS; H_2SiCl_2) is the main HC reaction by-product. DCS yield is typically 20-30 times lower than TCS. HC reaction selectivity to DCS is proportional to TCS. DCS is produced in the following reactions. Reaction 3 is catalyzed by aluminum chloride ($AlCl_3$). $AlCl_3$ is produced from reactive aluminum present in the MGS fed to the HC reactor.

$$HSiCl_3\ (g) + H_2\ (g) = H_2SiCl_2\ (g) + HCl\ (g) \quad (2)$$

$$2HSiCl_3\ (g) = H_2SiCl_2\ (g) + SiCl_4\ (g) \quad (3)$$

DCS is a desired by-product if the HC unit is part of a silane plant as DCS is a desired intermediate in the conversion of TCS to silane. DCS can be a desirable and / or undesirable by-product if the HC unit is part of a TCS-based polysilicon plant. Some DCS can be co-fed with TCS to the TCS Siemens polysilicon reactors. High pure DCS can also be sold to semiconductor producers. Excess DCS can be redistributed with STC to produce TCS.

The HC reaction can be run with separately added catalyst. The catalyst helps drive the HC reaction closer to equilibrium and higher TCS yield. Copper is the preferred catalyst and can be added to the HC FBR as copper oxide, metallic copper, copper chloride or copper-silicon alloy. Eta phase (Cu_3Si) is believed to be the catalytically active form of copper in the HC reaction [3, pp. 27-28]. Proof of eta phase as the catalytically active form of copper in the HC reaction has not been published.

Unlike the Rochow-Müller direct process reaction, the HC reaction can be run successfully without use of external catalyst; the only result is lower TCS yield. MGS impurities, such as Al and Fe, always provide in-situ catalysis for the HC reaction. Optimization of MGS composition represents an opportunity to improve commercial HC TCS yield regardless of external catalyst use. Detailed information about industrial HC unit operation and optimization of TCS selectivity has been published [9].

Anhydrous HCl is produced as a by-product in the TCS-based polysilicon CVD process. HCl produced in the TCS Siemens reactors is recovered and recycled to the HC FBR. While the normal form of makeup chlorine for the HC reaction is STC, anhydrous HCl can also be used. The added HCl will react fast with MGS and may alter the product distribution. The net impact of HCl co-feed on final TCS yield from the HC reactor has not been reported and represents potential future work.

Direct Chlorination

The process to produce TCS by reaction of ground MGS and anhydrous HCl has been given several names. Direct chlorination (DC) has become a common name and is used in this paper. Alternate names for the reaction are low-pressure chlorination, direct TCS process and, to make things a bit confusing, hydrochlorination. The TCS selectivity in the DC process is controlled by kinetics. Therefore, it is important to avoid elements and conditions that promote equilibrium (opposite of optimum HC conditions). The silicon requirements are different compared to the HC process. The DC reaction is comprised of one main reaction step and two side reactions. The main reaction is written:

$$Si\ (s) + 3HCl\ (g) \rightarrow HSiCl_3\ (g) + H_2\ (g) \qquad (4)$$

The main side reaction is the production of STC. This reaction can be written as a parallel reaction to the TCS synthesis reaction (Reaction-5) or as a consecutive TCS reaction (Reaction-6) [10]. It is important to note that STC is a by-product of the DC reaction as opposed to a reactant in the HC reaction. Formation of by-product STC is undesirable as the production of TCS is reduced with a fixed flow of HCl to the DC FBR. It should also be noted that with a fixed flow of HCl (most common operational practice) the consumption of silicon will be reduced with lower TCS selectivity simply because formation of STC requires an additional HCl molecule.

$$Si\ (s) + 4HCl\ (g) \rightarrow SiCl_4\ (g) + H_2\ (g) \qquad (5)$$

$HSiCl_3$ (g) + HCl (g) → $SiCl_4$ (g) + H_2 (g) (6)

DCS is a minor but important DC reaction by-product. DCS yield is about 80 times lower than TCS. DCS is produced by previously provided Reaction-2 and Reaction-3. The options for handling by-product DCS are similar to those discussed for the hydrochlorination TCS synthesis reaction.

DC has been the main commercial route for production of TCS for use in production of polysilicon and organofunctional silanes. One of the first patents teaching the reaction chemistry was issued to Wacker in 1961 [11]. The DC reaction is conducted in fluid bed reactors that contain a large internal heat exchanger to remove the high heat of reaction generated by the strongly exothermic reaction. Design of the internal heat exchanger is a critical aspect for safe, reliable operation of a commercial DC process. Reaction temperatures can exceed 1200 ºC if the reactor is operated with poor fluidization. Very tight temperature control is required to ensure safe industrial DC FBR operation and to maintain desired TCS selectivity.

Ground MGS is fed to the reactor with anhydrous HCl. Industrial DC processes consume ground MGS with a wide range of particle size distributions that are selected to match desired fluid bed reactor designs. Higher reaction temperatures favor higher production of STC [12] since increased temperature moves the process towards equilibrium. Typical DC reaction temperatures are 280 - 380 ºC and typical operating pressures are 1.03 – 3.45 barg (15 – 50 psig). The DC process can be catalyzed by feeding external copper [13] to reduce the operating temperature. Iron is reported to promote higher levels of STC [14]. Aluminum and iron react with HCl to form problematic aluminum trichloride ($AlCl_3$) and ferric chloride ($FeCl_3$).

The fluid bed DC TCS synthesis process should not be confused with a similar fixed bed process [15]. Anhydrous HCl with or without hydrogen co-feed is fed to a fixed bed reactor that consumes large lump silicon to produce a mixture of STC and TCS.

Hydrogenation

The process to produce TCS by the high temperature reaction of STC and hydrogen has been given several names. This paper will refer to this reaction as hydrogenation. Alternate names for this reaction / process are high temperature hydrogenation, STC hydrogenation, STC converters, hot hydrogenation and hot conversion. The term “hydrogenation” should not be confused with the use by REC Silicon (Union Carbide, Advanced Silicon Materials) of hydrogenation to describe the hydrochlorination reaction (see Reaction 1). The equilibrium hydrogenation reaction is written:

$SiCl_4$ (g) + H_2 (g) = $HSiCl_3$ (g) + HCl (g) (7)

The hydrogenation reaction has been used by industrial TCS-based polysilicon producers for many years to convert by-product STC to TCS. One of the first patents teaching the reaction chemistry was issued to Motorola in 1976 [16]. The endothermic high temperature STC conversion reaction can be operated in a wide range of reactor designs and process conditions [17, 18, 19]. The reaction is run at temperatures ranging from 600 – 1200 ºC and can be catalyzed. The best hydrogenation reactor designs minimize both electrical energy consumption and the contamination of TCS with hydrocarbons.

Polysilicon Deposition

Almost all TCS-based polysilicon is produced in batch operated chemical vapor deposition (CVD) reactors. TCS can be produced by hydrochlorination, direct chlorination and / or hydrogenation. TCS produced from the initial synthesis reactions must be purified to remove all impurities, especially volatile carbon compounds, volatile donor (As, P, Sb) compounds and volatile acceptor (Al, B) compounds. In general terms, the purity of TCS fed to the Siemens CVD reactor is the same as the final desired polysilicon purity, i.e. production of 10N pure poly requires 10N pure TCS.

The CVD reactor design was originally developed by Siemens AG in the 1950's and has become known by many as "Siemens" reactors. Chemistry of TCS-based polysilicon production is complex but the overall reaction can be written as Reaction-8. An excess of hydrogen is blended with the TCS fed to the Siemens CVD reactors. Reaction-8 does not show production of by-products such as HCl, DCS and polychlorosilanes (Si_2Cl_6, Si_3Cl_8, Si_4Cl_{10}, etc.). Specific operation of industrial TCS-based Siemens CVD reactors is complex and can be based on producer-specific parameters.

$$4HSiCl_3\ (g) \rightarrow Si\ (s) + 3SiCl_4\ (g) + 2H_2\ (g) \qquad (8)$$

TCS Synthesis Metrics

A primary metric of industrial HC and DC process operation is the amount of TCS produced in the HC or DC reaction. The metric is called "TCS yield", "TCS conversion" and / or "TCS Selectivity". One of the main goals with industrial operation of HC or DC processes is to maximize TCS selectivity. Higher TCS selectivity is directly proportional to higher polysilicon production.

TCS selectivity for both HC and DC is controlled through careful industrial plant design, raw material specification and active process control. Since industrial plant design is difficult to change once the plant has been built, experience shows that raw material and process control optimization represent the best ways to maximize TCS selectivity. Raw material optimization is normally focused on MGS impurity content. Experience shows that there is no single parameter (raw material, process control) that has a significant influence on TCS selectivity in industrial HC operation. Reaction temperature has a significant impact on TCS selectivity for the DC reaction [12]. Higher temperatures reduce TCS selectivity in favor of greater by-product STC. Table 1 compares typical TCS selectivity for the HC and DC reactions.

Table 1: Comparison of TCS selectivity for hydrochlorination and direct chlorination. TCS "Crude" refers to the mixture of all chlorosilanes that exit the industrial HC or DC process unit as a liquid stream on a hydrogen and HCl-free basis.

Metric	Hydrochlorination	Direct Chlorination
By-products	DCS, trace (10's of ppmw) polychlorosilanes	DCS, STC, Polychlorosilanes (Si_2Cl_6, Si_3Cl_8, Si_4Cl_{10}, etc.)
Non-silicon impurities (volatile As, B, C and P compounds)	Not included in TCS crude composition	Not included in TCS crude composition
Traditional TCS selectivity units	Mole % or Weight %	Weight %
TCS Selectivity	Does not include unreacted Hydrogen or HCl	Does not include unreacted Hydrogen or HCl
TCS Selectivity =	100 * TCS in TCS crude / (total TCS crude [DCS, TCS, STC])	100* TCS in TCS crude / (total TCS crude [DCS, TCS, STC, Polychlorosilanes])
Typical TCS crude content	DCS: 0.1 – 0.5 weight % TCS: 12 – 30 weight % STC[1]: 70 – 88 wt. % Polychlorosilanes: trace [1] *STC present in TCS crude is unreacted; STC is not a by-product*	DCS: 1 - 3 weight % TCS: 82 - 88 weight % STC: 8 - 15 weight % Polychlorosilanes: 0.2 – 1.0 wt.%

Volatile Phosphorus Compounds

MGS is the primary source of reactive phosphorus entering the industrial HC and DC TCS synthesis processes. Removal of these volatile phosphorus impurities is a significant focus of the TCS purification part of the overall polysilicon process. Optimum design of a purification system requires knowledge about the specific chemical form of the impurities.

At least four volatile phosphorus compounds can be formed in the hydrochlorination and direct chlorination TCS synthesis reactions: phosphorus oxychloride ($POCl_3$), phosphorus trichloride (PCl_3), dichlorophosphine (DCP; $PHCl_2$) and monochlorophosphine (MCP; PH_2Cl). MCP is provided in this list but the amount formed is believed to be very low compared to the other compounds and, given the low boiling point, removal of MCP during TCS purification is not problematic. Tokuyama has proposed, but not confirmed in the open literature, the presence of two additional volatile phosphorus compounds: SiH_3PH_2 (similar boiling point to DCS) and $SiCl_2HPH_2$ (similar boiling point to TCS) [20].

Phosphine is not produced in HC or DC. Phosphine (PH_3) can be produced in the hydrogenation TCS synthesis reaction (Reaction-7) and within the Siemens CVD reactors given the presence of excess hydrogen, phosphorus from materials of construction [21]

(Reaction-9) and traces of DCP present in feed TCS (Reaction-10). Table 2 provides the normal boiling point of these volatile phosphorus compounds along with DCS, TCS and STC.

$$P\ (s) + 1.5H_2\ (g) \rightarrow PH_3\ (g) \quad (9)$$

$$PHCl_2\ (g) + 2H_2\ (g) \rightarrow PH_3\ (g) + 2HCl\ (g) \quad (10)$$

Table 2: Normal boiling points (NBP) of volatile phosphorus compounds produced in hydrochlorination, direct chlorination and hydrogenation TCS synthesis reactions. The NBP of dichlorosilane, trichlorosilane and silicon tetrachloride are provided for reference. Where: HC = Hydrochlorination; DC = direct chlorination; HYD = hydrogenation; CVD = Siemens TCS polysilicon reactor

Name	Abbreviation	Formula	Source	NBP °C
Phosphine	-	PH_3	HYD, CVD	-87.7
Monochlorophosphine	MCP	PH_2Cl	HC, DC	0
Dichlorosilane	DCS	H_2SiCl_2	HC, DC, CVD	8.2
Trichlorosilane	TCS	$HSiCl_3$	HC, DC, HYD, CVD	31.9
Dichlorophosphine	DCP	$PHCl_2$	HC, DC	45
Silicon tetrachloride	STC	$SiCl_4$	DC, CVD	57.6
Phosphorus trichloride	-	PCl_3	HC, DC	75.5
Phosphorus oxychloride	-	$POCl_3$	HC, DC	105.8

DCP is the most troublesome volatile phosphorus impurity formed in TCS synthesis by HC or DC for TCS-based polysilicon production due to suspected strong binary interactions between DCP and TCS. The strong binary interactions result in DCP being present in TCS and difficult to remove entirely by distillation. DCP is believed to be formed in the HC reactor via Reaction-11 [22].

$$PCl_3\ (g) + H_2\ (g) \rightarrow PHCl_2\ (g) + HCl\ (g) \quad (11)$$

An approximate distribution of volatile phosphorus compounds produced from the reaction of phosphorus present in MGS in the HC and DC processes is provided in Table 3 [22].

Table 3: Approximate distribution of volatile phosphorus compounds produced from reactive phosphorus (present in MGS) in the hydrochlorination (HC) and direct chlorination (DC) TCS synthesis reactions. The percentage of reactive phosphorus present in MGS converted to volatile compounds has not been reported.

Compound	HC weight %	DC weight %
$POCl_3$ (phosphorus oxychloride)	~ 5	5
PCl_3 (phosphorus trichloride)	75 - 80	92 - 93
$PHCl_2$ (dichlorophosphine)	10 - 15	2 - 3
PH_2Cl (monochlorophosphine)	trace	trace

Significantly lower DCP production in DC is explained by 1) significantly lower concentration of excess hydrogen in the DC process (HC process is intentionally run with a significant excess hydrogen) and 2) single pass flow of PCl_3 in the DC process. PCl_3 is the main form of volatile phosphorus produced in both HC and DC. With the HC process, unreacted STC that exits the HC reactor is combined with by-product STC from the TCS-based CVD polysilicon production reactors and recycled back to the HC reactor. The unreacted STC can contain 10's or 100's of ppmw of PCl_3 and this PCl_3 is recycled back to the HC reactor with the STC feed. The higher concentration of PCl_3 present in the HC reactor (from recycle STC and produced from reaction of phosphorus present in MGS) combined with excess hydrogen enables a higher generation of DCP.

Why is low Phosphorus content important?

Polysilicon with the lowest phosphorus content can be used in the widest range of semiconductor and solar applications. Consistent, minimum phosphorus content polysilicon is normally sold for higher prices. All semiconductor applications require minimal phosphorus content.

Only a limited number of industrial TCS-based polysilicon producers presently have capability to intentionally produce polysilicon with minimized phosphorus content suitable for use in the semiconductor industry. Almost all polysilicon producers can unintentionally produce polysilicon with minimized phosphorus content. There is a significant difference between intentional production and unintentional production. Intentional production implies the producer understands what is required to control phosphorus content.

Polysilicon purity metrics

Phosphorus (and any periodic table Group 5 element such as arsenic) is an electron donor. Boron (and any periodic table Group 3 element such as aluminum) is an electron acceptor. Almost all polysilicon is "n-type" because phosphorus content is always higher than boron content. When the phosphorus content is higher than boron content an excess of negatively charged (hence the term "n-type" with n for "negative") electrons are present. When boron content is higher than phosphorus content there is a deficit of electrons (hence the term "p-type" with p for "positive"). The metric "net doping concentration" is frequently used and is obtained from subtracting n-dopant concentration (Phosphorus) from p-dopant concentration (Boron).

The best measures of overall polysilicon purity used by the semiconductor and solar industry are 1) donor (As, P) – acceptor (B) concentrations; 2) resistivity (ohm-cm) and 3) total metallic impurities (transition elements such as chromium, iron and nickel). Impurities (donors, acceptors, metallic) are commonly reported as ppba (parts per billion-atom) or ppta (parts per trillion-atom). There is good correlation between resistivity and net donor concentration. It is important that the method to quantify levels of donors, acceptors and metallic impurities be specified to ensure accuracy of reported impurities.

It remains common to use the "N" or "nines" designation to differentiate between grades of polysilicon. The "N" designation is acceptable for general discussions but is not used in actual

product specifications. Polysilicon purity is commonly measured using the "N" or "nines" metric. Solar grade polysilicon is typically 6N – 8N or 99.9999 weight% (there are 6 "nines") to 99.999999 weight % (8 nines). Electronic grade (or semiconductor grade) polysilicon purity ranges from 9N – 11N. The "N" designation normally does not account for the oxygen and carbon content. The highest purity electronic grade polysilicon contains close to 1 ppma of oxygen and carbon. Typical solar purity polysilicon contains 10's of ppma of oxygen and carbon. The silicon content by itself is not the important factor in the silicon quality, but rather the specific content of impurities.

As demands for higher efficiency solar cells increase, an overlap of the traditional "solar grade" and "electronic grade" polysilicon exists. Some solar applications require use of electronic grade, although the full qualification protocol required in the semiconductor industry is not necessarily followed. Regardless of whether polysilicon is solar or electronic grade and regardless of the exact method used to quantify overall purity, it still remains that all polysilicon is some of the highest purity materials produced in the world.

Polysilicon applications versus purity

Excessive amounts of phosphorus results in the inability to produce acceptable single crystal wafers for production of semiconductors. Recent trends in the solar sector show strong growth in demand for monocrystalline wafers, which yield the highest efficiency solar cells. Production of the most efficient monocrystalline solar wafers requires polysilicon having a phosphorus content and overall purity similar to some semiconductor applications. Some analysis shows that the present global supply of high purity polysilicon (9N+) does not meet the present demand [23]. Despite these reported changes in trends, the large majority of solar cells are made with standard solar-grade (6N – 8N) polysilicon that is converted to p-type silicon wafers via ingot doping with boron.

Polysilicon phosphorus content is an important technical requirement for polysilicon used to produce all semiconductors and the highest efficiency monocrystalline silicon solar wafers. Polysilicon purity requirements for many solar applications extend beyond technical justification. Sales and marketing are a very important factors that can provide individual producers significant market advantages.

Since most polysilicon producers are not integrated with wafer, cell and module production they must sell polysilicon on the open market. The use of purity, and, most importantly, phosphorus content, can be a strong selling feature for the polysilicon producer regardless if the wafer – cell – module producer absolutely requires high purity, minimized phosphorus content polysilicon.

Polysilicon phosphorus industrial values and limits

Phosphorus specification limits of solar grade polysilicon taken from standard Chinese specifications are provided in Table 4 [24, 25].

Table 4: Solar-grade polysilicon phosphorus specification limits for Chinese production. Resistivity is also included.

Solar Product	P spec maximum ppba	P spec maximum ppta	Resistivity minimum ohm-cm
Grade 1 (Super)	1.5	1500	100
Grade 2 (Ultra)	3.76	3760	40
Grade 3 (Standard)	7.74	7740	20

Wacker Polysilicon, which is a major electronic grade polysilicon producer, reports their highest purity polysilicon has a baseline phosphorus content of 30 ppta (0.03 ppba) with a resistivity of 4250 ohm-cm [26]. Osaka Titanium shows electronic grade polysilicon to have 160 ppta maximum (0.160 ppba) phosphorus content for nominal 11N purity [27]. GCL Polysilicon shows electronic grade polysilicon to have 300 ppta maximum (0.30 ppba) phosphorus content with a minimum resistivity of 1000 ohm-cm. [25].

TCS Purification: Phosphorus Removal

Perhaps the most challenging aspect of industrial high purity polysilicon production is minimizing phosphorus in the TCS that is fed to the Siemens CVD polysilicon reactors. Reliable removal of volatile phosphorus compounds from crude TCS is strongly influenced by overall plant configuration. Raw material specifications and specific purification unit operations are equally important. Additional factors such as plant operator experience, overall plant technology, equipment design, maintenance practices and adherence to standard operating practices and procedures are also important.

Polysilicon plant configuration

An industrial polysilicon plant can be located on a site that is integrated with adjacent / fence-line production of fumed silica, organofunctional silanes, silicates and / or additional specialty materials. Alternatively, an industrial polysilicon plant can be a stand-alone facility where the only product is polysilicon. Most long-term producers operate integrated polysilicon plants that have historically supplied the highest purity polysilicon to the semiconductor industry.

As the demand for solar-grade polysilicon has increased the number of stand-alone plants has increased. The main justifications for stand-alone polysilicon plants are 1) the only business of the plant operator is solar-grade polysilicon and 2) there is no economic justification to integrate new polysilicon capacity with fumed silica, organofunctional silane or similar capacity that consumes technical grades of TCS and STC. Almost all of the recent, under-construction and planned solar-grade TCS-based polysilicon capacity in China are stand-alone plants.

Integrated polysilicon plants provide benefits to the plant operator in terms of the final polysilicon product purity, polysilicon product consistency and overall plant economics. An important benefit of an integrated plant is the ability to optimize polysilicon product purity. Stand-alone polysilicon plants enable the plant operator to only focus on polysilicon

production. The ability to reliably produce consistent quality high purity, low cost polysilicon (9N+) may be difficult with stand-alone plants due to lack of external customers for TCS and STC "purge" streams and lack of available TCS purification technology.

Integrated Plants

Integrated polysilicon plants have, by intentional design, large chlorosilane "purge" streams. These streams are most likely not known as "purge" streams by the plant operators. Distillation is used to reject volatile phosphorus compounds into the TCS fraction that is not consumed to produce polysilicon, i.e. the "purge" streams. Several ppbw of phosphorus is of no concern to non-polysilicon (Solar or semiconductor grades) applications such as organofunctional silane production.

Organofunctional silanes are a broad class of silicon-based materials that find a wide range of applications. TCS is an important feed material used to produce organofunctional silanes. A considerable amount of the total TCS produced in the TCS synthesis unit can be consumed by the organofunctional silane plant. The TCS purification train can be operated in a manner that rejects volatile phosphorus compounds to the organofunctional silane TCS feed stream.

Fumed silica (nano-size silica; sometimes called pyrogenic silica; SiO_2) is used as a reinforcing filler in many silicone products such as heat cured rubber (HCR) and room temperature vulcanizing (RTV) silicone rubber. Fumed silica can be produced with feed streams ranging from 100% STC to 100% methyltrichlorosilane (MTCS; M1; Tri; CH_3SiCl_3) with any combination of TCS, STC and M1 in between. Many fumed silica plants are integrated with silicone production, hence the use of M1.

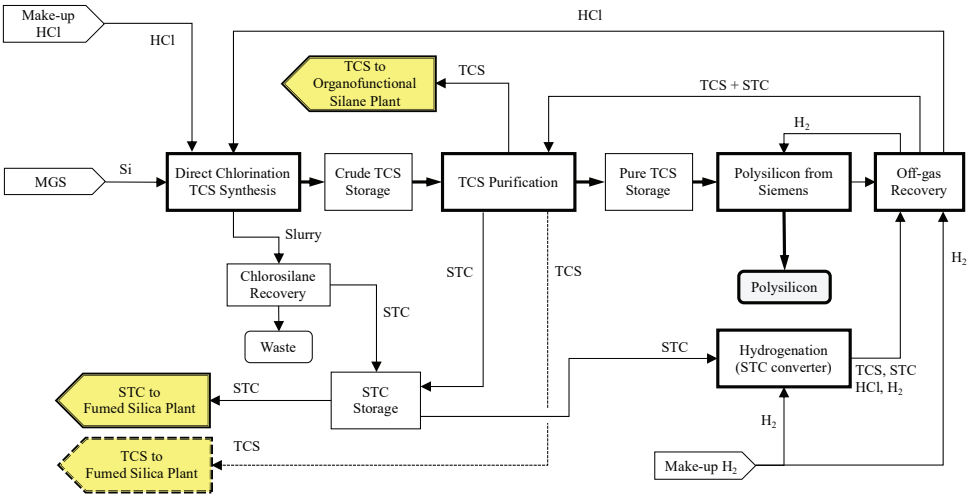
A polysilicon plant integrated with fumed silica production may require conversion of some by-product STC (produced in the DC TCS synthesis reaction and polysilicon production reaction) to TCS. For some producers or depending on demands and capacities of TCS synthesis units, all by-product STC could be used as fumed silica feedstock. The fumed silica plant can also consume some amount of TCS. Supply of STC and / or TCS to a fumed silica plant represents another intentional "purge" for control of final TCS purity, especially phosphorus, for feed to TCS-based polysilicon production. Distillation is used to generate these "purge" streams.

The overall economics of integrated polysilicon plant operation are difficult to accurately calculate given the complexity of plant design, operation and specific needs and costs associated with each industrial operator. Given the non-polysilicon outlets for TCS and STC, these plants are operated without the need to waste chlorosilane streams as part of the phosphorus removal strategy.

Almost all TCS-based integrated polysilicon plants synthesize TCS by a combination of DC and hydrogenation. DC provides the initial TCS synthesis route and hydrogenation is used to balance the overall supply / demand of STC. The hydrogenation section of the plant has the option to consume all STC (by-product from DC TCS synthesis and polysilicon production) or partial streams of STC. Wacker operates a plant with this type of configuration [28]. An

overall block flow diagram of a DC + Hydrogenation TCS synthesis polysilicon plant integrated with fumed silica and organofunctional silane production is shown in Figure 1.

Figure 1: Block flow diagram showing a typical integrated polysilicon plant where TCS is synthesized by direct chlorination and hydrogenation. Some portion of TCS is used for production of organofunctional silanes. Some portion of STC is used for production of fumed silica.



Stand-alone Plants

Most stand-alone polysilicon plants were designed to produce lower purity solar-grade polysilicon (6N – 8N). The designs of most stand-alone plants are such that intentional chlorosilane purges, to aid in purity control, are minimized as such purges represent a yield loss of silicon, chlorine and hydrogen. Unit operations to enable specific removal of volatile phosphorus compounds (see next section) do not appear to exist compared to the use of silica gel for removal of boron trichloride (BCl_3) [29].

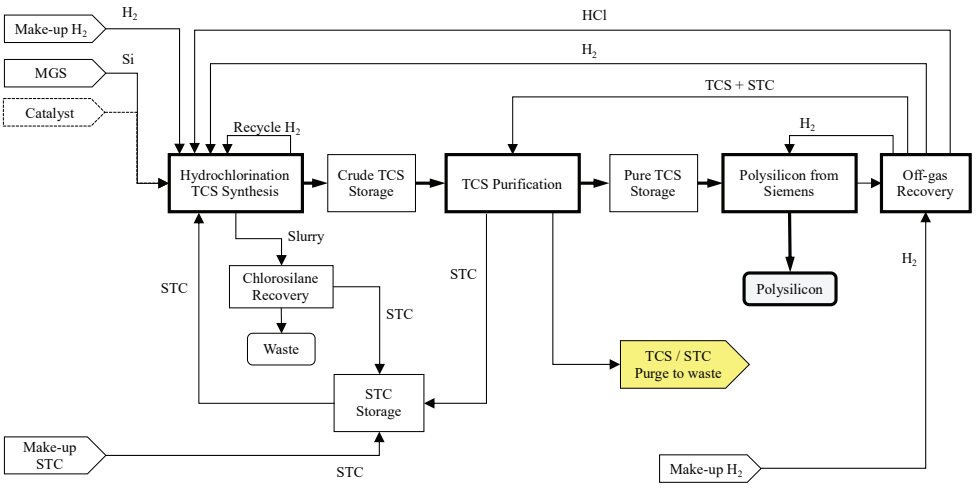
Most stand-alone TCS-based polysilicon plants synthesize TCS by HC. By-product STC from polysilicon production is recycled back to the HC unit. Polysilicon plants that use HC as the route to TCS synthesis are well suited to be stand-alone as by-product STC is consumed by the HC reaction and a separate high temperature STC hydrogenation unit is not required. HC plants are normally net consumers of STC. STC is the common source of make-up chlorine for these plants. Osaka Titanium is one such producer with this type of plant configuration [30]. An overall block flow diagram for a stand-alone HC TCS-based polysilicon plant is shown in Figure 2.

Stand-alone TCS-based polysilicon plants easily operate within the overall 6N-8N solar grade polysilicon purity range. At times these plants may *unintentionally* produce higher purity

(9N+) polysilicon, but intentional higher purity production is normally not possible without making changes to operation of the overall TCS purification section of the plant. As the demand for higher purity (9N+) polysilicon for the solar industry is increasing, operators of stand-alone TCS-based polysilicon plants are investigating methods to increase the capability to produce higher purity polysilicon. Control and minimization of the volatile phosphorus content of TCS is most likely a major focus of these upgrade plans.

These stand-alone plants cannot be operated economically with the significant chlorosilane "purge" streams (STC and / or TCS feed for production of fumed silica and / or organofunctional silanes) found in the integrated plants. The minimum purge required to remove sufficient volatile phosphorus compounds to enable reliable production of higher purity (9N+) polysilicon has not been published but is most likely higher than present purge rates (for solar purity) from these stand-alone plants. Selling large volumes of chlorosilane purges to external customers engaged in production of fumed silica and / or organofunctional silanes is possible, but most likely not economical. Alternate methods are required to enable reliable production of higher purity polysilicon by these stand-alone producers.

Figure 2: Block flow diagram showing a typical stand-alone polysilicon plant where TCS is synthesized by hydrochlorination. There is a minimal chlorosilane purge stream to enable minimal removal of impurities. This stream is normally wasted by water hydrolysis.



Raw Material Specification

An important method to control of phosphorus content of polysilicon is to minimize the entry of phosphorus into the plant through raw materials. Metallurgical grade silicon (MGS) and make-up chlorine are the two raw materials that have the possibility to introduce phosphorus into the overall polysilicon plant.

MGS

The main entry point for phosphorus into any polysilicon plant is MGS. Phosphorus can enter as an internal MGS impurity or an external impurity via steel contamination from crushing and grinding. Depending on the source of MGS, the total internal phosphorus content ranges from 20 – 200 ppmw although 30 – 50 ppmw is the common range. Reactive phosphorus is present in both the intermetallic phases and the silicon matrix. The percentage of reactive phosphorus present in MGS that is converted to volatile compounds has not been reported.

Any polysilicon producer can receive a benefit with regards to control of phosphorus content of polysilicon product by placing a careful specification on the maximum allowable phosphorus content of purchased MGS.

Make-up chlorine

Chlorine is lost through normal TCS-based polysilicon plant operations. Lost chlorine must be replenished to enable stable overall plant operation. The type of primary TCS synthesis determines the makeup chlorine options.

A. Make-up Chlorine: Direct chlorination TCS Synthesis

Anhydrous HCl is the major source of make-up chlorine required for plants that produce TCS by direct chlorination. Chlorine can enter the plant boundaries in several forms including anhydrous HCl, strong aqueous HCl (28-35%), chlorine (Cl_2) and salt (NaCl). Aqueous HCl must be distilled to produce anhydrous HCl; disposal / recycle of the 21% HCl (aq) azeotrope by-product is important. Cl_2 can be reacted with H_2 to produce anhydrous HCl. Cl_2 can be produced by electrolysis of NaCl (aq) and then reacted with H_2 to produce anhydrous HCl. There are numerous advantages and disadvantages of the various forms of make-up chlorine used for TCS synthesis by DC. Whereas many impurities can be introduced into the polysilicon plant by these various sources of chlorine, there are no reported specific problems related to phosphorus from these sources.

B. Make-up Chlorine: Hydrochlorination TCS Synthesis

The traditional source of make-up chlorine for plants that produce TCS by hydrochlorination is STC. TCS or a mixture of TCS and STC can also be used. Anhydrous HCl can also be used with chlorine entering the HC TCS plant in the same forms as previously described for TCS synthesis by DC. Volatile phosphorus can enter the plant when STC or TCS is the form of makeup chlorine.

STC can introduce phosphorus trichloride (PCl_3) and TCS can introduce dichlorophosphine (DCP; $PHCl_2$). The polysilicon producer does not have many options available with regards to minimization of phosphorus content entering the plant via purchased STC or TCS since these are generally low-cost technical grades. While purchase of high purity STC or TCS is possible, the added cost would be excessive and the majority of volatile phosphorus compounds continue to be produced within the HC TCS synthesis reaction.

The polysilicon producer using HC to synthesize TCS should be aware that volatile phosphorus compounds enter the plant through purchased STC or TCS. Upper specification limits for total phosphorus are recommended.

Phosphorus-specific removal unit operations

Distillation is the standard general unit operation used by all TCS-based polysilicon producers to removal volatile phosphorus from crude TCS. The ideal method to remove volatile phosphorus from TCS would be a specific unit operation designed to remove specific volatile phosphorus compounds. There does not appear to be a single, reliable, well-known unit operation to facilitate removal of volatile phosphorus compounds from TCS based on a review of open literature. Conversely, boron trichloride (BCl_3) is reliably removed from TCS by use of silica-gel beds [29].

A review of intellectual property associated with volatile phosphorus compound removal from TCS (and STC) produces over 40 unique patents. The first patent was issued to Bell Telephone in 1958 [31] showing this to be an old problem! The 40+ patents teach a wide range of removal techniques including: 1) Adsorption / absorption (analogous to use of silica gel beds to remove BCl_3); 2) Catalytic destruction; 3) In-situ complex formation (volatile phosphorus compound is converted to a high boiling compound by reaction with an existing compound present in the process) and 4) Additive (gas, liquid or solid is added to the process to enable formation of a high boiling complex with the volatile phosphorus compound). There is no way to know if the teachings of any of these patents have been reduced to routine industrial practice. Proprietary unit operations may be currently used by one or more industrial producers to enable reliable production of minimal phosphorus content polysilicon.

One of the main challenges to develop a unit operation that enables reliable removal of volatile phosphorus compounds from TCS is identification of the actual phosphorus compound(s) to be removed. Most researchers assume that PCl_3 is the volatile form of phosphorus to be removed from TCS but, as discussed previously, PCl_3 is not the TCS impurity to remove. Positive identification of the proposed volatile phosphorus compounds present in TCS represents one challenge; having access to these volatile phosphorus compounds to enable laboratory scale process development is another challenge. Development and industrial implementation of a unit operation to remove volatile phosphorus from TCS (and STC) is possible but would require significant research and development resources along with access to streams of crude TCS produced by industrial TCS synthesis units.

Experimental Results

A series of laboratory experiments were run with the DC and HC TCS synthesis reactions. The purpose these experiments was to measure the effect of phosphorus content on TCS yield of the DC and HC reactions. Another purpose was to quantify the accumulation and distribution of phosphorus, that enters the synthesis reactions with feed silicon, within the reaction system. These experimental results are presented in this section.

Direct chlorination experiments

Experiments were run on a continuous fluidized lab scale DC reactor system. The reactor is continuously operated at 1.15 barg (16.7 psig), 340 °C with continuous addition of ground silicon to maintain 5 grams of reaction mass. The ground silicon particle size distribution range is 125 – 250 microns. A mixture of anhydrous HCl and a small amount of argon is continuously fed to the reactor. Argon is used to provide a standard for the on-line gas chromatograph (GC). A filter is located outside of the reactor to capture entrained fines and to make sure that some impurities are removed during operation.

The cleaned process gas stream is automatically sampled by a continuous on-line GC. The main metrics are total silicon consumed (up to 70 grams of silicon) and TCS selectivity. TCS selectivity is defined as weight percent TCS present in the product stream relative to all chlorosilanes produced (TCS, STC, DCS, high boilers). TCS selectivity is reported on a hydrogen-free and HCl-free basis.

Four silicon samples were prepared for evaluation in the lab scale DC reactor. Table 5 provides a summary of the samples. The four samples were prepared in the laboratory starting with polycrystalline silicon and adding desired levels of aluminum, calcium and iron. The values selected for Al and Ca are typical of these impurities found in MGS consumed in industrial DC TCS synthesis reactors. One sample was prepared with significantly lower Fe compared to typical values. The phosphorus content of Sample D, 35 ppmw, is within the normal phosphorus range (30 – 50 ppmw) found in MGS used for industrial TCS synthesis. No additional impurities were present in the four samples.

Table 5: Composition of silicon samples used in laboratory scale direct chlorination TCS synthesis reaction to evaluate the effect of phosphorus. The base silicon for the four samples was polycrystalline silicon.

Sample	Al (weight %)	Ca (weight %)	Fe (weight %)	P (ppmw)
A	0.14	0.032	0.02	0
B	0.16	0.023	0.28	0
C	0.16	0.023	0.28	10
D	0.16	0.023	0.28	35

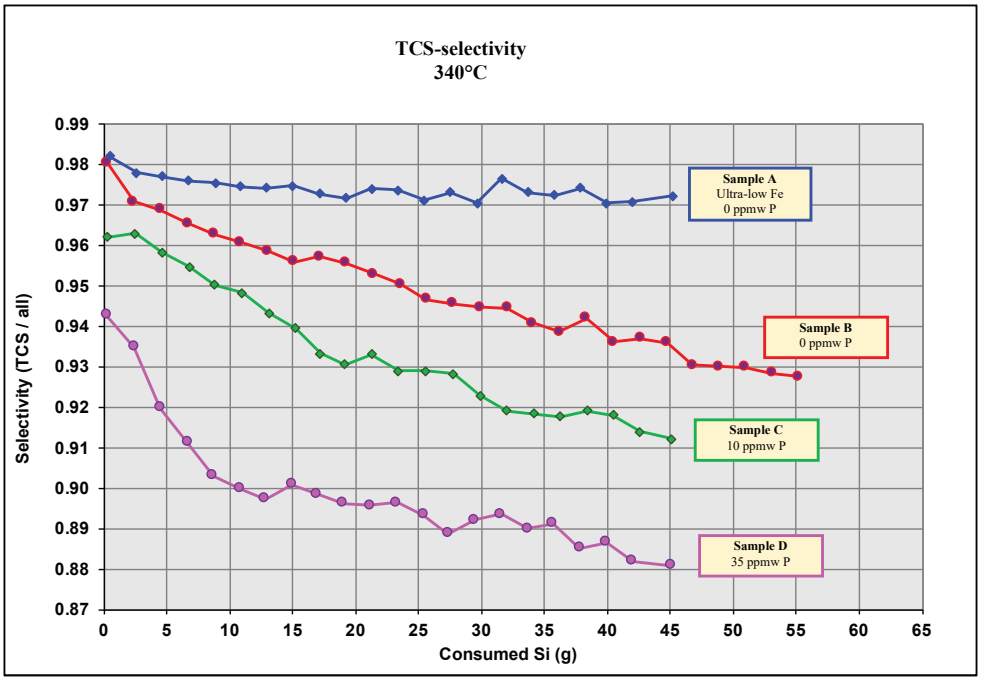
The four samples were run under identical reaction conditions described above. Figure 3 provides representative results from running the four samples in the laboratory scale DC reaction system. Each lab experiment was run with multiple reactor bed volumes. The intent of the experiments was to identify significant TCS selectivity changes as a function of feed silicon composition.

The reproducibility of the direct chlorination apparatus is ±0,4% in the measured TCS selectivity and the four experimental run results shown in Figure 3 have a statistically significant difference. Conversion of about 10 reactor volumes is the maximum possible in a long working day. Industrially the run length will be significantly longer (+100 reactor

volumes). It can be seen from the graphs in Figure 3 that the TCS selectivity is still declining, meaning that we have not reached the steady state situation.

The steady state TCS selectivity will depend strongly on the amount of impurities in the silicon. Typically, more impure silicon will reach steady state quicker. The samples used in this work are very pure (no trace elements except the intentionally added ones) and therefore better TCS selectivity is achieved compared to industrial MGS. TCS selectivity is provided as a function of total silicon consumption. The results of Samples B, C and D clearly show that as phosphorus content of silicon is increased, TCS selectivity decreases.

Figure 3: Laboratory-scale DC TCS synthesis reaction results for silicon Samples A, B, C and D that show the effect of increasing phosphorus content on TCS selectivity. The results also show the effect of iron on TCS selectivity.



The results also show the detrimental effect of iron on TCS selectivity when Sample A (0.015 weight % Fe) is compared with Sample B (0.28 weight % Fe). The Al and Ca content of Sample A and B are almost identical and neither sample contains P. The results suggest that when the DC reaction is run at "normal" Fe levels such as found in Samples B, accumulation of Fe in the reaction mass promotes formation of the undesired STC by-product (see Reaction-5 and 6). The more rapid drop in TCS selectivity for the early part of Sample D reaction suggests that "normal" levels of P combined with "normal" levels of Fe amplifies initial TCS selectivity loss.

Tokuyama investigated the effect of phosphorus on the DC TCS synthesis reaction [14] but did not vary the phosphorus content of MGS. Phosphorus was added externally as red phosphorus and at significantly higher levels. TCS selectivity decreased as the amount of red phosphorus added was increased.

Hydrochlorination experiments

A lab-scale hydrochlorination reactor was used to run a similar set of experiments to investigate the impact of phosphorus on TCS yield. A continuous FBR lab reactor was used in these experiments. The reactor is operated at 550 °C, 10 barg (145 psig), 1 weight % Cu (as CuCl) and a constant 2:1 STC to H_2 molar feed ratio. Ground silicon with a PSD range of 125 – 180 micron was fed to maintain a constant bed mass of 5 grams. The direct chlorination process is controlled by kinetics and elements that promote equilibrium will reduce TCS selectivity. On the other hand, the best TCS yield to achieve in the hydrochlorination process is the equilibrium concentration and elements which promote equilibrium will be beneficial.

The addition of 50 ppmw phosphorous to a low reactive silicon gave a small increase in the TCS selectivity of the lab-scale hydrochlorination reaction. The TCS selectivity increase was not as significant as the reported changes in TCS yield for the direct chlorination reaction (Figure 3). The addition of 50 ppmw phosphorous to a high reactive silicon did not have any significant impact on the TCS selectivity. As will be discussed in the next section, the negative effect of adding volatile phosphorous into the product gas completely overrules the small effect of improved TCS selectivity by adding phosphorous into the hydrochlorination reactor.

Phosphorus accumulation experiments

The phosphorus in the silicon added to the DC or HC reactor will accumulate in three locations: 1) the solid reaction mass in the reactor; 2) leave the reactor in the solid state as part of the total entrained fines and 3) enter the product gas as volatile phosphorous compounds. The continuous addition of silicon with the same phosphorous level to the reactor will quickly give a stationary situation where the phosphorous level in the three different forms are constant. This observation is independent of specific TCS selectivity. However, changing the input level of phosphorous (up or down) will give a new stationary situation between the different locations of phosphorous. The amount phosphorus present in the three locations will depend on the design of the plant. Each producer should set up and conduct a mass balance for phosphorous content in the different streams as part of the overall phosphorus control strategy.

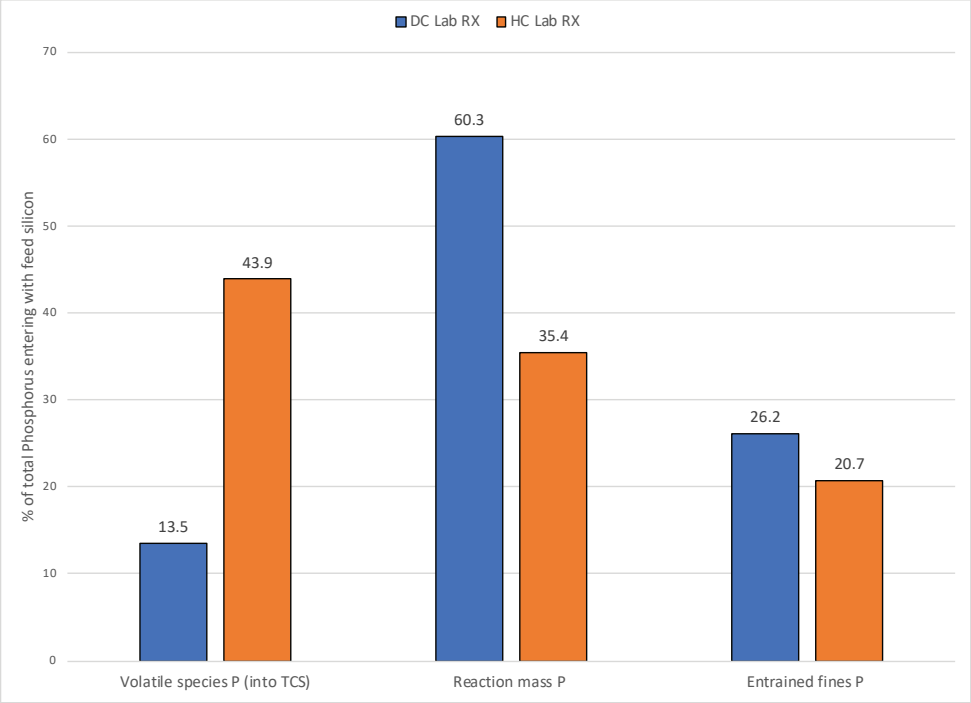
Lab-scale DC and HC experiments were run to quantify the distribution of phosphorus in the three locations listed above. The same lab reactors as previously described were used. Phosphorus content of the MGS added to the DC and HC reactors was held constant at 35 ppmw. At the end of each reaction, phosphorus content was measured by inductively coupled plasma optical emission spectrometry (ICP-OES) in the solid reactor residue (solids remaining in the reactor at the end of each run [spent reaction mass / spent bed]) and entrained

fines (fine particles that exit the reactor and are subsequently removed from the product gas). The specific forms of solid phosphorus were not identified. The amount of entrained fines is less than 0.5 weight % of total ground silicon fed to the reactor, which is much lower than typically observed with an industrial DC or HC fluid bed reactor.

The amount of volatile phosphorus present in the gas product stream was calculated by subtracting the measured amount of phosphorus present in the spent bed and entrained fines from 100%. Quantification of volatile phosphorus present in the reactor product stream was beyond the analytical capability of the laboratory. It should be noted that quantification of volatile phosphorus compounds present in TCS produced in the lab or industrially is not a trivial challenge. It is hypothesized that volatile phosphorus is present as one or more of the phosphorus compounds listed in Table 2 produced by reaction of phosphorus present in the feed MGS. It is possible that some phosphorus may leave the reactor as higher vapor pressure complexes with additional metal chlorides such as $AlCl_3$.

Results of the phosphorus accumulation quantification clearly show that for the DC synthesis reaction, a majority of phosphorus present in the MGS feed remains in the solid phases, i.e. spent reaction mass and entrained fines. A limited amount of phosphorus exits the DC reactor as volatile species that contaminate the product gas stream. The results show that for the HC synthesis reaction, a significant amount of phosphorus present in the MGS feed is converted to volatile phosphorus compounds that contaminate the product gas stream. Figure 4 provides a summary of the phosphorus distribution results.

Figure 4: Comparison of phosphorus distribution for lab-scale DC and HC TCS synthesis reactions. The phosphorus content of MGS fed to the DC and HC reactors was 35 ppmw in all experiments. The phosphorus distribution of spent reaction mass and entrained fines was measured by ICP-OES and volatile phosphorus distribution was calculated by difference from 100%.



Direct chlorination phosphorus accumulation discussion

When we analyze the reactor residues (spent bed and entrained fines) after running an experiment in the direct chlorination process, a strong accumulation of phosphorous was observed (86.5% of the phosphorus fed to the reactor remained in the solid phases). The accumulation of phosphorous depends strongly on the chemical content (such as aluminum, iron and nickel) of silicon fed to the reactor. For example, a higher degree of accumulation is observed when the iron content is higher. We believe that the reason for this observation is that phosphorous can form rather stable phosphides with several elements such as Al, Fe and Ni.

The strong phosphorus accumulation in the reactor is also the reason for the strong negative impact on TCS selectivity (See Figure 3). We have shown, in un-published work, that FeP strongly reduces the TCS selectivity of the process. The positive aspect of strong accumulation in the solid phase (reactor residue + entrained fines) is that a small fraction of the phosphorous goes into the product gas as undesired volatile compounds. We hypothesize

that the temperature is a very critical parameter in controlling the phosphorous content in the reactor.

Hydrochlorination phosphorus accumulation discussion

The hydrochlorination process is operated at significantly higher reactor temperature (500-600°C) than the direct chlorination process (280-380°C). The phosphorus accumulation results provided in Figure 4 clearly indicate that higher HC reaction temperature results in a significantly higher amount of phosphorus exiting the process as undesired volatile contaminates in the product gas stream (43.9% for HC compared to 13.5% for DC). The HC results confirm the hypothesis that temperature is a critical parameter to determine the distribution of phosphorus in the DC and HC processes.

Phosphorus accumulation conclusion

Therefore, these results indicate that it will be more challenging to minimize the phosphorus content in the final TCS product used for polysilicon production when operating the hydrochlorination process compared to the direct chlorination process. A larger burden is placed on the sections of the TCS purification train designed to remove volatile phosphorus compounds. One possible solution will be to use silicon with minimal phosphorus content for TCS-based polysilicon producers using the hydrochlorination process. Minimal phosphorus content silicon also is recommended for use in the DC process to promote higher TCS selectivity.

Conclusions

1) The growing trend of stand-alone TCS-based polysilicon plants combined with the increased demand for high purity (9N+) polysilicon for monocrystalline solar applications will place a stronger emphasis on the development of reliable methods to remove volatile phosphorus compounds.

2) TCS-based polysilicon producers that operate plants integrated with fumed silica and / or organofunctional silane plants are able to easily reject volatile phosphorus compounds by distillation to TCS and STC feed streams for these non-polysilicon plants. This enables integrated polysilicon plants to reliably produce high purity polysilicon.

3) The growth of stand-alone polysilicon capacity will continue to exceed the growth of fumed silica and organofunctional silanes. These stand-alone polysilicon plants will not have easy access to external TCS and STC consumers that enable purging of TCS and STC feed streams which contain volatile phosphorus compounds.

4) Any TCS-based polysilicon producer, and especially stand-alone plants, can benefit from specifying minimum phosphorus content metallurgical grade silicon. MGS is generally the main source of phosphorus entering any polysilicon plant. Use of minimum phosphorus content MGS reduces the amount of reactive phosphorus entering the plant.

5) Laboratory results indicate that a minor amount of phosphorus entering the direct chlorination synthesis reactor with MGS feed exits the process as volatile species present

in the product stream. Most phosphorus remains in the solid phases (reaction mass and entrained fines). Conversely, almost half of the phosphorus entering the hydrochlorination synthesis reactor with MGS exits the process as volatile phosphorus species present in the product stream.

6) The laboratory direct chlorination reactor results show TCS selectivity increases as phosphorus content of MGS decreases. Higher TCS selectivity is translated to higher polysilicon capacity and lower cost production.

7) Laboratory hydrochlorination reactor results show that TCS selectivity slightly increases when the phosphorus content of MGS increases for some grades of MGS. Any TCS selectivity increase is negated by contamination of the TCS product stream with higher amounts of volatile phosphorus species.

References

1. G. F. Wagner, C. E. Erickson, *Hydrogenation of Halosilanes*, U.S. Patent 2,595,620, 1952.
2. J. Y. P. Mui, *Final Report on Investigation of the Hydrochlorination of $SiCl_4$*, JPL Contract 956061, 1983, https://ntrs.nasa.gov/archive/nasa/casi.ntrs.nasa.gov/19830025051.pdf, pp.1-2.
3. J. Y. P. Mui, D. Seyferth, *Final Report: Investigation of the Hydrochlorination of STC*, JPL Contract 955382, 1981. http://ntrs.nasa.gov/archive/nasa/casi.ntrs.nasa.gov/19810019076.pdf
4. W. M. Ingle, M. S. Peffley, *Kinetics of the Hydrogenation of Silicon Tetrachloride*, J. Electrochem. Soc, **132(5)**, 1985, pp. 1236-1240.
5. P. Cygon, *Technical Reaction Studies of the Hydrochlorination of Silicon in a Laboratory Fluidized Bed Reactor*, Diploma Thesis, University of Köln, 1999.
6. T. Sill, *Hydrochlorination Study of Silicon for the Trichlorosilane Synthesis in a Fluidized Bed Reactor*, PhD Thesis, Ruhr-University Bochum, 2001.
7. R. J. Lehnen, *Studies Concerning the Catalytic Hydrochlorination of Metallurgic Silicon with Silicon Tetrachloride and Hydrogen in a Laboratory Fixed Bed Reactor*, PhD Thesis, Ruhr-University Bochum, 2002.
8. F. Becker, Modeling and Simulations of the Hydrochlorination of Silicon to Trichlorosilane for the Development of a Technical Fluidized Bed Reactor, Doctor - Engineer Thesis, Rheinisch-Westfälischen Technischen Hochschule Aachen, 2005.
9. A. Crawford, *Cost saving of using a metallurgical grade silicon with higher trichlorosilane yield in the hydrochlorination based polysilicon process*, Silicon for the Chemical and Solar Industry XIII, L. Nygård, B. Pachaly, H. Rong, M. Tangstad, H. Tveit, I. Page Eds., (Kristiansand, Norway), 2016, p. 203.
10. U. Kürschner, U. Pätzold, K. Hesse, H. Lieski, *Studies on Trichlorosilane Synthesis*, Silicon for the Chemical and Solar Industry VII, H.A. Øye, A. Holås, L. Nygård, Eds., (Tromsø-Bergen, Norway), 2004, pp. 177-188.
11. E. Enk, J. Nickl, H. Teich, *Continuous process for the manufacture of silicon tetrachloride and / or trichlorosilane*, West German patent DE 1105398B, 1961.

12. E. Enk, J. Nickl, H. Teich, *Apparatus for the continuous production of silicon chloroform (trichlorosilane) and / or silicon tetrachloride,* U. S patent 3,148,035, 1964.
13. E. Ehrich, T. Lobreyer, K. Hesse, H. Lieski, *Action of copper in Trichlorosilane Synthesis*, Silicon for the Chemical and Solar Industry IV, H.A. Øye, H. Rong, L. Nygård, G. Schüssler, J. Tuset, Eds., (Geiranger, Norway), 1998, pp. 113-122.
14. S. Wakamatsu, K. Hirota, K. Sakata, *Study of selectivity in Trichlorosilane producing reaction*, Silicon for the Chemical and Solar Industry IV, H.A. Øye, H. Rong, L. Nygård, G. Schüssler, J. Tuset, Eds., (Geiranger, Norway), 1998, pp. 123-132.
15. H. Vollbrecht, *Temperature regulating process for vibratory grate reactors,* U. S patent 3,754,075, 1973.
16. M. Rodgers, *Process for production of polycrystalline silicon*, U. S. Patent 3,933,985, 1976.
17. H. Hamster, F. Köppl, *Device for treating gases at high temperatures*, U. S. Patent 4,536,642, 1985.
18. R. Burgie, P. Harder, D. Sawyer, *Process for hydrogenation of tetrachlorosilane*, U. S. Patent 5,422,088, 1995.
19. S. Fahrenbruck, B. Hazeltine, A. Schweyen, S. Skinner, *Apparatus and methods for conversion of silicon tetrachloride to trichlorosilane*, U. S. Patent 9,217,609, 2015.
20. K. Oda, *Production of polycrystalline silicon with low phosphorus content*, Japanese Patent JP 3878278-B2, 2007.
21. H. Prigge, R. Rurländer, M. Schwab, H. Bortner, A. Englmüller, *Process for removing N-type impurities from liquid or gaseous substances produced in the gas-phase deposition of silicon*, U. S. Patent 4,892,568, 1990.
22. L. Coleman, *private communication*, 2015.
23. OCI Company Ltd., Investor Relations, *Financial results for the Fourth quarter ended December 31, 2017*, Slides 14 and 15, February 2018.
24. Chongqing Daqo New Energy Co., Ltd., *Solar grade chunk polysilicon technical data sheet*, http://www.dqsolar.com/down/1263362910.pdf, March 2018.
25. GCL-Poly Energy Holdings, Ltd., *Solar and electronic grade polysilicon technical data sheet*, March 2014.
26. Wacker Polysilicon, Capital Markets Day Burghausen, *High Quality Polysilicon – The basis for high wafer yields and high efficiency solar cells*, Slide 16, 25-July-2007.
27. Osaka Titanium Technologies Co., Ltd. Web site, *Polysilicon product details*, www.osaka-ti.co.jp/e/e_product/pdf/table_e.pdf, March 2018
28. Wacker Polysilicon, Capital Markets Day Burghausen, *High Quality Polysilicon – The basis for high wafer yields and high efficiency solar cells*, Slide 19, 25-July-2007.
29. B. Ceccaroli, E. Ovrelid, S. Pizzini (Eds.), *Solar Silicon Processes - Technologies, Challenges and Opportunities*, Boca Raton, Florida, USA: CRC Press; 2017, pp. 203-204.
30. Osaka Titanium Technologies Co., Ltd. Web site, *Silicon Manufacturing Process*, www.osaka-ti.co.jp/e/e_product/silicon/index.html, March 2018
31. J. Whelan, *Method of purifying silicon tetrachloride and germanium tetrachloride*, U. S. Patent 2,821,460, 1958.

Silicon for the Chemical and Solar Industry XIV
Svolvær, Norway, June 11 – 14, 2018

Exploring thermal pyrolysis of monosilane through gas chromatography-mass spectrometry measurements of higher order silanes

Guro M. Wyller, Thomas J. Preston, Marte O. Skare, Hallgeir Klette, Anjitha S. G, Erik S. Marstein
Institutt for energiteknikk (IFE), Box 4, 2027 Kjeller, Norway

Abstract

We develop and demonstrate an advanced combination of gas chromatography and mass spectrometry (GC-MS) for detection of higher order silanes. In a recent contribution we have successfully identified the three tetrasilane isomers *n*-tetrasilane (*n*-Si_4H_{10}), silyltrisilane (*i*-Si_4H_{10}) and cyclotetrasilane (*cyclo*-Si_4H_8), as well as the four pentasilane isomers *n*-pentasilane (*n*-Si_5H_{12}), silyltetrasilane (*i*-Si_5H_{12}) disilyltrisilane (*neo*-Si_5H_{12}) and cyclopentasilane (*cyclo*-Si_5H_{10}) using our system. We further presented the mass spectra of these species. In this contribution, we introduce optimizations of the GC-MS setup that enhances measurement sensitivity, especially for silanes with high boiling points. We combine the GC-MC setup with our novel millilitre per minute flow scale reactor – Milly – with excellent temperature, pressure and flow control. Subsequently, we determine the relation between boiling point and retention time of higher order silanes, and finally use this relation to identify the two hexasilane isomers cyclohexasilane (*cyclo*-Si_6H_{12}) and *2*-silylpentasilane and/or 3-silylpentasilane.

Introduction

Pyrolysis of SiH_4 in solar silicon industry

Reducing the energy consumption during production of polysilicon can significantly reduce the energy payback time of solar cells and modules. A recent study [1] indicates that reducing the energy consumption for solar grade silicon production by 15–17 kWh/kg-Si gives – in a CO_2 emission perspective – the same result as a 1 % increase in the baseline efficiency for mono- and multicrystalline silicon solar modules. In today's solar cell industry, more than 80% of the consumed polysilicon is produced by the Siemens process [2], a relatively expensive and energy demanding process in which gaseous trichlorosilane (TCS/$SiHCl_3$) is converted to solid silicon by thermal decomposition (pyrolysis). The TCS-based Siemens process can be replaced by pyrolysis of monosilane (SiH_4), which can be carried out, for example, in a fluidized bed reactor (FBR) or a centrifugal chemical vapor deposition (C-CVD) reactor. These monosilane-based reactor technologies have the proven capability to produce polysilicon with significantly lower energy use than the Siemens reactor [1], [3], [4]. These reactor technologies do, however, encounter challenges related to dust formation during the silane pyrolysis process [3]–[5]. When reactant gas molecules decompose homogeneously (in the gas phase), rather than heterogeneously (on a surface), dust

(fines) is formed instead of the desired solid silicon product [6], [7]. Fines formation is, in other words, a competing chemical pathway causing reduced overall chemical yield in the pyrolysis process [5], [8]. Fines formation does also lead to mechanical challenges, such as reactor clogging [9], as well as to reduced material quality [8]. Overcoming these challenges requires understanding of the chemical pathway through which the pyrolysis proceeds.

Pyrolysis of monosilane can schematically be described through the overall reaction (1) in which gaseous monosilane (SiH_4) is converted to solid silicon and gaseous hydrogen:

$$SiH_4(g) \rightarrow 2H_2 + Si(s) \quad (1)$$

This overall reaction does, however, hide a lot of chemical complexity. There is a general consensus that the pyrolysis occurs through a network of chemical reactions including Si-Si bond formation and hydrogen elimination, producing silanes with increasing number of silicon atoms [10]–[15]. Within one silane family, 1,2-hydrogen shifts (rearrangement in which a hydrogen atom moves from one silicon atom to another) and ring opening and closing reactions lead to interconversion between different isomers [10], [11], [16], [17].

Many kinetic models of the monosilane pyrolysis process have an impressive degree of detail. Some of these include hundreds of species with up to 10 silicon atoms and more than one thousand chemical reactions [10], [11], [18]–[20]. Experimental works in the field, on the other hand, are typically limited to measurements of silanes with no more than three or four silicon atoms, and have a lack of differentiation between isomers [12], [13], [21], [22]. There is, in other words, a mismatch between the degree of detail in the experimental and modelled works, and hence few available methods for validating detailed silane pyrolysis models. Therefore, even if several studies, experimental, as well as based on modelling, have been conducted on the topic of thermal pyrolysis, a lot of its chemical complexity remains hidden.

The GC-MS measurement technique that we apply and develop in this work contributes to enlighten this chemical complexity by allowing measurements of separate higher order silane isomers in monosilane pyrolysis exhaust. These isomer-resolved measurements enable validation of detailed models of monosilane pyrolysis.

In a recent publication [23], we demonstrated our GC-MS method and presented the mass spectra of mono-, di- and trisilane, as well as mass spectra of the tetrasilane isomers n-tetrasilane (*n*-Si_4H_{10}), silyltrisilane (*i*-Si_4H_{10}) and cyclotetrasilane (*cyclo*-Si_4H_8) and of the pentasilane isomers n-pentasilane (*n*-Si_5H_{12}), silyltetrasilane (*i*-Si_5H_{12}) disilyltrisilane (*neo*-Si_5H_{12}) and cyclopentasilane (*cyclo*-Si_5H_{10}). Six of these mass spectra were previously unpublished. All these mass spectra are shown in Figure 1. For monosilane (SiH_4), disilane (Si_2H_6) and trisilane (Si_3H_8), spectra from literature are shown for comparison. The literature spectra for monosilane and trisilane are taken from the NIST WebBook [24], whereas that of disilane – which is unavailable in that database – is taken from the newest available publication including that spectrum [25].

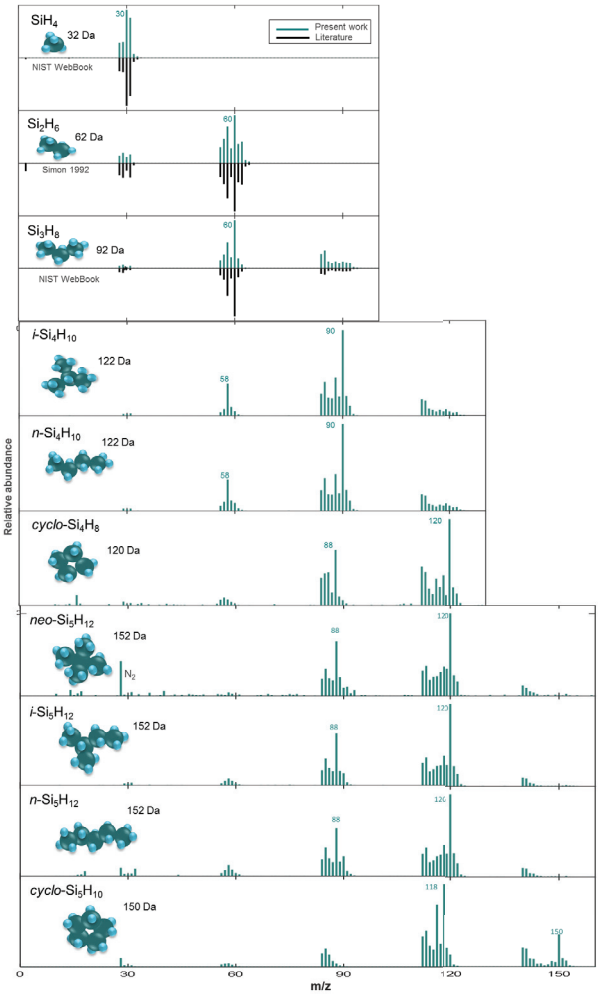


Figure 1: Reprinted from our previous work [23]. 70 eV electron ionization mass spectra of 10 silane isomers with number of silicon atoms ranging from 1 to 5. The masses of the most abundant peaks are indicated. In the three lowest order silanes (SiH_4, Si_2H_6 and Si_3H_8), mass spectra measured by our setup (green) are compared to mass spectra appearing in the literature (black). For more detail on how our spectra and their uncertainties are calculated, see ref.[23].

Experimental setup

GC-MS system

The GC-MS system applied in this work consisting of gas chromatograph Agilent 7890B GC and a mass spectrometer Agilent 5977A MSD (subtype G7038, quadrupole MS with electron ionization) is largely the same as the system already presented in ref.

[23]. Readers are therefore referred to our previous work in ref. [23] for a thorough description of the setup. In the gas-chromatographic system, silane isomers are being separated in time, due to their differences in boiling points and, accordingly, also in their migration time through gas-chromatographic columns. Different isomers do therefore elute to the mass spectrometer at different times.

As a part of this work, some improvements are introduced to the gas handling and loading system, which is also an integrated part of the GC-MS setup. Most importantly, the temperature of the gas handling and loading system is elevated to about 120 °C (as opposed to 60 °C in the former setup). The elevated temperature provides increased sensitivity by preventing large, high-boiling silanes from condensing in the system before they reach the gas chromatographic columns. High temperature in the gas handling system is facilitated by pneumatically controlled valves. The new pneumatic system allows the electronic parts, by which valves in the gas inlet system are controlled, to be placed separately from the valves themselves: the valves are placed in a tailor-made oven, heated to 120 °C, whereas the electronics, having a lower temperature tolerance, are placed outside the oven. The so-called Argon Piston, presented in ref. [23], is in the new GC-MS setup replaced by a smaller inert sampling coil built into the heated oven, securing that the temperature also in this part is kept at 120 °C.

Silane pyrolysis reactor - Milly

Our GC-MS setup can be connected to any silane pyrolysis reactor to automatically sample the reactor exhaust. For the experiments described in this work, a horizontal silane pyrolysis reactor (see Figure 2 a and b) was used.

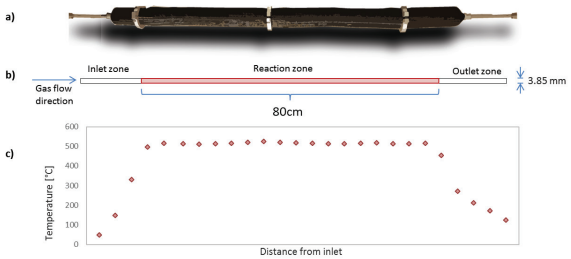


Figure 2: Our novel millilitre-per-minute flow silane pyrolysis reactor - Milly. a) Simplified photo of the reactor. b) Schematic drawing of the reactor, including inlet zone, reaction zone and outlet zone. c) Measured temperature profile along reactor centreline.

The reactor setup consists of a 124 cm long 1/4'' stainless steel pipe with Swagelok fittings in both ends. The inner diameter of the tube is 3.85 mm. Process gases (SiH_4, H_2 and Ar) are routed from a gas interface cabinet into the reactor in which the gas is heated, causing production of higher order silanes. The reactor exhaust is led to the GC-MS for analysis. The temperature of the transfer line from the reactor to the GC-MS is kept above 120 °C to prevent high boiling species from condensing at the tube walls. The reactor temperature and pressure as well as mixing ratio and flow rate of the process gases (SiH_4/H_2/Ar) are controlled by the reactor operator. For the experiment presented here we used a fixed pressure of 1.2 bar, a fixed temperature of 500 °C and a fixed flow of 0.095 slm Ar and 0.005 slm SiH_4.

Figure 2c displays the temperature profile along the centerline of the reactor with the total gas flow and temperature settings used in the experiment. Due to the small reactor diameter and good insulation, we obtain a very stable reactor temperature with less than 15 °C deviation among the highest and lowest temperatures in the reaction zone.

Results and discussion

Figure 3 shows a total ion chromatogram (TIC) of a typical GC-MS injection of silane pyrolysis exhaust. The chromatogram is acquired by scanning all masses from *m/z* 10 to *m/z* 300. The masses of some abundant polluting ions (*m/z* 18, 28, 32, 40, 44 corresponding to H_2O, N_2, O_2, Ar and CO_2 respectively) are subtracted for an enhanced signal-to-noise ratio. The chromatogram includes peaks from isomers with number of silicon atoms $n_{Si} \geq 3$. The assignment of the chromatographic peaks in Figure 3 to silane isomers is partly based on the mass spectral signatures of those peaks (see Figure 1), but also on the assumption that the retention time of a silane isomer from the GC column correlates with its boiling point to some degree. Boiling points of silane isomers are not frequently tabulated and are generally substantially less thoroughly addressed in the literature than boiling points of hydrocarbons. In our previous work [23] the relevant boiling points available in the literature were collected and presented.

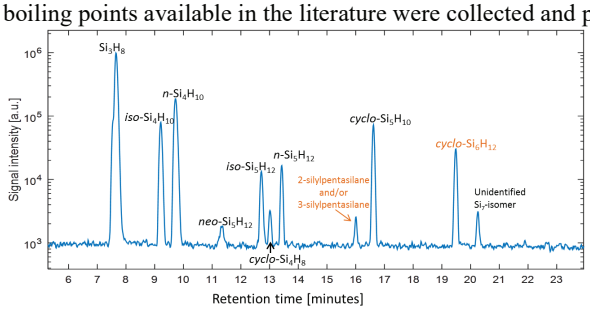


Figure 3: Total ion chromatogram (TIC) of a typical GC-MS injection of silane pyrolysis exhaust. The masses of some abundant polluting ions (m/z 18, 28, 32, 40, 44 i.e. H_2O, N_2, O_2, Ar and CO_2 respectively) are subtracted for an enhanced signal-to-noise ratio. Peaks are identified based on their mass spectra (see Figure 1, labelled in black) and based on their boiling points (See Figure 4, labelled in orange).

In Figure 4, retention times of the elutes shown in Figure 3 are plotted against the inverse boiling points of the corresponding species. Filled symbols indicate chromatographic peaks with corresponding silane isomers that we already identified in ref. [23]. Open symbols indicate chromatographic peaks and species that we identify herein. The boiling points of all the species are found in the literature [23], [26]–[32].

For two of the species included in Figure 4 (*cyclo*-Si_5H_{10} and *neo*-Si_5H_{12}), there are two unequal boiling points reported in the literature. So far there is no general consensus on what the actual boiling points are. In these cases, we have therefore included both reported boiling point values in the figure. For *cyclo*-Si_5H_{10} Hengge and Bauer [30] reported a boiling point of 195 °C, whereas Günter [31] reported 173.3 °C. As explained in ref. [23] we have reason to believe that the boiling point reported by Hengge and Bauer [30] is the more trustworthy. The boiling point reported by Günter [31] is therefore grey in Figure 4. As indicated by the dashed line in Figure 4, we observe a linear relation when plotting the logarithm of the retention time versus the inverse boiling point. The linear relation seems to hold true for all the known species

(filled symbols). The origin of this linear behaviour is focus of current work. Note that the point reported by Günter [31] appears as an outlier in Figure 4, supporting our theory that the boiling point reported by Hengge and Bauer [30] is the more trustworthy of the two. For disilyltrisilane (*neo*-Si_5H_{12}), boiling points of 130 °C (Höfler and Jannach [28]) and 134.3 °C (Fehér and Freund [29]) are reported. The linearity of our data (see also next paragraph) suggest that the first of the two (130 °C [28]) is the more trustworthy. The latter is therefore also indicated grey in Figure 4.

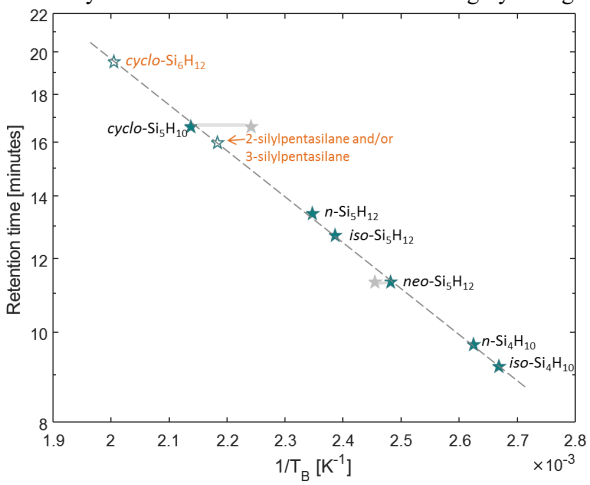


Figure 4: Semilogarithmic plot of retention time versus inverse boiling points of several higher order silane isomers. Closed symbols correspond to previously identified chromatographic peaks/species. Open symbols correspond to chromatographic peaks/species that we identify in the present work.

Based on the remarkably clear linear relation between the logarithm of the retention time of the known species and their inverse boiling point temperature, we assume that a similar linearity holds true for all elutes. We are thereby able to tentatively assign also some of the so-far unknown species (open symbols) to chromatographic peaks in Figure 3. As seen by the good adherence to the line in Figure 3, our data suggest that we have one peak corresponding to cyclohexasilane (*cyclo*-Si_6H_{12}) and one peak corresponding to 2-silylpentasilane and/or 3-silylpentasilane. These peaks, which we have tentatively assigned based on Figure 4, are labelled in orange in Figure 3.

Interestingly, the boiling points of *n*-hexasilane (*n*-Si_6H_{14}) and *n*-heptasilane (*n*-Si_7H_{16}) [27] do not correspond to any of our chromatographic peaks, meaning that in the present experiment these species were not produced, or were produced at a concentration below our detection limit. The cyclic species cyclopentasilane and cyclohexasilane, on the other hand, have intense chromatographic peaks (see Figure 3), indicating that these species are produced at relatively high concentrations. This observation is in line with kinetic simulations by Wong et al. [19], who found cyclopentasilane to be the most abundant Si_5 species during silicon nanoparticle formation. Several authors [11], [18], [33], [34] (and others) have stated that ring formation plays a key role in the formation of large hydrogenated silicon clusters. Elimination of silylene from cyclic species requires simultaneous breakage of two Si-Si bonds, and is therefore less likely than elimination of silylene from non-cyclic species [33]. Cyclopenta- and cyclohexasilane which, as opposed to the cyclic species with

fewer silicon atoms, are entirely free of ring strain [35], are therefore likely to be produced at high concentrations. Our experimental results, indicating high concentrations of cyclic species, are in line with these theoretical considerations.

Conclusion

With recent optimizations of our unique gas chromatography-mass spectrometry (GC-MS) setup for separation and detection of higher order silanes, we are able to identify and measure the three tetrasilane isomers *n*-tetrasilane (*n*-Si_4H_{10}), silyltrisilane (*i*-Si_4H_{10}) and cyclotetrasilane (*cyclo*-Si_4H_8), as well as the four pentasilane isomers *n*-pentasilane (*n*-Si_5H_{12}), silyltetrasilane (*i*-Si_5H_{12}), disilyltrisilane (*neo*-Si_5H_{12}) and cyclopentasilane (*cyclo*-Si_5H_{10}) and finally the two hexasilane isomers cyclohexasilane (*cyclo*-Si_6H_{12}) and 2-silylpentasilane and/or 3-silylpentasilane. The hexasilane isomers, which we were previously not able to assign to chromatographic peaks, are now identified based on an observed linear relation between the logarithm of the retention time and inverse boiling point of a species.

Our GC-MS, with its proven capability of detecting separate higher order silane isomers is a unique tool for validation of monosilane pyrolysis models. Such models can enhance the understanding of the pyrolysis process and thus allow for optimization of monosilane based polysilicon reactor technologies.

References

1. D. Ravikumar, B. Wender, T. P. Seager, M. P. Fraser, and M. Tao, "*A climate rationale for research and development on photovoltaics manufacture,*" Appl. Energy, **189**, 2017, p.245–256.
2. G. Cellere, H. Forstner, T. Falcon, M. Zwegers, and J. Bernreuter, "*International Technology Roadmap for Photovoltaic,*" no. March, 2016, p.1–37.
3. A. Ramos, W. O. Filtvedt, D. Lindholm, P. A. Ramachandran, A. Rodríguez, and C. del Cañizo, "*Deposition reactors for solar grade silicon: A comparative thermal analysis of a Siemens reactor and a fluidized bed reactor,*" J. Cryst. Growth, **431**, Dec. 2015, p.1–9.
4. W. O. Filtvedt, T. Mongstad, H. Klette, A. Holt, S. Sørensen, and J. Filtvedt, "*Novel low cost production through centrifuge chemical vapor deposition ,*" *Silicon for the Chemical and Solar Industry*, **XII**. Trondheim, 2014.
5. J. Li, G. Chen, P. Zhang, W. Wang, and J. Duan, "*Technical challenges and progress in fluidized bed chemical vapor deposition of polysilicon,*" Chinese J. Chem. Eng., **19**, no. 5, 2011, p.747–753.
6. T. Murthy, N. Miyamoto, M. Shimbo, and J. Nishizawa, "*Gas-phase nucleation during the thermal decomposition of silane in hydrogen,*" J. Cryst. Growth, **33**, no. 1, 1976, p.1–7.
7. G. Hsu, R. Hogle, N. Rohatgi, and A. Morrison, "*Fines in Fluidized Bed Silane Pyrolysis,*" **157**, no. March, 1984, p.660–663.
8. G. Bye and B. Ceccaroli, "*Solar grade silicon: Technology status and industrial trends,*" Sol. Energy Mater. Sol. Cells, **130**, 2014, p.634–646.
9. W. O. Filtvedt *et al.*, "*Development of fluidized bed reactors for silicon production,*" Sol. Energy Mater. Sol. Cells, **94**, no. 12, 2010, p.1980–1995.
10. S. L. Girshick, M. T. Swihart, M. R. Mahajan, and S. Nijhawan, "*Numerical Modeling of Gas-Phase Nucleation and Particle Growth during Chemical*

Vapor Deposition of Silicon," J. Electrochem. Soc. Soc., **147**, no. 6, 2000, p.2303–2311.
11. M. T. Swihart and S. L. Girshick, "*Thermochemistry and Kinetics of Silicon Hydride Cluster Formation during Thermal Decomposition of Silane,*" J. Phys. Chem. B, **103**, no. 1, 1999, p.64–76.
12. J. O. Odden, P. K. Egeberg, and A. Kjekshus, "*From monosilane to crystalline silicon, part II: Kinetic considerations on thermal decomposition of pressurized monosilane,*" Int. J. Chem. Kinet., **38**, no. 5, 2006, p.309–321.
13. A. A. Onischuk *et al.*, "*Aerosol formation under heterogeneous/homogeneous thermal decomposition of silane: Experiment and numerical modelling,*" J. Aerosol Sci., **31**, no. 8, Aug. 2000, p.879–906.
14. A. J. Adamczyk, M.-F. Reyniers, G. B. Marin, and L. J. Broadbelt, "*Kinetic correlations for H2 addition and elimination reaction mechanisms during silicon hydride pyrolysis.,*" Phys. Chem. Chem. Phys., **12**, no. 39, 2010, p.12676–96.
15. A. A. Onischuk and V. N. Panfilov, "*Mechanism of thermal decomposition of silanes,*" Russ. Chem. Rev., **70**, no. 4, 2001, p.321–332.
16. A. J. Adamczyk, M. F. Reyniers, G. B. Marin, and L. J. Broadbelt, "*Exploring 1,2-hydrogen shift in silicon nanoparticles: Reaction kinetics from quantum chemical calculations and derivation of transition state group additivity database,*" J. Phys. Chem. A, **113**, no. 41, 2009, p.10933–10946.
17. A. J. Adamczyk, M. F. Reyniers, G. B. Marin, and L. J. Broadbelt, "*Hydrogenated amorphous silicon nanostructures: Novel structure-reactivity relationships for cyclization and ring opening in the gas phase,*" Theor. Chem. Acc., **128**, no. 1, 2011, p.91–113.
18. S. Nijhawan *et al.*, "*An experimental and numerical study of particle nucleation and growth during low-pressure thermal decomposition of silane,*" J. Aerosol Sci., **34**, no. 6, 2003, p.691–711.
19. H. Wong, X. Li, M. T. Swihart, and L. J. Broadbelt, "*Detailed Kinetic Modeling of Silicon Nanoparticle Formation Chemistry via Automated Mechanism Generation,*" **108**, 2004, p.10122–10132.
20. B. L. Slakman, H. S. Simka, H. Reddy, and R. H. West, "*Extending Reaction Mechanism Generator (RMG) to silicon hydride chemistry,*" Ind. Eng. Chem. Res., **55**, no. 49, 2016, p.12507–12515.
21. A. A. Onischuk, V. P. Strunin, M. A. Ushakova, and V. N. Panfilov, "*Studying of silane thermal decomposition mechanism,*" Int. J. Chem. Kinet., **30**, no. 2, 1998, p.99–110.
22. F. Slootman and J.-C. Parent, "*Homogeneous gas-phase nucleation in silane pyrolysis,*" J. Aerosol Sci., **25**, no. 1, 1994, p.15–21.
23. G. M. Wyller, T. J. Preston, H. Klette, T. T. Mongstad, and E. S. Marstein, "*Identification of higher order silanes during monosilane pyrolysis using gas chromatography-mass spectrometry,*" J. Cryst. Growth, **Accepted**, 2018.
24. M. S. D. C. NIST and S. E. Stein, "*Mass Spectra,*" in *NIST Chemistry WebBook, NIST Standard Reference Database Number 69, Eds. P.J. Linstrom and W.G. Mallard*, Gaithersburg MD: National Institute of Standards and Technology, 2018.
25. J. Simon, R. Feurer, A. Reynes, and R. Morancho, "*Thermal dissociation of disilane: quadrupole spectrometry investigation,*" J. Anal. Appl. Pyrolysis, **24**, 1992, p.51–59.

26. F. Feher, H. Keller, G. Kuhlbörsch, and H. Luhleich, "*Isomerie in der Silan-reihe,*" Angew. Chemie, **70**, no. 13, 1958, p.402.
27. F. Feher, P. Hädicke, and H. Frings, "*Beitrage zur Chemie des Siliciums und Germaniums XXIII(1) Physicalisch-chemische Eigenschaften der Silane von Trisilan bis Heptasilan,*" Inorg. Nucl. Chem. Lett., **9**, 1973, p.931–936.
28. F. Höfler and R. Jannach, "*Zur Kenntnis des Neopentasilanes,*" Inorg. Nucl. Chem. Lett., **1**, 1973, p.723–725.
29. F. Feher and R. Freund, "*Contributions to the chemistry of silicon and germanium, xxii (i) new silanes, bromosilanes and phenylsilanes,*" Inorg. Nucl. Chem. Lett., **9**, 1973, p.937–940.
30. V. E. Hengge, G. Bauer, A. Chemie, T. Itochschule, and O. Mit, "*Darstellung und Eigenschaften yon Cyclopentasilan,*" Monatshefte für Chemie, **512**, 1975, p.503–512.
31. W. Günter, "*Beitäge zur Chemie des Cyclopentasilans,*" Universität zu Köln, 1976.
32. E. Hengge and D. Kovar, "*Darstellung und Characterisierung von Cyclohexasilan Si6H12,*" Zeitschrift für Anorg. und Allg. Chemie, **456**, 1979.
33. S. Veprek, K. Schopper, O. Ambacher, W. Rieger, M. G. J. Vep, and J. Yvon, "*Mechanism of Cluster Formation in a Clean Silane Discharge,*" J. Electrochem. Soc., **140**, no. 7, 1993, p.5–12.
34. K. Tonokura, T. Murasaki, and M. Koshi, "*Formation Mechanism of Hydrogenated Silicon Clusters during Thermal Decomposition of Disilane,*" J. Phys. Chem. B, **106**, no. 3, 2002, p.555–563.
35. W. W. Schoeller and T. Dabisch, "*Anomaly in the Ring Strain Behaviour of Cyclopropane, Cyclobutane, and Cyclopentane, compared with their Silicon Analogues; a Theoretical Study,*" J. Chem. Soc., Chem. Commun, no. 1706, 1985, p.1706–1707.

Silicon for the Chemical and Solar Industry XIV
Svolvær, Norway, June 11 – 14, 2018

New approaches to the investigation of carbon formation in the Direct Synthesis of Methylchlorosilanes

Amalie Tysseland[1)], Estelle M. M. Vanhaecke[1)], Ingeborg-Helene Svenum[2)], Edd A. Blekkan[1)], and Hilde J. Venvik[1)]

1) *Department of Chemical Engineering, NTNU - Norwegian University of Science and Technology, 7491 Trondheim, Norway*
2) *SINTEF Industry, P.O.Box 4760 Torgarden, 7465 Trondheim, Norway.*

Abstract

The underlying mechanisms for the formation of carbonaceous species on the Si/catalyst contact mass during synthesis of methylchlorosilanes from CH_3Cl and Si remain to be understood to the extent that enables inhibition or a high degree of predictability. Building on experience obtained studying carbon formation aspects on heterogeneous catalysts applied in the conversion of natural gas, biomass and crude oil, we report an effort to bring alternative approaches and recent advances in instrumentation into this field. Characterization of the Si/catalyst contact mass, and the carbonaceous species in particular, was made by TGA/DSC/MS, Raman spectroscopy, XPS and pyrolysis GC/MS. SEM/EDX analyses were also performed. Si/catalyst contact mass samples extracted from ongoing as well as terminated fluidized bed experiments were investigated to assess the applicability of the methodology.

Combined, the experimental results imply that the carbonaceous materials are highly reactive species, amorphous in nature, i.e. with a low degree of graphitization. This suggests that their formation, as well as their decomposition in the industrial process, may be sensitive to the reaction conditions and the (local) structure and composition of the contact mass. Given that activation of CH_3Cl is desired, it may prove difficult to completely suppress the formation of carbonaceous deposits, but better predictability and/or partial inhibition could be feasible.

Our analyses indicate significant concentrations of oxygen in the samples. The presence of oxygen has implications for TGA/DCS/MS, the peaks in the Raman spectra, the functional groups of the decomposition products during pyrolysis, as well as the core level shifts in XPS. The relevance of these observations to the actual reaction environment must be established. Moreover, the effect of Cl on the Cu and Si oxidation states and on the decomposition products should be separated from the effect of O. This suggests the need for inert sample transfer routines and equipment, and – if possible – efforts towards in situ characterization.

Introduction

The silicone industry is one of the largest markets for silicon and a key step is the synthesis of methylchlorosilanes, often referred to as the Direct Process or Müller-Rochow synthesis. As a continuous, heterogeneously catalyzed industrial process, it is somewhat unique in the sense that both the catalyst (Cu-based) and one of the two reactants (Si) are in the solid phase, while the other reactant (chloromethane, CH_3Cl) is in the gas phase. The process is tricky to carry out with a high degree of predictability, and the reaction rate as well as the product distribution depend on many factors. In addition to the temperature and (partial) pressure(s) in the reaction zone, these include the nature, purity and degree of conversion of the silicon starting material, the copper catalyst and possible promoters, the morphology of the solid phase, and the type of reactor used. A range of methylchlorosilanes, $(CH_3)_xSiCl_{1-x}$, is formed, with dimethyldichlorosilane (x=2) as the predominant (70-90%) and most desired species. In addition to these, there are many side products that can be isolated, including hydrogen and hydrocarbons as well as chlorosilanes and a number of high-boiling silanes, polysilanes, and siloxanes. In summary, this makes the Direct Process complicated and several aspects are still not fully understood (see e.g. [1] and references cited therein).

One main challenge in lab-scale investigations as well as industrially is the formation of carbon containing species on the surface of the solid phase, which may inhibit the formation of the desired product(s). More specifically, the actual mechanism of the carbon formation, the nature of the carbon formed and its relation to the abovementioned factors are – to the extent of the authors' knowledge – missing to a large degree. Carbon formation is extensively studied in heterogeneous catalysis, since it impacts both safety and cost associated with the industrial processes that involve conversion of hydrocarbons under conditions typically depleted of sufficient oxygen and/or steam to promote carbon gasification. A range of methodologies is applied to better understand the formation of carbon/coke and thereby minimize, control and predict its consequences and associated risk and cost [2, 3]. Certain categories of carbon formation are particularly well described, however, it remains clear that even if the thermodynamic driving force is a boundary condition, the extent of carbon formation is highly dependent on the nature of the solid surfaces present; catalysts, reactor materials, and in the present case – the catalyst-reactant contact mass. This means that the kinetics of the surface reactions determine the extent of carbon formation, and thereby implies a potential for controlling or suppressing the carbon formation by tuning the surface chemistry and the relative rates of the elementary reaction steps proceeding.

Carbon formation from carbon monoxide, methane and lower alkanes is a common issue in all technologies for synthesis gas ($CO+H_2$) production. The phenomenon affects the catalysts and materials applied, as well as the room for optimizing the product composition to the downstream application or the energy efficiency. In this case, the carbon formation mainly proceeds over certain metal nanoparticles in their reduced state, the most efficient catalysts being Ni, Fe and Co and alloys thereof. The presence of Ni and Fe is tricky to avoid as they have important properties with respect to syngas formation catalysis (Ni) and high temperature tolerance of the equipment (Ni, Fe) [4]. Typically, CO is dissociated, oxygen is removed from the surface in the form of CO_2 or H_2O, and the elementary carbon eventually forms graphite-like structures; carbon nanofibers or nanotubes. The size, shape and composition of the solid phases present

strongly affect the nature of the carbonaceous materials, as well as the temperature, pressure and composition of the gas [5]. Moreover, it has been debated whether this mechanism proceeds via dissolution of carbon in the metal, or directly on the surface with certain facets and defects playing a role [5, 6]

The other much studied and described type of carbon formation proceeds via acid sites on a catalyst surface, the most prominent example being the fluid catalytic cracking (FCC) of heavy hydrocarbons widely applied in the oil refineries [2, 3]. The acidic surface is typically an oxide or sulfide, and the chemistry involves the formation of carbonium ion intermediates from the hydrocarbon feedstock of which some interact with each other or other unsaturated species to form a large and complex variety of carbonaceous materials. The classic FCC catalyst is a zeolite (aluminosilicate) type material with a well-defined microporous structure and composition, for which the pore geometry and the chemistry, i.e. the strength and density of acid sites, affects the carbon formation as well as the desired cracking chemistry.

It goes beyond the scope if this contribution to describe the accumulated knowledge on these and related types of carbon formation. But this knowledge has been acquired by applying an extensive experimental and theoretical toolbox addressing the structure and chemistry of the surfaces involved, the corresponding characteristics of the carbonaceous products and their intermediates, and - if possible - the intrinsic kinetics of the reactions involved. We find, however, that although significant contributions exist, this methodology seems to have found limited application with respect to carbon formation during the production of methylchlorosilanes. In this work, we present results from a preliminary investigation in an effort to illustrate the potential for improved understanding of the carbon formation through an integrated experimental approach. Working with a small series of contact mass samples from different stages of a fluidized bed reaction experiment, we have applied thermogravimetric analysis (TGA) combined with differential scanning calorimetry (DSC) and mass spectrometry (MS) to assess the stability and reactivity of surface species as a function of temperature. Pyrolysis gas chromatography combined with mass spectroscopy (pyrolysis GC/MS) was used to capture possible decomposition products from the carbonaceous deposits and Raman spectroscopy was utilized further to investigate structural characteristics of the carbon on the surface; the latter is also sensitive to certain other surface phases, typically oxides. X-ray photoelectron spectroscopy (XPS) was used to capture details of the surface chemistry, and this was combined with the more frequently applied and somewhat less surface sensitive scanning electron microscopy and energy dispersive x-ray analysis (SEM/EDX). The scope of the work has been to explore the potential of these methods, and selected results and preliminary conclusions will be presented. The difficulties and challenges encountered with respect to interpretation and precision will also be addressed, and we will briefly discuss how the approach could be further improved and extended.

Material and methods

The solid samples applied were obtained from Elkem Silicon Materials. The main series was extracted from a fluidized bed experiment performed at 4 bar and 300 °C feeding chloromethane and Ar at a rate of 285 and 10 mL/min, respectively. The contact mass consisted of Si particles (metallurgical grade) and a CuCl catalyst promoted with Zn and Sn, for which the remaining details on impurities and promoters are proprietary.

Samples S1-S4 were extracted at different times (~4, 21,5, 27,5, 46 hours) from the bed during fluidization by inserting and opening a small cylinder containing inert gas at ambient pressure. S5 was obtained from the same contact mass after termination of the experiment at 51h and cooling in inert atmosphere. S0 represents a Si feedstock sample prior to reaction and was used for comparison. In addition, we have investigated some older samples from terminated experiments under similar conditions, in order to have a larger sample amount during exploration. These are named SX1 and SX2, denoting a low and high extent of carbon formation, respectively.

The mass loss, heat exchange and CO_2/H_2O formation from the samples was measured with a Netzsch STA 449C Jupiter TGA/DSC coupled with a Netzsch Aërlos QMS 403C MS. Each sample was heated from 35 °C to 800 °C at 10 °C /min The gas flow applied was either 25 ml/min of Ar (purging gas) and 75ml/min of 20% O_2 in N_2 (oxidative atmosphere) or pure Ar at 100 ml/min (inert atmosphere). The sensitivity to moisture accumulating on the samples was addressed through comparing experiments with and without pre-drying overnight 100 °C in air.

Pyrolysis GC/MS is normally applied to analyze decomposition products from organic samples in the absence of an oxygen atmosphere. Here, samples of approximately 0.5 - 1 mg of contact mass were loaded into a Single-Shot Pyrolyzer ”PY-3030S” from Frontier Lab. Flash pyrolysis was used at a furnace temperature of 500 °C for both samples. The resulting gaseous species were separated on a Agilent 7820A gas chromatograph equipped with an Ultra ALLOY® capillary column, and the eluted compound further analyzed on an Agilent 5977 MSD. The analysis result was compared to the NIST chemical data base using the instrument software.

Raman spectroscopy is nowadays a common tool for evaluating the forms of carbon materials. In fact, with a rapid scan and without destroying the sample, one can easily have access to the 1000-2000 cm^{-1} region where carbon materials present D (around 1330 cm^{-1}) and G (around 1580 cm^{-1}) peaks at visible excitation (633 nm laser source used in this study). In our study the Raman spectra were collected by focusing on a Horiba Jobin Yvon LabRAM HR800 spectrometer. The spectra were obtained by using a x50 LWD objective with a motorized x-y stage. Spectral measurements were performed with continuous scans in the range of 100-3000 cm^{-1}. Acquisition parameters were optimized in order to diminish the background contribution. None of the spectra shown in the study were subject to smoothing or background removal.

X-ray photoelectron spectroscopy was performed on samples SX1 and SX2 using an Axis UltraDLD XP spectrometer from Kratos with monochromatic Al Kα radiation (hv=1486.6 eV). The samples were mounted on carbon tape and the analysis area is approximately 300 × 700 μm^2. A pass energy of 80 eV was used for survey scans and 40 eV for the individual core levels. Charge compensation was used and the binding energy scale is calibrated to elemental Si at 99.4 eV.

The scanning electron microscopy (SEM) topography and elementary distribution (EDX) analysis was performed on a Hitachi S-5500 S(T)EM, applying a voltage of 10kV and 5A-7A current. The STD sample holder was used, onto which ethanol mixed with the sample was dropped and left to dry.

Results and discussion

Scanning electron microscopy images obtained for series S1-S5 as well as S0 generally reveals a large variety of morphology at different magnification scales. Drawing definite inferences on the morphological developments as a function of time and reaction conditions must therefore be done with care. Figure 1 compares representative micrographs from SEM on samples S0 and S3 at a similar scale. Although the Si feedstock contains fine particles (< 1 µm) on the external surface of the particles in the main size range, 100-300 µm, it seems apparent that the reaction between the solid Si leads to roughening of the contact mass particle surface. Part of this seems to be best described as pits dug into the surface, in agreement with previous investigations such as [7]. Intriguing dendritic growth structures occur here and there, but the significance of these could not be established.

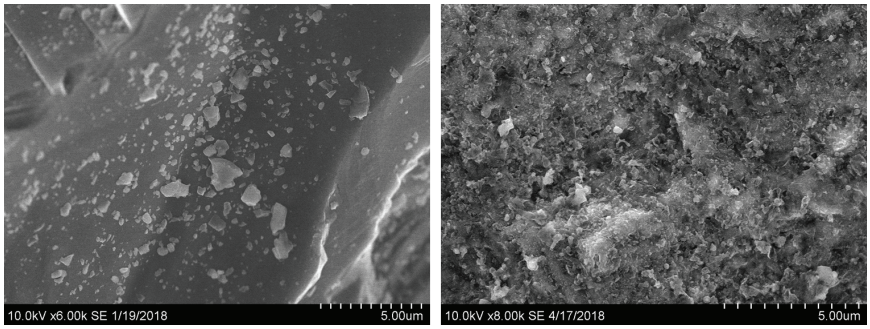


Figure 1: SEM micrographs at comparable magnification showing (left) the surface of a Si particle before exposure to reaction conditions and (right) the surface of an S3 Si particle after ~27,5 hours on stream under CH_3Cl with the Cu based catalyst present.

The EDX analysis shows that the Cu based catalyst is relatively evenly distributed, and it is possible to identify small Cu-rich particles on the surface of the Si particles. Certain regions appear enriched in oxygen, and partly associated with the Cu. Cl is also present and evenly distributed.

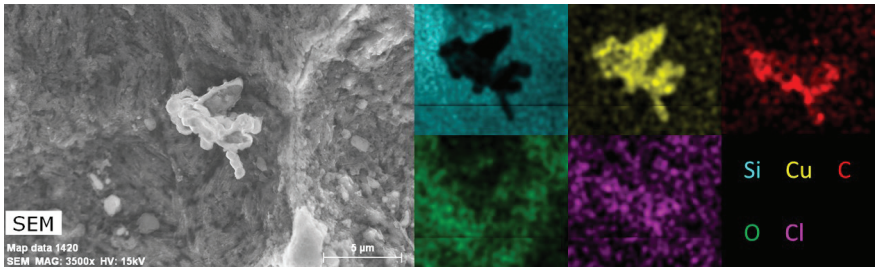


Figure 2: SEM micrograph focussing on a specific particle in sample S2 (~21,5 h on stream), with corresponding elemental analysis for Si, Cu, C, O, Cl by EDX

An interesting result from the elemental analysis is shown in Figure 2. It shows a fragmented Cu particle seemingly not alloyed with the Si. The surrounding Si surface

may contain Cu in lower amounts. The particle is partly overlapping with the C signal, so it is either covered by carbon or is carbidic in nature. The EDX micrograph indicates O depletion in the same area, but generally the O signal is moderately strong and varying. Previous investigations have also reported bulk Cu as more active with respect to carbon formation than Si and Cu_3Si. [8-10]

The TGA/DCS/MS analysis was more challenging than expected. This is related to several aspects. Firstly, due to the nature of the samples, i.e. dense and non-porous, the absolute and relative mass changes are small even if the surface is covered in carbonaceous material. Likewise, the associated CO_2 formation is small, with the potential formation of H_2O dependent on the H-content of the carbonaceous material but presumably also small. This makes the precision sensitive to buoyancy effects in the balance, leaks and the detection limits of the MS and the calorimeter, as well as the humidity of the samples. Higher precision may be achieved through increasing the sample mass for each experiment and running reproductions, but as the method is destructive, this poses demands on the amount of sample required. In our S1-S4 case, the amount of sample available was very limited.

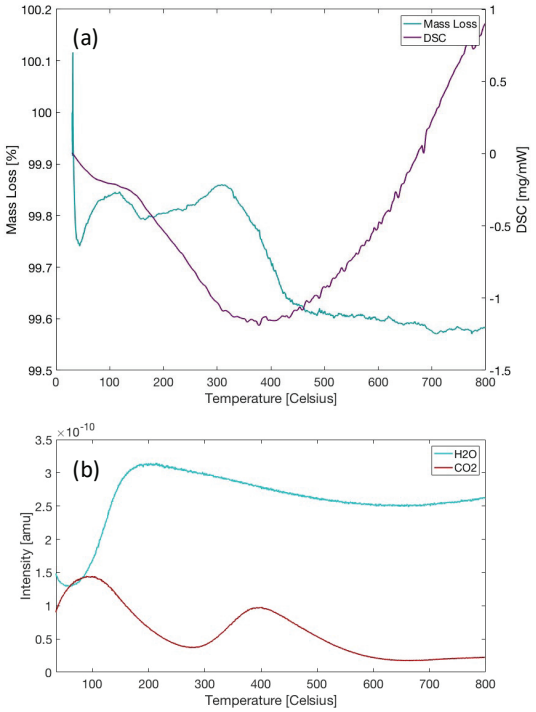


Figure 3: Results of the thermogravimetric analysis of sample S5, obtained after 51 h on stream and subsequent cooling under inert atmosphere, showing (a) the relative mass change and associated exotherm and (b) formation of CO_2 and H_2O as recoded by MS as a function of increasing temperature under oxidizing conditions (20% O_2 in N_2).

Figure 3 shows the TGA/DSC/MS results from sample S5. The mass loss (Fig 3a) around the 350-400 °C signifies the decomposition of contact mass deposits under exposure to oxygen. It is associated with an exotherm in the DSC signal and a peak in the CO_2 formation as measured by MS. The graphs also illustrate the complications encountered with these experiments. Release of CO_2 during the initial heating and other fluctuations during the start-up affect the determination of the mass reference (100%), and in view of this, the mass loss during gasification may be determined as to be 0,3±0,1 %. The H_2O MS signal is difficult to interpret and suggests a gradual release from 100 °C and onwards. Adsorbed humidity may be released upon heating, and at higher temperatures H may be released from C-H bonds and OH groups, but here it must be concluded that the H_2O MS measurement is not sufficiently sensitive to conclude about the chemistry involved. It may also be noted that the formation of CO_2 in the range 300-500 °C from samples subjected to heating ramps under an inert atmosphere was also observed (not shown). In view of the results presented below, this is likely due to oxide phases present in the contact mass samples that upon heating reacts with the carbon species, or carbonate decomposition.

Figure 4 displays Raman spectra obtained from the S1-S4 series. Spectra for S2-S4 have been offset along the y-axis for clarity, but the relative intensities remain the same. The strong peak at 517-520 $cm^{-}$is attributed to Si, and the sharp and intense appearance of the band suggests the presence of crystalline Si [11, 12]**.** One can thus assume that other Raman bands may be detectable in the range of the investigation (100-3000 cm^{-1}) such as the peak at 300 cm^{-1} corresponding to a Si mode and the band at 947 cm^{-1} which could be attributed to Si-H vibrations/Si overtones. The bands at ~430 and ~615 cm^{-1} have not been uniquely assigned at this point since they are small and the composition of the samples is complex, but both bands could also be related to (partly oxidized or chlorinated) Cu species [13-15].

Central to the carbon species are the peaks usually assigned as disordered (D) and graphite (G) peaks around 1330 cm^{-1} and 1580 cm^{-1}, respectively [16]. The G-band is known as due to the relative motion of sp^2 hybridized C atoms while the D band is due to the breathing vibrational mode of six-membered rings. A first general observation is the increase in carbon signal with residence time of the contact mass in the reaction, confirming a gradual accumulation of carbonaceous species. Relative to Si, the modes attributable to carbon deposits are quite weak, despite the generally strong scattering of/ high sensitivity for these particular modes. Hence, the amount of carbonaceous deposits is not very large.

A high intensity ratio of G to D is indicative of high ordering of the carbon, i.e. “graphitic”, and this ratio may change with time, surface or conditions to indicate a (gradual) ordering/disordering. This ratio does not seem to change significantly throughout the series, and the general degree of ordering is relatively low. This is further signified by a lack of intensity in the 2560-2660 cm^{-1} region (2D band). This latter band is highly sensitive with the layer number of graphene and is characteristic to the second order Raman peak of graphite. The carbonaceous layer present on the samples thus consists of mainly amorphous carbon, likely with some locally ordered graphitized carbon [16].

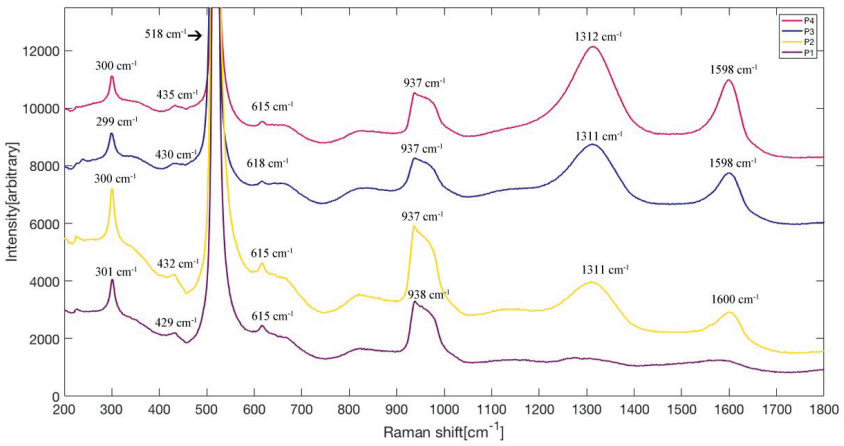


Figure 3: Raman spectra obtained for the S1-S4 sample series(~4, 21,5, 27,5, 46 hours on stream, extracted during reaction), with spectra for S2, S3 and S4 offset for clarity.

X-ray photoelectron survey spectra (EB=0-1200eV) of samples SX1 and SX2 (not shown) confirm the presence of C, Cl, Cu, Si, trace amounts of Zn, and –notably – a considerable O 1s peak in both samples. This may explain significant CO_2 formation observed under non-oxidative TGA for these samples. The extent of oxygen present under the (overall reducing) reactions conditions remains to be established, since oxidation may also proceed during sample transfer and storage. This calls for precautions and measures with respect to preparing and transferring samples and is of great importance with respect to interpreting the decomposition product data discussed below.

XPS spectra of the respective high intensity peaks from sample SX1 and SX2 are displayed in Figure 5. The Si 2p spectrum (Fig 5a) contains contributions that indicate a variety of surface chemistry in addition to the two spin orbit split Si^0 (Si $2p_{3/2}$, Si $2p_{1/2}$) peaks at 99.4 eV and 100 eV. A minimum of two peaks are required to fit this part of the spectrum. Due to their broad nature these peaks are fitted with one component each. The one at the high binding energy side at 103.3-103.5 eV is typical for SiO_2. The other species, denoted Si^{x+}, at somewhat lower binding energy (~102.2 eV), usually representative of less oxidized or organically bound Si.

The C 1s spectrum indicates one broad peak with some minor contributions on the high binding energy side. It is difficult to find a unique and consistent set of peaks to fit, and typical location of relevant C chemical bonds are thus just indicated in the figure. It may be noted that C-C bonding seems to represent a major contribution, but with additional single and double bonds to H, Cl, Si and O. Minor amounts of carbidic Si cannot be ruled out. Sample SX2 is higher in elemental Si as well as carbon; the latter consistent with findings from Raman spectroscopy on these samples (not shown).

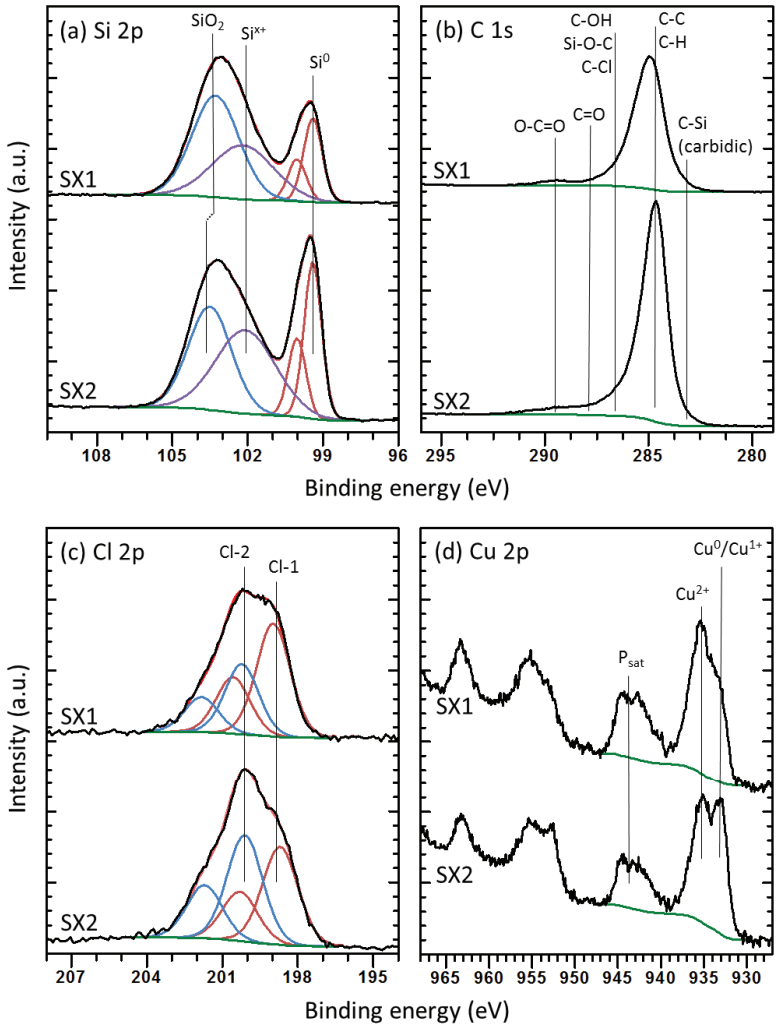


Figure 5: X-ray photoelectron spectra of samples SX1 and SX2 showing the (a) Si 2p, (b) C 1s, (c) Cl 2p, (d) Cu 2p core levels, with some typical peak position for various chemical shifts indicated.

The Cl 2p core level (Fig 5c) has two spin orbit split components (Cl $2p_{3/2}$ and Cl $2p_{1/2}$) separated by 1.6 eV. Two different Cl species are detected, Cl-1 and Cl-2, with the Cl $2p_{3/2}$ component at binding energies of ~198.8 eV and ~200.1 eV, respectively. The Cl-1 component is consistent with M-Cl type (M is Si and/or Cu) and Cl-2 with C-Cl type species [17, 18]. The relative amount of Cl-2 to Cl-1 is higher in SX2, indicating that more chlorine is bonded to carbon in the sample with a larger amount of carbon. This

may not be consistent with the assumption of maintaining the methyl-Cl bond as key to avoiding C-C bond formation.

With respect to the Cu 2p core level, the spin orbit splitting (Cu $2p_{3/2}$ and Cu $2p_{1/2}$) is about 19.8 eV, and the peak shape indicates Cu^{2+} as well as Cu^{0} or Cu^{1+} type species. Moreover, the satellite peak at 940-946 eV is associated with Cu^{2+} type species, and the relative amount of such species is slightly lower in sample SX2. The XPS data hence seem to suggest an overall higher degree of reduction in the sample with more carbon on the surface. This could be a result of the experimental conditions or a difference in the contact mass properties during reaction, but a difference in the propensity to oxidize under ambient conditions (sample transfer) cannot be completely ruled out. Beyond the Zn, no peaks attributable to Si impurities were captured in the survey scan. This signifies their overall low concentrations, but may depend upon the surface sensitivity. It can be enhanced beyond the 5-10 nm into the surface prevailing in these analyses by tuning the incident photon energy to the optimum range using monochromated synchrotron radiation.

Pyrolysis GC/MS results from sample S4 are presented in Figure 6 together with the interpretations suggested upon comparison with the NIST database. It may be noted that, in addition to CO_2, paraffinic and olefinic hydrocarbon chains in the C_{10}-C_{20} range with functional groups attached dominate. In addition, an acetate as well as an aromatic specie are identified. Oxygen is included in most species, either as part of the chain or as part of a functional group. Notably, a predominant functional group is carboxyl, i.e. several decomposition products have acidic nature. Nitrogen functional groups, N≡ and NH_2- are also found.

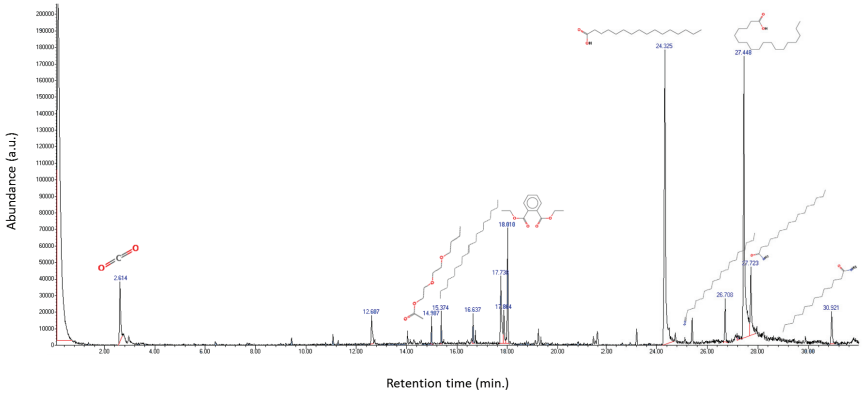


Figure 6: Chromatogram showing the carbon decomposition products obtained from Pyrolysis GC/MS analysis of sample S4 (~37h on stream under CH_3Cl)

Similar chromatograms were obtained for all the samples in the S1-S5 series. There is a slight variation in the molecular structure of the species detected, but the overall chain characteristics and functional groups remain the same. The quality of the fits vary in the range 70-90 %. Many reproductions in additions to standards are required for high precision determination of the decomposition products, but it may be concluded that the

C=C, C-O-C and C=O bonds and the functional groups represent a signature of chemically reactive carbonaceous species on the surface.

Conclusion

This is a preliminary investigation, but this combined TGA/DSC/MS, Raman spectroscopy, XPS pyrolysis GC/MS and SEM/EDX approach seems to offer some possibilities for improved understanding of the underlying mechanisms for the formation of carbonaceous species on the Si/catalyst contact mass during synthesis of methylchlorosilanes from CH_3Cl and Si. The joint data imply that the carbonaceous materials are highly reactive species, amorphous in nature, i.e. with a low degree of graphitization and stability. This suggest that their formation as well as their decomposition in the industrial process may be sensitive to the reaction conditions and the (local) structure and composition of the contact mass. Given that reactant activation is desired, it may prove difficult to completely suppress the formation of carbonaceous deposits. However, better predictability and/or partial inhibition could be feasible. In agreement with previous investigations, the SEM/EDX results suggest that the presence of metallic Cu may have a role in the accumulation of carbon on the Si/contact mass surface.

The spectroscopic data (Raman, XPS) suggest the presence of Cu^{2+} or Cu^{1+}, but it is generally difficult to distinguish the role of oxygen from that of chlorine, both clearly present in the samples. The presence of oxygen also affects the TGA/DCS/MS results and the functional groups of the decomposition products during pyrolysis. Advancing the methodology further thus suggests even better control of all experimental parameters. In particular, it seems essential to avoid post reaction exposure of the samples to air and possible partial oxidation of some of the phases present. This suggests inert sample transfer routines and equipment, and – in line with state-of-the-art catalysis science– efforts towards in situ characterization. Additional investigations addressing the acidic properties of the contact mass surface and the general surface chemistry of the fresh and exposed contact mass by e.g. infrared spectroscopy could also be useful.

Acknowledgement

Dr. Harry Rong and Torbjørn Røe at Elkem Silicon Materials are acknowledged for initiating the investigation, supplying the samples, and for interesting discussions. Professor De Chen, Dept. Chem. Eng, NTNU, is thanked for some the initial suggestions and for making the Pyrolysis GC/MS available. Isaac Yeboah, Dept. Chem. Eng, NTNU, is gratefully acknowledged for assistance and training on the Pyrolysis GC/MS.

References

1. W. Kalchauer and B. Pachalay. Müller-Rochow synthesis: *The direct process to methylchlorosilanes.* Handbook of Heterogeneous Catalysis, Chapter 12.6 p.2635, 2008.
2. C. H. Bartholomew. *Mechanisms of Catalyst Deactivation.* Applied Catalysis A: General, 212, 2001, p17.

3. D. L. Trimm. *Catalyst Design for Reduced Coking (Review).* Applied Catalysis, 1983.
4. P. V. D. S. Gunawardana, T. T. Minh Nguyen, J. C. Walmsley, and H.J. Venvik, *Initiation of Metal Dusting Corrosion in Conversion of Natural Gas to Syngas Studied under Industrially Relevant Conditions,* Industrial Engineering Chemistry Research, 53, 2014, p. 1794.
5. De Chen, K.O. Christensen, E. Ochoa-Fernández, Zixin Yu, B. Tøtdal, N. Latorre, A. Monzón, A. Holmen, *Synthesis of carbon nanofibers: Effects of Ni crystal size during methane decomposition,* Journal of Catalysis 229, 2005, p. 82.
6. S. Helveg, C. López-Cartes, J. Sehested, P.L. Hansen, B.S. Clausen, J.R. Rostrup-Nielsen, F. Abild-Pedersen, and J.K. Nørskov, *Atomic-scale imaging of carbon nanofibre growth,* Nature 427, 2004, p. 426
7. W. F. Banholzer, N. Lewis, and W. Ward, *Active site formation in the direct process for methylchlorosilanes,* Journal of Catalysis 101, 1986, p. 405.
8. T. C. Frank, K. B. Kester, and A. L. Falconer. *Surface Analysis of Methylchlorosilane Formation Catalysts.* Journal of Catalysis 95, 1985, p. 396
9. T. J. Wessel and D. G. Rethwisch, *Deactivation of CuSi and CuZnSnSi Due to Coke Formation During the Direct Synthesis of Methylchlorosilanes,* Journal of Catalysis 161, 1996, 861.
10. J.R. Anderson and B.H. McConkey, *Reactions of methyl chloride and of methylene chloride at metal surfaces: II. Reactions over evaporated films of titanium and other metals,* Journal of Catalysis 11, 1968, p. 54.
11. P.A. Temple and C.E. Hathaway, *Multiphonon Raman Spectrum of Silicon,* Physical Reviews B, 7, 1973, p. 8.
12. T. Kallen, M. Dammak, J. Wang and W.M. Jadwisienczak, *Raman characterization and stress analysis of AlN:Er^{3+} epilayers grown on sapphire and silicon substrates,* Materials Science and Engineering B, 187, 2014, p. 46.
13. Frost, R. L., and Williams, P. A., *Raman spectroscopy of some basic chloride containing minerals of lead and copper,* Spectrochimica acta. Part A, Molecular and biomolecular spectroscopy 60, 2004, p. 2071.
14. G. Socrates, *Infrared and Raman Characteristic Group Frequencies: Tables and Charts,* 3rd ed. John Wiley & Sons, Inc., 2001, p. 198.
15. Yilin Deng, A.D. Handoko, Yonghua Du, Shibo Xi, and Boon Siang Yeo, *In Situ Raman Spectroscopy of Copper and Copper Oxide Surfaces during Electrochemical Oxygen Evolution Reaction: Identification of Cu^{III} Oxides as Catalytically Active Species,* ACS Catalysis 6, 2016, p. 2473.
16. A.C. Ferrari, and J. Robertson, *Interpretation of Raman spectra of disordered and amorphous carbon*, Physical Review B, 61, 2000, 14095.
17. T.H. Andersen, I.-H. Svenum, A. Gabrielsen, and A. Borg, *Investigation of 1,1-dichloroethene interacting with the Si(111)–7×7 surface studied by scanning tunneling microscopy,* Surface Science 603, 2009, p. 84.
18. W. Sesselmann, and T.J. Chuang, *The interaction of chlorine with copper: I. Adsorption and surface reaction,* Surface Science 176, 1986, p. 32.

Optimizing ZT Power Factor Variables in a Porous Silicon Thermoelectric Material

John Carberry[1)], Devin Roberts[1)], Robert Tesch[1)], Timothy Wilson[1,2)]

1) *Silniva Corporation, Jefferson City TN 37760*
2) *Artiman Ventures, Palo Alto CA*

Abstract

But for its bulk thermal conductivity of 149 W/m·K, silicon is an ideal thermoelectric material. It can be doped for high electrical conductivity, high Seebeck coefficient, has high temperature utility, a very low coefficient of thermal expansion, is affordable, and available in commercial and industrial scales. After initially mastering a process for making porous conductive silicon structures with thermal conductivity well below 1 W/m·K, the authors have worked to optimize variables, some of them interactive, and processes, most of them interactive for Seebeck, thermal conductivity, electrical conductivity, and geometric designs to optimize performance.

Introduction

Just as a P N semiconductor can turn light (photons) into electricity (solar cells), or electricity into light (LEDs), a P N semiconductor can also turn heat (phonons) into electricity (thermoelectric generator, TEGs) or electricity into cold (thermoelectric cooler, TECs). But for its high thermal conductivity, silicon is one of the most ideal materials for making such semiconductors. It is the object of our work to adapt silicon through nano structures to solve the challenge of high thermal conductivity and make very efficient TEGs and TECs. Given that 68% of all energy generation is lost as waste heat, and between 16 and 21% of utilities are for cooling, we believe this new technology can have important economic and environmental contributions.

We began our work focusing on using silicon as a Thermoelectric Material (TEMat) eight years ago and first introduced our approach and work in 2012, at this conference, and at the American Ceramic Joint Physics conference in Daytona Beach that same year.

The theme of our work and those presentations was that "but for its thermal conductivity silicon can be the perfect TEMat." As can be seen from the formula, a low thermal conductivity is a prerequisite for success:

The thermoelectric figure-of-merit, ZT, for a thermoelectric material (TEMat) is a dimensionless measure of its efficiency. Z is calculated by multiplying electrical conductivity (σ) and Seebeck Coefficient (S) squared and dividing by thermal conductivity (κ), or:

$$ZT = \frac{S^2\sigma}{\kappa} T^K \qquad (1)$$

At that time, it was presented the following analysis of the competitive comparative attributes of various TEMat candidates (as in Table 1).

Table 1: Comparative attributes of TEMat candidates

Material Parameter		CTE	Oper	Seebeck	Seebeck	Elec	Elec	Thermal	Thermal	ZT	ZT	Rare Earth?	Cost	Properties	Large X
Unit	Tensile	PPM	Temp	microvolts/k	microvolts/k	Siemens	Siemens	W/mK	W/mK			Precious?		Temp	Sections?
	Strength		Kelvin	lower	upper	lower	upper	Upper	Lower	Lower	Upper			Stable?	mm
Bi2Te3 & family		18	550	0.00008	0.00014	50,000	80,000	2.5	1.5	0.07	0.57	yes	High	No	Minus 1 mm
Oxides		8	900	0.00008	0.00012	12,000	18,000	3	2	0.02	0.12	?	High	Yes	Minus 1 mm
Lead Telluride		16	400	0.00014	0.00018	20000	30000	3	1.5	0.05	0.26	yes	High	No	Minus 1 mm
Half Heusler		16	600	0.00012	0.00018	40,000	80,000	2.5	1.5	0.14	1.04	yes	High	No	Minus 1 mm
Skutterudites		16	750	0.00012	0.00018	40,000	80,000	10	1.5	0.04	1.30	Yes	High	No	Minus 1 mm
ZNTL		12	700	0.00012	0.00018	40,000	80,000	2.5	1.5	0.16	1.21	Yes	High	no	Minus 1 mm
L AST		14	700	0.00014	0.00018	20000	30000	0.8	0.5	0.34	1.36	yes	High	No	Minus 1 mm
Magnesium Silicide		11.5	700	240	300	6000	32000	6	3.6	0.30	0.80	no	moderate	No	Thin
Micro Channels		3.6	900	0.00012	0.00018	25,000	35,000	1.5	0.6	0.22	1.70	No	High	Yes	Minus 1 mm
Nano Fiber		3.6	900	0.00012	0.00018	25,000	35,000	1.5	0.6	0.22	1.70	No	High	Yes	Minus 1 mm
Silicon Germanium		4	1400	0.00014	0.00028	20,000	40,000	60	2.5	0.01	1.76	Germanium	High	Yes	10 +
Porous Silicon		2.6	1400	0.00017	0.00062	5,000	75,000	0.16	0.72	1.26	56.06	No	Low	Yes	25+

The purpose of our presentation today is to show the updated work and progress that has been made in the preceding six years. We believe we are at the cusp of presenting modules made with porous silicon legs and yet we have had to address and solve a very large number of problems during this work.

Thermal Conductivity: Kappa

The thermal conductivity of pure crystalline silicon is about 149 Watts per meter degree kelvin (149 W/m·K), which is clearly a disqualifier for a TEMat where the ZT values are calculated in a formula where thermal conductivity is in the denominator.

The phonon necessitated pathway, which is temperature dependent, is much larger than the electrical conductivity necessitated pathway for kappa sub phonon compared to kappa sub electron. Most of the heat flow is K_p. At room temperature it is close to 200 nm, for 500°C it is about 80 nm. This provides a window where a material can be effectively engineered to "decouple" the electrical and thermal properties.

There is also the nature of phonon scattering at "Fermi Surfaces" in the same vein, where the reflection and scattering of the phonons is very high at those free surfaces.

We find there is a curve for kappa in a porous silicon structure, where the density below 68%, and optimally below 60%, provides values below 0.7 W/m·K and as low as 0.16 W/m·K:

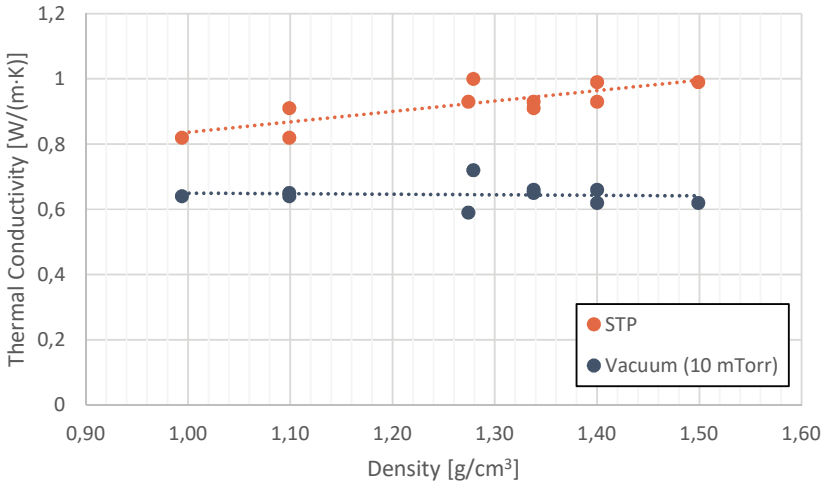


Figure 1: Measured Kappa in air and vacuum

The measurement of thermal conductivity is as much art as technology. Most thermal measurement devices apply an effusivity sensor to infer diffusion and thermal conductivity.

We know our porous silicon objects are fully reticulated: placing a pellet on a drop of water will very quickly bring water to the top surface. Therefore, in most thermal conductivity measurements a signal is sent and received and read in a time domain. When the object is not a bulk material and there are two pathways, as there is in a reticulated porous object, one must be diligent to interpret the data and the test circumstances in these regards.

We have used several methods to measure kappa. The industry standard, for instance used at GA Tech's Thermal transfer laboratory taken in air and a vacuum differ. Here is the reasoning:

- Our pellet's porosity is reticulated, continuous from one side to the other.
- We have small necks, nano sized three-dimensional arrow heads
- The sonic velocity for silicon is 8433 m/s.
- IF our kappa in the porous structure is indeed 0.2-0.6 W/m·K, then the sonic velocity at the end of the day is 0.2/149 times 8433 or 9 m/s.
- For air it is 343 m/s
- For water it is 1498 m/s.
- Density of air is 1.225×10^{-3} g/cm^3, water is 1 g/cm^3, silicon is 2.33 g/cm^3.
- Water is 816 times the density of air, and silicon 1902 times denser.
- Whether we are transient or steady state, we are dealing with the movement of phonons in terms of time signatures and steady state respectively and literally the heat transfer efficiency of the two systems.
- When we do the transient in vacuum, all the signal goes through the silicon, none, or nearly none through the vacuum. I am sure we are all agreed on that?
- When filled the porosity with water, through which the signal would go much faster through the water but the increase in mass by 816 results in huge thermal transfer losses from one side to the other in the recorded time domains. In both the case of the vacuum filled porosity and the water filled porosity the value measured is through the silicon, in the case of air it is mostly through the air.

Jean-Marie Lebrun in his doctoral thesis studied and worked on ways to make a fully or nearly fully dense wafer for solar cells. [1] Though his efforts did not obtain the desired results, his work and data have been of enormous utility to us. His failure to turn powdery silicon into a fully dense silicon wafer were based on the tendency at temperatures below silicon's melting point to form necks which grow very slowly and inhibit densification.

We have found that we can go to very high temperatures, and even hold for very long times, and hold density to very controlled levels of porosity.

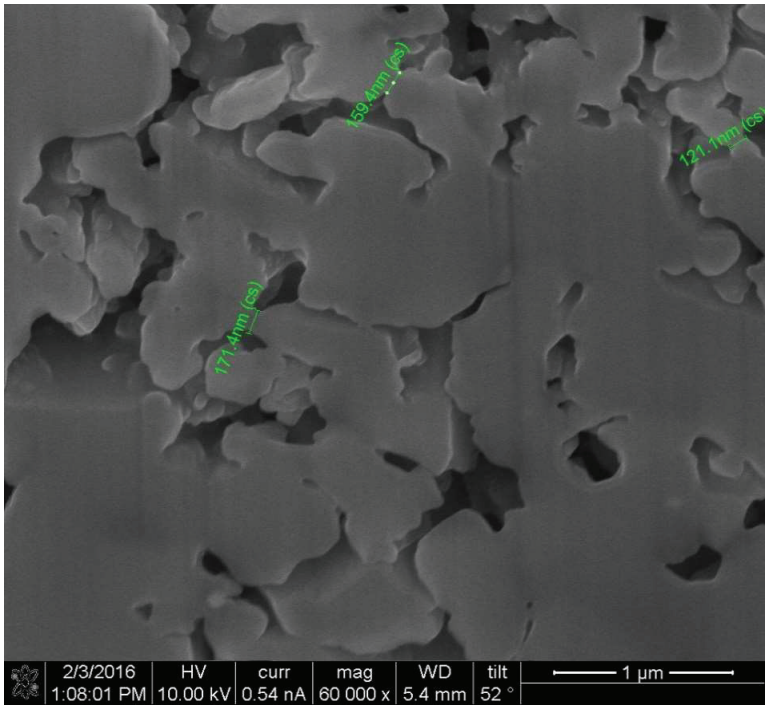


Figure 2: A polished (FIB) cross section SEM 60,000 X of our porous silicon. Starting particle size was D50 by number about 600 nanometers.

Our milling process, performed in a high energy mill with a cold jacket and using a solvent such as acetone or ethanol, is fast, economical and provides a high yield. We have good control over particle size, distribution and surface are with the controls in place, such as RPM, charge density, solvent content, time, media size as well as the morphology of the starting charge.

We have concluded that an engineered process for making porous highly doped silicon with very low thermal conductivity has been achieved.

Electrical Conductivity

Both classical and quantum physics show there is dimensionality to Ohm's law behaviors: nano structures can provide high electrical conductivity while providing very low thermal conductivity. For instance, when an object has a porous structure where the nano or micron dimensioned structures are "necked" at the dimensional limits, there is a boundary condition where electrical conductivity happens and where it does not. In silicon connections where the special dimensions are less than $2\pi/K_f$, where K_f is the fermi wave vector, then Ohm's law no longer applies, and electrical conduction is almost eliminated.

For silicon and many similar materials this dimension is about 8 nm. So, we want our necks to be more than 8 nm in all cases.

Edwin Bosco Ramayya in his 2010 PhD thesis examined the dimensionality in silicon with respect to quantum size nano effects and electron mobility. [2]

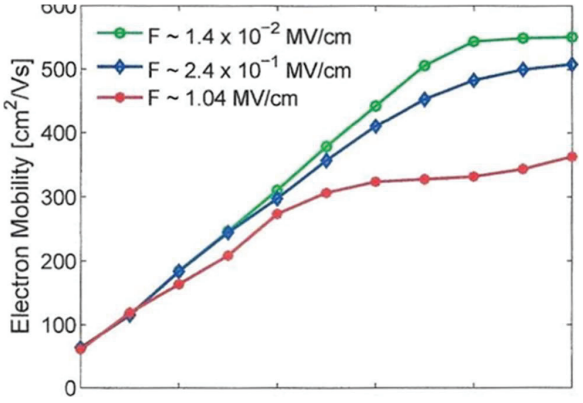


Figure 3: Wire thickness and width (Ramayya, 2010)

We have struggled with sigma, and have had variable results, and we have found the behavior of the phosphorous and boron or arsenic doped materials behave very differently. We have studied the effect of doping levels, both on sigma and Seebeck. We have also studied various sintering profiles and atmospheres, times, and temperatures to affect the growth of necks to achieve high sigma. We have had results in phosphorous and boron well over 30,000 S/m.

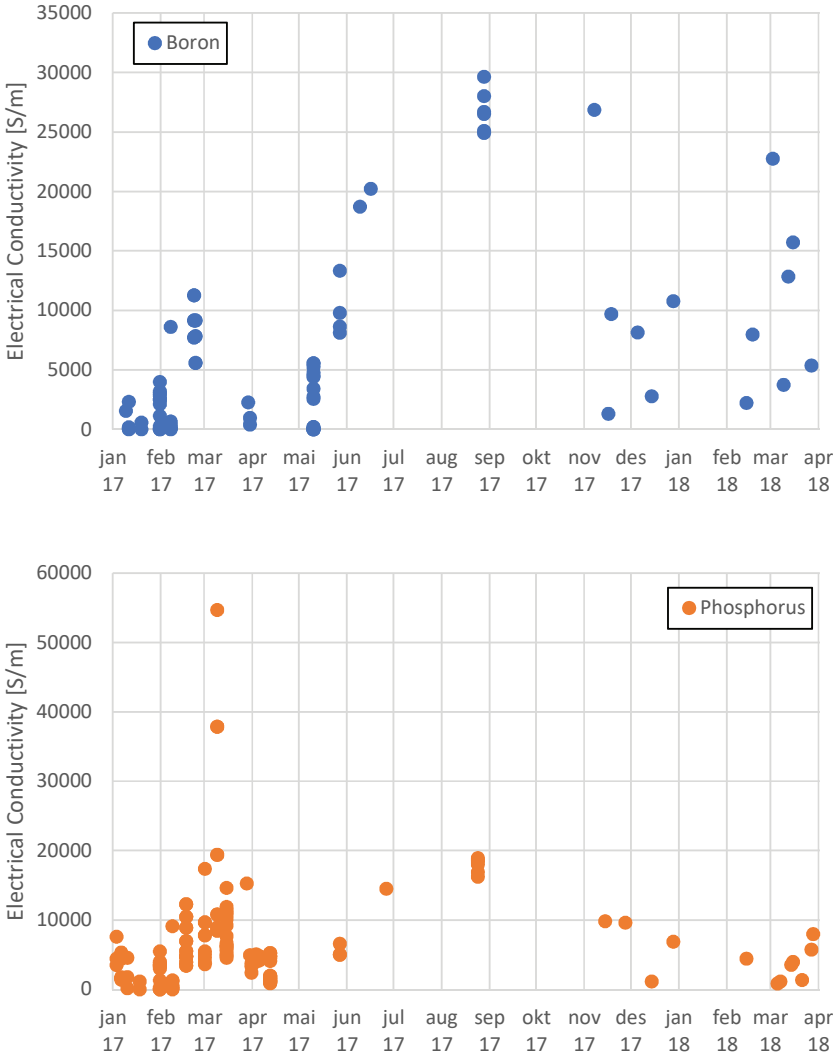


Figure 4: scatter plot of sigma readings in porous sintered highly doped Si.

Recently we have understood that the rates of sublimation can be very different at the necks than in the bulk surface, and very different for boron and phosphorous.

The first major clue that hinted that this was true was the “flipping” of the sign on the Seebeck Coefficient in the phosphorous and arsenic doped materials but not in the boron doped silicon (Figure 5).

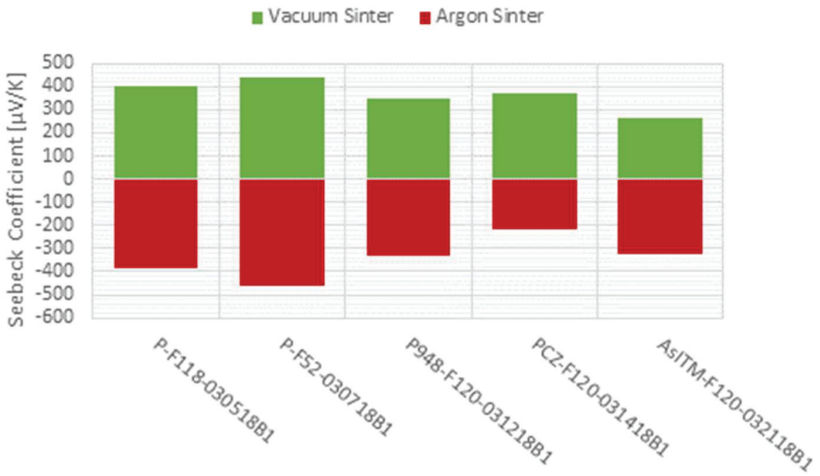


Figure 5: Argon flipping from negative to positive on same pellets in vacuum, back to negative in argon with phosphorous and arsenic doped silicon

We reasoned as to how this could happen and why it did not happen with boron. Then we reviewed *Vacuum Refining of Molten Silicon* by Jafar Safarian and Merete Tangstad and could see that our problem in harvesting high sigma from the necked silicon structures and the cause of this "Flipping" was sublimation, higher rate in the necks than in the bulk surfaces. [3]

Safarian and Tangstad show that:

- The vapor pressure at about 1400°C for boron is 1E-5 Pa, whereas phosphorus is 1E+8 Pa.
- The separation coefficients at this temperature is -10 for phosphorus and +22 for boron.

But we surmise that this unattractive behavior is happening in boron also but at slower rate and scale.

Simultaneously we read Rachow's et al paper *Degradation of silicon wafers at high temperatures for epitaxial deposition*: which showed that we could also be suffering from long times at high temperature. [4]

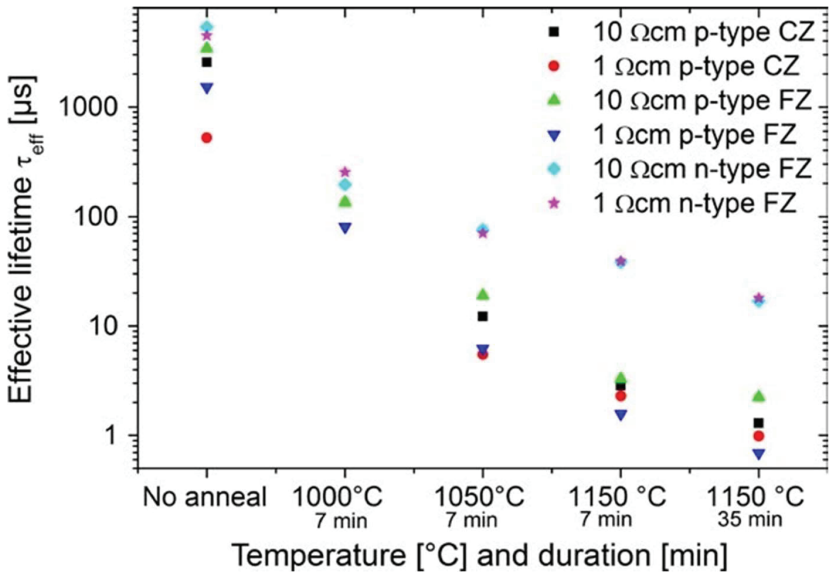


Figure 6: Effective lifetimes at various Temperatures (Rachow, 2016)

Our efforts now are focused on perfecting a process where we can limit time at temperatures over 900°C, use over pressure, use overpressure of phosphine gas, spark plasma sintering and other means. We believe we will find several alternatives.

Seebeck Coefficient

Lee, Galli and Grossman reported: "The authors ascribed the sharp increase in ZT to the reduction in κ and the phonon drag effect, the latter of which has been known to be small or negligible in previously studied TE materials." [5]

One of the things we questioned was the sharp righthand turn the Seebeck Coefficient makes with respect to doping in Lee's graph (Figure 7). So, we decided to explore small doping increments.

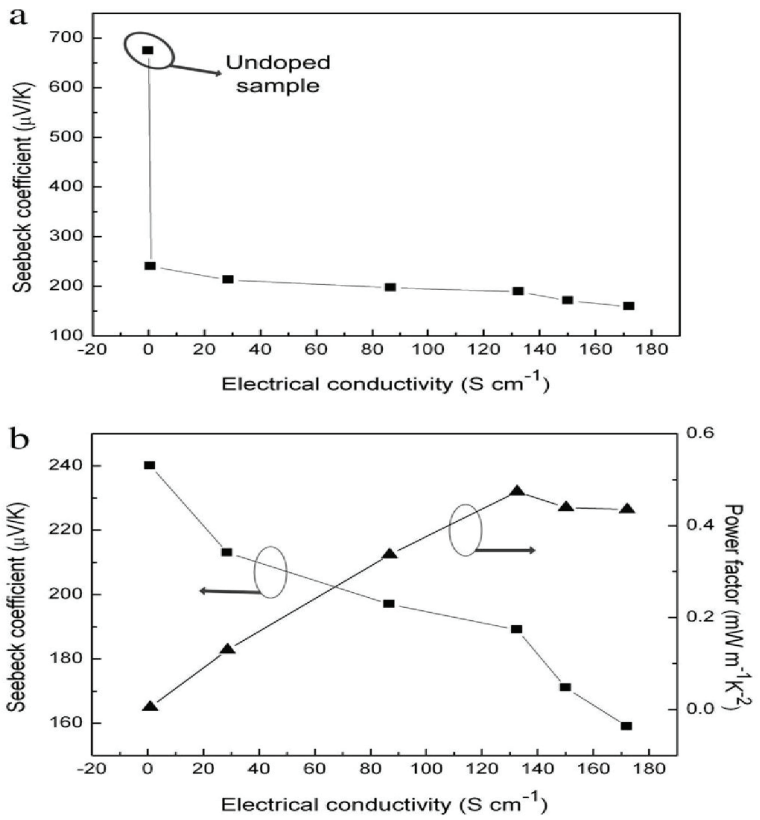


Figure 7: (a) Absolute Seebeck coefficient of samples with and without doping
(b) Seebeck coefficient and Power Factor for given Electrical Conductivity
(Lee, 2016)

To our delight we found that while the curve for sigma in these doping regimes was gentle, the curve for Seebeck in these ranges was quite steep, as shown in Figure 8.

From this work we have been able to identify optimal doping levels to harvest the maximum Seebeck and Sigma.

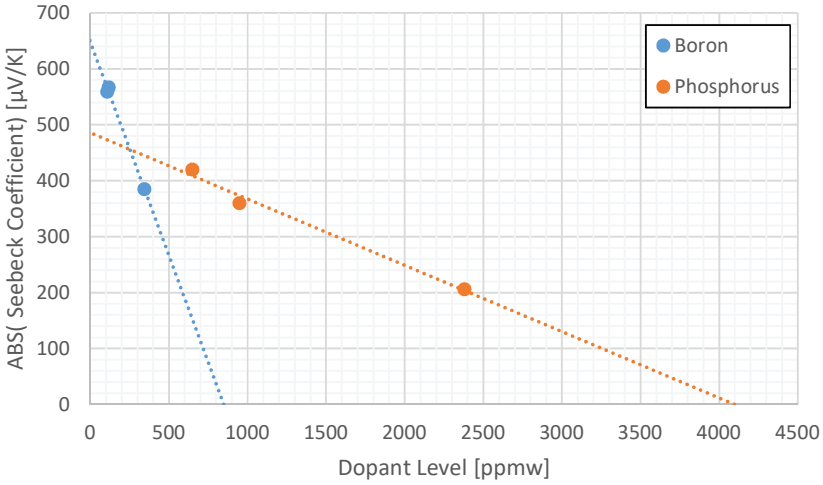


Figure 8: Seebeck Coefficients for given dopant levels

Table 2: Measured Properties for Tested dopant levels

					Boron ppm	Resitivty	Conductivit	Phos ppm	Resitivty	Conductivity
Sample	**Dopi**	**Dopant Level PP**	**Temp (K**	**S (μV/K)**	1.30E+17			4.53E+16		
SVA – 4	B	250	300	0.000567	3.24E+19	0.0022030	45,393			
SVA – 3	B	500	300	0.000559	6.49E+19	0.0018680	53,533			
SVA – 2	B	1000	300	0.000385	1.30E+20	0.0010030	99,701			
SVA – 8	P	425	300	-0.00042				1.93E+19	0.0034	29,343
SVA – 7	P	850	300	-0.00036				3.85E+19	0.0019	52,576
SVA – 6	P	1700	300	-0.00021				7.70E+19	0.0011	94,877

Coefficient of Performance

Most TEMats have a very high coefficient of thermal expansion, 14 to 20 ppm per degree. This inhibits the designer's freedom to optimize the coefficient of performance with respect to leg geometry.

One of the phenomena we have observed that our friends from Linseis and Ulvac have confirmed and designed into their systems is that a minimal delta T is required to tease out the intrinsic highest Seebeck coefficient in a subject material. This delta T is about 5 degrees between the probes which in the case of Linseis are about 4 mm spaced. Given even very low thermal conductivity, we have found that a dimensionality from the hot to the cold side of a minimum of about 10 mm.

So for instance when we measure a 12 mm diameter pellet from one side of the diameter to the other and when we measure through the face 4 mm to the other the Seebeck Coefficient is about a third less through the shorter distance.

Pietrzyk et al in their paper *Thermoelectric module design strategy for solid-state refrigeration,* provide models we have used to make a portrait of COP versus leg height. [6] Given our CTE of silicon of 2.6 ppm, we have unlimited freedom to design legs of most any size or geometry we desire.

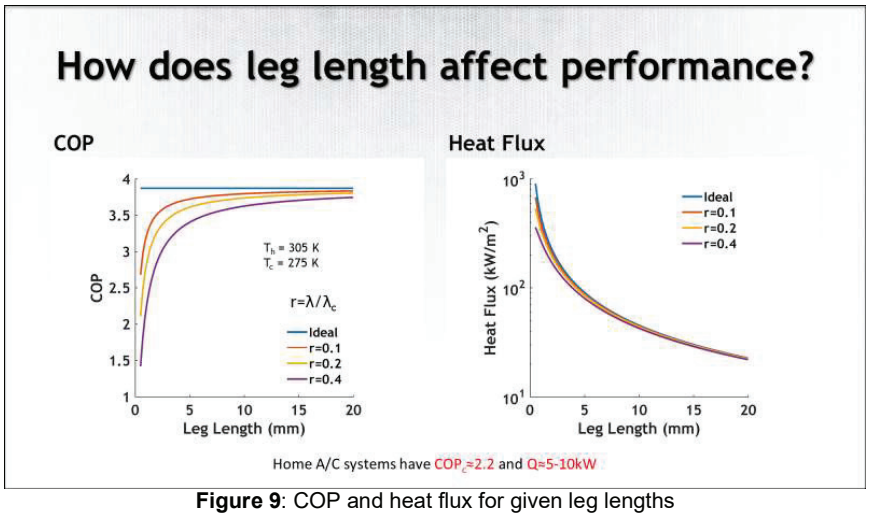


Figure 9: COP and heat flux for given leg lengths

References

1. J.M. Lebrun. *Investigation of Oxidation and Sintering mechanisms of Silicon powders for photovoltaic applications*. Material chemistry. Institute National Polytechnique de Grenoble - INPG, 2012.
2. E.B Ramayya, *Thermoelectric Properties of Ultrascaled Silicon Nanowires*, University of Wisconsin- Madison, 2010.
3. J. Safarian and M. Tangstad, *Vacuum Refining of Molten Silicon*, Metallurgical and Materials Transactions B, **43B**, 2012, p1427-1445.
4. T. Rachow et. al., *Degradation of silicon wafers at high temperatures for epitaxial deposition*, Energy Science and Engineering, **4(5)**, 2016, p344-351.
5. Lee, G. A. Galli, and J. C. Grossman, *Nanoporous Si as an Efficient Thermoelectric Material*, Nano Letters, **8 (11)**, 2008, p.3750–3754.
6. K. Pietrzyk et al, *Thermoelectric Module Design Strategy for Solid-State Refrigeration*, Energy, **114**, 2016, p823-832.

Silicon for the Chemical and Solar Industry XIV
Svolvaer, Norway, June 11 - 14, 2018

Molten silicon at the heart of a novel energy storage system

A. Ramos[1)], A. Datas[1)], C. Cañizo[1)] and A. Martí[1)]
1) Instituto de Energía Solar - Universidad Politécnica de Madrid, ETSI Telecomunicación, Avda. Complutense 30, 28040, Madrid, Spain

Abstract

AMADEUS (www.amadeus-project.eu) is a FET-OPEN project funded by the European Commission to research a new generation of materials and solid state devices for ultra-high temperature energy storage and conversion. By exploring silicon-based alloys as new phase change materials (PCMs), latent heat in the range of 1000-2000 kWh/m^3 is achievable; which means an order of magnitude greater than that of typical salt-based PCMs used in concentrated solar power (CSP). In addition, silicon-based PCMs lead to storage temperatures well beyond 1000 ºC, and so this project aims at breaking the mark of ~ 600 ºC rarely exceeded by current state of the art thermal energy storage (TES). This paper describes the project R&D activities and first results, and comments on challenges towards new systems combining latent heat energy storage in molten silicon and hybrid thermionic-photovoltaic (TIPV) heat-to-power conversion. Also, numerical steady-state and transient simulations of a lab-scale TES prototype are presented; where silicon phase-change, heat loss mechanisms and heat-to-power conversion analyses are conducted. For real cases studied, percentage of energy stored available for conversion strongly depends on the scale, design and materials; with conversions above 75-85% considered feasible for medium-large scale applications.

Introduction

Greater penetration of renewable energy sources is necessary to address some of the major challenges that the present world economy faces: energy security, pollution, sustainability and climate change [1]. Reaching the climate goals of the Paris agreement (2015) will require increasing quantities of renewable energy to be generated in the urban environment and the availability of energy storage technologies at competitive cost structures. The latter is essential in order to manage a future electric system based on renewables.

In this paper we present a novel latent heat thermal energy storage (LHTES) system that has the potential to achieve one of the highest energy densities among existing energy storage solutions. The proposed LHTES [2,3] considers silicon-based alloys as new phase change materials (PCMs) combined with novel solid-state heat to power conversion technologies able to operate at temperatures above 1000 ºC, in particular hybrid thermionic-photovoltaic (TIPV) devices. Silicon-based alloys latent heat falls within the range of 1000-2000 kWh/m^3 and melting points far above 1000 ºC. In Figure 1 the latent heat of fusion of different materials as a function of the melting temperature is shown. This figure illustrates the potential of silicon (1230 kWh/m^3) and boron (2680 kWh/m^3) compared with latent heats of typical salts used in CSP, such as $NaNO_3$ (110 kWh/m^3) and KNO_3 (156 kWh/m^3). Figure 1 also shows that silicon and boron PCMs provide higher storage energy densities than most forms of energy storage, including electrochemical batteries and pressurized hydrogen.

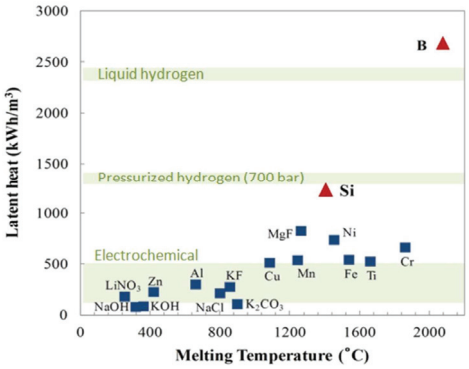


Figure 1: Latent heat of fusion of different materials as a function of the melting temperature.

The main challenge of the proposed LHTES solution is the very high operating temperature, especially concerning the heat-to-power conversion system. Nonetheless, solid state converters, such as thermionics [4], thermophotovoltaics (TPV) [5,6] and hybrid thermionic-photovoltaics [7], are perfectly suited for such high temperatures, mainly because they are based on the direct emission of electrons and photons through space (non-direct contact), eliminating the need for a working fluid and moving parts. These converters also benefit from extremely high power densities (power-to-weight and power-to-volume ratio), low maintenance costs due to the absence of moving parts, and silent operation. The latter is relevant for energy storage applications in an urban environment. Figure 2 presents a sketch of the LHTES concept under development in the AMADEUS project. It can be observed how part of the energy storage will be converted into electricity by a hybrid TIPV device, while the remainder is delivered in the form of heat (e.g. it could be used for hot water and/or heating appliances).

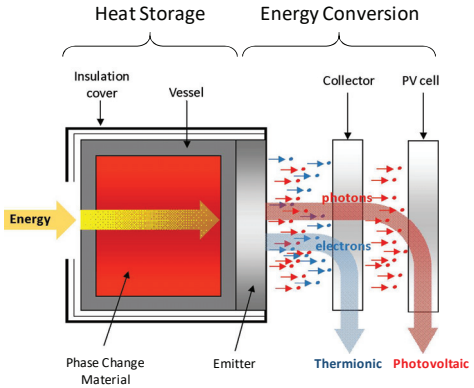


Figure 2: Sketch of the AMADEUS LHTES concept.

AMADEUS project

AMADEUS is a FET-OPEN research project funded by the European Commission for the development of a new generation of ultra-compact energy storage devices based on

molten silicon and solid state heat-to-power converters [8]. The AMADEUS project is coordinated by the IES-UPM and, including the coordinator has the participation of seven European partners with experience in the fields of high temperature materials (NTNU and FRI), fluid-dynamics and finite elements analysis (CERTH), thermal insulation (USTUTT), and solid state heat-to-power conversion based on thermionics (CNR and Ionvac) and photovoltaics (IES-UPM) [8].

Started in January 2017, the AMADEUS project has a budget of ~ 3.3 M€ (3 years) and the final aim is to demonstrate the proof-of-concept of a new LHTES concept based on ultra-high temperature PCMs and solid state heat-to-power converters. In order to reach the final goal of the project, a number of materials and technologies have been investigated, and two proofs of concept are scheduled:

- novel PCMs based on the silicon-boron system with ultra-high melting point and latent heat,
- novel refractory lining composites based on carbides, nitrides and oxides for the PCM container walls,
- advanced thermally insulated PCM casing enabling small heat losses,
- proof of concept of a novel hybrid thermionic-photovoltaic (TIPV) device [7],
- proof of concept of the final complete LHTES device comprising the elements described above.

The project is subdivided into two main blocks: developing a high temperature heat storage unit, and developing a high temperature energy conversion module. The first block comprises the study of silicon-boron PCMs, PCM-container interaction, heat transfer analysis in the PCM and thermal insulation. The second block of the project studies the high temperature operation of TIPV converters. All of the advances performed over the first years of the project will serve as a basis for the design and construction of a LHTES prototype during the last year of the project, which will allow demonstration of a proof of concept for the complete system.

As mentioned above, silicon-boron PCMs are a smart choice as this binary alloys allow very high energy storage densities. The selection of proper Si-B alloys and the alloys container material at elevate temperatures is studied through experimental and theoretical (FactSage software) thermodynamic work at NTNU [9]. First conclusions indicate that the alloys closer to the eutectic point in the Si-B system (i.e. ~3% in weight of B) are the best candidates as they have a larger enthalpy of fusion at solidus and a slightly lower melting point (~1385 ºC) [10], additionally, boron is significantly more expensive than silicon, so a small addition is more feasible. These binary alloys also present the advantage of a decrease of volumetric change during liquid-solid states transitions. Other kinds of binary and ternary alloys including Si, B, Cu, and Fe (among others) are currently under investigation in the AMADEUS project by NTNU and FRI. One of the main challenges faced in this project is to develop standard procedures and instrumentation for examining thermo-physical properties of silicon and silicon-boron alloys in semi-liquid and liquid states.

PCM-container interaction is also being investigated at FRI and NTNU [9]. Both silicon and boron are active elements and they are susceptible to oxidation, nitridization and carburization in contact with O, N, and C, which are typical constituents of high temperature refractory materials (e.g. C, SiC, Si_3N_4, BN, etc.). The behavior these refractories in contact liquid Si-B alloys is being investigated within the project [10].

During the first year, both C and BN have been identified as interesting candidates. The main difference is that graphite is wetted by liquid silicon, while boron nitride is not. It has also been found that alloying silicon with boron results in a decrease the wetting of boron nitride (BN) containers [11]. More details of this particular research, conducted between FRI and NTNU, can be found in [12].

Analysis of the complex heat transfer mechanisms occurring inside the proposed PCM is being developed on the basis of the ANSYS® Fluent platform by CERTH [13]. This model will allow the study of the PCM solidification/melting process, with incorporation of the parametric study on the heat loss variation under different emitter surfaces and container volumes. The final aim is the thorough investigation of the stress-strain between the PCM and its container. Regarding heat transfer analysis of the overall system, a CFD model has been developed in COMSOL® [14]. This model incorporates all relevant properties of a number of suitable thermal insulation materials which can stand temperatures up to 2000 ºC. Initially, a multi-layer thermal insulation is being considered, aiming at defining an overall insulation which accomplishes a compromise solution between minimum single-layers thickness and low-cost [13].

Finally, energy conversion block activities are devoted to the proof of concept of the novel thermionic-photovoltaic (TIPV) device [7]. While both technologies (thermionic -TI- and thermophotovoltaic -TPV-) have been demonstrated separately by researchers participating in this project [15,16], the hybrid TIPV device has only been considered theoretically [7]. The TIPV device (Figure 3) consist of a tandem arrangement between a thermionic and a photovoltaic cell, comprising two main elements: the TIPV cathode (or emitter) and the TIPV anode. The TIPV cathode is the radiating element; it irradiates electrons and photons when heated due to a low work function and high optical emissivity. The TIPV anode comprises the thermionic collector and the TPV cell; the former will absorb the electrons (since its work function is even lower than that of the emitter) and the TPV cell will absorb the emitted photons, generating an electron-hole pair. Electrons collected in the thermionic collector recombine with holes photo-generated in the TPV cell; thus closing the circuit and series connecting the thermionic and photovoltaic sub-devices. Finally, the emitter and the TPV cell anode are externally connected to deliver external electrical power. The combination of both devices is expected to provide a significant increment of the power density compared with the independent thermionic and photovoltaic devices.

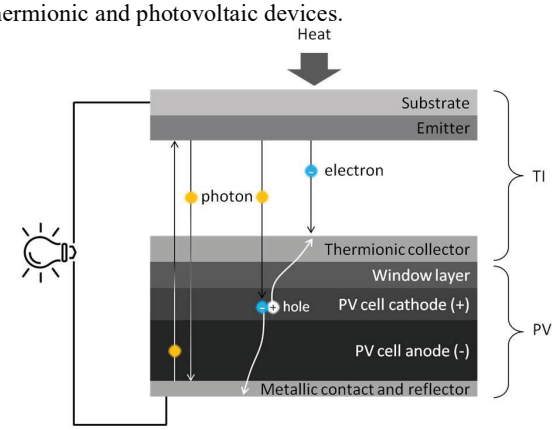


Figure 3: The thermionic-photovoltaic (TIPV) device [7].

TIPV converter has the potential of achieving efficiencies of ~ 40% [7]. Furthermore, a TIPV generator illuminated by a 1400 ºC radiant source may produce more than 100 kW/m^2 of electricity, which is about 500 times the power density of conventional flat plate PV systems (~200 W/m^2). In regards to the challenges faced in this block of activities, the main ones are the need of a vacuum atmosphere and micro-spacers (for the separation between the TIPV anode and cathode) that are indispensable conditions for the successful operation of the TI device.

Applications

Thermal energy storage for power generation is almost exclusively used in concentrated solar power (CSP) systems, where the sun's energy is stored in the form of sensible heat in molten salts and converted upon demand into electricity using a conventional Rankine engine. The combination of (low energetically dense) molten salts and Rankine engines has resulted in the construction of very large CSP power plants of typically 100's of MWs that are placed in distant locations; thus requiring complex civil engineering, new wiring and grid adaptation. The construction of smaller (kW-class) CSP systems is interesting in order to bring modularity to this technology. The remarkably high energy density of molten silicon (~1200 kWh/m^3) and the very high power density of solid state converters such as TIPV (~100 kW/m^2) will bring a new paradigm to the CSP sector, enabling extremely compact designs that could be used in smaller and simpler configurations, even integrated in urban areas.

The ultra-high energy density of molten silicon also opens the door to a new kind of application for thermal energy storage, which is the direct storage of electricity using an electric furnace for melting. Although thermodynamically counterintuitive, the extremely low prices of the electricity produced by renewable sources, such as wind and solar, are suggesting that using electricity for heating will become more economical than burning fuels. In this scenario, the proposed LHTES system could be used for electricity storage and co- or tri-generation in domestic applications (electricity/heating and electricity/heating/cooling). Besides, many other niche applications may appear in the future, including waste heat storage and recovery in industrial processes, space power storage and conversion, etc.

In principle, the proposed LHTES device could cover from a few kilowatts-hour (kWh) of capacity for domestic applications to some megawatts-hours (MWh) in the case of large accumulators. However, optimum sizing of the system is a key design aspect that is being carefully investigated, and must take into account the specific application requirements and the system performance (mostly heat transfer and thermal insulation requirements). It is worth mentioning that despite focusing on the potential of a lab-scale (very small) LHTES prototype, aimed at proof of concept of the proposed solution, scaling up a LHTES will lead to higher storage efficiencies (lower heat losses) and subsequently, higher full-cycle efficiencies and performance ratios per unit of storage capacity. Nevertheless, we will also give some insight on this in the following section.

Lab-scale prototype

The final goal of the AMADEUS project is to realize, first, a proof of concept of the TIPV device, and then a proof of concept of the full LHTES device. The later activity will start in the third year of the project, when all the other elements have been properly defined. However, the activities concerning the design, materials selection and sizing of the LHTES prototype have already started. In this section we present the CFD modelling

developed for the LHTES prototype, which accounts for all material properties, realistic boundary conditions, and the silicon-based alloy phase change. Once developed, this model allows both steady-state and transient simulations in order to reproduce in a quite realistic manner the charge-discharge of the system during real operation, by means of heat transfer and structural mechanic calculations.

System Model

In order to select the final prototype design a number of possible configurations for the AMADEUS Project prototype have been modelled and analyzed; aiming for the best compromise in performance and simplicity at lab-scale. We have addressed the problem definition (materials selection, thermal and mechanical analysis), followed by a CFD analysis in both steady-state and transient scenarios. Finally, on the basis of modelling results, analysis and discussion, a final prototype design has been proposed, that aims to maximize a merit function defined as the quotient between the radiated power towards the TIPV converter and the overall heat losses (P_{rad}/P_{tot}). Accordingly, in chronological order the following parameters have been improved/defined: heat losses through the outer walls, crucible geometry and crucible holder shape, insulation layer thickness and disposition, materials and overall sizing. In this model, only photon radiation is considered for simplicity; thus disregarding the electron emission from the TIPV cathode/emitter.

The design proposed for the LHTES prototype is sketched in Figure 4; where the different elements and materials are indicated. The overall dimensions of the prototype are 40 cm diameter and 37 cm high; the volume of silicon-alloy contained in the crucible is 0.5 L (~ 1.16 Kg Si). The external casing of the prototype is made of stainless steel. Graphite fiber board (RFA), fumed silica board (WDS Ultra) and graphite fiber mat (GFA) are considered as possible insulation materials. The crucible holder is made of a rigid graphite fiber board (MFA), and the crucible could be made of a graphite composite or a high density graphite. Results presented below consider a graphite composite crucible. For the heat input during the charging stage of the prototype a graphite resistance heater was selected.

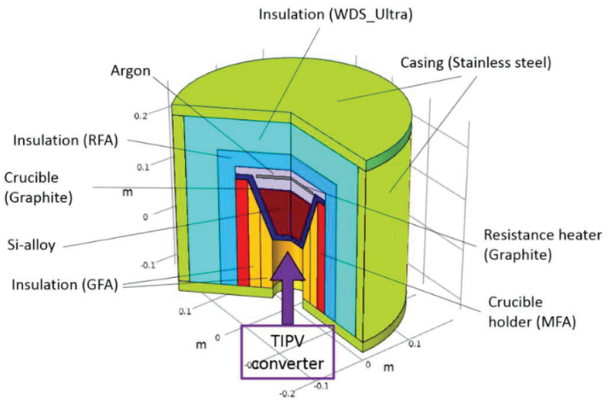


Figure 4: Proposed design and materials for the LHTES prototype.

The TIPV device (which will be water cooled) is not included in Figure 4, however its presence and performance is simulated by means of the boundary conditions defined at the bottom surface of the crucible and inner surface of the cylindrical GFA insulation

layers. In the real prototype the TIPV converter (anode) will be placed underneath the bottom of the crucible; the bottom surface of the crucible will act as the cathode (emitter). Finally, the inner cavity of the prototype will be filled with argon gas at atmospheric pressure; while the TIPV device would be kept in a vacuum atmosphere by means of an infrared radiation-transparent quartz chamber precisely occupying the vacant volume beneath the crucible in Figure 4.

Relevant properties for the simulations conducted with all of the selected materials are presented in Table 1; except for the thermo-chemical properties of the Si-alloy that are presented in Table 2. Single values indicated in Tables 1 and 2 correspond to the particular value of each property at the referred conditions; however, properties are defined as a function of the temperature in the model developed. The silicon phase-change is simulated considering its latent heat of fusion; adding this magnitude at the phase-change temperature to the silicon heat capacity. In addition, at the melting point (T_m) of the pure silicon, its properties are simulated with a sharp phase transition (within a few degrees Celsius); being the properties for $T < T_m$ and $T > T_m$ those corresponding to the solid state and liquid state, respectively.

Table 1: Properties of the LHTES prototype involved materials.

Material	Thermal conductivity, k [W/(K·m)]		Max. operation temperature [ºC]	Thermal expansion, α [m/K]
	T = 25 ºC	T > 1000 ºC		
WDS_Ultra	0.034	-	1000	-
RFA	-	0.3	2000	-
GFA	-	0.5	2200	-
MFA	-	0.3	2000	-
Graphite composite	1.7	3.2	> 2500	3.5×10^{-6}
High density graphite	140	70	> 2500	4.8×10^{-6}
Stainless steel	240	-	940	2.4 e-5
Argon (gas)	0.02	0.05	-	-

Table 2: Thermo-physical properties of pure silicon (T_m=1414ºC), which is selected as the PCM for this model.

Property	Temperature [ºC]		Phase change (T = T_m)
	T < T_m	T > T_m	
Density, ρ [kg/m^3]	2535	2520	-
Thermal conductivity, k [W/(K·m)]	25	50	-
Heat capacity, C_p [J/(kg·K)]	1040	1040	-
Dynamic viscosity, μ [kg/(m·s)]	-	0.06	-
Latent heat, L [J/kg]	-	-	1.8×10^6
Thermal expansion coef., α [m/K]	2.6×10^{-6}	-	-
Emissivity, ε [-]	0.7	0.2	-

Now, in Figure 5 (left) the boundary conditions (BCs) and the heat transfer mechanisms for the thermal modelling are indicated. Conduction heat transfer phenomena occurs in all materials/elements; and the thermal conductivity as function of the temperature (k(T)) for each element/material is considered for conductive heat transfer. Convective heat losses are defined at the outer walls and at the inner surface of the GFA insulation; the convective heat transfer coefficients (h) are 20 W/(K·m^2) and 5 W/(K·m^2), respectively. Radiation occurs at the heater surface (ε = 0.9), at the top surface of the Si-alloy (ε = 0.7-

0.2), at the bottom surface of the crucible (ε = 0.3) and at the inner surface of the GFA insulation (ε = 0.9). The emissivity considered at the bottom surface of the crucible of 0.3 does not correspond to that of the crucible material but to a rough estimation of the so called effective emissivity; which is the emissivity resultant from the net radiative balance between the emitter (attached to the bottom of the crucible) and the TIPV anode. Eventual modifications of the emitter (e.g. selective coatings) will change the effective emissivity and will dramatically impact the heat transfer within the PCM. Thus, a more thorough analysis of the radiative exchange in the actual emitter surface is required to accurately determine the effective emissivity. This will be done in future work.

In Figure 5 (right), BCs for the structural mechanical modelling are presented. It can be observed that the insulation elements effect are disregarded (those are considered flexible) and that the remaining surfaces BCs are divided between free displacement and fixed boundaries.

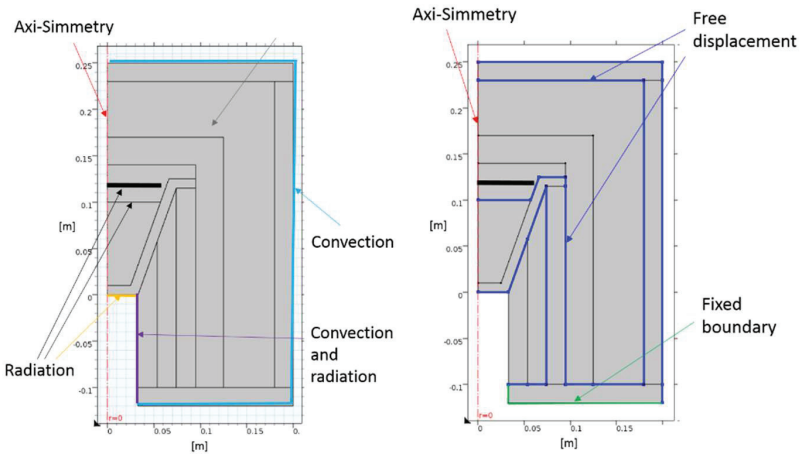


Figure 5: Boundary conditions and heat transfer mechanisms for the thermal calculations in the model (left), and BCs for the structural analysis modelling. Axi-symmetric view of the prototype.

Steady-state analysis

The model of the LHTES prototype is used for thermal and structural mechanic calculation at steady-state. The most demanding operating conditions (higher temperatures and temperature gradients) of the prototype occur when its charging stage finishes and right before the discharge stage initiates, i.e. the bottom part of the PCM is slightly beyond 1414 ºC, the silicon's melting point. Thus, this time is the one analysed below.

In Figure 6 (left), the temperature distribution of the LHTES prototype is presented. The highest temperatures are at the heating element (1567 ºC) and top surface of the silicon-alloy (1511 ºC), and the temperature of the radiant surface towards the TIPV device (crucible bottom surface) is about 1103 ºC, which implies a temperature gradient of 97 ºC in the bottom crucible wall (not considering convective flow of the liquid). The temperature at the outer walls is below 35 ºC, which is a reasonable temperature since the real prototype wall will be water-cooled; and it has also been assured that no material reaches its maximum operation temperature.

In Figure 6 (right), results of the thermal and structural mechanics analysis combined are presented. The von Mises stress criteria is used to evaluate whether the different materials will yield when subjected to the strains associated with thermal expansion [17]. The von Mises stress is compared to the material's yield stress (or to the ultimate tensile stress when it is lower than the former), to determine whether any material would yield or fracture. The maximum displacement due to deformation is also obtained from these calculations. In all cases, strain suffered by the materials are below their limits (as well as under their maximum operation temperature); the most critical conditions occur at the crucible holder, followed by the interfaces at the crucible holder-crucible, crucible holder-wall and alloy surface-crucible. At these points surface coatings and clearances, facilitating free displacement parallel to the corresponding interfaces, will reduce mechanical stress due to thermal expansion.

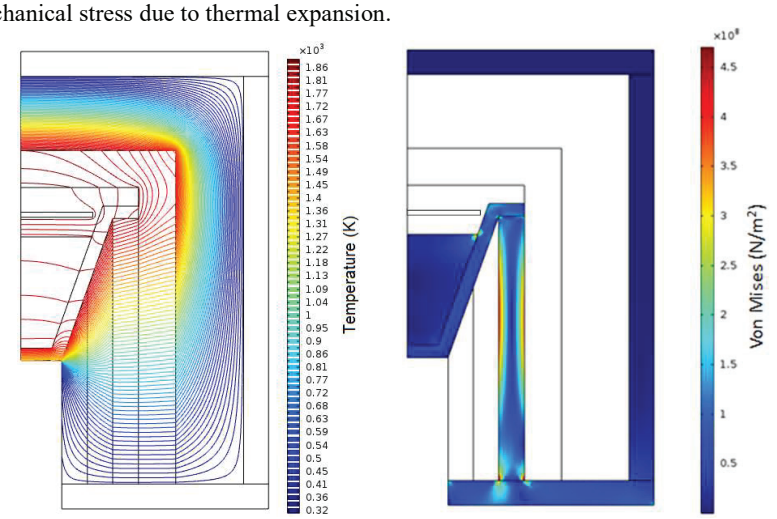


Figure 6: Temperature distribution (left) and Von Misses (structural mechanics analysis) when the system is completely charged (all Si-alloy melted).

As mentioned above, this design was optimized aiming to maximize the merit function P_{rad}/P_{tot} (expressed in percentage); which is obtained to be 62.9%. This means that 62.9% of the storage energy is available for the subsequent conversion by means of the TIPV device. It is worth mentioning that scaling up the system will result in significantly lower heat losses through the outer wall, due to the lower surface-to-volume ratio. For a real LHTES, P_{rad}/P_{tot} ratios above 75-85% are considered feasible (and above 90% desirable) when scaling up the system and optimising its design at the same time.

Other factors, besides the scale of the LHTES unit, will also affect the merit function P_{rad}/P_{tot}. A slight variation in the materials properties of the crucible (in particular thermal conductivity), is translated to a relevant decrease/increase of the merit function. E.g. varying the thermal conductivity from 2 to 70 W/(K·m) leads to an increase of P_{rad}/P_{tot} ratio from 62.9% to 78.4%; since the increase of P_{rad} is greater than that of P_{tot}. This effect is damped with the scale, but it will never be negligible. It is worth noticing here, that very low thermal conductivities of the crucible are not desired since this will be translated to a lower temperature of the emitter (due to higher temperature gradient at the base of the crucible).

Dynamic analysis

Transient simulations of the discharge of the LHTES prototype were also conducted. The interest is in analysing the temperature distribution, the length of the discharge periods and the rate of power generated.

In Figure 7, the temperature distribution along the vertical axis in the Si-alloy and crucible during discharge is presented; discharge takes 80 minutes. The silicon bottom (crucible bottom) temperature goes from 1414 to 1337 ºC (1103 to 1072 ºC), and according to an in-house (idealized) TPV model based on InGaAsSb semiconductor devices (bandgap of 0.51 eV), this is translated to a power generation per unit area in the range 3.85-2.94 W/cm^2 [18]. It must be noticed the important drawback of the large temperature gradient in the crucible. If TPV cells were operated at 1414ºC (temperature at point A in the inset of Figure 7), the power generation density (watts per unit of device area) would be as high as 11.4 W/cm^2 [18]. Besides, this power could be doubled by using TIPV instead of TPV up to ~20 W/cm^2 (1000 times greater than conventional solar PV cells) [7].

The expected output electric power, temperature at emitter and TIPV device, and discharge times will be strongly affected by the effective emissivity. Thus, it is only possible to predict with the generated power density with reasonable accuracy. Furthermore, the electrical energy that can be removed will also vary significantly if a rear reflector is placed in the cells, thus return heat to the emitter. The latter will increase the efficiency, although it will not change the density of electrical power; that is, it will take longer to solidify since the power density of the TIPV conversion remains constant for a given emitter temperature.

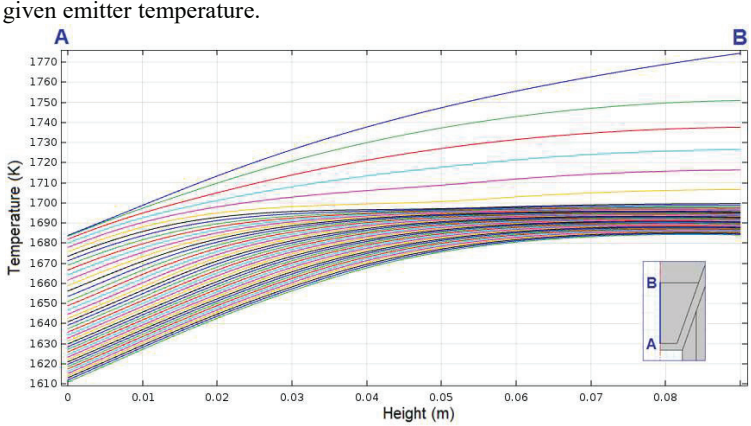


Figure 7: Temperature distribution along vertical axis in the crucible during discharge (time step: 120 sec).

In Figure 8 (left), convective and radiative heat losses are shown. Radiation towards the TIPV device (P_{rad}), convective losses to the ambient (P_{conv}), and convective (P_{conv_cav}) and radiative (P_{rad_cav}) losses through the cavity for the TIPV devices are presented separately. Ideally, we would like to minimise all heat losses with the exception of P_{rad}; thus maximising the P_{rad}/P_{tot} ratio. In Figure 8 (right), radiated power (from the emitter) over total power losses (P_{rad}/P_{tot}) during the discharge time is presented. It can be observed that P_{rad}/P_{tot} ratio decreases from 62.9 to 60.0% during discharge (61.5% average) due to the temperature drop at the emitter surface. These values are acceptable for the initial lab-scale system prototype, where system size must be kept at a minimum to facilitate

experimentation and reduce fabrication costs. Larger P_{rad}/P_{tot} ratios will be attained by scaling up the system and optimizing the design to larger sizes. Indeed, this analysis will allow the determination of the minimum system size in future works.

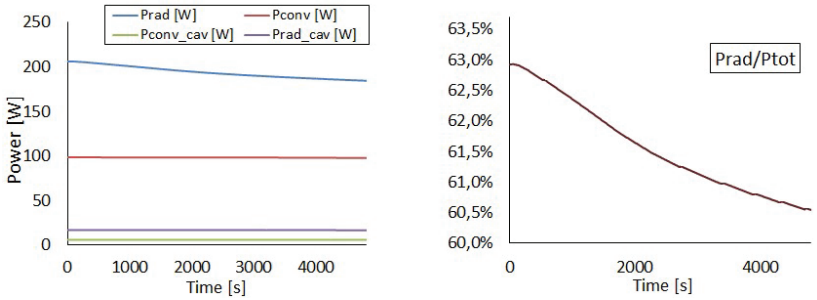


Figure 8: Convection and radiation heat losses (left) and radiated power (from the emitter) over total power losses, P_{rad}/P_{tot} ratio (right), during the discharge time.

Conclusions

In this paper we have described a new energy storage system based on molten silicon and solid state energy conversion devices. This system is the target of a FET-OPEN European funded Project named AMADEUS (www.amadeus-project.eu) that started in January 2017 and will finish in December 2019. The main advantage of the concept relies on the extremely high latent heat of silicon and silicon alloys (~1200 kWh/m^3) that clearly surpass most forms of energy storage, including batteries (< 500 kWh/m^3) and molten salts (<100 kWh/m^3). Examples of possible applications range from a few kilowatt-hour (kWh) of capacity to some megawatt-hours (MWh), in the case of large accumulators. Specifically, the proposed system could be used for electricity storage (using electric furnaces) for co- or tri-generation in domestic applications, direct solar energy storage (CSP), and energy storage at industrial waste heat recovery systems, among many others.

A small lab-scale prototype, which will eventually be fabricated within the AMADEUS project, is analysed in this paper. This prototype is a proof of concept, it is not optimized in terms of energy storage efficiency, but in terms of flexible experimentation. This lab-prototype contains 0.5 litres of silicon, representing a latent heat storage capacity of ~ 615 Wh_{th}. According to CFD simulations, solidification of silicon will last about 80 min, during which ~ 63 % of the latent heat will be delivered as radiation towards the solid state energy converter, which will convert part of this radiation into electricity. Assuming a conversion efficiency of 40%, it means that 25% of the stored latent heat will be retrieved as electricity. This relatively low conversion efficiency is mostly attributed to the small dimensions of the lab-scale prototype, characterized by a large surface-to-volume ratio that results in relatively large losses through the thermal insulation. Scaling up the system is expected to produce conversion efficiencies in the range of 30-40%; thus, future work will focus on determining the minimum size of the system that will enable the profitability of the system in different applications.

Acknowledgements

The project AMADEUS has received funds from the European Union's Horizon2020 research and innovation program, FET-OPEN action, under grant agreement 737054. The sole responsibility for the content of this publication lies with the authors. It does not necessarily reflect the opinion of the European Union. Neither the REA nor the European

Commission are responsible for any use that may be made of the information contained therein. Authors also acknowledge the financial support from the Comunidad de Madrid through the Programme MADRID-PV (Grant Nº. S2013/MAE-2780) and from the Spanish Ministerio de Economía y Competititvidad through the Project TORMES (Grant Nº. ENE2015-72843-EXP). Authors acknowledge Mr. Stephan Lang for valuable discussions on the selection of the thermal insulation materials.

References

1. K. J. Chalvatzis and A. Ioannidis, Energy supply security in the EU: Benchmarking diversity and dependence of primary energy, Appl. Energy 207, pp 465-476, 2017.
2. G. N. Hatsopoulos and E. P. Gyftopoulos, Thermionic Energy Conversion, 2 vols. Cambridge, Massachusetts: The MIT Press, 1979.
3. A. Datas et al., Ultra high temperature latent heat energy storage and thermophotovoltaic energy conversion, Energy 107, pp. 542-549, 2016.
4. A. Datas el at., Steady state analysis of a storage integrated solar thermophotovoltaic (SISTPV) system, Sol. Energy 96, pp. 33-45, 2013.
5. T. Bauer, Thermophotovoltaics: Basic Principles and Critical Aspects of System Design. Springer, 2011.
6. D. L. Chubb, Fundamentals of thermophotovoltaic energy conversion. Elsevier, 2007.
7. A. Datas, Hybrid thermionic-photovoltaic converter, Appl. Phys. Lett. 108, pp. 143-503, 2016.
8. AMADEUS Project. Website: http://amadeus-project.eu/
9. A. Datas et al., AMADEUS Project Deliverable 1.4: Annual Technical Progress Report, January 2018. DOI: 10.5281/zenodo.1163387
10. A. Datas, et al., AMADEUS: Next Generation Materials and Solid State Devices for Ultra High Temperature Energy Storage and Conversion, Solar PACES Conf., 2017.
11. W. Polkowski, et al., Wetting Behavior and Reactivity of Molten Silicon with h-BN Substrate at Ultrahigh Temperatures, J. of Materi. Eng. and Perform., 2017
12. W. Polkowski, et al., Silicon and silicon-boron alloys as phase change materials in thermal energy storage units, Silicon for the Chemical and Solar Industry XIV conference, Norway, 2018.
13. A. Datas, et al. Molten Silicon Storage of Concentrated Solar Power with Integrated Thermophotovoltaic Energy Conversion, Poster, Solar PACES conference 2017. DOI: 10.5281/zenodo.1154768
14. S. Lang, et al., Thermal Insulation of an Ultra-High Temperature Thermal Energy Store for Concentrated Solar, Poster, Solar PACES conference 2017. DOI: 10.5281/zenodo.1123404
15. A. Bellucci et al., Preliminary characterization of ST2G: Solar thermionic-thermoelectric generator for concentrating systems, AIP Conf. Proc. 1667, 2015.
16. A. Datas and C. Algora, Development and experimental evaluation of a complete solar thermophotovoltaic system, Prog. Photovolt. Res. Appl. 21, pp. 1025-1039, 2013.
17. K. D. Hjelmstad, Fundamentals of Structural Mechanics, Second Edition. Urbana-Champaign, Illinois: Springer US, 2005.
18. A. Datas, Optimum semiconductor bandgaps in single junction and multijunction thermophotovoltaic converters, Sol. Energy Mat. Sol. Cells 134, pp. 275-290, 2015.

Silicon and silicon-boron alloys as phase change materials in thermal energy storage units

Wojciech Polkowski[1)], Natalia Sobczak[1)], Merete Tangstad[2)], Jafar Safarian[2)], Jian Meng Jiao[2)] and Bettina Grorud[2)]

1) *Foundry Research Institute, Zakopiańska 73 Str., 30-418 Krakow, Poland*
2) *Department of Materials Science and Engineering, Norwegian University of Science and Technology, Alfred Getz vei 2, 7491 Trondheim, Norway*

Abstract

Although Si and Si-B alloys seem to be perfect candidates as high temperature PCMs (phase change materials) (in terms of their high melting points and latent heat values), a number of scientific/technical challenges have to be faced before introducing them into real Latent heat thermal energy storage (LHTES) devices. A special attention should be paid to a proper selection of reliable refractories for building the PCM container. For this purpose, the involved teams from the Foundry Research Institute in Krakow (FRI) and Norwegian University of Science and Technology (NTNU), have agreed to explore two distinctly different approaches: (i) "Non-wetting + negligible reactivity concept" and (ii) "Self-crucible concept", respectively. In the former attempt, it has been assumed that the selected refractory material will be inert towards the contacting PCMs, i.e. the system will be characterized by non-wetting behaviour and a lack of significant dissolution of the refractory in molten PCM as well as no new reactively formed products. On the contrary, the principles of the latter approach include a reactive formation of continuous interfacial product layer at initial stages of PCM/refractory interaction. The reactively formed layer should play a role of barrier coating, and thus forms a "self-crucible" inside the PCM vessel.
In order to accomplish the Project's goals, Si and Si-B alloys were fabricated by using various metallurgical routes (including an induction melting or an electric arc melting). After that, their high temperature solid/liquid state interaction with refractories selected in accordance to both proposed approaches, was examined. Additionally, a proper thermodynamic assessment of phase equilibria was performed in order to support obtained experimental data.

Introduction

A thermal energy storage (TES) is considered as a good way to overcome drawbacks of concentrated solar power (CSP) systems regarding an energy availability during sunless periods. Among physical TES methods, those involving a latent heat evolution have gather a special attention. The latent heat thermal energy storage (LHTES) is based on absorption or release of heat from a material when it undergoes a *solid↔solid*, *solid↔liquid* or *liquid↔gas* phase change processes (Fig. 1) [2]. Such material is referred to as phase change material (PCM) and is the main player determining the overall output of the TES system. When a PCM is subjected to heating it absorbs the energy which amount is proportional to applied temperature (called as a sensible heat).

However, when temperature reaches a corresponding threshold of phase change, the PCM takes up a large amount of energy (so called latent heat or heat of fusion ΔH) to cover the transformation process. During a subsequent cooling step, the process goes in a reverse way and the absorbed energy is released. This effect has become a basis for the development of new energy storage and conversion units.

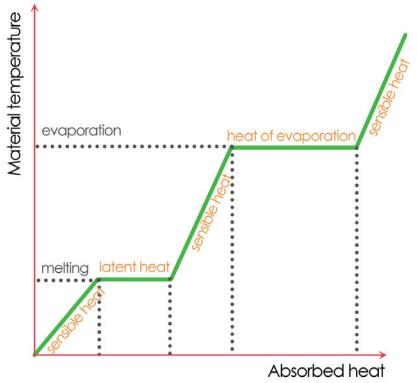


Figure 1: The heat evolution during heating of phase change material (based on [2]).

As it was already mentioned, the most important feature of every LHTES system is a PCM determining its performance, while temperature is the crucial operating parameter (generally, the higher the temperature the higher the unit potential). Unfortunately, current state-of- the-art systems are limited to temperatures around 800ºC, due to a lack of suitable materials and devices. In this regard, the following main requirements should be fulfilled by PCM candidates [3, 4]:

1) a high melting point near the required operational temperature range of the TES system;
2) a high latent heat per volume to improve energy storage density of the system;
3) a high thermal conductivity and heat capacity in both solid and liquid states to provide an additional sensible energy storage and lower charging and discharging times;
4) a high chemical and thermal stability of structure and properties upon thermal cycling operations.

So far, a wide range of various organic and inorganic materials have been proposed and examined as potential PCMs (e.g. [4-6]). Metals constitute a class of PCMs with a potentially higher energy density, thermal conductivity and possible operation temperatures than their organic counterparts (that are mostly based on molten salts) (Table 1).

Table 1: A comparison of selected thermophysical properties of organic and inorganic PCM candidates (T_m – melting point, $\Delta H°$ – latent heat, k – thermal conductivity) [4,7].

Class	Material	T_m [°C]	$\Delta H°$ [MJ/kg]	k [W/mK]	Ref.
Organic	Paraffin Wax	317 – 379	0.07 – 0.21	0.19 – 0.75	[7]
	Fatty Acids	268 – 344	0.05 – 0.21	0.14 – 0.17	
	Hydrated Salts	281 – 1170	0.12 – 0.49	0.46 – 5.0	
low melting point metals	Mercury	234	0.01	8	[4]
	Cesium	302	0.02	17	
	Rubidium	312	0.03	29	
	Indium	430	0.03	36	
	Bismuth	544	0.05	8	
	Tin	505	0.06	15	
	Gallium	303	0.08	29	
	Lithium	459	0.43	41	
high melting point metals	Copper	1356	0.193	350	[7]
	Niobium	2750	0.29	82	
	Nickel	1728	0.3	83	
	Scandium	1814	0.31	16	
	Ruthenium	2607	0.38	80	
	Molybdenum	2896	0.38	84	
	Chromium	2180	0.4	48	
	Vanandim	2183	0.45	51	
	Beryllium	1560	1.31	69	
	Silicon	**1687**	**1.79**	**20**	
	Boron	**2350**	**4.6**	**10**	

As it comes from the comparison shown in Table 1, silicon and boron exhibit significantly greater $\Delta H°$ than any other materials, showing potentially available volumetric energy storage capacities an order of magnitude greater than typical salts used in CSP such as $NaNO_3$ (Fig. 2). Thus, it has been assumed that introduction of Si-B alloys as PCMs should allow overcoming already existed limitations of TES systems as well as will also allow reaching energy densities similar to that available for other storage technologies (e.g. those based on pressurized or liquid nitrogen) (Fig. 2).

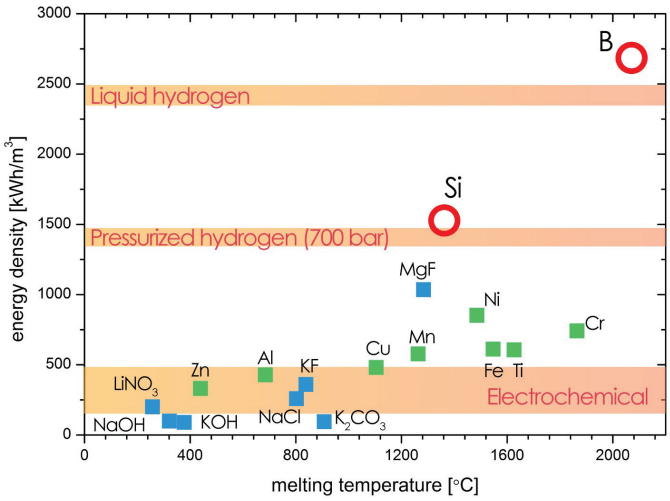


Figure 2: A possible energy density coming from latent heat of different materials as a function of melting temperature compared with the energy density of other storage technologies (based on [1]).

Of course, one of the main questions summarizing technological challenges related to the assumptions of AMADEUS Project is: *What kind of refractory material should be used for building a container dedicated for a long-term storage of solid/liquid Si and Si-B alloys at ultra-high temperatures (up to 2000°C)?*
Giving the right answer on this question seems to be a not very easy task, since there is a prominent lack of reported data on (i) interaction of pure Si with refractories at very high temperatures (T>1500°C); (ii) interaction of Si-B alloys with refractories at any temperature. For this reason, there is a strong need to evaluate basic high temperature capillarity phenomena (wetting, spreading, infiltration) and interfacial reactivity in Si(-B)/ceramic systems at temperatures higher than corresponding melting points of selected PCM candidates.
Consequently, in order to solve this problem and provide technological recommendations for a selection of container materials, the involved teams from the *Foundry Research Institute (FRI)* and *Norwegian University of Science and Technology (NTNU)*, have agreed to explore two distinctly different approaches.

"Non-wetting and negligible reactivity" approach (FRI)

In this attempt, it has been assumed that the selected refractory material will be inert towards the contacting PCMs, i.e. the system will be characterized by non-wetting behavior and a lack of significant dissolution of the refractory in molten PCM as well as no new formed products under conditions corresponding to those predicted for the LHTES system. It was decided to start with evaluation of pure Si/ceramic systems, and after that to examine the effect of boron addition on behavior of Si-B/ceramic couples.
High temperature capillarity phenomena in Si/ceramic systems have been so far investigated mostly concerning manufacturing and processing of photovoltaic Si. In this matter, it is worth to recommend comprehensive review papers by Yuan et al. [8] and

Drevet and Eustathopoulos [9]. A wide range of refractories has been examined including various oxides, carbides, borides and nitrides. It has been documented that due to a high chemical affinity of silicon to oxygen, nitrogen and carbon most of ceramics show the contact angle θ values close to or lower than 90º at temperatures <1500°C, i.e. almost all of them are well-wetted by molten silicon, except hexagonal boron nitride (h-BN) that exhibits an unique ability to be not wetted (Fig. 3).

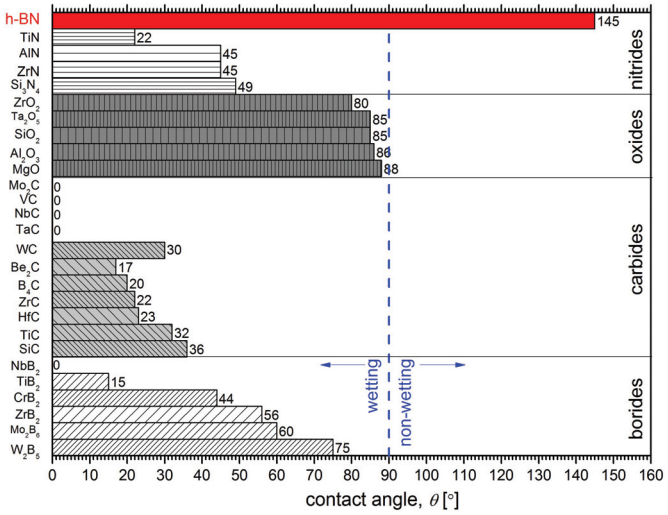


Figure 3: A brief overview on contact angle values reported in the literature for various Si/ceramic systems at T<1500°C.

As it was discussed by Yasinskaya [10], the θ value in Si/nitrides, Si/carbides and Si/borides systems is affected by the character of chemical reaction of the contacting materials. When, a chemical reaction is either absent or negligible (only for Si/h-BN), the surface of ceramics is non-wetted or slightly wetted by Si. In the case of reaction taking place between a ceramic and liquid Si leading to the formation of a wettable product, a good or even complete wetting takes place. The effect of interfacial product formation on wetting behavior might be well presented on example of Si/oxide ceramic systems. It was reported that an involved reaction mechanism in Si/Al_2O_3, Si/ZrO_2, Si/SiO_2 or Si/MgO systems at temperatures <1500°C [9] is mostly based on the dissolution of a ceramic substrate followed by the reprecipitation of SiO_2 product layer at the interface. Since the equilibrium contact angle of molten silicon on silica is around 80-90°, the behavior of all oxide ceramics is very similar. For carbides and nitrides, the situation is analogous since in contact with molten silicon they form well-wettable carbides, nitrides or silicides based interfacial products.

Thus, by taking into account the "non-wettability and non-reactivity" criteria, h-BN has been selected as the material of the first choice. However, it should be noted that although the contact angle values reported in the literature for Si/h-BN couples tested by using various materials and conditions are within the non–wetting regime (θ>90°) (Table 2), all available data are limited to 1500°C, and in fact – do not allow fully predicting the materials performance at higher temperatures.

Table 2: Contact angle θ values reported in the literature for the Si/h-BN system [4,7].

Substrate	Substrate remarks	Testing conditions	Contact angle, θ [°]	Ref.
h-BN		Vacuum; **1500°C**	110	[12]
c-BN			95	
BN		Argon; **1420°C**; 1200 s	145	[8]
p-BN	Pyrolytic BN		144	
p-BN	Pyrolytic BN	Vacuum; **1500°C**	105	[13]
BN	Hot pressed, no binder	Inert gas; **1412°C**; 300 s	122	[14]
p-BN	Pyrolytic BN; R_a=30 nm	Argon; lowp_{O2};**1430°C**; 600 s	117	[15]

Therefore, in order to fill the existed gap and to verify the limits of materials applicability, a sessile drop experiments (Fig. 4) were performed by using dedicated complex for examining high temperature phenomena [11]. Ultra-high purity silicon (7N) pieces were placed on commercially available h-BN sintered substrates, and then subjected to heating to 1750°C in static argon atmosphere (850-900 mbar) in accordance to the temperature profile shown in Fig. 4c. During the tests, images of sessile drop couples were *in-situ* recorded by a CCD high speed camera, and then used for a calculation of wetting kinetics. After the tests, solidified couples were subjected to a detailed structural characterization by means of light microscopy (LM) and scanning electron microscopy coupled with energy dispersive spectroscopy (SEM/EDS).

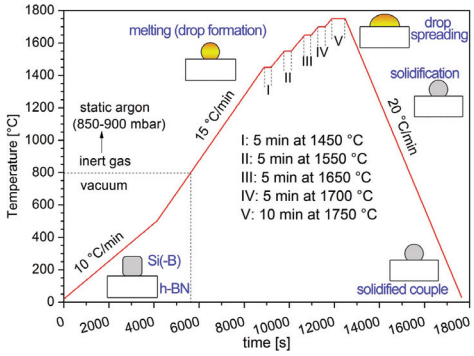


Figure 4: An experimental procedure used for sessile drop method examinations of ultra-high temperature phenomena in Si/h-BN system.

The results of our research (more details are presented elsewhere [16]) demonstrated that increase in temperature improves wetting in the Si/h-BN system, and consequently, non-wetting-to-wetting transition takes place at around 1650°C (Fig. 5a). However, the contact angle of $\theta = 90\pm5°$ is maintained at temperatures up to 1750°C. Based on the results of conducted sessile drop experiments and structural characterization, it was documented that the high-temperature interaction between molten Si and h-BN is mainly controlled by a dissolution/reprecipitation mechanism. It means that h-BN is slightly dissolved (the dissolution rate depends on applied temperature) during a contact with molten Si at high temperature, what results in (i) a modification of chemistry of initially pure Si towards Si-B alloys (Fig. 5b) and (ii) a formation of gaseous nitrogen. Subsequently, new h-BN crystals are precipitated at the interface during cooling. What

is important, any wettable interfacial products were formed upon the ultrahigh temperature interaction. In a combination with a platelets-like morphology of reprecipitated h-BN crystals (Fig. 5c), it was reflected by a dewetting effect (i.e. a substantial increasing of contact angle) (Fig. 5a) during cooling from 1750°C. Since, overall behaviour allows for a preliminary assessment of h-BN as a good candidate for application in the Si-based LHTES system working at temperatures up to 1650°C, its performance upon a thermal cycling operation, has to be further examined.

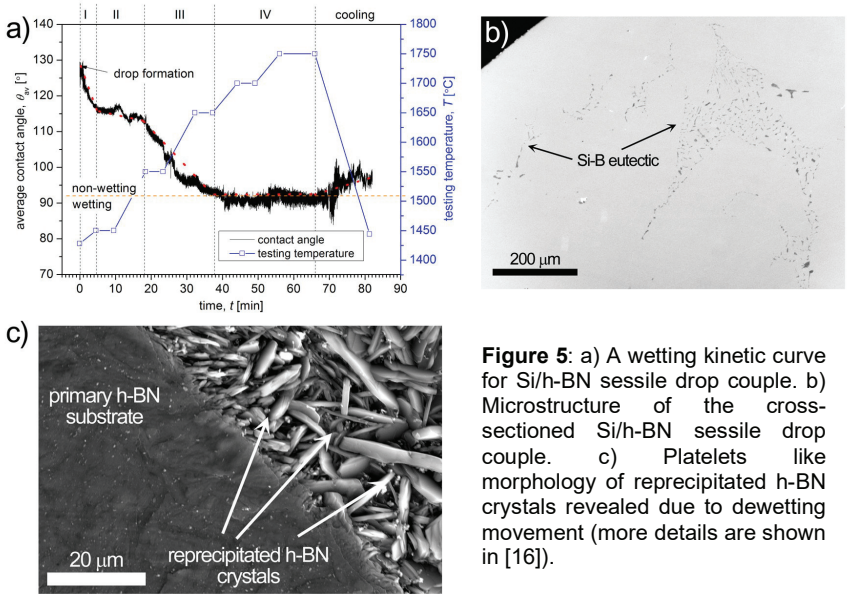


Figure 5: a) A wetting kinetic curve for Si/h-BN sessile drop couple. b) Microstructure of the cross-sectioned Si/h-BN sessile drop couple. c) Platelets like morphology of reprecipitated h-BN crystals revealed due to dewetting movement (more details are shown in [16]).

Subsequently, in order to evaluate the effect of boron addition on wettability in Si-B/h-BN system, a series of binary Si-B alloys were produced by a crucible-less electric arc melting method (in *IFW Dresden, Institute for Complex Materials, Germany*). Small specimens with a mass varying between 0.2 and 0.6 g (Fig. 6a), were fabricated from pure elements by melting pre-prepared mixtures having hypoeutectic, eutectic and hyper eutectic compositions, respectively (in accordance to the Si-B binary phase diagram [17]) (Fig. 6b).

The Si-B alloys were subjected to the same testing procedure as the pure silicon previously. The contact angle values obtained for Si, Si-1B, Si-3.2B and Si-5.7B (wt%) alloys on h-BN substrates at various testing temperatures are listed in Table 3 and compared with other reference Si/ceramics couples tested under the same conditions. What is clearly found is that the addition of boron to silicon lowers the wettability with h-BN – for each Si-B alloy the contact angle is stabilized at a very high level of ~130-150° in the whole temperature range (up to 1750°C). Furthermore, it should be noted that the highest values (around θ =150°) were measured for hypo- and eutectic Si-B alloys. Therefore, it might be recommended that for the sake of ensuring a lack of wetting in Si-B/h-BN system it is beneficial to use near eutectic concentration of boron. Since, we have already discussed that the mechanism of high temperature interaction in Si/h-BN system is dominated by the dissolution/reprecipitation of h-BN platelets, the results obtained for Si-B alloys clearly point towards a hindering of dissolution of h-BN

ceramic in molten Si through additions of boron. Additionally, during cooling the Si-B alloys droplets were spontaneously detached from h-BN substrates, confirming a very low reactivity in the system.

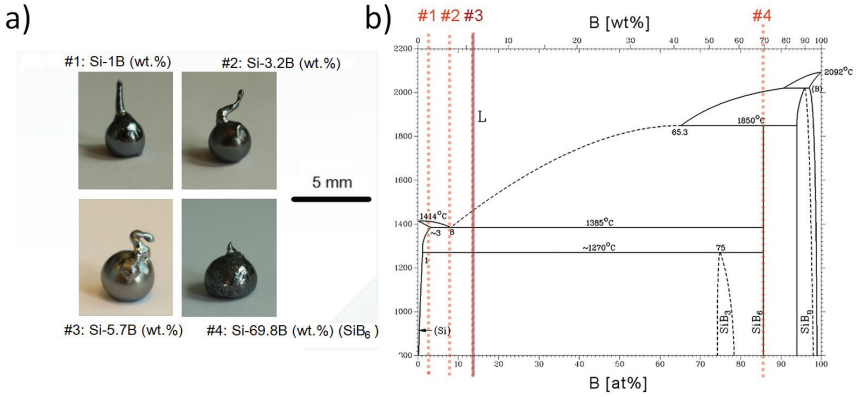


Figure 6: a) Macroviews of exemplary Si-B alloys fabricated by electric arc melting. The Si-B binary phase diagram [17] with marked nominal compositions of fabricated alloys.

Table 3: Contact angle θ values measured by sessile drop method for Si and Si-B alloys on h-BN substrates and the other reference ceramic materials.

	Si/h-BN	**Si-1B/h-BN**	**Si-3.2B/h-BN**	**Si-5.7B/h-BN**	**Si/SiC**	**Si/ZrO_2***
T [°C]	contact angle values after 5 min test, θ [°]					
1450	115	147	146	145	43	100
1550	97	150	144	143	45	96
1650	94	150	147	136	44	96
1700	92	152	150	134	44	92
1750	90	151	151	131	0	92

* During the test, a substantial drop movement ("a dancing drop" effect) was observed as the direct effect of the formation of volatile oxide products.

"Self-crucible" approach (NTNU)

As opposite to the assumptions described above of negligible reactivity between contacting materials, principles of the latter approach include a reactive formation of continuous interfacial product layer at initial stages of PCM/refractory interaction. The reactively formed layer should play a role of barrier coating, and thus presents a "self-crucible" inside the PCM vessel.

In order to realize this idea, the NTNU team has decided to choose graphite (C_{gr}) as the potential refractory material for PCM container. Graphite is widely used in the fabrication and processing of photovoltaic grade silicon due to its favorable set of thermophysical properties including compatible thermal expansion with Si, good thermal shock resistance, high thermal conductivity, and excellent machinability [18]. Nevertheless, a present selection of this material is justified mostly by a well-recognized behavior in molten Si/C_{gr} system leading to the formation of SiC interfacial continuous product layer [18]. The involved reaction between molten Si and C_{gr} originates from a lack of chemical equilibrium in the system – the interaction is not terminated until either

the melt completely infiltrates into the porous graphite substrate, or the SiC layer is produced. The competition between infiltration and formation of the product layer is governed by many factors, e.g. a size and shape of pores, surface roughness, temperature and contact time [19]. Furthermore, as it comes from our thermodynamic assessment of phase equilibria in the Si-C-B ternary system (performed by using FactSage database - Fig. 7), addition of boron strongly contributes to a type of products formed at the interface. It was estimated that when the content of boron in molten Si-B alloy is higher than 3-5 wt%, the interaction with graphite goes in two stages including the formation of product layer composed of (i) SiC and (ii) B_4C layers (Fig. 8). Otherwise (i.e. when B <3-5 wt%), only SiC is formed at the interface.

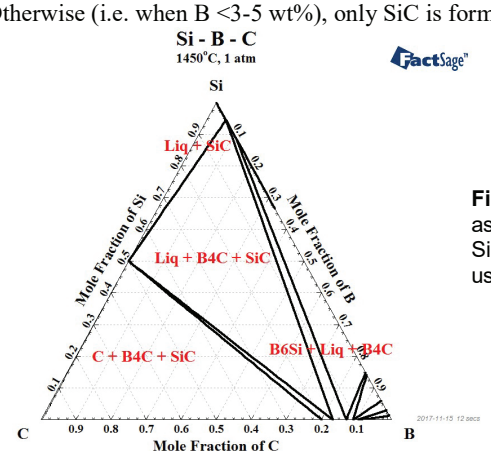


Figure 7: A thermodynamic assessment of phase equilibria in the Si-C-B ternary system (performed by using FactSage database).

In order to validate these thermodynamic calculations, a number of Si-B alloys having the nominal boron content of 2, 3, 5, 8, 11, 15 and 25 (wt%) were produced by induction melting of pure elements inside graphite crucibles, in argon atmosphere, at temperatures between 1450 and 1750°C. The molten Si-B mixtures were held for 2 hours at selected processing temperatures, then cooled down to room temperature and subjected to microstructural evaluation (Fig. 9).

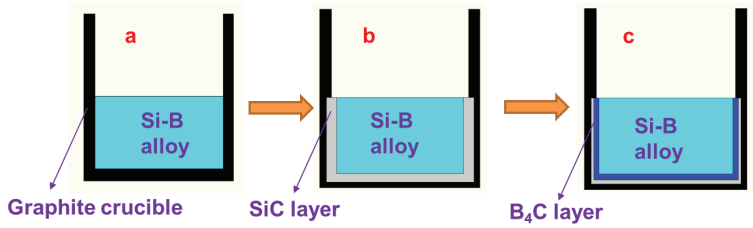


Figure 8: The interaction stages between Si-B alloys and a graphite crucible. When the content of boron in molten Si-B alloy is higher than 3-5 wt %, the interaction with graphite goes in two stages (a→b→c) [20].

Regarding the interface between the alloy and the crucible, it is found that a thin SiC layer is created (Fig. 9a). At high B contents, B_4C layer was also produced at the surface of the crucible (Fig. 9b). This layer probably originates from the reaction of SiC with B near the crucible surface. When B_4C is produced it consumes a lot of B in the alloy and

the B content in the alloy is decreased. It should be noted that some of the B_4C was found also in the alloy phase. At low B contents (less than 5 wt%), SiB_6 and B_4C are not present and the alloy is relatively clean.

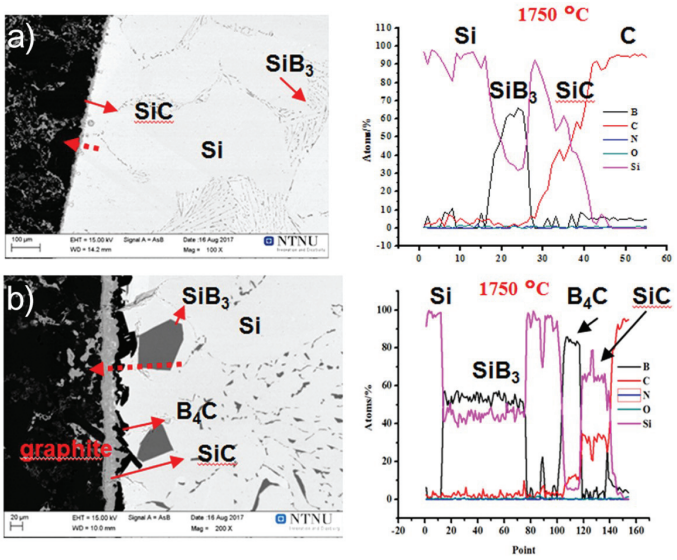


Figure 9: SEM images and EDS profiles of the interface between Si-B and C_{gr} for two Si-B compositions: (a) Si-2wt% B and (b) Si-8wt%B. Experiments were carried out up to 1750°C. For the larger B content (bottom), a double layer of SiC/B_4C is formed at the interface. For the lower amount of B, only SiC is formed [20].

Subsequently, long-term high temperature annealing experiments (up to 48 h) were performed to examine thermal stability of Si-B alloys and interfacial products. Near eutectic compositions of Si-B alloys were selected for these tests, since they are also beneficial in terms of relatively lower melting temperatures combined with even higher latent heat than that of pure Si. It was documented that molten Si(B) penetrates the crucible and produce SiC quite fast (Fig. 10), and after that the reaction is very slow. By taking into account that the Si(B) penetration strongly depends on the porosity of graphite, a dense crucible is needed. Besides, as observed during the short term experiments, a dense SiC barrier layer is produced on the surface of the crucible, which decreases the further reactions. It was found that, this layer may rarely leave the crucible surface and be found in the alloy. Nevertheless, during the experiments the eutectic alloy remained quite clean from SiC at the eutectic composition. Additionally, we observed that cycling of temperature, above the melting temperature, does not affect the alloy composition. Therefore, when C_{gr} crucibles are applied, the Si-B alloy composition should be within the area of the eutectic composition (3 wt% B), e.g. between 2-5 wt% B, due to a suppressed formation of SiB_6 and B_4C solid particles. A lack of solid particles should be reflected in the following beneficial effects:

1) an increase of latent heat of fusion per volume unit;
2) no boron depletion of Si-B alloy;
3) a more controlled solidification process;
4) viscosity and other parameters are determined by the melt properties only.

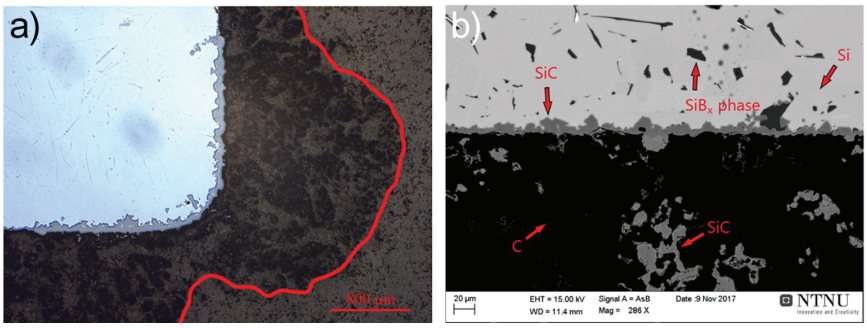


Figure 10: Eutectic Si-B alloy/ C_{gr} interface after 48h of interaction at 1550ºC.

Conclusions

In order to provide practical recommendations for the selection of crucible material for Si and Si-B based LHTES systems working at ultra-high temperatures, two distinctly different approaches have been explored: one assuming an inertness between contacting PCM and refractory, while the other was based on a reactively formed interfacial barrier layers. Regarding the former attempt, it was documented that h-BN is the only one ceramic fulfilling criteria of the non-wetting and negligible reactivity with molten silicon at temperatures up to 1650°C. Additionally, it was found that Si-B alloys exhibit even lower wetting with h-BN at temperatures such high as 1750°C, as compared to pure silicon. The decreased reactivity originates from hindering of dissolution of h-BN ceramic in boron enriched silicon alloys.

In the later approach, graphite proved its ability to form a barrier layer composed of SiC or (SiC+B_4C), depending on boron content in PCM. The *in-situ* formed products showed also a high thermal stability upon short and long term (up to 48h) holding at temperatures up to 1750°C. Therefore, both dense graphite and SiC crucibles could be used as container material. As both carbon and SiC wet the alloy, over time a thin silicon layer should cover the crucible. In other processes, this has been stopped by adding a non-wetting band in the top of the crucible (e.g. h-BN).

Since, at the early stage of the AMADEUS project, both considered attempts seems to be reasonable (but each having some advantages and disadvantages), the final selection of materials requires further study on behavior of selected PCM/refractory couples upon cyclic melting/solidification steps.

Acknowledgments

The project AMADEUS has received funds from the European Union's Horizon2020 research and innovation program, FET-OPEN action, under Grant agreement 737054. The sole responsibility for the content of this publication lies with the authors. It does not necessarily reflect the opinion of the European Union. Neither the REA nor the European Commission is responsible for any use that may be made of the information contained therein.

References

1. A. Datas, A.B. Cristobal, C. del Cañizo, E. Antolín, M. Beaughon, N. Nikolopoulos, A. Nikolopoulos, M. Zeneli, N. Sobczak, W. Polkowski, M. Tangstad, J. Safarian, D.M. Trucchi, A. Bellucci, M. Girolami, R. Marx, D. Bestenlehner, S. Lang, A. Vitulano, G. Sabbatella, A. Martí, *AMADEUS: Next Generation Materials and Solid State Devices for Ultra High*

Temperature Energy Storage and Conversion, SolarPaces 2017, Santiago, Chile, 2017. Article submitted to AIP Conference Proceedings (Open Access)
2. B. Cárdenas, N. León, *High temperature latent heat thermal energy storage: Phase change materials, design considerations and performance enhancement techniques*, Renewable and Sustainable Energy Reviews **27**, 2013, 724–737
3. G. Alva, L. Liu, X. Huang, G. Fang, *Thermal energy storage materials and systems for solar energy applications*, Renewable and Sustainable Energy Reviews, **68,** 2017, 693-706
4. S.A. Mohamed, F.A. Al-Sulaiman, N.I. Ibrahim, Md. H. Zahir, A. Al-Ahmed, R. Saidur, B.S. Yılbaş, A.Z. Sahin, *A review on current status and challenges of inorganic phase change materials for thermal energy storage systems*, Renewable and Sustainable Energy Reviews, **70**, 2017, 1072-1089
5. L. F. Cabeza (Ed.), Woodhead Publishing Series in Energy: Number 66, *Advances in thermal energy storage systems methods and applications*, Woodhead Publishing, Camridge, UK, Elsevier 2015
6. K. Pielichowska, K. Pielichowski, *Phase change materials for thermal energy storage*, Progress in Materials Science, **65**, 2014, 67-123
7. M.R. Gilpin, D.B. Scharfe, M.P. Young, R.N. Webb, *Experimental investigation of latent heat thermal energy storage for bi-modal solar thermal propulsion*, Propulsion and Energy Forum, 12th International Energy Conversion Engineering Conference, July 28-30, **2014**, Cleveland, USA
8. Z. Yuan, W.I. Huang, K. Mukai, *Wettability and reactivity of molten silicon with various substrates*, Applied Physics A, **78**, 2004, 617–622
9. B. Drevet, N. Eustathopoulos, *Wetting of ceramics by molten silicon and silicon alloys: a review*, Journal of Materials Science, **47**, 2012, 8247–8260
10. G.A. Yasinskaya, *The wetting of refractory carbides, borides, and nitrides by molten metals*, Soviet Powder Metallurgy and Metal Ceramics, **5**, 1966, 557–559
11. N. Sobczak, R. Nowak, W. Radziwill, J. Budzioch, A. Glenz, *Experimental complex for investigations of high temperature capillarity phenomena*, Materials Science and Engineering A, **495**, 2008, 43–49
12. Y.V. Naidich, *The wettability of solids by liquid metals*. In: D.A. Cadenhead, J.F. Danielli (eds.), *Progress in Surface and Membrane Science*, Academic Press, New York, 1981, 353 - 487
13. J.A. Champion, B.J. Keene, S. Allen, *Wetting of refractory materials by molten metallides*, Journal of Materials Science, **8**, 1973, 423-426
14. Y. Maeda, T. Yokoyama, I. Hide, T. Matsuyama, K. Sawaya, *Releasing material for the growth of shaped silicon crystals*, Journal of Electrochemistry Society, **133**, 1986, p440-443
15. B. Drevet, R. Voytovych, R. Israel, N. Eustathopoulos, *Wetting and adhesion of Si on Si_3N_4 and BN substrates*, Journal of European Ceramic Society, **29**, 2009, 2363–2367
16. W. Polkowski, N. Sobczak, R. Nowak, A. Kudyba, G. Bruzda, A. Polkowska, M. Homa, P. Turalska, M. Tangstad, J. Safarian, E. Moosavi-Khoonsari, A. Datas, *Wetting behavior and reactivity of molten silicon with h-BN substrate at ultrahigh temperatures up to 1750 °C*, Journal of Materials Engineering and Performance, 2017, article in press, doi.org/10.1007/s11665-017-3114-8
17. R.W. Olesinski, G.J. Abbaschian, *The B-Si (Boron-Silicon) system,* Bulletin Alloy Phase Diagrams, **5**, 1984, 479-484
18. J.F. White, L. Ma, K. Forwald, D. Sichen, *Reactions between silicon and graphite substrates at high temperature: in situ observations*, Metallurgical and Materials Transactions B, **45**, 2014, 150–160
19. D. Camel, B. Drevet, N. Eustathopoulos, *Capillarity in the processing of photovoltaic silicon*, Journal of Materials Science, **51**, 2016, 1722–1737
20. J. M. Jiao, J. Safarian, M. Tangstad, *High temperature interaction of Si-B alloys with graphite holder in thermal energy storage systems*, Mat. Met.Trans B, to be published in 2018

Prediction of through-thickness microstructure during metallurgical silicon solidification

S. Gouttebroze[1)], M. M'Hamdi[1)]
1) SINTEF Industry, Pb.124 Blindern, 0314 Oslo, Norway

Abstract

A microstructure model, Sistruc, has been previously developed to predict the phase formation during solidification of metallurgical silicon. The model includes the four major elements Al, Ca, Fe and Ti in addition to B and P. The model has been designed to predict the average microstructure based on the nominal alloy composition. Nevertheless, silicon material produced industrially are not homogeneous in terms of composition. The main expected variation is through the thickness due to macrosegregation.

In the present paper, the extension of Sistruc capabilities to simulate macrosegregation and through thickness microstructure variation is presented. The macrosegregation and heat transfer model is described and explained. Finally, the new model is applied to a synthetic alloy to perform a numerical study of the effect of cooling rate and casting thickness. The importance of considering macrosegregation is also demonstrated.

Introduction

A general trend for the silicon markets is the need for small sized particles with tailored intermetallics. Therefore, silicon producer must find a way to control the solidification process to reach customer requirements. During solidification, metallic impurities will segregate and form intermetallic phases mostly at the grain boundaries. Depending on the solidification process (especially the cooling rate) and melt quality, different particles can nucleate and grow. Iron, aluminium, calcium and titanium are usually the main elements in metallurgical grade silicon. Other elements are referred to as trace elements. Previous studies have provided a description of the intermetallic phases found in MG-Si material produced with standard process route [1, 2, 3, 4, 5]. The main intermetallic phases are FeSi2, Al3FeSi2, FeSi2Ti, Al2CaSi2, Al6CaFe4Si8, CaSi2, Al6Fe4Si6 and TiSi2.

Previous work [6] has focused on developing a microstructure model to predict the amount of intermetallics phases based on local composition. Experimental evidences and numerical modelling have shown that the cooling rate impacts the grain size and intermetallics shape but does not significantly affect the microsegregation.

Nevertheless, at the macroscale, the composition is not uniformed as measured by M.F. Møll [5].

The purpose of this paper is to present the improvement of our microstructure model, Sistruc, by coupling it with a macrosegregation model. Sistruc model, presented in [6], is mainly calibrated from gathered literature data covering the major binary and ternary systems. The segregation profile is predicted by a finite volume solver. This paper will describe the microstructure and macrosegregation model, and a simple application to illustrate the effect of cooling rate and casting thickness on material microstructural homogeneity.

Microstructure model

The microstructure model, hereafter referred to as Sistruc, has been initially developed in 2009 by A.L. Dons following a similar approach as for the Alstruc model [7]. The main objective of this tool is to be predictive, fast and user-friendly which implies that one has to balance complexity with some simplifications and approximations. The main equations of the model have been presented in Gouttebroze et al. [6] and are briefly summarized below. In the following, unless written otherwise, the temperature T and the concentration c are in K and wt%, respectively.

Model description

Sistruc considers up to 6 elements Al, Ca, Fe, Ti, B and P. Two main values need to be computed by the model to determine the phase formation path: i) the concentration dependence of the liquidus temperature and ii) the solubility of the different phases. The generic formula to compute the liquidus temperature is given by:

$$T_{liq}(°C) = 1414 + \sum_i \sum_{k=1}^{3} \alpha_i^k {C_i}^k + \sum_i \sum_{j \neq i} \beta_{ij} C_i C_j \quad (1)$$

where i denotes the solute element (and C the concentration in the liquid, α_i^k are the coefficients of the third order polynomials.

The solubility limit for solute element i is given by:

$$C_i^* = A_i e^{-\frac{B_i}{T}} \quad (2)$$

where T is the temperature in Kelvin.

The formation of the intermetallic compounds is generally defined by a combination of the previous information and the particle composition. For example, for Al_3FeSi_2 phase, precipitation occurs when:

$$\frac{C_{Fe}}{C_{Fe}^*} \cdot \left(\frac{C_{Al}}{C_{Al}^*}\right)^3 > 1 \quad (3)$$

At the microscopic scale, the solidification of Si and liquid enrichment is, in the current version, simply computed assuming no diffusion in the solid phase and complete mixing in the liquid phase.

Macrosegregation model

Model description

A finite volume model has been implemented separately and coupled to Sistruc. The model, when called from Sistruc, addresses the simplified problem described in Figure 1.

The model solves heat transfer, via an enthalpy approach, and the solute diffusion:

$$\frac{\partial h}{\partial t} = \nabla \cdot (k \nabla T)$$
$$\frac{\partial c}{\partial t} = \nabla \cdot (\mathrm{D} \nabla \mathrm{c})$$

Where h is the enthalpy, k the conductivity, T the temperature, and c the concentration.

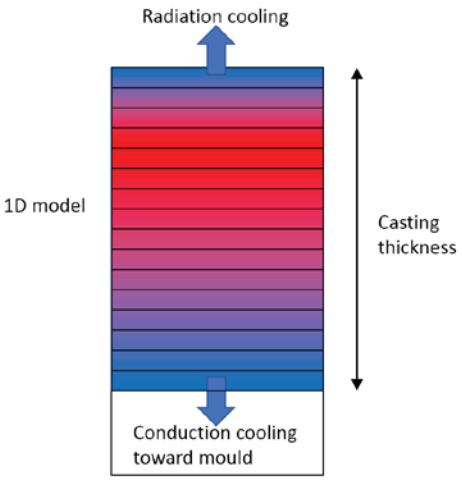


Figure 1. Solution domain and boundary conditions

A volume-averaged based approach has been implemented to deal with the phase change, the material being considered as a mixture of solid and liquid. The macro transport equations are solved using an explicit time scheme.

At the micro-scale, segregation is modelled using Scheil's equation with an imposed eutectic transformation at 90% solid. The values used for the partition coefficients and diffusivity are physical values while often effective values are used to consider other physical phenomena. Before applying the previous model to industrial cases, a calibration procedure should be applied to determine the effective values for that specific process.

User interface

An additional panel has been added to the user interface. The nominal composition of the material, the cast thickness and the heat transfer coefficient are the main input of the simulation. From the simulation, plots of the segregation profile of the different elements are available. Local composition can be extracted from the simulation and directly send to Sistruc main solver for prediction of the microstructure at different ingot heights.

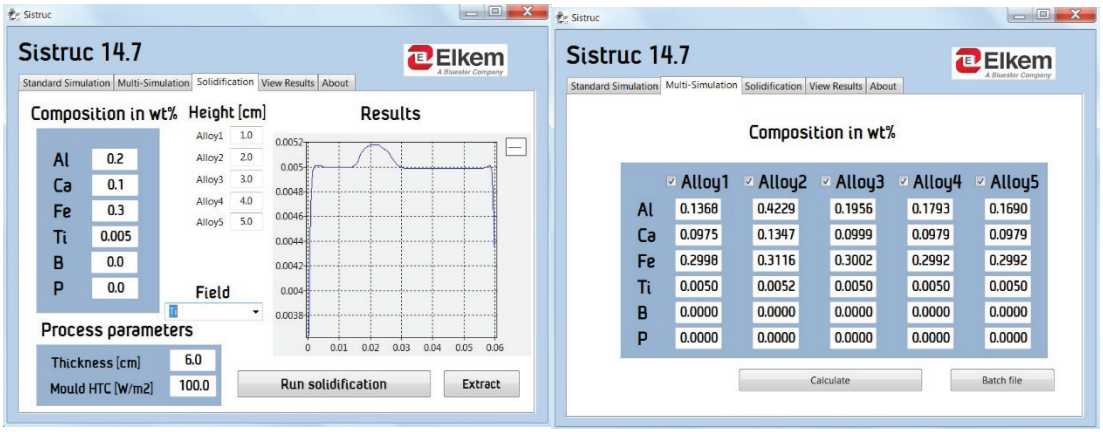


Figure 2. User-interface for solidification simulation and extraction of local composition.

Application

Sistruc is an industry-oriented tool that should run easily and rapidly to test different casting operations, predict trends and provides quantitative estimations. More advanced approaches based on thermodynamic modelling and database description might be more accurate but would require expert user and far larger resources. Nevertheless, the following study will demonstrate the potential of this tool to support product development. Please note that the macrosegregation results presented here are not calibrated with industrial process parameters and are only used to develop new understanding.

A synthetic alloy was selected with the following composition: Al 0.2 wt%, Ca 0.1 wt%, Fe 0.3 wt%, Ti 0.005 wt%. The study focuses on the effect of process parameters on the microstructure and demonstrate the importance of segregation when analysing the microstructure through the thickness. Three macrosegregation simulations were carried out: a) 6cm thick casting with heat transfer coefficient (HTC) equal to 100 W/m^2/K, b) 6 cm and 50 W/m^2/K, c) 3 cm and 100 W/m^2/K. From these simulations, local composition was extracted at five points regularly spaced.

Effect of cooling rate on macrosegregation

The standard casting procedure, illustrated in Figure 1, leads to concurrent silicon crystallization at the contact surface with the mould and from the top surface due to radiation cooling.

For a 6 cm thick ingot, the solidification and macrosegregation simulation result in the segregation profile presented in Figure 3. Two essential aspects can be highlighted: *i*) the curves usually present a peak where the two solidification fronts merge, *ii*) elements will segregate strongly or not, based on their partition coefficient and diffusivity. The cooling rate imposed by the heat transfer coefficient value strongly affects the position and height of the peak. Based on intrinsic (not effective) values for partition coefficient and diffusivity, the model predicts decreasing segregation from Al, to Ca, to Fe (and Ti). Nevertheless, the segregation profile for Fe is not well predicted and calibration is required.

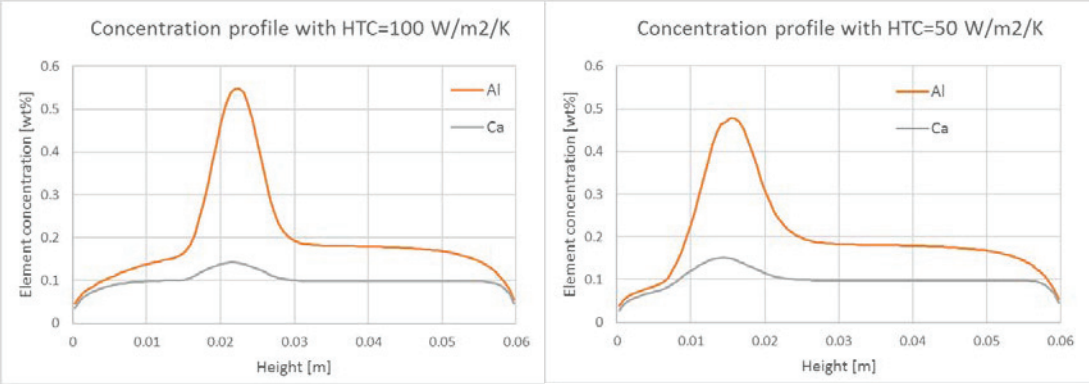


Figure 3. Segregation profile through the thickness of the casting

Effect of macrosegregation on microstructure

The previous profile has been discretized to run parallel microstructure simulations based on local composition. As illustrated in Figure 4, the segregation of elements modifies significantly the amount and relative ratio of the intermetallics through the thickness. The results are compared with the prediction based on the nominal composition. Indeed, the previous version of Sistruc relies solely on the nominal composition with no influence from the casting parameters.

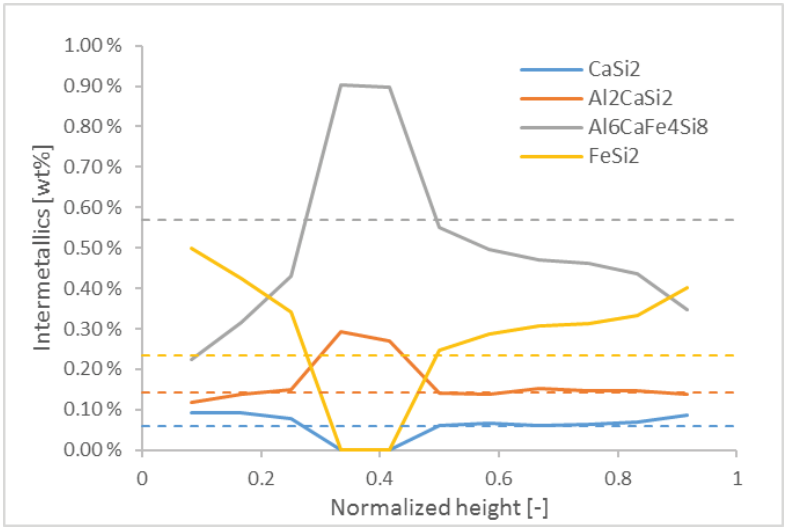


Figure 4. Amount of intermetallics through the thickness of the casting (6cm, HTC=100 W/m^2/K). Dash lines indicates the predicted microstructure based on nominal composition

The curves presented in Figure 4 correspond to 11 separate microstructure simulations. The standard in Sistruc is by default 5 values. Preliminary results indicate that this number might be too small to provide a good description of the profile and then compute the amount of intermetallics. This point should be further investigated to assess that effect and also provide guidelines for material characterization.

Effect of process parameters on microstructure

As stated previously, standard calculation relies on nominal composition. We have therefore selected this average calculation as our reference case to assess the effect of process parameters when considering macrosegregation. Figure 5 present the difference in averaged values over the thickness for the main intermetallic particles.

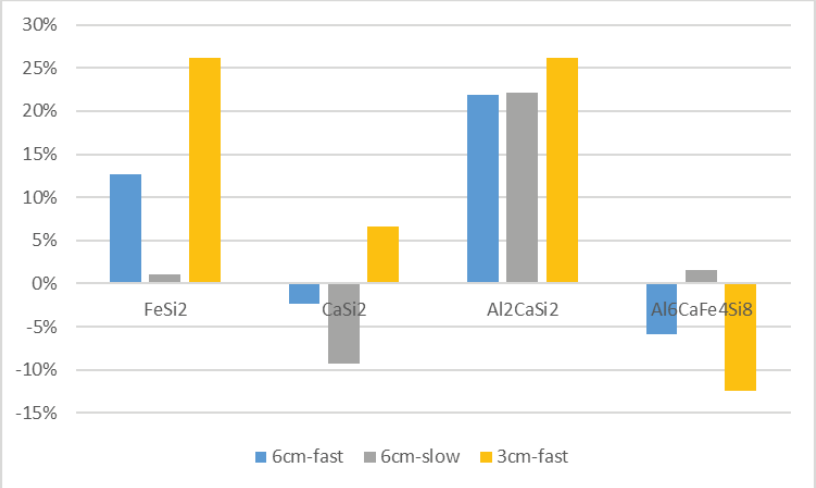


Figure 5. Deviation from microstructure prediction using nominal composition

The first observation is that average calculation based on nominal composition is insufficient to optimize the process: including the effect of macrosegregation, relative variation up to 25% are observed in the amount of intermetallics. The second observation is the different behaviour of phases: Al_2CaSi_2 phase is not affected while the FeSi2 and the quaternary phase are varying strongly due to differential segregation between (Al, Ca) and Fe.

Conclusion

A user-friendly microstructure model, Sistruc, has been improved to simulate the effect of macrosegregation during silicon solidification and its consequences on the microstructure. The model has been applied to study the effect of process parameters on the amount and distribution of intermetallic particles. Large variations in amount and type of intermetallics are observed over the sample thickness.

As a conclusion, the current version of Sistruc is a good tool for industrial optimization of metallurgical silicon composition to reach specific requirements. Processing parameters seems to strongly affect the spatial distribution of intermetallics through the thickness. The new understanding provided by this tool should be compared with advanced characterization of silicon samples through thickness. Nevertheless, this type of analysis is very challenging due to amount of data required to generate good statistical representation of the particles.

Acknowledgments

The financial support from Elkem and the Norwegian Research Council through the CORSICA project is greatly acknowledged.

References

[1] T. Margaria et al., "Intermetallic compounds in metallurgical silicon," in *INFACON 6*, 1992.

[2] J. C. Anglezio et al., "A study of the Si-rich domain of the Al-Ca-Fe-Si quaternary system," *Calphad,* vol. 18, no. 3, p. 311, 1994.

[3] T. Margaria, "Influence of cooling on silicon structure," in *Silicon for the Chemical Industry III*, Trondheim, 1996.

[4] G. C. Vogelaar, "Analysis of intermetallic phases in silicon ingots of different thickness," in *Silicon for the Chemical Industry III*, Trondheim, 1996.

[5] M. F. Møll, "Solidification of silicon - Macro- and microstructure as functions of thermal history and composition," PhD thesis, NTNU, 2014.

[6] S. Gouttebroze et al., "Sistruc: A microstructure model for optimization of silicon materials," in *Silicon for the chemical and solar industry XIII*, Kristiansand, Norway, 2016.

[7] A. L. Dons et al., "The alstruc microstructure solidification model for industrial aluminum alloys," *Met. Mat. Trans. A,* vol. 30, no. 8, p. 2135, 1999.

[8] S. Ciu et al., "Thermodynamic optimization of Ca-Fe-Si system and its application to metallurgical grade Si-refining process," *Met. Mat. Trans. E,* vol. 1, p. 67, 2014.

[9] N. Krendelsberger et al., "On the reaction scheme and liquidus surface in the ternary system Al-Fe-Si," *Met. Mat. Trans. A,* vol. 38, 2007.

[10] V. Raghavan, "Al-Fe-Si (Aluminum-Iron-Silicon)," *J. Phase Equilibria,* vol. 23, no. 4, 2002.

[11] V. Raghavan, "Fe-Si-Ti (Iron-Silicon-Titanium)," *J. Phase Equilibria,* vol. 30, no. 4, 2009.

[12] FactStage, [Online]. Available: http://www.crct.polymtl.ca/fact/facthelp/FS61new.htm.

[13] J. Safarian et al., "Liquidus of silicon binary systems," *Met. Mat. Trans. BB,* vol. 42, p. 852, 2011.

[14] V. Raghavan, "Al-Si-Ti (Aluminum-Silicon-Titanium)," *J. Phase Equilibria,* vol. 30, no. 1, 2009.

Fume collection in FeSi/Si plants – Regulations and Technical measures

Ragnhild Jensen [1)], Jens Christian Fjelldal [2)]
1) Process Metallurgist, Project Manager, Elkem ASA Technology
2) Environmental Manager, Elkem ASA Corporate

Abstract

All Elkem's Norwegian (ferro-)silicon plants have developed detailed plans regarding reduction of process dust generation, reduced personnel dust exposure and improved dust collection.

The Doghouse extraction system and air curtain shall be implemented at the plants for tapping smoke collection, and online dust measuring equipment installed, so that all dust sources in the production halls can be identified. If practically feasible, dust astray shall be eliminated, and dust collected.

A new generation of emission permits is emerging, with a significantly increased burden for the smelting plants for controlling, measuring and reporting on emission. Removal or reduction of diffuse process fume in indoor environment has a positive secondary effect by reduced fugitive emission from the production plant.

Introduction

Production of silicon and ferrosilicon involves a series of critical processes, such as raw material handling, furnace operation, tapping, refining and casting, and further mechanical processing, to produce the desired product quality. The different process steps create in varying degree environmental challenges as emissions to indoor working environment. Focus has in recent years been on reducing the process dust exposure [18, 19]. Sources to fume astray are mapped, the main being from the tapping, refining and casting process. Measures are taken to prevent, reduce, or protect working personnel against exposure to fumes in the production areas. Methodology for developing technical facilities and results of industrial implementation are presented.

Process Fume and main initiatives in the Industry

Process dust (fume) from the silicon and ferrosilicon industry consist mainly of amorphous silica, and studies on the health effect shows risk for obtaining Chronic obstructive pulmonary disease (COPD) [1]. The Norwegian Labour Inspection Authority has increased the focus on COPD with the objective to reduce the dust exposure for workers in the Norwegian smelting industry [2]. Elkem has over many years worked with the challenges of dust exposure, both by internal programs and projects, and in collaboration with other parties such as Norwegian Ferroalloy Producers Research Association (FFF), FUME programme (FFF), ECAST (FFF) and DeMaskUs

(Researh Council program Nano 2021), see illustration in figure 1.

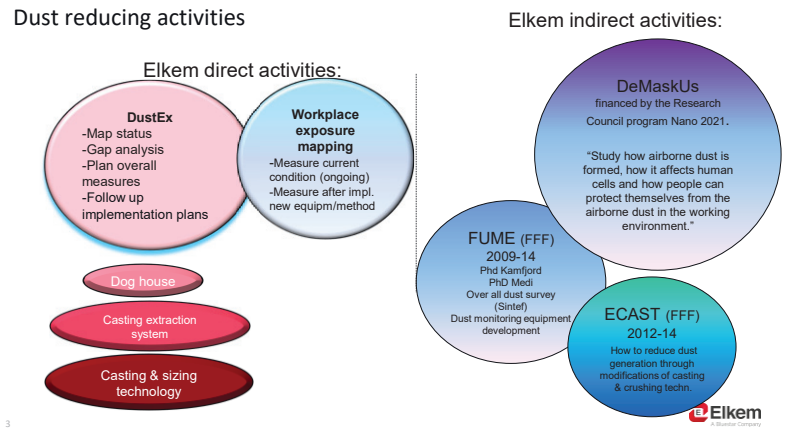


Fig. 1. Dust reducing programs and projects in Elkem and with partners.

Elkem started its process dust mapping program already in 1999, with a final report in 2005 [3] concluding with a risk of being inflicted reduced lung capacity due to exposure to smelting plant dust levels over a prolonged period. The tapping area showed to be one of the most exposed areas. Extra effort was put into improving the working conditions in the tapping area, this was enhanced with the result of the Johnsen Ph.D. Thesis [1].

To protect plant workers from developing COPD, first step was to impose use of dust masks in the exposed areas. To work with permanent measures to reduce spread of fume in indoor environment, resources were allocated to work with process understanding and possible technical solutions to the challenge. In 2006 the project "Promiljø" was initiated [4]. "Promiljø" was followed by the "Fume" project in 2009 [5].

Elkem is also partner in DeMaskUs, a four-year research program started in 2015 as a follow-up to FUME. DeMaskUs is an interdisciplinary research project financed by the Norwegian Research Council. Participants are the Norwegian ferroalloy, silicon and silicon carbide industry, with Norwegian research partners. The primary objective of DeMaskUs is understanding the origin of-, protection from- and potential health effects of ultrafine particles in the ferroalloy and SiC industry. One of the main focuses is respiratory protection with dust masks, researching the effectiveness of various dust masks against ultrafine particles, the importance of personal customisation of masks, the psychological aspects related to using a dust mask and psychological aspects that influence the use of dust masks in the industry [6,7]. Elkem's production plants participates actively in this important work.

The Elkem "DustEx" program

Elkem initiated the internal program "DustEx" in 2012 for further initiatives to reduce the process dust exposure, with the goal to, by permanent technical measures, remove or reduce the process dust to an acceptable level and/or personnel shall be less exposed by changing working routines: 1) remove or reduce dust generation, 2) reduce personnel's exposure to dust, 3) handle remaining dust by improved collection.

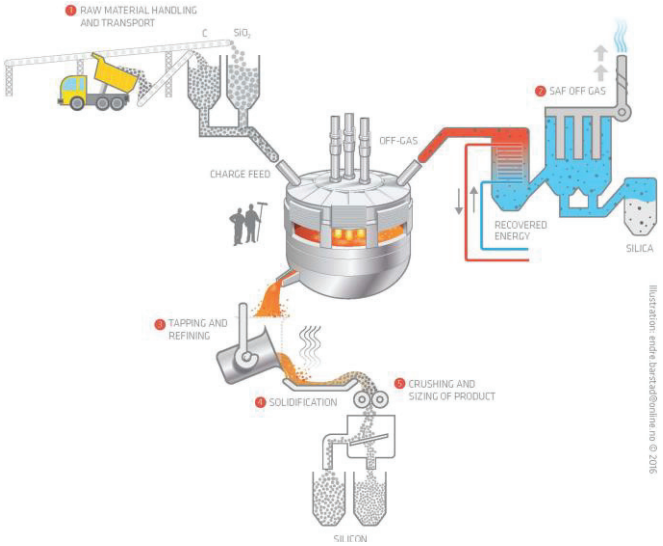


Figure 2. Main dust source areas at Norwegian ferroalloy smelting plants. [8]

The desired situation includes that "best practice" and available technological solutions are known and taken/planned taken into use at all plants, and that use of respiratory protection is reduced to a minimum. Collected dust is a valuable material and contributes to circular economy.

Dust level limits

To comply with Norwegian Labour Inspection Authority injunction regarding dust in the working environment, Elkem internal goals were set on dust level limits (table 1) [9].

Table 1. Dust exposure limits, working environment, Elkem.

Dust type / Limit	**Threshold limit value (TLV)**	**Elkem internal limit for taking measures ****
Total respirable dust *	*≤ 2.5 mg/m³*	≥1,25
Respirable amorphous Si02	*≤1.5 mg/m³*	≥0,38

* *The standard TLV for "respirable dust" is ≤ 5 mg/m³ but since the plant dust has a high content of amorphous silica, the figure for dust of amorphous Silica applies.*
** If value is *≥1/4 of norm, plan to reduce level is required.*

The dust exposure level in the working environment is measured by personnel carrying a filter pump during a whole working day (8 hours).

Another factor to consider are periods with high exposure dust levels caused by special operations or working tasks. As a rule of thumb, following dust levels are acceptable for a 15min exposure period (provided that the 8 hours value are according to the requirements):

- Respirable dust ≤ 10 mg/m3
- *Respirable Amorphous SiO2 ≤ 3 mg/m³*

Example from Elkem Bremanger: High exposure dust level periods were identified and measured for the tapper at Elkem Bremanger Foundry, with exposure of 12 mg/m^3 i.e. above the defined maximum level (Fig. 3), i.e. use of filter mask is mandatory for the tapper.

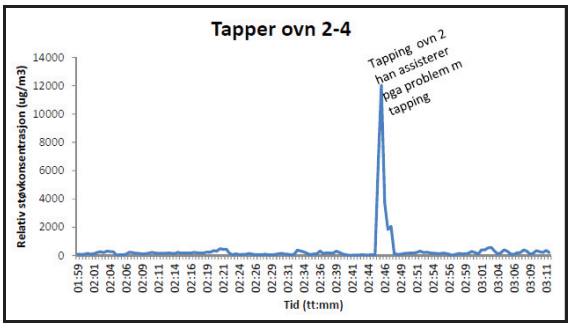


Fig. 3. High dust exposure situation, problems during tapping, Elkem Bremanger Foundry furnace 2 and 4.

Process dust characteristics

Dust at the Elkem plants can be divided into two main categories; thermal generated dust, mainly amorphous SiO_2, and mechanical generated dust, particles of Si, FeSi, C, SiO2 (crystalline). Mechanical dust is typically generated by crushing, grinding, cutting and handling processes, and create dust particles normally in the range between 1 µm og 10 µm.

Thermal generated dust is formed at high temperature through combustion or evaporation, such as during tapping, refining and casting. Thermal generated dust has typical particle sizes from 0.01 µm to 1 µm (fig 4.) [10]. The tapping gas is a result of a small overpressure in the furnace (0.03-0.06 bar) caused by the process, and consists mainly of CO gas and SiO gas that burns, forming CO_2 and amorphous SiO_2 particles.

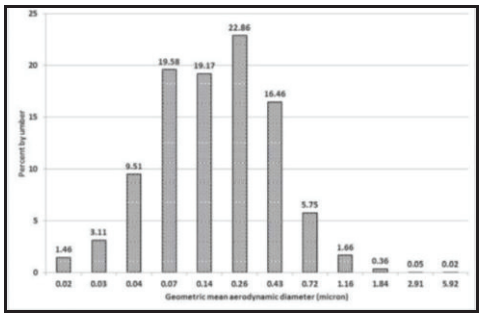


Figure 4. Particle size distribution of fume generated during tapping of Si. [10]

Focus in our industry has been, and is, more on the thermally generated process dust than mechanical produced dust, reasons being that fumes represents: 1) large quantities, 2) small particle size, 3) respirable dust with potential health risks, 4) widely spread, long residence time, 5) thermal effects spreads dust and ultimately leads to emissions to

the outside environment, 6) negative process yield impact. Some main properties to process dust vs mechanical dust is shown in table 2.

Table 2. Typical properties thermal dust vs mechanical dust, FeSi / Si

Property	Thermal dust	Mechanical dust
Size	Fine	Coarse
Specific weight	Low	High
Temp:	Hot	Cold
PAH	(+)	-
Radioactive (norm)	(+)	-

Environmental requirements and measuring challenges

Various stakeholders affect development and framework conditions within the environmental area. Elkem's vision, Norwegian legislation, the European Union, Customers are among the important stakeholders. A new generation of emission permits is emerging, with a significantly increased burden for the smelting plants for controlling, measuring and reporting on emission.

New requirements for measurement plans includes:

- Assessment of measurement uncertainties
- Requirements for accredited analyzes
- Documented assessment of sample representativeness
- Regular 3rd party control for all regulated parameters
- Requirements for control of suppliers' measurement plans (C-containing materials)

Use of resources on emission measurements is and will increase significantly. For a number of regulated parameters, measuring uncertainty is high due to issues with non-channelized gas flow, e.g. sample taking, analyzing methods, low concentrations etc. Examples of reportable parameters are PAH, heavy metals, and dust.

For priority environmental pollutants, “no emission is small enough“. There is no lower limit for regulation and annual reporting. Reporting is currently taking place using model calculations, there is a need to gain more control, and reduce the content of these elements. For example, the elements arsenic, copper, chrome, is included in environmental accounts, and there are currently no standardized measurement methods. These elements will however be included in new emission permits.

Our industry is facing new challenges, with mandatory emission permit for radioactive nuclides (norm). The limit value for emissions of radioactive nuclei is regulated [11], and when releasing several nuclides, you must sum up the contributions. If you release above threshold limit, application must be issued to the Norwegian Radiation Protection Authority. Standard raw materials used in our industry are subject to emission permits and we must know quantities and emissions.

The environmental emission requirements are for some areas challenging due to uncertainties in the measuring systems / devices /methods used, this includes measuring process dust conditions in the smelting plant.

Most dust meters are designed to measure particle sizes down to approx. 1 µm; they are suitable for measuring on mechanically-generated dust, but not thermally generated dust. It is mostly only custom made and expensive dust meters that can measure particles below 1 µm, or filter pumps as used for the measuring campaigns on personnel

exposure. To install on-line dust surveillance systems in working environment is challenging on several levels.

Increased dust collection will typically require more filter capacity and not least technology for extracting the fume as close to the source as possible. With temperature levels in the silicon and ferrosilicon tapping processes at ca. 1550 °C to 1750 °C, and a high energy load [20], designing sustainable technical solutions for fume collection is challenging.

DustEx - Elkem program on dust exposure reduction

Elkem allocates significant resources to combat silicon and ferrosilicon dust in the working environment. With the DustEx program, efforts to meet with the Labour Authorities requirements and have a working environment without need for using respiratory protection are worked with from several angles. The overall goal is to have feasible solutions for reduction of dust to acceptable level for all sources that are identified, and that "best practice" and available technological solutions are known and taken or planned taken into use at all plants, for the dust levels to be reduced to below TLV.

All Norwegian Elkem plants have performed a complete mapping of the dust status in working environment in the different processes and working areas, example of mapping is shown in table 3. Succeeding the mapping, risk evaluation and accompanying action plans were developed. They revealed the fact that there was and still is a need for development of new technology for reduction and/or capturing of process generated dust.

Table 3. Example of dust mapping, Bremanger furnace 4 for different working groups (tapper, furnace operator, mechanic)

		Number of samples	Avrg. Con. (mg/m^3)	Stdev. (mg/m^3)	Min.level (mg/m^3)	Max level (mg/m^3)
Tappers	1999-2003	19	4,1	2,30	1,20	10,00
	2012	19	2,7	1,40	0,69	6,80
Furnace operators	1999-2003	10	2,1	0,78	0,90	3,20
	2012	12	2,1	0,94	0,20	3,10
Mechanical engineers	1999-2003	8	4,5	2,30	1,80	8,40
		8	5,1	2,30	1,00	10,00

Based on the mapping results, focus areas for fume reduction involving technological development was concentrated to design optimization of the “Doghouse system”- a local exhaust system for tapping fume. Based on the technical challenges with measuring process dust in indoor environment, focus was also set on dust measurement systems, including on-line surveillance in furnace /production halls, to gain better understanding of the complex processes and working operations in the smelting plants.

Principles and challenges with tapping gas collection

To collect tapping fume there are some main principles to caretake (fig.5)
Extremely high temperatures and ultra-fine particles that disperse very quickly makes it especially difficult to capture dust generated during the tapping and casting processes. The tapping fume escaping collection using conventional tapping off gas extraction

system is a main source for emission to indoor environment. Elkem, together with R&D partners has successfully gained greater understanding of these challenges and developed better solutions for dust collection [12].

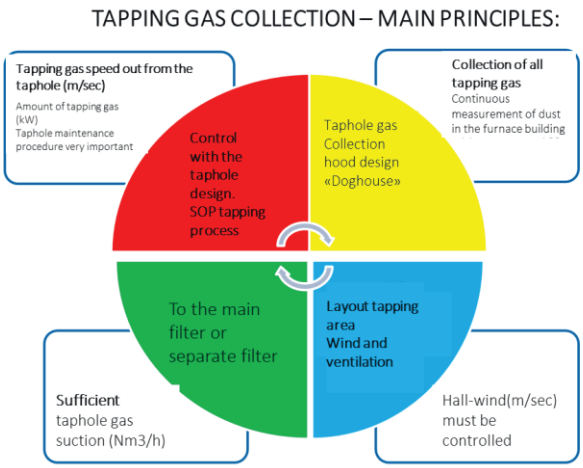


Figure 5. Tapping gas collection – main principles [13].

Since silicon furnaces are rotating, finding robust and durable technological solutions for collecting the tapping fume is demanding. An issue with the tapping gas is that the gas velocity out of the taphole occasionally may be very high, making fume collection difficult. A working tapping fume collection system must safeguard using tapping tools, maintenance operations and comply with the established safety standards.

Extraction solutions require customization on the individual furnaces, and furnace outage for several days is required for implementation of the new doghouse technology.

"Doghouse" technology

The tapping area is one of the most difficult emission points for combatting dust. Standard tapping hoods does not capture sufficient amounts of the produced tapping gas, resulting in fume astray and need for tapper to use personal respiratory protection.

Elkem has been developing new types of highly effective local dust collection and extraction systems for the tapping area, commonly called 'Doghouse' technology after the first prototype. As each furnace is unique with respect to processing and structural conditions, the technology must also be tailored to each furnace.

The doghouse technology has been installed at several Norwegian plants: -An industrial pilot was installed on Thamshavn furnace 1 in 2011, this was based on results in the Kadkhodabeigi PhD thesis in 2011 [14, 15], as a succession of full scale testing at Elkem Thamshavn and Elkem Salten (B.Faaness / N.E.Kamfjord) in 2010, that again was based on conceptual test phase by K.H.Berget in 2009, established on new ideas for better design of tapping hoods by K.H.Berget / J.E.Christiansen in 2008. The validation of the Thamshavn doghouse pilot was positive and further activities commenced, illustration of the design development is shown in fig. 6. Second generation doghouse was designed for Thamshavn, not installed yet, but the basis from this project is used for the on-going execution project with doghouse implementation at Elkem Salten furnace 2.

An Elkem internal procedure for developing industrial doghouse design was established in 2012-2014, (R. Jensen). Under the DustEx program, the first plant to install the industrialized doghouse solution was Elkem Foundry Bremanger furnace 4 in 2015-2016 (R. Jensen). After meticulously planning and design work, the doghouse system was installed on Bremanger Foundry furnace 4 and set into operation in January 2016. The design was developed by calculations of the convection flow rate, hall wind surveys, and physical and thermal conditions in the tapping area.

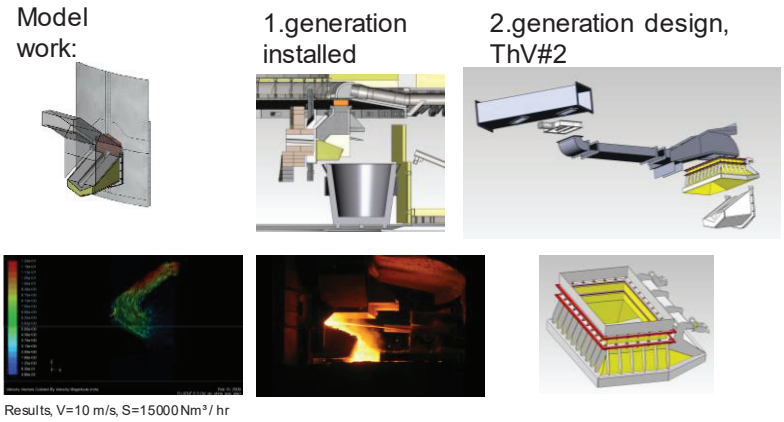


Figure 6. Development of the Doghouse system

Computational fluid dynamic analysis

To verify (and adjust) the doghouse design, computational fluid dynamic analysis (CFD)was used (Fig.7) [15].

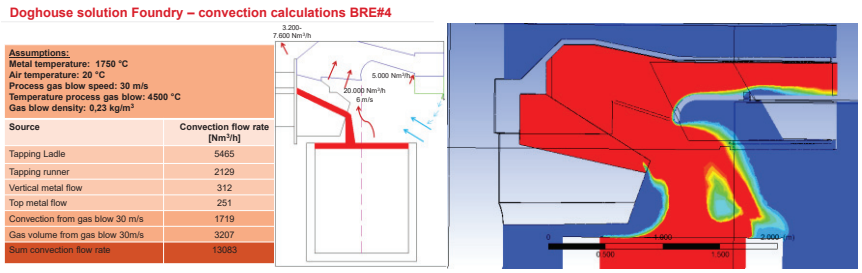


Figure 7. Convection flow rate calc., and CFD analysis, Bremanger Furnace no. 4. [15]

To determine the local hall wind conditions in the furnace building at Elkem Bremanger Foundry, simple smoke measurements and more extensive furnace building pressure conditions were mapped and the result used as input to the CFD model.

The CFD modeling was performed in steps to eliminate any model errors and ensure understanding the different parameter effects.

Air curtain solution.

The Bremanger furnace 4 doghouse solution includes an air curtain system as supplement to preventing tapping smoke astray. This add on has shown to be a success, and further development work is on-going on design and utilization of air curtain technology.

The developed air curtain solution for Bremanger furnace 4 producing ferro silicon was caused by the fact that tapping is done without lid on the tapping ladle (i.e. no concentration, directing of the tapping gas), and discontinuous tapping, challenging as to amount of tapping gas produced per time. The tapping fume is in general generated from four main locations: 1) tap hole, 2) tapping runner, 3) tapping ladle surface, 4) refining (if oxygen/pressurized air is added to the tapping ladle during tapping).

The air curtain has three main functions: 1) stop fume from moving away from the extraction point(s), by an air impulse, 2) keep fume within a confined area until it is removed at the extraction point(s), 3) stabilize flow ratios in the tapping zone, and reduce the negative impact from any hall winds.

The air curtain will assist to efficiently collect process gases and prevent dust from spreading into the surrounding air / internal working environment by directing the fume towards the extraction point(s), effect is in fig.8. The air curtain is supplied by air from air fan(s).



Figure 8. Demonstration of Air Curtain effect at Bremanger Furnace 4.

To achieve desired effect of the air curtain, some adjustable parameters are required: 1) nozzle gap width, 2) volume flow of air in the distribution channel, 3) exit velocity (rate should be between 20 m/s and 30 m/s), 4) the outlet direction, angle of the air flow.

The air curtain does not produce excess pressure that pushes the fume astray, and the convection flow in the tapping zone is none or little affected. The main reason for this is that the exhaust volume from the doghouse system is much greater than the airflow supplied from the air curtain. It seems as the air curtain assists to set up a swirl with rising air under the tapping hood close to the furnace, and downward air at the outer edge located with the out at the air curtain nozzle. This swirl stabilizes the conditions in the tapping zone [17].

Doghouse implementation Bremanger Foundry

The complete doghouse design for Bremanger furnace 4 is illustrated in fig. 9, together with pictures of the tapping smoke situation before and after start-up of the doghouse. Implementation of doghouse to remove tapping smoke from the indoor environment has highly contributed to reduce exposure at Elkem Foundry Bremanger.

The Foundry Division followed up by copying and installing the Doghouse system also at Bremanger Foundry furnace 2 in June 2016. The effect on fume astray is very satisfying (fig.10).

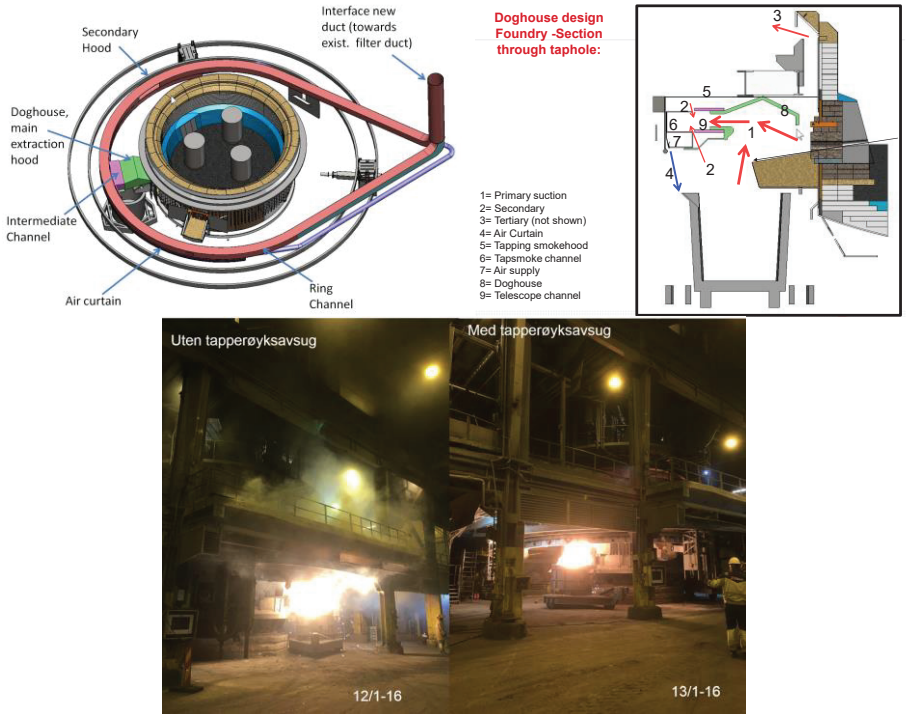


Figure 9. Doghouse principle solution at Elkem Foundry Bremanger furnace 4. Change in dust astray situation at Elkem Bremanger Foundry, before (left) and after (right) doghouse installation at furnace 4 (Jan. 2016).

Further doghouse implementation

Installing the new doghouse solution requires available filter capacity. Due to this fact, several of the Elkem furnaces will in the period 2017-2020 be provided with upgraded extraction capacity for tapping (and refining) gas.

A detailed plan for further deployment of doghouse systems in Elkem is developed. Installation of doghouse at Salten furnace 2 is planned for in 2019, equipment already being produced and pre-installations in initial phase. Design solution is developed for Elkem Thamshavn furnace 2 and for Elkem Salten furnace 1, ready for main study and execution phase according to Elkem investment program. Concept design solution for Rana furnace 5 and Bremanger furnace 5 are developed, and both main studies are in initial phase. The current plan is that all Norwegian Elkem furnaces have installed satisfactory tapping gas extraction solutions by 2020/2021.

Dust measurement devices.

At present instrumentation for monitoring and documenting dust exposure is by use of expensive solutions. Calibration of operating on-line dust measurement devices is

ambiguous and often tends to be neglected. This in turn makes demonstrating effect of dust reducing measures difficult to monitor.

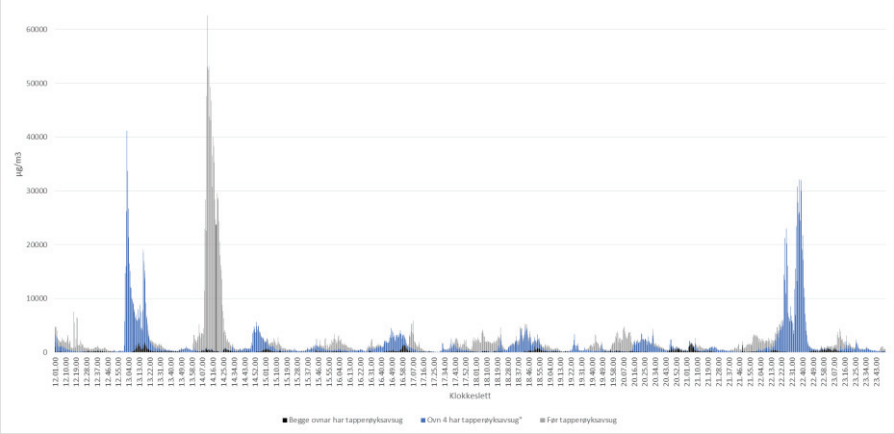


Figure 10. Dust levels in tapping area, Elkem Bremanger Foundry, before and after doghouse installations. Dust astray measured over 12 hours, before doghouse (grey), with doghouse furnace 4 (blue), with doghouse furnace 4 and 2 (black).

On line laser dust measurement

Current laser dust measurement device for on-line surveillance of process fume astray in working environment has some issues with calibration, requiring external expertise, limitations in dynamics in dust dispersion, and they are expensive. Example of use is shown in fig.12.



Figure 12. On-line laser gauge for smoke detection in indoor environment, Elkem Salten.

Smoke detection image analysing tool

A "machine vision" system is in planning for complementing the existing laser dust measurement devices and wind gauges placed in field. The intention is that on-line machine vision dust monitor shall display silica dust "concentration", relative area and elongation of the smoke plume astray.

To develop more inexpensive tools for smoke monitoring, the idea is to develop a new method for process smoke surveillance, using state of the art components; digitalization and data analysis. Video picture algorithms shall be established for digitalization of the smoke distribution, smoke astray. The goal is to have a "Smoke

Area Factor" to measure the smoke plume propagation. Example is shown in figure 13, from a casting process.

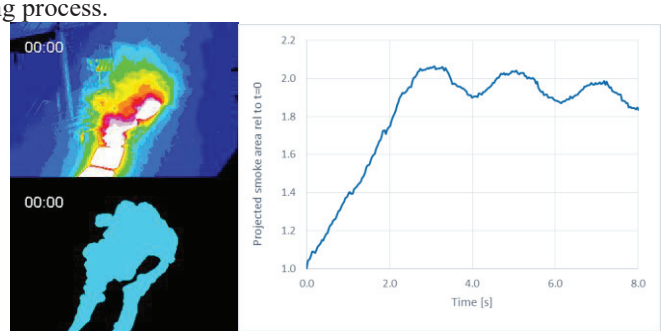


Figure 13. *Smoke plume at casting process, with a resulting "smoke area factor" in %.*

A graphical representation of dust contamination (as illustrated above) or similar shall also be generated to visualize contamination status. The limits, upper and lower, shall be set within the normal range of smoke distribution in the relevant Process Area. The goal is to have a "Smoke Area Factor" as a parameter to measure the variation in the smoke plume propagation. The goal is to calibrate the "Smoke Area Factor" with measured smoke concentration levels. Work on this is commenced.

On-line hall wind measurement

To better understand the cause and effect of hall winds and subsequent effect on smoke distribution inside the furnace halls, a pilot system with wind surveillance is installed at Elkem Salten (fig. 14). The outside wind gauge is used to calibrate against actual weather conditions; learn how the wind speed and direction and impacts on the internal hall winds, and also use the information to understand the effect of open / closed gates in the furnace hall.



Figure 14. Wind measurement gauge in furnace hall and outside, Elkem Salten.

Other dust reducing initiatives

Refining: Bremanger Foundry has newly installed a new Refining station including an off-gas hood, connected it to the Doghouse off-gas infrastructure utilizing available extraction capacity. Elkem Salten furnace 2 is working with installation of similar solution. **Casting:** Elkem is also working with the development of extraction hoods for capturing process gas during casting. This is challenging because it involves several

moving systems and multiple points of dust generation. A preliminary study has been done at the Salten plant in Norway and is ready to be followed up with a pilot test.

References

1. H.L. Johnsen, *Lung function, respiratory symptoms, and occupational exposure*, Ph.D. Thesis, University of Oslo, Oslo 2009.
2. Arbeidstilsynet, *Strategi for reduksjon av yrkesbetinget KOLS 2010/2011.*
3. S.M. Hetland, *Kartlegging av eksponering for luftforurensninger i arbeidsatmosfæren ved Elkem ASA*, Elkem Internal, 2005.
4. Norwegian Ferroalloy Producers Research Association (FFF), Promiljø, Research program 2006-2011.
5. Norwegian Ferroalloy Producers Research Association (FFF), FUME, Research program 2009-2014.
6. Ø. Robertsen, H.C.B. Vangberg, S. Føreland, M.N. Hegseth, *Predicting the use of protective equipment in the Norwegian smelter industry*, Infacon XV, Feb. 2018, pp.103
7. M.N. Hegseth, Ø. Robertsen, A. Aminoff, H.C.B. Vangberg, S. Føreland*, Reasons for not using respiratory protective equipment and suggested measures to optimize use in Norwegian silicon carbide, ferro- and silicon-alloy industry*, Infacon XV, Feb. 2018, pp.104.
8. Ida Kero, Svend Grådahl & GabriellaTranell, *Airborne Emissions from Si/FeSi* Production, JOM The Journal of The Minerals, Metals & Materials Society (TMS)
9. *Siri Helland-Hansen, Elkem internal Memo,* 2013.
10. Ida Kero, Mari Næss, Gabriella Tranell, *Fume characterization in the ferro alloy industry*, INFACONXIII_Vol2_p945-955
11. Klima- og miljødepartementet, *Forskrift om radioaktiv forurensning og avfall,* Lovdata 01.01.2011.
12. Dr. Halvard Tveit, Mr. Vegar Andersen, Mr. Kjell Håkon Berget, Ms. Ragnhild Jensen, Elkem AS**,** *The tapping process in silicon production,* SAIMM Furnace Tapping Conference 2014.
13. Dr. Halvard Tveit, *Elkem internal memo*, 2017.
14. M. Kadkhodabeigi, H. Tveit and K. H. Berget, *SILICON PROCESS- NEW HOOD DESIGN FOR TAPPING GAS COLLECTION*, HELSINKI, FINLAND, , INFACON XII – JUNE 6-9, 2010,
15. Modeling of Tapping Process in Submerged Arc Furnaces Mehdi Kadkhodabeigi Doctoral Thesis NTNU April 2011
16. Ø.V.Nygaard (Sweco), *Doghouse design,* Elkem internal report 2013.
17. Ø.V.Nygaard (Sweco), Målerapport luftgardin BRE 4, Elkem internal report 2017.
18. Elkem AS, *Sustainability report*, 2015.
19. Elkem AS, *Sustainability report*, 2016.
20. Mass and Energy Balances of the Silicon Process – Improved Environmental Standards Nils Eivind Kamfjord Doctoral Thesis NTNU April 2012.

Silicon for the Chemical and Solar Industry XIV
Svolvær, Norway, June 11 – 14, 2018

Statistical Model for Locating Micro Slag Droplets in MG-Si production

Erlend Lunnan Bjørnstad[1)], and Gabriella Tranell[2)]
1) PhD Candidate, SFI Metal Production, IMA, NTNU, Trondheim
2) Professor, SFI Metal Production, IMA, NTNU, Trondheim

Abstract

Representative metal sampling in the oxidative ladle refining(OLR) of MG-Si is challenging, creating difficulties for industry and researchers alike in describing the system. One of the problems associated with this comes from the contamination of micro slag droplets(MSD). This work proposes a model for finding metal samples contaminated by micro slag droplets OLR, when only a small number of samples are available for each ladle. To achieve this, the behaviour of [Ca] and [Al] from different ladles are compared to allow for greater statistical resolution. The model has been tested on published data sets, and simulated sets with different population variance, and has been found to represent the system adequately, with a type I and II error less than 10%.

Introduction

Metallurgical grade silicon(MG-Si), is a widely used silicon source in many industries, ranging from aluminum alloy production to photovoltaics. It is produced by carbothermic reduction of quartz in a submerged arc furnace, and undergoes further refining to meet customer specifications. Oxidative ladle refining(OLR) is one these refining processes. In OLR, the melt is tapped into a ladle, which is purged with oxygen enriched air, through a bottom mounted porous plug, as seen in figure 1. The oxygen reacts with the melt, forming an immiscible slag phase, which will contain an equilibrium amount of oxide forming impurities. While a large range of minor oxide-forming impurities are present, the primary slag forming impurities are [Ca] and [Al], giving a predominantly SiO_2-CaO-Al_2O_3 slag. To specify that a species El is in the metal it is written in square brackets, [El]. When customer specification has been reached, the melt will continue to casting, while the slag is removed. While performing OLR it is customary to take product samples during the process, to ensure compliance with customer demands.

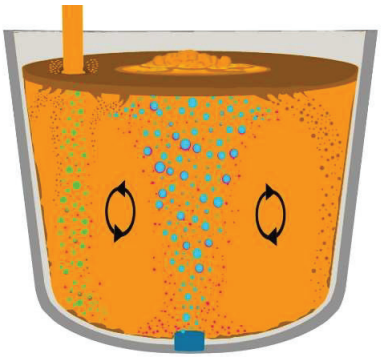


Figure 1: OLR, with gas bubbles in blue, and slag droplets in pink.

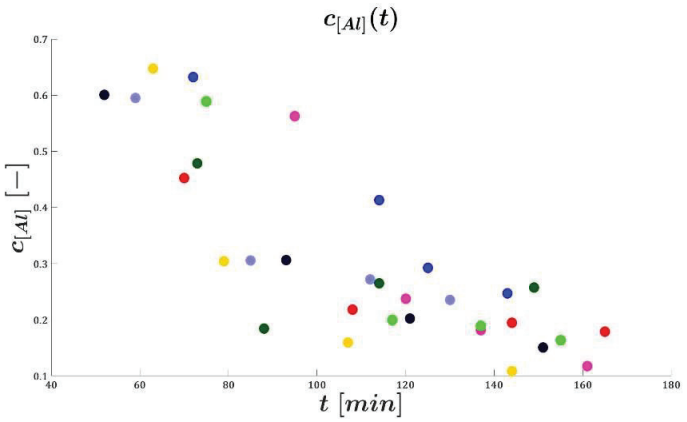


Figure 2: Normalized [Al] concentration, with respect to the initial value, as a function of time.

Sampling however, poses many challenges. High temperatures, ranging from 1823-1923K(1550-1650°C), and an aggressive environment, limits the number of available sampling techniques, and in addition necessitates extensive EHS procedures. Representative sampling poses additional challenges, as a ladle can contain upwards of 7tonns of Si-melt. In addition, there is a moderate chance that micro slag droplets will be present in the sample. These micro slag droplets(MSDs) contaminate the sample, but due to the high uncertainty present in small sample sizes, it can be difficult to distinguish slag-contaminated, and non-contaminated samples. While there exists well studied outlier analysis procedures, like the general extreme Studentized deviate(ESD) many outlier procedure, they are often not applicable due to the limited sample size [1]. This is not only an issue facing the industry, but also researchers working with this process.

By utilizing information regarding the expected refining behavior of the primary slag forming impurities, [Ca] and [Al], and assumed sampling behavior, this work proposes a model for locating slag-contaminated samples in OLR of MG-Si. The aim of the model is to provide a useful approximation for the system currently at hand, where inconsistent sampling intervals and high uncertainties are frequent. Thus higher errors are expected, as not enough information is currently provided to perform a more thorough analysis. This model was evaluated using industrial data sets analyzed by Kero et al. [2], and simulated sample sets with different population variance. Due to limited experimental data and fundamental knowledge, this model is currently limited to samples taken after the ladle is 50% full.

Figure 2 shows the normalized [Al] concentration, with respect to the initial value, $c_{[Al]}$, from Kero et al. [2]. Here the initial point is not shown, as the sets are transformed such that the initial concentration is 1, at time 0. The expected behavior can be approximated as a simple transient decay, with the refined concentration as its steady state. An example of this is the red and yellow ladle in figure 2. $c_{[Ca]}$ will behave similarly.

Expected Behaviors and Assumptions

A common theme in experimental analysis is that the less one knows about a systems behavior the more samples are needed to describe it. While the actual number of necessary samples will depend on system variance, desired resolution, effect size, etc..., this theme is especially important when describing data sets containing small sample sizes. To visualize this fact, one can think of sampling 5 out of 10^5 people, where 1% of the population has red hair. The probability that no one in the sample has red hair is ≈95%. This experiment is not able to see the effect(red hair), let alone give any indication of the effect size(1%). Now, if the occurrence of red hair is increased to 60%, the probabilities that 0, 2, 3, or 4 people, out of 5 sampled, have red hair are respectively ≈<1%, 23%, 34%, and 26%. Here one is expected to see the effect, and additionally the sample can give a rough estimate of the actual effect size(3/5=0.6). Consider the 1% case once more, but now it is known that almost all of the red haired people live in a single city with a population of 2000. The chance of getting a number of red haired people, out of 5 possible, can be seen in table 1.

Table 1: Probability of getting *x* red haired people out of 5 total, in a population of 2000, where 1000 have red hair.

x	0	1	2	3	4	5
p(x) [%]	3	16	31	31	16	3

With this extra knowledge it is now possible to see and estimate the effect. This is an example of the fact that knowledge of a system can allow one to measure effects that could not otherwise be measured. It is also shown that a small sample size cannot see or estimate small effect sizes, since one cannot attain the necessary statistical resolution. The weight fractions of [Ca] and [Al], $\omega_{[Ca]}$, $\omega_{[Al]}[-]$, are in the order of 10^{-3} in a typical tapped MG-Si, after the ladle is half full. $\omega_{[Ca]}$ and $\omega_{[Al]}$ are considered small, compared to their respective counterpart oxides in the slag. Therefore, it is assumed that MSDs contamination has a large effect on the metal analysis. In principle this means that small deviations can be disregarded. It is additionally assumed that the deviation will always be positive, when compared to similar non-contaminated metal samples. This assumption states that the lowest measured $\omega_{[Ca]}$, $\omega_{[Al]}$ values at any given point in time are more likely to represent the population than the highest. In turn, this allows one to compare the samples to the measured minimum, rather than the average. As previously assumed, the slag contains large amounts of both Al and Ca. This means that a sample containing MSDs, can be assumed to show large deviations in both $\omega_{[Ca]}$ and $\omega_{[Al]}$. If the variance is high, then there will naturally be a large spread in the refining curves. This assumption allows one to better distinguish between this natural spread, and MSDs contamination. One can still mark a non-contaminated sample as contaminated, if both concentrations have a naturally high positive deviation, giving a false positive or type I error. However, this assumption will later be shown to greatly reduce these errors, justifying its inclusion.

The assumptions up until this point have all been quite general, but they are not enough to get a proper model. Next, comes therefore some assumptions which are more specific, to allow for a better system description. In figure 2, each ladle is only sampled a few times. Additionally, the samples are not taken at similar absolute times, with regards to refining initialization, but rather at process breakpoints, like 50% full ladle, or full ladle. While the absolute sampling times are, in most cases, not widely different, they still cause scatter when comparing different ladles. Comparing the behavior of $\omega_{[Ca]}$ and $\omega_{[Al]}$ in

different ladles would be of great benefit, as the increased sample size greatly increases the statistical resolution. To decide which ladles/batches behave similarly it is assumed that, the combination of m similar sample sets, from N total sets, starting at 50% full ladle and normalized with respect to the actual initial concentration, will contain a set of k points, each the minima of their respective absolute time interval τ_i.

$$\vartheta_{[El],i} = \min(c_{[El]}(t_j)), \quad t_j \in \tau_i, \quad \tau_i = t_i \pm \Delta t_i, \quad i = 1,2,...,k \tag{1}$$

These points will adequately follow a model on the form:

$$\hat{\vartheta}_{[El]}(t) = \hat{\omega}_{[El],\min}(t) / \omega_{[El]}^{in} = \theta_1 + (\theta_2 - \theta_1)\exp(-\theta_3 t) \tag{2}$$

For this model specifically, time is shifted to the left by the first measured point at 50% full ladle, making this the new initial point. The first time interval will then have t_1-Δt_1=$t_{0,min}$=0. This is to help the regression. $\theta_{1\text{-}3}$ are all fitted values, but for the model to be adequate one should roughly have $\theta_1 \approx c_{[El],min}(k)$, $\theta_2 \approx c_{[El],min}(1)$, and $\theta_3 \in [0\ 1]$. Equation 2 is a simplified version of the batch refining equation found in Engh [3], and while it does not represent the whole refining process adequately, it can approximate the current time interval well enough to be of use. If all points in a set are marked as contaminated, except for the final points or the final points tend towards the general equilibrium concentration, then the set is not considered to be similar with the rest. This essentially states that similar sample sets show approximately the same behaviors within a given time interval.

With the previous observation, it can also be noted that even with dissimilar sampling times there will be a point where $c_{[Ca]}, c_{[Al]} \approx c^{\infty}_{[Ca]}, c^{\infty}_{[Al]}$. Even if these points are scattered over a wide time interval they can still be assumed to represent the same population value. This provides a greater sample size to perform tests on. It is then assumed that the actual variance is the same over the whole refining curve. Finally, it is assumed that the initial value, which is normalized against, is not contaminated. If this is the case, then the set should have a large negative deviation, with regards to the other ladles. Final list of assumptions:

1. MSDs contamination has a large effect on the metal analysis.
2. MSDs contamination will produce a positive deviation in $c_{[Ca]}$ and $c_{[Al]}$.
3. Contamination by MSDs will be seen with respect to both Al and Ca.
4. $c_{[El],min}(i)$ can be adequately fitted to equation 2.
5. Even if scattered over a large time interval, $c_{[Ca]}, c_{[Al]} \approx c^{\infty}_{[Ca]}, c^{\infty}_{[Al]}$ all represent the same population value.
6. The actual variance is the same over the whole refining curve.
7. The value normalized against contains no slag.

Model

First, all of the sample sets are normalized with respect to their respective initial value and sorted by time. Starting at a time, after/at 50% full ladle, all of the values within a specified time interval are checked to find the smallest among them, before moving

forward a given distance and checking again. It is advised to use smaller time steps, and to allow the intervals to overlap, so that multiple points are considered in every time interval. This should lower the chance of getting a minimum point at odds with the other minima. For the data from Kero et al. [2] a step size υ=5min, with the interval Δt=10min was used. t_i can then be written as:

$$t_i = t_{0,\min} + \upsilon \cdot i \tag{3}$$

According to assumption 4, the minima are fitted to equation 2, by the fminunc function in MATLAB R2016b. From this function one can find which points are close to equilibrium. This step could potentially be substituted by visual inspection of the data if one desires. For the set considered here the last 10 points are used.

Next the 95% confidence interval(CI), using the t-distribution with respect to the mean, is calculated for the equilibrium points. If the CI does not contain the smallest equilibrium point, then the point with the largest positive deviation is discarded, and the CI is recalculated. Here assumption 2 is used, as it is assumed that the minimum is a better description of the true values. This is performed until the CI contains the minimum.

Then an interval equal to the CI is placed on top of the minimum values already found for each respective time interval, as such:

$$\varphi_{[El],i} = \vartheta_{[El],i} + \max(CI) - \min(CI) \tag{4}$$

Every point which lies above the line drawn by $\varphi_{[El],i}$ is marked as a potential outlier. For a point to be marked as contaminated, it must lie above both $\varphi_{[Ca],i}$ and $\varphi_{[Al],i}$. If most of a set is marked as contaminated, then it is considered not similar to the rest.

The model on the data from Kero et al. [2] can be seen in figures 3 and 4. Here the blue sample set is not considered similar to the rest. The samples which are marked as outliers are the first points in the pink and green ladle, together with the last point in the dark green ladle.

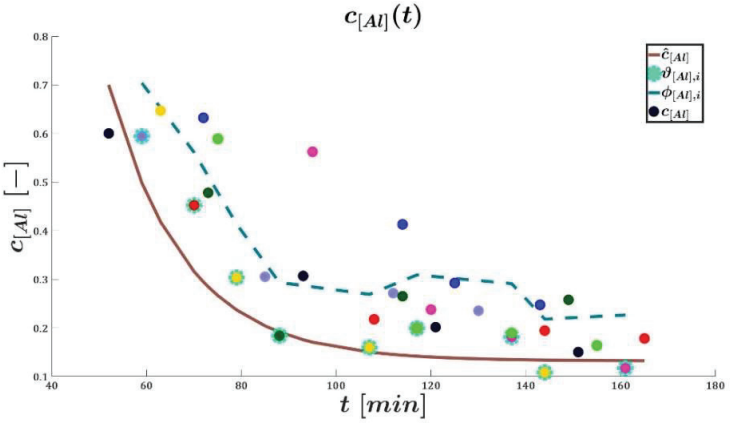


Figure 3: Data from Kero et al. [2] for [Al]. Different colored dots indicate different ladles.

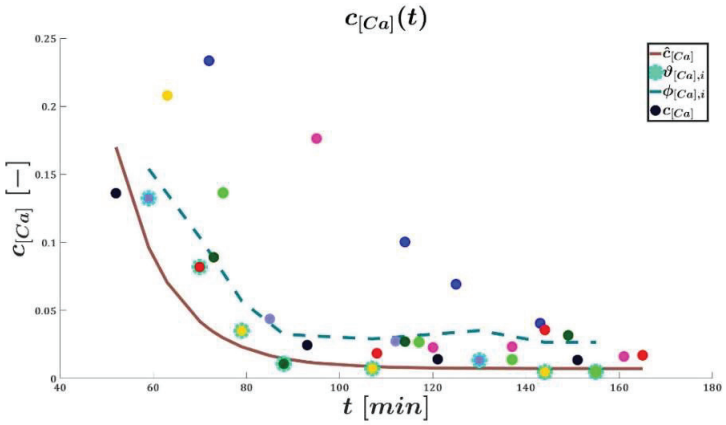


Figure 4: Data from Kero et al.[2] for [Ca]. Different colored dots indicate different ladles.

Simulated Sets

To test the model simulated sets were generated using equation 2 with $\theta_{[Ca]}$=[6.1e-3, 0.17, 8.34e-2] and $\theta_{[Al]}$=[0.15, 0.7, 6.23e-2]. Each point was given a normally distributed displacement around the line with a standard deviation $\sigma_{[Al]} \in$[0.02, 0.06] where $\sigma_{[Ca]}=0.5\sigma_{[Al]}$, by Matlab R2016b's normrnd function. Within each generated set $\sigma_{[Al]}$ was kept constant. Each point for $c_{[Al]}$ had a specific contamination chance, and thus was displaced further by a random integer between 10 and 50, which was then multiplied by 10^{-2}. $c_{[Ca]}$ has half of the displacement of $c_{[Al]}$. The contamination chances tested were 5, 10, 15, 20, 25, and 30%. When running a simple time series from 0 to 100 minutes, with one point for each minute, including 0, and υ=2.5, Δt=5min, one gets the errors seen in figure 5. It can be seen from figure 5 that the model performance is heavily affected by the contamination chance.

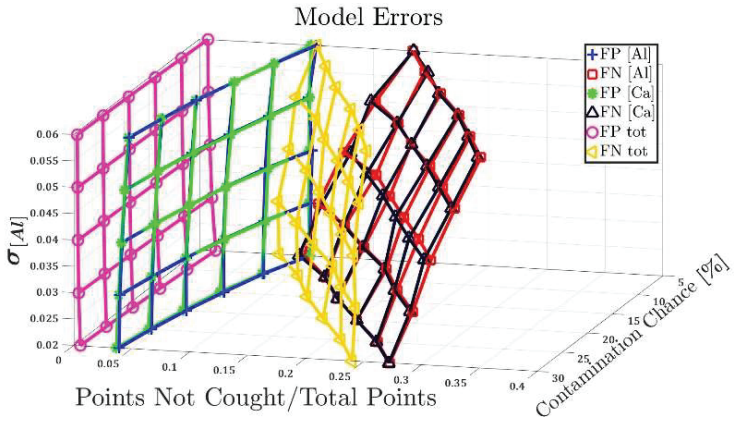


Figure 5: Model Errors. False Negative(FN) and False Positive(FP) for [Al], [Ca], and when they are combined. Each point is generated from 10^5 sets. The last 10 points in each set generated the CI.

This is due to the large variance one gets when there are many contaminated points in the points used to generate the CI. The figure also shows that assumption 3 is quite valuable, as it lowers the error considerably. For a single species one can get the case where a minima does not belong far down the distributions tail. This shifts $\varphi_{[El]}$, making it non-representative. However, the chance is quite small that this occurs in both species. Another problem which might occur is that the rapid change in the initial part of the curve is not fully represented, due to large υ and/or Δt. This can be seen quite easily and fixed however. Figures 6 and 7 show different behaviors for the simulated sets.

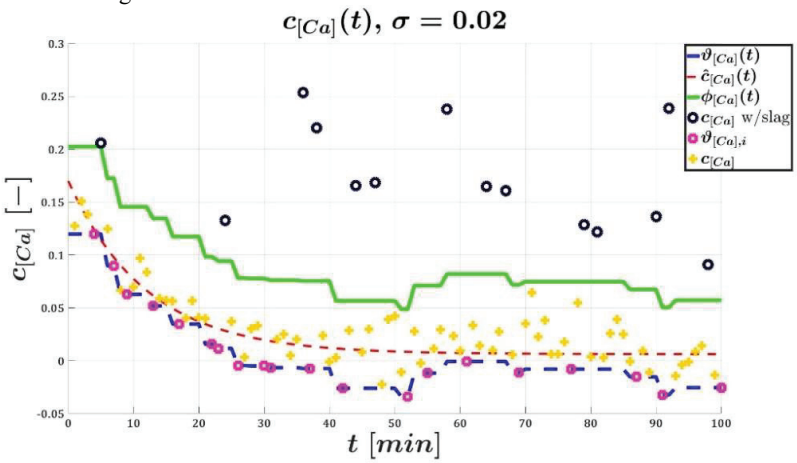


Figure 6: Simulated set of [Ca] with no model error.

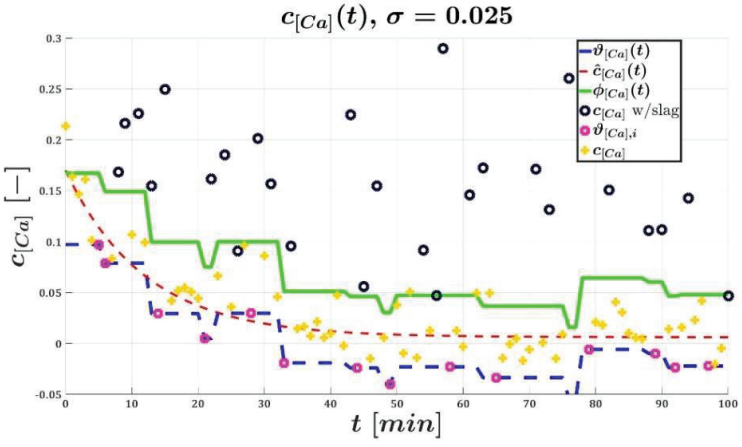


Figure 7: Simulated set of [Ca] with some model error.

Discussion

The proposed model is apt at finding which points are contaminated by MSDs. As seen from figures 3 and 4, all obvious points, like the first point for the light green and pink ladles, lie above the line, and are therefore marked as contaminated. The blue ladle is marked as not similar to the rest, as only one of its points is not above the line for both [Al] and [Ca]. It also does not allow one to remove points which might be considered an outlier at first glance, like the first yellow point. From $c_{[Ca]}$ alone, it might be tempting to discard the point, but this model states that it should be kept. If the sample set from which it generates the CI itself is heavily contaminated, then its performance worsens considerably, as seen in figure 5. This performance drop is primarily due to φ becoming too large, increasing the number of false negatives. If one sees that the final points clearly contains a large group of contaminated samples, it is advised to remove these before running the model. The theory in the proposed model can additionally be expanded on if new relations between the species are found. Sampling designs made to achieve a better representation of a ladle as a whole would also help massively, but this would require each industrial site to change their sampling routines. Due to the small sample size, any positive change would strengthen the set considerably. Further work will be performed to look at how to make the model less sensitive to each minima, but rather uses their joint behavior. Additionally, new relationships between the species will be looked for to add further behavioral restrictions.

Conclusion

A model for determining MSDs contamination in MG-Si has been proposed. It has tested on experimental [Ca] and [Al] data from Kero et al. [2], and simulated sets. From this, it has been found that the model is able to aptly find MSDs contaminated samples.

Acknowledgements

This work has been funded by SFI Metal Production, (Center for Research-based Innovation, 237738). This author gratefully acknowledges the financial support from the Norwegian Research Council and partners of SFI Metal Production.

References

[1] Bernard Rosner. Percentage Points for a Generalized ESD Many-Outlier Procedure. *Technometrics*, 25(2), 1983, p165.

[2] Ida Kero, Mari K. Nass, Vegar Andersen, and Gabriella M. Tranell. Refining kinetics of selected elements in the industrial silicon process. *Metallurgical and Materials Transactions B*, 46(3), 2015, p1186.

[3] T.Abel Engh. *Principles of Metal Refining*. Oxford University Press, 2 edition, 1992.

Silicon for the Chemical and Solar Industry XIV
Svolvær, Norway, June 11 – 14, 2018

The EHS Achilles Heel of the Silicon Furnace – the Potential for Energy out of Control

Halvard Tveit [1)] and Mark Breidenthal [2)]
1) Adjunct Professor at NTNU, Corporate Specialist Elkem
2) VP Environment, Health and Safety & Corporate Social Responsibility Elkem ASA

Abstract

Both the process specific hazards and the general workplace hazards are discussed. For the general workplace hazards a comprehensive safety plan should be made for the factory. Some plant specific factors are presented.

The general reason for the process specific accidents are presented. The silicon process requires huge amount of potential energy in the form of chemical energy and thermal energy. Normally these energy is under full control. However, there are some ways that the potential energy may be released in a very short time – and create dangerous and hazardous situations.

Some potential hazards and the learning from accidents are presented.

General causes of accidents and injuries in the silicon industry

Primary production of silicon has not changed substantially for many decades. It is still traditional heavy industry with large processing units, heavy duty equipment and challenging working conditions. It is also often characterized by a large concentration of dangerous activities in old buildings that were not designed for today's requirements to a safe and healthy workplace. There is also a high amount of shift work as the process must run 24/7.
Most of the injuries we see at silicon plants today are very similar to what we would expect to see at any industrial site; like injuries related to the use of mobile equipment, elevated work, bruises, cuts and burns in connection with mechanical work, and ergonomic issues with difficult working positions. These types of incidents and injuries can also be manged with standard, well know prevention tools and methods developed for all types of work.

The silicon industry does however have other major safety challenges that are specific to this type of production and that can have extreme consequences compared to general industrial hazards. The main metallurgical processes include very high temperatures and high amounts of energy. The thermal energy and the energy flow is normally controlled safely in the process, but may also come out of control creating a high potential for fatal injuries. The combination of water leakages from cooling systems and high thermal energy in the reduction furnace may create extremely hazardous situations.

Safety in Elkem

Environment, Health and Safety have top priority in Elkem. During the past 20 years the number of recordable injuries has been substantially reduced.

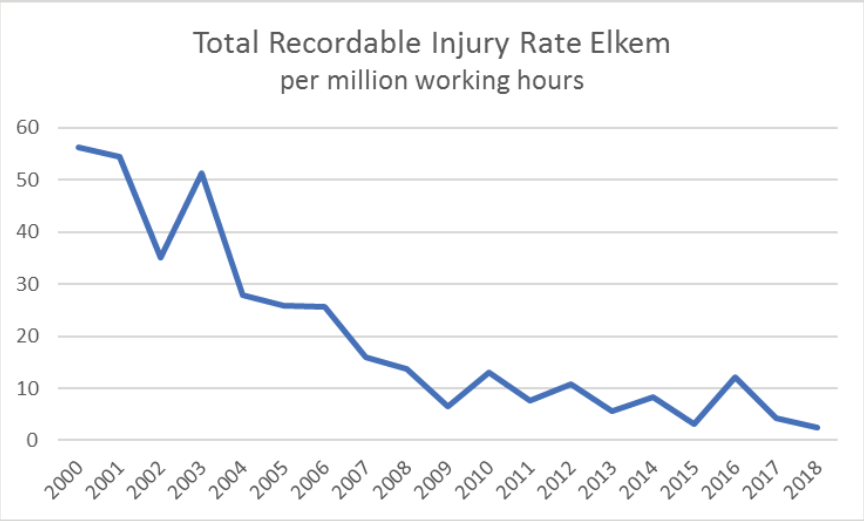


Figure 1 Incident reduction since 2000

The main drivers to attain these results have been:

- Management commitment and a zero-harm philosophy
- The implementation of a structured EHS management system and clear standards
- A high focus on general and job specific EHS training
- A high level of deviation and incident reporting with good incident management
- Close follow-up on compliance and behaviour
- Company values that promote respect, precision, continuous improvement and involvement

Process related hazards require additional focus

Despite all our improvement activities and success with our safety results, we have still experienced horrific explosions and tragic fatalities at our production plants during these same years. These have been related to the metallurgical process itself and show that general safety provisions are not enough to prevent them from happening. We need a greater understanding of the specific hazards in the process and how we can control them.

The main candidates for process related incidents with silicon smelters are:

- Cooling water leakages combined with the huge amount of thermal energy may create rapid release of energy
    - If water is encapsulated in molten slag or silicon the rapid water expansion (1600x) will create high pressure and may create explosions – the size and type of explosion is dependant of the amount of water and the accessible energy in the warm media
    - If a large amount of water is heated – a dangerous superheated water vapour may spread outside the furnace
- The raw materials feed into the furnace contain water and coal. Water from the raw materials may act like a water leakage. Coal may defragment if heated very rapidly and the fine coal particles may burn with a very high speed and huge thermal energy release. Volatiles in the coal may also evaporate and flow outside of the furnace where they ignite in contact with oxygen
- Some silicon furnaces have energy recovery systems. If the recovery process includes high temperature and pressure steam or super-heated water this may also pose a potential hazard in connection with overpressure and/or leakage
- Silicon dust from crushing, sizing and packaging operations can enter the areas with molten silicon of slag giving the opportunity for a secondary explosion after a primary explosion caused by water and molten material.

Hazards caused by water leakage or fresh charge materials into a silicon reduction furnace

During the reduction process CO_2, H_2O, condensed silica fume and some minor gasses are created. The off-gas system for a silicon furnace will normally take care of these in a safe manner in addition to ensuring necessary cooling air to achieve the design off-gas temperature.

The amount of off-gas from a 10 MW furnace is shown in table 1. The off-gas will vary somewhat with different charge mix such as the amount of coal, coke and wood-chips.

Table 1 shows the typical amount of off-gas from a 10 MW silicon furnace

Off-gas temperature	Off-gas volume	Corresponding amount of water steam at 400°C
300 C	32 Nm^3/sec	26 kg H_2O
500 C	18 Nm^3/sec	15 kg H_2O
700 C	12 Nm^3/sec	10 kg H_2O

Table 1 also shows the amount of water vapor that the off-gas system can handle if the water is evaporated within one second for a 10 MW furnace and all other off-gas. The amount of water decreases with increasing off-gas temperature due to decreased off-gas volume. (To find the water volume for a given furnace the temperature may be linear extrapolated and the furnace size X (MW) should be multiplied with X/10.)

Table 1 gives very low numbers for the amount of water the off-gas system can handle. These numbers are much lower than the real safety limit for water leakages. The main reason for this is:

1. A certain amount of water is needed before a section of the charge is cooled down enough to allow liquid water to accumulate. If the power supply to the furnace is turned off before the water leakage is stopped the section will also cool down quicker increasing the risk of water accumulation instead of evaporation.

2. The eruption may last for more than 1 second – models and videos from a real case show eruption lasting from 2-5 seconds

3. To create a hazardous situation outside the furnace the amount of water vapor must be much higher than the numbers in table 1.

4. Charge materials containing water and coal act as a water leakage if the amount is too big to allow sufficient evaporation before entering the reaction zone.

All of this shows that a water leakage into the furnace must be handled with upmost care! The following cases show what can happen if it is not managed correctly.

Case 1 – the 2006 Elkem Thamshavn accident

On the 12th of April 2006, an eruption took place in Furnace #1. One operator was critically wounded and died four weeks later. The direct cause of the incident was a major water leakage in the electrode cooling system. A comprehensive investigation was carried out to find the root cause of the incident and measures to avoid similar accidents in the future. In line with the Elkem ASA policy of being open with information that may help others avoid serious incidents and injuries a presentation of the incident was published in 2008 /1/.

The investigation included reviews of other similar incidents showing that water vapour eruptions from silicon and ferro-alloy furnaces did happen occasionally, and often resulted in multiple fatalities. The paper describes 5 known accidents with up to 7 fatalities.

Case 2 – the 2010 Elkem Iceland accident

The tragic incident at Elkem Iceland on the 29th of June in 2010 was a new reminder of the inherent risk involved with the production of high silicon containing alloys. A severe eruption of gasses from Furnace #1 ignited, killing one young operator.

Again, an investigation had to be carried out in order to find the root causes and how to avoid similar incidents.

The first hypothesis suggested a major water leakage like the Thamshavn case, but no water leakages were found, and the furnace was in normal operation when the eruption took place.

Video footage from CCTV cameras in the area gave valuable input to the investigation and the modelling of the incident. Figure 1 shows time stamped pictures from the video that allowing us to see how the eruption progressed

The investigation concluded that the incident was an eruption of process gasses from the furnace that ignited in contact with oxygen outside of the furnace. The findings strongly indicate a major furnace cavity collapse allowing fresh, newly feed charge to fall into the reaction zone before moisture and volatiles were evaporated. (Ref figure 2.)

The investigation, modelling and necessary calculations gave a frightening worst case potential for fatal incidents when substantial amounts of fresh raw materials are mixed with very warm charge material and/or molten silicon. The literature suggests that high volatile coal may defragment (or explode and be converted into small pieces) if it is heated too quickly. The resulting fragments of coal may release volatiles and have an extremely fast combustion with the release of huge amounts of energy.

Several combustion and mixing scenarios were calculated. The worst-case scenario indicated an energy release in the order of 16 GW during 1 second – i.e. the total effect of the Norwegian electricity production. This is not the most probable scenario, but all the calculated scenarios resulted in an overload of the off-gas system according to the observations and measurements.

Both cases mentioned above are extreme examples of what is typically called a furnace blow-out. Gasses and materials will be ejected through furnace openings when an imbalance occurs in the off-gas evacuation system. Fans that normally create a constant evacuation through the chimneys are no longer sufficient when the amount of process gas increases rapidly, replacing some of the cooling air and increasing temperature in the furnace hood. Blow-outs on a smaller scale happen frequently in silicon furnaces and can be anything from small amounts of smoke and particles to burning flames and charge materials that can cause damage and fires in the area. This phenomenon will sometimes be heard as slamming of the furnace doors due to the change of gas pressure and the reverse of the cooling gas flow to the furnace.

The Elkem Iceland 2010 incident was an extreme blow-out from the furnace. The root cause for the blow-out was an increase in the process gas or increased thermal energy from the charge. The rapid increase in process gas was caused by a cavity collapse and large amounts of fresh raw materials falling into the hottest zone of the furnace.

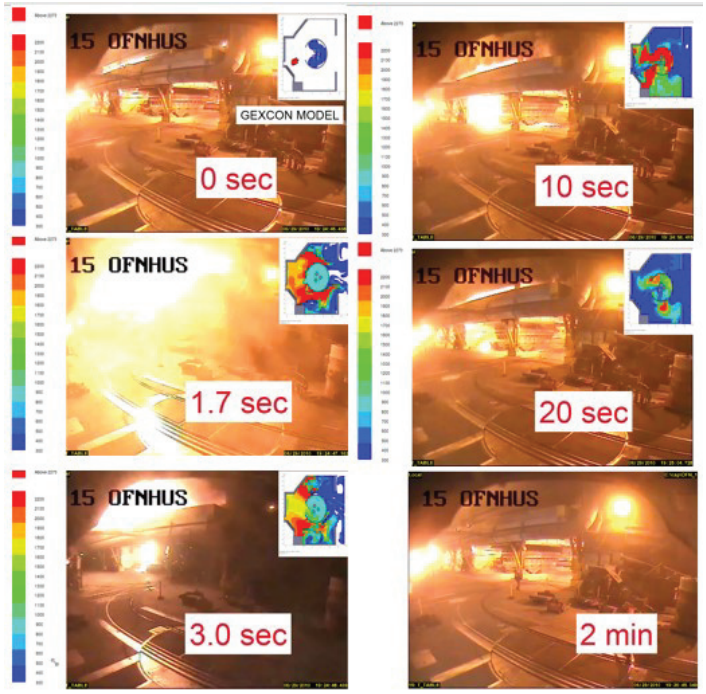


Figure 1. The snap from a video shows the speed of the eruption at Elkem Iceland together with the model from Gexcon /5/. There was 2 maximum – after 0.7 and 1.7 sec. The major eruption time was about about 1 sec – and after 2 minutes no trace of the accident could be seen at the video.

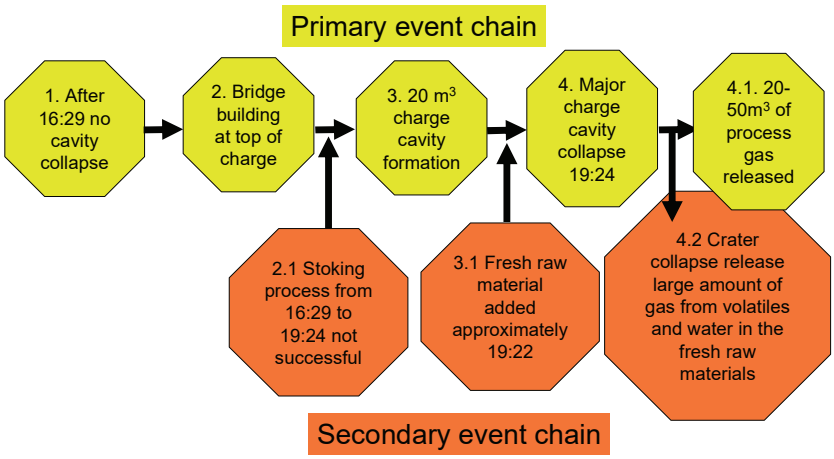


Figure 2 shows the most likely chain of events. The figure is based on the fact that a major cavity of 20m³ was found at the top of the charge. The reason why the cavity did not collapse during the 3 hours of stoking is not fully understood.

The main measures after the Elkem Iceland accident were changes to the charging process and limitations of access to the stoking floor area.

Explosion due to water encapsulated in molten or very hot metals and materials

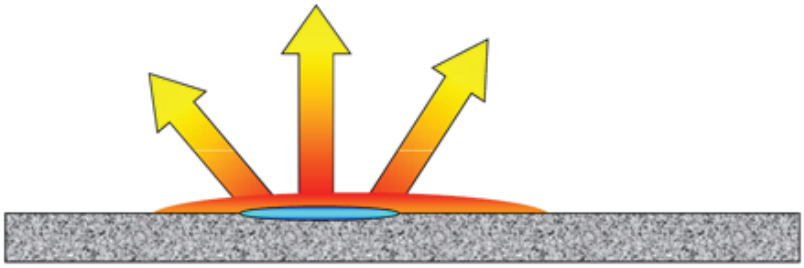
Liquid water or humidity encapsulated in molten or very hot metal immediately evaporates. This will create a sudden expansion and possible pressure build-up creating an explosion. The molten substances may be ejected with high force and velocity and harm people and equipment in the proximity by contact or by resulting fire.

There is practically no lower limit to the amount of water needed for this type of incident to occur. Liquid water at 25°C – if heated to 1000°C – will become water vapour with a volume enlarged 1600 times. This means that the tolerance of water – that can be trapped in liquid silicon is zero. Candidates for this type of explosion in silicon production are liquid silicon or slag that entraps water from equipment leakages, rain or snow. It can also be residual moisture that is not sufficiently dried in refractory materials, or concrete floors.

The phenomena of explosions caused by water enclosed in metal have also been investigated in the steel and aluminium industry /2/. The explosive effect of 1000 kg of aluminium or steel is presented for different amounts of water entrapped:

Amount of water	1 litre	10 litres	100 litres
Explosive power (kg TNT)	3	32	200

1 kg of TNT will destroy all windows within a radius of 30 m, 80 kg TNT will destroy all windows within a radius of 250 m and destroy a normal roof at a 40 m distance and all walls at 23 m distance from the explosion.



The figure 3 *shows the principle of the start of a water explosion – i.e. water enclosed by liquid or warm silicon or slag.*

The enthalpy of silicon both for the volume and for mass is much higher than for aluminium and iron – so the explosion strength may be higher for silicon. This type of explosion can harm people in multiple ways, both by pressure and temperature. A pressure wave can injure people both directly and indirectly by moving debris, particles and equipment at high speeds. Temperature can injure people directly with severe burns caused by contact or fumes caused by fires.

Table 2 shows the enthalpy release through 100 ΔC and solidification /6/

	Temp in	Temp out	kWh/kmol	kWh/1000 kg	kWh/Nm3
Al	700	600	-4	-144	-389
Fe	1600	1500	-5	-91	-714
Si	1500	1400	-15	-524	-1221

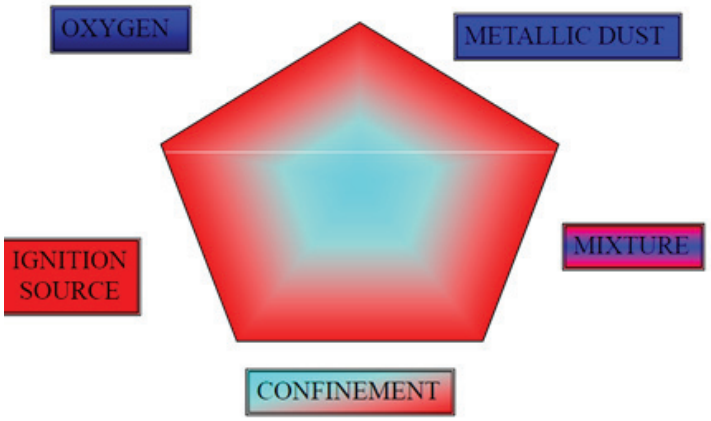
Dust explosions – primary and secondary explosions or the formation of explosive gases or metal fines after a primary explosion

Most of the dust in primary silicon production facilities is SiO_2 and will not cause dust explosions as it is inert. Further processing of silicon alloys however, involves operations with crushing and sizing of silicon that create combustible dust. There will therefor almost always be the potential for combustible dust in a silicon facility and the silicon industry has experienced dust explosions with fatal consequences /4/ /5/.

There are four conditions that must be in place for a dust explosion to happen:
1) The dust must be combustible
2) Particles must be able to form a cloud exceeding min. explosion concentrations.
3) Dust must be confined, and

4) An ignition source must be present.

Most types of silicon alloy dust are difficult to ignite. If they do ignite however, the explosions can be extreme because of the stored energy. The fact that molten silicon alloys may be processed in the same area as combustible dust is present on walls and structures increases the risk of explosion as the molten silicon has more than sufficient energy to ignite the dust.



The figure 4 shows the principle necessary conditions for a metallic dust explosion

The candidates for dust explosion in the silicon industry are carbon material fines in the transportation system, and silicon fines in the crushing and screening plants.

Burning of skin due to contact with warm gas or liquid or warm silicon

This type of injury is by far the most common when we experience blow-outs or explosions, and may give anywhere from minor superficial burns to fatal burns. Breathing hot gases can also cause fatal burn injuries as it may affect a person's throat and lungs.
Most of the minor to medium severity burns in the silicon production happen in the tapping and post taphole areas where there is close contact between molten silicon and operators. High pressure process gas ejection from the taphole or loss of confinement of molten silicon from ladles or casting molds are the main causes of this type of incident. Fatal burn injuries are more connected to major explosions like the ones described in case 1 and 2 above.

Conclusion

Production of silicon alloys has a high inherent risk of explosion and serious injury because of very high temperatures and very high amounts of energy. Fully understanding the mechanisms behind this risk is of the upmost importance to be able to

operate the process safely and prevent harm from happening. Controlling this risk involves fully understanding the process, implementing equipment, automation and methods to remove operators from dangerous work, and the use of better personal protective equipment.

The referred literature gives more details as well as advice about how to avoid accidents in silicon production.

References

1. Halvard Tveit & al, *Water leakages in ferroalloy and silicon reduction furnaces – experience gained from a severe accident in 2006*, Silicon for the Chemical and Solar Industry IX
2. I.V. Babaitsev and O.V. Kuznetsov. Labor Protection. *Energy of Explosions occurring when water falls onto a layer of molten metal.* Metallurgist, Vol 45, Nos. 5-6, 2001
3. Tasneem Abbasi, S.A. Abbasi *Dust explosions–Cases, causes, consequences, and control* Journal of Hazardous Materials 140 (2007) 7–44 (Available at Sciencedirect.com)
4. R.K. Eckhoff et al., "*Ignitability and Explosibility of Silicon Dust Clouds. Influence of Dust Fineness"*, *L* Electrochem. Soc" 133, 1986, pp. 2631-2637
5. Gexcon AS - DSEAR, Fire and Explosion Consultants www.gexcon.com Gexcon AS, Bergen Norway
6. HSC version 7.00 Outotec Research Oy, 19794-2009 https://www.outotec.com/products/digital-solutions/hsc-chemistry/

Will there be another China?

Jorn P. de Linde
CRU

Abstract

China is set apart from other countries in several important ways, notably by the size and rapid growth of its economy. It has also experienced a remarkably swift build-up of production capacity on an unprecedented scale in a wide range of industries, including silicon, silicones, polysilicon and aluminium, dramatically boosting both silicon demand and supply in China. No other country is about to equal China as the key driver of the growth in global silicon demand. However, an increased focus on value-added manufacturing, combined with curbs on the expansion of power-intensive and polluting industries, means that other countries will account for a larger share of future silicon supply. Meanwhile, the difference between production costs in China and other locations is expected to diminish, which in turn will reduce regional differences in silicon prices.

Introduction

China has played a pivotal role in the development of the silicon market and industry over the past several decades. No other country has had a comparable influence for such an extended period of time. During the second half of the 1980s, Brazil emerged as a leading producer of silicon in a span of just a few years. Subsequently, the break-up of the Soviet Union precipitated a major shift in international trade flows. These events principally affected silicon supply, however, they did not materially alter silicon demand and they did not have a lasting effect on a scale like that of China.

Looking ahead, what happens in China will continue to have a substantial impact on global silicon demand and supply. But will other countries play a larger role in shaping the future of the silicon market and industry? Specifically, will there be another China?

The position of China

In addressing the question of whether there will be another China, a useful starting point is to review the evolution of silicon demand and supply in China and assess the country's current position in the market. There are no definitive data, but CRU estimates that in 2017 China represented more than 37% of total silicon demand and nearly 66% of global output. Reflecting the gap between Chinese production and demand, the country has also consistently been by far the world's biggest silicon exporter, providing more silicon to overseas consumers for an extended time than all of the other suppliers combined.

Facilitated by a massive expansion of local production capacity, Chinese silicon output has risen more than five-fold since 2000. The country has accounted for more than 92% of the net increase in global silicon production since that time. The rapid expansion of

Chinese silicon production has been supported by growing international demand, but rising domestic consumption has fuelled most of the gain in local output over the past decade. Chinese silicon demand is now more than 16 times larger than it was in 2000, with China having contributed more than 60% of the total growth in total demand over the past 17 years. In 2009, China overtook the USA as the single largest market for silicon and, two years later, Chinese silicon demand surpassed that of the EU for the first time. In 2016 another milestone was reached, as Chinese silicon demand exceeded the combined total of that in the USA and the EU.

Historically, much of Chinese demand was related to the manufacture of aluminium alloys but, since 2008, the chemical sector has emerged as the main driver of consumption growth. Chinese chemical-related silicon demand has increased more than fivefold between 2008 and 2017 and the country has accounted for upwards of 76% of the total increase in chemical-related consumption during this time.

The rapid rise in Chinese demand reflects large increases in siloxane and polysilicon production, sustained by massive expansions of local production capacity that have far exceeded the corresponding capacity additions in the rest of the world. Coinciding with this build-up, China has turned from a large net importer of silicones to a significant net exporter. The country remains a substantial net importer of polysilicon. In fact, China imported a record amount of polysilicon in 2017, indirectly supporting nearly 200,000 t of silicon consumption in other countries.

The aluminium industry continues to play a much smaller, but still important, role in the rapid expansion of Chinese silicon demand. As is the case in other countries, most aluminium castings in China are consumed in the transportation sector. Since 2009, China has been the largest producer of cars and commercial vehicles. Although the growth in local auto production is slowing down, the aluminium intensity of Chinese autos is increasing. The rapid rise in the production of primary foundry ingot in China partly reflects the growing requirements of local manufacturers for aluminium wheels. A significant part of this production is exported. Thus, Chinese aluminium-related silicon consumption is also affected by trade.

China has a nameplate silicon capacity of more than 5 Mt/y, but the effective capacity is much lower, likely in the range of 2.7-3.2 Mt/y, adjusting for furnaces that have been closed for extended periods of time for economic reasons and for production units that do not meet government rules and regulations, including environmental standards. Further reducing capacity on an average annual basis and, thus, the actual output of silicon, many furnaces in Southwest China operate only during the rainy season when lower-cost electric power is available. More recently, furnaces have also been idled due to shortages of raw materials and electrodes or because of environmental inspections.

The rapid growth in Chinese silicon demand would not have been possible without the addition of vast amounts of production capacity in downstream industries. We estimate that Chinese siloxane capacity totalled nearly 1.32 Mt/y at end-2017, compared with around 1.16 Mt/y in the rest of the world, and more than four times the siloxane capacity China possessed at end-2008. Nameplate polysilicon capacity in China has also grown rapidly and now exceeds that in other countries combined as well. China has an even more dominant position in primary aluminium, accounting for more than 58% of

global capacity and more than 57% of total production in 2017. China's share of primary foundry alloy (PFA) output is about half of what it is for primary aluminium, but the country is by far still the world's largest producer of PFA, well ahead of the UAE, Russia, Canada, Norway and Qatar. China has an even more dominant position in the manufacture of secondary aluminium foundry alloys.

What makes China unique?

China has undergone a remarkable economic transformation. The Chinese economy has advanced at a CAGR of more than 9.6% over the past two decades, catapulting the country from a position as the world's seventh largest economy in 1997 to becoming the second largest in 2009, just 12 years later. However, the rapid pace of industrialisation and growth has come at a considerable cost, leading the Chinese government to more strictly enforce environmental regulations as part of broader economic reforms.

Historically, economic growth in China has been heavily reliant on external trade and fixed asset investment rather private consumption. Easy access to credit contributed to extensive overinvestment in many sectors of the economy, including manufacturing. Over time, this path of development resulted in significant economic imbalances and created large public and private sector debt burdens within China and sparked numerous trade conflicts with other countries.

The Chinese government has instituted an array of supply-side reforms aimed at sustaining economic growth, which remains the paramount objective, while at the same time attempting to curb excessive lending, eliminate surplus capacity across a wide range of industries and reduce pollution. This attests to the critical role played by the central government not only in establishing and implementing policies but in actively managing the economy and safeguarding growth, while seeking to prevent unwanted outcomes. Although the silicon industry in large part is privately-owned, State-Owned Enterprises (SOEs) hold key positions in most segments of the Chinese economy.

China is the world's leading producer of coal and it also mines vast amounts of quartz, not surprising for a country with a large landmass. However, the quality of local raw materials can be a challenge. Frequently, high-quality quartz is not available near silicon plants that have access to inexpensive electric power. Moreover, much of the coal mined in China is comparatively high-cost or low-grade. Still, most of the inputs used in the manufacture of silicon are obtained from domestic sources, although China has imported some large-diameter carbon electrodes and, most importantly, relied on substantial amounts of charcoal from neighbouring countries.

What also sets China apart are the large shifts that have occurred in the location of domestic silicon production. Over time the industry has moved progressively Westward, from Hunan towards Guizhou, Guangxi, Heilongjiang, Inner Mongolia, Sichuan and Yunnan and, most recently, Xinjiang. This relocation has mainly occurred in response to regional differences in the availability and cost of electric power. As a result, newly-constructed silicon plants have steadily displaced existing, higher-cost operations.

Who are the most likely candidates, if any, to rival China?

Over the past decade, quite a few countries, mostly located in Asia, have experienced rates of economic growth substantially above the world average. One of these countries, India, even has a population close to that of China, although the Indian economy is only one quarter the size of the Chinese economy. When it comes to silicon, the difference between the two countries is an order of magnitude larger. Indian silicon demand has advanced at a CAGR of nearly 11% since 2008, but total consumption remains less than 5% of that in China. In fact, within Asia, Indian silicon consumption also trails that of Japan, South Korea and Thailand, clearly demonstrating the impact that the chemical sector has on total silicon demand in individual countries.

In addition to China and India, economies that currently rank among the world's 50 largest and that also grew substantially faster between 2008 and 2017 than the world average of 2.4%/y are Turkey, Indonesia, Ireland, Malaysia, Nigeria, the Philippines and Singapore. However, only Malaysia has attained a silicon demand of 25,000 t or more in a single year.

South Korea has experienced by far the biggest increase in silicon demand after China. However, the approximate net 86,000 t rise in South Korean demand since 2008 dwarfs the corresponding jump in Chinese demand of nearly 790,000 t. Gains in other countries have been much smaller. Offset in part by significant losses in Japan, Italy and Brazil, total silicon demand outside China advanced by less than 250,000 t between 2008 and 2017. Indian demand grew by more than 31,000 t over this period, ahead of the USA, Thailand, Qatar, Germany and Mexico. No other country experienced a net gain in silicon demand of more than 20,000 t since 2008, although Mexico and Malaysia came close.

One of the factors impeding the growth in silicon demand in countries like South Korea and India is high power costs. The availability and cost of power has also had a substantial impact on the location of new silicon capacity both in China and elsewhere. For many years, capacity additions outside China were mostly in the form of furnace conversions, capacity creep and furnace rehabilitations, but numerous greenfield silicon plants, as well as several significant brownfield expansions, have been completed in other countries since 2010.

No single country has dominated the growth in silicon production or capacity outside of China. Using 2000 as a point of reference, led by France, most of the net increase in non-Chinese silicon output has occurred in Europe. Different base years will yield different results, especially in terms of net gains or losses in the USA, Brazil, South Africa and Asia, but to put these variations into perspective, while French silicon production rose by 67,000 t between 2000 and 2017, Chinese output jumped by more than 1.52 Mt during the same time.

Expected changes in the years to come

Underpinned by continued strong gains in chemical-related silicon consumption, we expect that global silicon demand will advance at an underlying rate of 4.5-5.0%/y over the next decade, which is close to the historical average and well above the corresponding rate of world economic growth. Considering current levels of silicon

demand in individual markets, forecast rates of economic growth and expected developments in the key end-use sectors for silicon, in the foreseeable future, no other country will replace China as the key driver of global silicon demand. Notably, CRU projects that China will account for more than two-thirds of the growth in total silicon demand over the next five years.

Although a shift in policy priorities could contribute to slower GDP growth in China going forward, the country's economy will likely continue to advance at a rate substantially above the corresponding world average. Moreover, an increased focus on value-added manufacturing and the environment will support substantial gains in the local manufacture of silicones and polysilicon production, although part of this growth will be offset by lower silicon demand in other countries.

Nearly half of the projected rise in silicon consumption outside China over the next five years will be associated with the solar sector, mostly spread among existing polysilicon plants in the USA, Germany, South Korea, Japan, Malaysia and the Middle East. Future gains in aluminium-related silicon demand outside China will be confined largely to other parts of Asia, Russia and the Middle East, reflecting structural shifts in auto production and in the manufacture of primary foundry alloys. However, excluding China, no single country will account for more than 5% of the expected growth in global silicon demand through to 2022.

Turning to silicon supply, we expect that Chinese output will continue to advance substantially, supported by future capacity additions and rising demand. Much of the growth in Chinese silicon production will take place in Xinjiang, which is expected to contribute more than two-thirds of total Chinese silicon supply within a few years, up from around 25% in 2015. Part of this growth will come at the expense of output in Yunnan and Sichuan, but the steepest declines in production will occur in locations where power is more expensive. Thus, Xinjiang, Yunnan and Sichuan together will account for more than 90% of total output at the end of this decade, compared with around 68% in 2015.

As the Chinese silicon industry has shifted Westwards, power rates have fallen but transportation distances to ports have increased considerably. Xinjiang in many respects represents the last frontier and likely marks the end to the steady migration of Chinese production capacity, thereby making it increasingly difficult to contain operating costs simply through the relocation of silicon plants. Moreover, measures taken by the Chinese government to curb the expansion of power-intensive and polluting industries are likely to progressively slow the rate of growth in local silicon supply.

Concurrent with this slowdown, Chinese silicon exports will gradually fall as a much larger share of local production is absorbed by the domestic market. As the net gains in silicon capacity and production in China moderate due to structural reforms, other countries will gradually meet a higher proportion of global silicon demand. We project that China will account for about 45% of the increase in total production over the next five years, less than half the share contributed during the previous five years.

The expected output growth outside of China will require a steady expansion of silicon capacity. Investment decisions are guided by a host of factors, including strategic

concerns, but greenfield silicon projects will gravitate towards locations that offer a stable supply of affordable electric power combined with access to suitable raw materials. Other important considerations include attractive construction costs, investment incentives, a local pool of skilled labour, unrestricted market access and a stable political and financial environment.

Several locations in the USA fit most of these criteria as do, to varying extents, multiple sites in quite a few other countries. Given lead times of 24-36 months, the timing and size of capacity additions beyond the end of this decade are still subject to considerable speculation, but it is highly unlikely that any one country will account for most of the additional silicon production outside China.

Conclusion

No single country is likely to evolve into another China in the foreseeable future. Rather, a range of countries will make significant contributions to total silicon supply, together filling more of the role in global supply traditionally played by China. As the central government persists in transitioning the Chinese economy from export and investment-led growth towards domestic consumption and value-added manufacturing, China will continue to account for much of the gains in global silicon demand.

Although a much larger share of future capacity expansions will shift to other countries, China will retain its position as the world's largest producer and exporter of silicon and the long-term trend in international silicon prices will, to a considerable degree, still be determined by what happens to Chinese demand, supply and production costs.

Author Index

Acker, Jörg 11
Anjitha S. G. 267
Bade, Stefan 21
Becker, Robert Becker 97
Bertakis, Evangelos 63
Biazutti, Luciano 105
Bjørnstad, Erlend Lunnan 349
Blandhol, Kjell 163
Blekkan, Edd A. 277
Bleskin G.S. 121
Breidenthal, Mark 357
Broggi, Andrea 139
Bullón Camarasa, Javier 91
Butakova T.V. 121
Carberry, John 289
Colomb, Matthias 217
Crawford, Alan 243
Datas, Alejandro 303
de Faria, Rodrigo Silva 105
De Linde, Jørn 367
de Oliveira, Valdiney Domingos 105
del Cañizo, Carlos 303
Eidet, Trygve 77
Esteves, Gabriel 105
Eulenberger, Ronald 63
Fjelldal, Jens Christian 335
Frings, Bodo 21
Gaal, Sean 231
Gouttebroze, Sylvain 327
Grorud, Bettina 315
Hegdal Chapana, Randi S. 63
Herold, Steven 11
Hoel, Jan-Otto 243
Höfler, Andreas 21
Hosseinpour, Ali 173
Jayakumari, Sethulaksmy 125
Jensen Ragnhild, 335
Jiao, Jian Meng 315
Jusnes, Karin Fjeldstad 39
Kjønli, Henning 243
Klette, Hallgeir 267
Kvanin A.L. 121
Langner, Thomas 11
Leite de Lima, Moysés 193
Leye, Johann 97
Lyubina, Julia 21
Marstein, Erik S. 267
Martí, Antonio 303
Martorano, Marcelo Aquino 193
Matveev A.V 121
M'Hamdi, , Mohammed 327
Mikkelsen, Øyvind 77
Murgau, Adrian 183
Nascimento, Denir Paganini 193
Neto, João Batista Ferreira 193
Palanki, Srinivas 217
Parous, Lou 105
Polkowski, Wojciech 315
Preston, Thomas J. 205, 267
Ramos, Alba 303
Ribeiro, Tiago Ramos 193
Rimböck, Karl 153
Ringdalen, Eli 29, 39
Roberts, Devin 289
Røe, Torbjørn 163
Rong, Harry M. 163, 243
Saadieh, Raghed 51
Safarian, Jafar 183, 315
Schafer, Ryan 231
Sieber, Tim 11
Skare, Marte O. 267
Sobczak, Natalia 315
Spektoruk A.A 121
Stachowiak, Scott 231
Störger, Reiner 21
Svanem, Johan P. 163, 243
Svenum, Ingeborg-Helene 277
Sylvester, Nicholas D. 217
Tafaghodi, Leili 173
Tangstad, Merete 39, 51, 125, 139, 315
Tesch, Robert 289
Tranell, Gabriella 349
Traunspurger, Gerhard 153
Tveit, Halvard 357
Tysseland, Amalie 277
Vanhaecke, Estelle M. M. 277
Venvik, Hilde J. 277
Vinck, Nadia 1
Wegge, Harald 51
Wilson, Timothy 289
Wyller, Guro M. 267

PARTICIPANTS 1992-2018

Argentine

Carmona, José Luis	1998

Australia

Breit, Wolf	1998, 2000, 2002
Brosnan, James Gerard	2014, 2016
Brosnan, Jim	2000
Bultitude-Paull, John	1994
Ferraro, Mike	1998
Harris, Leighton Drew	2016, 2018
Hubert, Alyssa Jane	2018
Lund, Chris	2000
Matisons, Janis	2002, 2004
Miles, David	1998, 2000, 2004, 2006
Miyashita, Masaru	2000
Naude, Christiaan Petrus	2016
Ryabova, Elena	2000, 2002
Simpson, Andrew Vincent	1994, 2002
Snow, Brad	2006
Spratt, Michael	2002
Spratt, Mike	1994, 1996
White, George	1998

Austria

Grogger, Christa	2004
Schlosser, Viktor	2010
Stueger, Harald	2004

Bahrain

Jahnke, Uwe H.	1998, 2000
Agasti, Bhakta Hari	2018

Belgium

Blümlein, Otto K.	1996, 1998, 2000, 2002, 2004, 2006
De Poortere, Michel	2006
Fiat, Michel	1996
Germain, Pierre	2016
Seys, Freddy	2000
Verniers, Francois	1992, 1996, 1998, 2000, 2002
Vinck, Nadia	2016, 2018
Zijlema, Tjakko	2006

Brazil

Amaral, Luciano	1998, 2000
Augusto, Thales Xavier	1998, 2000, 2002, 2004, 2006, 2008, 2010, 2012, 2014, 2016, 2018
Azvedo Cysne, Marcos J. de	1996
Barbosa Vilaboim, Luiz F.	2004
Bolzer, Walter	2002, 2004
Borges, Cezar	2006
Caracas, Ronaldo Winter	1994, 1996, 2000
Daher, Nelson	1996
Eulálio de Souza	2004
Fernandes, José G.	2002, 2004, 2006, 2018
Fialho, Paulo Cezar	1998, 2002
Flavio Lúcio	2004
Fonseca, Roberto G. Da	1994
Freitas Nogueira, Paulo de	1998
Fudaba, Masayuki	2002, 2004, 2006
Gomes, Gabriel Mousinho	1998
Hugo Mitsuo	2010
Jordao, Marco	1998, 2004
Keller, Peter	1998
Lage, Braulio	2006
Ledic, Marco Luz	2010
Nacif, Mario Odiniz	1998
Nascimento, Denir Paganini	2018
Neto, David dos Santos	2002, 2004, 2006, 2008
Neto, Joao Batista Ferreira	1996, 1998
Parreiras, Bruno dos Santos	1994, 1996, 2002, 2004, 2006, 2008`, 2012, 2014
Patrus, Marcos Caram	1996, 1998, 2000, 2002, 2004, 2006, 2008, 2010, 2012, 2014, 2016, 2018
Pecora, Luis A.	1994, 1996
Pereira, Guilherme Antunes	2016
Pujatti, Arquimedes	2006
Ramos Ribeiro, Tiago	2016
Rodrigues, Átila Benito P.	2010, 2014
Rodrigues, Daniel	2000
Santos, Everaldo E. dos	1998, 2000, 2002
Schmidt, Jorg	2002, 2004, 2006
Senna, Marco	2000
Spinola, José Carlos	2002, 2004, 2006, 2016
Tsukamoto Goto	2010
Versiani dos Anjos, Fernando	1998, 2000
Vicintin, Bruno Bello	2004
Vicintin, Ricardo	1996, 1998, 2000, 2002, 2004
Zica, Felipe Simões	2006, 2008, 2010, 2012, 2016
Zica, Henrique Simões	1998. 2000, 2002, 2004, 2006, 2008, 2010, 2012, 2014, 2016

Canada

Barati, Mansoor	2010, 2014
Boisvert, Rene	1996, 1998, 2000, 2002, 2004, 2006, 2008 2010
Choo, Roland	2010
Dold, Peter	2008
Haertel, Lutz	2004
Ksinsik, Dieter W.	1994, 1996, 1998, 2000, 2002, 2004, 2006
Lalancette, Michel	1996, 1998, 2000
Leblanc, Dominic	2008, 2010
Nichol, Scott	2008
Sagan, Nicholas	2006, 2008, 2010, 2012
Shahverdi, Ali	2018
Tafaghodi, Leili	2016, 2018
Utigard, Torstein	2010

Chile

Camino, Nicolas	2002
Pena, Roberto J.	2016

China

Cao, Jizhuang	2012
Chen, Xiaoyan	2018
Hu, Jingjun	2018
Jun, Fan	2010
Liu, Alanzo	2006, 2008
Liu, Tao	2002
Marsilio, Matteo	2008
Su, Zhiyi	2014
Tao, Wei	2010
Xiaodan, Hu	2008
Xijin, Zhang	2008
Xue, Jilai	2006
Yang, Wang	2008
Yuegang, Shao	2004, 2006, 2010

Cyprus

Vinogradov, Andrey	2004

Denmark

Hadsbjerg, Casper	2012

Egypt

ElSabee, Karim Maher	2012, 2014, 2016

FINLAND

Palo, Juha	2016, 2018

France

Apostolou, Georges 1994
Bandelier, Pascal 1996,1998, 2000
Baud, Luc 1994, 1996, 1998
Bertolini, Jean-Claude 1996, 1998, 2000, 2006
Blaser, Eugénie 2018
Borel, Jean-Marc 1996, 1998, 2000
Bricou, Alain 1998
Brown, Michael 2000
Bucher, Jean Philippe 1994, 1996, 1998, 2000
Bulteau, Thierry 1998, 2000
Caillod, Lisa 2004
Casulli, Stephane 1994
Chaal, Mohammed 2012, 2014, 2016, 2018
Choulet, Jean-Claude 1994
Colin, Pascale 1996, 1998, 2000, 2002, 2004
Decourtive, Bernard 1992, 1994, 1996
Degoulange, Julien 2014, 2018
Doguet, Loic 1996
Dubois-Quilbeuf, Isabella 2002
Floquet, Nicole 1992
Garcia-Escomel, Cristina 2006
Garcin, Eric 2006
Gautier, Pascal 2002
Geantet, Christophe 2018
Glasson, Thomas 1996, 1998
Guerin, Pascal 2002
Huet, Michel Henri 2016
Humbert, Gilles 2012, 2014, 2016, 2018
Jenck, Jean-Francois 1992
Jugnet, Yvette 2000
Kewes, Eloi 2014
Laroze, Gilles 1992, 1994, 1996
Lecordix, Jean-Pascal 2008, 2012, 2014, 2018
Linglois, Alain 2008
Margaria, Thomas 1994, 1996, 1998, 2000, 2008, 2010, 2012
Martinon, Jean 1996, 1998, 2000
Morin, Nathalie 2008
Muratet, Jean-Claude 1996
Neulat, Laurent 2000, 2002, 2004
Nilssen, Benedicte Eikeland 2016
Ollivier, Benoist 2018
Pelletier 2012
Plagne, Jean-Louis 1992, 1994
Portal, Jerome 2012, 2014, 2016, 2018
Ramé, Frédéric 2002, 2004
Roche, Christian 1998
Rogier, Jean-Baptiste 1998
Rondeau, Jacques 1992, 1994
Roques, Yves 2002
Rosier, Cécile 2006, 2008, 2012, 2014, 2016, 2018
Rouvière, Philippe 2010
Ruckebusch, Alain 1996, 1998, 2000, 2002
Saillant, Bruno 1998
Traversaz, Frank 1996
Troude, Pierre 2000, 2002, 2004
Victorin, Marc-Olivier 2018

Germany

Acker, Jörg 1998, 2000, 2002, 2004, 2012, 2014, 2016, 2018
Ackermann, J. 1998
Alber, Anne 2008, 2010
Antel, Detlef 1994, 1998
Antel, Hans-Detlef 2000, 2006, 2008, 2012, 2014, 2016, 2018
Armbrust, Ralph 1998
Auner, Norbert 2000, 2004, 2006, 2008, 2010, 20122014
Bade, Heinz 1994, 1996
Bauer, Stefan 2012, 2014, 2018
Becker, Robert Karl 2016, 2018
Berendes, Eckart 2010, 2012
Berg, Gerd 2010, 2012
Bernreuter, Johannes 2016
Bertakis, Evangelos 2018
Bidlingmaier, Thomas 2010
Block, Hans-Dieter 2000
Bockholt, Andreas 2016
Boersting, Alfred 1994
Bramsiepe, Friedhelm 1994, 1998, 2000, 2006, 2008, 2012
Brantl, Stefan 1998, 2000
Braun, Rudolf 2008
Brenske, Michael 2012
Brumme, Johannes 1992, 1994, 1996
Candussio, Anton 2004
Conrad, Jürgen 2002
Damiotti, Dario 2008, 2010
Degel, Rolf 2014
Dembek, Joerg 2012, 2014
Deusser, Hans 1996, 1998
Diedrigkeit, Klaus 2012
Domingos, Valdiney 2014, 2016
Rimböck, Karl-Heinz 2016
Ehrich, Heike 1996, 1998
Fabry, Laszlo 2016
Fischer, Bernd 1992
Frey, Volker 1992
Frings, Albert 2000
Fritz, G. 1994
Froehling, Christian 2014
Furrer, Tanja 2018
Gamon, Norbert 1996, 1998, 2002
Garcia-Alonso, Nuria 2006
Gebauer, Klaus 1998, 2000
Goetze, Brigitte 2006, 2010, 2012, 2014, 2016
Goetze, Ulrich 1994
Gomon, Dmytro 2008, 2010
Gottschalk-Gaudig, Torsten 2016
Gross, Jochen 2000
Groth, Thomas 2008, 2012
Gruenleitner, Walter 2002, 2004, 2008, 2010, 2006
Hackl, Michaela 2016, 2018
Hager, Rudolf 1996
Harrmann, Martin 2000
Hecker, Erik 2014, 2016
Heinrichs, Arne 2002
Heitmann, Claus 2000
Hennecke, Dieter 2010
Hesse, Karl 1994, 2000, 2004, 2008
Heuer, Matthias 2014, 2016
Heyen, Erk Thorsten 2012, 2014, 2016
Hock, Sebastian 2006, 2010
Höcker, Harald 1998, 2000, 2006, 2008
Hoffmann, Volker 2006, 2008
Höfler, Andreas 2012, 2014, 2016, 2018
Holl, Sven 2002, 2004
Horn, Guido 2008

Horns, Udo 1994, 1996, 1998, 2000
Hübner, Dieter 2010
Ilies, Dinu Mihai 2016
Immenkeppel, Michael 2000
Kai, Petter 2008
Kalchauer, Wilfried 1994, 1998, 2000, 2002, 2004, 2006, 2008
Kalisch, Michael 2016
Kammergruber, Konrad 2004
Kappler, F.R. 1998
Kerat, Uwe 2010
Kessler, Dietmar 2012, 2014
Kiese, Siegfried 2006
Kirchner, Holger 2002
Klengel, Sascha 2012, 2014
Kletersteeg, Karin van de 2006, 2008, 2010, 2014, 2016, 2018
Kliem, Susanne 2002
Klingbeil, Christian 2008
Klingebiel, Uwe 2002, 2004, 2008
Knittel, Gerhard 1998, 2000
Koch, Michael 2016
Köhler, Bernd 2000
König, Sabine 2012, 2014
Köther-Becker, Sven 2008
Kroell, Michael 2010
Kroke, Edwin 2006
Krueger, Joerg 2006
Kuhnlein, Markus 2006, 2008, 2010
Kunert, Jan 2006, 2008, 2010
Kuzma, Mieczyslaw 1994
Lamhofer, Gerhart 1994, 1996
Langner, Bernd E. 1996
Lemke, Stefan 2016
Lersch, Peter 1994
Leye, Johann Christian 2016, 2018
Licht, Elke 1992, 1994
Lieske, Heiner 1992, 1994,1996, 1998, 2000, 2002, 2004, 2006
Linden, Wolfgang 2016
Lobreyer, Thomas 1996, 1998
Lorat, Helmut 1996
Lorey, Lars 2000
Lossin, Adalbert 1998
Lyubina, Julia 2018
Mäcker, Ralf 2000, 2016
Mai, Jan-Philipp 2010, 2012, 2014, 2016
Maier, Günther 2002
Mais, Bernard 2004, 2006, 2008
Mais, Bernhard 1996
Majumdar, Oliver 2016, 2018
Martin, Andreas 2006
Mautner, Konrad 2004
Mees, Rainer-Andreas 2004, 2010
Mleczko, Leslaw 2000
Mohsseni, Javad 2014, 2016
Möller, Hans Joachim 1998
Monkiewicz, Jarek 2004
Monkiewicz, Jaroslav 1998, 2008
Morgenstern, Dieter 1994
Mueller, Armin 2008, 2010, 2014
Mueller, Manfred 2000
Müller, Michael 2016
Müller, Steffen 2014
Neumeyer, Felix 2014
Nörthemann, Ralf 2016
Nürnberg, Peter 1994, 1996, 1998
Oeinck-Lanfer, Ilse-Cathrin 2010, 2012, 2014, 2016
Ohler, Tobias 2008
Okyere, Christiana 2016
Olek, Maciej 2008, 2010, 2012
Pachaly, Bernd 1992, 1994, 1996, 1998, 2016
Parous, Louis Charles 2014, 2016, 2018
Pätzold, Uwe 2002, 2006
Petkov, Peter 2016, 2018
Petter, Kai 2010
Pfeifer, Karl 1992
Pfolk, Erhard 1994, 1996
Popp, Alfred 2004
Ramirez-Weyershausen, Paula 2016, 2018
Rauch, Klaus 1992
Rauleder, Hartwig 1994
Reber, Stefan 2008, 2010
Rich, Jonathan 1998, 2000
Riepe, Stephan 2010
Rietig, Anja 2016
Ritz, Linda Luisa 2010
Rocher, Anja 2008
Roewer, Gerhard 1998, 2004
Rösch, Lutz 1992, 1996, 2000, 2002, 2004
Röver, Ingo 2000, 2002, 2004
Rüdinger, Christoph 2012
Ruff, Andreas 2006, 2008, 2010, 2012
Savvopoulos , Iordanis 2000
Schaaff, Friedrich 2012, 2014
Schartau, Wolfgang 1996
Schierlinger, Christian 2014
Schindler, Christopher 2010
Schmidbauer, Hubert 1998, 2000, 2002
Schmidt, Dietrich 1994, 1996, 2000
Schmidt, Jörg 2016
Schmidt, Jörg 2008, 2010, 2012, 2014, 2016, 2018
Schmidt, Klaus-Jörg 1992, 1994, 1996, 1998, 2000
Schmitz, Jürgen 1998, 2000, 2002
Schneider, Stefan 1996
Schork, Rheinhold 2004
Schulze, Friedrich-Wilhelm 2012
Schulze, Manfred 1992
Schumacher, Berent 1996
Schumann, Herbert 2000, 2002
Sofina, Natalia 2014, 2016, 2018
Sonnenschein, Raymund 2004, 2006, 2010
Spiess, Markus 1994, 1996, 1998, 2000, 2002
Sprung, Christoph 2008
Srebny, Hans-Günther 1992, 1994
Standke, Burkhard 2002
Stanjek, Volker 2010
Stantke, Peter 1996, 1998
Stary, Fridolin 2012
Steding, Frank 1996
Steiner, Matthias 1996, 1998, 2002, 2004, 2006, 2008
Steinhorst, Michael 1992
Stoerger, Reiner 2016, 2018
Straussberger, Herbert 1996
Sundermeyer, Wolfgang 1992, 2000, 2002
Tacke, Reinhold 2010
Tamme, Gudrun 2000
Tillmann, Jan 2014
Topp, Klaus-Dieter 2014
Traunspurger, Gerhard 2018
Troll, Harald 2006
Valenti, Cathrin 2010
VanDongeren, Hans 2004
Vendt, Bernd 2000

Wagner, Gebhard 1992, 1994, 1998, 2000
Walter, Holger 1998
Wardenga, Ulf 1992
Weber, Frank 2012, 2014
Weber, Rainer 1998, 2000
Weidner, Richard 2000, 2004
Weissberger, Felix 2012
Wenzel, Peter 2012, 2014
Wildemann, Adolf 1994, 1996, 1998, 2000, 2002, 2004, 2006, 2008, 2010, 2012
Wilms, Axel 1996
Ziche, Wolfgang 1998

Hong Kong

Alary, Thierry 2004

Iceland

Bjorn, Helgi 2014
Björnsson, Hákon 2014
Dembek, Jörg 2016, 2018
Fenger, John 2014
Gardarsson, Magnus 2014
Gargarsson, Magnus 2012
Gudnason, Edvard G 2012
Gunnarsson, Jökull 2016
Jonsdottir, Stella Marta 2012
Saadieh, Raghed 2016
Thorhallsson, Helgi 2016
Viktorsson, Hafsteinn 2016
Wenzel, Peter 2016

India

Bachal, Sanjiv 1998
Badani, Manish 2002
Chandola, Pankij 1998
Padubidri, Sushama 1994, 1996, 1998, 2000, 2004, 2008
Paman, Ajeet S. 2000
Paulmer, Robert 1998
Samala, Murali 1998

Italy

Angelis, Daniele de' 2000
Broggi, Andrea 2016, 2018
Cerofolini, Gianfranco 1996
Damiotti, Dario 2002
Foglia, Foglia Gianmichele 2012
Marangoni, Giovanni 2006
Osvaldo, Brioni 2012
Pasolli, Claudio 2008, 2010
Scandola, Pietro 2008
Smagghe, Alain 2012

Japan

Abe, Mitsuo 1996, 1998
Arai, Fumio 1998
Araki, Isamu 2002
Aramata, Mikio 1998, 2000, 2002, 2004, 2006, 2008, 2010
Arita, Yoji 2010
Bolzer, Walter 1996, 1998, 2000
Ehara, Yoshitaka 2018
E, Piljoon 2012
Grandum, Svein 2008
Gunji, Toru 1996
Hanaoka, Hiroaki 1998
Harada, Katsuyoshi 2002, 2008, 2010
Hasegawa, Takao 1994
Iida, Katsunori 2010
Ikeda, Tatsuya 2004
Inoue, Yuji 2000
Kambara, Makoto 2010, 2012
Kato, Yoshiei 2016
Kirii, Seiichi 1992
Kishimoto, Hiroyuki 2002, 2004,
Kohno, Hiroshi 1994
Komada, Norikazu 2016
Kondo, Katsumi 1998
Kusama, Shin-ichi 2002
MA, Xiaodong 2012
Miyata, Masahiro 1992, 1994, 1996
Morita, Kazuki 2008, 2010, 2012, 2014, 2016
Muraida, Akio 2004
Murakami, Kazushiro 1996
Nakanishi, Tetsuo 1996
Nakano, Mamoru 2004
Nakayasu, Akio 2016
Nishikawa, Mitsuhiro 1996, 1998
Ochiai, Mitsuji 1992
Oda, Hiroyuki 1992
Ohtani, Jiroh 1998, 2000, 2002
Okamoto, Masaki 1996
Ono, Yoshio 1994, 1998
Otani, Eiichi 2000
Sakaguchi, Hiroki 2014
Sakai, Sho 1998
Sakai, Tetsuo 2014
Samori, Hirosi 1996
Sandberg, Bjorn 2008
Sato, Yuzuro 2006, 2008, 2010
Shimada, Shiro 2006
Shimizu, Hiroshi 1992, 1994, 1996, 1998, 2000, 2002
Sugiura, Kengu 2004
Takahashi, Takashi 2000
Tanaka, Shoichi 1992
Terada, Ikuhiro 1998
Tsumura, Hiroshi 1994
Uesugi, Nobuyuki 2004
Umehara, Mitsuiro 1994
Wakamatsu, Satoru 1998
Wang, Ye 2014
Yamashita, Toru 1996
Yoshizawa, Hironori 2012, 2014
You, Yuliu 2016

Kazakhstan

Zhandayev, Nurlan Makataevich 2014

Mexico

Aguilera, Alberto F. 1992, 1994, 2000, 2002, 2004, 2010, 2012
Cervantes, Jorge 1992, 1994, 1996, 1998, 2000, 2002, 2004, 2010
Plascencia, Gabriel Plascencia 2010

New Zealand

Harris, Graeme 2004
Matheson, Andy 2002
Simpson, Andrew Vincent 2004

Norway

Aabakken, Skjalg 2014
Aasly, Kurt 2006, 2016
Abrahamsen, Thorstein 2010

Andersen, Geir 2000, 2002, 2004, 2012
Andersen, Vegar 2012
Andresen, Birger 1996, 1998, 2000, 2002, 2004, 2006, 2008, 2010, 2012, 2014, 2016, 2018
Backström Iversen, Cecilie 2010
Bakke, Per 2008
Berget, Kjell Håkon 2012, 2014
Bergkvist, Anders 2002, 2004
Bjørnstad, Erlend Lunnan 2018
Bjørseth, Alf 1998, 2006
Breidenthal, Mark 2010
Brekken, Henrik 1994, 1996, 1998, 2000, 2002, 2004, 2006, 2008, 2010, 2012, 2014
Brevik, Sigbjørn 2002, 2004
Buseth, Torfinn 1994, 1998, 2000
Carlsson, Per 2016
Ceccaroli, Bruno 1992, 1994, 1996, 1998, 2006, 2008, 2012, 2014, 2016, 2018
Christiansen, Glenn Scott 2014
Christiansen, Stein 2014, 2018
Ciftja, Arjan 2006, 2010
Delbeck, Håkon 2000
Dolme, Marit 2018
Dybwad, Nils 2000, 2002, 2004, 2008, 2010, 2012 2014, 2016, 2018
Eckhoff, Rolf K. 1996
Egeberg, Per Kristian 2000
Eidet, Trygve 2018
Eik -Nes, Bodil 2010
Eikeland, Inger Johanne 1996
Eikevik, Tine 2010
Einarsson, Gudmundur 1996, 1998
Ellingsen, Eivind 2016
Enger, Ole 1998
Engh, Thorvald A. 2006
Eulenberger, Ronald 2014
Faaness, Bente Merete 2012
Filtvedt, Werner O. 2010, 2012, 2014, 2016
Foosnæs, Trygve 2004, 2006, 2008
Forwald, Karl R. 1992, 2012, 2014
Fossheim, Rune 1996
Galler, Patrick 2014
Galteland, Inge 1994
Garcia , Jorge 2012, 2014
Gausemel, Håvar 2008, 2010
Gjestland, Haavard 2008
Gløkner, Ronny 2008
Gouttebroze, Sylvain 2016
Gudnadottir, Harpa 2014, 2016, 2018
Gullbrekken, Øystein 2014
Håland, Kjell 2012
Halland, Torbjørn 2008, 2010
Halvorsen, Gunnar 2008, 2010
Hansen, Henry 1994, 1996, 1998, 2000, 2002, 2006, 2008, 2010, 2012, 2014
Hårstad, Tor Inge 1998
Haug, Alf Tore 2008, 2016
Haugesten, Lise Helmine 2016
Haugland, Vidar 2010
Haverhals, Arjan 2004
Heide, Johan 2000, 2016
Hellsten, Thomas 2014, 2016
Hildal, Kjetil 2000
Hoel, Jan-Otto 1996,1998, 2000, 2002, 2012, 2014
Holås, Arnfinn 2004
Holta, Halvor 1994, 1996
Jagtøyen, Anne 1992, 1994, 1996, 1998, 2000, 2002, 2004, 2006
Jakobsson, Lars Klemet 2012
Jayakumari, Sethulakshmy 2016, 2018
Jensen, Ragnhild 2018
Jusnes, Karin Fjeldstad 2016, 2018
Katylevskaya, Ludmila 2008, 2010, 2012
Kawamoto, Ryosuke 2016
Kero, Ida Teresia 2016
Klette, Hallgeir 2012, 2014, 2016
Krystad, Egil 2014
Ksiazek, Michal 2014, 2016
Kuhnlein, Markus 2016
Kvande, Rannveig 2010
Lamy, Raphael 2016
Larsen, Karin E. 1996
Li, Fei 2016
Lindstad, Lars H. 2018
Lindstad, Tor 1992, 1994, 2008
Ljungquist, Dag 2008
Lohne, Otto 2008
Løkke-Øwre, Erik 2000, 2002, 2004
Lorentsen, Kolbjørn 2002, 2008
Lunde, Torgeir 2008
Meland, Jon A. 2010
Mokkelbost, Tommy 2018
Møll, Maria Førde 2010, 2012, 2014
Møller, Sverre 1996, 1998, 2006
Mongstad, Trygve 2016
Moor, Jürg 2018
Mørk, Knut 2016
Morkemo, Roy 2000
Motzfeldt, Ketil 2004, 2008
Mykland, Kjell-Åge 1998, 2000
Myklebust, Hilde 2008, 2010, 2018
Myrhaug, Edin Henrik 2002, 2012
Nilsson, Camilla 2008
Nordstrom, Kjell 2008, 2012
Nygaard, Lars 1992, 1994, 1996, 1998, 2000, 2002, 2004, 2006, 2008, 2014, 2016
Nygård, Paul 2012
Nyhus, Jørgen 2010
Odden, Jan Ove 2000, 2002, 2008
Ødegård, Cecilie 2004, 2006, 2008
Olafsen Sjåstad, Anja 2008, 2010
Olsen, Erlend 2018
Ossenkamp, Gabriel 2012
Ott, Emmanuelle 2008, 2010
Ovesen, Bjørnar 2016, 2018
Øvrelid, Eivind J. 2006, 2008, 2016
Øye, Harald A. 1992, 1994, 1996, 1998, 2000, 2002, 2004, 2006, 2008, 2010, 2012, 2014, 2016
Page, Ingrid Gamst 2016, 2018
Pedersen, Bjørnar 2016
Preston, Thomas 2018
Raaness, Ola S. 1992, 1994, 2000, 2006, 2008
Rasch-Olsen, Preben 2008
Ringdalen, Eli 2014, 2016, 2018
Røe, Torbjørn 2000, 2002, 2004, 2012, 2014, 2016, 2018
Rong, Harry 1992,1994, 1996, 1998, 2000, 2002, 2004, 2006, 2008, 2010, 2012, 2014, 2016, 2018
Rosenkilde, Christian 2008
Rosenqvist, Terkel 2004
Roszinski, Jan Olaf 2016, 2018
Sæterstad, Trond 2014
Sæther, Sverre 2004
Sadieh, Raghed 2018
Safarian, Jafar 2010, 2014, 2018
Samset, Oddgeir 2008, 2010
Samstad, Odd 1998, 2000

Sandberg, Bjørn 2006, 2010, 2012
Saugestad, Bjørn 2014
Schei, Anders 1992
Schüssler, Gunnar 1992, 1994, 1998, 2000, 2002, 2004, 2006, 2008, 2010, 2014
Sindland, Caroline 2018
Skjølberg, Einar Martin 2002, 2004, 2008
Søiland, Anne-Karin 2014
Solberg, Birger 1994, 1996
Sommerfeldt, Hanne-Marthe 2010
Sørensen, Sverre 2014
Sørheim, Håvard 1992, 1994, 1996, 1998, 2000
Sørli, Øyvind 1994, 1996
Sørvik, Arvid Inge 1996, 2010, 2014
Søvik, Asbjørn 1998
Stanghelle, Helge 2004
Staubo, Bjørn 1992, 1994, 1996
Stubhaug, Elin 2012
Sundsli, Kjell 1994, 1996
Svanem, Johan Pääaho 2016
Sveine, Arne 1992
Syran, Christopher 2012, 2014, 2016, 2018
Syran, Lasse 2012
Talle, Steinar 2010
Tangstad, Merete 2014, 2016, 2018
Tathgar, Harsharn 2008, 2010
Tranell, Gabriella 2016, 2018
Tronstad, Ragnar 2012
Tuset, Johan Kr. 1992, 1994, 1996, 1998, 2000, 2002, 2004, 2006
Tvedt, Øyvind 2000
Tveit, Halvard 1998, 2000, 2002, 2004, 2008, 2010, 2012, 2014, 2016, 2018
Ulriksen, Arve 2012
Vaksdal, Ragnar 1998, 2000
Venvik, Hilde J. 2018
Vik, Jan-Børre 2012
Vitsø, Herulf E. 1998, 2000, 2002, 2004, 2006, 2008, 2012, 2014
Voll, Morten Magnus 2014
Wærnes, Aud Nina 2010, 2012, 2014, 2016, 2018
Werge-Olsen, Arne 2016
Werner, Tobias Mohn 2018
Westengen, Håkon 2008
Windfeldt, Magnus Kyrre 2018
Wyller, Guro Marie 2016, 2018

Portugal

Chen, Jinxiang 2018

Poland

Brandsvoll, Ralph E. 2016
Marciniec, Bogdan 1992
Nielsen , Alex 2012, 2014, 2016, 2018
Polkowski, Wojciech 2018
Prezekop, Robert, 2016
Smyczek, Piotr Benedykt 2018
Wisniewski , Marek 2012, 2014, 2016, 2018

Russia

Anatoliy, Matveev 2016
Arkhipov, Mikhail 2008
Babich, Yuriy 2006
Bezushenko, Andrey 2012
Borisov, Igor 2008
Chemezov, Oleg 2010
Chuvasheva, Olga 2004
Dushanin, Boris M. 1994
Endovin, Yury P. 1996, 1998
Fedossenko, Viatcheslav 2000, 2002
Kibkalo, Maria 1994
Kim, Stanislav 2008
Kokhanovski, Sergei 2000
Kubar, Dmitry S 2016
Kuzmina, Irina 2008
Nemchinova, Nina 2008
Nepomnyaschikh, Alexander 2002, 2004
Novikov, Alexey 2004
Pan'kov, Andrey 2006
Pererva, O.V. 1996, 1998
Pereveznyuk, Ludmila 2016, 2018
Petrova, Tatiana 2006
Pirogova, Anna 2002
Poliak, Victor 2000
Polivanov, A.N. 1998
Sadykov, Ildar 2004
Sharonov, Juriy 2000
Skornyakov, Alexander 2006
Suponenko, Alexander 2016
Voluinski, Alexander 2000
Yaremenko , Natalia 2008
Zolotaiko, Alexander 2000
Zolotayko, Alexandr 2004

Saudi Arabia

Khokhar, Abdul Aleem 2010

Slovakia

Jablonski, Andrzej 2016

South Africa

Barker, Ian J. 2002, 2006
Barrett, William 1994
Bennie, John P.W. 1994, 1996
Brown, Michael H. 1994, 1996, 1998
Giese, Mark 2008
Lagendijk, Herman 2016
Mahony, Charles 1998, 2002
McDougall, Isobel Tenova 2014
Oertel, Chris 2018
Strydom, Johan C. 1996, 1998
Veldsman, Ben 2012

South Korea

Ahn, Gui Ryong 2012
Cho, Ayoun 2014
Cho, Gyu-jong 2008
Choi, Guen 2008
Choi, Jae-Won 2006
Choi, Seong Ho 2012
Choi, Won Choon 2010, 2012
Eom, Tae Jun 2012
Han, Joo Hee 2012
Huh, Weon-Hoe 2000
Jang, G.H. 2008
Jeon, Jiwon 2010
Jun, Yoon-Soo 2010
Jun, Youn-Soo 1994, 2000
Jung, Il Nam 1994, 2002
Kang, Kyoung Hoon 2006
Kim, Byoung Ki 2012
Kim, Gil Ho Hanwha 2014
Kim, Hee Young 2010
Kim, Hyun Woo 2002

Kim, Jongsoo 2012
Kim, JunHo 2010
Kim, Myung Ho 2006
Kim, SungHoon 2006
Konmani, Santi 2010
Lee, Chang Bae 2006
Lee, Dohyun 2010
Lee, Hwa-Sung 1996
Lee, Jungwoo 2010
Lee, Sang-Kyu 2010
Lee, Woohyun 2006
Lee, Wook Ki 2004, 2006
Moon, Sin Chul 2006
Park, Jo Moon 2008
Park, Jumoon 2010
Park, Soo Whan 2008, 2010
Rim, Jeong Oan 2010
Sangho , Choi 2008
Seo , Jin-Seok 2010
Seo, Hyun Sik 2012
Seok, Seongho 2010
Shim, Kyung Bo 2010
Sohn, Jung Min 2008
Sung, Changwan 2008
Yang, O-Bong 2010
Yeon, Seung Ho 2012

Spain

Bermudez, Alfredo 2000
Bullon Camarasa, Javier 2014, 2016, 2018
Bullon, Javier 1994, 1996, 2000, 2002, 2008, 2012
Canizo, Carlos del 2014
Coso, Conzalo del 2008
de Canizo, Carlos 2012
del Coso, Gonzalo 2010
Gallego, Victor 1994,1996
Gorny, Zbigniew 1994, 1996, 1998, 2000
Hoffman, Volker 2010
Larrea, Pedro 2016
Lelièvre, Jean-Francois 2008
Mendez Gimenez, Laura 2014
Mendez, Laura 2006, 2008
Meseguer, Francisco 2012
Miguez Novoa, Jose Manuel 2018
More, Anton 2002, 2004
Oller, Santiago 2002, 2004, 2012, 2014
Ordás Babía, Ramón 2014
Ordas, Ramon 2010, 2012, 2016
Ramos Cabal, Alba 2012, 2018
Ramos, Alba 2014
Rodriguez, Araceli 2006, 2008, 2010
Rodriquez, Hugo 2008
Tellaeche Palomar, Oscar 2014
Tellaeche, Oscar 2002, 2004, 2012

Sweden

Andreasson, Mikael E.Å. 2018
Fagerberg, Magnus 2016
Glaser, Julius 2006, 2008, 2010
Nordström, Kjell 2016
Sylvén, Peter 1998, 2000, 2002
Toth, Imre 2006
Trägårdh, Johan 2016
Trägårdh, Martin 2014, 2016

Switzerland

Borisov, Roman 2008, 2010
Fischer, Jean-Claude 2014
Hattangadi, Arun 2008
Hefti, Franz 2016
Kaeppeler, Johannes 2016
Kallfelz, Peter L. 1994, 1996, 1998, 2000, 2002, 2004, 2006 2008, 2010, 2012
Keller, Hans-Peter 2002
Selinger, Adrian 2014
Serra, C. 2002
Suter, Roland 2006
Tattersall, Alex 2002

Taiwan

Chang, Wen Hao 2012
Lin, Jason 2012

The Netherlands

Gutjahr, Astrid 2000
Sanders, Doron 2010, 2012, 2014
Stern, Yaron 2014, 2016
Takayama, Shigeyuki 2006
Tanaka, Toshiharu 2000
van den Ven, Philippe 2012
van der Stap, Pablo 2014
van Noort, Wilhelms 2012
van Noort, Willem 2014
Veltkamp, A. C. 2010

Ukraine

Benderskiy, Vasiliy V. 2004
Buchovska, Iryna 2010
Lyaskovskyi, Oleksandr 2012
Shevchenko, Yu. N. 1996
Yandyuk, Andrii 2010

United Kingdom

Allsop, Mark 2008
Baron, Michael 1992, 1994, 2000
Bentley, David 2004, 2006, 2008
Bettie, Cameron P. 1998
Bowrey, Malcolm 1998
Brookes, Karen 1994, 1996
Egen, Gregg 2000, 2002
Fulford, David J. 1996, 1998
Jones, Andrew 1996
Joyner, Richard W. 1994
Kerbey, Mark 2000
Kirkwood, Tony 2002
Kohane, Joseph P. 1998, 2000
Madavo, Fidelis 1994
Mead, Jonathan 1996
Neely, John D. 1996
Siddiqui, M. Rafiq H. 1992
Timms, Peter 1992
Welborn, Patrick 1996, 1998
Tatlock, Gordon J. 1996

USA

Able, Brett 1998
Anderson, Richard 1996
Ausikaitis, Joseph 2012
Bablin, John M. 2000, 2002
Barr, Mark K 2000, 2002
Barton, Thomas J. 1998
Boardman, Timothy R. 1998
Boardwine, Carl E. 1992, 1996, 1998, 2000
Boddner, Mark 1998

Bowes, Christopher 2016
Breneman, William 1996
Brimhall, Daniel 1998, 2000, 2002
Brown, Larry C. 1996, 1998, 2002. 2004. 2008
Buck, Wayne M. 2000
Carberry, John 1994, 2012, 2016, 2018
Chudzinski, Peter J. 1994, 1996
Coleman, Larry 2012, 2014, 2016
Colomb, Matthias Andre 2018
Crawford, Alan Carson 1996, 1998, 2000, 2002, 2006, 2008, 2014, 2016, 2018
Daher, Nelson 1994
Dassel, Mark W. 2016
de Linde, Jørn P. 1994, 1996, 1998, 2000, 2002, 2006, 2008, 2010, 2012, 2014, 2016, 2018
Dery, Alain 2012
Dosaj, Vishu 1992, 1994, 1996, 2000, 2002, 2004, 2006, 2008, 2010, 2012, 2014
Dray, Larry 2008, 2010
Duncan, Kirk 2000
Falconer, John L. 1992, 1994
Finn, Walter W. 2004
Fontana, Robert 1994
Freeburne, Steven K. 1996, 1998
Gaal, Sean 2014, 2016, 2018
Gadre, Sarang 2010
Galteland, Inge 1996
Green, Jonathan 2008
Griffith, Chuck 2012
Gross, Dave 2002, 2004
Hall, Charles A. 1996
Halm, Roland 1992, 1994
Hanna, Krista 2012
Harder, Patrick 2002, 2010
Haworth, Joseph D. 2002
Haynes, Marcia 2000, 2002
Hazeltine, Bruce 2012
Herron, William 2010
Holsclaw, Brian 2014, 2016
Houser, Daniel E. 1992
Jarrett, Eugene 1998
Jordao, Marco 2000, 2002
Jurisch, Randall 2012
Kaiser, Robert 1994, 1998
Kaiser, Robert H. 2002
Kamei, Takeshi 2012
Kanner, Bernard 2006
Kennedy, Cristopher 1996
Kern, Thomas F. 1998, 2000, 2002
King, Thomas 1994
Klar, Erhard 1992, 1994, 1996
Klatt, Kim 1998, 2000, 2002
Klotz, James A. 1998
Kohane, Joseph P. 1996
Komitsky, Frank 1998
Kopp, Steven 2000
Kremer, Paul W. 1998, 2002
Kremer, Vladimir 1998
Kroupa, Mike 2002
Kuivila, Charles S. 1996, 1998
Kurin, Larry J. 2004
Ladner, Steven 2018
Lage, Braulio M. 1996, 1998, 2000, 2002, 2016
Leicht, James T. 1996
Lewis, Kenrick 2002, 2006
Lewis, Kenrick M. 1994, 1996, 1998, 2000
Lewis, Larry 1998, 2000, 2002
Lynch, David 2002, 2004
Mackey, Thomas 2004
Mackey, Thomas Michael 2016
Marion, Paul J. 1996, 1998, 2000, 2002, 2004, 2006, 2014
Maxwell, Josh 2000
May, James B. 1996, 1998, 2000, 2004
McDermott, John B. 1998
Mendicino, Frank D. 1998, 2000
Miller, Matthew Joseph 2014
Moore, Michael P. 2008
Murphy, Thomas 2000
Murphy, Thomas M. 2004
Myers, Katrina 2008
Neely, John 2000
Negrych, John A. 1996, 1998
Nelson, Kenneth E. 1996
Nettles, Bryan 2012, 2018
Nguyen, Binh T. 2006, 2008, 2010
Niswonger, D. Scott 2000, 2002
Noglows, William P. 1996
Nordstrom, Kjell 2000, 2002
Olakangil, Job 2000
Oleson, John 1992, 1998
Ollmann, James 1998
Ott, Emmanuelle 2012
Pannell, Keith H. 2004
Perkins, J. Marlin 1998, 2016
Perkins, Marlin 2000, 2010, 2012
Petras, James 1996
Pillai, Unni 2006
Piolpre, Jean Philippe 2008
Preuth, Joseph 2000
Prokai, Bela 2002
Rao Gangaraju, Venkat 2010
Ray, C. Tom 1996
Rethwisch, David G. 1996, 2000, 2002, 2006
Ritscher, James S. 1998
Ritzer, Alan 1992, 1994
Rochow, Eugene 1994, 1998
Rogers, Kimberly 2016
Ryan, Patrick 1998, 2000, 2002, 2008
Sanderson, James L. 1998, 2000, 2002
Schilling, Jr., Curtis L. 1998
Searcy, Mike 2008
Smith, Kenneth D. 1996
Sobeck, Dan 2010
Srinivasan, Lakshminara 2004
Stafford, Craig 2002
Strongin, Daniel R. 1998
Tabit, George E. 1992, 1996, 1998, 2000, 2002, 2004, 2008
Tatterson, Robert L. 1994
Tetrick, Stephen 1992
Thompson, Tony 2010
Torbic, John A. 1996, 1998
Triebell, Edward 2012
van Dongeren, Hans 2002
Vitcavage, Jack 1992, 1994
Vogelaar, Glen 1994, 1996, 1998, 2000
Ward, William 2000
Ward, William J. 1996, 1998
Wengrovius, Jeffrey 2010
Wenske, James R. 1996
West, Robert 1994
Whiteley, Darrel 2000
Wilding, Jr., Oliver K. 1994, 1996
Wilkerson, Brock E. 1996
Wilson, Matthew Paul 2016

Wineland, Jon	2002, 2004, 2006, 2008
Wolf, Richard	2012
Wood, Larry H.	2000, 2002, 2004
Wright, Antony	1998
Xue, Genqiang	2016
Yilmaz, Sefa	2000
Young, Martin D.	1994, 1996